WOODHEAD PUBLISHING IN MATERIALS

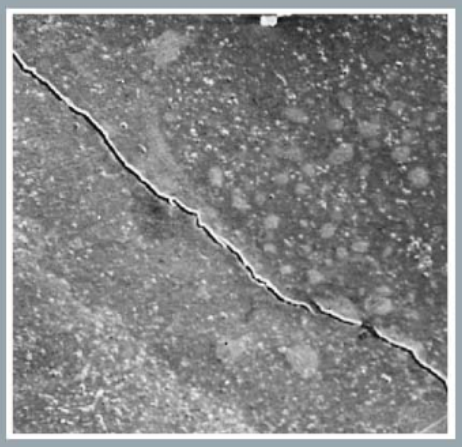

Weld cracking in ferrous alloys

Edited by Raman Singh

CRC

WP

Weld cracking in ferrous alloys

Related titles:

Cumulative damage of welded joints
(ISBN 978-1-85573-938-3)
Fatigue is a mechanism of failure that involves the formation of cracks under the action of different stresses. Stresses can be a wide range of magnitudes. To avoid fatigue it is essential to recognise at the design stage that the loading is such that fatigue may be a possibility and to design the structure with inherent fatigue strength. However, fatigue strength is not a constant material property. It may be assessed by fracture mechanics, but such characteristics are based on quantitative analysis and mere assumption. Fatigue cracks are exceedingly difficult to see, particularly in the early stages of crack growth. Cracks can progress to a significant extent before they are discovered. This book is primarily concerned with fatigue under variable amplitude loading, unlike most tests performed under constant loads.

Processes and mechanisms of welding residual stress and distortion
(ISBN 978-1-85573-771-6)
This volume outlines theoretical treatments on heat transfer, solid mechanics and materials behaviour that are essential for understanding and determining the welding residual stress and distortion. The approaches for computational methods and analysis methodology are described so that even non-specialists can follow them. There are chapters discussing the various techniques for control and mitigation of residual stress and distortion. Residual stress and distortion results for various typical welded structures are also provided. The second half of the book looks at case studies and practical solutions, and provides insights into the techniques, challenges, limitations and future trends of each application. The book will be useful for advanced analysis of the subject and provides examples and practical solutions for welding engineers.

Fatigue assessment of welded joints by local approaches Second edition
(ISBN 978-1-85573-948-2)
Local approaches to fatigue assessment are used to predict the structural durability of welded joints, to optimise their design and to evaluate unforeseen joint failures. This completely reworked second edition of a standard work provides a systematic survey of the principles and practical applications of the various methods. It covers the hot spot structural stress approach to fatigue in general, the notch stress and notch strain approach to crack initiation and the fracture mechanics approach to crack propagation. Seam-welded and spot-welded joints in structural steels and aluminium alloys are also considered.

Details of these and other Woodhead Publishing materials books can be obtained by:

- visiting our web site at www.woodheadpublishing.com
- contacting Customer Services (e-mail: sales@woodhead-publishing.com; fax: +44 (0) 1223 893694; tel: +44 (0) 1223 891358 ext. 130; address: Woodhead Publishing Limited, Abington Hall, Granta Park, Great Abington, Cambridge CB21 6AH, England)

If you would like to receive information on forthcoming titles, please send your address details to: Francis Dodds (address, tel. and fax as above; e-mail: francis.dodds@woodheadpublishing.com). Please confirm which subject areas you are interested in.

Weld cracking in ferrous alloys

Edited by

Raman Singh

CRC Press
Boca Raton Boston New York Washington, DC

WOODHEAD PUBLISHING LIMITED
Cambridge New Delhi

Published by Woodhead Publishing Limited, Abington Hall, Granta Park,
Great Abington, Cambridge CB21 6AH, England
www.woodheadpublishing.com

Woodhead Publishing India Pvt Ltd, G-2, Vardaan House, 7/28 Ansari Road, Daryaganj,
New Delhi – 110002, India

Published in North America by CRC Press LLC, 6000 Broken Sound Parkway, NW,
Suite 300, Boca Raton, FL 33487, USA

First published 2009, Woodhead Publishing Limited and CRC Press LLC

British Library Cataloguing in Publication Data
A catalogue record for this book is available from the British Library.

Library of Congress Cataloging in Publication Data
A catalog record for this book is available from the Library of Congress.

Woodhead Publishing ISBN 978-1-84569-300-8 (book)
Woodhead Publishing ISBN 978-1-84569-545-3 (e-book)
CRC Press ISBN 978-1-4200-7963-0
CRC Press order number WP7963

The publishers' policy is to use permanent paper from mills that operate a sustainable forestry policy, and which has been manufactured from pulp which is processed using acid-free and elemental chlorine-free practices. Furthermore, the publishers ensure that the text paper and cover board used have met acceptable environmental accreditation standards.

Project managed by Macfarlane Book Production Services, Dunstable, Bedfordshire, England (e-mail: macfarl@aol.com)
Printed by TJ International Limited, Padstow, Cornwall, England
Typeset by Replika Press Pvt Ltd, India

Contents

Contributor contact details *xi*

Introduction *xv*

RK Singh, *Monash University, Australia*

Part I Welding technology and design to prevent weld cracking

1 Selection of weld-crack resistant stainless steels 3

JN DuPont, *Lehigh University, USA*

1.1 Introduction 3
1.2 Types of stainless steels 3
1.3 Cracking mechanisms in stainless steel welds 17
1.4 Preventing weld cracking 24
1.5 References 30
1.6 Appendix of terms 32

2 Robust welding technologies for ferrous alloys 34

AK Bhaduri, SK Albert and B Raj, *Indira Gandhi Centre for Atomic Research, India*

2.1 Introduction 34
2.2 Weldability of austenitic stainless and other steels 35
2.3 Weldability evaluation of austenitic stainless steels 39
2.4 Weldability of modified chromium–molybdenum ferritic steels 47
2.5 Dissimilar metal welding 55
2.6 Improving welding in practice: development of special purpose electrodes 73
2.7 Hardfacing of austenitic stainless steel components 78
2.8 Conclusions 92
2.9 References 94

3 Design against cracking in ferrous weldments 96

P Chellapandi and SC Chetal, *Indira Gandhi Centre for Atomic Research, India*

3.1 Introduction 96
3.2 Weld design rules for pressure vessel components (ASME section VIII division 1) 97
3.3 Weld design rules for nuclear power plant pressure vessels (ASME section III division 1) 102
3.4 Design rules for welds as per RCC-MR 113
3.5 Design of welds with crack-like defects 115
3.6 Effect of mismatch creep properties on weld design 122
3.7 Conclusions 125
3.8 References 125

4 A discussion of the current procedures for design of welds against fatigue 127

JWH Price, *Monash University, Australia*

4.1 Introduction 127
4.2 Weld failures and design problems 127
4.3 Fatigue design concepts and their influence 133
4.4 Manufacturing codes: acceptable sizes of surface cracks caused by welding 134
4.5 Assessing the strength of welds 135
4.6 Current approaches to design against fatigue cracking at welds 135
4.7 Case studies 142
4.8 Discussion 147
4.9 Conclusions 148
4.10 References 148

Part II Weld crack behaviour, evaluation and repair

5 Mechanical behaviour of stainless steel, ferritic steel welds and weld joints 153

K Bhanu Sankara Rao, MD Mathew, K Laha, R Sandhya and B Raj, *Indira Gandhi Centre for Atomic Research, India*

5.1 Introduction 153
5.2 Fatigue behaviour of stainless steel weldments 155
5.3 Creep–fatigue interaction behaviour of stainless steel welds and weld joints 160
5.4 Creep behaviour of austenitic stainless steel welds 166

5.5	Creep rupture strength of ferritic steel weld joints	174
5.6	Creep of dissimilar weld joints	181
5.7	Acknowledgements	182
5.8	References	182
6	Fracture toughness in the design and operation of ferrous weldments	185
	SK Ray and G Sasikala, *Indira Gandhi Centre for Atomic Research, India*	
6.1	Introduction: the importance of fracture properties	185
6.2	Fracture properties for materials qualification	186
6.3	Dynamic and quasi-static fracture properties	187
6.4	Metallurgical inhomogeneities	192
6.5	Strength mismatch and residual stress	193
6.6	Characterisation of fracture properties: dynamic fracture properties	197
6.7	Quasi-static fracture toughness	205
6.8	Subcritical crack growth characterisation of welds	212
6.9	Conclusions	215
6.10	References	216
7	Testing and evaluation of weld cracking in ferrous alloys	222
	B Raj, T Jayakumar and P Palanichamy, *Indira Gandhi Centre for Atomic Research, India*	
7.1	Introduction	222
7.2	Quality assurance and qualifications	224
7.3	Testing and evaluation of welds	229
7.4	Non-destructive tests	230
7.5	Semi-destructive testing: metallography	258
7.6	Hardness testing	259
7.7	Destructive testing	264
7.8	Testing methods for corrosion assessment	271
7.9	Measurement of residual stresses in weldments	277
7.10	On-line weld monitoring and intelligent welding	294
7.11	Welding codes and standards	302
7.12	Conclusions	305
7.13	Acknowledgements	305
7.14	References and further reading	305
	Appendix 7.1: compilation of standards on weld testing	307
	Appendix 7.2: ASTM material specifications for welded components with NDT requirements	310

Appendix 7.3: standards for semi-destructive and destructive techniques 311

8 Lessons learnt from failures in ferrous weldments 314

B Raj, KV Kasiviswanathan, N Raghu, NG Muralidharan and V Karthik, *Indira Gandhi Centre for Atomic Research, India*

8.1 Introduction 314
8.2 Welding processes for ferrous alloys 315
8.3 Major failure mechanisms associated with ferrous weldments 317
8.4 Reducing failures in weldments 322
8.5 Case studies in failure investigation 328
8.6 References 351

9 Cracking in high performance superduplex stainless steel welds 353

A Comer, *Dublin City University, Ireland*

9.1 Introduction 353
9.2 Microstructure of superduplex stainless steel welds 354
9.3 Toughness and corrosion resistance of superduplex stainless steel welds 361
9.4 Hydrogen embrittlement 364
9.5 Corrosion fatigue cracking of stainless steel welds 366
9.6 Crack propagation in a benign environment 372
9.7 Crack propagation in seawater under high electrochemical potential 378
9.8 Crack propagation in seawater under negative imposed electrochemical potential 381
9.9 Future trends 387
9.10 Sources of further information and advice 388
9.11 References 389

10 Weld metal cracking in cellulosic girth welds of pipelines 393

D Dunne, *University of Wollongong, Australia* and D Nolan, *BlueScopeSteel, Australia*

10.1 Introduction 393
10.2 Keyhole welding 394
10.3 Cellulosic welding 395
10.4 Pipeline construction 396
10.5 Hollow bead defect 398

10.6 Solidification cracking 406
10.7 Cold cracking 421
10.8 Conclusions 428
10.9 Acknowledgements 430
10.10 References 430

11 Repair of weld cracks 433

R Ibrahim, *Monash University, Australia*

11.1 Introduction 433
11.2 Weld defects 434
11.3 Weld cracks 434
11.4 Crack locations 436
11.5 Other welding defects 440
11.6 Resultant welding process microstructures 441
11.7 Repair welding 444
11.8 Welding heat treatment 445
11.9 Techniques for tempering and grain refinement of the HAZ without PWHT 447
11.10 Conclusions 455
11.11 References 456

12 Measurement of residual stresses in weld repairs in steels 459

J Price, *Monash University, Australia,* A M Paradowska, *Rutherford Appleton Laboratory, UK* and T Finlayson, *University of Melbourne, Australia*

12.1 Introduction 459
12.2 Experimental procedure 461
12.3 Residual stress measurement 462
12.4 Residual stress estimation 465
12.5 Results and discussion 468
12.6 Conclusions 472
12.7 Acknowledgements 473
12.8 References 473

Part III Environment-assisted weld cracking

13 Corrosion issues in ferrous weldments 477

RK Dayal, H Shaikh and N Parvathavarthini, *Indira Gandhi Centre for Atomic Research, India*

13.1 Introduction 477

13.2 Different forms of corrosion 479
13.3 Effect of defects on the corrosion properties of weld metal 486
13.4 Effect of residual stresses on the corrosion properties of weld joints 488
13.5 Corrosion of austenitic stainless steel weld joints 490
13.6 Corrosion of ferritic steel weldments 506
13.7 Conclusions 517
13.8 References 517

14 Advances in techniques for determination of susceptibility of welds to stress corrosion cracking (K_{ISCC}) 521

RK Singh, *Monash University, Australia*

14.1 Stress corrosion cracking (SCC) of welds and threshold stress intensity for SCC (K_{ISCC}) 521
14.2 CNT testing 524
14.3 Determination of K_{ISCC} by CNT testing 528
14.4 CNT testing of welds 530
14.5 Conclusions 532
14.6 Acknowledgements 532
14.7 References 532

15 Less explored types of environment-assisted cracking of welds: industrial issues and research opportunities 534

RK Singh, *Monash University, Australia*

15.1 Introduction 534
15.2 Cr–Mo ferritic steel welds: high temperature corrosion 535
15.3 Microbiologically influenced corrosion of stainless steel weldments in the marine environment 540
15.4 References 543

Index *546*

Contributor contact details

(* = main contact)

Editor and Chapters 14 and 15

Dr Raman K. Singh
Department of Mechanical and Chemical Engineering
Building 31 Monash University
Victoria 3800
Australia

E-mail:
Raman.Singh@eng.monash.edu.au

Chapter 1

Professor John N. DuPont
Energy Research Center
Lehigh University
Bethlehem, PA 18015
USA

E-mail: jnd1@Lehigh.EDU

Chapter 2

Dr Arun Kumar Bhaduri*, Dr Shaju K. Albert and Dr Baldev Raj
Indira Gandhi Centre for Atomic Research
Kalpakkam 603 102
India

E-mail: bhaduri@igcar.gov.in
shaju@igcar.gov.in
dir@igcar.gov.in

Chapter 3

Dr P. Chellapandi*and S. C. Chetal
Indira Gandhi Centre for Atomic Research
Kalpakkam 603 102
India

E-mail: pcp@igcar.gov.in

Chapter 4

Dr John W. H. Price
Mechanical and Aerospace Engineering Department
Monash University
Wellington Road
Clayton
Victoria 3800
Australia

E-mail: john.price@eng.monash.edu.au

Chapter 5

Dr K. Bhanu Sankara Rao*, M. D. Mathew, K. Laha, R. Sandhya and Baldev Raj
Indira Gandhi Centre for Atomic Research
Kalpakkam 603 102
India

E-mail: bhanu@igcar.ernet.in
bhanu@igcar.gov.in

Chapter 6

Dr S. K. Ray and Dr G. Sasikala*
Indira Gandhi Centre for Atomic Research
Kalpakkam 603 102
India

E-mail: saradivdo.ray@gmail.com
gsasi@igcar.gov.in

Chapter 7

Dr Baldev Raj*, Dr T. Jayakumar and P. Palanichamy
Indira Gandhi Centre for Atomic Research
Kalpakkam 603 102
India

E-mail: secdmg@igcar.gov.in

Chapter 8

Dr Baldev Raj*, K. V. Kasiviswanathan, N. Raghu, N. G. Muralidharan and V. Karthik
Indira Gandhi Centre for Atomic Research
Kalpakkam 603 102
India

E-mail: kasi@igcar.gov.in
secdmg@igcar.gov.in

Chapter 9

Dr Anthony Comer
School of Mechanical and Manufacturing Engineering
Dublin City University
Dublin 9
Ireland

E-mail: anthony.comer@gmail.com

Chapter 10

Emeritus Professor Druce Dunne*
Faculty of Engineering
University of Wollongong
Wollongong
NSW 2522
Australia

E-mail: druce@uow.edu.au

Dr David Nolan
BlueScopeSteel
PO Box 202 Port Kembla
NSW 2505
Australia

E-mail:
David.Nolan@bluescopesteel.com

Chapter 11

Associate Professor Raafat Ibrahim
Monash University
Mechanical and Aerospace
Engineering Department
Wellington Road
Clayton
Victoria 3800
Australia

E-mail:
raafat.ibrahim@eng.monash.edu.au

Chapter 12

Dr John W. H. Price*
Mechanical and Aerospace
Engineering Department
Monash University
Wellington Road
Clayton
Victoria 3800
Australia

E-mail: john.price@eng.monash.edu.au

Dr Anna M. Paradowska
ISIS Facility, Science and
Technology Facility Council
Rutherford Appleton Laboratory
Harwell
Didcott OX11 0QX
UK

E-mail: a.paradowska@rl.ac.uk

Associate Professor Trevor R.
Finlayson
School of Physics
University of Melbourne
Victoria 3010
Australia

E-mail: trevorf@unimelb.edu.au

Chapter 13

Dr R. K. Dayal*, Hasan Shaikh and
N. Parvathavarthini
Corrosion Science and Technology
Division
Indira Gandhi Centre for Atomic
Research
Kalpakkam 603 102
India

E-mail: rkd@igcar.gov.in

Introduction

R K SINGH, Monash University, Australia

Welding emerged as a result of engineering necessity for joining two metal pieces. However, to me, what makes fabrication and performance of steel welds most fascinating is that it is possibly the only single topic that necessitates education in almost the entire spectrum of metallurgical engineering. For example, ensuring sound performance of a cracking-resistant welded steel vessel for handling a corrosive fluid would need an understanding of:

- metallurgy of solidification and solid state phase changes associated with fabrication (and sound microscopic evaluation of the phase changes);
- non-destructive evaluation (NDE) of defects and stresses in welded structure;
- corrosion and synergistic influence of stress and corrosion causing cracking;
- fracture mechanical evaluation of the design and remaining life of the welded structure;
- NDE of the extent of damages in the aged welded structure;
- fractography and failure analyses of cracked structure; and
- metallurgy and NDE evaluation of the repair of cracked structure.

Adequate modelling coupled with key experimentation and validation approaches are essential inputs for quality and cost-effective welding management. Welding technology concerns traditional metallurgical engineering, which is underpinned by the fundamentals of physics, chemistry, materials and mechanical engineering. Unfortunately, metallurgical engineering in most modern materials engineering curricular contents has been dwindling worldwide. However, welding will continue to be an indispensable fabrication process for industrial structures, and the problems associated with welding will continue to perplex designers, manufacturers and plant operators. Because of the lack of adequately trained engineers in the field of traditional welding/metallurgical engineering, more and more professionals from other disciplines (such as mechanical and chemical engineers, who will be required to design, manufacture the components and run the plants) will have to shoulder the responsibilities of weld design, fabrication and robust operation over the lifetime of the plant.

In the planning and development of this book, particular care has been taken to make the chapters suitable for professionals from other disciplines who will need to learn and apply the information provided to the welds and their cracking/failures. Therefore, wherever possible, each chapter provides short descriptions (either within the main text or in an appendix) of the traditional metallurgical terminology and/or phenomena.

This book benefits tremendously from the participation of international experts in complementary topics of welding technology and research. The chapters deal invariably with the most recent technological advances in the respective topics while keeping an eye on the other primary purpose of the book, i.e. to make the chapters suitable for those without formal training in welding/metallurgical engineering (for the reasons described above).

The book has three parts. Part I aims at providing fundamentals as well as most recent advances in the areas of welding technology, design and material selection for preventing weld cracking. This part consists of chapters on such topics as robust welding technologies, component design against cracking and selection of crack-resistant stainless steels.

Part II discusses weld crack behaviour, evaluation and repair of cracking/cracked welds. NDE is the most critical tool for monitoring the health of welded components as well as their life prediction. The book benefits from an extensive and robust chapter on the topic of NDE and quality control that is contributed by one of the strongest non-destructing evaluation and development groups in the world. There is another chapter on the specialised use of neutron diffraction in evaluation of residual stresses of weldments. Chapters on fracture toughness and other common mechanical properties of welds deal with the role of fundamental metallurgical aspects on these properties and their evaluation. Some of the sets of data included in these chapters have been generated over extended testing and are extremely relevant to the performance of actual welds and their cracking. The chapter on the application of cellulosic girth welding provides an elaborate fundamental treatment of the major issue of weld cracking in the millions of kilometres of pipelines of welded steel structure. Similarly, the chapter on weld repair provides modern metallurgical approaches for restoration of the cracked welded structure. To develop an appreciation for the direct industrial relevance of these topics, Part II includes a chapter on a few typical case histories of weld cracking in different industrial situations and the systematic engineering and metallurgical approaches that were adopted to mitigate the problem of weld cracking in each case.

Part III covers environment-assisted weld cracking. Corrosion in conjunction with stresses (called stress corrosion cracking, SCC) can lead to catastrophic cracking. Such failures are particularly severe in the case of welded structures that are invariably under considerable residual stresses, which can lead to

SCC failures if the welds are not suitably stress relieved. Therefore, environment-assisted weld cracking has received tremendous research and development attention over the several decades. This part includes an elaborate chapter on corrosion and corrosion-assisted cracking of steel weldments. It also has chapters on a modern technique on evaluation of SCC susceptibility, and on relatively less explored types of corrosion-assisted failures of welds and the existing research and development potentials.

The editor finds it extremely fulfilling to have been able to receive participation of a galaxy of experts in the complementary areas of welding technology, design, evaluation and maintenance. However, special thanks must go to Indira Gandhi Centre for Atomic Research (IGCAR), a reputable research centre of Indian Atomic Energy and its distinguished director, Dr Baldev Raj. IGCAR is possibly the most self-sufficient centre for welding technology, design and evaluation, having extensive programmes on each of the areas listed earlier. Dr Raj has been the key factor in encouraging his colleagues for the participation in this book, and in ensuring that a sound mechanism was in place for the delivery of the committed chapters.

1

Selection of weld-crack resistant stainless steels

J N DUPONT, Lehigh University, USA

Abstract: Stainless steel alloys are used in a wide variety of applications that often involve welding. Depending on the specific alloy type and composition, these alloys can be susceptible to various forms of cracking during welding. This chapter provides an overview of the various types of stainless steels, descriptions of potential cracking mechanisms, and techniques for avoiding cracking.

Key words: stainless steels, solidification cracking, HAZ cracking, liqud cracking, hydrogen cracking, primary solidification mode.

1.1 Introduction

Stainless steels are used in a wide range of applications that require good resistance to corrosion along with various combinations of strength, ductility, and toughness. Most applications will require fabrication by fusion welding. Although stainless steels are generally readily weldable, there are some forms of cracking that can occur during welding that need to be avoided. The objective of this chapter is to provide an overview of cracking mechanisms that can occur during welding of stainless steels. A brief description of the physical metallurgy applicable to various classes of stainless steels is provided first. The types of cracking mechanisms that are operable in stainless steels are then reviewed. In this section, particular attention is given to solidification cracking and heat-affected zone (HAZ) liquation cracking, since these are the most common problems that need to be avoided. The chapter concludes with general recommendations for avoiding the various types of cracking that can occur in stainless steels during welding.

1.2 Types of stainless steels

1.2.1 Martensitic stainless steels

Table 1.1 summarizes compositions of some common martensitic stainless steels. These alloys generally contain 11.5 to 18 wt% Cr for corrosion resistance. The strength of these alloys is primarily obtained by an austenitize-cool-temper heat treatment procedure that is designed to form a tempered martensitic microstructure with carbides. Additional strength can be imparted due to solid solution hardening by the presence of dissolved solute elements (such

Table 1.1 Compositions of some common martensitic stainless steels. All values in weight percent. Unless noted, single value is a maximum

Alloy	UNS no.	C	Cr	Mn	Si	Ni	Other
403	S40300	0.15	11.5–13.0	1.00	0.50	–	–
410	S41000	0.15	11.5–13.5	1.00	1.00	–	–
420	S42000	0.15 min.	12.0–14.0	1.00	1.00	–	–
431	S43100	0.20	15.0–17.0	1.00	1.00	1.25–2.50	–
440A	S44002	0.60–0.75	16.0–18.0	1.00	1.00	–	0.75 Mo
CA-6NM	–	0.06	11.5–14.0	1.00	1.00	3.5–4.5	0.4–1.0 Mo

as Ni and Cr), the precipitation of carbides during tempering, and by control of the prior austenite grain size. Since martensite is the primary strengthening mechanism, the hardness and strength of these alloys increase significantly with increasing carbon content. Cold working also provides a significant increase in strength, but the ductility and toughness are adversely affected, so this strengthening mechanism is typically not exploited in practice.

The austenitizing treatment is required as the initial step so that martensite can form from the austenite during cooling. Formation of fully martensitic structures in simple Fe–Cr alloys is limited to ~ 10–12 wt%. Above this Cr level, austenite is replaced by ferrite at higher temperatures, thus restricting the ability to form martensite during cooling. Additions of elements such as C, N, and Ni are useful in this regard because they widen the austenite phase field. This permits the addition of higher Cr contents while allowing formation of a fully austenitic structure at higher temperatures. Unlike low alloy steels, the relatively high Cr content of these alloys leads to high hardenability, so that quenching is generally not required to form a uniform martensitic microstructure during cooling. The as-quenched martensite exhibits very high hardness and strength, but is usually of insufficient toughness for most engineering applications. Thus, tempering is required to impart adequate toughness and ductility (with a concomitant reduction in strength and hardness).

Master tempering curves are often available to correlate changes in mechanical properties to heat treatment time and temperature. An example of this for a 12Cr–0.14C martensitic stainless steel is shown in Fig. 1.1 [1]. In this plot, the change in hardness is plotted against a Larson–Miller type

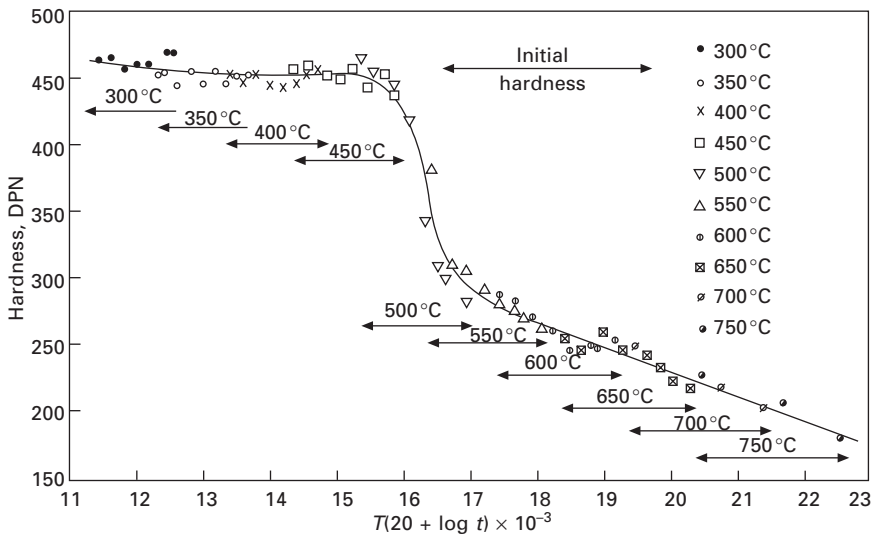

1.1 Master tempering curve for a 12Cr–0.14C martensitic stainless steel.

tempering parameter (where T is temperature and t is time). This type of information permits one to determine various combinations of time and temperature that produce equivalent results in terms of tempering and resultant properties. The reduction in hardness occurs due to release of carbon from the super saturated martensite, which is also accompanied by precipitation of various carbides. It is worth noting, however, that the tempering temperatures between 475 and 550 °C are generally avoided in martensitic stainless steels in order to avoid temper embrittlement. This form of embrittlement produces a significant reduction in toughness that is associated with segregation of tramp elements to the prior austenite grain boundaries during tempering.

1.2.2 Ferritic stainless steels

Table 1.2 lists typical compositions of some common ferritic stainless steels. The presence of austenite stabilizing elements in these alloys is lower than the martensitic stainless steels and, as a result, these alloys generally remain ferritic from room temperature up to melting. Thus, they cannot be strengthened by heat treating. Some alloys can contain minor amounts of martensite, but most alloys are fully ferritic. Ferritic stainless steels exhibit inferior mechanical properties compared with martensitic and austenitic stainless steels, and are susceptible to various forms of embrittlement at service temperatures above ~ 400 °C. However, they have good resistance to general and localized corrosion (e.g. stress corrosion cracking). Thus, these alloys are typically used where low temperature corrosion resistance, rather then mechanical properties, is of primary concern.

Ferritic stainless steels are susceptible to several types of embrittlement phenomena that induce severe losses in toughness and ductility and warrant brief discussion. These include 475 °C embrittlement, sigma phase embrittlement, high temperature embrittlement, and notch sensitivity. Alloys with Cr levels from 15 to 70 wt% can undergo 475 °C embrittlement. This process is generally believed to be associated with the formation of a coherent α' precipitate at temperatures below 550 °C, which is expected from the miscibility gap that exists in the Fe–Cr system. Alloys aged below this temperature can form a two phase microstructure that consists of Fe-rich (α) and Cr-rich (α') phases. The rate of precipitation increases with increasing Cr content and increasing cold work. This form of embrittlement can also reduce corrosion resistance due to selective attack of the low Cr α phase. The brittle σ phase can form in alloys with 20–70 wt% Cr when exposed to temperatures from 500 to 800 °C. As with 475 °C embrittlement, the rate of σ phase formation increases with plastic deformation and increasing Cr content. Sigma phase embrittlement can be reversed if the alloy is heated above 800 °C, which results in dissolution of the σ phase.

High temperature embrittlement occurs when alloys are heated above ~

Table 1.2 Compositions of some common ferritic stainless steels. All values in weight percent. Unless noted, single value is a maximum. P levels are typically < 0.04, and S levels are typically < 0.03

Alloy	UNS no.	C	Cr	Mn	Si	Ni	Other
405	S40500	0.08	11.5–14.5	1.00	0.50	0.60	0.10–0.30 Al
409	S40900	0.08	10.5–11.75	1.00	1.00	0.50	Ti = 6 × C – 0.75
434	S43400	0.12	16.0–18.0	1.00	1.00	–	0.75–1.25 Mo
446	S44600	0.20	23.0–27.0	1.50	1.00	0.75	0.25 N
468	S46900	0.03	18.0–20.0	1.00	1.00	0.50	0.03 N, 0.07–0.30 Ti, 0.10–0.60 Nb

950 °C. Since this is well above the service temperature of ferritic stainless steels, this process can occur during processing operations such as casting, welding, and/or thermo-mechanical processing. The level of interstitial elements such as carbon, nitrogen, and oxygen, have a strong influence on high temperature embrittlement. At high temperatures, these elements can be dissolved. During cooling, their presence can lead to precipitation of Cr-rich carbides, nitrides, or carbo-nitrides that induce a severe reduction of impact toughness and increase in the ductile to brittle transition temperature. Even when ferritic stainless steels can be processed without the three forms of embrittlement described thus far, they still exhibit notch sensitivity. As shown in Fig. 1.2, notch sensitivity is a strong function of Cr content and the combined interstitial level (carbon + nitrogen) [2].

1.2.3 Austenitic stainless steels

Austenitic stainless steels represent the most widely used alloys of all the stainless steels. This can be attributed to their combination of good corrosion resistance, ease of fabricability by a variety of techniques (e.g., casting, welding, and various forming processes), and good mechanical properties. Table 1.3 lists the composition of some common grades of austenitic stainless

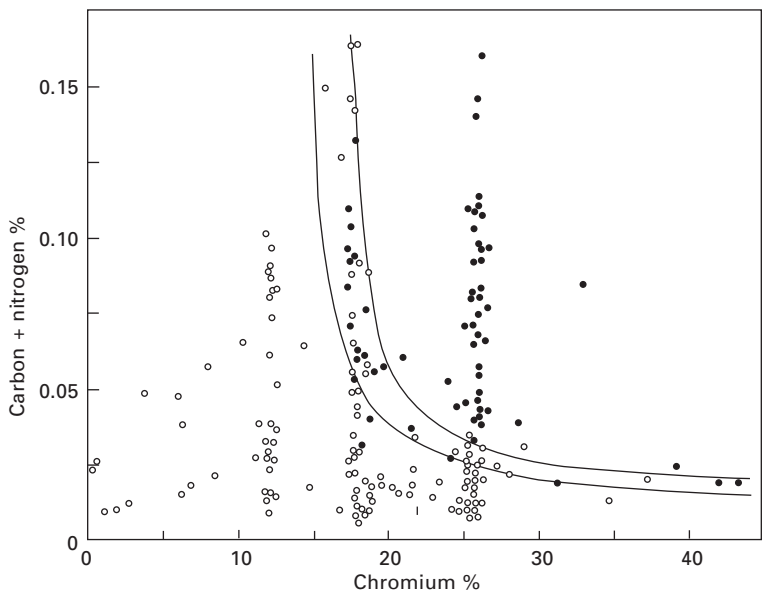

1.2 Notch sensitivity of ferritic stainless steels as function of Cr content and combined C + N content. Open circles represent high impact strength alloys; closed circles represent low impact strength alloys.

Table 1.3 Compositions of some common austenitic stainless steels. All values in weight percent. Unless noted, single value is a maximum. P is < 0.045 and S is < 0.03

Alloy	UNS no.	C	Mn	Si	Cr	Ni	Other
304	S30400	0.08	2.0	1.0	18.0–20.0	8.0–10.5	–
308	S30800	0.08	2.0	1.0	19.0–21.0	10.0–12.0	–
309	S30900	0.20	2.0	1.0	22.0–24.0	12.0–15.0	–
316	S31600	0.08	2.0	1.0	16.0–18.0	10.0–14.0	2.0–3.0 Mo
321	S32100	0.08	2.0	1.0	17.0–19.0	9.0–12.0	Ti = 5 × C – 0.70
347	S34700	0.08	2.0	1.0	17.0–19.0	9.0–13.0	Nb = 10 × C – 1.00

steels. It should be noted that this is only a small list from a very wide range of commercially available alloys. These alloys are based on the Fe–Ni–Cr system and generally contain a minimum of ~ 8 wt% Ni that is added to stabilize the γ-austenite matrix to low temperatures. The influence of Ni is readily observed from isothermal sections of the Fe–Ni–Cr ternary system shown in Fig. 1.3 [3]. Austenite (γ) and ferrite (referred to as either α or δ) are the primary phases that cover most of the temperature–composition space associated with the Fe–Ni–Cr system. The brittle σ phase can also form at lower temperatures and higher Cr concentrations. Although the kinetics associated with formation of the σ phase are typically sluggish, it has been

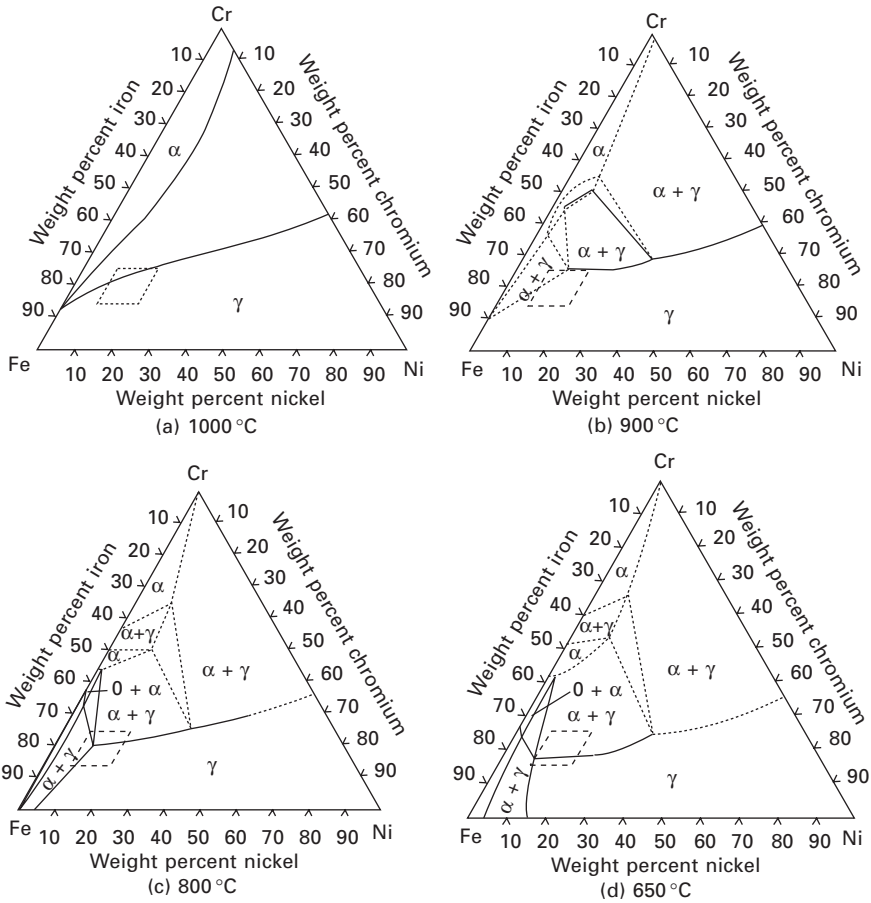

1.3 Isothermal sections of the Fe–Ni–Cr ternary system shown at various temperatures. The small boxes (dotted lines) represent the typical range of Ni (~ 8–20 wt%) and Cr (~ 15–25 wt%) concentrations found in many commercially austenitic stainless steels.

observed in several higher Cr alloys and can compromise both mechanical properties and corrosion resistance [4]. The small boxes (dotted lines) shown in Fig. 1.3 represent the typical range of Ni (~ 8–20 wt%) and Cr (~ 15–25 wt%) concentrations found in many commercially austenitic stainless steels. Note that most alloys will be fully or nearly fully austenitic.

Austenitic stainless steels can exhibit either primary ferrite or primary austenite solidification modes [5,6]. This can be understood by reference to the 70 wt% Fe isopleth section extracted from the Fe–Ni–Cr system that is shown in Fig. 1.4 [7]. The ternary liquidus projection for this system exhibits a line of twofold saturation that separates primary δ-ferrite solidification from primary γ-austenite solidification. This line has a slope of ~ 3Cr : 2Ni on the ternary liquidus projection, and the line is reduced to a 'eutectic point' on the isopleth section of Fig. 1.4. Alloys rich in Ni located to the left of the eutectic will exhibit primary γ solidification, and γ will generally remain stable after solidification (as previously mentioned, the σ phase can potentially form in some higher Cr alloys). Alloys higher in Cr located to the right of the eutectic will solidify as primary δ. However, in most commercial austenitic stainless steels, this ferrite is not stable with decreasing temperature and can transform to austenite with continued cooling. Depending on alloy composition and cooling rate, the alloy may contain some remnant ferrite (either stable or unstable), or may be fully austenitic.

Although the phase diagrams shown in Figs 1.3 and 1.4 are useful for understanding phase transformation sequences and potential microstructures,

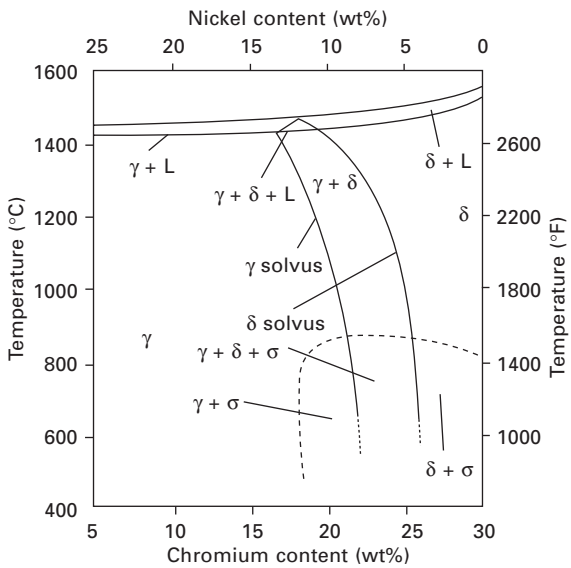

1.4 The 70 wt% Fe isopleth section extracted from the Fe–Ni–Cr system.

commercial austenitic stainless steels contain many other elements that affect the position of the phase boundary lines and, therefore, can significantly alter the final microstructure. It is well known that elements such as Ni, Mn, C, and N stabilize austenite, while elements such as Cr, Mo, and Si stabilize the ferrite phase [8]. Numerous constitution diagrams are available for stainless steels that take these higher order alloying effects into account. Two of the most common diagrams utilized for controlling weld metal microstructures in stainless steels are shown in Fig. 1.5 – the Schaeffler (Fig. 1.5a) and WRC

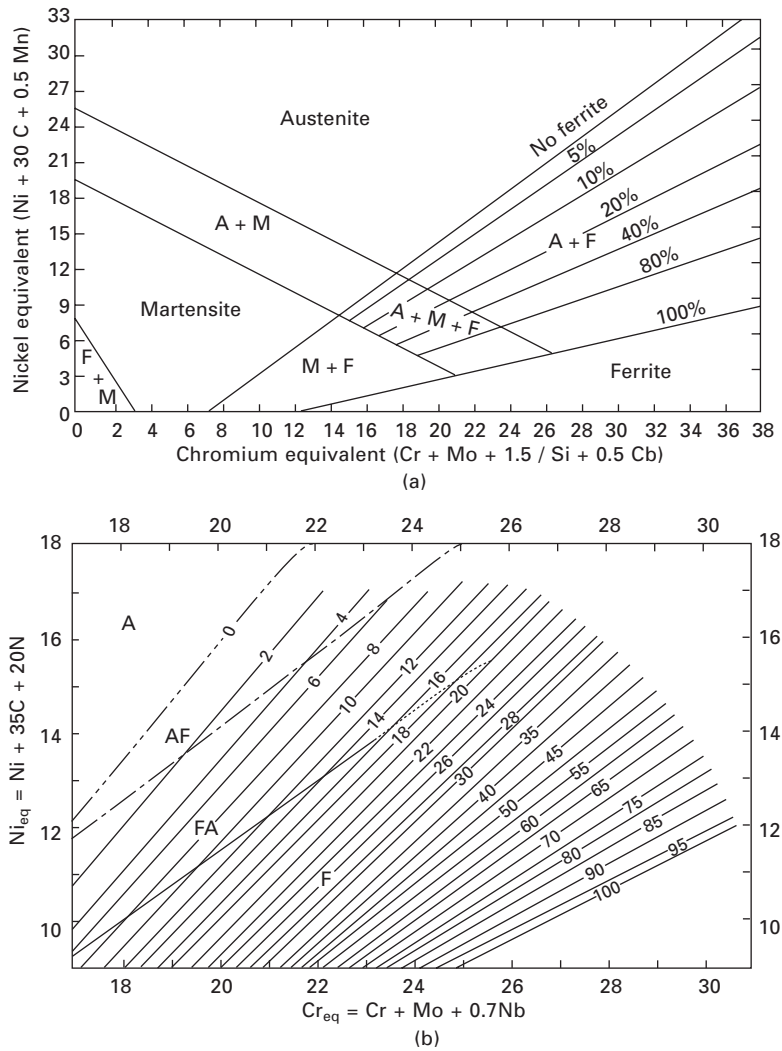

1.5 (a) Schaeffler and (b) WRC constitution diagrams for stainless steels.

(Fig. 1.5b) [9,10]. (These diagrams are intended to provide estimates of the final weld microstructure after cooling, so they do not account for transformations that may occur during long-term aging at elevated temperatures.) These diagrams each utilize the concept of an equivalent chemical composition, in which the influence of various elements on phase stability is taken into account relative to that of Ni (and its ability to stabilize γ) or Cr (and its ability to stabilize δ).

The Schaeffler diagram is useful because it provides information on phases that will exist over a wide range of compositions. The diagram is somewhat limited in that it provides no direct information on the primary solidification mode. As explained in more detail in Section 1.4, the primary solidification mode is of paramount importance for avoiding solidification cracking in stainless steel welds. The WRC diagram (Fig. 1.5b) is more useful in this regard because it can be used to directly estimate the primary solidification mode (A, AF, FA, or F) from knowledge of alloy composition. The WRC diagram can be used for applications involving ferritic, austenitic, and duplex stainless steels, while the Schaeffler diagram can be used for the same alloy groups in addition to martensitic stainless steels.

1.2.4 Duplex stainless steels

Table 1.4 lists the chemical composition of some typical duplex stainless steels. These alloys generally have higher Cr_{eq}/Ni_{eq} ratios than austenitic stainless steels. As a result, they always exhibit a fully ferritic solidification mode. This is shown schematically in the pseudo-binary phase diagram in Fig. 1.6 [11]. Most duplex stainless steels have a Cr_{eq}/Ni_{eq} ratio of about 2.3–3.5. Upon cooling, much of the as-solidified ferrite will transform to austenite, with partitioning of ferrite stabilizing elements (e.g. Cr, Mo, W) to ferrite and austenite stabilizing elements (e.g. Ni, C, N, Cu) to austenite. The chemical composition and thermo-mechanical processes used with these alloys are typically controlled to produce a microstructure that consists of an approximate 50/50 volume mix of austenite and ferrite. Nitrogen is an important alloying element that is added to accelerate the formation of austenite and also improve corrosion resistance. Because of the relatively complex and careful control required during processing, these alloys are generally more expensive than austenitic stainless steels.

Duplex stainless steels provide a very good combination of corrosion resistance and strength. Their strength level is generally above that of the austenitic alloys, and they are often substituted for austenitic alloys where stress corrosion cracking is a concern. However, these alloys are also susceptible to formation of various undesirable phases such as sigma and chi phases (to name a few) at temperatures above ~ 300 °C. The susceptibility of forming these phases increases with increasing additions of Cr, Mo, and W, and this

Table 1.4 Compositions of some common duplex stainless steels. All values in weight percent. Unless noted, single value is a maximum. P is typically < 0.045 and S is typically < 0.03

Alloy	UNS no.	C	Mn	Si	Cr	Ni	Mo	N	Cu
2304	S32304	0.03	2.5	1.0	21.5–24.5	3.0–5.5	0.05–0.60	0.05–0.20	0.05–0.60
2205	S32205	0.03	2.0	1.0	21.0–23.0	4.5–6.5	2.5–3.5	0.08–0.20	–
329	S32900	0.08	1.0	0.75	23.0–28.0	2.0–5.0	1.0–2.0	–	–
255	S32550	0.04	1.5	1.0	24.0–27.0	4.5–6.5	2.9–3.9	0.10–0.25	1.50–2.50
2507	S32750	0.03	1.2	0.80	24.0–26.0	6.0–8.0	3.0–5.0	0.24–0.32	0.50

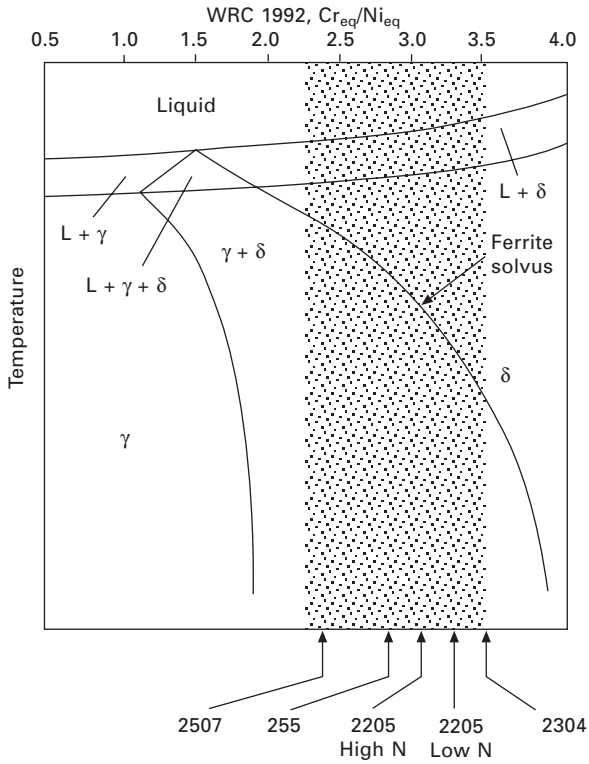

1.6 Pseudo-binary phase diagram of FeNiCr system showing typical Cr_{eq}/Ni_{eq} ranges for duplex stainless steels.

problem needs to also be considered during post-weld heat treating (PWHT) and multi-pass welding applications. In addition, the alloys exhibit a ductile-to-brittle transition, which limits their use at cryogenic temperatures.

1.2.5 Precipitation hardened stainless steels

Precipitation hardened stainless steels are available in three classes, depending on their predominant microstructure – semi-austenitic, austenitic, and martensitic. Table 1.5 lists compositions for several of each type of alloy class. These alloys form very high strength levels due to the presence of a precipitation element such as Ti, Cu, Al, or Nb. The austenitic grades exhibit the highest Ni content and, as a result, will solidify with a fully austenitic microstructure. These alloys are commonly supplied in the solution annealed condition in which they are relatively soft, as this facilitates fabrication. They are then aged at temperatures in the range of approximately 670–750 °C to form various precipitate phases such as Ni_3Ti. The final microstructure consists of an austenitic matrix with fine precipitates.

Table 1.5 Compositions of some common precipitation hardened stainless steels. All values in weight percent. Unless noted, single value is a maximum. P is typically < 0.04 and S is typically < 0.03

Alloy	UNS no.	C	Mn	Si	Cr	Ni	Mo	Other
Martensitic grades								
13-8Mo	S13800	0.05	0.20	0.10	12.25–13.25	7.50–8.50	2.0–2.5	0.90–1.35 Al, 0.01 N
15-5PH	S15500	0.07	1.0	1.0	14.0–15.5	3.5–5.5	–	2.5–4.5 Cu
17-4PH	S17400	0.07	1.0	1.0	15.0–17.5	3.0–5.0	–	3.0–5.0 Cu
Custom 450	S45000	0.05	1.00	1.00	14.0–16.0	5.0–7.0	0.50–1.00	1.25–1.75 Cu, Nb = 8 × C – 0.75
Semi-austenitic grades								
15-7Mo	S15700	0.09	1.0	1.0	14.0–16.0	6.50–7.75	2.0–3.0	0.75–1.50 Al
17-7PH	S17700	0.09	1.0	1.0	16.0–18.0	6.50–7.75	–	0.75–1.50 Al
Austenitic grades								
A-286	S66286	0.08	2.00	1.00	13.5–16.0	24.0–27.0	1.0–1.5	0.35 Al, 1.0–1.5 Ti, 0.1–0.5 V
JBK-75	–	0.03	0.20	0.10	13.5–16.0	29.0–31.0	1.0–1.5	0.15–0.35 Al, 2.0–2.3 Ti, 0.1–0.50 V

The reduced Ni content of the semi-austenitic grades results in solidification to essentially all ferrite, but most of the ferrite is transformed to austenite with further cooling. Slow cooling will then generally produce a microstructure that is mostly austenitic with a small amount of remnant ferrite. In this condition, the alloy is quite soft and can be easily worked. After fabrication, the alloy is then re-heated to 'condition' the austenite, which results in precipitation of carbides, a reduction in the carbon content in the austenite, and a concomitant increase in the martensite start (Ms) temperature. On cooling, the higher Ms temperature results in formation of martensite. The alloy is then given a final, lower temperature heating to induce the primary precipitation reaction. Thus, the final microstructure can generally contain a martensitic matrix with remnant ferrite along with carbides and an additional precipitate that depends on the exact alloy.

The martensitic type alloys also solidify fully as ferrite, but nearly all the ferrite transforms to austenite with further cooling so that very little remnant ferrite persists after cooling. Homogenization treatments can be used to eliminate any remnant ferrite, and subsequent cooling will then produce martensite. These steels can also contain retained austenite after cooling. After cooling to form martensite, these alloys receive a final aging treatment to increase the strength by precipitation.

1.3 Cracking mechanisms in stainless steel welds

1.3.1 Fusion zone solidification cracking

The formation of solidification cracks in the fusion zone of stainless steels is a primary concern in alloys that exhibit a primary austenitic solidification mode, although it can occur in any of the stainless steel alloy types under conditions of very high restraint. In general, fusion zone solidification cracks can form during the terminal stages of solidification when a liquid film is distributed along grain boundaries and interdendritic regions. At this stage, shrinkage strains across the partially solidified boundaries can become appreciable. If the terminal liquid is distributed along the boundaries as a continuous film, the strains cannot be accommodated and the boundaries separate to form a crack [12]. Figure 1.7 shows an example of solidification cracks in the fusion zone of an austenitic stainless steel [13]. Note that the cracks reside within the grain boundary and interdendritic regions that are the last locations to solidify, and this is a key feature that can be used to identify the cracking mechanism.

In a general sense, the solidification temperature range as well as the amount and distribution of the interfacial terminal liquid are primary factors that control solidification cracking susceptibility of engineering alloys [14]. Solute redistribution plays an important role in solidification cracking as it

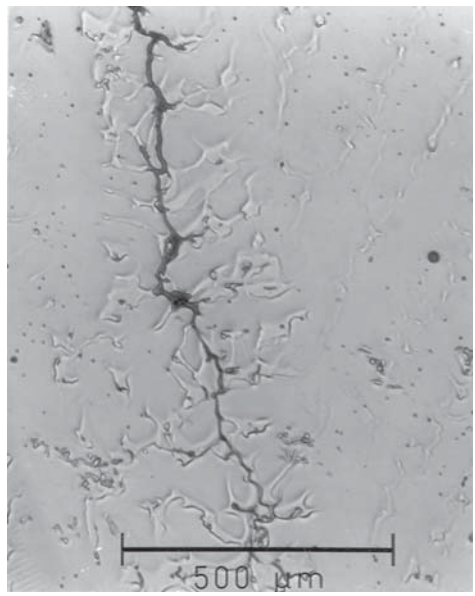

1.7 Light optical photomicrograph showing an example of solidification crack in the fusion zone of an austenitic stainless steel.

affects the solidification temperature range and amount of terminal liquid. The effect of the solidification temperature range can be understood in simplified terms by considering its influence on the size of the solid + liquid (mushy) zone. During welding, the mushy region trails behind the liquid weld pool. It is this mushy region which is susceptible to cracking under the influence of shrinkage strain and external restraint. The interface between the liquid weld pool and mushy zone (i.e. start of the mushy zone) is located where the actual temperature intersects the liquidus temperature of the alloy (assuming dendrite tip under-cooling is negligible). Similarly, the interface between the mushy zone and completely solidified weld (i.e. end of the mushy zone) is positioned where the actual temperature intersects the terminal solidus temperature of the alloy. For a fixed temperature gradient in the mushy zone (constant processing parameters), composition variations which promote low temperature reactions at the terminal stages of solidification will widen the solidification temperature range and generally aggravate cracking tendency by expanding the crack-susceptible mushy zone.

In stainless steels these factors are controlled to a large extent by the primary solidification mode. The primary solidification mode is, in turn, controlled mainly by alloy composition. This is shown schematically in Fig. 1.8 [15]. High Ni alloys with low Cr_{eq}/Ni_{eq} ratios have their nominal alloy composition located to the far left of the eutectic composition that separates primary austenite and primary ferrite solidification modes. Thus, these alloys

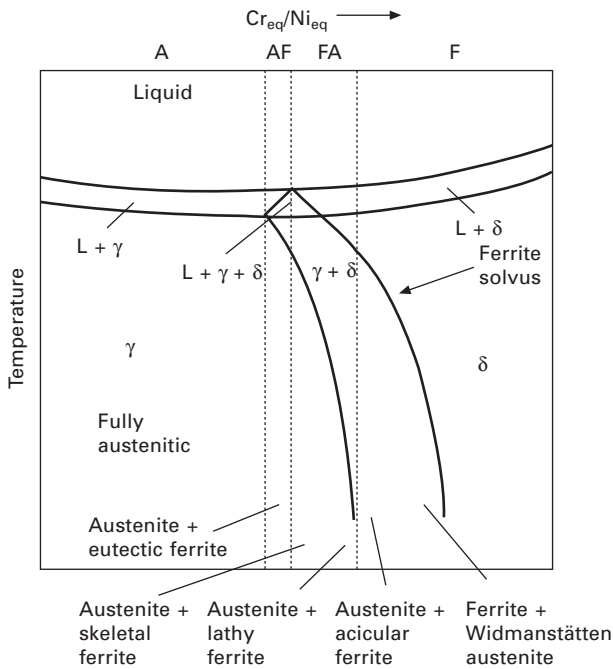

1.8 Schematic illustration showing influence of Cr_{eq}/Ni_{eq} ratio on primary solidification mode and microstructure of stainless steels.

exhibit a primary austenite solidification mode. Because the nominal alloy composition is far removed from the eutectic transition, the interdendritic liquid is never enriched sufficiently in solute to reach the eutectic composition, and no ferrite forms in the interdendritic regions, resulting in a fully austenitic solidification mode (A). Figure 1.9(a) shows an example of this type of microstructure [6,16].

For alloys with slightly higher Cr_{eq}/Ni_{eq} ratios, the interdendritic liquid can reach the eutectic composition during solidification, which will promote interdendritic eutectic ferrite and austenite forming at the terminal stages of solidification. These alloys are classified as the AF solidification mode and can be identified by the presence of ferrite in the interdendritic regions (Fig. 1.9b). With increasing Cr_{eq}/Ni_{eq} ratio, the nominal alloy composition will cross the eutectic composition and the primary solidification phase will change from austenite to ferrite. Alloys with a Cr_{eq}/Ni_{eq} ratio located on the Cr-rich side of the eutectic, but relatively close to the eutectic composition, can form interdendritic ferrite and austenite at the end of solidification. This type of solidification mode is classified as FA (Fig. 1.9c). Most of the ferrite that forms during solidification is unstable and will transform to austenite during further cooling by a diffusion-controlled transformation. The austenite generally

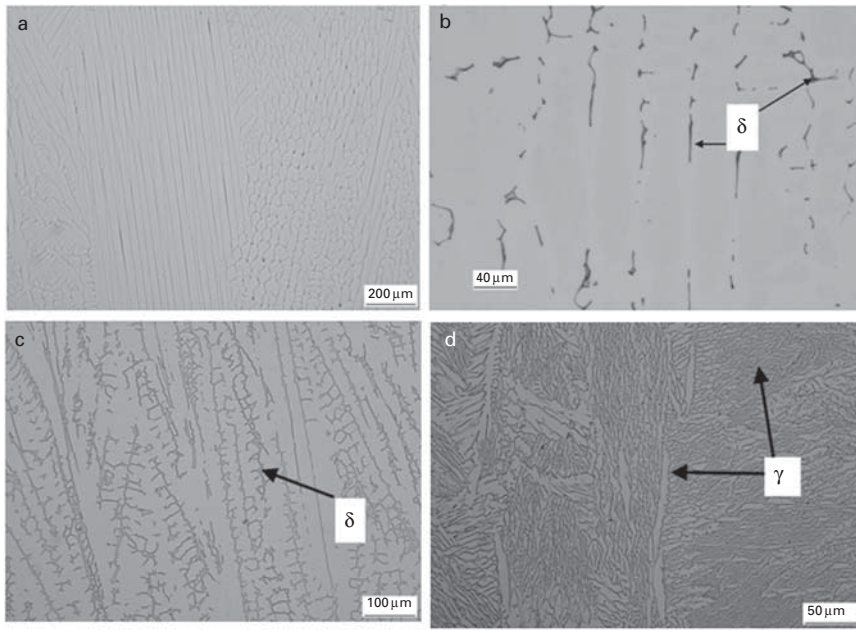

1.9 Light optical photomicrographs of austenitic stainless steel microstructures associated with various solidification modes: (a) A solidification mode, (b) AF solidification mode, (c) FA solidification mode, (d) F solidification mode.

grows epitaxially from the pre-existing austenite that formed during solidification. However, since the ferrite formed first, any remnant ferrite is now located at the cell cores (as compared with the interdendritic regions in the AF mode). Lastly, alloys with high Cr_{eq}/Ni_{eq} ratios located to the far right of the eutectic composition will undergo solidification completely as ferrite and exhibit the F solidification mode. As with the FA alloys, the ferrite is unstable and will transform to austenite during cooling. However, in this case, there is no pre-existing austenite that formed during solidification (as with the FA mode). Thus, austenite formation requires both nucleation and growth. As a result, the austenite is typically present as grain boundary and Widmanstätten-type austenite (Fig. 1.9d) [5,6,16].

It is well established that alloys which solidify in the primary austenite (A) or austenite–ferrite (AF) solidification modes are most susceptible to cracking [17]. Of these, alloys that solidify in the A mode are most susceptible. During fusion welding of these alloys, care should be exercised to reduce the level of restraint and weld pool size in an effort to reduce cracking tendency. The relatively high cracking susceptibility of these alloys is attributed to the low solubility of tramp elements in austenite (most notably P and S), and the relatively smooth austenite/austenite solidification grain boundaries that form

during solidification [17]. The low solubility of P and S leads to segregation of these elements along the interdendritic and grain boundaries which, in turn, stabilizes low melting point, solute-rich films along the boundaries that aggravate cracking. The straight, smooth austenite/austenite boundaries promote wetting of the boundaries by the liquid film and also provide little resistance to crack propagation in the fusion zone. Each of these factors lead to increased cracking susceptibility.

Alloys that solidify in the ferrite–austenite (FA) mode exhibit excellent resistance to solidification cracking due to the presence of primary ferrite. The benefits of primary ferrite have been attributed to [17]: (1) higher solubility of tramp elements in ferrite, thus reducing segregation of these elements; (2) reduced wetting of liquid films at the ferrite/austenite boundaries; and (3) increased difficulty of crack propagation along the tortuous ferrite/austenite grain boundaries. Although alloys that exhibit the F solidification mode are also quite resistant to cracking, they are slightly more susceptible than alloys that solidify in the FA mode because they form rather straight solidification grain boundaries. Thus, benefit (3) above is not operative. In summary, the resistance to solidification cracking varies as FA > F > AF > A. Since the solidification mode is governed primarily by alloy composition, much effort has gone into establishing constitution diagrams for control of solidification mode and resultant cracking susceptibility. These will be described, along with secondary factors that affect cracking susceptibility, in the next section.

1.3.2 HAZ liquation cracking

All engineering alloys melt and solidify over a range of temperatures. In general, the higher the alloy content, the larger the melting/solidification temperature range. During welding, the region outside the fusion zone will experience a range of peak temperatures that is between the liquidus and terminal solidus temperature of the alloy. The material within this region will thus undergo partial melting and is appropriately referred to as the partially melted zone (PMZ). Liquation cracking can occur in the PMZ in stainless steels when the liquid within the locally melted region cannot sustain the residual and external strains and thus ruptures to form a crack. An example of this type of cracking in a cast stainless steel is shown in Fig. 1.10 [18]. Note that the cracking in the HAZ is associated with localized melting of a secondary constituent (arrowheads).

The formation of these residual liquid films and the associated cracking can generally occur by three types of mechanisms. For stainless steel alloys which are single phase, the PMZ will exist where the actual temperature is between the liquidus and solidus temperatures of the alloy. Even though the alloy is single phase, tramp elements with low solubility such as S and P often segregate to the grain boundaries and cause a local depression of the

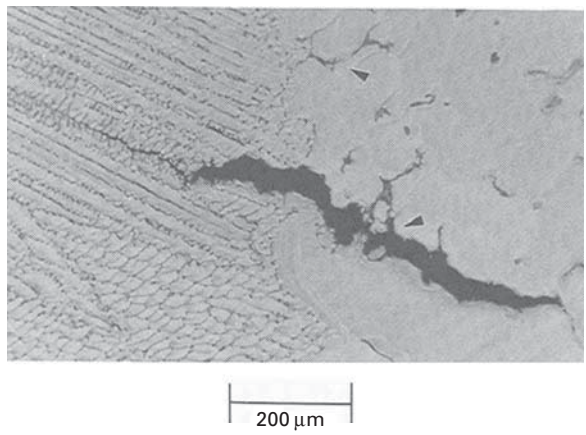

1.10 Example of liquation cracking in a cast stainless steel.

melting temperature [17]. Thus, the grain boundaries typically undergo liquation within the PMZ of single phase materials. It has been suggested that grain boundary segregation can be increased during grain growth within the HAZ as solute elements are swept into and accumulate in the migrating boundary [19]. Subsequent solidification of the solute-rich grain boundaries can often be observed in the PMZ as thick boundaries.

Liquation can also occur in alloys that contain secondary constituents such as intermetallic or carbide phases by a process known as constitutional liquation [20]. In this case, the rapid heating associated with the weld thermal cycle does not permit sufficient time for dissolution of the secondary phase within the matrix. Upon heating above the eutectic temperature, the secondary phase reacts with the matrix to form an interfacial liquid film that is at the eutectic composition. Lastly, localized melting can also occur for alloys that have residual eutectic constituents in a manner similar to that just described for constitutional liquation. In this case, the rapid heating cycle does not permit sufficient time for dissolution of the eutectic constituent, and localized melting of the eutectic begins at the eutectic temperature. If the alloy is above its maximum solid solubility, the eutectic constituent cannot dissolve regardless of the heating rate, and localized melting will always occur.

Localized melting is generally not enough in itself to promote cracking, as the locally meted regions are initially isolated. However, intersection of the moving boundaries with the liquid (due to grain growth in the HAZ) causes the liquid to penetrate and wet the boundaries, often leading to complete grain boundary coverage of the liquid film. It is difficult for the boundaries to support localized strain in this condition, and cracks can form. It is worth noting that the last two liquation mechanisms (constitutional liquation and

eutectic melting) are generally more detrimental from a cracking perspective than the first (grain boundary liquation). This is true for two main reasons. First, constitutional liquation and eutectic melting generally produce more residual liquid and, second, the melting occurs over a wider temperature range. Grain boundary liquation typically occurs between the solvus and liquidus temperatures, where liquation of the other two types occurs from the eutectic temperature to the liquidus. Based on the discussion above, there are apparent differences between the types of liquation and associated degree of cracking susceptibility expected between single phase stainless steels (e.g. fully austenitic) that are in the solid solution condition, and alloys that are strengthened by precipitation treatments. The first liquation mechanism (grain boundary liquation) is most typical for solid solution strengthened alloys, and the cracking susceptibility is therefore generally lower than that of precipitation hardened alloys. Ferrite content also has a strong influence on HAZ liquation cracking susceptibility. Alloys that form a small amount of ferrite are generally more resistant to cracking than fully austenitic alloys because the ferrite/austenite boundaries are not as easily wet by the liquid films, and the presence of ferrite helps reduce grain growth.

Cracking susceptibility is also influenced by tramp element concentration. The influence of P and S on liquation cracking is similar to that of fusion zone solidification cracking, where these elements are known to be particularly harmful. These elements all aggravate cracking by segregating aggressively to the grain boundary and causing localized melting of the grain boundaries at low temperatures. Thus, these elements should be kept as low as possible from a cracking perspective.

1.3.3 Reheat cracking

Reheat cracking (also referred to as strain age cracking or, PWHT cracking) can occur in stainless steels that form carbides or other precipitates during a PWHT operation. The phenomenon is similar to that which occurs in low alloy steels and Ni base superalloys. During welding, the cooling rate in the fusion zone and HAZ is rapid enough to prevent carbide precipitation during cooling, thus leading to a super-saturated solid solution in these areas. During re-heating (from subsequent passes in multi-pass welds, or during PWHT), the precipitates can form from the super-saturated solution. The carbides typically form as a fine distribution within the grains, but the grain boundary regions are often depleted of carbides and therefore relatively soft. As a result, the residual strain from welding is often relieved by localized straining along the soft, carbide depleted grain boundary regions, resulting in cracking. The cracking tendency is controlled in large part by alloy composition and the PWHT temperature. Austenitic stainless steels that form carbides are obviously most susceptible to this form of cracking. For example, this problem

has been observed in type 347 stainless steel that contains Nb and forms NbC during PWHT [21]. The higher carbon grades such as 316H can also exhibit this type of cracking. Techniques for mitigating cracking are covered in Section 1.4.3.

1.3.4 Hydrogen cracking

Hydrogen cracking can occur when four factors are simultaneously present, including a source of hydrogen, residual tensile stresses, temperatures below about 200 °C, and a susceptible microstructure. The first three factors will always be present in any welding application, and means for controlling these factors for purposes of mitigating hydrogen cracking are discussed in the next section. In terms of stainless steel welds, 'susceptible microstructure' can essentially be taken as any microstructure that exhibits hard and brittle martensite. Thus, the martensitic and precipitation hardened martensitic grades of stainless steels are susceptible to this form of cracking. Hydrogen cracks form along the prior austenite grain boundaries and are predominately found in the HAZ. Although several theories have been proposed to explain the cracking process, each one has similar features. During welding, hydrogen can be liberated in the arc from a number of sources (e.g. moisture in electrode coatings, contaminants on the base metal surface) or can exist as residual hydrogen in the base metal. The hydrogen will diffuse to the grain boundaries where it is generally thought to reduce the cohesive atomic strength, and any residual tensile stresses from welding will then be relieved by localized cracking along the grain boundaries. Cracking is generally confined to lower temperatures where the hydrogen is unable to migrate away from the grain boundaries due to reduced diffusion rates. Hard martensitic structures are susceptible to this form of cracking because they cannot relieve residual welding stresses via plastic deformation.

1.4 Preventing weld cracking

1.4.1 Fusion zone solidification cracking

As described in the previous section, the solidification cracking susceptibility of stainless steels is controlled primarily by the primary solidification mode and amount of impurity elements. The primary solidification mode is, in turn, controlled mainly by composition. Thus, there has been much progress in developing correlations between alloy composition and cracking susceptibility. The simplest, and often most effective, approach for controlling solidification cracking susceptibility is through use of the WRC diagram – Fig. 1.5(b). With this diagram, the alloy composition can be used to directly estimate the primary solidification mode and the resultant susceptibility to

cracking, where alloys that solidify in the FA mode are most resistant to cracking (see Section 1.3.1). It should be noted that, when evaluating particular alloys for cracking susceptibility, the full range of Ni_{eq} and Cr_{eq} values permitted within specification should be plotted on the diagram. Some alloys can exhibit composition variations that are within specification and can exhibit both AF and FA solidification modes. In this case, it may be necessary to develop tighter composition limits in order to ensure the desired FA solidification mode, although this will likely come with added alloy cost.

Kujanpaa and Suutala and co-workers have developed a very useful diagram that accounts for both solidification mode and impurity content (P + S) on the solidification cracking susceptibility of stainless steel alloys [22]. Their diagram is shown in Fig. 1.11 and plots the cracking behavior as a function of combined P + S content and the Cr_{eq}/Ni_{eq} ratio. This diagram was developed through a review of a wide range of solidification cracking studies. The Cr_{eq} and Ni_{eq} values used for Fig. 1.11 are those developed by Hammar and Svenson and are given by [23]:

$$Cr_{eq} = Cr + 1.37Mo + 1.5Si + 2Nb + 3Ti \quad 1.1a$$

$$Ni_{eq} = Ni + 0.31Mn + 22C + 14.2N + Cu \quad 1.1b$$

Note that there is a substantial increase in cracking resistance at Cr_{eq}/Ni_{eq} values above ~ 1.5. This is associated with a change in solidification mode, from the crack-susceptible AF alloys with Cr_{eq}/Ni_{eq} values below ~ 1.5 to the

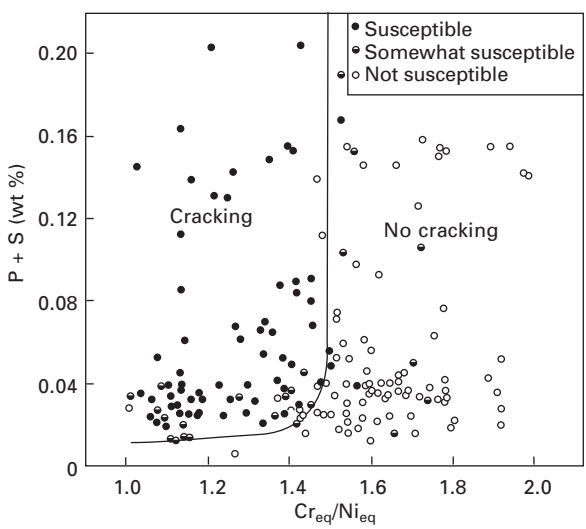

1.11 Suutala diagram showing influence of Cr_{eq}/Ni_{eq} ratio and impurity content (P + S) on the solidification cracking susceptibility of stainless steel alloys.

crack-resistant FA alloys with Cr_{eq}/Ni_{eq} values above ~ 1.5. Alloys that solidify in the primary austenitic solidification mode can be welded without cracking, provided the impurity alloy content is held to low values.

Welding conducted at higher cooling rates with high energy density processes (i.e. laser and electron beam) can undergo a shift in the primary solidification mode and resultant cracking susceptibility. At higher cooling rates, dendrite tip under-cooling can cause alloys that normally solidify in the FA mode to exhibit a change to the AF solidification mode [5]. Under these conditions, Figs 1.5(b) and 1.11 are no longer accurate, since they were developed under cooling rate conditions typical of arc welding and cannot account for conditions in which dendrite tip under-cooling becomes significant. Pacary *et al*. have modified the Suutula diagram shown in Fig. 1.11 to account for these effects, and their diagram is shown in Fig. 1.12 [24]. The diagram is similar to that of Fig. 1.11, except that boron is included in the impurity elements and, more importantly, the welds were prepared with the pulsed laser process. The previous crack/no crack boundary from Fig. 1.11 is shown for reference on the diagram. Note that higher Cr_{eq}/Ni_{eq} values (above ~ 1.7) are required to prevent cracking at these high solidification velocities.

The welding parameters and degree of restraint can also be controlled in an effort to reduce the occurrence of solidification cracks. Lower heat input leads to smaller weld sizes that, in turn, reduce solidification shrinkage strains. Lower heat inputs also decrease the size of the crack-susceptible solid + liquid region. An example of this is demonstrated by the results provided in Fig. 1.13 [13], which shows the maximum crack length (measured from the Varestraint test) as a function of welding current for autogenous welds in the stainless steel alloy 20Cb-3. Welds were also made with three

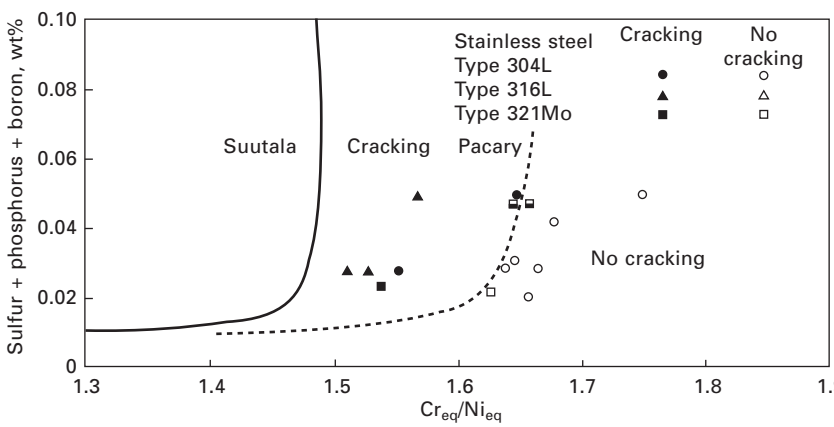

1.12 Cracking susceptibility diagram of stainless steels under laser beam processing conditions.

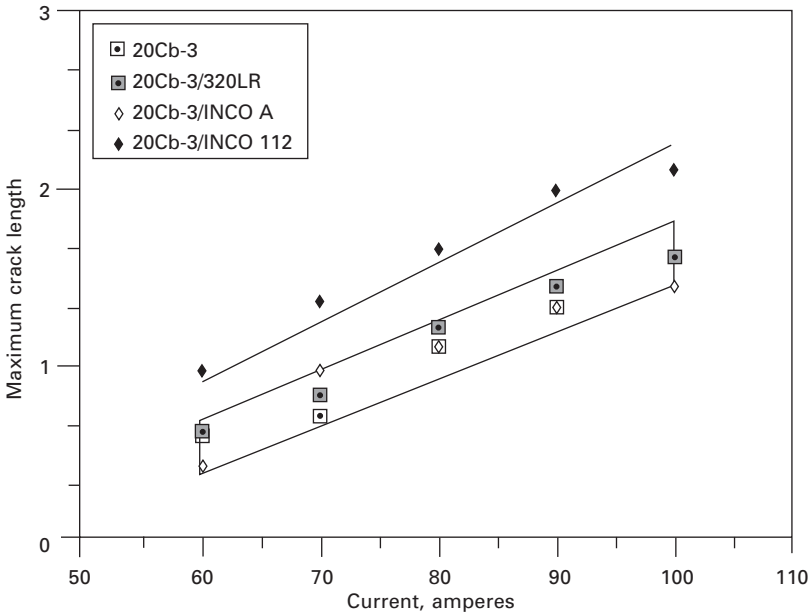

1.13 Maximum crack length (measured from the Varestraint test) as a function of welding current for autogenous welds in the stainless steel alloy 20Cb-3. Welds were also made with three different filler metals.

different filler metals. In each case, there is an increase in maximum crack length with increasing welding current, indicating that the size of the crack-susceptible mushy zone is increasing with higher currents. This can be understood from simple heat flow considerations. Higher heat inputs lead to lower temperature gradients, which, in turn, increase the distance between the liquidus and terminal solidus temperatures. This widens the crack susceptible range and aggravates the cracking problem.

The weld pool shape can also influence solidification cracking susceptibility by controlling the grain morphology as shown schematically in Fig. 1.14. The grains generally grow perpendicular to the solid/liquid interface. The fusion line in welds that are narrow with deep penetration (Fig. 1.14b) will be nearly straight and parallel. As a result, the weld metal grains will tend to grow towards and converge at the weld centerline, forming a centerline grain boundary. In this case, much of the shrinkage strain and solute segregation must be accommodated by this single centerline grain boundary, which promotes cracking. This can be avoided with wide and shallow welds (Fig. 1.14a) in which the fusion line exhibits more curvature. This promotes grain growth from the bottom of the weld toward the top and can eliminate centerline grain boundaries and the associated increased risk of cracking.

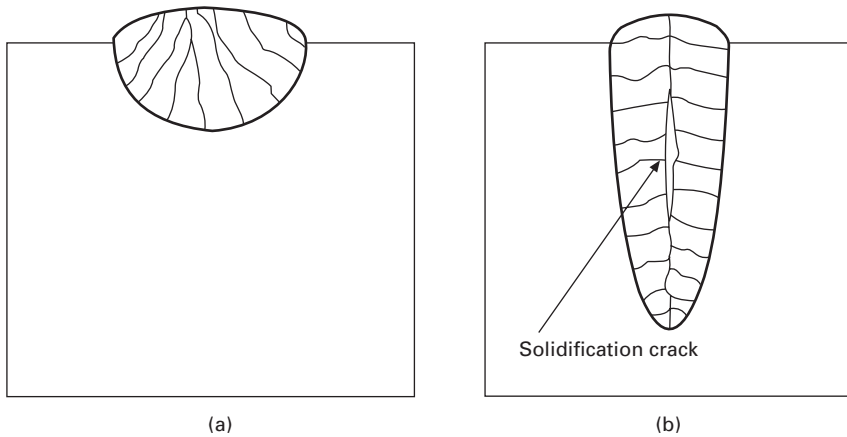

1.14 Influence of weld pool shape on solidification cracking susceptibility. (a) Shallow and wide weld that exhibits fusion line curvature and low cracking susceptibility. (b) Deep and narrow weld in which the fusion lines will be nearly straight and parallel that will exhibit high cracking susceptibility.

1.4.2 HAZ liquation cracking

There are four major factors that can be controlled during fabrication in order to minimize or eliminate liquation cracking – base metal microstructure, alloy composition, welding parameters, and degree of restraint. In terms of the base metal microstructure, the ferrite content has a strong influence on HAZ liquation cracking susceptibility. Alloys that form a small amount of ferrite are resistant to cracking because the ferrite/austenite boundaries are not as easily wet by the liquid films, and the presence of ferrite helps reduce grain growth. Liquation cracking susceptibility can also be minimized to some degree by control of the initial microstructure of the base metal as affected by heat treatments. For example, heat treatments that dissolve intermetallic phases and eutectic-type constituents will eliminate the possibility of liquation at lower temperature and improve cracking resistance. In addition, fine-grained materials are more resistant to liquation cracking than large-grained materials. Larger grain sizes increase cracking susceptibility by promoting more extensive grain boundary wetting by the liquid films and inducing higher stress concentrations.

The influence of alloy composition has already been discussed in detail. Tramp elements such as S, P, and B should be minimized. It is also useful to limit elements that promote the formation of low melting point eutectic-type constituents. However, such elements are typically added to improve a particular property, and alloy composition must be selected to balance both weldability and performance.

In terms of welding parameters, lower heat inputs are favorable for minimizing liquation cracking because they decrease the size of the partially melted zone. Cracking of any form cannot occur without some level of tensile strain. Tensile strains in the weld region will develop due to residual stresses from mechanical restraint and solidification shrinkage. Low heat input combined with reduced levels of restraint each help to reduce the level of tensile strain experienced by the HAZ. In multiple pass welding, filling of the joint with a larger number of smaller passes is beneficial because it reduces heat input, residual stress, and shrinkage strains.

1.4.3 Reheat cracking

As described in Section 1.3.3, reheat cracking can occur in alloys that are strengthened by precipitation hardening. The cracking susceptibility is controlled by alloy composition and the PWHT temperature. In general, these types of cracks can form when precipitation occurs over the same time and temperature regimes over which the stress begins to relax. An example of the time and temperature dependence of reheat cracking in Type 347 stainless steel is shown in Fig. 1.15 [21]. These results were obtained by thermo-mechanical simulation (using the Gleeble tester) in which weld metal samples were heated to various temperatures at 75% or 100% of the yield strength, and the time required for fracture was recorded. The closed symbols did not fracture during the test. Note that failure occurs the fastest (i.e. the alloy is most susceptible to cracking) over the temperature range of approximately 750 to 1000 °C. This type of 'C' curve behavior is similar to that exhibited by the precipitation kinetics of NbC in this alloy, and this is the same temperature range over which the carbides form in this alloy.

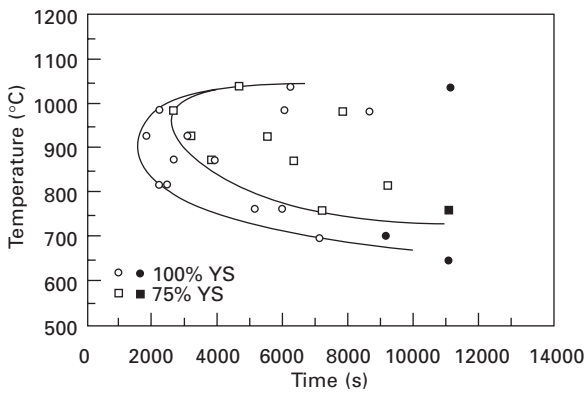

1.15 Time–temperature dependence of reheat cracking in Type 347 stainless steel.

The type of data shown in Fig. 1.15 is useful from a practical standpoint because it identifies the time/temperature ranges for PWHT that should be avoided in order to prevent reheat cracking. Unfortunately, there are very few data available in the open literature for stainless steels that can be used for this purpose because the tests are time consuming. There are also practical difficulties. The use of PWHT below the precipitation temperature may not be adequate for reduction of residual stress. On the other hand, the use of higher temperatures is also problematic because large components will be heated slowly through the precipitation range, which can induce cracking during the heating stage of the PWHT cycle. In applications where this form of failure is a problem, it may be possible to avoid cracking by avoiding any reheating after welding. This would involve removal of the PWHT and/or replacement of multipass welds with a single pass weld.

1.4.4 Hydrogen cracking

Hydrogen cracking in martensitic stainless steels can generally be avoided through control of preheat, heat input, degree of restraint, and welding process. Application of preheating is beneficial for removing residual hydrogen. The use of preheat, combined with higher heat inputs, will also reduce the weld cooling rate. This allows more time for the martensite to temper during the cooling stage, which reduces cracking susceptibility. Joint designs that minimize restraint will be beneficial for reducing cracking tendency, although this is generally not as effective as control of the preheat and heat input. Last, low hydrogen processes, such as gas tungsten arc welding (GTAW) and gas metal arc welding (GMAW), are preferred over higher hydrogen processes such as shielded metal arc welding (SMAW). The flux in SMAW electrodes can also act as sources for hydrogen. Thus, in conditions that require use of this process, lower hydrogen electrodes should be employed and should be heated prior to use.

In some applications an austenitic filler metal can be used for mitigating hydrogen cracking in martensitic stainless steels. This produces a weld metal that is austenitic and has high solubility for hydrogen combined with improved toughness and ductility. The reduced strength of the weld metal needs to be accounted for through design. This approach is often used for 410 martensitic stainless steels, which are welded with type 309L filler metal. In this case, the 309L weld metal provides strength levels that meet those required for the 410 base metal.

1.5 References

1. K.J. Irvine, D.J. Crowe and F.B. Pickering, The Physical Metallurgy of 12% Chromium Steels, *Journal of the Iron and Steel Institute*, Vol. 195, August, 1960, pp. 386–405.

2. W.O Binder and H.R. Spendelow, The Influence of Cr on the Mechanical Properties of Plain Chromium Steels, *Transactions of the American Society for Metals,* Vol. 43, pp. 759–772.
3. H. Baker, Ed. *Alloy Phase Diagrams*, ASM International, Materials Park, OH, 1992, pp. 3–44.
4. A.M. Talbot and D.E. Furman, Sigma formation and its effect on the impact properties of iron-nickel-chromium alloys, *Transactions of the American Society for Metals*, Vol. 45, 1953, pp. 429–440.
5. J.W. Elmer, S.M. Allen and T.W. Eagar, Microstructural Development During Solidification of Stainless Steel Alloys, *Metallurgical and Materials Transactions A*, Vol. 20A, 1989, pp. 2117–2127.
6. T.D. Anderson, M.J. Perricone, J.N. DuPont and A.R. Marder, Phase Transformations and Microstructural Evolution of Mo-bearing Stainless Steels, *Metallurgical and Materials Transactions A*, Vol. 38, No. 1, 2007, pp. 86–99.
7. J.C. Lippold and W.F. Savage, Solidification of Austenitic Stainless Steel Weldments: A Proposed Mechanism, *Welding Journal*, Vol. 58, 1979, pp. 262s–374s.
8. J.C. Lippold and D.J. Kotecki in *Welding Metallurgy and Weldability of Stainless Steels*, Chapter 3, Wiley Interscience, Hoboken, New Jersey, 2005, pp. 19–55.
9. A.L. Schaeffler, Constitution Diagram for Stainless Steel Weld Metal, *Metal Progress,* Vol. 56, 1949, pp. 680–681B.
10. T.A. Siewert, C.N. McCowan and D.L. Olson, Ferrite Number Prediction to 100 FN in Stainless Steel Weld Metal, *Welding Journal*, Vol. 67, 1988, pp. 289s–298s.
11. J.C. Lippold and D.J. Kotecki in *Welding Metallurgy and Weldability of Stainless Steels*, Wiley Interscience, Hoboken, New Jersey, 2005, p. 235.
12. J.C. Borland, Generalized Theory of Super-solidus Cracking in Welds and Castings, *British Welding Journal*, Vol. 20, 1960, pp. 508–512.
13. J.N. DuPont, unpublished research on solidification cracking of stainless steels, Lehigh University, 2002.
14. J.N. DuPont, Microstructural Development and Solidification Cracking Susceptibility in the Fusion Zone of a Stabilized Stainless Steel, *Welding Journal*, Vol. 78, 1999, pp. 253s–263s.
15. J.C. Lippold and D.J. Kotecki in *Welding Metallurgy and Weldability of Stainless Steels*, Wiley Interscience, Hoboken, New Jersey, 2005, p. 153.
16. T.D. Anderson, M.J. Perricone, J.N. DuPont and A.R. Marder, The Influence of Molybdenum on Stainless Steel Weld Microstructures, *Welding Journal*, Vol. 86, No. 9, September, 2007, pp. 281s–292s.
17. J.A. Brooks, A.W. Thompson and J.C. Williams, A Fundamental Study of the Beneficial Role of Delta Ferrite in Reduced Welding Cracking, *Welding Journal*, Vol. 63, 1984, pp. 71s–83s.
18. *ASM Handbook*, Vol. 6, *Welding, Brazing, and Soldering*, ASM International, Materials Park, OH, 1992, p. 92.
19. J.C. Lippold, W.A. Baeslack and I. Varol, Heat Affected Zone Liquation Cracking in Austenitic and Duplex Stainless Steels, *Welding Journal*, Vol. 71, 1992, pp. 1s–4s.
20. J.J. Pepe and W.F. Savage, Effects of Constitutional Liquation in 18-Ni Maraging Steel Weldments, *Welding Journal*, Vol. 46, No. 9, 1967, pp. 411s–422s.
21. W. Lin, J.C. Lippold and S. Luke, Unpublished research performed at Edison Welding Institute, 1994.
22. V. Kujanpaa, N. Suutula, T. Takalo and T. Moisio, Correlation Between Solidification

Cracking and Microstructure in Austenitic and Austenitic-Ferritic Stainless Steel Welds, *Welding Research International*, Vol. 9, 1979, p. 55.
23. O. Hammar and U. Svenson, *Solidification and Casting of Metals*, Metal Society, London, 1979, pp. 401–410.
24. G. Pacary, M. Moline and J.C. Lippold, *A Diagram for Predicting the Weld Solidification Cracking Susceptibility of Pulsed Laser Welds in Austenitic Stainless Steels*, 1990, EWI Research Brief B9008.

1.6 Appendix of terms

Austenite – The face centered cubic (FCC) crystal structure found in stainless steels.

Austenitize – To heat an alloy in order to convert the body centered cubic (BCC) ferrite phase to the face centered cubic (FCC) austenite phase.

Cell cores – The center of the cells. Cells are substructural features that form within the grains during solidification.

Cold working – Increasing the strength of an alloy by plastic deformation.

Dendrite tip under-cooling – The depression of the dendrite tip below the liquidus temperature that can occur under rapid solidification conditions.

Ductile to brittle transition temperature (DBTT) – The temperature in which there is a significant decrease in toughness, typically associated with stainless steels containing ferrite.

Ferrite – The body centered cubic (BCC) crystal structure found in stainless steels.

Gleeble tester – A thermo-mechanical simulation device that permits samples to be exposed to a wide range of thermal and mechanical cycles, either separately or in combination. This device is very useful for simulating the heat-affected zone thermal cycles in welds on relatively large samples.

Hardenability – The ability of an alloy to form 100% martensite during cooling from the austenite phase.

Isopleth section – A vertical section (or 'slice') taken from a ternary phase diagram along the direction of constant composition for one element.

Larsen–Miller parameter – A semi-empirical parameter that is used to exchange the effects of time and temperature on diffusion-controlled processes such as creep and tempering.

Liquidus temperature – The temperature above which the alloy is all liquid.

Martensite – The body centered tetragonal (BCT) crystal structure found in stainless steels, usually containing supersaturated carbon.

Martensite start temperature – The temperature at which martensite begins to form from austenite during cooling.

Maximum solid solubility – The maximum amount of solute that can be dissolved by a particular solvent.

Miscibility gap – A region of the phase diagram in which two phases form with similar crystal structures but different compositions.

Primary solidification mode – The phase that forms first from the liquid during solidification.

Sigma – a Cr and/or Mo rich intermetallic phase found in stainless steels that is hard and brittle.

Solvus temperature – The locus of temperature/composition points on a phase diagram that separates a single phase solid solution field from a two phase field.

Solution annealed – Heating of an alloy in order to dissolve the solute elements.

Tempered martensite – Martensite that has been heated in order to promote formation of carbides. The formation of carbides leads to relief of lattice strain that occurred from super-saturated carbon, thus leading to a reduction in hardness and strength and an increase in toughness and ductility.

Terminal solidus temperature – The temperature below which the alloy is all solid.

Varestraint test – A test used to determine the susceptibility of engineering alloys to solidification cracking. In this test, a sample is strained in a controlled manner during solidification of a weld in order to induce cracking. The extent of cracking is typically quantified using a stereomicroscope or light optical microscope, and is quantified by the total crack length and/or maximum crack length on the sample.

2

Robust welding technologies for ferrous alloys

A K BHADURI, S K ALBERT and B RAJ,
Indira Gandhi Centre for Atomic Research, India

Abstract: Weldability issues of two major classes of materials, viz. austenitic stainless steels and chromium-molybdenum ferritic steels, have been discussed. While for the austenitic stainless steels the issue of hot cracking in the weld metal and heat-affected zone have been addressed, for the Cr–Mo steels the issues of hydrogen assisted cracking and optimisation of post-weld heat treatment for achieving required weld metal toughness have been dealt with. These weldability studies led to the development of special-purpose welding electrodes of E316-15 and modified 9Cr–1Mo steel. Also, the development of two dissimilar metal weld joints, viz. transition metal joints between austenitic stainless steel have also been discussed in detail. Finally, technology development towards hardfacing of austenitic stainless steel components with a nickel-base alloy has been dealt with, which encompasses identification of suitable hardfacing alloy as an appropriate hardfacing technology for industrial-scale implementation.

Key words: weldability, austenitic stainless steels, modified 9Cr–Mo steel, dissimilar metal welding, hardfacing, welding elecrodes.

2.1 Introduction

Weldability of two major classes of materials is of concern with regard to fabrication. These are (i) austenitic stainless steels (SS) and (ii) chromium–molybdenum ferritic steels. In the case of austenitic SS, e.g. in Alloy D9 and to a lesser extent for 316L(N), hot cracking in the weld metal and heat-affected zone (HAZ) is a major issue. In the case of Cr–Mo steels, e.g. modified 9Cr–1Mo (grade 91), the weldability problems are related to hydrogen-assisted cracking (HAC) as well as optimisation of post-weld heat treatment (PWHT) for achieving required weld metal toughness. Weldability studies were carried out on two austenitic SS, D9 and 316L(N), to quantify solidification (weld metal) cracking and HAZ cracking as a function of composition using Varestraint hot cracking tests supplemented by detailed microstructural studies. It was also required in the course of the work to examine criteria relating cracking in the Varestraint test to actual weld behaviour. Weldability studies on grade 91 were conducted in two phases. In the first phase, the objectives were to determine critical preheat temperature and hydrogen levels to avoid HAC. In the second, the objective was the development of shielded metal arc (SMA) welding consumables to obtain

weld metal of adequate impact toughness and microstructural characteristics. Industrial manufacturers of welding electrodes were developed for manufacturing grade 91 and 316L(N) welding electrodes. In order to predict the delta-ferrite content from chemical composition, a generalised Bayesian Neural Network (BNN) model has also been developed.

Transition metal joint (TMJ) between austenitic SS and Cr–Mo steel is used widely in steam generators of power stations. In certain applications, steam generator (SG) pipes of grade 91 are welded to 316L(N) SS pipes from Intermediate Heat Exchanger (IHX)[1], for which an improved trimetallic TMJ of austenitic SS/Alloy 800/Cr–Mo steel has been developed, based on international experience. Also, for the dissimilar metal weld (DMW) joint between A48P2 carbon steel (CS) and 316L(N) SS, the soundness and life of DMW joint was studied [2] through investigations on susceptibility of the joint to hot cracking, effect of partially mixed zone (PMZ) and unmixed zone (UMZ) on joint properties, impact properties of weld metal, weld/ base metal interfaces and CS-HAZ, and residual stress distribution in as-welded condition and after exposure at 453 K for 120 h (which is equivalent to cumulative exposure over an operating life of 40 years).

A number of austenitic SS components may encounter severe wear in the form of adhesive wear, abrasive wear due to sliding movement, and erosion due to high velocity liquid metals such as sodium. The self-welding tendency increases to a limited extent with rising temperature [3]. Hard coatings required for high temperature wear resistance were developed over several stages of technology development. The first stage was identification of materials, process and technology appropriate for each relevant component. The second stage involved laboratory-scale development, and in the third stage industrial-scale implementation was carried out. Simultaneously, data had to be generated on performance of the coatings for ensuring compliance with design criteria. For the major part of the requirements, the efforts have succeeded in taking the technologies to the third stage of development. The location of these parts and their accessibility also influence the selection of hardfacing alloy. For components in which the radiation dose is very high and accessibility is nil, activation products formed in the hardfacing alloys (e.g. Co^{60} in the case of stellites) will result in additional activity of the already active primary circuit. In the case of certain components that should be accessible for maintenance, such induced activity should be minimised.

2.2 Weldability of austenitic stainless and other steels

Various codes for fabrication such as RCC-MR and ASME section III provide for hot cracking tendency of austenitic SS during welding by either specifying limits on ferrite content in weld metal or by simple usability tests. RCC-MR

specifications for welding filler materials make a distinction for ferrite content based on service temperature. As per RS 3334, 5–15% ferrite is specified for components operating below 648 K. For components operating above this temperature, these limits do not apply and the user must specify ferrite limits. Weld ferrite content is determined by either Schaeffler or DeLong diagram or by magnetic saturation method. When ferrite content of the deposited weld is below 5%, RS 2536 stipulates a groove cracking test for qualification of welding consumables as per RS I 900 or 930. The test consists of depositing (undiluted) five lengths of weld metal (50 or 60 mm length) within an 80° groove. The deposits are then examined for cracking using liquid penetrant test. Filler materials or electrodes must exhibit freedom from cracking, including crater cracking, to qualify. ASME section III NB-2433.2 does not make a distinction based on service temperature but accounts for the hot cracking tendency by specifying a minimum ferrite level as per WRC-92 ferrite diagram. Similar criteria have been recommended by Lundin *et al*. [4] for nuclear grade SS including 316L(N). Delta-ferrite is restricted in weld metals intended for elevated temperature service because it results in poor creep properties due to its microstructural instability under service conditions.

As discussed above, the code stipulations rely on conservative tests and additional requirements such as ferrite level specification to provide for resistance to cracking susceptibility. However, the codes do not adequately address the necessary tests for hot cracking behaviour of weld metals intended for high temperature service in several areas. The first is the possibility of HAZ cracking in the base metal and multipass stainless steel weld metal that is not taken into account in the codes. The second drawback is that there are no guidelines for weldability evaluation of fully austenitic material such as D9. There was therefore a need for detailed weldability evaluation to obtain clear quantitative guidelines for excluding the possibility of cracking while at the same time avoiding excessive conservatism.

2.2.1 Weldability of modified 9Cr–1Mo steel

The major technological issues in weldability of grade 91 steel are determining the critical preheat temperature to avoid HAC and achieving adequate toughness in the weld metal. Though ASME code, section IX, has stipulated PWHT at a minimum of 977 K for 1–2 h for grade 91 steel, it does not address the issue of preheat temperature. On the other hand, developers of this alloy recommended [5] a mandatory minimum preheat temperature of 477 K. The job thickness, hydrogen content of the electrode, carbon equivalent and weld heat input need to be considered together to determine the preheat temperature required to prevent cold cracking. International experience [6,7] shows that the critical preheat temperature is a sensitive function of composition, but the results of various studies are not conclusive.

Achieving good toughness in the weld metal, especially in those produced by processes that involve fluxes (like shielded metal arc welding, SMAW, submerged arc welding, SAW, and flux-cored arc welding, FCAW) has been an uphill task ever since the development of modified 9Cr–1Mo steels. During the initial stages of development it was difficult to achieve good toughness in the weld metal with a composition optimised for the plate or pipe materials. Systematic studies on the effects of various alloying elements on weld metal toughness revealed that Ni is beneficial while Nb and Si are detrimental. Accordingly, Ni was added to the welding consumables, and Nb and Si were reduced [8]. Further, an upper limit for the total of Ni + Mn was also recommended. In the initial stages of electrode development for SMAW, it was found that the desired properties could not be achieved when synthetic electrodes were used [9].

For steels with Cr > 9 wt%, the microstructure of weld can contain a small volume fraction of delta-ferrite in both the HAZ and the weld metal. Two formulas for predicting volume fraction of delta-ferrite in welds of these steels have been reported in the literature [10]. The toughness of both HAZ and weld metal is found to decrease with an increase in volume fraction of delta-ferrite. Accordingly, compositions of both base metal and welding consumables are optimized [11] to have no delta-ferrite in the weld metal or HAZ.

2.2.2 Dissimilar metal welding

The austenitic SS/Cr–Mo steel TMJ has long been recognised to pose a potential problem [12,13], because of large thermal stresses generated owing to the different thermal expansion characteristics of the two steels. Thermal cycling during power plant operation plays a major role in premature service failure of this joint. Although similar failures are reported in creep-rupture tests [14,15], there is general agreement that in operating plants, stresses responsible for failure of this TMJ are due to thermal cycling that occurs during plant start-ups and shut-downs [16]. Laboratory test results [14,17,18] and service experience [19–21] have shown that a significant improvement in service life of TMJ can be achieved by using Ni-base welds instead of austenitic SS welds [20,22]. However, service failures of TMJ with Ni–base welds have also been reported [19,20]. Indeed, Ni–base welds buy more time, but eventually fail before the plant's design life. Among various approaches attempted [23] for development of improved TMJs, one approach is a trimetallic TMJ with transition piece having coefficient of thermal expansion (CTE) intermediate to the ferritic and austenitic steels. This provides a more gradual change in CTE and consequent decrease in magnitude of stresses from thermal cycling [24]. Alloy 800, the most attractive choice for the transition piece, reduces hoop stress near the root of the ferritic steel by 37% [24,25], besides providing excellent resistance to oxidation and creep at elevated temperatures [24].

A box-type structure, made of A48P2 CS specified in RCC-MR code, consists of a bottom plate and a top plate with the space between them being partially filled with concrete. This box-type structure is a massive structure of 12.9 m diameter, 1.8 m height and weighs about 650 tonnes. The fabrication of the box-type structure involves a DMW joint between A48P2 CS and 316L(N) SS plates at the bottom of the structure. The thickness of the plate was chosen to be 30 mm from the consideration that stress-relieving heat treatment is not mandatory for this thickness as per various fabrication codes. Austenitic SS fillers are commonly used for this DMW when operating temperatures do not exceed 648 K. The commonly used welding consumable E309, containing 12–14%Ni and 22–25%Cr, was chosen for this A48P2/316L(N) SS joint. This high alloy content in E309 consumable is sufficient to prevent the formation of martensite or bainite in the weld even after dilution by the base metal, and also to retain some residual amount of delta-ferrite for minimising the possibility of hot cracking during welding under severe restraints. During the fabrication of a similar structure [26,27], a stress-relieving heat treatment was given to all the shop-fabricated parts to ensure dimensional stability of the components, even though the plate thickness involved in most of the weld joints was only 35 mm, i.e. they qualified for exemption from stress-relieving heat treatment as per the applicable codes. In this case, only the site-integration weld joints were not subjected to stress-relieving heat treatment.

Industrial manufacturers of welding electrodes have been developed for manufacturing 316L(N) welding electrodes. For prediction of delta-ferrite content from chemical composition, a generalised BNN model has been developed, which has the best accuracy of prediction among all predictive models currently available (including WRC-1992 diagram). Manufacturers have also been developed for manufacturing grade 91 welding electrodes.

2.2.3 Hardfacing of austenitic stainless steel components

Ni–base hardfacing alloys (e.g. Colmonoy) have already been used with satisfactory results. Tests on six liquid sodium pumps, with 304 SS bearings hardfaced with Colmonoy 6 and the shafts/journals hardfaced with Colmonoy 5, operating at 748–798 K have accumulated 20 000 hours for each pump without failure of the bearing area [28]. In some applications Colmonoy-faced sleeves and shafts have been used in the hydrostatic sodium-lubricated pumps [29]. Bearing operation in almost all cases has been satisfactory, but all operations were at temperatures below 813 K. However, a seizure occurred in one of the cases in an intermediate (secondary) pump before attaining an operating temperature of 823 K. The cause of the failure is not known. Another primary pump seizure occurred sometime later and its probable cause was

lack of wear resistance in the bearing material. The temperature of the pumps was then limited to 723 K. All previous prototype bearings were made of Stellite but for these particular pumps, a change to Colmonoy was made. The use of the proven material, Stellite, might have eliminated the seizures [29].

2.3 Weldability evaluation of austenitic stainless steels

Weldability evaluation of austenitic SS usually involves application of strain or some form of restraint during welding and assessing the deposited weld for cracking [4]. Weldability assessment of austenitic SS was done using the Varestraint test [5]. Evaluation using this test is done using criteria such as total crack length (TCL), maximum crack length (MCL) or brittleness temperature range (BTR). BTR is essentially the temperature range over which the weld metal is prone to cracking during solidification due to the presence of low melting eutectics. It is derived from the MCL by converting length into temperature using the centreline cooling curve and welding speed.

2.3.1 Weldability of austenitic stainless steels D9 and 316L(N)

316(N) and 316L base metals, three heats of D9, and four modified 316 weld metal compositions were evaluated for solidification cracking as well as HAZ cracking. The compositions are given in Table 2.1. The D9 alloys differed among themselves only in the level of Ti. The 316L and 316L(N) were used to study the effect of N addition, by controlled additions through the shielding gas during Varestraint testing. N was varied in the range 0.04–0.19%. Varestraint test specimens were prepared from the solution annealed blanks of 3 mm nominal thickness. Chemical analysis of weld metal composition for all elements except nitrogen was done by standard wet chemical techniques on chips extracted from the weld metal. Nitrogen analysis was obtained using a Leco nitrogen analysis of the weld chips.

2.3.2 Hot cracking tests

The specimens were prepared from sheet and tested using longitudinal Varestraint and trans-Varestraint tests. In the longitudinal Varestraint test, specimens of dimensions $127 \times 25 \times 3\,mm^3$ were used and autogenous gas tungsten arc (GTA) weld beads were deposited along the length as shown in Figs 2.1(a) and (b). When the weld puddle reached the middle of the specimen, strain was applied pneumatically by bending rapidly over a ram of fixed radius. The straining was completed within 15 milliseconds, so that the weld puddle was essentially ‘frozen’ in position. The strain experienced by the

Table 2.1 Chemical compositions of the stainless steel weld metals tested (wt%)

Code	FN*	C†	Mn	Cr	Ni	Si	Mo	N†	P†	S†	Other
316L(N)	0.7 ± 0.07	0.03	1.45	16.8	11.1	0.53	2.06	0.073	0.031	0.001	0.27 Cu
316L	2.7 ± 0.2	0.029	1.8	17.0	11.9	0.7	2.25	0.036	0.035	0.012	–
D9-A	0	0.052	1.5	15.1	15.0	0.5	2.26	0.066	0.011	0.002	0.21 Ti
D9-B	0	0.051	1.5	15.0	15.1	0.5	2.25	0.068	0.011	0.002	0.32 Ti
D9-C	0	0.052	1.5	15.1	15.3	0.52	2.26	0.064	0.012	0.002	0.42 Ti
316-A	3.9 ± 1	0.049	1.1	18.8	12	0.44	2.5	0.067	0.026	0.012	
316-B	4.8 ± 1.5	0.044	1.2	18.4	11.4	0.36	2.5	0.091	0.025	0.015	
316-C	5.0 ± 1.6	0.043	1.3	18.7	11.0	0.36	2.5	0.097	0.025	0.016	
316-D	3.9 ± 1	0.046	1.3	18.4	10.5	0.33	2.5	0.12	0.027	0.015	

* Standard deviation is indicated beside the FN.
† Accuracy of analysis 10 ppm.

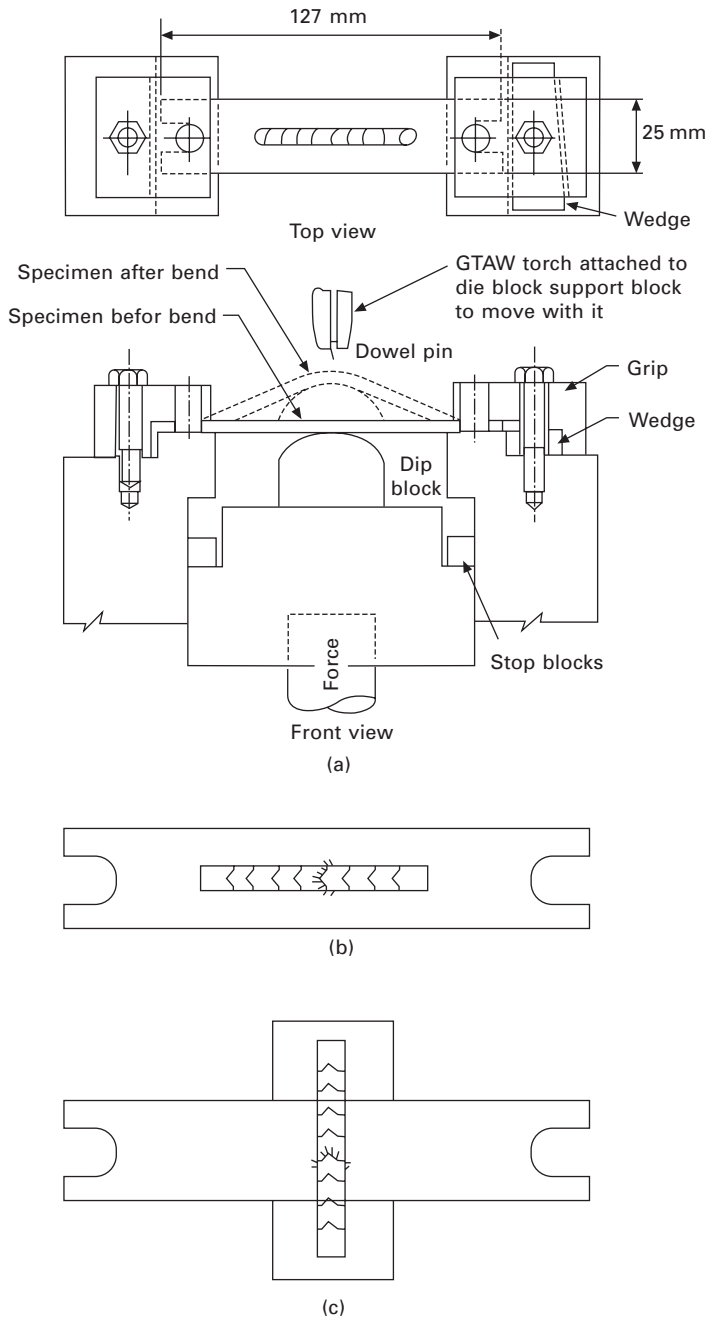

2.1 Schematic diagram of the Varestraint test equipment: (a) equipment, test procedure and weld orientation in (b) longitudinal mode and (c) trans-Varestraint mode.

specimen is related to the radius of the die block by the relation $e \cong t/2r$ where e is the strain in the outer fibre, t the specimen thickness and r the radius of the die block. In the trans-Varestraint test (TVT), the weld bead was applied transverse to the specimen length (Fig. 2.1c). Run-on and run-off tabs were attached by tack welding on the underside so that the weld bead was long enough to ensure thermal equilibrium at the instant of straining. Welding conditions used for testing were current 100 A at 12 V, welding speed 4.2 mm s^{-1}, and shielding gas flow rate of 12 l min^{-1}.

To evaluate cracking in the HAZ, in addition to the fusion zone, a three-bead test technique [5] was followed. The test weld bead is applied overlapping a previously deposited weld bead. Cracking in the base-metal HAZ and weld-metal HAZ occurring on either side of the test weld bead was then evaluated. BTR measurements were derived from maximum crack lengths obtained in the Varestraint test. The variation of BTR as a function of strain for D9 and 316L(N) stainless steel base metals, and the modified 316 weld metals are shown in Figs 2.2(a) and (b), respectively [3,6]. It is well known that BTR and solidification cracking are strong functions of the solidification mode in stainless steels. Therefore, the cracking data are shown as a function of WRC Cr_{eq}/Ni_{eq} ratio in Fig. 2.3. In Fig. 2.3, data for D9, 316L(N) and modified 316 weld metals are shown. Also represented are data corresponding to nitrogen-added 316L or 316L(N) base materials in the range 0.04–0.19%N. Some data are also shown for nickel-added compositions for comparison. The BTR values are low for high Cr_{eq}/Ni_{eq}, i.e. above a value of 1.3, which corresponds to a ferritic solidification mode. Stainless steel base and weld metals solidifying in the FA (ferritic/austenitic) mode of solidification have a BTR of 30 K or lower and are highly resistant to solidification cracking. The cracking tendency increases with decreasing Cr_{eq}/Ni_{eq} ratio, i.e. decreasing ferrite content, while the solidification mode changes to AF (austenitic/ferritic) and to A (fully austenitic). The modified 316 weld metal is observed to be in the safe regime with FA solidification mode. However, the D9 alloys being fully austenitic can be considered to be highly susceptible to solidification cracking [7].

Solidification cracking, however, is also a function of the level of impurity elements, S and P, and minor elements such as Ti and Si. Although a direct correlation between the composition, impurity levels and cracking is not available at present, the diagram of Kujanpaa *et al*. of Cr_{eq}/Ni_{eq} vs. P + S content can be used (the Cr and Ni equivalents correspond to that of Hammar and Svensson) [10]. In this diagram (Fig. 2.4), susceptible compositions lie in the region of $Cr_{eq}/Ni_{eq} < 1.5$ and P + S > 0.015 wt%. Much higher impurity levels could be tolerated for higher Cr_{eq}/Ni_{eq} ratios and such compositions were not susceptible to cracking. In Fig. 2.4, cracking data for D9 and 316L(N) stainless steels have been shown in terms of Hammar–Svensson (H-S) Cr_{eq}/Ni_{eq} ratio and P + S contents. The BTR values at 4% strain corresponding to each material are indicated within parentheses beside

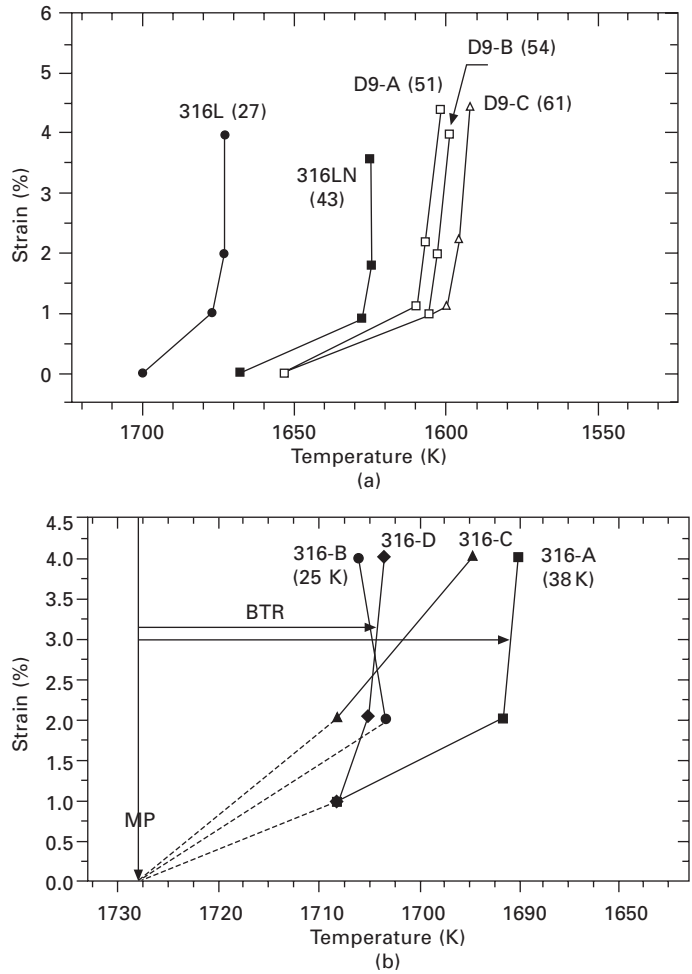

2.2 Brittleness temperature range (BTR) of stainless steel: (a) D9 and 316L(N) base metal [6], (b) modified 316 weld metals [9] (0.07–0.12 N) (BTR values in parentheses).

each datum point. The important feature here is that unstabilised stainless steels fit reasonably well into the diagram, with low BTR compositions finding a place in the less susceptible regions and the high BTR 304L-A and D9 alloys are placed in the 'highly susceptible' portion. On the other hand the stabilised stainless steels 321 and 347 show much higher susceptibility for equivalent Cr_{eq}/Ni_{eq} ratio and impurity content, compared with the unstabilised varieties. This is presumably because of the potent influence of Ti and Nb on the cracking tendency that is not taken into account in this diagram. Similarly, the D9 alloys, despite having low P + S (0.014 wt%), show high susceptibility, which can be attributed to the presence of Ti.

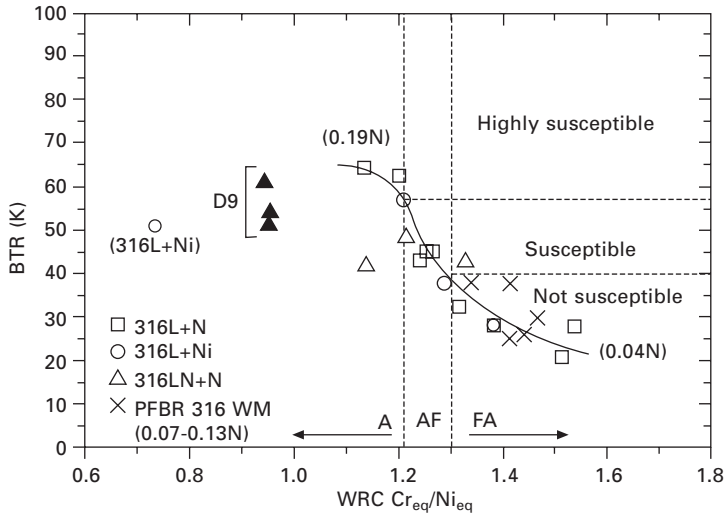

2.3 Solidification cracking in D9, 316L(N) and modified 316 weld metals as a function of WRC Cr_{eq}/Ni_{eq} ratio; experimentally observed solidification mode boundaries are indicated (A – austenitic, AF – austenitic/ferritic and FA – ferritic/austenitic).

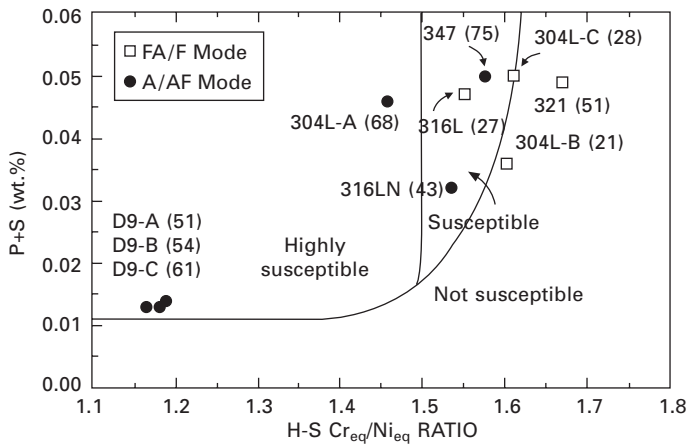

2.4 The modified Suutala diagram showing hot cracking behaviour as a function of Hammar–Svensson Cr_{eq}/Ni_{eq} and P + S content.

2.3.3 Effect of titanium and nitrogen on hot cracking

Specifically, the effect of Ti and N on cracking in D9 and 316L(N) is of interest. Extensive studies have been carried out on fusion zone and HAZ cracking in these materials [7]. Investigations of cracking in D9 welds showed that the cracking is due to segregation of Ti, S, N and C to the grain boundaries. A photomicrograph of hot cracks and segregation in a D9 weld metal is

shown in Fig. 2.5. Electrochemical extraction followed by X-ray diffraction analysis revealed that the segregate phases present in D9 were TiC, $TiC_{0.3}N_{0.7}$, and carbosulphides Ti_2CS and $Ti_4C_2S_2$, which apparently form eutectics with austenite and promote cracking. The relative amount of these phases increased with increasing titanium content, which was particularly high above a Ti/(C + 0.857N) ratio of 3. The weld metal tends to absorb a high level of N (about 200 ppm) during welding even with high purity gas, over and above the N level present in the base material. Since N participates in cracking, it is relevant to represent the effect of Ti in terms of Ti/(C + 0.857N) ratio (the factor 0.857 represents the ratio of the mass numbers of carbon and nitrogen), as shown in Fig. 2.6. It is observed from Fig. 2.6 that while Ti

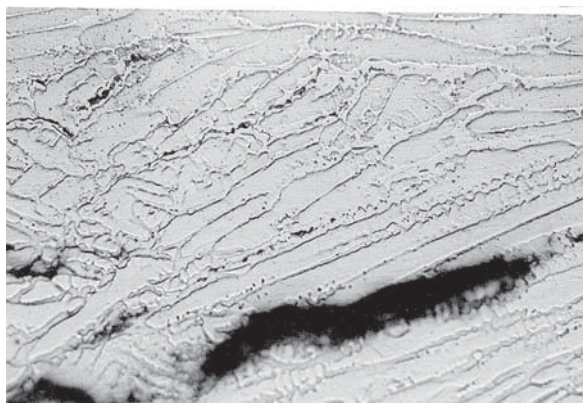

2.5 Microstructure of D9-B weld metal showing cracking and segregates along inter-dendritic regions and crack extensions.

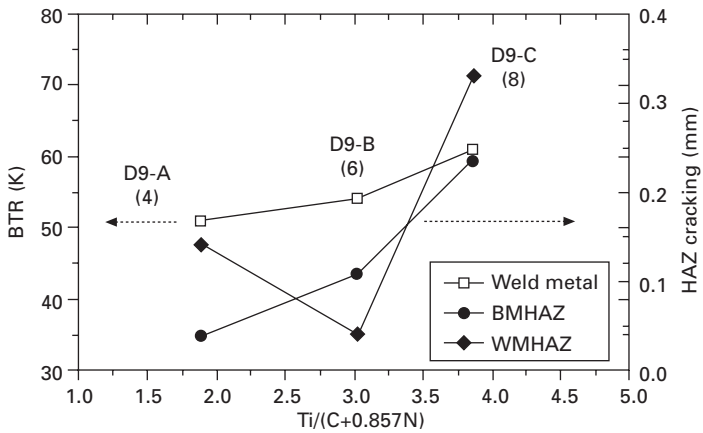

2.6 Effect of Ti/(C + N) ratio on cracking in D9 weld metal, base metal and weld metal HAZ (nominal Ti/C ratio given in parentheses; HAZ cracking follows right axis).

does not have a great influence on fusion zone cracking, the increase in HAZ cracking with Ti/(C + N) is significant.

The nitrogen effect on cracking in 316L(N) base metal [8] as well as modified 316 base metals [9] is well represented in Fig. 2.3. In Fig. 2.3, data for two types of weld are shown; N-added 316 and 316L(N) with N in the range 0.04–0.19%N, and modified 316 weld metals in which N was varied (0.07–0.12%N) while maintaining Cr_{eq}/Ni_{eq}. The essential observations from these data are that N has no detrimental effect on cracking if Cr_{eq}/Ni_{eq} is maintained to obtain a favourable solidification mode in the weld metal. N could be detrimental if ferrite is absent or solidification mode becomes austenitic (A mode) and when the S level is > 0.01%. This situation is possible during autogenous welding of the base metal or when HAZ cracking is envisaged. During structural welding of components the risk of cracking during autogenous welding is small due to stringent specifications, particularly for impurity elements. HAZ cracking has been shown to be a strong function of ferrite content or ferrite potential of the underlying material, but is likely only in extremely high restraint situations. Both these factors are therefore not a serious concern during structural welding.

2.3.4 Hot cracking assessment criteria

In actual welds, the amount of strain experienced by the weld metal is difficult to estimate in view of complex geometric and thermal conditions. Hence a controlled strain applied on a geometrically simple specimen is preferred for evaluation of cracking tendency. Several tests exist that satisfy the above condition, such as the Varestraint test, the PVR test (**p**rogrammierter **V**erformungs**r**isstest) and the Sigmajig test. These tests use any of several criteria such as total crack length, maximum crack length, strain threshold, strain rate threshold and brittle temperature range. While these criteria are very useful for comparison, direct application of hot cracking test data to actual fabrication is possible only if the restraint in the latter case can be quantified.

Application of Varestraint test criteria such as crack lengths and BTR to practical welding situations is complicated by the fact that in the actual case, strain, strain rate and stress are difficult to quantify as a function of weld geometry. Tests such as the Y-groove test [11] or the circular patch test [7] or actual weld joints have been used for correlation with Varestraint test results. However, there are reports that ranking based on BTR is more reliable than TCL from the Varestraint test. A review of the literature thus shows that there is no universal choice of criteria for cracking assessment when applied to actual welding situations. Investigations at the authors' organisation (IGCAR) show that the TCL parameter is subject to variations because of weld bead geometry, while BTR is not influenced by these factors that are related to

fluid flow effects in the weld pool. It has been shown [6] (Fig. 2.7) that if TCL is normalised using the weld width, the correlation with BTR is very good. the BTR parameter has been widely used in Japan for the past three decades [30].

It is observed from Fig. 2.3 that the modified 316 weld metal with limits of ferrite content of 3–7 FN is located in the FA mode of solidification and would essentially be free from hot cracking in the weld metal and HAZ. However, problems could arise during welding of D9, and welding conditions may require careful optimisation.

2.4 Weldability of modified chromium–molybdenum ferritic steels

Although modified 9Cr–1Mo (grade 91) steel is highly weldable, the major concerns in its fabrication are [31,32]: (i) HAC, also referred to as cold cracking or delayed cracking, and (ii) achieving good toughness in the weld metal when the joint is made using the SMAW process. The major source of hydrogen is the moisture present in the welding consumables that dissociates into hydrogen and oxygen in the welding arc. Cracking is caused by the complex interaction of dissolved hydrogen atoms with the defects in the crystal lattice. In addition to hydrogen, a susceptible microstructure and sufficient restraint are also necessary for cracking to occur. This section reports evaluation of HAC susceptibility of grade 91 steel using the UT-

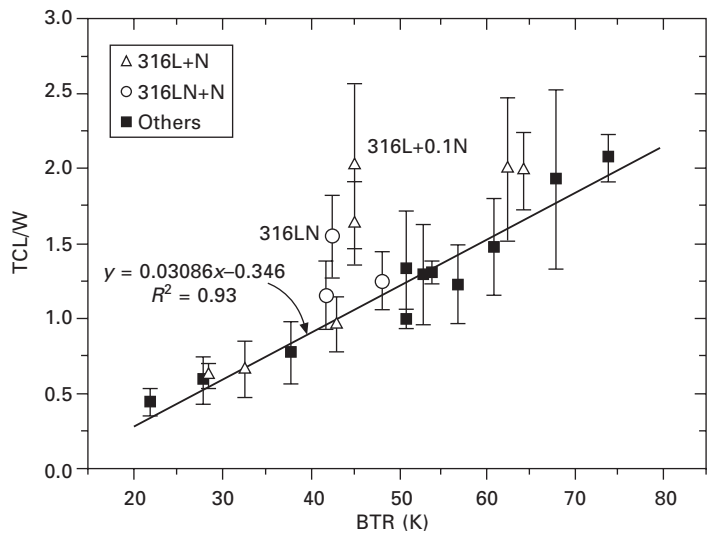

2.7 Correlation between normalised total crack length (TCL/W, W – weld width) and BTR criteria.

Modified Hydrogen Sensitivity Test and these results are compared with that of (plain) 9Cr–1Mo steel.

2.4.1 Hydrogen-assisted cracking studies

The University of Tennessee-modified Hydrogen Sensitivity Test was carried out [33,34] using autogenous bead-on-plate weld along the length of the 45 × 15 × 3 mm^3 blank of grade 91 steel in normalised (1333 K/25 min) and tempered (1023 K/1 h) condition using the gas tungsten arc welding (GTAW) process. Hydrogen content in the shielding gas was varied from 0.25 to 1.5% to obtain different levels of hydrogen content in the weld metal. The specimen was held in a copper fixture that had the facility for preheating to the desired temperature. After welding in the 1G position, the specimen was allowed to cool to room temperature and then strained in a fixture, as shown in Fig. 2.8. The nominal augmented strain ε on the surface is given approximately as ε ≈ $t/2R$, where t is the specimen thickness and R the bending radius. Die blocks of different radii were used to produce different strain levels varying from 0.5 to 4%. The susceptibility to cracking was determined by observing cracks formed on the specimen surface strained in tension for 24 h. Visual examination for cracking was carried out using a stereomicroscope at 60×. Crack surfaces were observed after heat tinting the specimen at 973 K for 15 minutes and opening the crack by hammering after cooling to liquid nitrogen temperature. Preheat temperature above which no specimen cracked for given

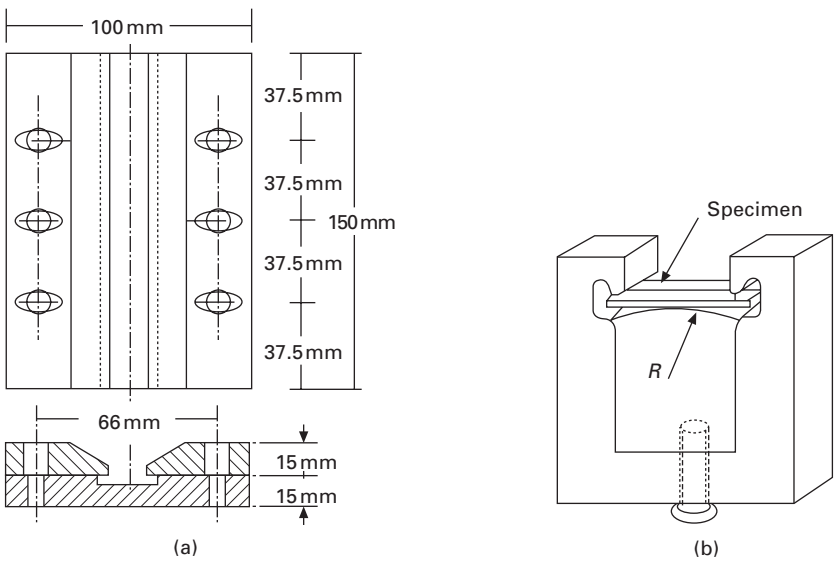

2.8 Setup for UT-modified hydrogen sensitivity test: (a) welding fixture (shown without preheating provision) and (b) straining jig.

hydrogen level and strain levels was chosen as the critical preheat temperature for that condition.

Effect of hydrogen and strain on critical preheat temperature

Specimens of grade 91 steel tested without hydrogen in the shielding gas did not show any cracking at room temperature. However, those tested with 0.25 vol.% H_2 in the shielding gas cracked without preheat. In the case of 9Cr–1Mo steel, no cracking was observed for the specimens prepared without preheat even with 0.5 vol.% H_2 in the shielding gas. The higher susceptibility of grade 91 steel to HAC than 9Cr–1Mo steel is thus established.

The variation of critical preheat temperature with strain is shown in Fig. 2.9(a). It is clear that under identical testing conditions critical preheat temperature is always higher for grade 91 steel than for the 9Cr–1Mo steel. It may also be noted that the critical preheat temperature increases in a stepped manner with increase in hydrogen content. This can be explained based on the minimum requirement of diffusible hydrogen to be present in the steel to cause cracking. Whatever the amount of hydrogen entering the weld metal, cracking occurs only when the preheat fails to remove the diffusible hydrogen below this threshold limit. The stepped variation as a function of hydrogen content is due to the existence of hydrogen traps in the microstructure, which release diffusible hydrogen in a stepwise manner with change in temperature.

The variations of critical preheat temperature with strain for different hydrogen contents in the shielding gas is shown in Fig. 2.9(b). For grade 91 steel, critical preheat temperature increased from 373 to 473 K with increase in strain for 0.25 vol.%, while the corresponding increase for 0.5 vol.%, hydrogen was from 398 to 498 K. However, for 9Cr–1Mo steel, this variation was less significant. For higher hydrogen levels, the critical preheat temperature at higher strain levels for grade 91 steel was above 523 K, the maximum temperature achievable in the experimental setup.

Role of composition and welding conditions in HAC

The reasons for the higher HAC susceptibility of grade 91 over 9Cr–1Mo steel are not very clear, although in general, the phenomenon is related to the degree of hydrogen trapping in the microstructure. The major difference between these steels is only in the micro-alloying elements Nb and V in the modified version, which imparts superior creep properties. It has been reported that in Cr–Mo steel with 2–3 wt% Cr, Nb and V do not significantly influence the cracking behaviour [35]. However, recent studies have shown wide variation in the critical preheat temperature for 9Cr–1Mo steel owing to minor variation in the composition [31]. Increase in Si content in the steel has been shown

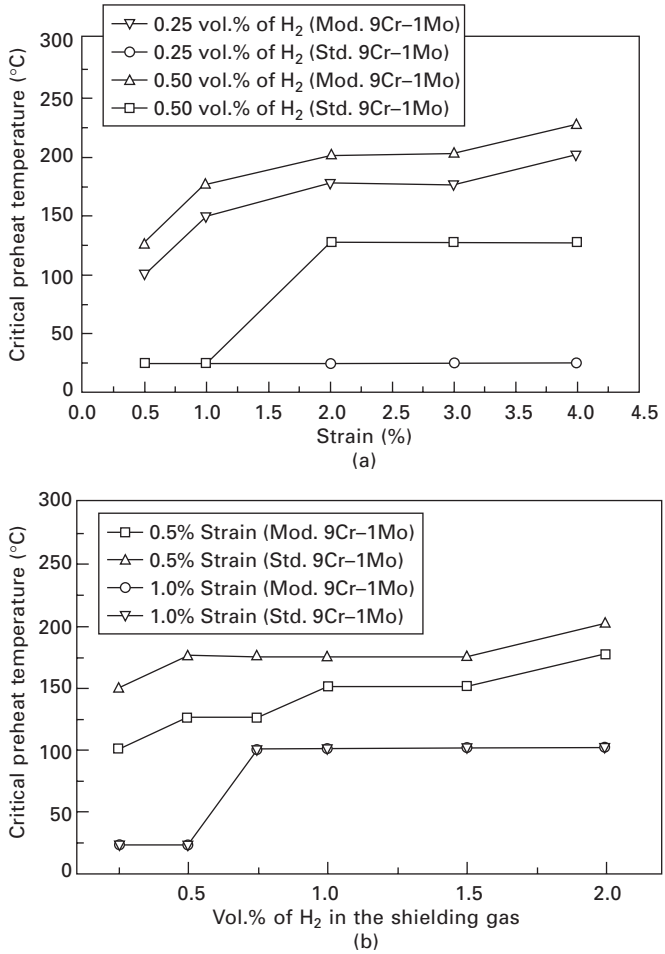

2.9 Critical preheat temperature for preventing HAC in grade 91 steel welds, as a function of (a) strain and (b) hydrogen in the shielding gas (the data points at 1% strain for both materials overlap each other).

to increase the HAC susceptibility. Further, the higher strength of grade 91 steel could also contribute to its increased susceptibility to cracking.

The lowest level of hydrogen used in our study, viz. 0.25 vol.% of hydrogen, which corresponds to about 1 ml hydrogen/100 g of weld metal, is much lower than the permissible hydrogen level of 4 ml/100 g of weld metal for low hydrogen electrodes (as per ASME section II-C SFA 5.5). The fact that HAC is caused even with such a low level of hydrogen in the case of grade 91 steel clearly shows that sufficient preheating and post-heating, baking of electrodes, etc., should be properly employed during welding of this class of

steel with SMAW process. Even while welding with GTAW process, it is advisable to ensure the quality of the gas so that the moisture content is kept sufficiently low. It must however, be noted that the behaviour of weld metal deposited by SMAW will be influenced in addition by the inclusion content, and other compositional variations. Data on SMA weld metal will be generated as and when the consumables become available.

2.4.2 Effect of composition and PWHT on toughness of SMAW metal

Grade 91 steel of 12 mm thickness was welded using 3.15 mm diameter (three different batches) and 5.0 mm diameter (one batch) welding consumables, and with 1.6 mm diameter filler wire (one heat). The chemical compositions of the base metal and weld metals designated as E1 (3.15 mm diameter synthetic electrode), E2 (3.15 mm diameter non-synthetic electrode), E3 (5 mm diameter synthetic electrode), E4 (3.15 mm diameter non-synthetic electrode) and FW (1.6 mm diameter filler wire) are given in Table 2.2. All these electrodes were obtained from different manufacturers.

All the weld pads were fabricated using a single V groove angle of 65°, with root gap of 3 mm for SMAW and 2 mm for GTAW process. The welding parameters used are given in Table 2.3. All electrodes were baked at 573 K for 1 h prior to welding. All the test pads were cut into two halves and subjected to PWHT at 1033 K for 3 h and 8 h. All the weld pads were subjected to X-ray radiography after PWHT and found to be defect-free except in a few regions. Specimens for metallography and hardness distribution measurement were taken at different heat-treated conditions and were studied using optical microscopy and microhardness measurement. Full-size Charpy V-notch (CVN) impact specimens were fabricated as per ASTM E23, with the V-notch located in the weld centreline along the direction of welding.

Microstructure and hardness of grade 91 weld metal

The microstructure of the grade 91 weld metals consists of untempered martensite in the as-welded condition, with the E3 weld metal also containing a significant amount of delta-ferrite in the weld metal. On PWHT, martensite gets tempered, with the martensite progressively losing its acicular features with an increase in the duration of PWHT, and the lath and lath boundary get decorated with precipitates. From Table 2.2 it can be seen that E3 weld metal has the highest Cr_{eq} (8.86) among the weld metals, causing more delta-ferrite to be retained in this weld metal. Delta-ferrite has been reported to decrease toughness and creep properties of grade 91 weld metal [36,37].

The microhardness distribution across the weld/base metal interface shows that PWHT at 1033 K for 3 h and 8 h reduces the hardness of the weld metal

Table 2.2 Chemical composition (in wt%) of grade 91 steel base metal, and SMAW and GTAW deposited weld metals

Elements	Base metal	SMA weld – electrode diameter and type				GTA weld 1.6 mm filler wire (FW)
		3.15 mm; synthetic (E1)	3.15 mm; non-synthetic (E2)	5 mm; synthetic (E3)	3.15 mm; non-synthetic (E4)	
C	0.097	0.09	0.062	0.06	0.085	0.065
Cr	9.29	9.00	9.0	9.8	8.30	8.5
Mo	0.92	1.0	1.1	0.8	1.0	1.0
Mn	0.37	0.55	1.5	0.6	0.7	0.4
Si	0.31	0.20	0.3	0.35	0.28	0.18
S	0.0047	0.007	0.01	0.015	0.015	0.007
P	0.018	0.015	< 0.007	0.015	0.015	0.01
Ni	0.38	0.6	0.9	0.1	0.5	0.7
Nb	0.08	0.06	0.03	–	0.069	–
V	0.26	0.07	0.012	0.012	0.004	0.09
N	0.052	0.033	0.03	0.025	0.025	0.032
Cu	–	0.05	< 0.05	0.05	0.05	0.05
Al	0.006	0.034	–	0.034	–	0.034
Fe	Balance	Balance	Balance	Balance	Balance	Balance
Cr_{eq}*	6.912	8.1	4.135	8.86	5.374	7.69
Ni + Mn	0.75	1.15	2.4	0.7	1.2	1.1

*Cr_{eq} = Cr + 6Si + 4Mo + 1.5W + 11V + 5Nb + 12Al + 8Ti–40C–2Mn–4Ni–2Co–30N–Cu [17]

Table 2.3 Welding parameters used for deposition of the grade 91 weld metals

Consumable	Welding process	Polarity	Voltage (V)	Current (A)	Number of passes	Heat input (kJ/mm)
E1	SMAW	DCEP	22	120	10	0.90
		AC	80	138	12	2.51
E2	SMAW	DCEP	22	120	10	1.02
		AC	80	138	13	2.84
E3	SMAW	DCEP	32	160	6	2.14
		AC	80	156	7	4.43
E4	SMAW	DCEP	–	–	–	–
FW	GTAW	DCEN	13	120	14	0.95

DCEP, direct current electrode positive; AC, alternating current; DCEN, direct current electrode negative.

and HAZ from 425 to 250 VHN and 460 to 220 VHN, respectively. This reduction in hardness is consistent with the microstructural observations. Hardness measurement showed that E2 weld metal had the highest hardness, which could be correlated with the presence of a high amount of austenite stabilising elements in the weld.

Impact toughness

CVN impact toughness values, with standard specimen configuration, of the direct current and alternating current (DC and AC) weld metals in different heat treated conditions are shown in Figs 2.10(a) and (b), respectively. Figure 2.10(a) shows that toughness of E1 and E2 weld metals is below acceptable values even after PWHT at 1033 K for 3 h. A further increase in PWHT duration to 8 h improves the toughness of all the DC weld metals [38]. But the values show complex variation. Low toughness of E2 weld metal can be correlated with the presence of high content of austenite stabilising (Ni + Mn = 2.4%) elements. A lower temperature tempering of 1013 K is likely to improve the toughness in this case. Figure 2.11 shows the effect of PWHT temperature and time on hardness of the weld metal. The behaviour of hardness vs. tempering time at various temperatures reflects the complex microstructural changes that are responsible for the hardness variation, particularly when the weld metal contains high austenite stabilising elements. PWHT temperature and time must therefore be carefully selected depending on composition and deposition process.

The present investigation also showed that although weld metal deposited by non-synthetic electrodes generally exhibited superior properties, the required toughness could be obtained with synthetic electrodes also, by increasing the duration of PWHT. Complementarily, non-synthetic electrodes alone cannot ensure good toughness unless the chemistry is balanced. Synthetic electrode

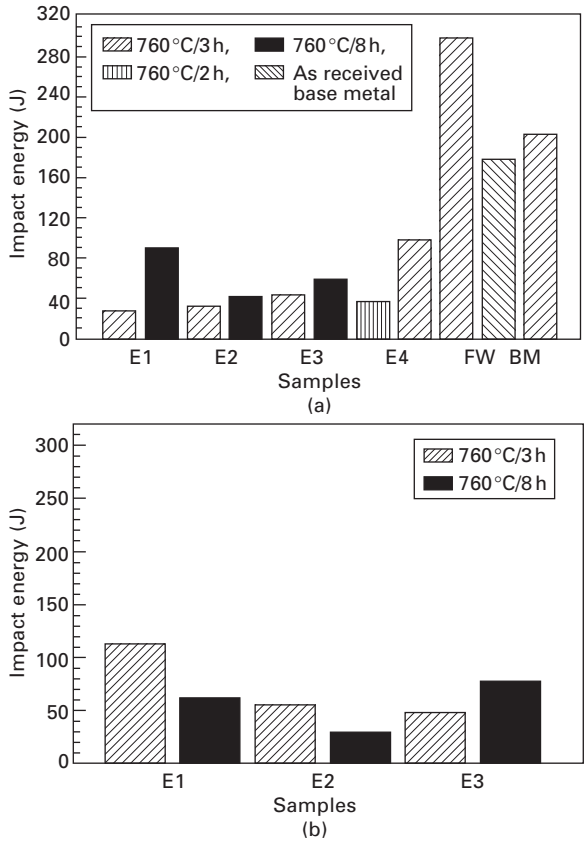

2.10 Effect of polarity during deposition of grade 91 weld metal on room temperature Charpy V-notch impact toughness: (a) DC weld deposits and (b) AC weld deposits (FW–GTA weld metal).

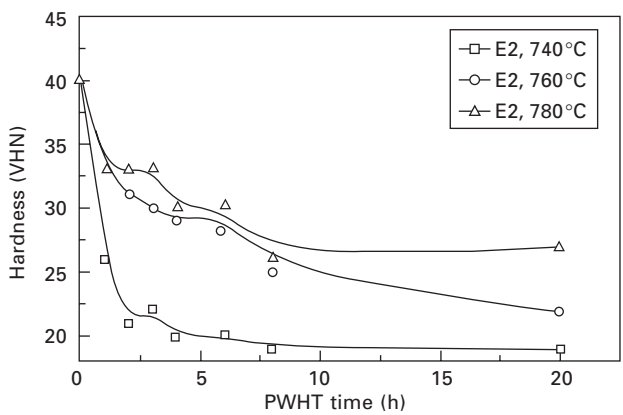

2.11 Effect of PWHT temperature and time on the hardness of the E2–DC weld metal.

E3 had a higher toughness than E1 and E2 though its microstructure showed presence of delta-ferrite in the weld metal. Relatively high toughness of E3 compared with E1 and E2 could be correlated with the use of high heat input, which gives rise to slow cooling rate and resulted in auto tempering. Only one weld metal, E4 (non-synthetic), showed high toughness (97 J) after 3 h PWHT as per specification, as against the requirement (45 J). In the present study, it was found that GTA weld metal gave much higher toughness than SMA weld metal and base metal for the same duration of PWHT. GTA weld metal shows high toughness [34] even in the as-welded condition. The high impact energy even in as welded condition may be due to the clean GTAW process, low oxygen content (< 20 ppm) in the GTA weld metal compared with the SMA weld (400 ppm) and use of higher number of passes than SMAW.

Interestingly, the toughness of AC weld metal was much higher than the DC weld metal for 3 h PWHT. Another point to be noted is that PWHT at 1033 K for 8 h reduces the toughness of E1 and E2. In E3 weld metal toughness is higher than the other two. Polarity during welding influences chemistry of the weld deposit, through factors such as arc temperature, decomposition of the flux ingredients and its influence on slag-metal reactions.

2.5 Dissimilar metal welding

In the trimetallic TMJ for the SG circuit (Fig. 2.12), Inconel 182 would be used for welding modified 9Cr-1Mo to Alloy 800, and ER 16-8-2 for welding Alloy 800 to 316L(N) SS. To characterise and evaluate this trimetallic TMJ, the following aspects are being investigated [1]:

- stability of microstructure and mechanical properties of 316L(N) SS/ Alloy 800 joint subjected to long-term elevated temperature ageing;
- optimisation of PWHT of Alloy 800/modified 9Cr–1Mo joint by studying the effect of PWHT and ageing on its microstructure and mechanical properties; and
- performance evaluation of trimetallic TMJ by accelerated thermal cycling of Alloy 800/modified 9Cr–1Mo joint subjected to the optimum PWHT.

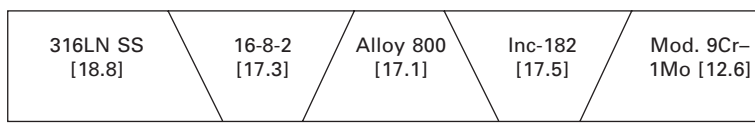

2.12 Schematic of configuration of the trimetallic TMJ developed (number below each material denotes mean CTE, in μm/m/K, in the temperature range 273–873 K).

2.5.1 Dissimilar 316L(N) SS/alloy 800 joint

The 316L(N) SS/Alloy 800 joints, GTA welded with ER 16-8-2, were subjected to accelerated ageing at 873 K for 200, 500, 1000, 2000 and 5000 h to simulate long-term service exposures. These aged joints were used to study the stability of their microstructure and mechanical properties against deterioration on prolonged service exposure at elevated temperatures.

Microstructure

The SS/weld interface comprises an *in-situ* melted and solidified unmixed zone, consisting of fine-grained austenite network (caused by localised melting and solidification of base metal without convective mixing with weld pool due to difference in their melting points), along with grain coarsening in the HAZ (Fig. 2.13a). The 16-8-2 weld has a cellular-dendritic structure with a small amount of delta-ferrite distributed in intercellular regions (Fig. 2.13b). The weld/Alloy 800 interface is sharp and well defined owing to compositional mismatch between 16-8-2 and Alloy 800, with average grain size of Alloy 800 HAZ being greater than SS HAZ (due to lower conductivity of Alloy 800 compared with SS and consequent slower heat dissipation) (Fig. 2.13c).

On prolonged ageing (for 5000 h), substantial precipitation of carbides occurs in SS HAZ resulting in a continuous grain boundary network of carbides, with the *in-situ* melted and solidified structure at SS/weld interface (observed in unaged condition) being also present (Fig. 2.14a). The cellular microstructure of 16-8-2 weld is more discernible after ageing than in an unaged condition, because of extensive precipitation of carbides and transformation products of delta-ferrite along cell boundaries (Fig. 2.14b). However, after long-term ageing, no appreciable change occurs in the microstructure along weld/Alloy 800 interface and of Alloy 800 HAZ, except for some grain boundary precipitation (Fig. 2.14c).

The delta-ferrite content at both the weld interfaces is lower than in the weld due to dilution of weld by austenite stabilisers from base metals: nitrogen from 316L(N) SS and Ni from Alloy 800 (Fig. 2.15a). However, in an unaged condition, ferrite content is much lower at weld interface with SS (0.4 FN) than with Alloy 800 (1.3 FN), because nitrogen is a stronger austenitiser (by a factor of 30) than Ni. With increased ageing, ferrite content at both weld interfaces decreases because of ageing-induced transformation of ferrite. As the initial ferrite content is lower at weld/SS interface, all ferrite here transforms within 1000 h of ageing, while the same occurs at weld/Alloy 800 interface only by 2000 h. In the weld, ferrite transforms very rapidly over the first 200–500 h of ageing (from 2.1 to 1 FN); thereafter it transforms much more gradually, with all ferrite transforming within 2000 h (Fig. 2.15a).

The ferrite content in the weld's root region is very low and increases

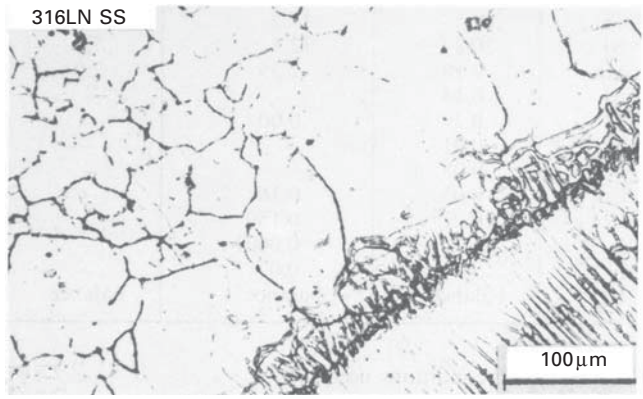

(a)

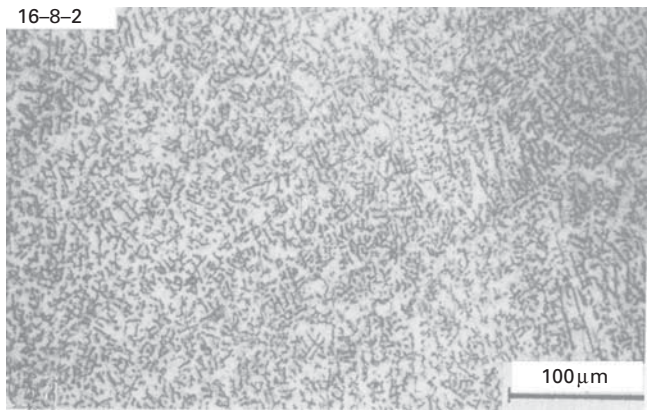

(b)

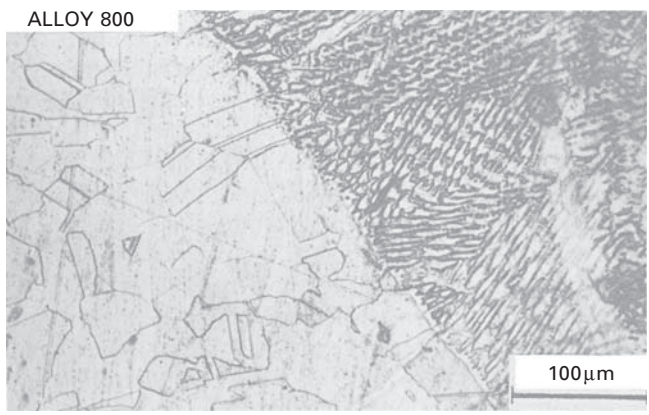

(c)

2.13 Optical micrographs of unaged joint: (a) 316L (N) SS/weld interface, (b) 16-8-2 weld and (c) weld/Alloy 800 interface.

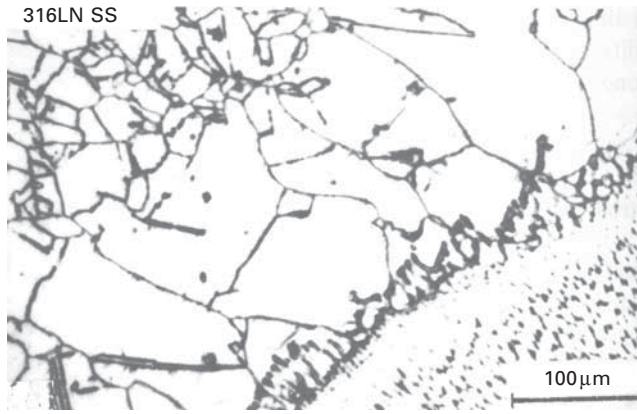

(a)

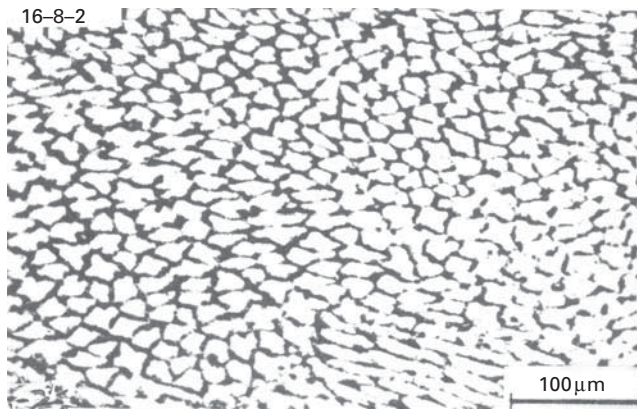

(b)

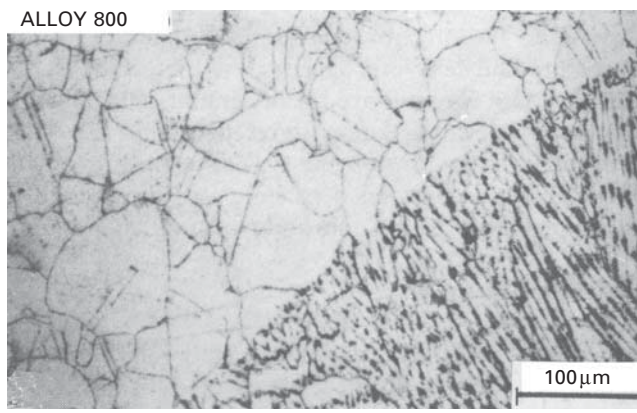

(c)

2.14 Optical micrographs of 873 K/5000 h aged joint: (a) 316L (N) SS/weld interface, (b) 16-8-2 weld and (c) weld/Alloy 800 interface.

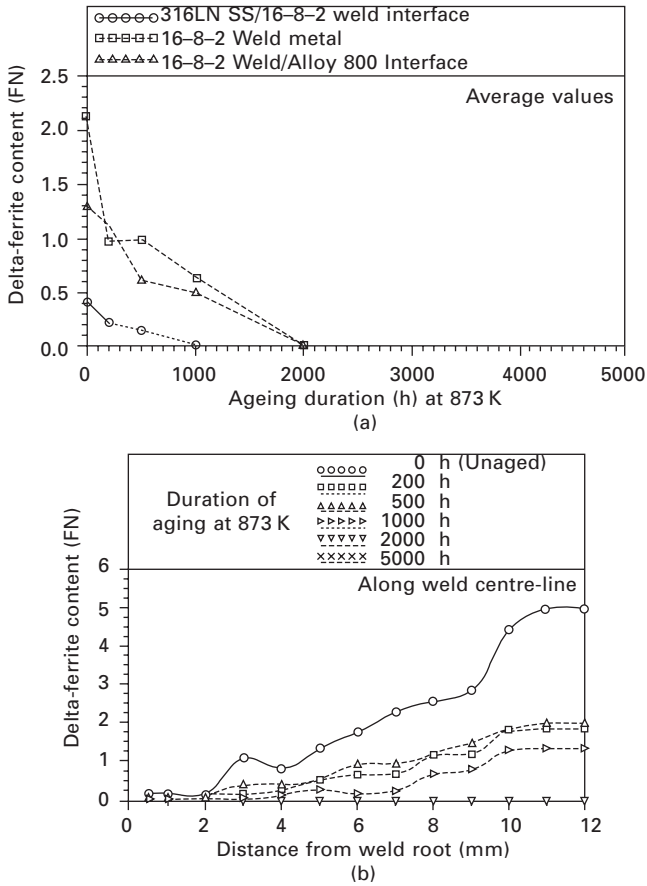

2.15 Effect of ageing duration at 873 K on ferrite content (a) in 16-8-2 weld and at weld/base metal interfaces, and (b) across the thickness of 16-8-2 weld.

progressively from root to face; in the unaged condition it increases from < 0.1 FN at root to about 5 FN at face (Fig. 2.15b). The decrease in ferrite content from the weld's face to root is caused by thermal cycling due to multiple welding passes partially transforming the ferrite present in earlier pass deposits. Obviously, the effect of multiple welding passes is more near the root. Additionally, at the root region there is extensive dilution of the weld by both base metals, both of which contain austenite stabilisers. As ageing duration increases, ferrite in the weld is progressively transformed to other phases, with the rate of transformation being faster over the first 200–500 h of ageing, and all ferrite is transformed within 2000 h of ageing. Hence, ferrite content throughout the weld is 0 FN for ageing durations of 2000 h and more.

Hardness

In the unaged condition, hardness across weld/SS interface and SS HAZ decreases steadily from about 225 HV in the weld to about 165 HV near SS base metal (Fig. 2.16). On ageing for 5000 h, there is no significant change in hardness level across SS HAZ, and hardness of the weld decreases marginally by about 10–20 HV. However, prolonged ageing over 5000 h results in appreciable dip in hardness near weld/SS interface due to diffusion of alloying elements across this interface having alloys of vastly differing compositions on either side. Across the weld/Alloy 800 interface, there is a sharp dip in hardness of the weld adjacent to the interface in both unaged and 5000 h aged conditions, due to good intermixing of weld and Alloy 800 during welding. In unaged condition, hardness of Alloy 800 HAZ decreases from about 250 HV near the interface to about 190 HV near unaffected base metal. On ageing for 5000 h, hardness of HAZ decreases by only about 30 HV on either side of the interface, and only marginally by about 10 HV near Alloy 800 base metal. Thus, even after prolonged ageing for 5000 h, there is only minimal change in hardness distribution across this joint.

Mechanical properties

The unaged and all aged joints have higher tensile strength and ductility at 298 K than at 773 K (Table 2.4). Almost all transverse-weld tensile specimens failed in the weld, indicating that the 316L(N)/Alloy 800 joint, GTA welded

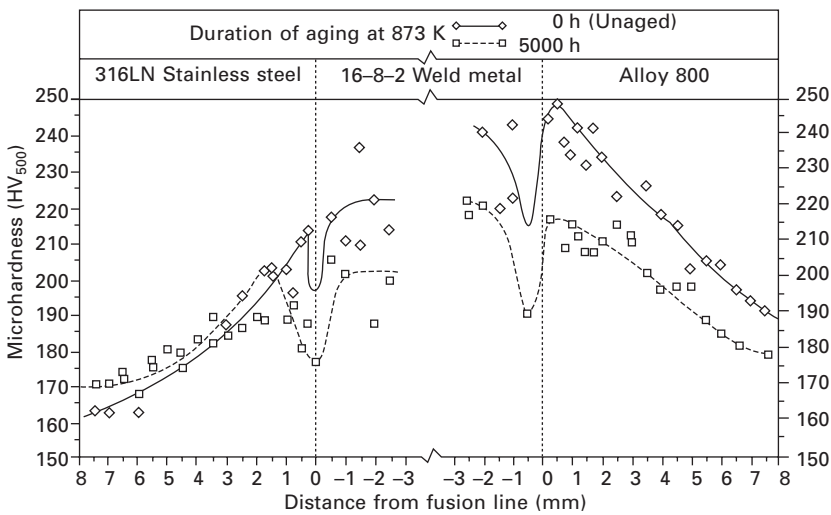

2.16 Hardness profile across 16-8-2 weld interfaces in unaged and aged conditions.

Table 2.4 Tensile properties of transverse-weld specimens of 316L (N) SS/Alloy 800 joint

Test temp.	Ageing time (at 873 K)	YS (MPa)	UTS (MPa)	UE (%)	TE **(%)**
298	Unaged	409	608	26	33
	200 h	444	631	22	27
	500 h	433	647	24	27
	1000 h	438	652	23	27
	2000 h	392	630	24	27
	5000 h	393	630	26	30
773	Unaged	307	478	18	21
	200 h	319	428	12	15
	500 h	305	451	11	13
	1000 h	317	433	10	14
	2000 h	270	413	11	15
	5000 h	280	404	10	13

with 16-8-2, is slightly under-matched. The joint strength, i.e. both yield strength (YS) and ultimate tensile strength (UTS), at both 298 and 773 K, do not change appreciably with ageing duration at 873 K. In addition, at both 298 and 773 K, the joint ductility, i.e. both uniform elongation (UE) and total elongation (TE), reduces rapidly within the first 200 h of aging at 873 K, and remains practically unchanged thereafter on further ageing up to 5000 h.

The ductile fracture toughness parameters, evolved at IGCAR [39,40], viz. Γ_f and η_f, determined from tensile tests of smooth cylindrical specimens, were used to determine the toughness of the weakest section in the specimen (i.e. where neck formation and ultimate tensile fracture occurs). While Γ_f estimates average energy per unit cross-sectional area of the neck required to cause fracture, η_f estimates average incremental plastic strain per unit volume consumed by the specimen per unit longitudinal plastic strain at the neck to sustain the fracture process. For ageing times longer than 2000 h, Γ_f and η_f remain constant (Fig. 2.17a) although UTS and percentage reduction in area (%RA) continue to change (Fig. 2.17b). The variation of Γ_f and η_f with ageing duration reflects the combined trends of UTS and %RA. Thus, Γ_f and η_f evaluated at 773 K, corresponding to weakest 16-8-2 weld, lead to the unambiguous conclusion that this joint has adequate resistance to ductile fracture after prolonged elevated temperature ageing, and therefore would show stable behaviour on long-term exposure to elevated service temperature.

2.5.2 Dissimilar Alloy 800/9Cr–1Mo steel joint

As investigations on Alloy 800/modified 9Cr–1Mo joint are currently in progress, results of the joint with the metallurgically similar 9Cr–1Mo are presented. The Alloy 800/9Cr–1Mo joints, welded using Inconel 182

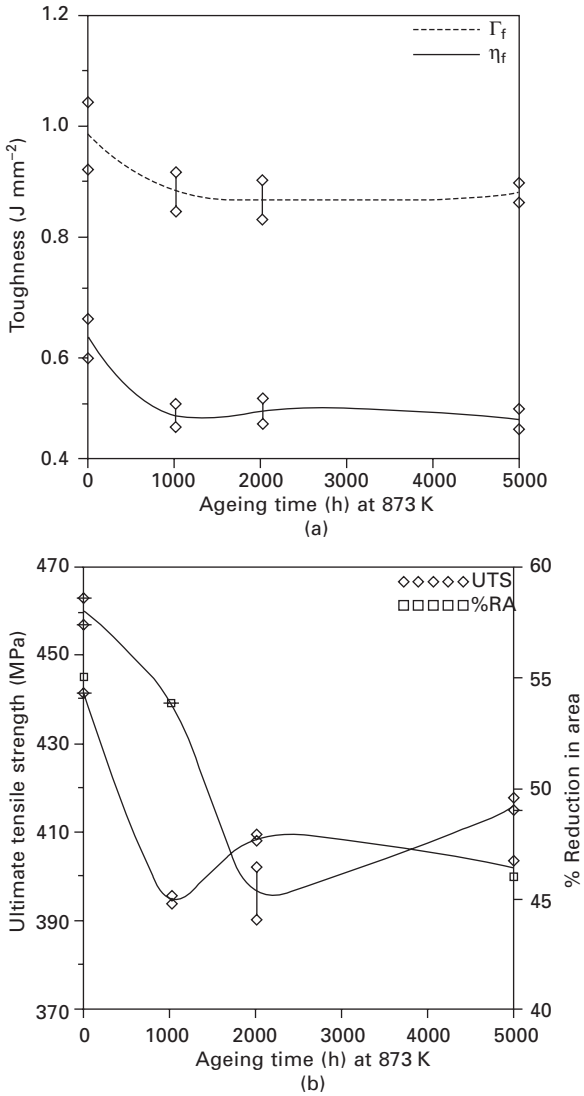

2.17 Effect of ageing on (a) ductile fracture toughness parameters (Γ_f and η_f) and (b) conventional tensile properties (UTS and %RA), all determined at 773 K.

consumable, were studied after subjecting them to PWHT for 1 h at 973, 998 or 1023 K, and ageing at 848 K for 100, 500, 1000 and 5000 h.

Microstructure

After 5000 h ageing, no substantial precipitation occurs at weld/ferritic steel interface and in ferritic steel HAZ. This indicates good microstructural stability

of ferritic steel HAZ on prolonged thermal exposure, irrespective of PWHT temperature. The limited precipitation at weld/ferritic steel interface is due to low carbon activity of 9Cr–1Mo steels resulting in low carbon activity gradient from ferritic steel to weld, thereby reducing carbon migration from ferritic steel HAZ.

After 1023 K/1 h PWHT, precipitation at weld/ferritic steel interface is negligible in unaged condition, with the extent of interfacial precipitation increasing only marginally with increasing duration of ageing. This further confirms the excellent resistance to ageing-induced microstructural instability of weld/ferritic steel interface and ferritic steel HAZ.

Hardness

The hardness at weld interface is highest (about 320 HV) in as-welded condition, and 230–250 HV in all PWHT conditions (Fig. 2.18a). The overall HAZ hardness decreases with increase in PWHT temperature, with the maximum HAZ hardness being 280–290 and about 260 HV after PWHT at 973–998 K and 1023 K, respectively. The width of ferritic steel HAZ in as-welded condition is about 3.5 mm, while that in PWHT conditions is about 2 mm. The reformed-martensite in as-welded HAZ in the region between 2 and 3.5 mm from the fusion line is tempered during PWHT; this results in reduction in its hardness to the base metal hardness level, and hence the difference in hardness becomes indistinguishable for the PWHT specimens. The hardness of unaffected (normalised and tempered) ferritic steel base metal is 190–220 HV in as-welded and PWHT conditions.

After 848 K/5000 h ageing, the hardness at the interface is highest at about 270 HV in as-welded condition, and 240–250 HV in PWHT conditions (Fig. 2.18b). The hardness of ferritic steel base metal in all the conditions is 200–220 HV. The width of ferritic steel HAZ in as-welded and PWHT conditions is about 2 mm. On 848 K/5000 h ageing, there is only marginal variation in hardness distribution across the HAZ in PWHT conditions, with the maximum hardness being 270–280 HV. The higher hardness of the HAZ up to about 0.75 mm from the fusion line indicates that relatively finer grain size of reformed-martensite is still retained and that tempering response of this low-alloy containing reformed-martensite continues to be poor at ageing temperature of 848 K.

Hence, PWHT is essential to reduce the extent and magnitude of hardness variation across the HAZ, and PWHT temperature and/or prolonged ageing even up to 5000 h has practically no effect on the hardness distribution across the ferritic steel HAZ. This further confirms that the HAZ of 9Cr–1Mo steels after PWHT at 973–1023 K will have a stable microstructure even after prolonged exposure at elevated service temperatures.

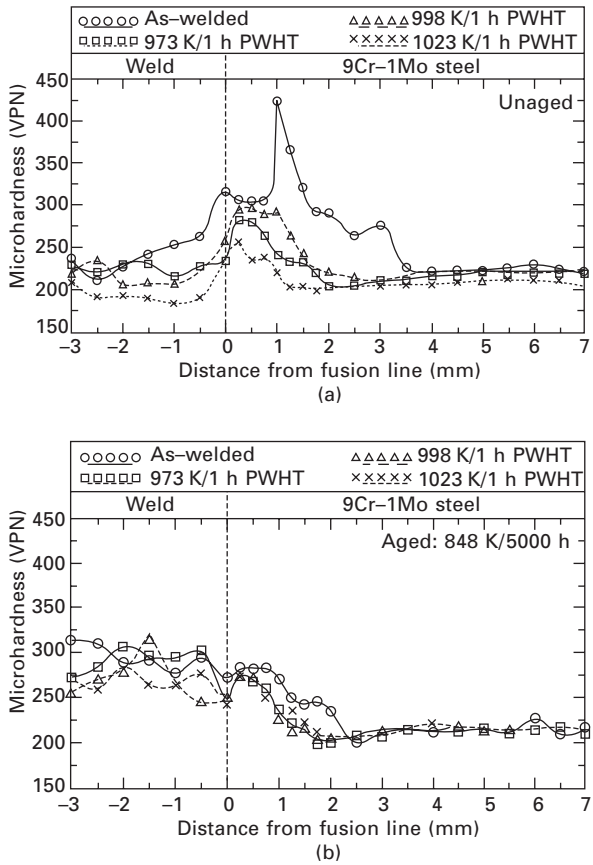

2.18 Microhardness profiles across Inconel 182 weld/ferritic steel interface for as-welded and PWHT joints in: (a) unaged and (b) 848 K/5000 h aged conditions.

Mechanical properties

All failures during tensile tests at 773 K occurred in ferritic steel HAZ, indicating that this HAZ is the joint's weakest region. In fact, the location of tensile failure coincides with the region near the fusion line, where a hump is observed in hardness profiles. Further, the location of failure does not change with either change in PWHT temperature and/or duration of ageing. In as-welded and PWHT conditions, 848 K/5000 h ageing results in an increase in YS to 377–394 MPa compared with 304–316 MPa in unaged condition. In contrast, after 5000 h ageing UTS decreases marginally to 439–465 MPa from 463–479 MPa in the unaged condition. However, %RA shows practically no variation on ageing, with RA in unaged and 5000 h aged conditions being 67–75% and 70–72%, respectively.

After ageing, the 998 K PWHT joint has a slightly higher YS than other PWHT joints, has consistently higher YS than in the unaged condition (Fig. 2.19a), and exhibits a minimal amount of fluctuation with progressive ageing. Further, after ageing, 973 and 998 K PWHT joints have marginally lower UTS than a 1023 K PWHT joint (Fig. 2.19b), and exhibit a minimal amount of fluctuation with progressive ageing. On ageing, 973 and 998 K PWHT joints exhibit minimum amount of fluctuations in RA (Fig. 2.19c), with RA for a 998 K PWHT joint being slightly higher than other PWHT joints.

The codes BS 5500, ANSI B31.3 and BS 3351 (BS 2633) specify PWHT temperature in the range 973–1033 K to achieve optimum high temperature properties in 9Cr–1Mo steels. PWHT carried out near 973 K will result in substantial reduction in regenerated residual stresses, while that carried out near 1033 K will cause maximum tempering of the martensitic HAZ of 9Cr–1Mo steels. In either case, however, subsequent in-service ageing will have only a marginal effect on the microstructure and tensile properties of this joint. It is noted that for this joint, the conventional structure–property approach

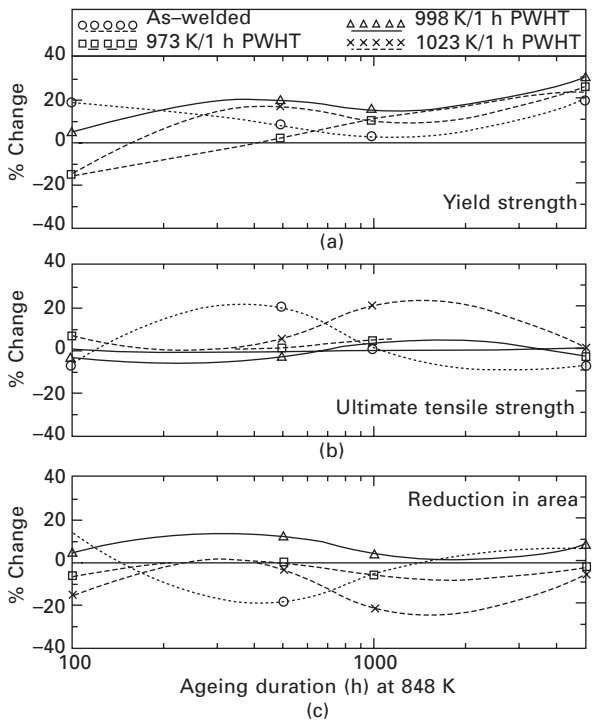

2.19 Effect of ageing duration at 848 K on (a) YS, (b) UTS and (c) %RA at 773 K for transverse-weld specimens of Alloy 800/9Cr–1Mo steel joint.

(discussed above) is unable to discern with certainty any unique optimum PWHT temperature, principally owing to the poor sensitivity of conventional parameters such as YS, UTS and %RA.

As tensile fracture in transverse-weld specimens of this joint occurs in the ferritic steel HAZ, ductile fracture toughness parameters, Γ_f and η_f, evaluated correspond to those for the weakest section in this HAZ. In the 1023 K PWHT joint, Γ_f first increases up to 500 h ageing at 848 K, then decreases over the next 500 h of ageing, beyond which it remains practically unchanged up to 5000 h ageing (Fig. 2.20a). For all ageing durations, the as-welded and 973 K and 998 K PWHT joints show similar variations in Γ_f, with the highest Γ_f in aged conditions being obtained for 1023 K PWHT joint (Fig. 2.20a). In contrast, with increasing ageing duration up to 5000 h, η_f increases continuously – rapidly at first (up to about 1000 h ageing) and then showing a tendency for saturation (Fig. 2.20b). However, for a given ageing duration, the range of η_f values for all joints is about 10%. Nevertheless, the 1023 K PWHT joint exhibits the highest η_f values for all ageing duration up to 5000 h (Fig. 2.20b). Thus,

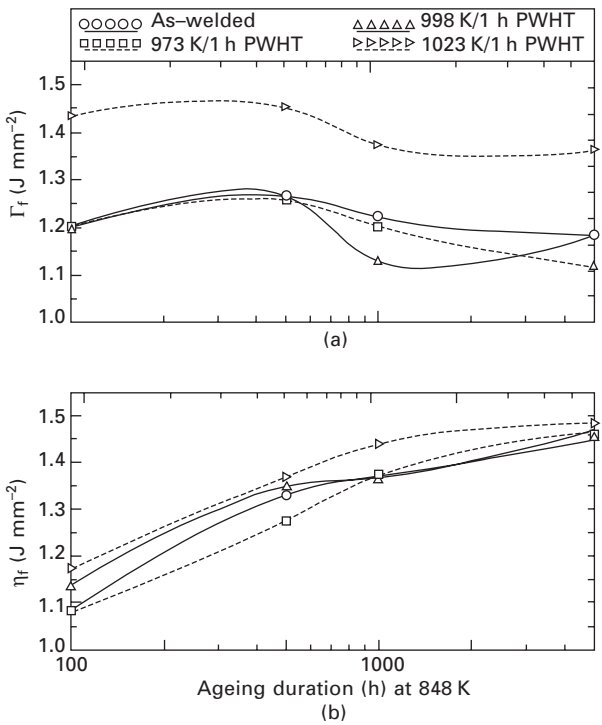

2.20 Variation in ductile fracture toughness parameters: (a) Γ_f and (b) η_f determined at 300 K with ageing time at 848 K for as-welded and PWHT joints.

from the ductile fracture toughness parameters Γ_f and η_f alone, the optimum PWHT temperature (within the range specified by codes) can be unequivocally identified as 1023 K.

For 1023 K PWHT joint, UTS increases by about 14% on 100–500 h ageing, increases by another 8% for the next 500 h ageing, and UTS decreases by 7% upon further ageing up to 5000 h ageing (Fig. 2.20a). The %RA initially increases by about 5% over the first 100 h ageing, but with prolonged ageing decreases to about 10% lower than that in unaged condition. Ageing for 100–500 h leads to an increase in Γ_f by about 35%; beyond which it decreases to saturate at about 27% net increase over the unaged condition. On the other hand, η_f increases steadily with increasing aging duration up to 5000 h, tending to saturate at 37% higher than the unaged condition. For 5000 h aged joints, an increase in PWHT temperature results in an increase in UTS and decrease in %RA (Fig. 2.20b). However, η_f after 5000 h ageing remains practically unchanged irrespective of PWHT temperature. On the other hand, though Γ_f decreases on PWHT at 973 K it increases with increasing PWHT temperature up to 1023 K, indicating thereby that better toughness would be obtained on PWHT at 1023 K.

The poor sensitivity of UTS and %RA to ageing (Fig. 2.20) indicates that the conventional structure–property analysis route would not distinguish the effect of different PWHT temperatures employed. For a 1023 K PWHT joint, UTS increases by about 14% on 100–500 h ageing and by another 8% for the next 500 h ageing, beyond which it decreases by 7% up to 5000 h ageing (Fig. 2.21a). The %RA initially increases by about 5% over the first 100 h ageing, but with prolonged ageing decreases to about 10% lower than that in unaged condition. Ageing for 100–500 h leads to an increase in Γ_f by about 35%, beyond which it decreases to saturate at about 27% net increase over the unaged condition. On the other hand, η_f increases steadily with increasing ageing duration up to 5000 h, tending to saturate at 37% higher than the unaged condition. For 5000 h aged joints, an increase in PWHT temperature results in increase in UTS and decrease in %RA (Fig. 2.21b). However, η_f after 5000 h ageing remains almost unchanged irrespective of PWHT temperature. On the other hand, though Γ_f decreases on PWHT at 973 K it increases with increasing PWHT temperature up to 1023 K, indicating thereby that better toughness would be obtained on PWHT at 1023 K.

The marginal improvement in η_f on increasing the PWHT temperature reflects the poor tempering response of the relatively fine-grained low alloy containing reformed-martensite present in the HAZ. The Γ_f and particularly η_f values unambiguously indicate the optimum (i.e. consistent within the specified temperature range) PWHT temperature to be 1023 K.

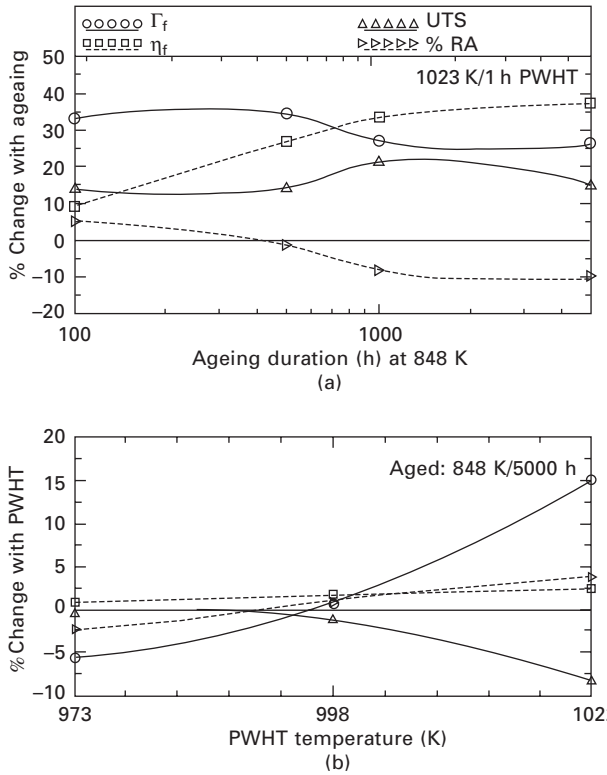

2.21 Change in Γ_f, η_f, UTS and %RA at 300 K with: (a) ageing duration at 848 K for 1023 K PWHT joints and (b) PWHT temperature for 848 K/5000 h aged joints.

2.5.3 Dissimilar metal weld joint between A48P2 carbon steel and 316L (N) SS

To study the soundness and life of this DMW joint the following aspects were investigated [41]: (i) susceptibility of the joint to hot cracking; (ii) effect of PMZ and UMZ on joint properties; (iii) impact properties of the weld metal, weld/base metal interfaces and CS-HAZ, and (iv) residual stress distribution in the as-welded condition and after exposure to 453 K for a cumulative time of 120 h that a joint is expected to experience in its operating life of 40 years.

The double-fillet weld test (as per DIN 50129 specification), which is specifically suitable for dissimilar metal welds, was carried out to evaluate the hot cracking resistance of the A48P2/316L(N) SS joint welded with E309 consumable, and the crack-free joints obtained confirmed the good hot

cracking resistance of the weld metal. A48P2/316L(N) SS joints with double-V and K joint geometries were welded using E309 electrodes of 4.0 and 3.15 mm diameters, respectively, considering the actual joint configurations that would be used during fabrication.

Mechanical properties

UMZ and PMZ are observed in the A48P2/316L(N) SS joints at the weld/CS interface, with the hardness of the UMZ and PMZ being significantly higher (350–370 HV) than the weld metal (220 HV) and base metal (180 HV).

During tensile testing, the transverse-weld specimens fractured in the CS base metal well away from the weld interface, indicating thereby that the PMZ near the weld interface has no effect on the overall tensile properties of this weld joint. However, this DMW joint exhibits higher YS and UTS but with lower ductility than the CS base metal, owing to the difference in tensile properties of the different constituents in this DMW joint (Fig. 2.22).

During the design-based loss of cooling condition, the temperature of this DMW joint is expected to rise from 293 K to 450 K, and remain at that temperature for up to 8–10 h. Such incidents of loss of cooling can occur over a maximum of 12–15 times during the entire lifetime of 40 years. To study the strength of this DMW joint, it was subjected to ageing at 450 K for 120 h. The tensile test of unaged and aged specimens (Table 2.5) shows that the YS and UTS of the CS base metal change marginally at 453 K in the unaged condition as well as after 453 K/120 h ageing. However, for this DMW joint, the YS and UTS both decrease by about 23% at 453 K in the as-welded condition and by about 20% after 453 K/120 h ageing.

CVN impact tests carried out at ambient temperature, for the weld metal, weld/CS interface, CS base metal and HAZ (Fig. 2.23a) show no difference in the impact energy of the weld metal and the weld/CS interface, indicating that the presence of PMZ does not have any effect on impact toughness. The impact toughness of the CS base metal and HAZ was found to be very good. The relatively lower impact toughness obtained for weld metal compared with that of the base metal can be attributed to the inclusion content, high dislocation density in the dendritic structure and the high delta-ferrite content in the weld metal. From the variation in impact energy with temperature for the A48P2 CS HAZ (Fig. 2.23b), the ductile to brittle transition temperature (DBTT) based on 40 J criterion is determined as 238 K (–35 °C). The impact energy of the CS base metal at ambient temperature is also in the same range as that of the HAZ (about 225 J). Compared with the specified minimum impact energy for the A48P2 material of 40 J at 253 K (–20 °C), the Charpy

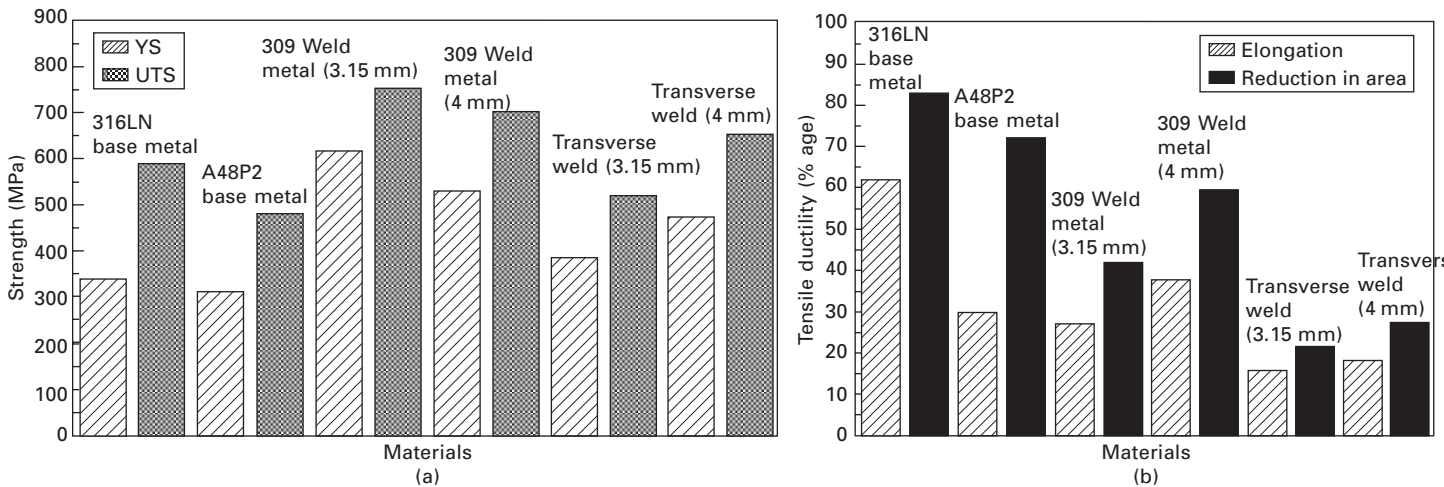

2.22 (a) Tensile strength and (b) tensile ductility of the base metals, all-weld metals and transverse-weld specimens of the A48P2/316L(N) SS dissimilar metal joint.

Table 2.5 Tensile properties of A48P2 base metal and A48P2/316L(N) SS DMW joint welded with 4.0 mm diameter E309 electrodes before and after 453 K/120 h ageing

		Test temperature			
		293 K		453 K	
Material	Condition	YS (MPa)	UTS (MPa)	YS (MPa)	UTS (MPa)
A48P2 base metal	Unaged	312	477	281	459
	453 K/120 h aged	311	491	–	–
A48P2/316L(N) SS joint	As-welded	469	650	356	508
	453 K/120 h aged	380	513	–	–

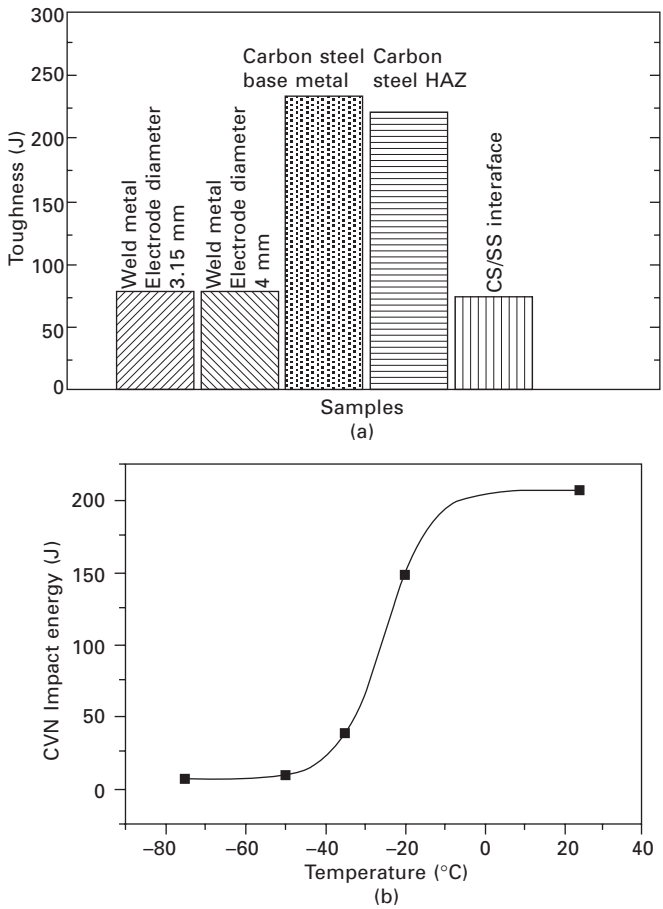

2.23 (a) Impact toughness of weld metal, carbon-steel (CS) HAZ and base metal, and CS/309 weld interface. (b) Ductile to brittle transition temperature for HAZ.

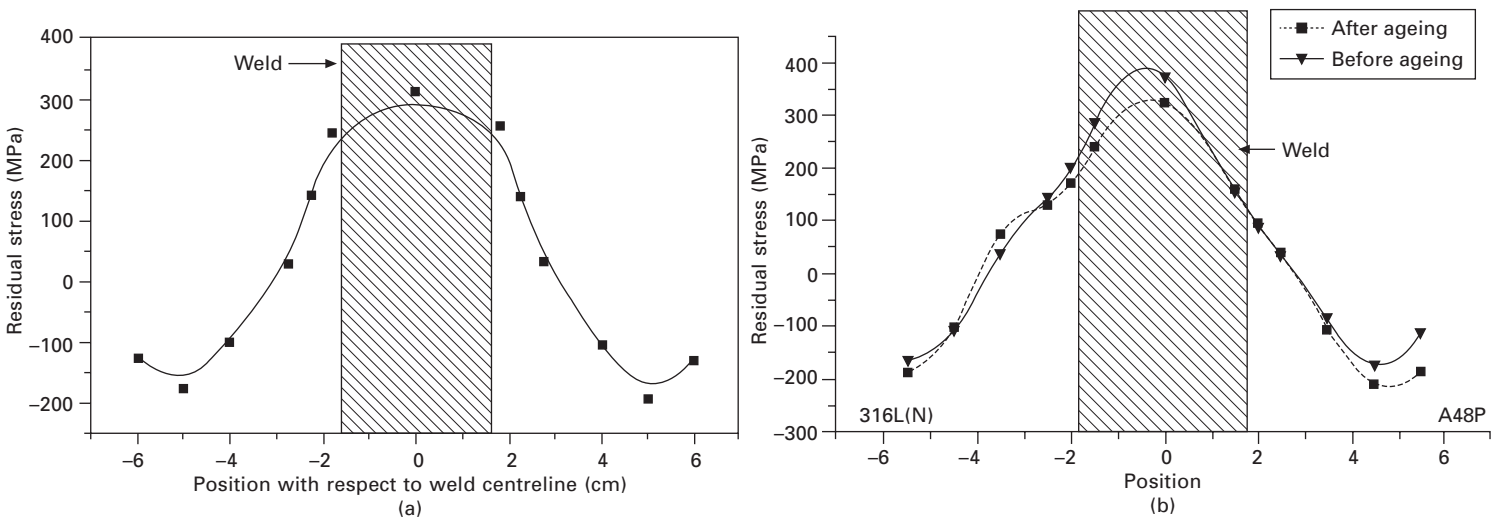

2.24 Residual stress distribution along longitudinal direction of K-groove joints: (a) A48P2/ A48P2 welded with E7018 and (b) A48P2/316L(N) SS welded with E309 before and after ageing at 453 K for 120 h.

impact energy evaluated at 253 K for the HAZ and CS base metal is 150 and 125 J, respectively. Thus, the results of impact tests on the A48P2 CS HAZ clearly show that the impact toughness of the CS HAZ is as good as that of the CS base metal even in the as-welded condition. The weld thermal cycles experienced by the HAZ during welding break down the ferrite–pearlite bands and transform them to more uniform structures, resulting in the higher impact toughness of the HAZ. In fact, these results indicate that the toughness of the CS HAZ could be marginally better than that of CS base metal owing to this microstructural modification.

Residual stress

The residual stress distribution in the A48P2/316L(N) SS DMW joint is different from that of similar metal joints involving the A48P2 material, because of the significant differences in the thermal conductivity and thermal expansion coefficients of the two dissimilar base metals. Hence, the residual stress distribution in this DMW joint (Fig. 2.24b) was compared with that in similar weld joints of A48P2 material (Fig. 2.24a). The result showed that the peak residual stresses at the centre of the weld are close to that of the YS of the weld metal. The peak residual stress in the A48P2/A48P2 similar metal joint made with E7018 carbon steel weld metal (~300 MPa) is lower than that in the A48P2/316L(N) SS DMW joint made with E309 SS weld metal (> 350 MPa). This can be attributed to the lower YS of the E7018 CS weld metal compared with that of the E309 austenitic SS weld metal. Further, for the A48P2/A48P2 similar metal joint, the residual stress distribution is symmetrical about the weld centreline, with the residual stresses being compressive beyond ~3 cm from the weld centreline. However, for the A48P2/316L(N) SS DMW joint, the residual stress distribution is asymmetrical about the weld centreline, with the residual stresses decreasing more rapidly with distance from the weld centreline in the CS side compared with that in the austenitic SS side. Further, ageing of this DMW joint at 453 K for 120 h has only a marginal effect on the residual stress distribution across the joint (Fig. 2.24b). Also, residual stress distribution across the A48P2/316L(N) SS DMW joint with double-V groove geometry is similar to that with K-groove geometry, indicating thereby that the two groove geometries do not affect the residual stress distribution in this DMW joint.

2.6 Improving welding in practice: development of special purpose electrodes

Modified E316-15 electrodes meeting the specifications have been developed and manufactured in collaboration with two electrode manufacturers (Table 2.6)

Table 2.6 Summary of results of quality assurance (QA) tests on modified E316-15 electrodes

As per specification		2.5 mm diameter	3.15 mm diameter	4 mm ϕ
Chemical composition (wt%)				
Carbon	0.045–0.055	0.055	0.050	0.055
Nitrogen	0.06–0.10	0.110*	0.120*	0.130*
Chromium	18.0–19.0	18.3	18.5	19.5*
Nickel	11.0–12.0	11.3	11.1	11.0
Molybdenum	1.9–2.2	1.8*	1.9	2.0
Manganese	1.2–1.8	1.4	1.4	1.5
Silicon	0.4–0.7	0.32*	0.46	0.53
Sulphur	0.020 max	0.008	0.006	0.003
Phosphorus	0.025 max	0.025	0.025	0.028†
Tantalum	0.10 max	< 0.010	< 0.010	< 0.010
Titanium		13 ppm	23 ppm	16 ppm
Niobium		< 0.07	< 0.07	< 0.07
Vanadium	–	0.070	0.075	0.100
Boron	20 ppm max	< 10 ppm	< 10 ppm	< 10 ppm
Copper	0.5 max	0.080	0.210	0.210
Cobalt	0.2 max	0.070	0.060	0.090
Delta-ferrite content				
By ferritescope	3–7 FN	4.4, [4.3, 4.6]§ FN	3.5, [4.1, 3.9]§ FN	5.1 FN
As per WRC-92		1.0 FN*‡	1.8 FN*‡	3.9 FN
By BNN model		2.8 FN (± 2.3)	3.8 FN (±2.2)	5.6 FN (±2.9)
Mechanical properties				
All-weld tensile properties at room temperature in as-welded state				
0.2% YS (MPa)	350 min	504	504	481
UTS (MPa)	550 min	614	621	611
Elongation (%)	35 min	35	32‡, [41, 39]§	38
R.A. (%)	To be noted	78	79	79
All-weld tensile properties at 550 °C in as-welded state				
0.2% YS (MPa)	116 min	317	339	318
UTS (MPa)	380 min	447	460	452
Elongation (%)	20 min	24	21	26
R.A. (%)	To be noted	58	56	51
Charpy U-notch impact strength (daj/cm^2) at ambient temperature				
As-Welded	7.0 min [on each of 3 specimens]	8.8, 8.2, 7.6	7.5, 8.1, 7.2	7.0, 7.6, 7.6
750 °C/100 h aged	3.0 min [on each of 3 specimens]	6.0, 5.1, 7.0	3.9, 3.8, 4.4	3.2, 3.7, 3.7
Other tests				
Slag detachability		Good	Good	Good
IGC Test (ASTM A 262 Practice E)		Fail‡ [Pass, Pass]§	Pass	Pass
Fillet Test (as per SFA 5.4)		Not required	Pass	Pass
Cracking test		Pass	Pass	Pass

* Accepted with minor variation (on DCR).
†S + P = 0.045 wt% (max) accepted (on DCR)
‡Retest required and carried out.
§Retest results accepted.

[42]. This developmental experience has shown that the identification of critical problems in production and their resolution through collaborative efforts, wherever necessary, have contributed to the success. During this developmental work it also became necessary to develop an artificial neural network (ANN)-based methodology to accurately estimate the delta-ferrite content from the chemical composition of the stainless steel weld metal.

2.6.1 Estimation of delta-ferrite content in 316L(N) stainless steel welds

Depending on service requirement, delta-ferrite content (in ferrite number, FN) in SS welds is often specified to ensure that weld metal contains a desired minimum and/or maximum ferrite level. Among various methods for predicting the FN in SS welds, such as constitution diagrams, function-fit model, feed-forward back-propagation neural network model, etc., the ANN method is reported to be a more accurate method. To avoid over-fitting of the training data set, a potential risk in ANN analysis, a Bayesian framework was adopted to control the complexity of the ANN, which also provided meaningful error bars for model predictions and automatically identified important input variables in the non-linear regression. A major breakthrough was achieved by successful development of a generalised BNN model for estimating ferrite content in austenitic and duplex SS welds from their chemical composition [43]. The accuracy of prediction by this BNN model vis-à-vis the measured ferrite content (Fig. 2.25), is better than that by all other presently available FN estimation methods, including the WRC–1992 constitution diagram. This BNN model also clearly brings out the significance of individual alloying elements (including those hitherto ignored) in SS welds on the ferrite number.

The major concern during welding of austenitic SS is hot-cracking, which is primarily influenced by the solidification mode that in turn is dependent on the weld-metal composition, i.e. the content of austenite and ferrite-forming elements. Hence, it is necessary to control the weldmetal composition so as to promote primary-ferritic (PF) solidification mode for minimising hot-cracking susceptibility of austenitic SS welds. The currently available methods for estimating solidification mode, such as constitution diagrams, are not always adequate, and a more reliable approach is by application of ANN-based model. A Bayesian classification neural network (BCNN) model for predicting the solidification mode in austenitic SS welds, as a function of weldmetal composition, has been developed [44]. The accuracy of this model, i.e. percentage of correct classification on the test data set, was determined to be 77%. Analysis based on the results from this model showed that the PF solidification mode is promoted with Mn > 6% and Ni < 10% (Fig. 2.26a). A three-dimensional plot of Cr_{eq}/Ni_{eq}, ratio, Ni content and probability of

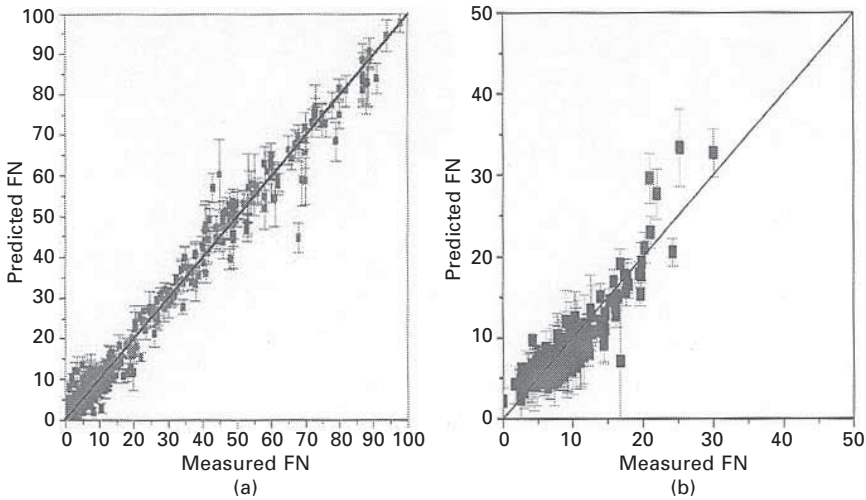

2.25 Comparison between measured and predicted FN values for (a) entire data set with RMS error of 2.1 and (b) independent data set not used in training with RMS error of 2.03.

ferritic solidification mode showed that PF solidification mode could be obtained with Cr_{eq}/Ni_{eq} ratio > 1.55 and Ni < 10% (Fig. 2.26b). The predictions of this model were validated by carefully planned experiments.

For accurate prediction of FN in 316L(N) austenitic SS welds, a generalised BNN model has been developed [45] using a database of 1020 data sets. This BNN model estimates the FN with much better accuracy than the constitution diagrams and all the other currently available FN estimation methods. The root mean square (RMS) value estimated for this BNN model of 2.03 is much superior to the other FN estimation methods, as it is 64% more accurate than the WRC–1992 diagram and 40% more accurate than the FNN-1999 model. In Table 2.7, the estimated FN values from this BNN model are compared with those estimated using the WRC–1992 diagram as well as with those measured by ferritescope. Figure 2.27 shows close agreement between ferritescope measured and BNN model estimated FN values (for electrodes from different manufacturers), with the estimated values having a maximum absolute error of 1.8 and mean error of 0.67.

2.6.2 Modified 9Cr–1Mo electrode

Development of modified 9Cr–1Mo electrodes, conforming to AWS classification E9016-B9 of ASME section II-C SFA-5.5, with Indian electrode manufacturers is in progress. One manufacturer sent two batches of full-size CVN impact specimen for initial screening. In the first batch of three CVN

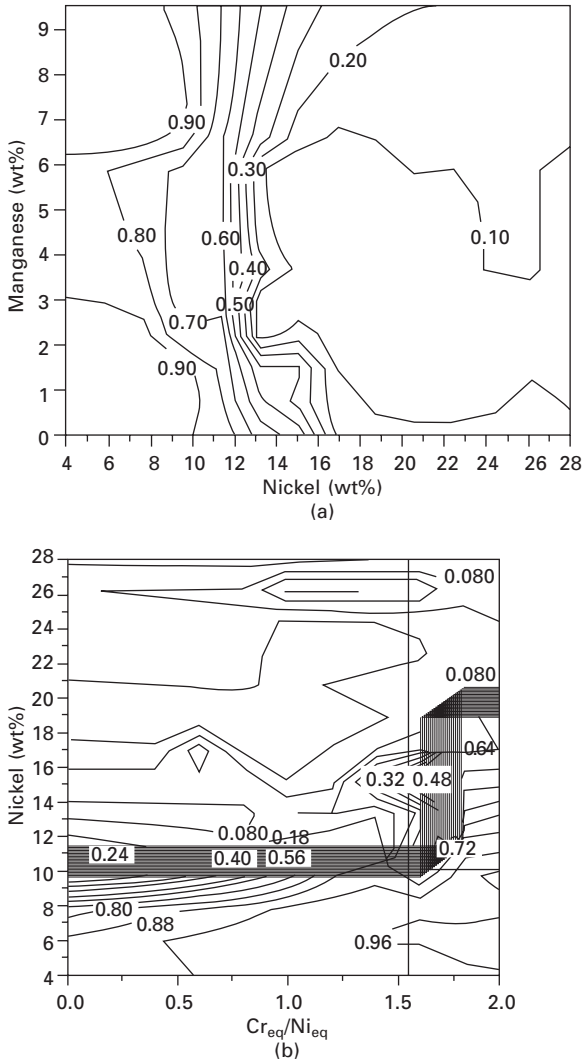

2.26 (a) Combined effect of nickel and manganese contents on probability of PF solidification mode. (b) Combined effect of Ni content and Hammar–Svensson Cr_{eq}/Ni_{eq} on probability of PF solidification mode.

specimens, impact toughness values of 90, 97 and 103 J were obtained after PWHT at 1033 K for 3 h. In the second batch (with same chemistry) of six CVN specimens, impact toughness values of 45, 50, 44.5, 68, 74 and 80 J were obtained (after the same PWHT). A summary of the qualification tests on the developmental lot of modified 9Cr–1Mo electrodes by one of the electrode manufacturers is given in Table 2.8.

Table 2.7 Comparison of RMS errors for different FN prediction methods

FN prediction method	RMS error	
	For complete training database	For independent data set not used in training
Bayesian neural network (BNN) model	2.1	2.03
FNN-1999 (back propagation neural network) model	3.5	2.3
WRC-1992	5.8	2.6
Function-fit model	5.6	5.1

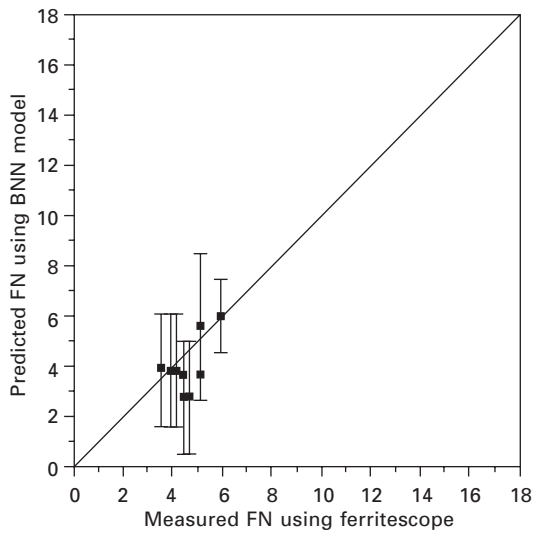

2.27 Comparison of FerriteScope measured and BNN model estimated FN values for 316L (N) welds.

2.7 Hardfacing of austenitic stainless steel components

Based on detailed activity and shielding calculations, the hardfacing taskforce has recommended nickel–base cobalt-free hardfacing alloys Colmonoy-5 and Colmonoy-6 for most of the components [3].

Hardfacing using Colmonoy has been chosen for a majority of the components. Hardfacing with Colmonoy by weld deposition is usually carried out using the GTAW process, for which no major technological development is involved. Therefore, a major objective of the studies was to obtain predictions

Table 2.8 Summary of results of QA tests on modified 9Cr–1Mo developmental electrodes

Chemical composition (wt%)				Impact toughness	
Element	Required	Analysis	Remarks	Impact energy (J)	Remarks
C	0.08–0.12	0.075 ± 0.005	C low by 0.05	90	Well above
Cr	8.0–9.5	9.4 ± 0.5	Cr high by 0.4	97	45 J specified
Mo	0.85–1.05	0.92 ± 0.05	OK	100	and consistent
Mn	0.5–1.2	0.6 ± 0.05	OK		
Si	0.15–0.3	0.28 ± 0.03	OK	45	Within 45 J
S	0.01 (max)	0.012 ± 0.001	High by 0.003	50	specified
P	0.01 (max)	0.012 ± 0.002	High by 0.003	44.5	
Ni	0.4–1.0	0.5 ± 0.05	OK	68	Well above
Nb	0.04–0.07	0.02	Low by 0.02	74	45 J specified
V	0.15–0.22	0.02	OK	80	
N	0.03–0.07	0.037 ± 0.005	OK		
Cu	0.25 (max)	< 0.05	OK		
Al	0.04 (max)	< 0.034	OK		
Fe	Balance	Balance	OK		

of long-term microstructural and hardness degradation of Colmonoy hardface deposits at the end of design life. Bushes of Colmonoy-6 alloy have been fabricated using technology developed in-house for use in the transfer arm gripper assembly. A major problem with weld deposition by GTAW is the high dilution and tendency for cracking of the weld deposit, necessitating stress relieving at high temperatures. One possible way to alleviate these problems, at least partially, is to deposit thinner coatings using the plasma transferred-arc welding (PTAW) process.

The Colmonoy hardfacing alloys, which contain high chromium and boron, form very hard chromium borides and abrasive resistance of the alloys is a function of amount of hard borides present in the matrix. However, the problems associated with the weld deposition of the nickel–base Colmonoy hardfacing alloys include low fluidity, generation of residual stress in the weld deposits that can lead to cracking, hard microstructure and significant dilution of deposit by the substrate material owing to the large difference in their respective melting points. Since the cracking resistance of hardfacing alloys is very poor, preheating and controlled slow cooling often needs to be adopted to avoid cracking. The selection of the hardfacing process depends on the form of filler material available. However, non-conventional weld deposition techniques such as laser welding and PTAW are found to be advantageous over the other processes that are generally used for hardfacing. Finally, selection of coating thickness has to be done judiciously considering corrosion and wear at elevated temperatures, at which the material softens

and the wear loss increases as a consequence. One of the most important concerns with Colmonoy alloys is the reduction in hot hardness (Fig. 2.28) above 723 K [46]. The effect of ageing temperature on hardness and microstructure with respect to dilution and predicted end-of-life ageing behaviour of Colmonoy alloys is discussed.

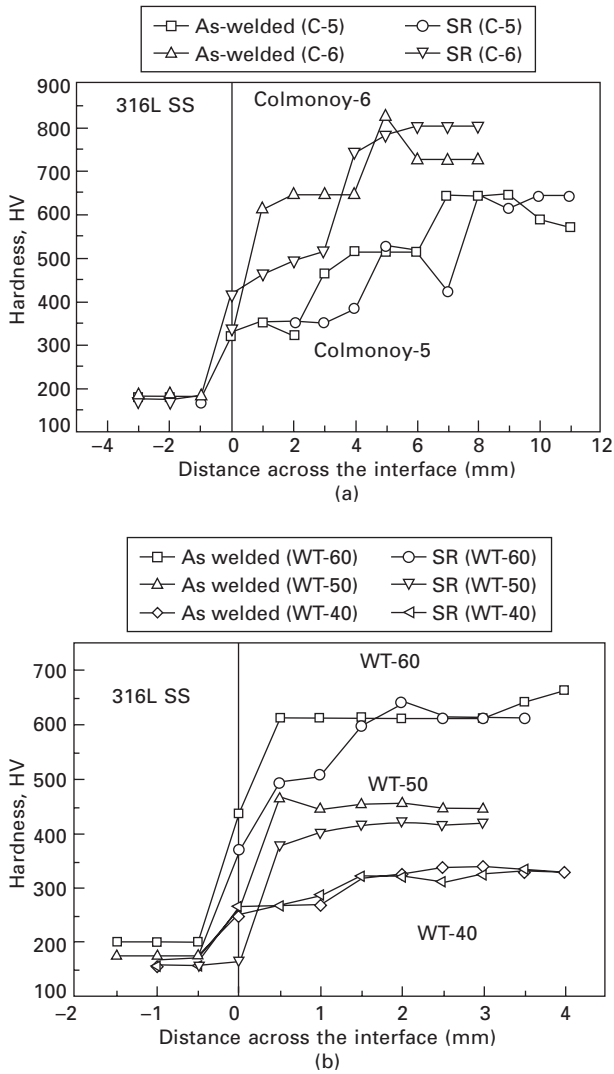

2.28 Variation in hardness across (a) tungsten inert gas (TIG) and (b) plasma transferred arc (PTA) deposits of NiCr hardface alloys.

2.7.1 Selection of hardfacing process and hardfacing alloy type

In NiCr hardfacing alloys, chromium borides and carbides contribute to their high hardness in addition to the solid solution strengthening by the alloying elements [47]. During deposition, dilution from the substrate material occurs and this could significantly alter the microstructure and mechanical properties of the hardface deposits near the deposit/substrate interface [48]. Further, the coating thickness is optimised from the consideration that, owing to differential thermal expansion of the deposit and substrate, an increase in thickness would cause an increase in the residual stress and the tendency of the deposit to crack and spall under thermal cycling conditions. Also, radiation-induced damage can aggravate the integrity of the hardface coatings. Finally, when designing coatings for wear resistance, corrosion resistance and other high temperature properties, the finished coating thickness is so chosen that it is greater than the permitted wear tolerance, especially for nuclear components in which refurbishing or repair is not envisaged.

While the undiluted hardface deposit provides the required wear resistance, the dilution zone at the deposit/substrate interface partially accommodates the stresses that arise during deposition or due to differential thermal expansion of the deposit and substrate during high temperature service. It is for these considerations that the best deposition process has to be adopted so that the width of the dilution zone is optimum and sufficient undiluted zone is available within the desired deposit thickness.

The effect of tungsten inert gas (TIG) and plasma transferred arc (PTA) welding processes on the dilution, and the effect of stress-relieving (SR) heat treatment on the properties of NiCr hardfacing alloys deposited on 316L SS were studied. For this purpose, E NiCr-A (Colmonoy 6, C-6) and E NiCr-B (Colmonoy 5, C-5) rods were deposited by the TIG welding process and E NiCr-A (WT-60), E NiCr-B (WT-50) and E NiCr-C (WT-40) powders were deposited by the PTAW process. Specimens for metallography, hardness measurements and SR heat treatment (at 850 °C for 4 h) were extracted from the deposits. The effect of dilution on microstructure of hardface deposits was characterised by scanning electron microscopy (SEM), energy dispersive analysis of X-rays (EDAX) and electron probe micro-analysis (EPMA).

The hardness profiles across the interface of TIG deposits (Fig. 2.28a) show that as-deposited hardness on the top surface of the C-5 deposit is 673 HV, while that of the C-6 deposit is 803 HV. However, the hardness of the C-5 deposit over a distance of about 1.5 mm from the substrate/deposit interface is only 350–400 HV, which increases to 550–650 HV over the next 1.5 mm of the deposit. For the as-deposited C-6 deposit, the hardness is about 575 HV over a distance of about 2.5 mm from the substrate/deposit interface, about 650 HV over the next 2.5 mm and about 800 HV over the

remaining thickness of the deposit. In both the C-5 and C-6 TIG deposits, SR treatment does not seem to affect their hardness.

The hardness profiles, across the interface of PTA deposits (Fig. 2.28b) show that in the as-deposited condition, the hardness of WT-40 deposit is 251 HV at the substrate/deposit interface and 350–360 HV over the rest of the deposit. Similarly, the hardness of WT-50 deposit is 317 HV at the substrate/deposit interface and 445–454 HV over the rest of the deposit. The corresponding values for WT-60 deposit are 437 and 612–663 HV, respectively. It is obvious that variation in hardness with increasing distance from the interface is much less in the PTA deposits than in the TIG deposits. A marginal decrease in hardness is observed after SR heat treatment of the WT-50 and WT-60 PTA deposits.

SEM images for C-6 TIG deposit with increasing distance from the interface are shown in Fig. 2.29. The microstructure of the deposit at 1 mm from the interface is significantly different from that near the top (8 mm from the interface). The volume fraction of blocky (dark) precipitates is very low near the interface, while both the volume fraction and the size of these precipitates increase with increasing distance from the interface. Further, near the interface, a eutectic mixture with a lamellar-like structure is present that disappears as the distance from the interface increases.

X-ray intensity profiles for Fe and Ni of the as-deposited C-5 and C-6 TIG deposits across the 316L SS/hardface deposit interface were obtained by EPMA. In C-5 TIG deposit (Fig. 2.30), the average Fe count of 119 was higher over a distance of about 1.5 mm from the substrate/deposit interface than in the rest of the deposit (46 counts), while the average Ni count of 257 was lower over a distance of about 1.5 mm from the interface than in the rest of the deposit (308 counts). In the C-6 deposit (Fig. 2.31), the average Fe count of 75 was higher over a distance of about 2.5 mm from the interface than in the rest of the deposit (< 50 counts), while the average Ni count of 400 was lower over a distance of about 2.5 mm from the interface than in the rest of the deposit (500 counts). Thus, the X-ray intensity profiles for Fe and Ni across the substrate/TIG deposit interface confirmed dilution from 316L SS substrate significantly affects the chemistry of these NiCr hardface deposits to the extent of about 1.5 mm into the E NiCr-B deposit and about 2.5 mm into E NiCr-A deposit.

The microstructure of WT-60 PTA deposit at the interface is different from those at different distances from the deposit/substrate interface (Fig. 2.32). However, there is no significant difference in the microstructure at about 2 mm from the interface and at the top of the deposit (about 3.5 mm from the interface), with the microstructure consisting of dendrites, carbides, borides and eutectic carbides. With increasing distance from the interface, the volume fraction of eutectic carbides decreases. The microstructures of WT-40 (Fig. 2.33a) and WT-50 (Fig. 2.33b) PTA deposits are considerably

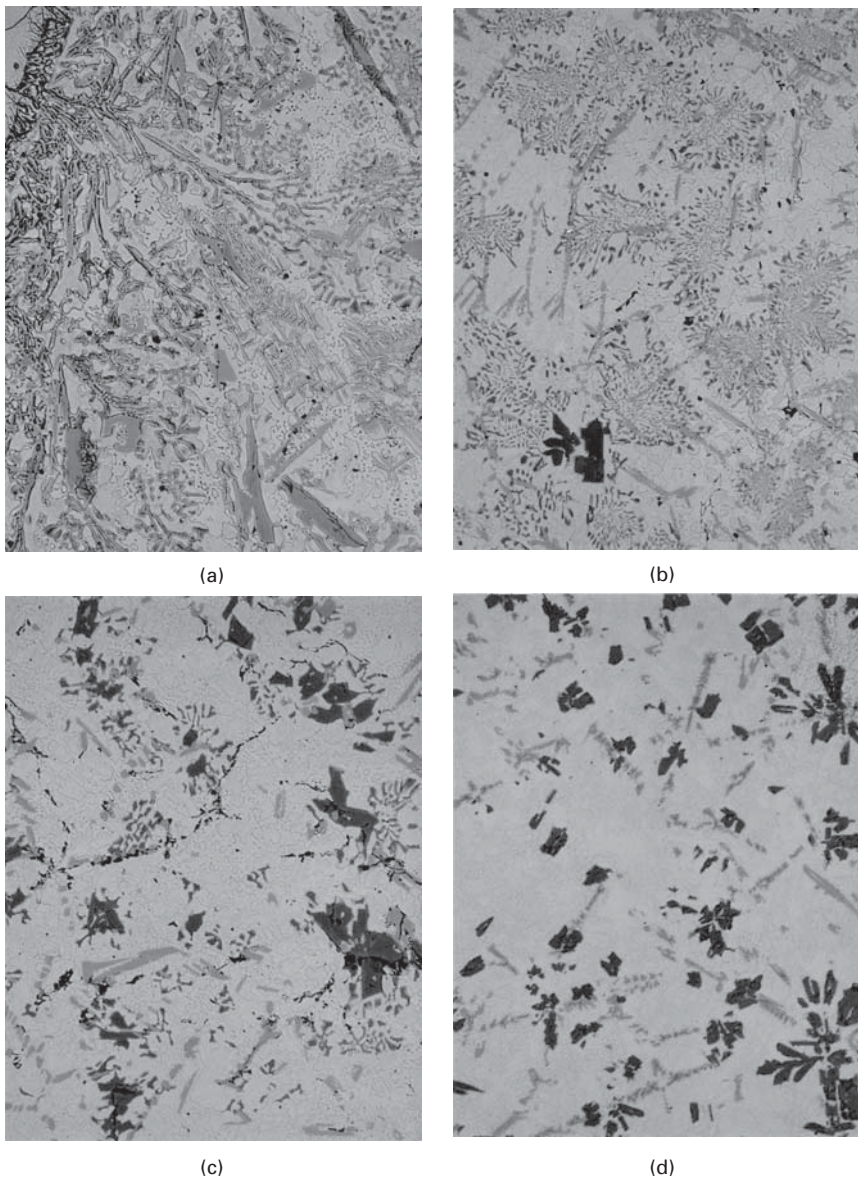

2.29 SEM micrographs of E NiCr-A (Colmonoy 6) TIG deposit at different distances from deposit/substrate interface of: (a) 0 mm (interface); (b) 1 mm; (c) 3.5 mm; (d) 8 mm.

different from that of the WT-60 deposit. The microstructure of WT-40 deposit consists of a pro-eutectic dendritic matrix with inter-dendritic precipitates with rod-like precipitates being practically absent. In the case of the WT-50 deposit, the volume fraction of the eutectic phase is significantly larger than

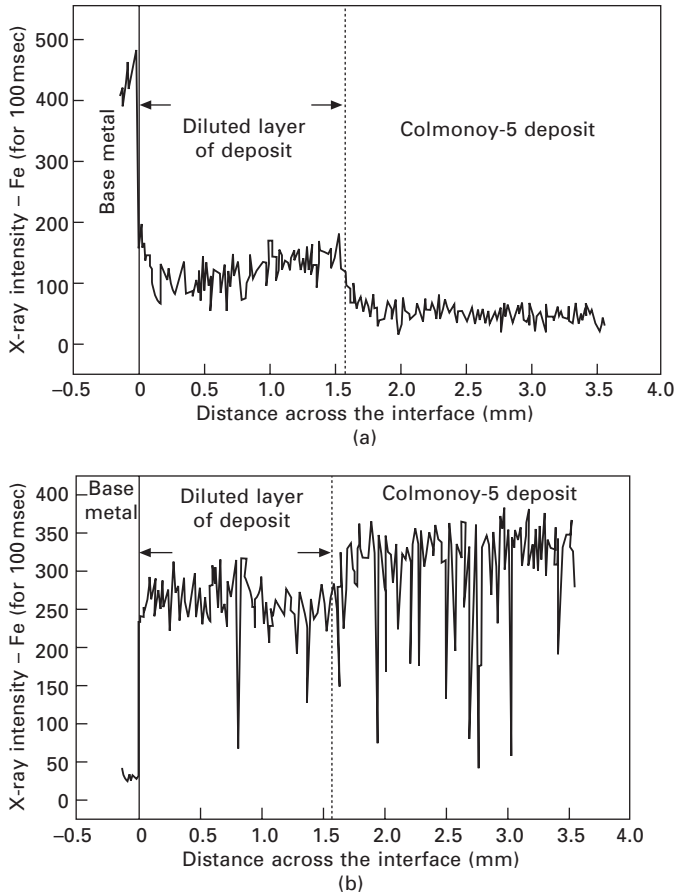

2.30 X-ray intensity profiles for (a) iron and (b) nickel across the E NiCr-B (Colmonoy 5) TIG deposit/316L SS substrate interface.

in the WT-40 deposit, with precipitates having a fish-bone morphology being observed. As in the WT-60 PTA deposit, in these PTA deposits also no significant variation in the microstructure is observed with increasing distance from the interface. The microstructure primarily consists of hypereutectic carbides, borides and a matrix with dendritic morphology. A comparison of the microstructure of the WT-50 PTA deposit after 850 °C/4 h SR heat treatment (Fig. 2.33c) with that of the as-deposited WT-50 (Fig. 2.33b) reveals that the SR heat treatment causes significant microstructural changes in the deposit, with the dendritic structure breaking down and the fish-bone type precipitates remaining unaltered.

Microstructure and hardness variation of the TIG deposits with increasing distance from the interface can be attributed to dilution of the deposit by the

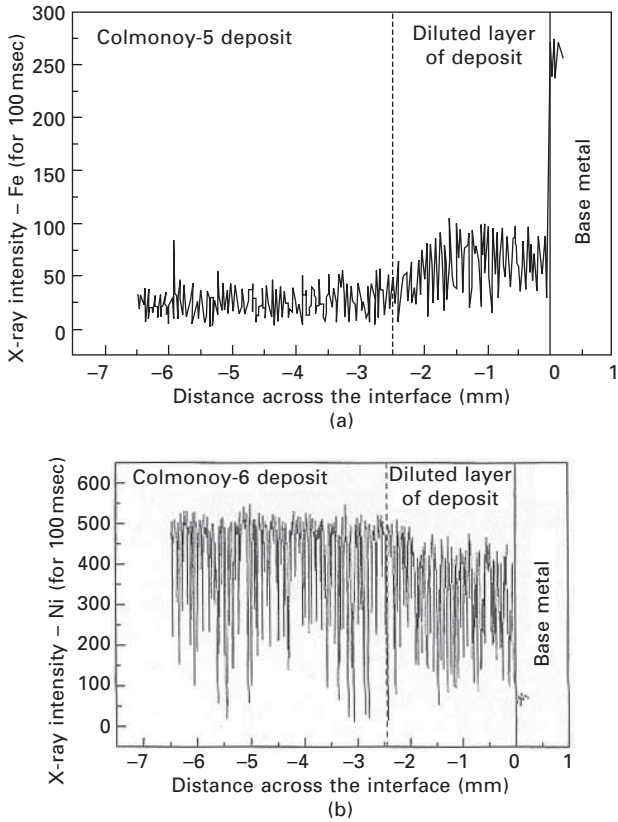

2.31 X-ray intensity profiles for (a) iron and (b) nickel across the E NiCr-A (Colmonoy 6) TIG deposit/316L SS substrate interface.

substrate. The step-wise increase in hardness can be attributed to the deposition of multiple layers. Dilution from the substrate is greatest in the first layer and hence its hardness is the lowest. During the deposition of the second layer, the molten metal mixes with the re-melted and diluted first layer of the deposit and hence the effect of dilution is reduced.

The results of EPMA studies (Figs 2.28 and 2.29) are in agreement with the results from microstructural examination and hardness measurements. There is almost one to one correspondence between the hardness profile and the EPMA profiles for elements Fe and Ni for both C-5 and C-6 TIG deposits. In C-6 TIG deposits, the high-Fe and low-Ni region extends over a distance of about 2.5 mm from deposit/substrate interface, indicating the extent of dilution of the C-6 TIG deposit by the substrate material. This is approximately the same distance over which the hardness was low in this deposit. Results for C-5 TIG deposits are also similar except that the distances over which these changes are observed are lower at about 1.5 mm. The reason for the

(a)

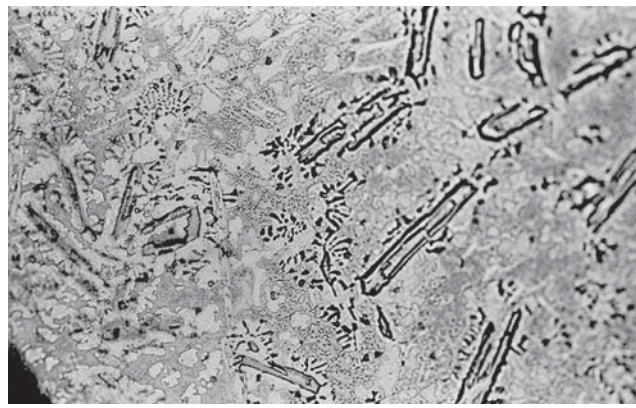

(b)

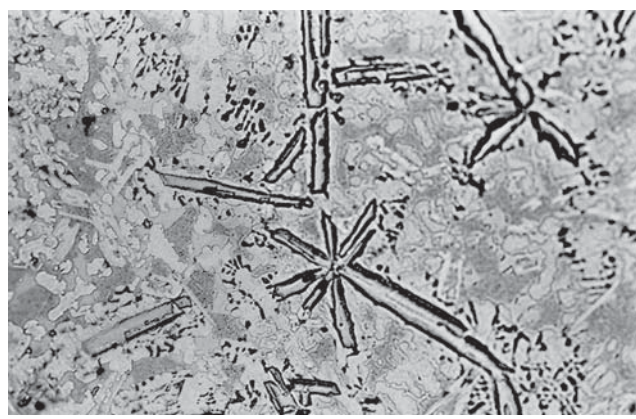

(c)

2.32 Microstructure of E NiCr-A (WT-60) PTA deposit at different distances from deposit/substrate interface of: (a) 0 mm (interface); (b) 2 mm; (c) 3.5 mm.

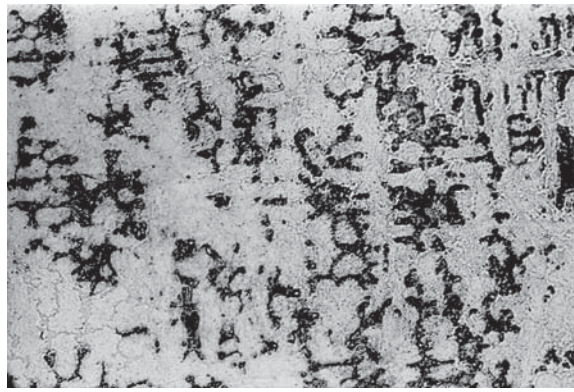

(a)

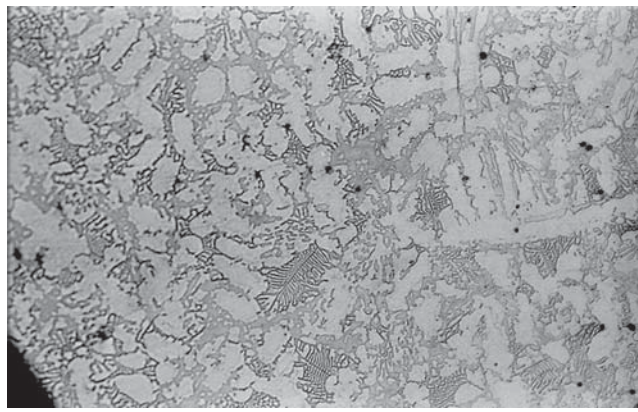

(b)

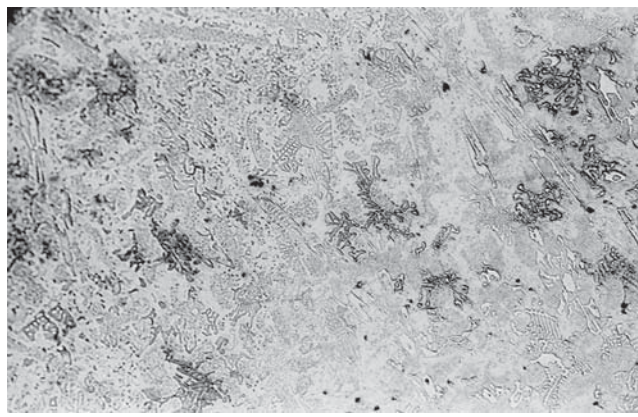

(c)

2.33 Microstructure of PTA deposits at 3.5 mm from deposit/substrate interface for: (a) as-deposited E NiCr-C (WT-40); (b) as-deposited E NiCr-B (WT-50); (c) 850 °C/4 h SR heat treated E NiCr-B (WT-50).

differences in the width of the diluted zones for the two deposits was not clear. Being multipass welds, it could be that these distances correspond to thickness of the first layer of the deposit at the location where both hardness measurements and EPMA analysis were carried out. As already stated, it is the first layer of the deposit that is most affected by dilution from the substrate.

In contrast to the results obtained for TIG deposits, the hardness and microstructural changes in the PTA deposits are confined predominantly over a short distance of about 0.5 mm near the interface. Fairly uniform microstructure and hardness beyond this distance suggest that dilution from the substrate material is significantly low in these PTA deposits.

Considering the various design requirements such as (i) minimising residual stresses (due to differential thermal expansion) both during deposition and service, (ii) avoiding cracking, (iii) ease of deposition and (iv) post-deposition machining, etc., the thickness of the deposit recommended for finished components is 1.5 mm. From the results discussed above, it is very clear that the hardness of TIG deposits of 1.5 mm thickness would be much lower than the minimum hardness achievable in the undiluted hardface alloy deposits. Hence, the PTAW process has been selected for hardfacing of the components.

Among the hardfacing alloys considered for deposition by the PTAW process, the hardness of E NiCr-C (WT-40) alloy is quite low while that of E NiCr-A (WT-60) alloy is too high. Also, the poor weldability of Ni base alloys makes it very difficult to achieve crack-free deposits using the E NiCr-A (WT-60) alloy. Hence, hardfacing alloys conforming to AWS specification E NiCr-B have been chosen for hardfacing of components. The hardness of the E NiCr-B hardfacing alloy also meets the minimum hardness requirement (40 $R_C \equiv 392$ HV) specified for the hardface deposits of components.

The SR heat treatment at 850 °C for 4 h is specified for many of the hardfaced components to ensure dimensional stability of these components during final machining and high temperature exposure during service. Since it was reported that high temperature hardness of NiCr hardfacing alloys reduces significantly with increase in temperature above 450 °C, it was necessary to ensure that SR heat treatment at 850 °C does not adversely affect the hardness of the hardface deposit. The hardness of TIG deposits subjected to SR heat treatment indicates that this heat treatment does not have any adverse effect on the properties of the TIG deposits (Fig. 2.28a). The small differences in hardness observed between the as-deposited and SR heat-treated TIG deposits are attributed to non-uniform distribution of precipitates. However, SR heat treatment of the PTA deposits seems to have some effect on its hardness and microstructure. As seen in Fig. 2.33(c), the dendritic microstructure of the matrix breaks down, resulting in a slight reduction in hardness (Fig. 2.28b). However, as the hardness reduction after SR heat treatment is only marginal, it is unlikely that the performance of hardfaced components would be adversely affected.

2.7.2 Metallurgical and ageing behaviour of hardface deposits on austenitic SS

Metallurgical characterisation of nickel-base Colmonoy 5 and 6 hardfacing alloy deposits on 316L(N) austenitic SS was carried out. Five layers of Colmonoy 5 and Colmonoy 6 hardfacing alloys were deposited separately using 4 mm diameter rods by GTAW process on a 316L(N) SS plate of dimensions $50 \times 50 \times 25\,mm^3$. Studies on Stellite 6 and Stellite 12 were used for comparison. The investigations carried out were on hardness, microstructure, dilution and long-term ageing effect at high temperature on room temperature properties of the coatings. For hardness, metallography and dilution studies, $10 \times 10 \times 10\,mm^3$ pieces of the deposit were cut using the electrical discharge machining (EDM) process and metallographically polished up to 0.25 µm. These hardfaced samples were also subjected to ageing at two different temperatures, viz. 823 and 923 K for 1000 h or longer durations.

Colmonoy 5 hardfaced 316 SS plates were also cut into $10 \times 10 \times 10\ mm^3$ pieces and subjected to ageing at three different temperatures, viz. 823, 873 and 923 K, for five different durations, viz. 200, 500, 1000, 2000 and 5000 h at each temperature. The Vickers hardness (VHN) values of the as-deposited and all the aged Colmonoy 5 deposits were measured at room temperature (RT) using a load of 10 kg.

The hardness profiles across the SS substrate/Colmonoy 6 and Colmonoy 5 deposits are shown in Fig. 2.34(a) and (b), respectively. The SR and ageing heat treatments do not have a significant effect on the deposit microstructure and hence its hardness up to 1000 h of ageing. Figure 2.34 also shows that there is a step-wise increase in hardness in the deposit. In the as-deposited condition, the minimum hardness in the deposit of about 575 VHN is observed near the interface over a distance of about 2.5 mm for Colmonoy 6, and of about 375 VHN near the interface over a distance of about 1.5 mm for Colmonoy 5. The hardness of the undiluted deposit is 650–800 VHN for Colmonoy 6 and 550–700 VHN for Colmonoy 5. Microhardness measurements also showed that the hardness of the matrix is 500–550 VHN, while those of needle-like and blocky precipitates are 1000–1250 and 2300–2800 VHN, respectively.

The hardness values of the as-deposited and all the aged Colmonoy 5 deposits, measured at RT using a 10 kg load, are presented in Fig. 2.35. The time–temperature correlation for these hardness values were obtained using the Larsen–Miller parametric approach, given by $LMP = T(C + \log_{10} t)$, where LMP is the Larsen–Miller parameter, T is the temperature in Kelvin, t is the time in hours, and C is a constant. The constant C was determined as 14.4 for Colmonoy 5 by least square fitting with the R^2 of the fit being about 0.97 (Fig. 2.36). Using C as 14.4, the hardness at RT of Colmonoy 5 after ageing at 823 K for the service-life of the various components, 2 and 30

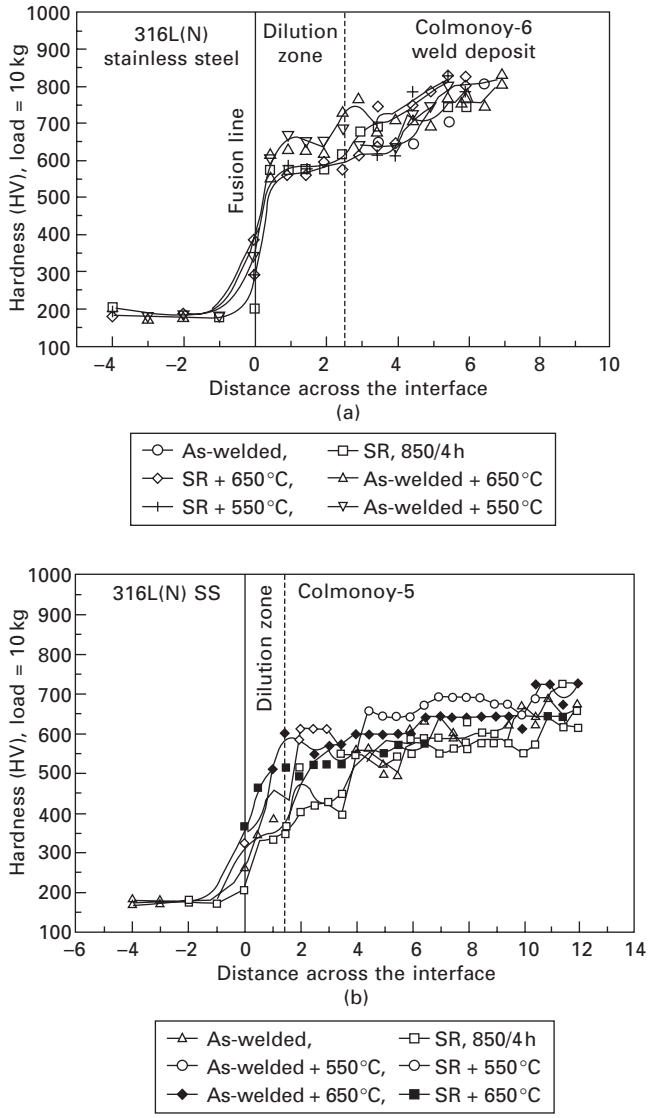

2.34 Hardness variation across substrate/hardface deposit interface for: (a) Colmonoy 6 and (b) Colmonoy 5.

years as also for intermediate durations of 3, 5, 10, 15, 20 and 25 years, was predicted and the same is plotted in the hardness vs. LMP plot in Fig. 2.36.

To predict the hot-hardness of the Colmonoy 5 on prolonged exposure at the different operating temperature of the various components, viz. 673 and 823 K, the average hot-hardness values of unaged Deloro 60 alloy (equivalent to Colmonoy 6) and Stellite 6 were used. The temperature dependence of

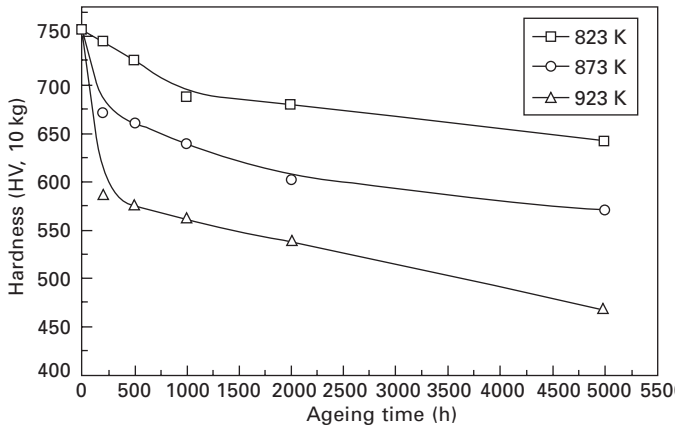

2.35 Variation of hardness (measured at RT) of Colmonoy 5 with ageing time.

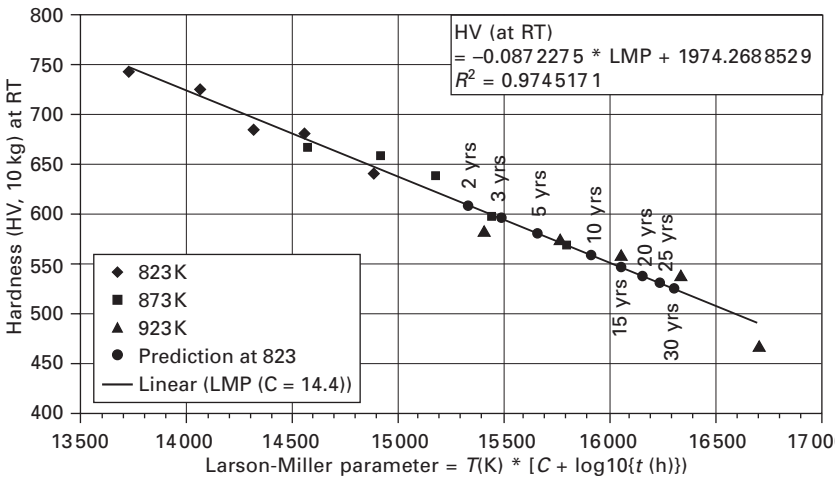

2.36 Hardness (at room temperature) vs. Larsen–Miller parameter plot for Colmonoy 5.

hardness of these hardface deposits was determined by an Arrhenius type plot of ln(hardness at RT/hardness at temperature) vs. $1/T$ (K^{-1}). Using the relationships for both the alloys over the specific temperature ranges as in Fig. 2.4, the hardness of Colmonoy 6 at 673 and 823 K can be predicted for prolonged exposure at 823 K, and the same is presented in Fig. 2.5. The hardness values of as-deposited Stellite 6 at 673 and 823 K are also presented in Fig. 2.5 for comparison. Thus, Figs 2.36 and 2.37 show that although there is expected to be about 30% reduction in the hardness of Colmonoy 6 after 30 years of exposure at 823 K, the hardness of Colmonoy 6 is expected

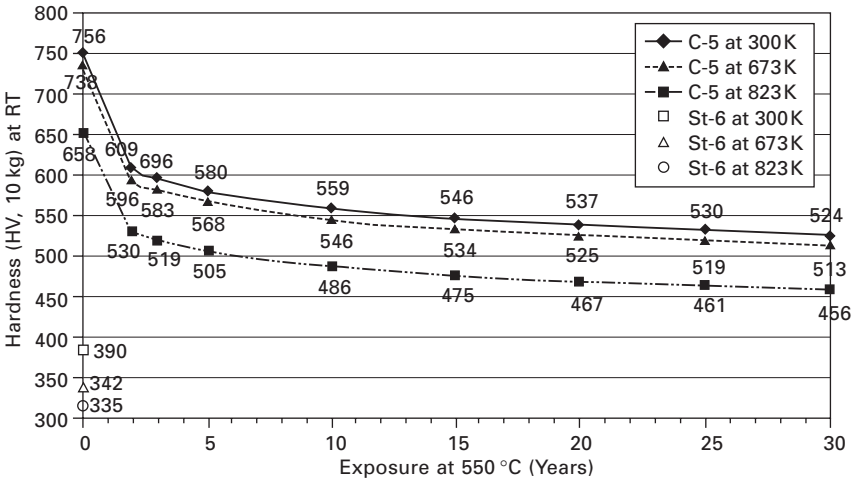

2.37 Projected hot-hardness of Colmonoy 6 on exposure (ageing) at 823 K (550 °C)

to remain sufficiently higher than the hardness of as-deposited Stellite 6. Hence, Colmonoy 6 deposits are expected to retain adequate hardness of about 525 VHN at RT and about 450 VHN at 823 K, after 30 years of exposure (ageing) at 823 K.

Reflected light microscopy observations showed that microstructures of both Colmonoy 5 and Colmonoy 6 deposits varied with distance from the substrate/deposit interface. The precipitates' size and volume fraction were significantly less in the Colmonoy 5 deposit than in the Colmonoy 6 deposit. The Colmonoy 6 deposit showed more needle-shaped carbides and borides compared with the higher fraction of rounded precipitates observed in Colmonoy 5 deposit. EPMA composition profiles showed iron dilution in line with the dilution zone width observed from the hardness variation.

2.8 Conclusions

1. Weldability of austenitic stainless steels as measured using brittleness temperature range criterion (BTR) from the Varestraint test correlated well with the experimentally observed solidification mode and according to the WRC-92 equivalent formulae. Normalising total crack length (TCL) with weld width gave better correlation with BTR, while variability was high when TCL alone was used.
2. Nitrogen in modified 316 weld metal within the specified range of 0.06–0.1% and up to 0.12% was not detrimental to weldability. Nitrogen in fully austenitic weld metal resulted in increased weld metal and heat-affected zone (HAZ) cracking when S level was over 0.01%.

3. Alloy D9 exhibited sensitivity to solidification and HAZ cracking because of the fully austenitic microstructure and the presence of Ti, S, C and N in the weld metal. Cracking, particularly in the HAZ, increased with Ti/(C + N) ratio. From the point of view of weldability, it is desirable to maintain this ratio as low as possible.
4. Grade 91 weld metal and HAZ are highly susceptible to hydrogen-assisted cracking (HAC). The degree of susceptibility is a strong function of composition. Diffusible hydrogen must be maintained as low as possible by way of initial content and baking of electrodes, along with control of preheat temperature to avoid HAC.
5. Toughness of grade 91 weld metal is a complex function of electrode manufacturing process, weld metal composition and heat treatment. The studies indicate that heat treatment cycle to obtain required toughness cannot be universally specified, but would have to be determined for every composition based on experimental data. There is a need to generate more information on the influence of microstructural variables on toughness and creep properties in order to optimise heat treatments for welded components.
6. In the trimetallic transition joint for the SG circuit, the 316L(N) SS/Alloy 800 joint, GTA welded with 16-8-2 would show stable behaviour during long-term elevated temperature exposure in service. For the Alloy 800/9Cr–1Mo steel joint, welded with Inconel 182, PWHT at 1023 K for 1 h would give optimal benefits including excellent resistance to ageing-induced microstructural degradation.
7. In the A48P2/316L(N) SS joint, welded with E309 consumable, residual stress distribution across the joint is not expected to be of serious concern. Tensile properties and residual stress distribution after ageing at 453 K for 120 h indicates that this joint will retain adequate mechanical properties and favourable residual stress distribution under loss of cooling condition over entire lifetime.
8. Modified E316-15 electrodes have been successfully developed indigenously with one electrode manufacturer. The generalised BNN model developed for estimating FN in austenitic SS welds is superior to all the presently available FN estimation methods, including the WRC–1992 diagram. Modified 9Cr–1Mo electrodes have also been developed indigenously with an electrode manufacturer.
9. Nickel–base cobalt-free Colmonoy hardface deposits on austenitic stainless steels are affected by dilution from the substrate, resulting in the hardness near the interface being lower than that in the bulk deposit. The dilution in Colmonoy 5 deposits is slightly less than that in Colmonoy 6 deposits. However, the Colmonoy deposits are expected to retain adequate hardness of about 525 HV at RT and ~ 450 HV at 823 K after 30 years of exposure at 823 K.

2.9 References

1. Bhaduri A K, Venugopal S, Srinivasan G, and Ray S K, *Development, Characterisation and Evaluation of Transition Metal Joint for PFBR Steam Generator Circuit*, Report IGC/MTD/MJS/2001/02, IGCAR, Kalpakkam, India (August 2001)
2. Albert S K, Das C R, Sreenivasan P R, Rai S K, and Bhaduri A K, *Characterisation of the Dissimilar Metal Joint between 316L(N) and A48P2 Steels in Roof Slab*, Report IGC/MTD/MJS/2002/05, IGCAR, Kalpakkam, India (April 2002)
3. Bhaduri A K, Indira R, Albert S K, Rao B P S, Jain S C, Ashok Kumar S, and Kuppusamy P, *Recommended Hardfacing Materials for NSSS Components*, Report IGC/HTF/05, IGCAR, Kalpakkam, India (November 2000)
4. Lundin C D, Lee C H, and Qiao C Y P, *Group Sponsored Study – Weldability and Hot Ductility Behaviour of Nuclear Grade Austenitic Stainless Steels. Final Report,* Univ. of Tennessee, Knoxville, USA (1988)
5. Lundin C D, and Henning J A, *Transformation, Metallurgical Response and Behavior of the Weld Fusion Zone and HAZ in Cr-1Mo steel for Fossil Energy Applications*, Report ORNL (1987)
6. Hart P H M, *Welding J*. **65** (1) (1989) 14s
7. Lundin C D, Milton R, Henning T A, and Richey M W, Hydrogen-Assisted Cracking Sensitivity of Cr-Mo Steels During Welding. *Advances in Welding Science and Technology* Ed. S.A. David, ASM International, Ohio, (1986) 585
8. Dittrich S, Gross V, and Heuser H, *Proc. National Welding Seminar*, Jamshedpur, India (1994)
9. Hainsworth, J, and Tanzosh, J M, Welding of 9Cr–1Mo–V Material. *Maintenance and Repair Welding in Power Plants*, AWS, Miami, Florida, USA (1991)
10. Barnes A, *Influence of Composition on Microstructural Development and Toughness of Modified 9Cr–1Mo Steel Weld Metal,* Report 509/1995, TWI, Abington, UK (1995)
11. Abe N, Ikoma T, and Tamura M, Weldability of Low C–9Cr–1MoNbV Steel (Development of Structural Steels for Fast Breeder Reactor – II), *Transactions of ISIJ* **24** (1984) 229
12. Reddy A S, Mannan S L, and Rodriguez P, Proc Sem *Welding in Boiler and Pressure Vessel Industry – Trends and Technologies for the 80's*, Ind Inst Weld, Tiruchirapalli, India (1979) G1
13. Lundin C D, *Weld J* **61** (1982) 58s
14. Nicholson R D, *Met Technol* **9** (1982) 305
15. Nath B, Proc. Conf. *Welding Technology for Energy Applications*, Amer Weld Soc, Gatlinburg, USA (1982) 597
16. Kleuh R L, King J F, and Griffith J L, *Weld J* **62** (1983) 154s
17. Jones W K C, *Weld J* **53** (1974) 225s
18. Slaughter G M, *Weld J* **43** (1964) 454s
19. Haas P E, Proc Conf *Joining Dissimilar Metals*, Amer Weld Soc, Miami, USA (1982) 37
20. Price A T, Proc Conf *Joining Dissimilar Metals*, Amer Weld Soc, Miami, USA (1982) 48
21. Wright V S, *Met Constrn & Br Weld J* **1** (12s) (1969) 1
22. Viswanathan R, Jaffee R I, and Dimmer J, Proc Conf *Joining Dissimilar Metals*, Amer Weld Soc, Miami, USA (1982) 7
23. Campbell G M, Elmer J W, Gibbs W S, Matlock D K, and Olson D L, Proc Conf

Trends in Welding Research in the United States, ed S A David, Amer Soc Metals, Metals Park, USA (1982) 443
24. King J F, Sullivan M D, and Slaughter G M, *Weld J* **56** (1977) 354s
25. Dalcher A W, Yang T M, and Chu C L, *J Eng Mater Technol* **99** (1977) 65
26. Branchu J, and Gigarel C, *Nucl Technol*, **68** (1985) 135
27. Lallement J, Morel A, and Perona M, *Nucl Technol* **68** (1985) 636
28. Allnatt N J, and Bell G R, Proc International Colloquium on *Hardfacing Materials in Nuclear Power Plants*, Avignon (1980)
29. *Large Sodium Pump Design Study*, Report no WARD-3762-1, Westinghouse Advanced Research Division, USA
30. Lundin C D, Lingenfelter A, Grotke G, Lessman G, and Mathews S, *WRC Bulletin* **280** (1982)
31. Shankar V, Gill T P S, Mannan S L, and Sundaresan S, *Mat. Sci. Eng*. **343** (2003) 170
32. Shankar V, Gill T P S, Thamban M, and Patel P, Proc Symp on *Joining of Metals*, Welding Research Institute, Tiruchirapalli, India (2000) paper WM-25
33. Kujanpaa V, Suutala N, Takalo T, and Moisio T, *Weld. Res. Int.* **9** (2) (1979) 55
34. Miura M, and Sumitomo J, *Metal* **34** (1) (1981) 201
35. Matsuda F, *Advances in Welding Metallurgy*, AWS (1990) 19
36. Shankar V, Muralidharan B G, Srinivasan G, and Gill T P S, Proc *Int Welding Conf* (1996) Ind Inst Welding, Mumbai, India (1996) paper A-056
37. Muralidharan B G, Shankar V, and Gill T P S, Proc *National Welding Sem* (1997) Ind Inst Welding, Bangalore, India (1997) 329
38. Srinivasan G, Shankar V, Gill T P S, and Sethi V K, Proc *Int Welding Conf*, Ind Inst Welding, New Delhi, India (1999) 617
39. Ray S K, Bhaduri A K, and Rodriguez P, *J Nucl Mater* **200** (1993) 70
40. Ray S K, Bhaduri A K, and Rodriguez P, *Int J Pressure Vessels Piping*, **75** (1998) 489
41. Albert S K, Das C R, Sreenivasan P R, Rai S K, and Bhaduri A K, *Characterisation of the Dissimilar Metal Joint between 316L(N) and A48P2 Steels in Roof Slab*, Report IGC/MTD/MJS/2002/05, IGCAR, Kalpakkam, India (April 2002)
42. Bhaduri A K, Srinivasan G, Ramasubbu V, Shanmugam K, Balasubramanian A, and Ramadasan P, *Development of Indigenous Modified E316-15 Electrodes for Shielded Metal Arc Welding*, Report IGC/MTD/MJS/2002/03, IGCAR, Kalpakkam, India (April 2002)
43. Vasudevan M, Bhaduri A K, and Raj B, *Welding in the World,* **51** (7/8) (2007) 15
44. Vasudevan M, Srinivasan G, Bhaduri A K, and Raj B, *Mathematical Modelling of Weld Phenomena – 8*, Eds. H Cerjak, H K D H Bhadeshia, E Kozeschnik, Verlag der Technischen Universität Graz, Austria (2007) 121
45. Vasudevan M, and Bhaduri A K, *Prediction of Delta Ferrite Content in Austenitic Stainless Steel Welds using Bayesian Neural Network Analysis*, Report IGC/MTD/MJS/2002/01, IGCAR, Kalpakkam, India (April 2002)
46. Deloro Stellite Limited, "Tribaloy" Product Catalogue, Deloro Stellite Limited, Swindon, UK
47. *ASM Metals Handbook*, Volume 6, 9th edition, ASM International, Materials Park, Ohio, USA (1993) 794
48. Das C R, Albert S K, Bhaduri A K, Sudha C, and Terrance A L E, *Surface Engineering* **21** (2005) 290

3

Design against cracking in ferrous weldments

P CHELLAPANDI and S C CHETAL,
Indira Gandhi Centre for Atomic Research, India

Abstract: The design procedure for the welds in pressure vessels as per nuclear and non-nuclear codes is presented with sufficient background. The design of welds as per non-nuclear code is done by using empirical correlations after choosing recommended weld configurations. As per nuclear codes, design is performed by detailed analysis. The analysis requirements are highlighted with particular emphasis to constitutive material models. The σ_d procedure for the welds which have creep-like defects, recommended in French assessment procedure RCC-MR Appendix A16, is presented with practical examples. The effect of weld mismatch creep properties on the creep rupture of fossil power plant pipes is quantified by detailed analysis.

Key words: weld design, nuclear codes, non-nuclear codes, acceptable weld configurations, weld mismatch properties, inelastic analysis.

3.1 Introduction

The primary requirement in any design process is to ensure that the component performs the intended function satisfactorily throughout the targeted life under the influence of all the service loadings. In order to comply with this requirement, the designer should choose correct materials, assess service conditions, which requires agreement with design and failure theories, and choose appropriate manufacturing and inspection methods. Despite fulfilling these, early failures can still occur since the welds are the weak links in the component. A specific case study on the failures in the worldwide fast breeder reactors indicates that about 50% are due to welds, as illustrated in Table 3.1 [1]. The major causes of failures in welds are high cycle thermal fatigue, fretting damage caused by flow-induced vibrations, hydrogen embrittlement, overheating of welds and development of longitudinal flaw during manufacturing process and reheat cracking.

Table 3.1 Weld failures in fast reactors

	DFR	PFR	PX	SPX	KNK	Total
Weld failures	3	7	17	1	10	38
Total number of failures	7	19	20	2	21	69

In the design stage, the welds are analysed in detail, strictly respecting the applicable design code criteria. Further, in the process of licensing of power plants for the extended operation, the welds are reviewed critically by non-destructive evaluation (NDE) techniques. In some situations, the defects observed in the components through NDE are analysed critically to decide upon their acceptance. Under these situations, it is essential to apply robust design rules/assessment procedures with complete understanding of behaviour of welds under operating conditions and the factors influencing their behaviour, particularly at high temperature.

The design codes provide rules based on the vast experience gained over the years. As ideal defect-free weld joints are not possible, it is necessary to specify the acceptable defects or deviations for the manufacturing purposes. In this regard, the codes specify the acceptable defects and inspection requirements as per the weld category. Various codes differ in their approach and they can be broadly classified into conventional and nuclear codes. For the purpose of illustration, the scope is restricted to a typical conventional design code called ASME section VIII division 1 [2] and nuclear code ASME section III: subsection NH [3]. The French code RCC-MR provides design rules exclusively for fast breeder reactor components [4]. The main failure modes that are precluded once design satisfies the code requirements are gross yielding and tensile rupture (time independent), and creep strain, creep rupture, creep and fatigue damage (time dependent). It is assumed that the components are free from cracks at the beginning of life and initiation of crack is the failure as per the design codes due to creep fatigue damage accumulation, apart from yielding and creep rupture.

Generally the rules recommended in the codes are followed for weld design. Accordingly, the highlights of the popular design codes, ASME section VIII, division 1 (conventional design), ASME section III, division 1: subsection NH (for high temperature components suitable for nuclear applications) and RCC-MR and annexure A16 (code exclusively for the fast reactor design) are presented. A few applications of nuclear codes, which call for detailed analysis, are brought out. In some special situations, detailed investigations based on numerical simulations are employed to understand the deformation and damage mechanisms. To illustrate this, a case study (premature creep cracking in low alloy steel weld reported in the literature) is presented employing inelastic analysis by finite element method (FEM).

3.2 Weld design rules for pressure vessel components (ASME section VIII division 1)

ASME section VIII division 1 is a popular and mature code for the design of conventional pressure vessel components. These rules can be applied for other components under similar service and loading conditions. The code

adopts the concept of 'design by thumb' rule, which means that it does not call for detailed analysis. The design does not address the complicated thermo-mechanical failure modes, which require detailed strain analysis. This important restriction should be kept in mind while using the code rules.

The first step in the weld design as per the code is the categorisation based on nature of stresses prevailing in the weld zone. In the circular shell, the hoop stress is the highest one, since the longitudinal stress is generally half the hoop stress. The stresses at the shell–nozzle and plate–shell junctions are generally local in nature. Subsequent steps are choosing proper weld configurations and estimation of thickness. These steps are highlighted below.

3.2.1 Weld categorisation

The weld joints in a typical pressure vessel are shown in Fig. 3.1. Category A welds are mainly the longitudinal joints within the main shell which see the hoop stress, communicating chambers, transitions in diameter, or nozzles; any welded joint within a sphere, within a formed or flat head, or within the side plates of a flat-sided vessel; circumferential welded joints connecting hemispherical heads to main shells, to transition in diameters, to nozzles, to communicating chambers.

Category B welds are circumferential welded joints within the main shell which are subjected to longitudinal stresses, communicating chambers, nozzles, or transitions in diameter including joints between the transitions and a cylinder at either the large or small end; circumferential welded joints connecting formed heads other than hemispherical to main shells, to transitions in diameter, to nozzles, or communicating chamber.

Category C welds are joints connecting flanges, tube sheets or flat heads to main shell, to formed heads, to transition in diameter, to nozzles, or to communicating chamber; any welded joints connecting one side plate to

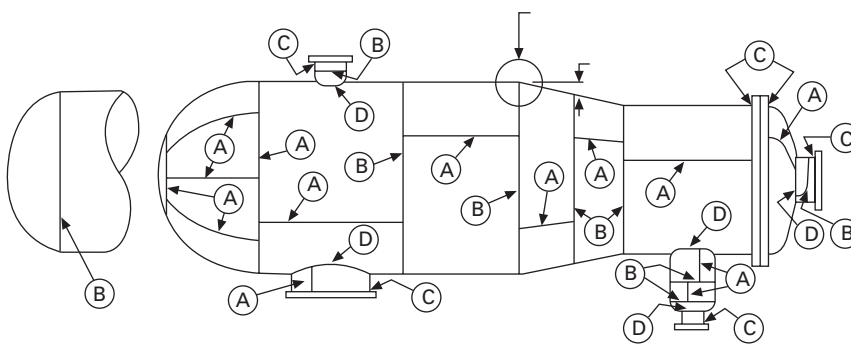

3.1 Typical Category A, B, C and D weld locations.

another side plate of a flat sided vessel. These welds are subjected to stresses which are local in nature.

Category D welds are joints connecting communicating chambers or nozzle to main shell, to sphere, to transition in diameter, to heads, or to flat-sided vessels; any joints connecting nozzles to communicating chambers (for nozzle at the small end of a transition in diameter, see Category B). The stresses developed at these joints are local in nature.

3.2.2 Permissible weld configurations

Certain important aspects should be considered while the design is performed as per the code. The dimensions and shape of the edges to be joined shall be such as to permit complete fusion and complete joint penetration. A tapered transition having a length not less than three times the offset between the adjacent surfaces of abutting sections shall be provided at joints between sections that differ in thickness by more than one-quarter of the thickness of the thinner section. The transition may be formed by any process that will provide a uniform taper. When the transition is formed by removing/adding material from the section, the minimum/maximum thickness of that section, after the material is removed/added, shall not be less/more than that specified by the code. For the lapped joints, the surface overlap shall be generally not less than four times the thickness of the inner plate. The fillet welds shall be added where necessary to reduce stress concentration. A few acceptable configurations for heads attached to shells are shown in Figs 3.2 and 3.3. Some joints between head and shell that are non-permissible as per ASME section VIII division 1 are shown in Figs 3.4 and 3.5.

3.2.3 Thickness estimation

The code has incorporated joint efficiency factors depending on the type and efficacy of radiographic inspection carried out. The formulas for thickness evaluation are as follows:

$$\text{Thickness based on circumferential stress, } t = \frac{PR}{SE - C_1 P}$$

$$\text{Thickness based on longitudinal stress, } t = \frac{PR}{SE - C_2 P}$$

where, t = minimum thickness of the section,
R = inside radius of the vessel
S = maximum allowable stress
P = design pressure
E = joint efficiency
$C_1 = 0.6$ and $C_2 = 0.4$.

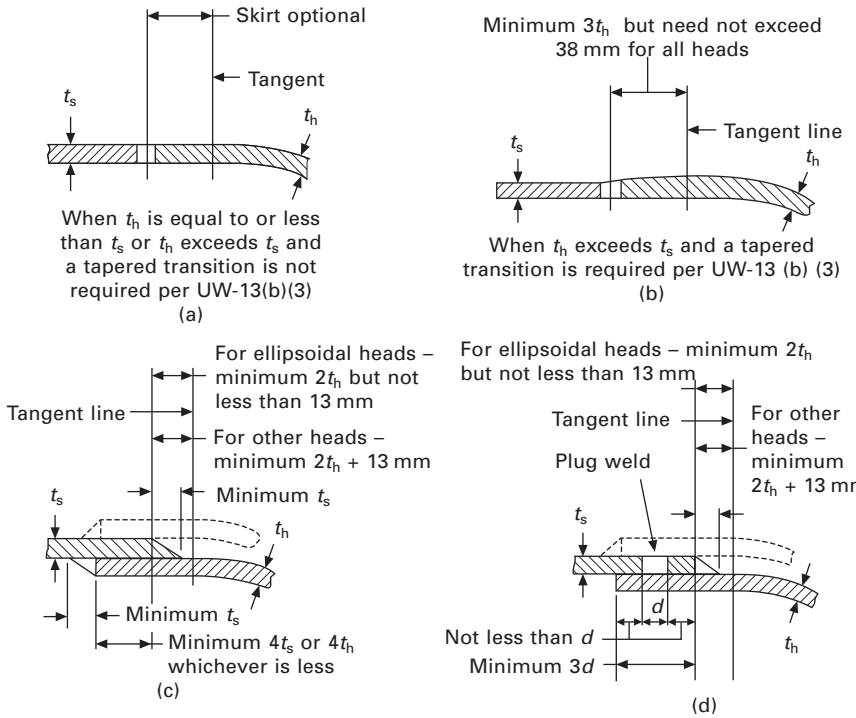

3.2 Acceptable weld joints between cylindrical shell and dished heads.

C_1 and C_2 are constants in the ASME modified formula to take into account both the thin and thick shell theories.

3.2.4 Weld joint efficiencies

In general, joint efficiency (E) depends only on the type of joint and on the degree of examination. Rules for determining the applicability of the efficiencies are found in the various paragraphs covering design formulas. Typical joint efficiencies for the arc and gas welded joints are as follows:

E = 1.0 if fully radiographed for the butt joints specified in Fig. 3.2(a) and (b).
E = 0.85 if spot radiographed for the butt joints specified in Fig. 3.2(a) and (b).
E = 0.7 if spot radiographed for the butt joints specified in Fig. 3.2(a) and (b).
E = 0.9 if fully radiographed for the butt joints specified in Fig. 3.2(c) and (d).

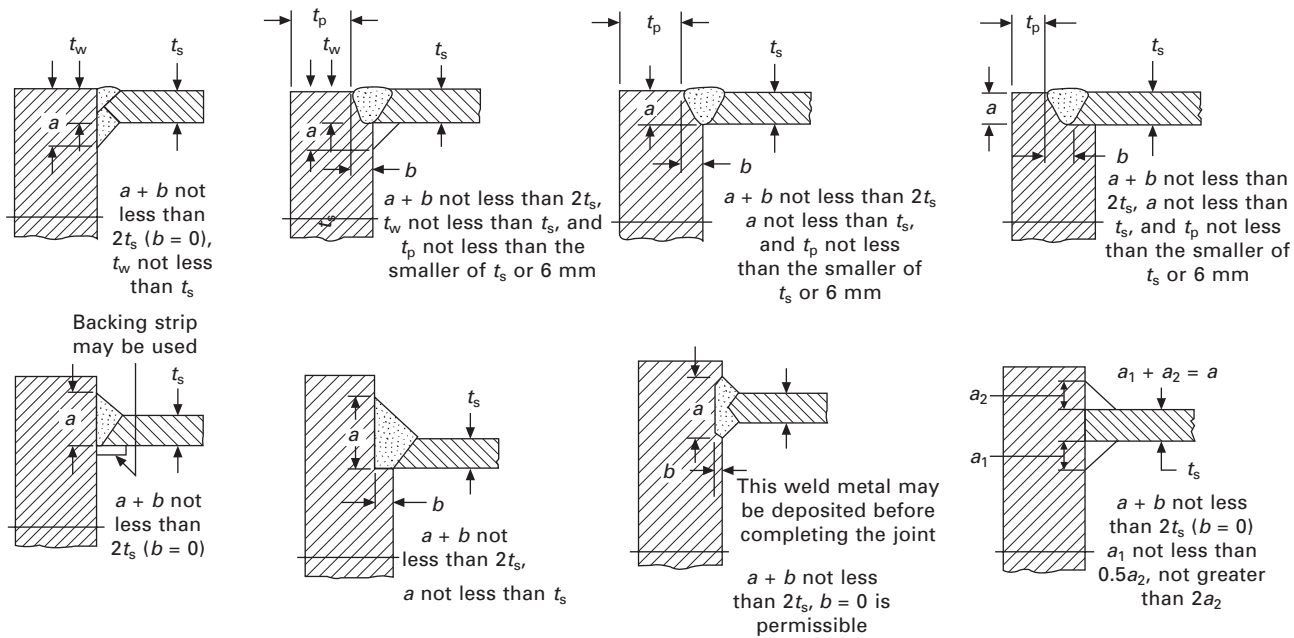

3.3 Acceptable corner joints for flat plates attached to shells.

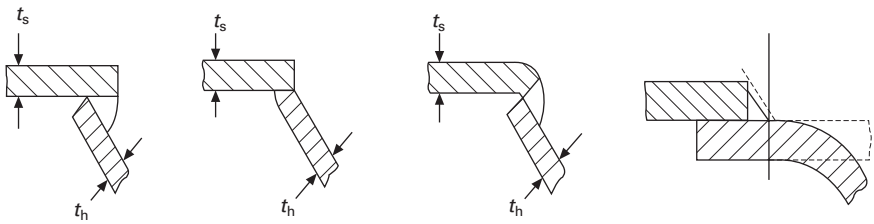

3.4 Non-permissible joints between shell and dished ends.

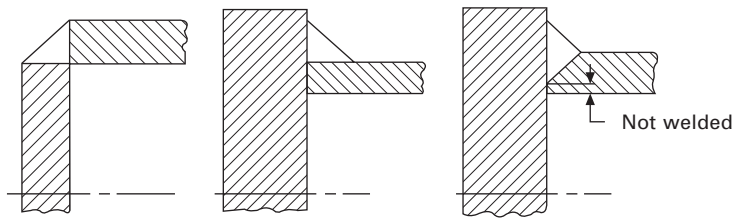

3.5 Typical non-permissible joints between shell and flat heads.

E = 0.8 if spot radiographed for the butt joints specified in Fig. 3.2(c) and (d).
E = 0.5 if spot radiographed for the butt joints specified in Fig. 3.2(c) and (d).

3.3 Weld design rules for nuclear power plant pressure vessels (ASME section III division 1)

ASME section III division 1 provides necessary design rules for nuclear power plant pressure vessels. Since the nuclear components are subjected to severe thermo-mechanical loadings, the design code addresses the possible failure modes due to static as well as cyclic temperature gradients. Accordingly, a 'design by analysis' approach is adopted in the nuclear code. The design analysis starts only after proper choice of weld configurations, as recommended by the code.

The analysis calls for determination of detailed stresses due to mechanical loadings to derive primary stresses and thermal gradients to derive secondary stresses. The code provides appropriate permissible stresses separately for the primary and secondary stresses. While primary stress limits ensure adequate structural integrity, the secondary stress limits protect against deformation-related failure modes accumulated over the plant life. For the purpose of stress and strain analysis as well as time-independent failure modes, the weld metal is assumed to have the same material properties as the parent metal. However, for the assessment of time-dependent failure modes, viz. accumulated strain, creep and fatigue damage, appropriate weld strength

reduction factors specified in the code are to be applied. The sub-section NB provides design rules for the safety-related components (class 1 components) in general and subsection NH provides additional rules to be respected for the design of components operating at high temperature (> 700 K for typical austenitic stainless steels).

A few important aspects of weld design rules specified in subsection NH are extracted and presented in the following paragraphs.

3.3.1 Permissible types of welded joints

The design of the vessel shall meet the requirements for each category of joint. The butt joints are full penetration joints between plates or other elements that lie approximately in the same plane. Category B angle joints between plates or other elements that have an offset angle, α, not exceeding 30° are considered as meeting the requirements for butt joints. Figure 3.6 shows typical butt welds for each category joint.

When Category B joints with opposing lips to form an integral backing strip or joints with backing strips not later removed are used, the suitability for cyclic operation shall be analysed using a fatigue strength reduction factor of not less than 2 under conditions where creep effects are insignificant. The corners of the end of each nozzle neck shall be rounded to a radius of one-half the thickness, t_n of the nozzle neck, or 19 mm ($^3/_4$ in.), whichever is smaller. *d* is the outside diameter of the nozzle. Where partial penetration welds are used, a fatigue strength reduction factor of not less than 4 shall be used for any related fatigue analysis under conditions where creep effects are insignificant. Oblique full penetration nozzles are permitted provided the following are satisfied:

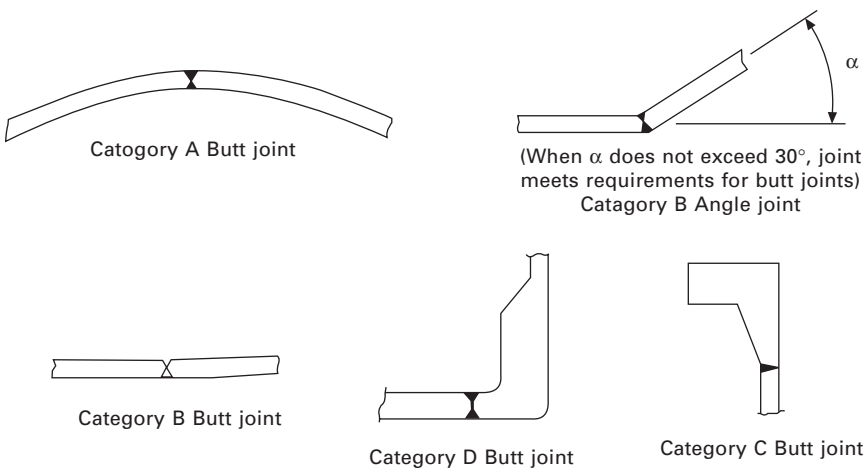

3.6 Typical butt welds for each category joint.

- The opening shall be completely reinforced, with the reinforcement located in the shell or head of the vessel.
- The nozzle shall be subjected to essentially no pipe reactions and no thermal stresses greater than in the vessel itself.
- The nozzle wall and the weld shall develop the full strength of the nozzle.

Two typical design details with thermal sleeves shown in Fig. 3.7 (not included in ASME) are recommended for high temperature applications. The diameter transition should typically be made using a standard reducer to provide increased structural flexibility and reduce the sharpness of the thermal gradient. Thus the thermal stresses as well as discontinuity stresses and the resulting fatigue damage are minimised.

The vessel supports, such as skirt, lug or column, should be attached to the vessel shell or head using full penetration welds. Two typical recommended configurations are shown in Fig. 3.8, one with a forged ring section and another with a weld build up. In both design concepts, clear access is provided for welding (butt weld) and also for inspecting, thus increasing the potential for achieving good overall weld quality. Further, skirt-supported vessels in high temperature applications will have a relatively high thermal gradient at the skirt-to-shell intersection. The local thermal gradient can be minimised by graded insulation. Another design concept often adopted is to provide slots in the skirt to increase the flexibility.

3.3.2 General guidelines of robust design

- Socket welds must be avoided for applications having risk of crevice corrosion. Further, socket welds have high stress concentration making them unsuitable for fatigue conditions.

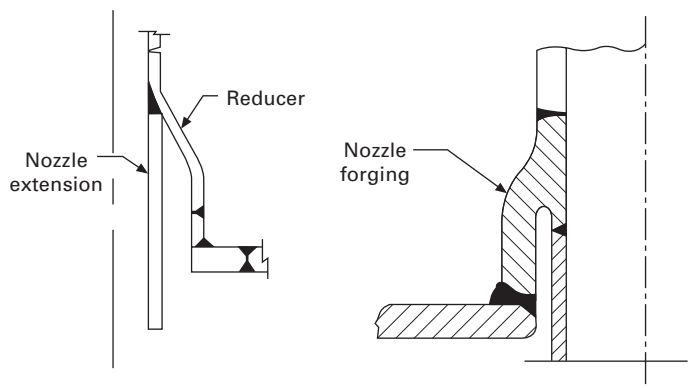

3.7 Nozzle welds with thermal sleeves for high temperature applications.

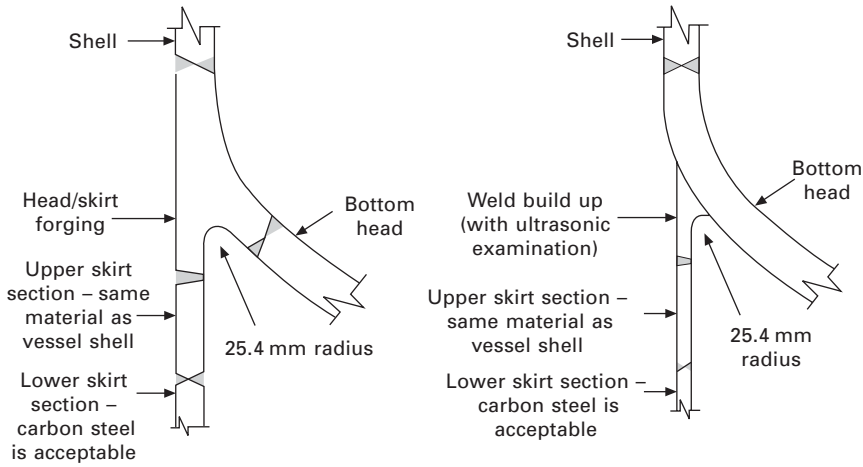

3.8 Typical preferred design for high temperature vessel supports.

- For an application involving fatigue loading, it is important to specify flush weld as against welded to minimise stress concentration factor. For more details, reference may be made to Table NB 3681 (as-1 of ASME section III, division 1 subsection NB class 1 component, ref [13]).
- For an application involving welding of two dissimilar steels of widely different thermal expansion and involving fatigue loading, for example of $2\frac{1}{4}$Cr–1Mo to austenitic stainless steel piping, it is advisable to incorporate an intermediate sleeve of a minimum length of $2.5\sqrt{RT}$ with an expansion co-efficient intermediate between the two base materials such as Alloy 800.
- For a heat exchanger, an application involving media not compatible with each other such as sodium and water in a sodium heated steam generator, it is worth making an economical comparison between the internal bore butt weld of tube to tube sheet with raised spigot and traditional rolled and welded joint. The spigot design has many advantages, such as the possibility of complete volumetric inspection, elimination of crevice corrosion and location of weld in low stress zone, in comparison with traditional rolled and welded joint. The additional cost of internal bore weld is likely to compensate the possible outage cost associated with the rolled and welded joint.

3.3.3 Primary stress limits

Primary stresses arise due to mechanical loadings such as gravitational force and pressure. Once the basic dimensions of the components including weld configurations are selected, stresses due to mechanical loadings should be

computed based on linear elastic analysis. For complex geometries, numerical methods such as the finite element method can be employed. From the computed stresses, primary stress intensities are computed based on which the failure of wall thickness is defined. Basically two stress intensities, viz. general primary membrane stress intensity (P_m) and primary bending stress intensity (P_b) are defined. These are calculated based on the linearised stress components (σ_{1m}, σ_{2m}, σ_{3m}, σ_{1b} , σ_{2b} and σ_{3b}) derived from the computed stresses, as follows:

$$P_m = \max \mid (\sigma_{1m} - \sigma_{2m}), (\sigma_{2m} - \sigma_{3m}), (\sigma_{3m} - \sigma_{1m}) \mid$$

$$P_b = \max \mid (\sigma_{1b} - \sigma_{2b}), (\sigma_{2b} - \sigma_{3b}), (\sigma_{3b} - \sigma_{1b}) \mid$$

For a simple uniaxial state of stress case, $P_m = \mid \sigma_{1m} \mid$ and $P_b = \mid \sigma_{1b} \mid$ which are schematically illustrated in Fig. 3.9.

The limits on primary stress intensities are defined in terms of basic allowable stress intensity called S_m in case the structural wall under consideration is operating in the non-creep regime (< 700 K for austenitic stainless steel and 645 K for carbon steel). If the structural wall is operating at the temperatures where creep is significant, basic allowable stress intensity, called S_t, is defined. S_t is defined as follows:

- 100% of the average stress required to obtain a total (elastic, plastic, primary and secondary creep) strain of 1%;
- 80% of the minimum stress to cause initiation of tertiary creep; and
- 67% of the minimum stress to cause rupture.

Stress limits

$$P_m \leq \text{lower of } S_m \text{ or } S_t$$

$$P_m + (P_b/K_t) \leq S_t$$

The factor K_t accounts for the reduction in extreme fibre bending stress due to the effect of creep. Thus, K_t is defined as ratio of creep stress ($-\sigma_c$)

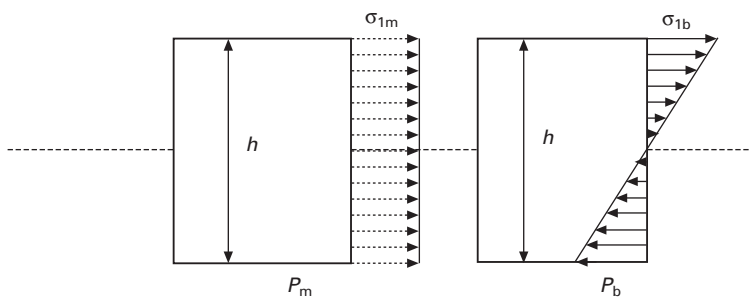

3.9 Primary membrane (P_m) and bending (P_b) stress intensities.

and elastically computed stress ($-\sigma_e$) at the extreme wall surface (Fig. 3.10).

For the welds, the S_t is equal to $0.8S_t \times R$, where R is the appropriate ratio of the weld metal creep rupture strength to the base metal creep rupture strength. S_r is the expected minimum stress-to-rupture strength. Figure 3.11 shows typical S_t values for weld for SS 316.

3.3.4 Secondary stress and strain limits

While elastic stress analysis is required for determining primary stresses, detailed inelastic analysis is needed to determine stress and strain due to steady state as well as cyclic thermal loads. This is because of the complicated deformation mechanisms such as cyclic plasticity and ratcheting under combined primary and cyclic secondary stresses, which cause accelerated strain growth. Inelastic analysis calls for realistic constitutive material models

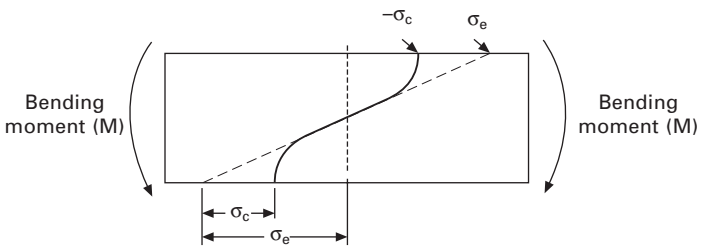

3.10 Basis for introduction of K_t parameter in subsection NH.

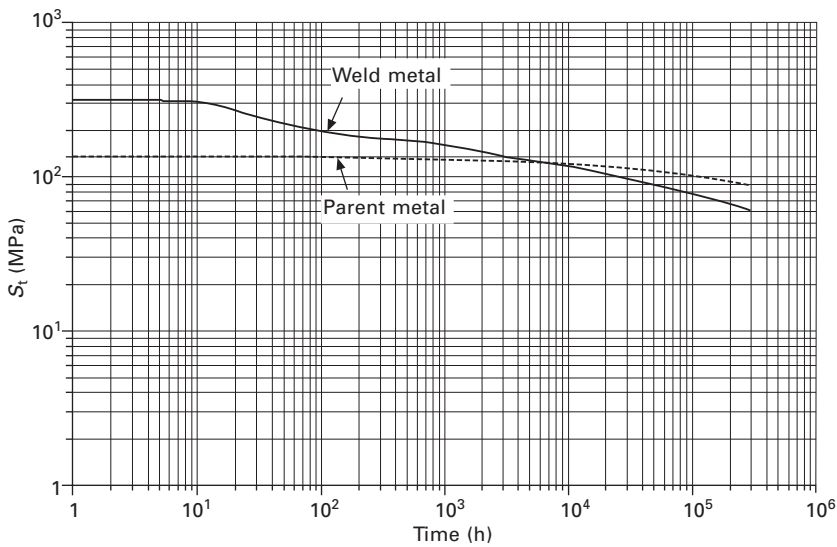

3.11 S_t values of welds for SS 316 at 550 °C.

to be employed in the finite element analysis. In view of these difficulties, the codes specify simplified techniques to determine inelastic stresses and strains based on elastically computed stresses. These simplified rules yield very conservative results. However, the 'elastic analysis route' is preferred in the design stage and, probably, inelastic analysis is preferred in the detailed design, to raise confidence as well as for life extension purposes.

Simplified analysis

The elasto-, plastic-creep stresses and strains of component wall subjected to monotonic/cyclic loads are estimated from elastically computed stresses, based on some robust theorems. Neuber's rule is commonly applied to estimate the elasto-plastic stress and strains. Accumulated inelastic strains on the component, subject to steady mechanical load (P, primary stress) and cyclic thermal loadings (ΔQ, secondary stress range) are computed using the O'Donnel–Porowski diagram. These methodologies are highlighted below.

Neuber's rule

As per Neuber's rule, the product of stress and strain is invariant with respect to stress strain curve. This implies that $\sigma\varepsilon$ = constant, which is a hyperbola. The constant can be determined based on elastically computed stress and strain. The intersection point of this hyperbola and actual elasto-plastic stress–strain curve defines the elastoplastic stress and strain. Under a multiaxial situation, the von Mises stress σ_{VM} can be used. Figure 3.12 illustrates the methodology.

O'Donnel–Porowski Diagram (OPD)

The accumulated inelastic strain is computed knowing the effective primary stress intensity $[P_m + (P_b/K_t)]$ and secondary stress range (ΔQ). By dividing these two quantities with average yield stress S_y, two parameters, viz. X and Y, are defined as: $X = [P_m + (P_b/K_t)]/S_y$ and $Y = \Delta Q/S_y$. Knowing X and Y, a parameter called dimensionless creep stress parameter Z is read from the OPD (Fig. 3.13), from which the effective core stress is computed as $\sigma_c = ZS_y$. The creep strain corresponding to σ_c for the total duration and specified temperature can be computed from the applicable isochronous stress strain curve provided in subsection NH.

Inelastic analysis

Inelastic analysis is essential for accurately predicting stress and strain history in the components subjected to mechanical and thermal loadings and thereby

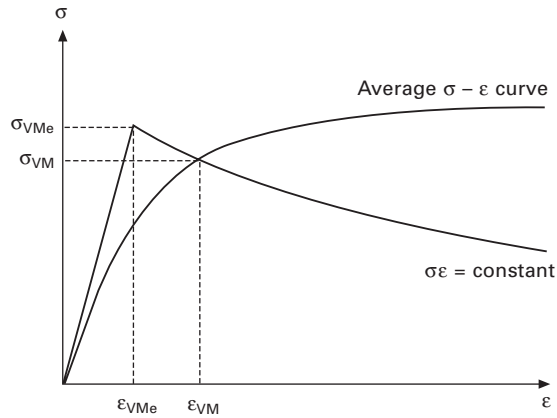

3.12 Neuber's rule for estimating elastoplastic stress and strain.

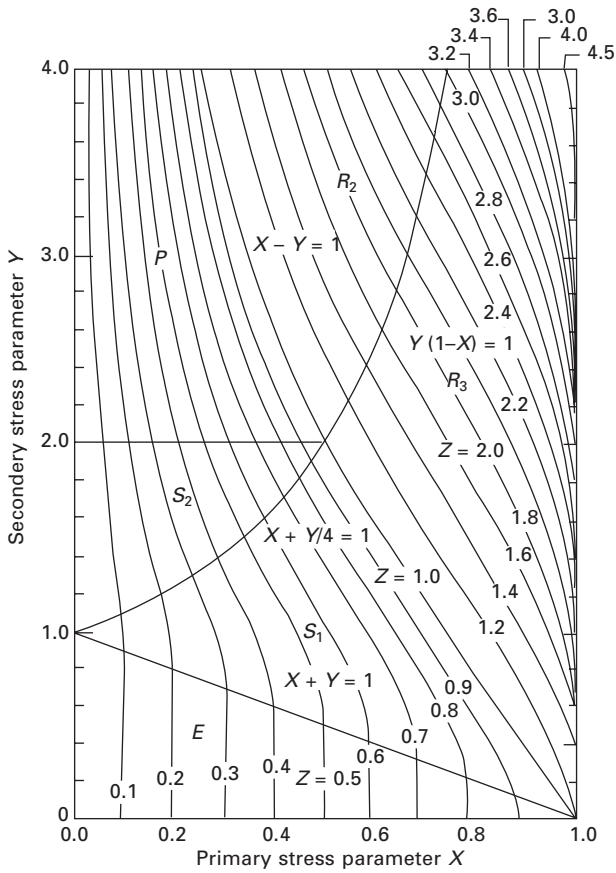

3.13 O'Donnel–Porowski Diagram.

for the accurate estimation of ratcheting, creep and fatigue damages. This calls for use of realistic material constitutive models to be employed in the numerical prediction of stress–strain history at all the critical locations. The constitutive model should be able to simulate accurately the complex material behaviour caused by monotonic and cyclic, mechanical and thermal loadings at high temperature. Apart from creep and creep relaxation, the material hardening behaviour by which the instantaneous yield stress and strain hardening behaviour changes continuously in stress or strain cycling is an important aspect need to be modelled. ASS exhibits cyclic hardening behaviour. Further, depending upon the values of primary and secondary stress ranges, the material point exhibits many complex behaviours, viz. elastic cycling, shake down and ratcheting. Under various cyclic loading, as illustrated in Fig. 3.14, there is no permanent strain at the end of each elastic cycling (Fig. 3.14a). Under shakedown, there is no accumulation of strains except strain cycling with a fixed magnitude (Fig. 3.14b). Under very high strain cycling (ratcheting), there is a possibility of progressive growth of strain, cycle by cycle, which can lead to development of unacceptable strains after application of a few number of load cycles (Fig. 3.14c).

The behaviour model to be considered will depend on the physical phenomenon and on the collapse mode to be analysed. Table 3.2 gives a guideline for cyclic hardening materials, but should be used with care when dealing with cyclic softening materials.

Strain limits

The design code specifies certain limits on the accumulated strain due to plasticity, creep and ratcheting. Accordingly, the principal strain components, viz. maximum positive membrane strain (ε_m), positive bending strain (ε_b) and positive local strain (ε_L), are to be limited as follows:

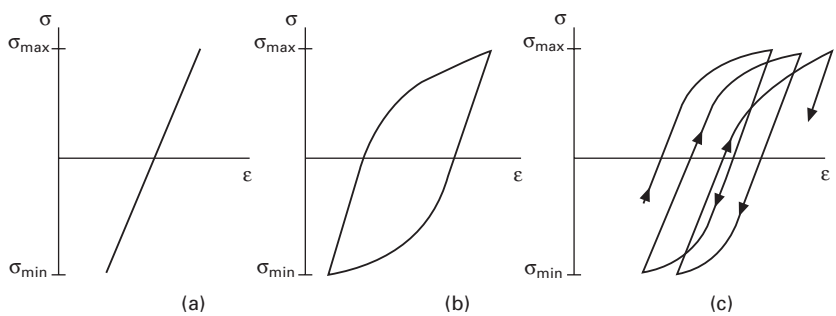

3.14 Various modes of cyclic loading under stress controlled condition: (a) elastic cycling, (b) shakedown and (c) ratcheting.

Table 3.2 Some guidelines for choosing appropriate material models

Behaviour model	Collapse mode		
	Excessive deformation, plastic instability	Progressive deformation	Creep-fatigue
Perfect plastic + creep rule	Suitable 	Avoid 	Avoid 
Isotropic strain hardening + creep rule	Suitable 	Avoid 	Avoid 
Linear kinematic hardening + creep rule	Avoid 	Use with care 	Use with care 
Combined hardening (Chaboche viscoplastic, etc.)	Suitable 	Use with care 	Suitable 

$$\varepsilon_m \leq 1\%,\ \varepsilon_m + \varepsilon_b \leq 2\% \text{ and } \varepsilon_m + \varepsilon_b + \varepsilon_L \leq 5\% \text{ for base metal}$$

Since the welds are less ductile than the base metal, strain limits for the welds are 50% of the values that are allowed for the base metal.

Creep damage

Creep damage, defined by Robinson's time fraction rule as $D_c = t/T_d$, should be less than 1, where t is the total duration of a given stress (σ_{eff}) at maximum temperature θ. T_d is allowable time duration determined from stress-to-rupture curves for the stress (σ_{eff}) at temperature θ. The computation of σ_{eff} from the individual stress components depends upon the kind of multiaxial rule followed for creep damage estimation. Giving due consideration for the role of the hydrostatic component in influencing the creep damage in addition to the von Mises component, ASME NH recommends the following expression for computing effective stress:

$$\sigma_{eff} = \sigma_{VM} \exp[C\ (J_1/S - 1)] \qquad 3.1$$

$$\sigma_{VM} = 1/\sqrt{2}\,[(\sigma_1 - \sigma_2)^2 + (\sigma_2 - \sigma_3)^2 + (\sigma_3 - \sigma_1)^2]^{1/2}$$

$$J_1 = \sigma_1 + \sigma_2 + \sigma_3$$

$$S = [\sigma_1^2 + \sigma_2^2 + \sigma_3^2]^{1/2}$$

C = material-dependent constant

= 0.24 for austenitic stainless steel (ASS)

where σ_i are the principal stresses. There is a need to apply a factor of safety K' by dividing σ_{eff}/K before entering into creep rupture curve. K' is 0.67 for ASS.

Fatigue damage

At any material point, fatigue crack initiation occurs if fatigue damage (D_f), defined by $D_f = n/N_d$, exceeds unity as per Minor's fatigue damage fraction rule, where n is applied number of strain cycles with the strain range of $\Delta\varepsilon$ at temperature θ. N_d is the permissible number of cycles determined from design fatigue curve. The design fatigue curves were determined from completely reversed loading conditions at appropriate strain rates by providing factor of safety on number of cycles and strain range on best fit curve.

Creep-fatigue interaction

When both creep and fatigue damages occur together, there can be strong interaction, which reduces the life significantly. Accordingly the sum of creep and fatigue damages should be limited to a specified value D as follows:

$$D_c + D_f \leq D$$

The value D is expressed as a function of either D_c or D_f as shown in Fig. 3.15. Figure 3.15 indicates that the creep–fatigue interaction is very strong for 9Cr–1Mo–V steel compared with austenitic stainless steel. Creep–fatigue damage would be a major life-limiting factor for this steel. In this respect, $2\frac{1}{4}$Cr–1Mo exhibits superior behaviour to 9Cr–1Mo–V.

Creep–fatigue damage for welds

In the vicinity of a weld (defined by ±3 times the thickness to either side of the weld centreline), the creep fatigue evaluation should utilise reduced values of the allowable number of design cycles N_d and the allowable time duration T_d. The N_d value should be one-half the value permitted for the parent material (Fig. 3.16). The T_d value should be determined from a stress-to-rupture curve obtained by multiplying the parent material stress-to-rupture values by the weld strength reduction factors (Fig. 3.17).

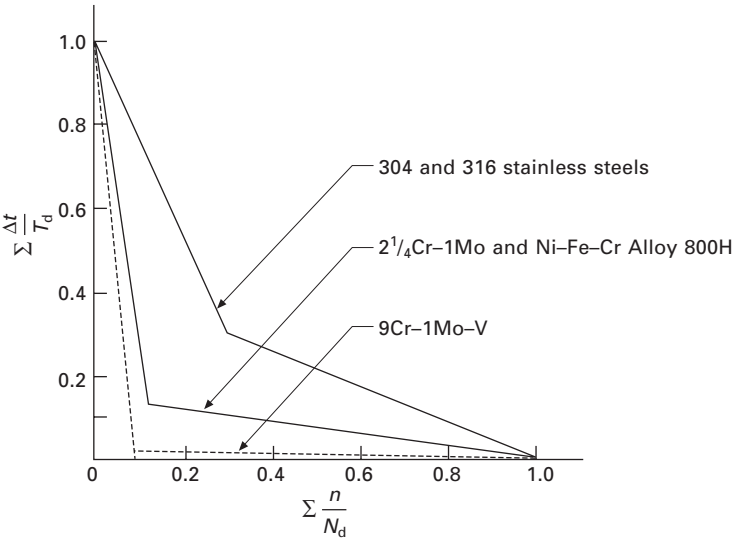

3.15 Creep–fatigue interaction of materials in NH.

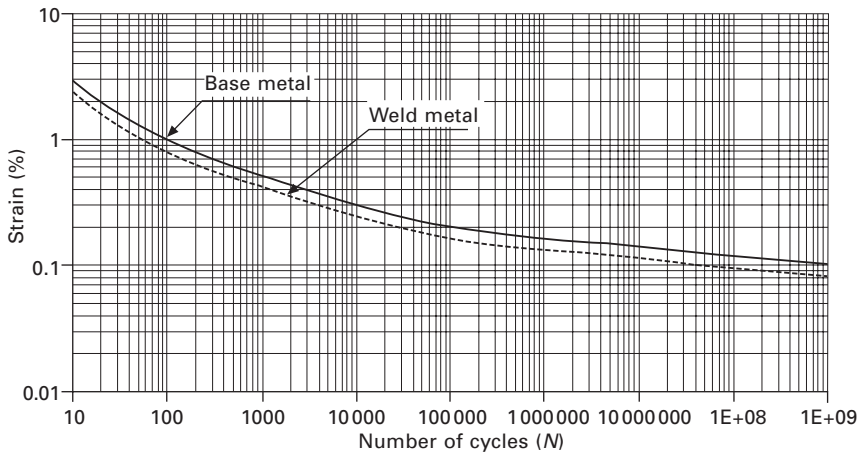

3.16 Design fatigue curves for base metal and welds (SS 316 at 550°C).

3.4 Design rules for welds as per RCC-MR

The approach followed by RCC-MR is conceptually similar to ASME-NH, as far as primary stress limits are concerned. However, there are a few differences in the treatment of secondary stresses. When the component wall is subjected to simultaneous primary stress (P) and cyclic secondary stress (ΔQ), RCC-MR introduces a concept of effective primary stress (P_{eff}).

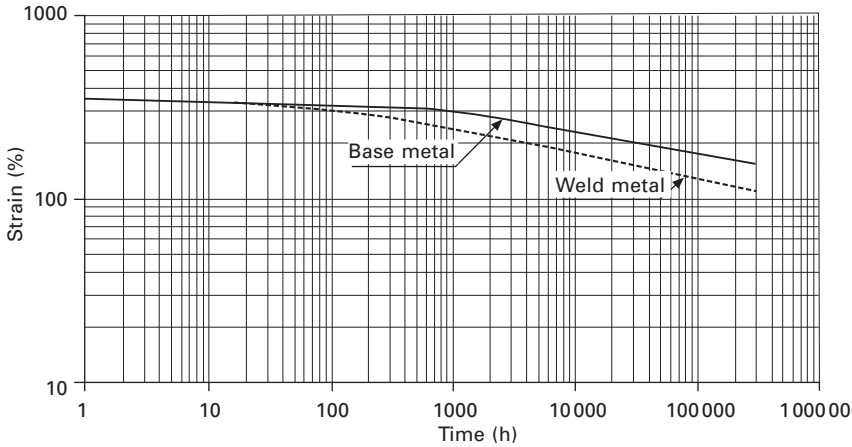

3.17 Creep rupture curves for base metal and welds (SS 316 at 550 °C).

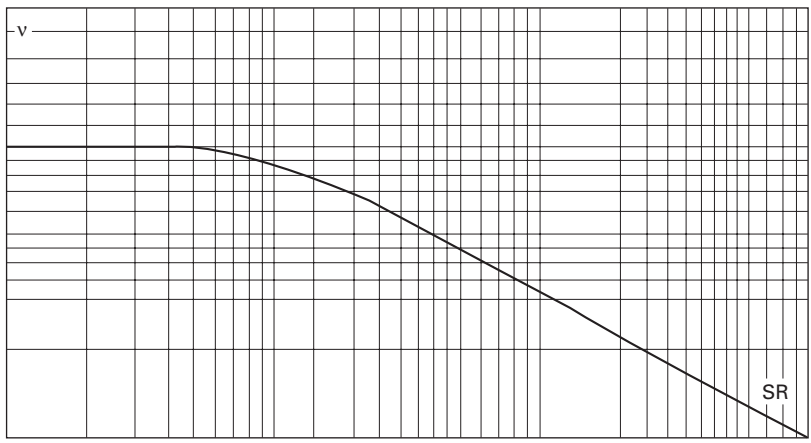

3.18 Efficiency index diagram given in RCC-MR.

Accordingly the ΔQ enhances the effectiveness of primary stress (P) by a factor 'ν' called the 'efficiency index', which depends upon the secondary stress ratio (SR). Two secondary stress ratios are defined: $SR_1 = \Delta Q/P_m$ and $SR_2 = \Delta Q/(P_m+P_b)$. Corresponding to these two stress ratios, two indices, ν_1 and ν_2, are extracted from the efficiency index diagram (Fig. 3.18).

If ν_1 and ν_2 are known, the effective primary membrane stress $P_{1eff} = P/\eta_1$ and effective primary membrane and bending stress $P_{2eff} = P/\eta_2$ can be computed. P_{1eff} is similar to σ_c introduced by the NH. Accumulated membrane and bending strains are calculated based on P_{1eff} and P_{2eff} in turn to check the appropriate strain limits.

In the creep–fatigue damage assessment for the welds, the RCC-MR introduces weld strength reduction factors, viz. J_t for S_t, J_r for S_r and J_f for $\Delta\varepsilon$. J_t and J_r are given as a function of temperature and time and J_f is equal to 1.25. For welds, the allowable S_t is J_tS_t, the allowable S_r is J_rS_r and allowable $\Delta\varepsilon$ is $\Delta\varepsilon/J_f$. It is worth noting that J_t and J_r are less than unity. The design rupture curves need to be lowered by a factor J_r and design fatigue curves are to be lowered by J_f to derive stress rupture and design fatigue curves for welds.

For the creep damage estimation, the following governing stress (σ_{eq}) is expressed as a function of both the von Mises stress (σ_{VM}) and the hydrostatic stress component (σ_H) as follows:

$$\sigma_{eq} = [2(1 + \nu)/3]\ \sigma_{VM} + [1 - 2\nu]\sigma_H \qquad 3.2$$

For Poisson's ratio $\nu = 0.3$, $\sigma_{eq} = 0.867\ \sigma_{VM} + 0.4\sigma_H$

3.5 Design of welds with crack-like defects

The nuclear codes specify stringent inspection requirements to ensure the high quality of structural materials and manufacturing standards. In view of the fact that welds are weak links in a structure, the codes do not permit welds without adequate and reliable inspection methodologies. Accordingly, the design procedures presented above are applicable for the welds having no deviations which are unacceptable by the design codes. However, in practice, a few difficult locations in the form of crack-like defects, termed 'geometrical singular points', are unavoidable. For such welded structures with crack like defects, RCC-MR provides special rules based on the 'σ_d approach' in annexure A16. As per this procedure, the creep and fatigue damage accumulated till the end of the design life is calculated at the characteristic distance '*d*' from the crack tip and should satisfy the creep–fatigue damage interaction limits (Fig. 3.15). The recommended value for *d* is equal to 50 μm for ASS in A16. However, the development of a visible crack (0.1–0.2 mm) is generally considered as crack initiation. Using the distance of 50 μm for calculating σ_d may be considered a conservative value for the assessment. Based on detailed investigation with the experimental data, 0.2 mm is considered for defining crack initiation life [5]. The method is illustrated by solving a benchmark problem given below.

3.5.1 Application of σ_d approach for the benchmark solution

Definition of benchmark

The experimental benchmark problem which is concerned with creep crack propagation in the welded joint incorporated in two standard plane sided 19

mm thick CT specimens is extracted from Hooton *et al*. [6]. The plane CT specimens are manufactured from a single heat of welded plates made of Type 316 LN steel plates using a matching manual metal arc (MMA) weld combination. The interface between the parent metal and the MMA weld metal is located parallel to the central line of the specimens. The specimens are pre-cracked at room temperature to generate initial crack lengths of 17.58 mm and 17.41 mm. Except for the initial crack size, the geometrical and loading conditions are the same for both specimens, which are shown in Fig. 3.19.

The creep crack propagation tests were conducted in air at 823 K by applying a constant axial load of 20 kN for the duration of the test. The time taken for creep crack growth of 0.2 mm was found to be 300 h and 400 h, respectively, which is considered as creep crack initiation times for the two specimens.

Linear elastic stress intensity factor

For the CT specimen, the stress intensity factor (K_I) is computed following section A16.8221.2, which recommends the following equation:

$$K_I = F_b \, \sigma\sqrt{\pi a} \tag{3.3}$$

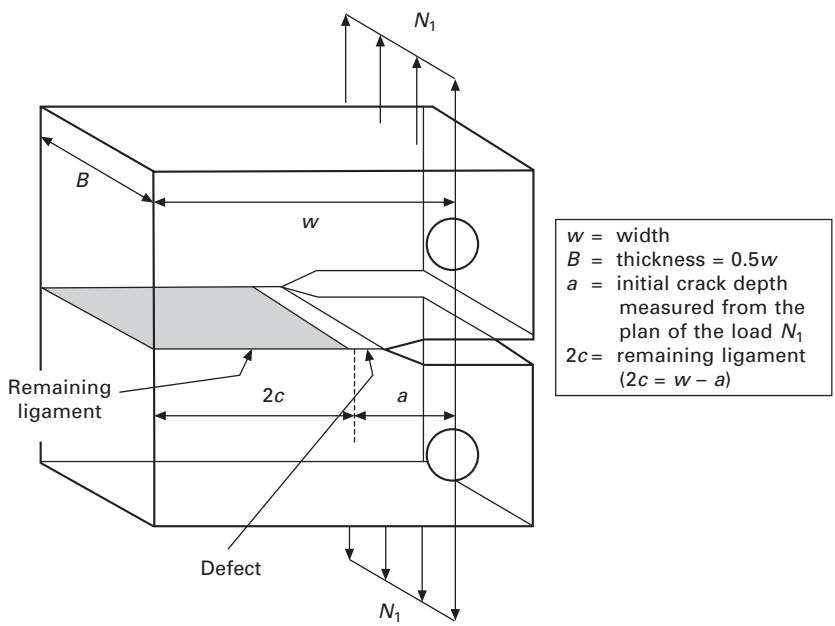

3.19 Details of benchmark problem.

where,

$$F_b = (2 + a/w)\ F_1/[(1-a/w)^{3/2}\sqrt{(\pi a/w)}]$$

$$F_1 = [(0.886 + 4.64(a/w) - 13.32(a/w)^2 + 14.72(a/w)^3 - 5.6(a/w)^4)]$$

$$\sigma = \frac{N_1}{wB}$$

The symbols are defined in Fig. 3.19. The width (w) is equal to 38 mm, thickness (B) equals 19 mm and axial force (N_1) equals 20 kN. K_I values for the two specimens whose initial crack lengths are 17.58 and 17.41 mm, are 46.67 MPa $m^{0.5}$ and 46.07 MPa $m^{0.5}$, respectively.

Elastically computed characteristic stress – σ_{de}

The value of σ_{de} is equal to the maximum principal stress = $K_I/\sqrt{2\pi d}$. The value of σ_{de} for specimen 1 whose K_I is 46.67 MPa $m^{0.5}$, is 2633 MPa at d = 50 μm. The corresponding value for specimen 2 whose K_I is 46.07 MPa $m^{0.5}$, is 2600 MPa.

Elasto-plastic characteristic stress – σ_d

σ_{VM} can be determined by solving the following equation using a modified Neuber's rule:

$$\sigma_{VM}\ \varepsilon_{VM} = \sigma_{VMe}\ [\sigma_{VMe}/E + B(\sigma_{ref})^{1/\beta}] \qquad 3.4$$

where E and B are elastic and plastic moduli of the material and β is the strain hardening index in a Ramberg–Osgood equation. The values of β and B are taken from Hooton *et al*. [6] as 0.138 and $(1/289.2)^{1/\beta}$ MPa respectively. The empirical correlation recommended in Table A16.8221.3 of A16 is used for determining σ_{ref} for a CT specimen under the assumption of von Mises plane strain conditions. The elastically computed σ_{He} can be corrected to obtain σ_H using the following equation:

$$\sigma_H = \sigma_{He}\left(\frac{\sigma_{VM}}{\sigma_{VMe}}\right) \qquad 3.5$$

Multiaxial creep damage criteria

The governing stress for creep damage estimation (σ_{eq}) is expressed as a function of both the von Mises stress (σ_{VM}) and the hydrostatic stress component (σ_H), as given in equation 3.2.

Relaxation of stresses

Secondary stresses generally undergo creep relaxation during sustained conditions at high temperature. For the present case, relaxation is considered for the von Mises stress. Since the value of von Mises stress at the crack tip is relatively small, the relaxation is limited and there is no concern of non-conservatism due to relaxation below the value required for equilibrium. The relaxation of the starting stress σ_{VM} is computed by using the following equation recommended in RCC-MR 3262.1:

$$\frac{d\sigma_{VM}}{dt} = -\frac{E\acute{\varepsilon}_c}{3} \quad \text{and} \quad \acute{\varepsilon}_c = K\sigma_{VM}^n \tag{3.6}$$

where K and n are constants associated with Norton's law which are provided in RCC-MR: Appendix Z as $K = 9.722 \times 10^{-30}$ and $n = 10.4707$ at 823 K. The relaxation of σ_H is assumed to vary in a similar manner to σ_{VM}.

Prediction of creep crack initiation life

The triaxial stress components at the characteristic distance determined using Creager's equations given in A16 are as follows.

For specimen 1 at d = *0.2 mm:* σ_x = 1313 MPa, σ_y = 1313 MPa and σ_z = 788 MPa. Application of Neuber's rule yields σ_{VM} = 174 MPa, σ_H = 376 MPa and σ_{eq} = 301 MPa.

Time variation of σ_{eq} and accumulation of creep damage are depicted in Figs 3.20 and 3.21 respectively. From Fig. 3.21, the time at which creep damage is equal to 1 is 435 h (T_{rd}).

For specimen 2 at d = *0.2 mm:* σ_x = 1297 MPa, σ_y = 1297 MPa, σ_z = 778 MPa, which yields σ_{VM} = 173 MPa, σ_H = 374 MPa, σ_{eq} = 300 MPa and T_{rd} = 451 h.

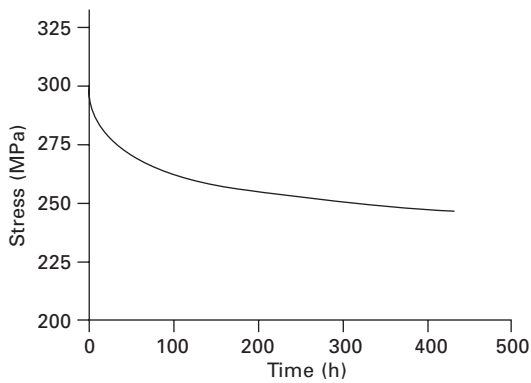

3.20 Relaxation of σ_{eq}.

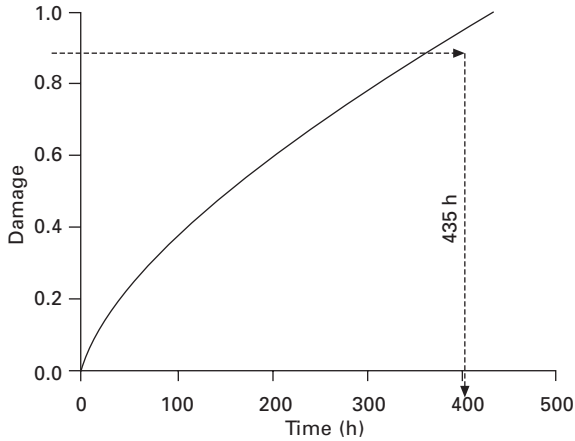

3.21 Cumulative creep damage.

Compared with the experimental data for these cases (300 h and 400 h), the improved procedure predictions (435 h and 451 h, respectively) show satisfactory experimental validation of the adopted procedure.

3.5.2 Application of σ_d approach for life prediction of fast breeder reactor (FBR) fuel pin end plug weld

The fuel pin end plug is welded after inserting the fuel pellets and other structural elements within the clad. A schematic of a typical weld configuration is shown in Fig. 3.22 along with important dimensions. The end plug welding is the most challenging task and some defects in the form of pockets are unavoidable in practical situations.

Since the fuel pin clad is one of the critical elements in the core sub-assembly, the weld configuration needs to be qualified thoroughly to ensure reliable operation without any failure so that this will not restrict the maximum achievable burn-up in the reactor. Creep damage is the governing failure mode for this weld and hence, it is simulated experimentally on a few practically achieved end plug welds. The temperature in the region of the end plug is 823 K under steady state operation. The fission gas pressure accumulated at the end of 200 GWday/t burn-up can be 12 MPa (maximum). The clad material is 20% cold worked SS 316 M.

Experimental details and results

Fuel pins with an end plug weld were tested at 973 K under an internal pressure of 20 MPa to account for possible uncertainties in the fission gas release phenomenon. A leak in the pin is the indication of failure, that is

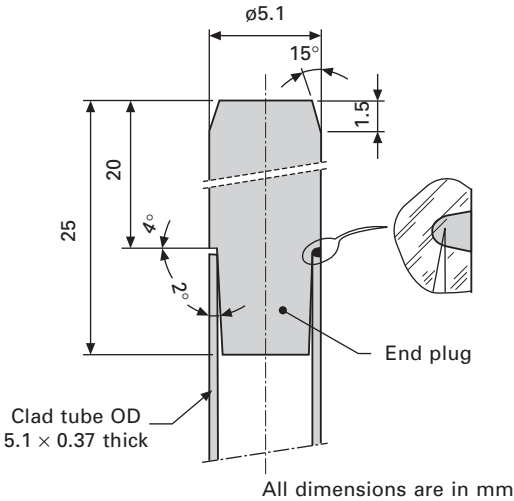

3.22 Details of end plug weld joint.

detected by a fall in the steady state pressure in the chamber. Six test specimens were placed inside the furnace. A total of six pins were tested and leaks occurred after 1104 h (min) and 1188 h (max). A typical tested pin showed bulging and a crack at the bulged location. The observed cracks were investigated thoroughly by image analysis. The cracks were longitudinal, caused by hoop stress effects, which is observed just below the weld joint.

Life prediction

The creep life is predicted by using the RCC-MR procedure described in section 3.4. The required stresses are determined by inelastic analysis using the finite element method. Analysis is carried out including creep deformation/relaxation in order to derive the governing stress σ_{eq} as per equation (3.1). The fuel pin along with end cap (dimensional details are shown in Fig. 3.22) is modelled using axisymmetric elements for the elastic-creep analysis by CAST3M computer code issued by CEA France. The creep law: $\sigma_c = 2.3046 \cdot 10^{-13}\ t^{0.6344}\ \sigma_{VM}{}^{4.60957}$ is adopted from RCC-MR: Appendix-Z, corresponding to 1S material (annealed condition) at 973 K. Analysis is performed for sufficiently long time (1500 h) to get the saturated state of stress. The distributions of saturated σ_θ and σ_l are depicted in Fig. 3.23. The peak σ_l occurs at the inner surface at the weld junction. The maximum σ_θ occurs on the outer surface, at a location ~ 1.5 mm below the weld junction. The σ_{eq} distributions are shown in Fig. 3.24.

While the maximum σ_{eq} on the outer surface of the pin is hoop stress dominant and load controlled, the peak σ_{eq} at the weld junction is longitudinal

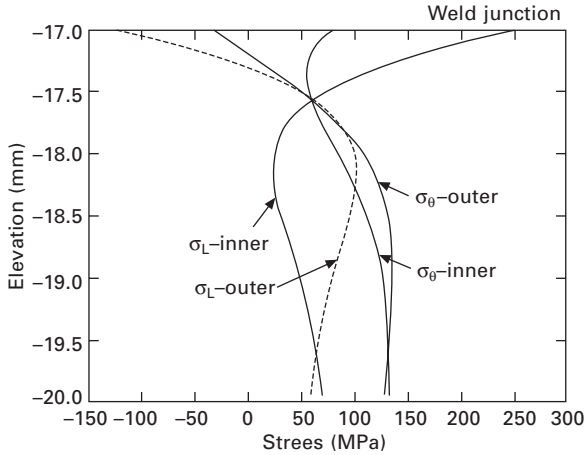

3.23 σ_θ and σ_l distributions.

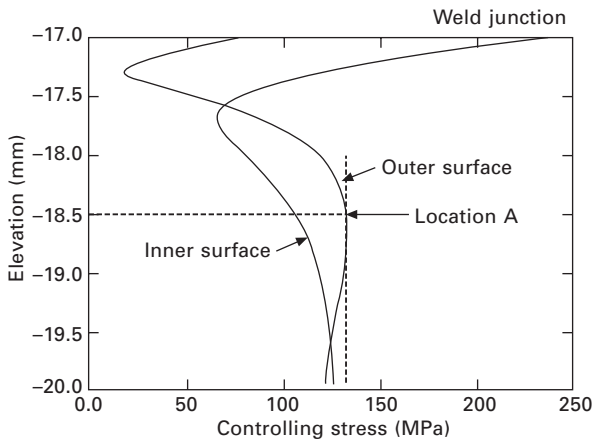

3.24 σ_{eq} distributions.

stress dominant and deformation controlled. Accordingly, there are two critical locations where creep crack initiation may start: one at the weld junction, where a circumferential crack initiates on the inner surface and propagates along the longitudinal direction, and another at the location A, where a longitudinal crack initiates on the outer surface and propagates across the depth direction, resulting in crack opening and subsequent leakage. As predicted, the crack at location A (Fig. 3.24) caused leakage of hot air, causing depressurisation after about 1100 h. Although a circumferential crack could have been initiated earlier, this could not have been quantified due to practical difficulties. The crack at the junction after propagation by a certain extent has branched, which is also a reason for not causing crack opening

earlier than the crack at location A. Based on the computed stress distributions, the creep crack initiation life is estimated using the experimentally generated average stress rupture curves as shown in Fig. 3.25, corresponding to the governing stress (σ_{eq}) of 133 MPa (Fig. 3.24) and predicted life is 1050 h, which compares well with the test results (1104 h minimum and 1188 h maximum). It is to be noted that σ_{eq} is nearly equal to σ_θ (135 MPa) which initiates the crack in the longitudinal direction. The predicted location of crack initiation (~ 1.5 mm below the weld junction as extracted from Fig. 3.24) is close to the observed crack location. The local bulging observed in the experiment developed during the tertiary creep stage.

3.6 Effect of mismatch creep properties on weld design

When a weldment is subjected to high temperature and stresses, its constituents, viz. base metal, weld and heat-affected zone (HAZ) will produce different creep strain rates depending upon the materials and welding procedures. The weld metal may exhibit a higher strain rate than the base metal when subjected to the same stress. It is called creep-soft weld. A creep hard weld exhibits a lower creep strain rate than the base metal. Thus the welding process produces mismatched weldment and, consequently, a non-uniform stress and strain field will develop with time owing to creep. These stresses and strains, developed due to weldment mismatch, may be enhanced by the weld geometry and the loading conditions. The design codes utilise the parent material properties for the analysis of welded component and subsequently design by

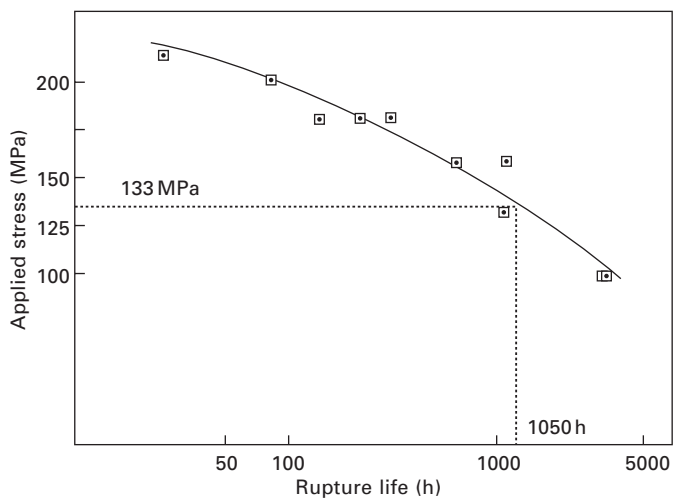

3.25 Creep rupture curve for 20% CW SS 316 M.

incorporating weld joint efficiencies on the allowable stresses. An estimation of stress and strain concentrations at the weldment due to the mismatched creep properties will help to assess the real factor of safety in the design codes. The effective way to solve this problem is the use of numerical simulation of creep of weldment by taking into account all the possible complexities that are associated with a weld design.

In order to depict the effects of mismatch creep properties, finite element calculations have been performed on longitudinal 'X' welds in a large diameter pipe to determine the stress concentrations for the material 2.25Cr–lMo at 811 K and results are compared with published data. The geometrical details of weldment and its finite element mesh are shown in Fig. 3.26.

The material data for 2.25Cr–1Mo steel at 540 °C used for the analysis are as follows:

Young's modulus = 1.42×10^5 MPa

Creep law for base metal = $1 \times 10^{-16}\sigma^8$/s

Creep law for weld = $5 \times 10^{-16}\sigma^8$/s

Creep rupture stress = 45.5 MPa

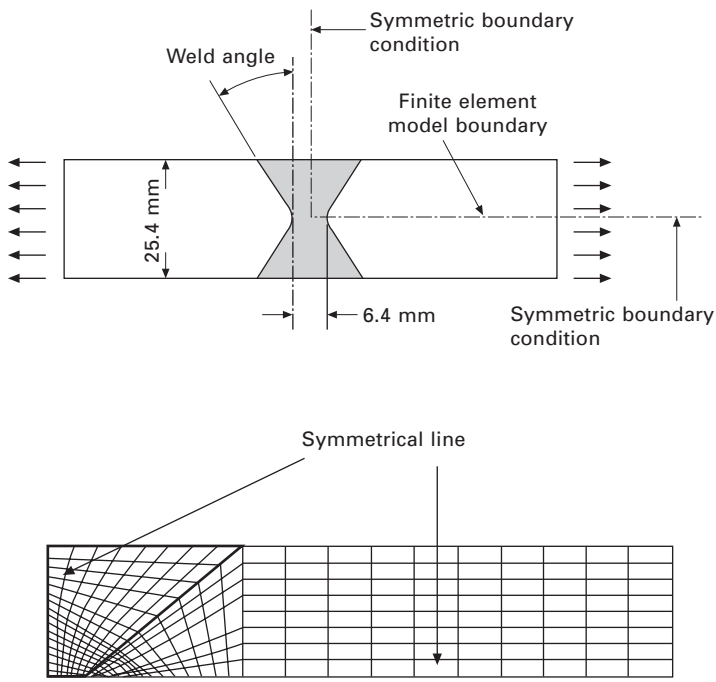

3.26 Analysis geometry and finite element mesh simulation.

Elasto-plastic creep analysis is performed and it is observed that the stress concentration develops at the weld fusion line on the neutral plane of the pipe wall as shown in Fig. 3.27.

Figure 3.28 shows the shaded stress contours after reaching the saturation above 104 h. It can be seen that the stress concentrations are highly localised and hence may not produce a significant increase in the membrane stress intensity across the wall thickness. Some additional bending stress intensity might have developed which will not exceed the code limits. The main concern is the strain concentrations which may exceed the creep ductility limit. Figure 3.29 shows the effect of weld angle from 0 to 45° on the saturated stress concentration factors. The higher weld angle produces higher stress concentrations, yielding a factor 1.5 for 45° weld angle. In this figure, the similar results obtained by Stevick [7] are included to demonstrate the validation of the predictions by FEM.

Possible mismatch of the creep properties of welds produces significant effects for 2.25Cr–1Mo, because a high stress concentration factor (~ 1.5) is

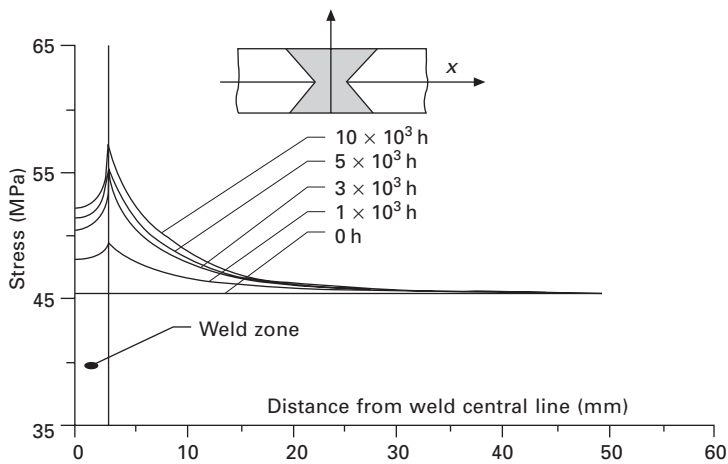

3.27 Development of stress concentration along neutral plan.

3.28 Saturated stress contours at 104 h.

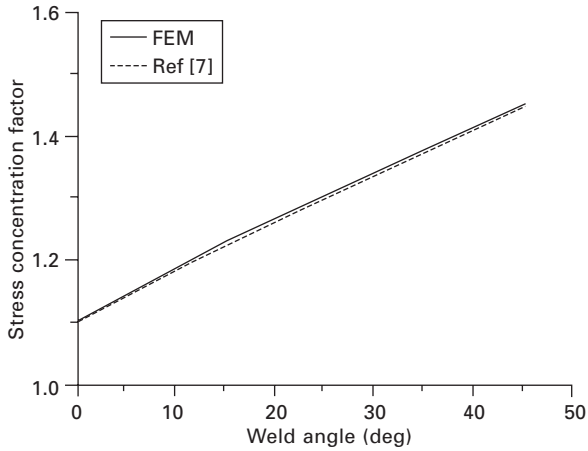

3.29 Effect of weld angle on stress concentration.

developed within one-tenth of design life. This explains the premature failure reported in this weld.

3.7 Conclusions

The design aspects of welds as per a typical conventional design code, viz. ASME section VIII division 1 and nuclear codes ASME section III, division 1: Subsection NH and RCC-MR (French Code) were covered with particular emphasis on high temperature operation. Further, the creep–fatigue design of welds having crack-like defects was highlighted with support of practical applications. Beyond the design by code rules, applications of the finite element method in quantifying the effects of mismatch in creep properties of base metal and welds, and also for simulating creep damage in the weldments having manufacturing deviations, were addressed. With the information presented in this chapter, it is expected that an inexperienced engineer with sufficient theoretical background can design a typical weld operating at high temperature.

3.8 References

1. *Structural Integrity of the Fast Reactor*, Report by the UK Nuclear Industry, Technical Advisory Group on Structural Integrity, AEA Technology, Risley, Warrington, WA3 6AT. 1992.
2. ASME section VIII division 1, *Rules for Construction of Pressure Vessels*, Edition 2007.
3. ASME section III division 1, *Rules for Construction of Nuclear Power Plant Components*, Subsection NH: Class 1 Components, Edition 2007.

4. RCC-MR Vol III, *Construction Rules for Mechanical Components of FBR Nuclear Island for Class 1 Components*, Subsection B: Class 1 Components, Edition 2002, AFCEN
5. Chellapandi, P., Chetal, S.C. and Baldev, R., 'Assessment of σ–*d* approach for creep damage estimation of FBR components with crack like defects at welds', *International Journal of Pressure Vessels and Piping*, Vol 82, 2005, pp 739–745.
6. Hooton, D.G., Bretherton, I. and Jacques, S., 'Application of the sigma-*d* (σ*d*) method for the estimation of creep crack incubation at austenitic weld boundaries', *Proc. 2nd Int. Conf. on integrity of high temperature welds*, 10–12 Nov 2003, London, 425–434.
7. Stevick, G.R., 'Failures of welds at elevated temperature', *WRC Bulletin*, Vol 390, 1994.

4

A discussion of the current procedures for design of welds against fatigue

J W H PRICE, Monash University, Australia

Abstract: The fatigue design of welds is the subject of large numbers of publications and a wide range of design approaches. This chapter describes the design approaches in common use and considers how they relate to the manner in which actual field failures occur. The questions raised are 'Are the design codes aimed at the actual way in which structural failures occur?' and 'Are there better design approaches?' This chapter suggests that cracking originating from manufacture of welds is the dominant factor in fatigue failures at welds. The logical approach would be to focus the design effort on controlling this cracking during manufacture rather than using the traditional design approaches based on the fatigue design or *S–N* (stress – number of cycles) curves. This would result in lighter and longer lived structures.

Key words: fatigue design, welded structures, hot spot stress, classification details, *S–N* curves.

4.1 Introduction

This chapter contains a review of the design of welded structures against fatigue cracking across a wide range of industries and techniques. The chapter also considers the way in which welds actually fail from fatigue and compares this situation with what is contained in the design codes.

One of the problems is that most of the design methods cover only a single industry (such as railway rolling stock, oil rigs, boilers and pressure vessels, ships or bridges) and are influenced by the history of that particular industry. The practitioners from these industries are not often in contact with each other. These design codes sometimes copy other codes and sometimes contain original concepts. Unfortunately often there is little explanation of the modifications. Sometimes an industry has an approach all to itself. The differences are often to do with historical issues; in most cases they have little to do with the physics of actual failure of welds.

4.2 Weld failures and design problems

It is clear from surveys of problems with structures that welds are a major problem[1]. After wear and generalised corrosion, the most common source of failure in industrial structures is damage at welds.

The main reason that fatigue damage occurs at welds is that welds are

complicated regions. A hot liquid metal has been deposited and it solidifies rapidly, reacting with its surrounds through an intense thermal cycle. The geometry of welds is often complicated. These severe conditions mean that welds are a focal point for damage including cracking.

4.2.1 A fatigue failure at a weld paradigm

To clarify the basics of weld failure it is worth using a paradigmatic case as an illustration. This particular failure occurred in a rail wagon with a fracture surface as shown in Fig. 4.1. The stages of the crack growth are sketched in Fig. 4.2, and the way the crack accelerates through its life (as measured in km travelled by the railway wagon) is illustrated in Fig. 4.3.

Explanation of regions on crack

1. Initial defect region. The shape in this region is strongly influenced by the stress field and stress concentration associated with weld. The initial flaw has a depth of about 6 mm from visual observation and probably was created during or shortly after the welding process.
2. Region of Paris Law or 'stable' crack growth where the size of the crack steadily increases at a slightly increasing rate.
   2A Crack is roughly circular, growing through the section.
   2B Crack is through thickness growing at one edge.
3. Region of fast crack growth
   3A Region marked by chevron marks indicating fairly brittle rapid failure (low plasticity in failure).
   3B No clear markings though there is a raised section which may be the damaged remnants of a plastic hinge.

4 Thin web plate. Fails by plastic tearing during which the crack grows to half a metre long at which point it is noticed by operators.

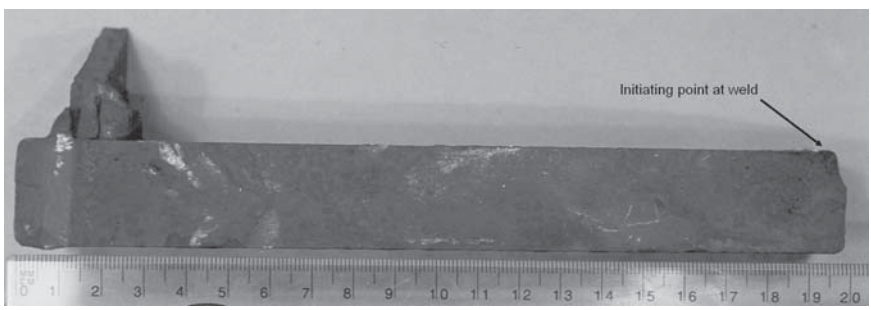

4.1 Fracture surface of a fatigue failure initiated at a weld.

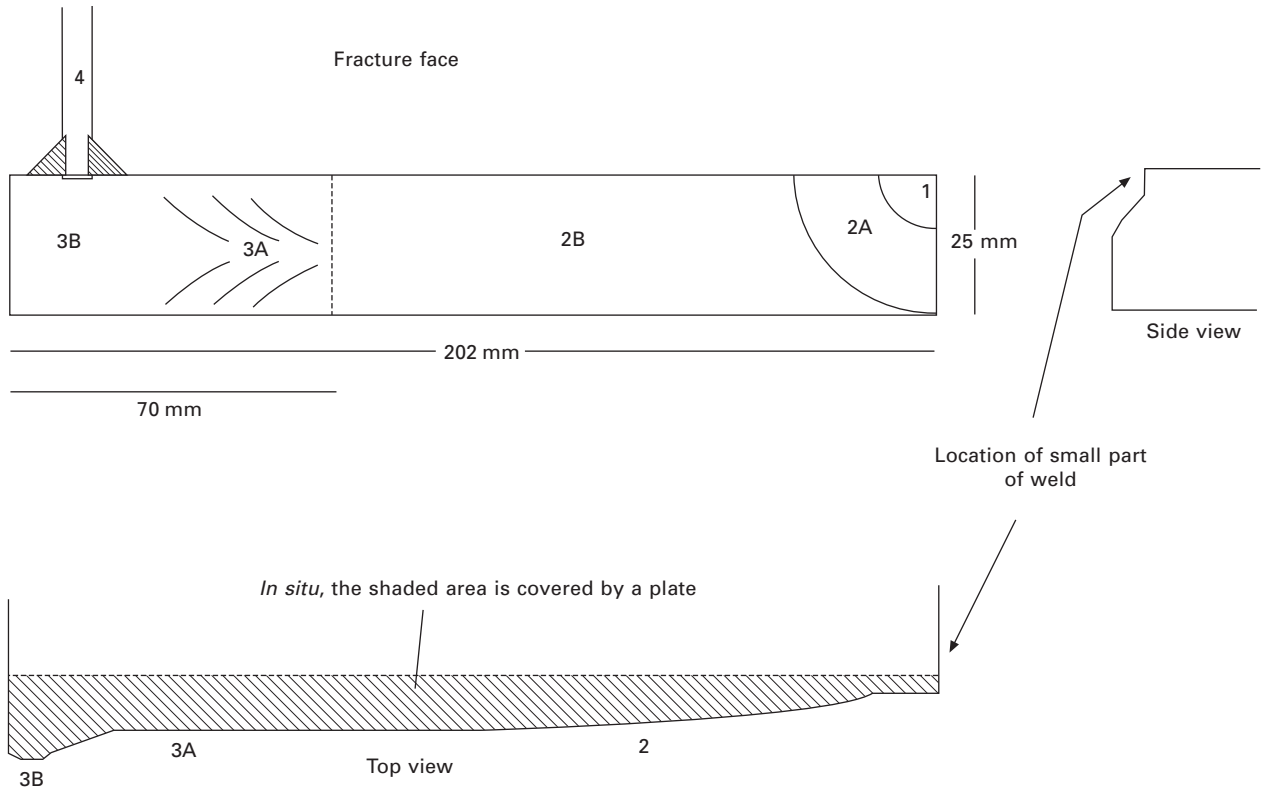

4.2 Fracture surface with observable regions for Fig. 4.1.

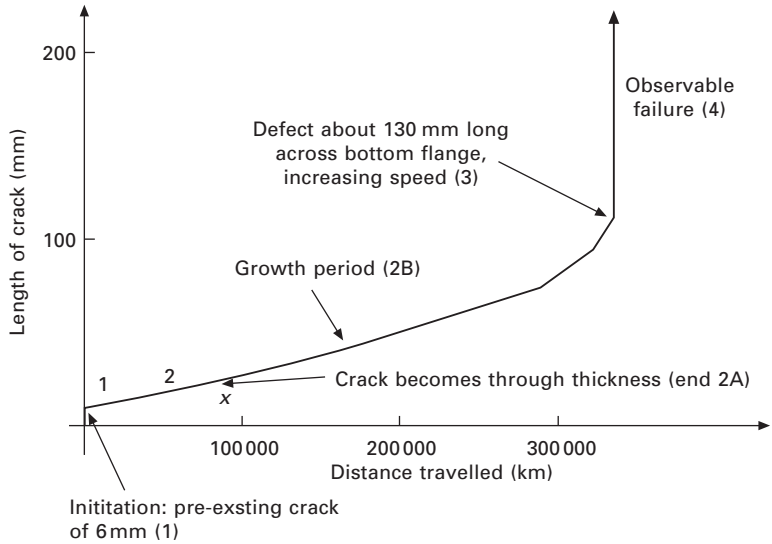

4.3 Crack length as a function of distance travelled.

Growth periods are shown in Fig. 4.2. The calculation is based on BS 7910[2].

In the case illustrated there was a crack at the weld dating from the time of welding. From visual examination this crack can be given a dimension of 6 mm. As is seen from Fig. 4.4, the weld itself is located to connect two extremely diverse members which flex independently as the wagon moves and this creates very high stresses.

Though this particular case probably was not properly designed it contains many of the key issues in the design of welds. The particular features which made this weld vulnerable and which exist in many other welds are as follows:

- *Stress concentration*. This often exists at welds due to the fact that welds almost always join one shape to another, resulting in sharp changes in section thickness. The presence of a stress concentration makes it difficult to estimate the stress that is actually applied to the weld.
- *Flaws in welding*. These are inclusions, cracking and sharp surface features left from the welding process. The issue with sharp features is they probably behave as pre-existing cracks and reduce the life expectancy of the structure dramatically.
- *Thermal cycle effects*. In the weld and the heat-affected zone ('HAZ') there are rapidly varying material properties including hard or weak regions. The interfaces between hard and weak regions are areas where damage is going to occur when deformation of the welded area occurs.
- *High residual tensile stresses*. Welds which are not heat treated after

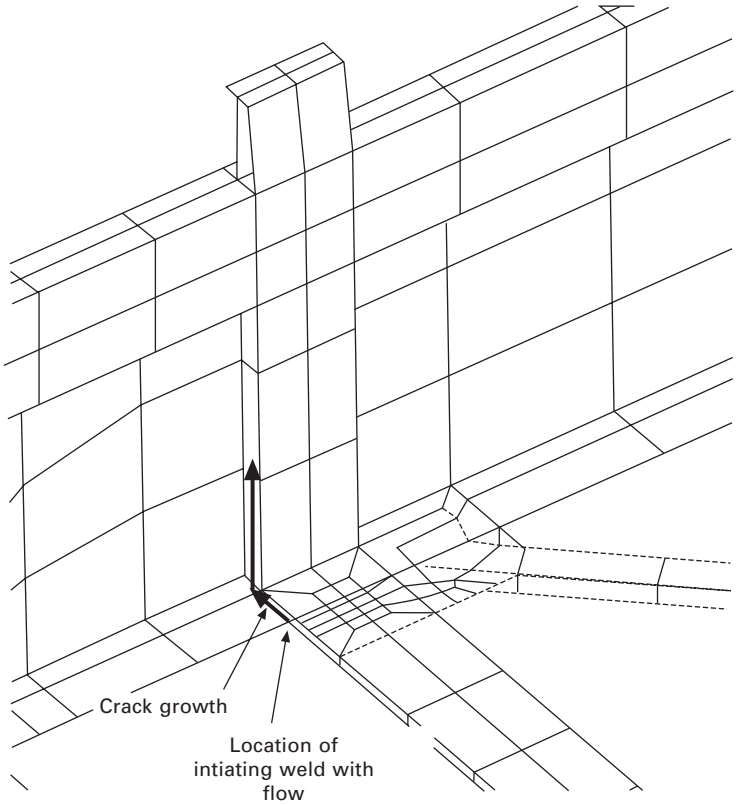

4.4 Layout of wagon showing location of weld at connection of two members.

welding have high residual stress resulting from the contraction of the metal from liquid to room temperature.

- *Environmental factors*. During the period the metal is hot and, while cooling, reactions such as oxidation, hydrogen absorption and other detrimental environmental effects can occur.
- *Quality control difficulties*. There are often limitations to the capabilities of quality control of the welding such as in the non-destructive testing ('NDT') at the complicated geometries at the weld locations.

In the paradigm, the steps by which failure due to cracking occurs can be divided into three stages:

1. The initiation of the crack. Initiation is normally not necessary in welding since cracks probably exist from manufacture (Period 1 in the example in Fig. 4.2).
2. The growth of the crack by application of cyclic loading, including

environmental effects. This period is sometimes called the 'stable crack growth' region though in fact the growth rate is slowly accelerating (Periods 2 and 3 as shown in Fig. 4.2).

3. The final failure by fracture of the remaining ligament (Period 4 in Fig. 4.2).

Design has to be aimed at reducing each of these stages. Of all these factors, the dominant factor in welds is probably undetected bad welding during construction which supplied the initiating crack.

In the example above, the stresses at the weld are particularly hard to estimate. Firstly there are very sharp features in the area of the weld leading to high stress concentrations. Secondly the detail is loaded by the relative movement of the structure of the rail wagon which is difficult to model and involves large-scale calculations.

The difficulties dealing with loadings and stress concentrations are illustrated by the work of Kalnins *et al*.[3] who analysed the pressure vessel detail shown in Fig. 4.5. In Table 4.1, it is seen that there is a large variation of predicted

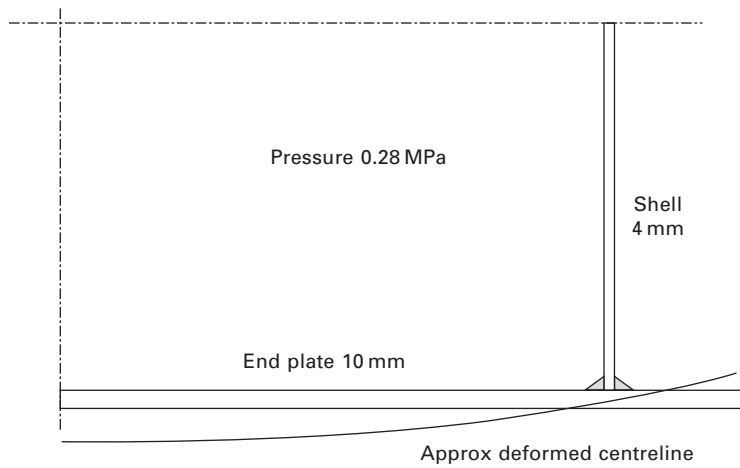

4.5 Vessel detail analysed by Kalnins *et al*.[3]

Table 4.1 Allowable cycles taken from Kalnins *et al*[3] using different S–*N* curve methods for a simple pressure vessel detail

Method	Allowable cycles
Dong and Hong (master *S*–*N* curve)	75 827
European Standards EN13445	14 489
Industry Practice (stainless)	39 541
Industry Practice (carbon steel)	4 835
Notch stress IIW	137 000

life of a pressure vessel detail based on the methods used and the way in which stress is calculated at the point of interest.

Hence it can be seen that not only do design codes have difficulty in dealing with the nature of welds, but also there are significant issues associated with the use of stress estimation as a design approach. The explanation of why this approach continues to dominate design codes lies in the history of the study of fatigue.

4.3 Fatigue design concepts and their influence

Design against fatigue damage in structures without welds has a long history. Fatigue damage was observed in shafts in early failures on railways in the mid-nineteenth century. Because of the importance of this type of failure, the engineering laboratories of the world for the next 100 years were filled with fatigue testing machines such as rotating/bending and three point bending. The tests were conducted on specially prepared specimens, cycled at fairly high frequencies, in laboratories where the effect of weather and in particular moisture was minimised. Failure was considered to be complete severance of the specimen since that was easy to measure.

The most import outcome of this work is a diagram which is termed the *S–N* curve. This diagram plots the cyclic stress against the number of cycles to failure. As testing continued, all kinds of influences such as surface finish and size were found to affect the results and eventually the effects of welds were also investigated[4]. The *S–N* curve thus became the basis for fatigue design, with the intention that actual in-service loadings, the accumulated sum of cyclic stress range ('*S*') at a particular number of cycles ('*N*'), was to be kept below this curve. There would be a safety factor included to cover 'material variations'.

The question that complicates design codes is that the *S–N* curve appears to have nothing to do with the three stages of fatigue failure listed above. The *S–N* curve has no direct connection to initiation, fatigue growth and final failure since it incorporates all of these factors. However, this leaves the problem that to be accurate, *S–N* curves have to be built up in painstaking detail for all possible variations of loading, weld quality and geometry.

The *S–N* approach is saved from invalidity by the fact that the first millimetre or so of the growth of a crack can occupy 90–95% of the life of the crack and by the incorporation of a safety factor. In a weld it is likely that there many pre-existing flaws, so the size of these flaws and whether they are sharp, crack–like features dominate the life. If the flaws are small, then the *S–N* curve may be a satisfactory model, if they are larger (this may mean anything over 1 mm in major dimension) and sharp, the *S–N* curve may not be conservative. In Fig. 4.3 for example, if the starting flaw had not been 6 mm in size the life of the component would have increased by a large factor.

Other examples of pre-existing flaws in practice are given later in this chapter. The safety factor in the design *S–N* curve accounts for some of the random variation of pre-existing flaws or cracks.

This leaves a significant issue: if welds always have pre-existing cracks, it is the size of these initiating cracks which dominates fatigue life, not the *S–N* analysis in the design codes. The standard engineering design procedures have little to say about permitted starting crack size – they basically assume that welds are 'defect-free'.

The size of cracking which can actually enter service is related to the quality control procedures which occur during the manufacture of the weld. The quality control procedures rely in large measure on the NDT procedures which are used on the weld.

4.4 Manufacturing codes: acceptable sizes of surface cracks caused by welding

Manufacturing codes basically do not allow cracks in manufacture. For example the ASME Boiler and Pressure Vessel Code VIII, states that 'Welds in which indications are characterised as cracks… shall be unacceptable'. This position is unrealistic. In fact all welds will have some small-scale cracks. The 'no-crack' criterion is really a statement about the resolution and reliability of the NDT procedures being used to seek 'indications'.

There are basically three levels of inspection conducted on welding:

1. *Supervisor visual inspection*. For most welds the only inspection required is an unaided visual inspection by an inspector. If the surface is rough and the weld beads not smoothed off (which is the case in most welds) then it is difficult to see surface breaking flaws of less than about 10–15 mm.
2 *Surface inspection*. Some manufacturing codes go further and require an enhanced visual (magnetic particle or dye penetrant) inspection of welds. These inspection techniques can only detect flaws on the surface. If the surface is smoothed before inspection (which is not always required) the visual enhancement makes detection of flaws of about 3–5 mm fairly reliable.
3. *Volumetric inspection*. Proper volumetric inspection is more expensive and is reserved for more important welds. In this case the cracks which can be detected are dependent on the resolution of the radiography, ultrasonics or other techniques used and the details of the tests carried out. These types of testing, in particular ultrasonic testing, have been getting better and are capable of better repeatability and resolution. Even so the wavelength of typical ultrasonic techniques means that cracks of 1 mm will not be reliably detected (Just[5] suggests 'a crack under the cladding

[of a nuclear vessel] with a through-wall dimension of 2 mm and a length of greater than 20 mm can be detected with a high degree of reliability'). It is to be noted that volumetric NDT is still only specified for some types of welds – those which have fairly simple geometries. Geometries such as those in branches or fillet welds remain too difficult for most industrial volumetric inspection techniques.

4.5 Assessing the strength of welds

Another historical problem in the design codes emerges from the concept that welds appear in tensile tests to be 'stronger' than the surrounding parent metal. This has led to the misconception that welds are less likely to fail than the parent metal. The basis of the concept that welds are stronger is that failures do not normally occur in the weld in tensiletests. This observation dominated early thinking about welds and still appears in modern engineering textbooks[6]. The requirement that a tensile test should break in the parent metal rather than the weld is still found in the codes for qualification of welding procedures[7]. The tensile test in fact confirms almost nothing of importance relating to cracking mechanisms in welds except perhaps proving that the weld is less ductile and has harder phases than the surrounding material.

Tensile loading is also not a particularly relevant test to the sort of loads seen in operation. Except in the case of major overloads such as explosions, the loading of welds in industrial application rarely replicates the simple tensile conditions of the weld qualification or over-load tests. Despite this situation, the simple uniaxial test is the basis of design of most welded structures in the world because it is simple in concept. This approach, however, means that tensile loaded structures are thicker and heavier than necessary.

4.6 Current approaches to design against fatigue cracking at welds

There are several main procedures in the literature for designing welds against fatigue, as follows.

4.6.1 Safety factor approach

In the safety factor approach the weld is assumed to have the same properties as the parent material and the possibility of this not being correct is accounted for by large safety factors within the conservatism of the design. The safety factor approach is the dominant simple procedure and is contained, for example, in the Design by Rule type approaches such as found in ASME Boiler and Pressure Vessel Code section VIII division 1 (Pressure Vessels)[8] and its

international variants[9]. These particular codes require the safety factor to be increased if the weld is not inspected to the top standards specified.

The mathematical concept behind the safety factor approach is illustrated in Fig. 4.6[10]. The idea of increasing the safety margin is that the failure area overlap is reduced.

The objections to this type of approach include the following:

- The safety factors are generally applied to the allowable tensile stress, though, as noted above, structures rarely fail in tensile over-load.
- The safety factors used are often excessive and lead to heavy designs in tension structures.
- Safety factors in fact do little to reduce high stresses at many types of stress concentrations including those associated with welds.
- Increasing safety factors does not compensate for dropping quality control standards in welding. This concept actually appears in design codes where thicker components are used to compensate for reductions in inspection levels (such as ASME VIII division 1 Clause UW-12 which has a lower 'joint efficiency' for less inspected welds). If large cracks are present then the concepts underlying Fig. 4.6 are completely violated.

A claim is often made in favour of the safety factor approach: safety factors have the weight of long and basically successful experience. This claim clearly has some weight because few traditionally designed structures fail catastrophically. However the safety factor approach thickens up the entire structure for the sake of creating strength at the really vulnerable areas. The vulnerable points are, in most cases, the welds. What would really be useful is a design approach which focuses on the connections and, in particular, the cracks in the welds at the connections. This is the route to the lightest and safest structures.

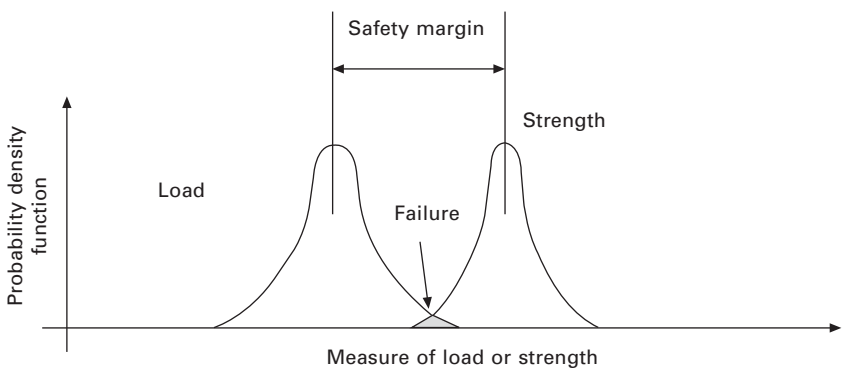

4.6 The statistical notion of how increasing the safety margin can reduce the probability of failure.

4.6.2 Peak stress approach

This approach requires an estimation of the maximum stress in the weld. The weld is basically assumed to have the same properties as the parent material but the view is taken that the stress to be used in the *S–N* table is more accurately estimated by using the peak stress. This is an approach which was originally used for shaft analysis and is the dominant method in the training of engineers[11]. The method has the severe disability in reference to the design of welds that the material is assumed to be 'defect free' and contain no pre-existing flaws.

The method is adopted in the important Design by Analysis approach of ASME and is the basis of design in the ASME Boiler and Pressure Vessel Code Section III (Nuclear Vessels) section VIII division 2 (Pressure Vessels Alternative Methods)[12] and their international variants[13]. The Design by Analysis approach requires the calculation of a peak stress and comparison with an *S–N* curve. The main *S–N* curves are illustrated in Fig. 4.7.

In the 2007 ASME VIII-2 analysis there are a number of modifications to the basic approach, including further description of how to determine the stresses (Annex 5A), factors which include size factors, the quality of the weld and any fatigue improvement treatment (perhaps surprisingly not including post-weld heat treatment, PWHT) and environmental factors (5.5.5 and 3.F). This process appears to introduce a further safety factor, typically 1.5, on the analysis as shown on Fig. 4.7.

There is also a new equation in ASME VIII-2, equation 5.76, which deviates from the defect-free approach of the rest of the code. This equation permits a user to consider a 'crack like flaw, i.e. undercut' of depth a in the weld. Equation 5.76 further increases the safety factor. It is to be noted that no weld inspection code permits 'crack like flaws' so whether this clause has any significance is hard to say but notionally it can allow flaws up to 15 mm deep in a 150 mm thick structure.

Variations of the *S–N* curve from the 2007 version of ASME VIII-2 to the older version (which dates from the 1980s) are also illustrated on Fig. 4.7. In addition a curve representing a typical structural steel design code (detail class 90 for transverse butt welds, see Fig. 4.9) is also shown. This latter type of standard is illustrated further in the next section.

The basic 2007 mean curve can be modified by factors including using the mean – 3 times standard deviation and a factor taking account of factors such as size and R value (an indicative division by 1.5 is thus added). The curve for a 90 detail classification weld has been added from a typical structural steel design code. Figure 4.7 has been compiled by the author.

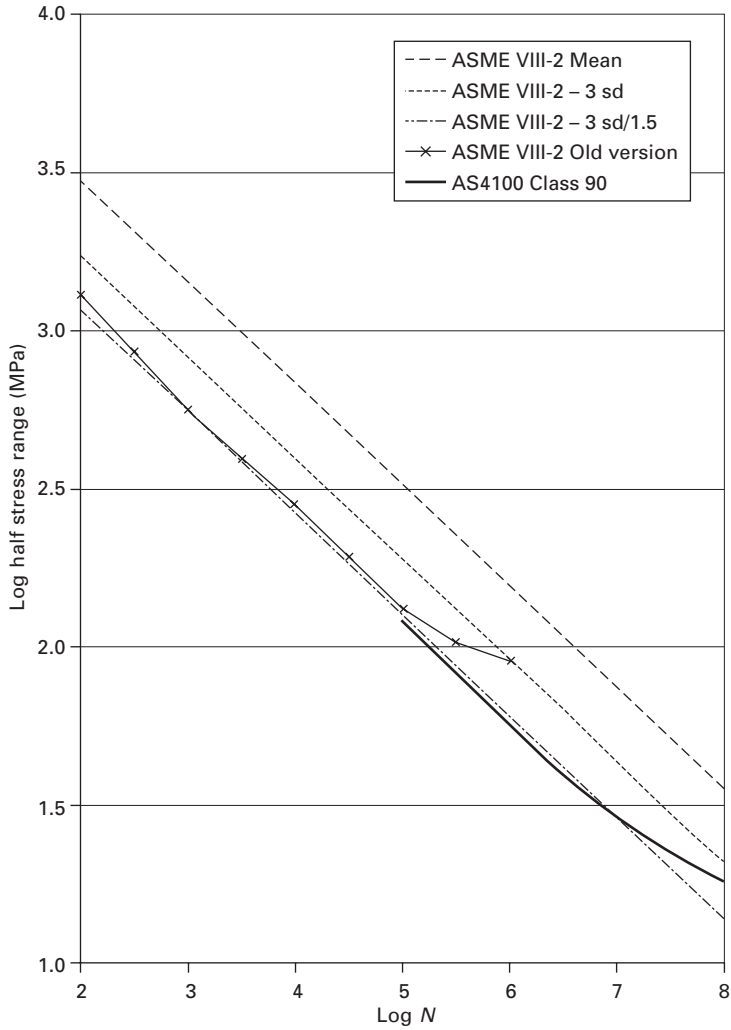

4.7 Comparison of versions of ASME VIII *S–N* curves. The basic 2007 mean curve can be modified by factors including using the mean – 3 times standard deviation and a factor taking account of factors such as size and *R* value (an indicative division by 1.5 is thus added).

4.6.3 Hot spot stresses

Another version for estimating the stress to be used in the *S–N* curve is the 'hot spot stress' approach. Here a representative stress is estimated for entry to the *S–N* curve. This method effectively estimates a stress concentration factor (SCF) based on geometry of the particular joint and includes the possibility of site measurements. The method is presented (among other

approaches) in the IIW and CIDECT guides[14]. The explanation given for the method is as follows:

> 'The hot spot stress method relates the fatigue life of a joint to the so-called hot spot stress at the joint rather than the nominal stress. … The hot spot stress range includes the influences of geometry and type of load but excludes the effects related to fabrication such as the configuration of the weld…'

There is a notional method of extrapolation from strain gauge measurements to a strain concentration factor (SNCF) as is illustrated in Fig. 4.8 which clearly demonstrates that the condition of the weld is not included in this approach. The hot spot stress method also has its own fatigue curves.

4.6.4 Other variants

Variations of the *S–N* and hot spot stress approaches are found in other references where the *S–N* curves are modified with factors to account for various effects of the welds. These variations are given different reasons in different codes. Example variations are:

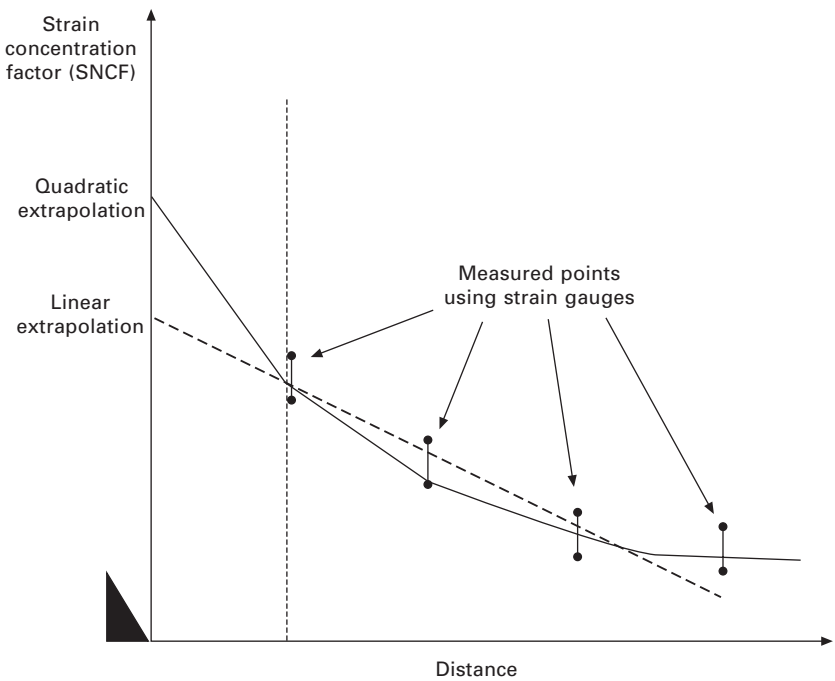

4.8 The notional methods of extrapolation of strains to the weld in the hot spot stress method.

- size, stress state[15,16];
- levels of inspection (visual, surface crack detection, volumetric or none at all)[16];
- surface smoothing such as grinding and blending (BS 7608[17], an improvement of a factor of 2.2 on life), and surface treatments such as peening; and
- post-weld heat treatment (PWHT) (BS 7608 permits use of 60% of compressive stresses in the stress range if PWHT is conducted).

4.6.5 Detail classification approach

This approach lists a number of types of welded joints (the 'details') which have been fatigue tested. The weld details are grouped into classifications. The classifications are then shown in a master *S–N* diagram as having various reduction factors on the basic parent metal fatigue curve. This approach originated in the road bridge industry (AAHSTO)[18] and has now been widely adopted internationally, not only for civil structures but also for pressure vessels and vehicles.

The method can be described as shown on Fig. 4.9. Firstly the type of welded detail is identified on the table, part of which is shown on Fig. 4.9(b). The nominal stress range in the members is determined in the direction as shown on the figure. The stress range is then used to find the permitted number of cycles for this nominal stress range on the detail on the graph shown in Fig. 4.9(a).

The advantage of this approach is that it can be claimed that all of the features important to determining the fatigue life of welds are automatically incorporated (with the exception of environmental factors). These would include normal residual stress and typical welding flaws.

There are, however, uncertainties in the approach. For example:

- There may be differences in the quality of welding and inspection which were involved in the test programs used to create the stack of *S–N* curves.
- It is unclear what has to be done if details do not appear on the table or stresses are applied on members in a way not defined. This will have an effect on the type of structures which are willingly designed by cautious engineers.
- The dominant version of the detail classification approach is found in typical steel structures code[19,20] but there are many variations of this basic theme such as those reviewed by the UK HSE[21].

Other major variations of the approach are found in the following.

- The Association of American Railroads code[22] which includes a modified Goodman approach. This permits consideration of the *R* ratio (maximum

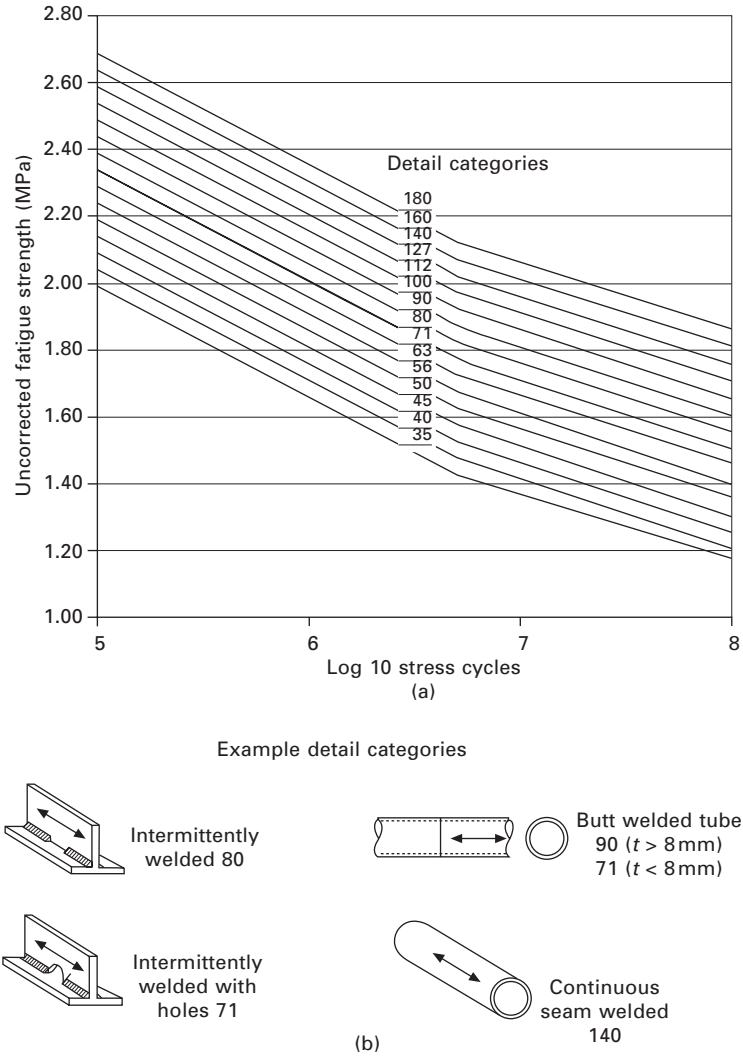

4.9 (a) S–N curves from a typical structural steel code. (b) Some typical construction details. The detail category (f_{rn}) indicates which of the curves on the S–N diagram is to be used.

stress divided by minimum stress) and has its own set of details. The AAR code is discussed further in the case studies section below.

- HSE report Steel 2001/015[23] which has a unique classification system for tubular structures.
- American Welding Society D1.1 has a full set of classifications and a different set of *S–N* curves[24].

4.6.6 Hypothetical defect and probabilistic approaches

The hypothetical defect approach also is sometimes described as 'damage tolerance'[25]. This is an approach which estimates the life of structure based on the assumption that

- there is a crack of the size that may have escaped detection during NDT;
- this crack is at a critical point in the structure;
- the flaw then grows this crack under a spectrum of loadings applied;
- in-service NDT inspections can also limit the size of the defect which remains undetected.

The approach is used for determining the life expectancy of the structure or in suggesting the frequency of NDT inspections. This approach is used in the aircraft industry where it is also described as a 'safe life' approach. In critical equipment where there may be areas where cracks cannot be inspected properly, an approach can be developed using BS 7910[2].

A development of the idea of assuming a size of crack which can escape detection by NDT is the probabilistic approach where it is assumed that all the processes discussed in the hypothetical defect approach are actually subject to various probability distributions. Hence there is a distribution of defects existing in the structure at the time of manufacture, there is a probabilistic distribution of the effectiveness of NDT to find the cracks, the cracks grow with a distributed range of growth laws and there is a probabilistic distribution of stresses which may be applied due to various incidents. This has been most extensively used in the nuclear industry starting with the notable report of Marshall[26] and in more recent work[27,28].

The probabilistic approach is too complicated for general engineering use, but the underlying principles should influence the development of the engineering design approaches.

4.7 Case studies

4.7.1 Ferritic stainless steel in rail wagon use

In this study, cracking problems in welded ferritic stainless steel rail wagons required the analysis of the various means of designing such welds. The dominant code in this area is the American Association of Railroads (AAR) code[22] which is a testing-based detail classification code which includes a modified Goodman type approach for differing R values ($R = \sigma_{min}/\sigma_{max}$). In addition it can be claimed that various other codes are relevant, for example BS 7608[29].

Figure 4.10 shows some of the data which were collected in this exercise. The weld detail for which the data in this case could be collected was the one sided fillet weld shown in Fig. 4.10(a). Figure 4.10(b) shows data from the

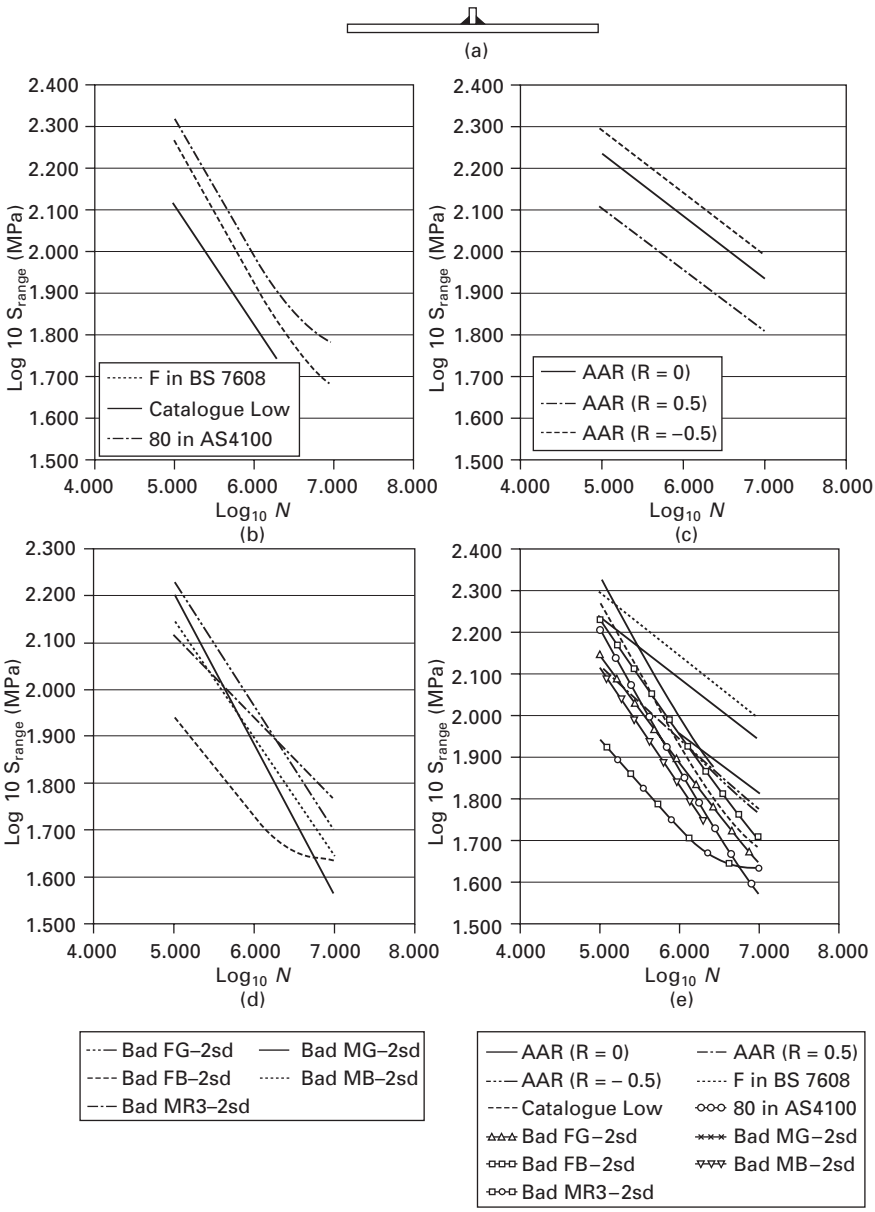

4.10 Comparison of various estimates and experimental tests of a joints fatigue life. (a) Joint design being considered.(b) Fatigue design by the detail classification approach (BS 7608 and AS 4100) and data from the catalogue for the ferritic stainless steel. (c)Fatigue design by the detail classification approach found in the AAR code which includes a modified Goodman approach with *R* factor. (d) Actual test data for a range of poorly made welds – 2 times standard deviation (the number of tests did not exceed 5). (e) All these curves brought together on a single graph. Compilations by the author.

manufacturer giving their recommended design *S–N* curve; the BS 7906 and AS 4100 data are also shown.

In Fig. 4.10(c) the AAR design curves are shown. There are two things to note:

- the curves are at variance with the other data in their slope; and
- the AAR code permits much higher stresses above 100 000 cycles, in particular as *R* changes.

In Fig. 4.10(d) data derived from sets of tests of deliberately faulty welds are shown[30]. The data from testing are lowered by 2 standard deviations, which will be quite a large margin since there is an average of five welds involved. The two bad cases listed are:

- 'MB' pitting on welds;
- 'MR' repair welds to the welds.

Figure 4.10(e) permits all the curves to be compared. As can be seen from this, the AAR design approach provides some interesting challenges:

- The AAR has a significant advantage in that it is less conservative and will produce lighter structures. With transport equipment, such as railroad rolling stock, reduction in mass makes a major on-going contribution to efficiency because fuel consumption is reduced.
- While the AAR slope of the *S–N* curve differs from the other design codes, the slope is presumably based on a significant collection of data. The reason for this difference would be worth exploring.

4.7.2 Mining dragline booms

Mining dragline booms are an interesting case study since they are among the most severely loaded welded structures[31,32]. These booms swing from side to side under high acceleration and deceleration about once every minute. The booms consist of a truss with about a hundred welded connections called nodes or clusters as shown in Figs 4.11 and 4.12.

Unlike many structures, mining dragline booms are in effect deliberately loaded until they crack. The reason for this is simple economics: there is a high value placed on the loads which can be put on them and the frequency of their movement. Owing to a warning system which can detect cracks in the booms there is presumed to be adequate protection against catastrophic failure.

The cracking in the dragline booms occurs at the welded intersections of the lacings with the main chords. The particular design of most interest in this analysis is a tubular structure where the intersections are called clusters. Table 4.2 reviews some of the design approaches which may be used to design the clusters and the predicted lives. The table also includes some data

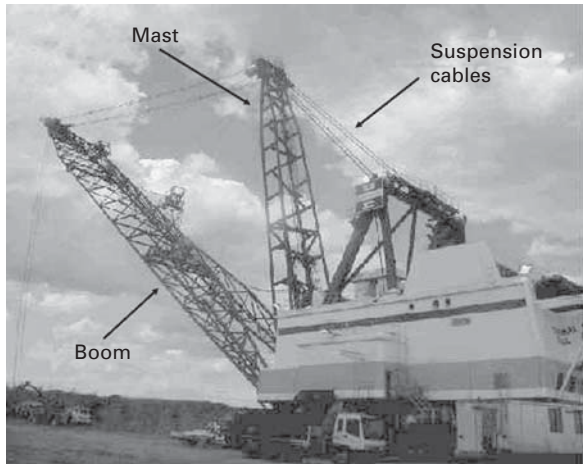

(a)

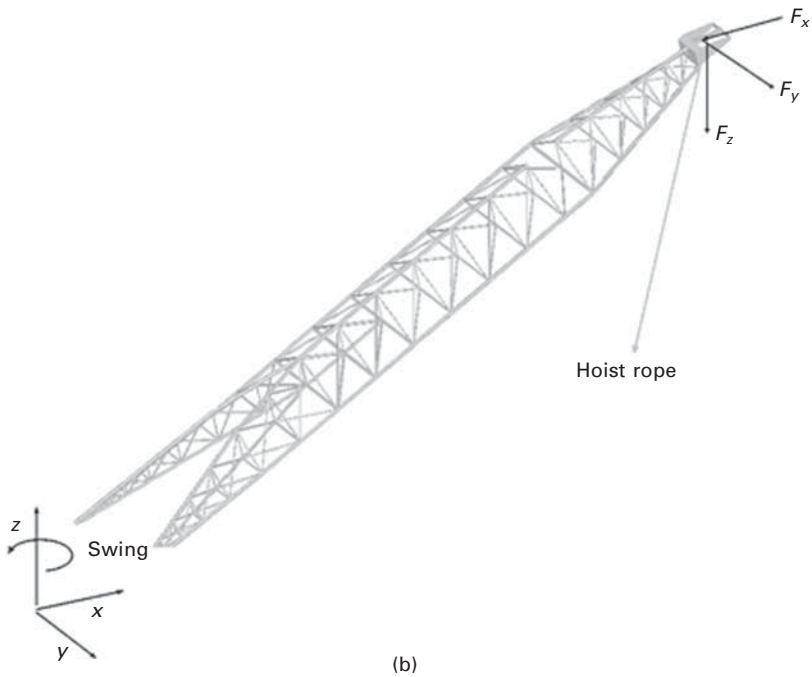

(b)

4.11 (a) A mining dragline; (b) the dragline boom (which is about 100 m long) and the loads imposed on it in service.

for cracking occurrence as detected by the protection system. When proper examination has been possible of cracked clusters, significant weld flaws have been found. The welds are made by hand, on-site and in quite difficult conditions. The cluster welds receive no inspection other than visual and are

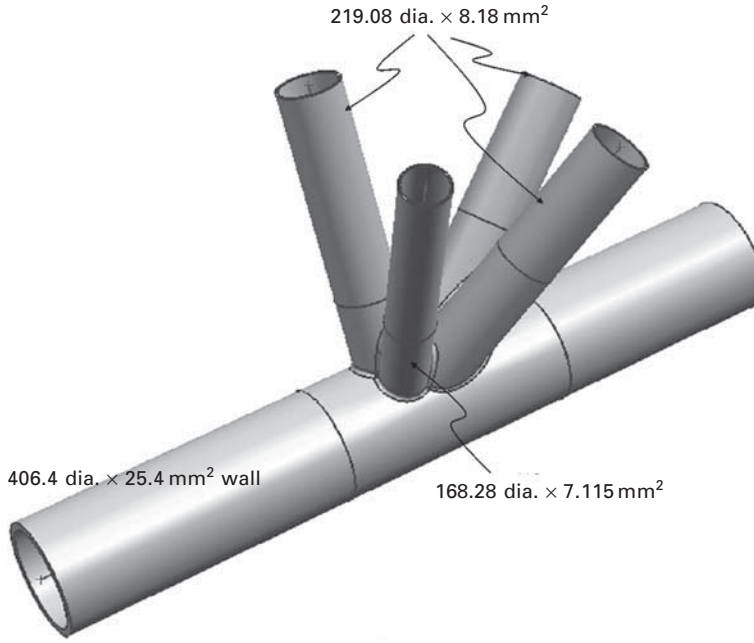

4.12 Typical cluster.

Table 4.2 Table of results for comparison of design procedures for a welded tubular connection on a mining dragline boom[33]

Design code/field observation	No. of cycles predicted for stress range of ~120 MPa	Approximate life of dragline cluster*
AWS D1.1:2000	1×10^6 cycles	2 years
AS 4100	7×10^5 cycles	1.4 years
OTR 2001/015 (tubulars in air)	2×10^6 cycles	4 years
OTR 2001/015 (tubulars in seawater)	6×10^5 cycles	1.2 years
ASME Boiler and PV Code (Section VIII-2) – Part 3 (Statistical Basis: -3σ)	4.1×10^5 cycles	0.8 year
ASME Boiler and PV Code (Section VIII-2) – Part 3 (Mean curve)	2.2×10^6 cycles	4.4 years
Field observation to early failures	$2.5 - 7.5 \times 10^6$ cycles	5 –15 years

*Assumes that the dragline cluster undergoes half a million stress cycles every year

not stress relieved. By comparison welds in the main chord are stress relieved and receive volumetric inspection. The main chord welds have not experienced major cracking.

The conclusion from this study is that the design codes are basically

conservative and the failures which occur do so because of poor welding processes and limited quality control. Improvement in the life of the dragline booms between cracking would be best achieved by using better welding procedures and conducting proper volumetric NDT. An alternative consideration is that the conservatism in the design codes increases the weight of the dragline booms, thus in itself increasing the loads due to acceleration and adding to the consumption of energy in each swing. A re-examination of these structures with respect to reducing conservatism of design and improving weld quality would be well rewarded.

4.8 Discussion

The current direction of design code development does not, in the author's opinion, reflect the real causes of weld failure. The paradigm of fatigue failure in welds is:

- there is an initial flaw in the weld;
- this flaw grows as cyclic loads are applied;
- eventually there is a noticeable failure.

Of the four main fatigue design procedures which are in use, only the most complicated and least used (the fourth point below) reflects this paradigm.

- *Safety factor approach.* This is the approach in design codes which regards welds as being no different from the parent metal but they apply a safety factor or safety margin to cover uncertainties. This is the type of approach which is used in simple design codes and is applied to millions of structures. The evidence of history suggests that in terms of catastrophic failure this approach is as successful as any of the other approaches. However the approach is conceptually faulty and will tend to produce heavy structures.
- *S–N curve approach.* Fatigue analysis was originally based on solid shafts and developed the *S–N* curve which plots the allowable stress range versus number of load cycles. Over the years this approach has been endlessly modified with extra factors covering a huge range of conditions including welding. Recent changes to the *S–N* procedures is in many ways attempting to overcome the fundamental problem that failure from cracks in welds do not follow the *S–N* failure paradigm.
- *Weld classification approach.* These codes are based on the testing of a range of specimens with varying weld details or classifications. Though the methods appear to be based on an *S–N* curve, the use of the welded specimens provides a number of advantages in developing the curves, including simplicity. Though this method is more recent in origin, there are several variants of the technique in use in various industries. The quality of the required weld is not clearly specified in the codes.

- *Hypothetical crack approaches.* These approaches are complex and applied only to structures such as nuclear pressure vessels where expensive engineering approaches are justified.

4.9 Conclusions

There are a wide range of engineering approaches to fatigue design stemming from the long history of the study of fatigue in various industries. However, these approaches may not result in good design since the current code approaches tend to favour thickening and strengthening the whole structure instead of concentrating on the causes of fatigue failure, which is cracks at welds.

The current approach can result in heavy, over-designed structures. In stationary structures such as bridges and pressure vessels this is a significant capital cost. In moving structures and transport vehicles, excess mass not only increases capital cost but also increases costs due to fuel consumption throughout life.

This chapter questions whether the design codes are actually focusing on issues which will genuinely make a difference to the reliability of structures. The chapter proposes that cracking in welds originating from manufacture is the dominant factor in determining the fatigue life of welded structures. As a result the logical approach would be to focus the design effort on controlling and reducing this cracking. This would result in lighter and longer-lived structures.

Improvements in weld reliability will mainly stem from improvements in weld procedures and non-destructive inspection. With the dramatic advances in technology and the reduction in cost of computer processing, automatic welding and advanced ultrasonic inspection can be more extensively used and the reliability of welds significantly improved.

4.10 References

1. ASME Section IX Task Group, Metal fatigue in operating nuclear power plants, *WRC Bulletin* 376, November 1992.
2. British Standards Institute, BS 7910 Guide on methods for assessing the acceptability of flaws in metallic structures, BSI, London. Section 8 Assessment for Fatigue, 2005.
3. Kalnins A, Bergsten V, Rana M, Fatigue assessment of a weld joint of a pressure vessel, *Proceedings of ASME Pressure Vessels and Piping Division Conference* 2005, Denver, Colorado, USA, PVP2005-71727.
4. Buch A, *Fatigue Data Handbook*, Transtech Publications, 1998.
5. Just T, Flaw detection ability of NDT techniques on clad surfaces of reactor pressure vessels, *Nuclear Engineering and Design*, Volume 151, Issues 2–3, 2 November 1994, pages 531–537.

6. Shigley JE *et al*., *Mechanical Engineering Design*, 7th ed., McGraw-Hill, New York, 2004.
7. A typical example is AS/NZS 3992 Pressure equipment – Welding and brazing qualification, Standards Australia, Section 7.4 Transverse tensile test.
8. ASME Boiler and Pressure Vessel Code, Pressure Vessels, section VIII division 1, American Society of Mechanical Engineers, New York.
9. For example: Australian Standards, Pressure Vessels, AS 1210, Standards Australia, Sydney.
10. Melchers RE, *Structural Reliability Analysis and Prediction*, Wiley, New York, 1985.
11. Khoshaba S, a comparison of the fatigue calculations process according to the Swedish and American textbooks for higher education, *UICEE 4th Asia Pacific Forum on Engineering and Technology Education*, Bangkok, September 2005.
12. ASME Boiler and Pressure Vessel Code, section VIII Rules for the construction of pressure vessels – Division 2 Alternative rules, American Society of Mechanical Engineers, New York 2007.
13. For example, Australian Standards, Pressure Vessels, AS 1210, Supplement 1, Advanced design, Standards Australia, Sydney.
14. Zhao X-L *et al*., Design guide for circular and rectangular hollow section welded joints under fatigue loading, Comité International pour le Développement et l'Etude de la Construction Tubulaire ('CIDECT'), TUV-Verlag, Germany, 2001.
15. Dong P, Cao Z, Hong, JK, Low-cycle fatigue evaluation using the weld master *S–N* curve, *Proceedings ASME Pressure Vessels and Piping Division conference*, Vancouver, Canada, 93607, 2006.
16. ASME Boiler and Pressure Vessel Code, section VIII division 2, 2007 edition, Chapter 5, Tables 5.11 and 5.12.
17. British Standards, Code of practice for fatigue design and assessment of steel structures, BS 7608:1993.
18. Barsom JM and Rolfe ST, *Fracture and Fatigue Control in Structures: Applications of Fracture Mechanics*, 3rd edition, ASTM MNL41, Butterworth-Heinemann, New York, 2000. Chapter 10.
19. Australian Standard, Steel structures, AS4100-1998, Standards Australia, Sydney, Australia.
20. Eurocode 3: Design Of Steel Structures – part 1–9: fatigue, National Standards Authority of Ireland.
21. Bomel Limited for the Health and Safety Executive, *Comparison of Fatigue Provisions in Codes and Standards*, Offshore Technology Report, 2001/83.
22. Association of American Railroads (AAR), Mechanical Division, *Manual of Standards and Recommended Practices*, Chapter 5.
23. Health and Safety Executive, *Steel*, Offshore Technology Report, 2001/015.
24. American Welding Society, Structural Welding code–Steel, AWS D1.1 2000.
25. Berkovits A *et al*., Consideration of effect of residual stresses on the fatigue of welded aluminium structures, *Fatigue and Fracture of Engineering Materials, and Structures*, volume 21, 1998, pages 159–170.
26. Marshall W, *An Assessment of the Integrity of PWR Pressure Vessels*, report by a Study Group chaired by W. Marshall, HM Stationery Office, London, UK, 1976.
27. Harris DO and Lim EY, Applications of a fracture mechanics model of structural reliability to the effects of seismic events on reactor piping, *Progress in Nuclear Energy*, Volume 10, No. 1, 1982, pages 125–159.

28. The Marshall work has also been reviewed for Public Enquiries in the UK. One occurred in 1983 in which the author was involved, see Davies LM *et al*., Second Marshall Study Group report on PWR pressure vessel integrity, *Journal of Pressure Vessel Technology*, Volume 105, No. 1, 1983.
29. British Standards, Code of practice for fatigue design and assessment of steel structures, BS 7608:1993.
30. Private communication, based on tests at BHP Steel.
31. Dayawansa D, Kerezsi B, Chitty G, Price J and Bartosiewicz B, Chronic Problem Areas, Repair Quality and Improved Repairs for Dragline Structurals, Project C11052, Australian Coal Association Research Program, 2005, available on www.acarp.com.au
32. Dayawansa P, Chitty G , Kerezsi B, Bartosiewicz H, Price JWH, Fracture mechanics of mining drag line, *Engineering Failure Analysis Journal*, Volume 13, No. 4, 2006, pages 716–725. doi:10.1016/j.engfailanal.2005.04.013
33. Joshi S, PhD Thesis, Design for Fatigue Life of Welded Nodes of Large Tubular Structures, Monash University, 2008.

5

Mechanical behaviour of stainless steel, ferritic steel welds and weld joints

K BHANU SANKARA RAO, M D MATHEW, K LAHA, R SANDHYA and B RAJ,
Indira Gandhi Centre for Atomic Research, India

Abstract: Creep and fatigue are important design considerations in the components subjected to start-ups and shutdowns and steady state operations at elevated temperatures. Weld joints are extensively used in the fabrication of high temperature components of fossil-fired power plants, chemical and petrochemical industries and nuclear power plants. In these industries, austenitic stainless steels, ferritic and ferritic/martensitic steels are major structural materials used for various components. From a microstructural view point, the welded joint comprises the base metal, weld metal and heat-affected zone (HAZ). Welding produces both metallurgical and mechanical discontinuities and performance of weldments is often the life-limiting factor in applications where creep and fatigue are important. Microstructures in the HAZ and weld metal are extremely complex and controlled by the interaction of thermal fields produced by the heat input from the welding process and by the phase transformations and grain growth characteristics of the materials being welded. These microstructures across the weldments can have greatly different mechanical properties and, as a consequence, cracking can arise both in the weld metal and HAZ when the weldment is subjected to creep and fatigue at high temperatures. This underlines the need for the critical assessment of the creep and fatigue behaviour of weld joints as well as the individual constituents of weldments in order to have a comprehensive understanding of their mechanical behaviour. This chapter provides concise and comprehensive information on creep, fatigue and creep–fatigue interaction behaviour of austenitic stainless steel welds and weld joints, and creep behaviour of ferritic/ferritic-martensitic steel welds and their similar and dissimilar weld joints. The creep and fatigue damage and cracking behaviour of welds and weld joints are rationalised on the basis of the initial microstructures generated during welding process, and the evolving microstructure at elevated temperatures during creep and fatigue.

Key words: austenitic stainless steels, ferritic steels, ferritic-martensitic steels, weld joints, creep, fatigue, creep–fatigue interaction, heat-affected zone cracking, delta-ferrite, sigma phase.

5.1 Introduction

Generally, from a microstructural view point, a welded joint is composed of base metal, weld metal and the heat-affected zone (HAZ). Therefore, significant variations in mechanical properties and fracture behaviour exist across the welded joint. In the case of thick-walled components that operate with frequent

start-up and shut-down modes, a reasonable assessment of creep and fatigue damage at elevated temperatures is an important issue. Often, fracture in fabricated engineering structures initiates at welded joints. The welding process produces local microstructural changes that are seldom considered in the operation design analysis. The metallurgical condition of the material is changed; local residual stresses of magnitudes well beyond the component design stress may be introduced and frequently defects are produced during the welding process, which sometimes go undetected. These defects, together with unfavourable design geometries, provide further stress concentrations. The combined effects of these on creep, low cycle fatigue (LCF) and creep–fatigue interaction behaviour are often overlooked by the designer, fabricator and user of the components. Failures in the welded joints are prevented through the use of safety factors on stresses and strains and by requiring the welds to be located in the regions of relatively low stresses. In the absence of substantial information on welds, ASME Boiler and Pressure Vessel code N-47 [1] imposes a limit on the design strains in the weld regions at one-half of the value permitted in the base metal for applications at elevated temperatures where creep effects are significant. The allowable number of fatigue cycles is also one-half of the value permitted for the parent metal. A factor of 1.25 on fatigue strain is recommended in the French RCC-MR design code [2]. There is a serious concern about the conservatism introduced in the design rules.

Austenitic stainless steels, particularly those that contain no ferrite, are susceptible to hot cracking during welding. Hot cracking refers to cracking that occurs during welding, casting or hot working at temperatures close to the melting point of the material. Austenitic stainless steels usually solidify during welding as a mixture of austenite and ferrite. The ferrite almost fully transforms to austenite on cooling, but there could be retention of a few percent of delta-ferrite in the weld metal. However, impurity elements such as sulphur and phosphorus and minor alloying elements such as boron, silicon, titanium and niobium promote hot cracking, particularly in fully austenitic steels. The duplex welds containing austenite and ferrite are less prone to hot cracking. In the welding consumables, the amounts of elements stabilising the austenite and the ferrite phases are suitably adjusted in order to produce about 3–10% δ-ferrite phase in welds. However, on exposure to high temperatures δ-ferrite undergoes decomposition to $M_{23}C_6$ carbides and intermetallic phase sigma [3–6], while low temperature ageing below 475 °C promotes spinoidal decomposition. The initial microstructure of the HAZ in the weld joints and the transformation behaviour of the δ-ferrite are the two important factors that determine the creep and LCF behaviour of SS welds and weldments.

Ferritic steels are extensively used in the fabrication of high temperature components of fossil-fired power plants, steam generators of nuclear power plants, and petrochemical industries owing to the combination of adequate

creep strength coupled with good thermal conductivity, low coefficient of thermal expansion and immunity to stress corrosion cracking in aqueous and chloride environments. Currently, several grades of Cr–Mo ferritic steels are in use. 2.25Cr–1Mo steel with tempered ferritic-bainitic structure and modified 9Cr–1Mo steel with tempered martensitic structure are widely used in the fabrication of various components in power plants. For successful service application of these steels and acceptance in practice, the long-term creep behaviour of ferritic steel weld joints is one of the most important aspects. During joining by fusion welding technique, weld thermal cycle generates an inhomogeneous microstructure in the HAZ of the base metal, resulting in a marked variation in microstructure and mechanical strength across the ferritic steel weld joint. Microstructures in HAZ and weld metal of Cr–Mo steels are extremely complex and are controlled by the phase transformations and grain growth characteristics of the steels being welded [7–12]. This chapter deals with creep, LCF and creep-fatigue interaction behaviour of various stainless steels and Cr–Mo steels.

5.2 Fatigue behaviour of stainless steel weldments

In general, the LCF behaviour of several stainless steel welds and weldments is similar. The LCF behaviour of 304 SS base metal, 308 SS weld metal and 304/308SS weld joints [13,14] is discussed here. The microstructure of 304 SS base metal is of equiaxed grains of 75 μm while weld metal is composed of columnar grains and vermicular δ-ferrite (ferrite number = 9) distributed in an austenite matrix. The weld joint shows a coarse-grained HAZ. The cyclic stress response of the base metal, weld metal and the weld joint differ considerably (Fig. 5.1). (The base metal shows rapid initial hardening followed by well-defined saturation stress stage at 823 and 923 K, which persists until the crack nucleation and growth impairs the load-carrying capacity of the specimen, as indicated by the rapid fall in stress towards the end of the test (Fig. 5.1a). Type 308 SS weld metal exhibits continuous cyclic softening (Fig. 5.1b). The cyclic stress response of the weld joints is marked by initial hardening followed by softening. The initial cyclic deformation of the weld joint is similar to that of its major constituent, base metal. Weldments subjected to a stress-relieving heat treatment (i.e. post-weld heat treatment, PWHT) display lower response stresses compared with the untreated weldments (Fig. 5.1c). The initial hardening observed in 304 SS base metal results from the combined effects of dislocation-solute atom (dynamic strain ageing) and dislocation–dislocation interactions, while the stress saturation is found to have correlation with the development of well-defined cell structure. The cyclic stress response of 316L(N) base metal, 316 SS weld metal and 316L(N)/316 SS weld joints exhibit similar trends [15,16].

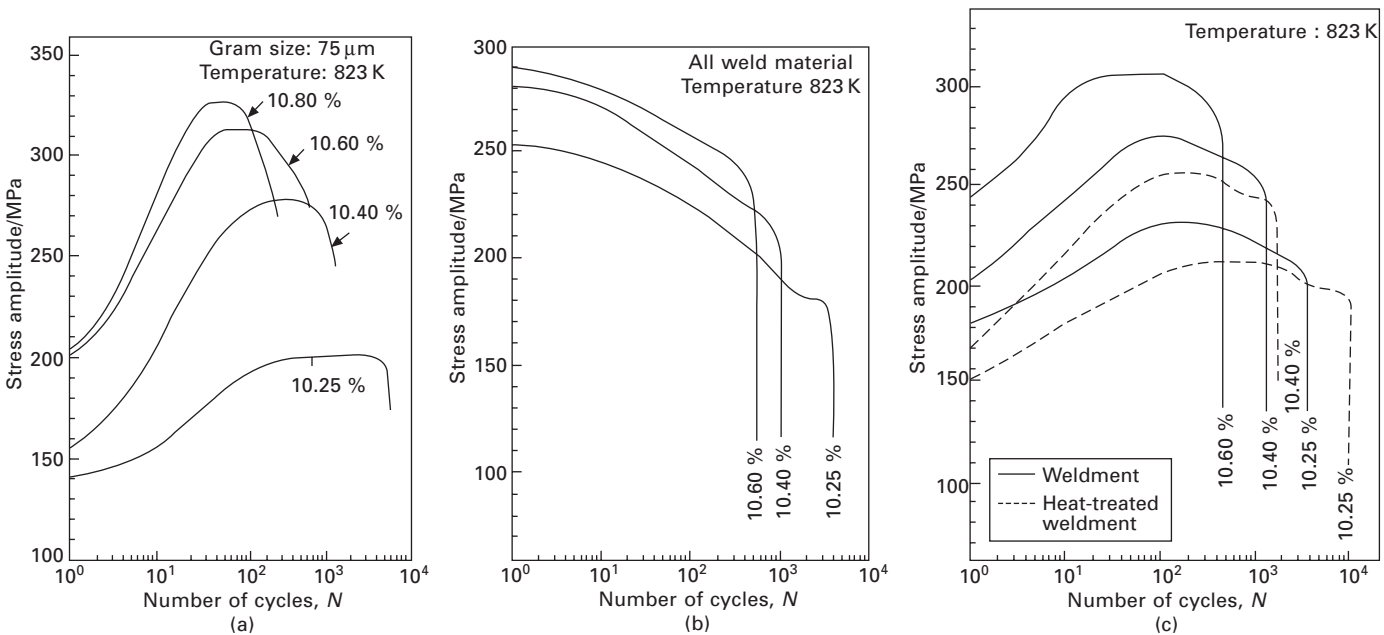

5.1 Cyclic stress response curves for (a) base, (b) all weld and (c) weldments specimens at 823 K [14].

Transmission electron microscopy on 316SS weld metal provided information on the origins of cyclic softening in austenitic weld metals [16]. The untested weld metal reveals very high density of dislocations and dislocation tangles in austenite matrix with a comparatively lower density of dislocations in δ-ferrite. After LCF testing, the dislocation density in austenite is considerably reduced, while δ-ferrite is free from dislocations. During LCF, dislocation tangles break down, and subsequent annihilation of dislocations of opposite sign promotes cyclic softening in weld metal [14].

Type 304 SS base metal displays superior LCF resistance while 304/308 SS weld joints show the least at 823 K and 923 K (Fig. 5.2). The reduction in life occurs for all the conditions with the raise in temperature from 823 to 923 K. The poor fatigue resistance of weld joints is ascribed to the shortening of crack initiation phase and to poor crack propagation resistance of the coarse-grained region of the HAZ. At 823 K, in base metal and weldments, crack initiation occurs in persistent slip bands, which signifies the occurrence of planar slip. Since the grain size governs the slip length, coarse grains develop larger slip steps at the surface, which would render the formation of intrusions and extrusions easier. Intrusions act as notches from which cracks originate. In alloys deforming by planar slip, an improved crack propagation resistance has been noticed with decreasing grain size. This is because the grain boundaries serve as natural barriers to transgranular crack propagation, causing the crack front to be held back and necessitating a crack re-initiation event to occur in each new grain. Solution annealing (at 1173 K for 3 h) the weldments prior to LCF testing result in improvement in fatigue life probably due to the elimination of residual stresses from the weld joint (Fig. 5.2). The reduction in life with increasing temperature is associated with the combined effects of an increase in inelastic strain generated in a cycle and from the effects of oxidation-assisted crack initiation and propagation in all the three material conditions. All weld 308 SS weld metal shows lower fatigue resistance compared with base metal, at both 823 and 923 K.

The LCF life is generally governed by the ductility of the material at high strain amplitudes and by strength of the material at low strain amplitudes. The lower ductility of weld metal causes reduction in its LCF life compared with the base material. Vermicular δ-ferrite in welds and weldments undergo transformation to $M_{23}C_6$ and σ-phase during LCF testing. The transformed amount of δ-ferrite increases with increasing number of cycles to failure and increasing temperature (Fig. 5.3). The transformation of δ-ferrite is more rapid in weldments than in all-weld metal. The fine duplex austenite–ferrite microstructure in the weld metal, with its transformed δ–σ phase boundaries, offers greater resistance to the extension of fatigue cracks by causing the deflection of crack path. Crack deflection could cause reduced stress intensity at the crack tip with an associated reduction in the crack propagation rate. The beneficial effects of δ–σ transformation could be clearly seen in the

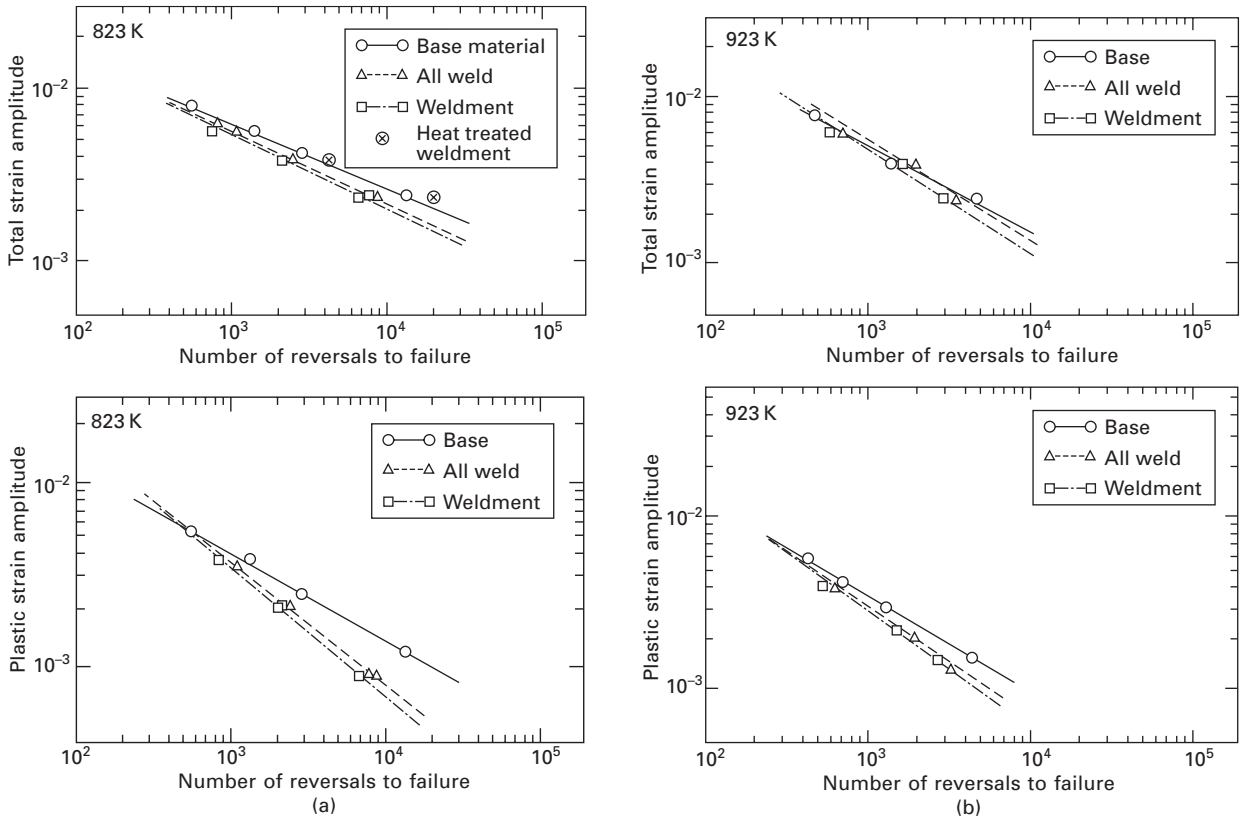

5.2 Strain-life plots for base, all-weld and weldments at (a) 823 K and (b) 923 K [14].

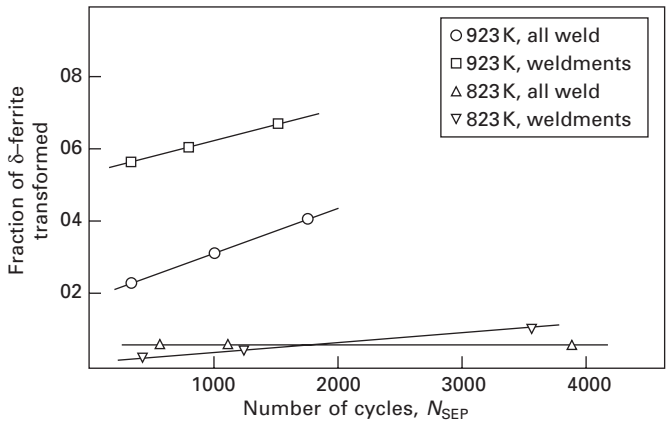

5.3 Influence of testing variables on the fraction of δ-ferrite transformed during fatigue deformation.

comparative evaluation [17] of fatigue lives of 316L(N) base and 316 SS weld metals at 773 and 873 K (Fig. 5.4). At 873 K, the LCF life of 316SS weld metal is superior to 316L(N) base metal, while at 773 K weld metal shows lower life. At 773 K, the transformation of the δ-ferrite to σ is less and the beneficial effects of crack deflection could not be fully realised.

Weld discontinuities play an important role on strain-controlled fatigue behaviour of 308 SS weld metal [14]. Fatigue resistance of defect-free 308 SS weld metal is substantially lower than 304 SS base material at low strain amplitudes. In base and sound weld metal, at all strain amplitudes, the crack initiation and propagation is generally transgranular. Discontinuities that are present on and near the specimen surface (Fig. 5.5, samples 1 and 3) are found to reduce the LCF life drastically compared with the defects located in the interior regions of the samples 4 and 6. Porosity present on the specimen surface is found to be particularly harmful and causes a reduction in life by a factor of seven relative to the sound weld metal. Combination of porosity and slag inclusions is found to be more detrimental than the case when either the slag inclusions or porosity (sample 5) alone is present in the interior regions. Porosity at one end of the gauge length (sample 4) is found to be less harmful to LCF life of weld metal. The shorter fatigue lives of the welds containing defects are associated with the initiation of fatigue cracks at discontinuities and rapid advancement of cracks.

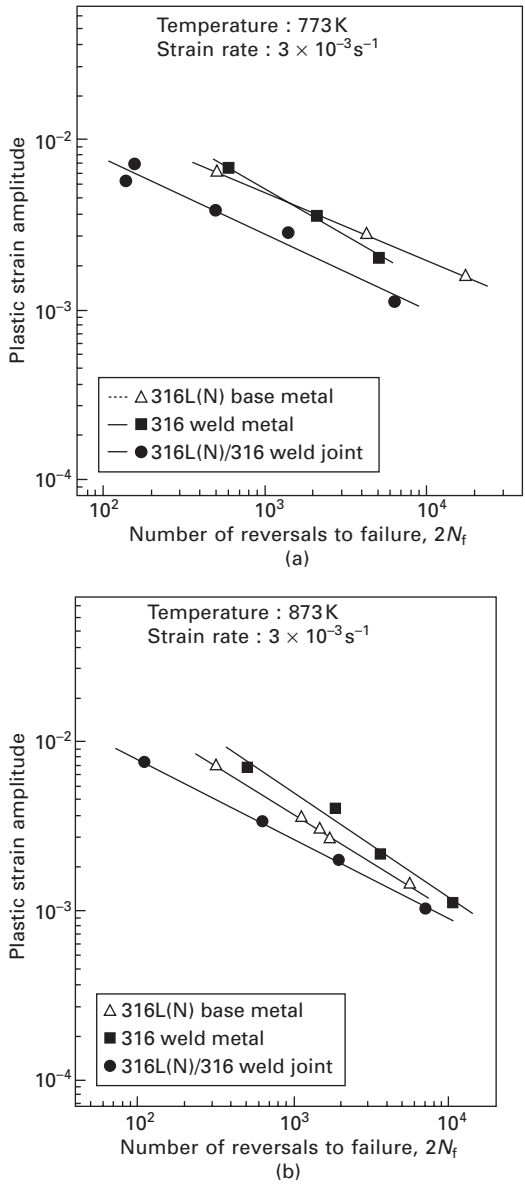

5.4 Comparison of fatigue lives of 316L(N) base metal, 316 weld metal and 316L(N)/316 weld joints at (a) 773 K and (b) 873 K [17].

5.3 Creep–fatigue interaction behaviour of stainless steel welds and weld joints

Creep–fatigue interaction is an important design consideration in plants that are subjected to steady state operation. The deformation and damage

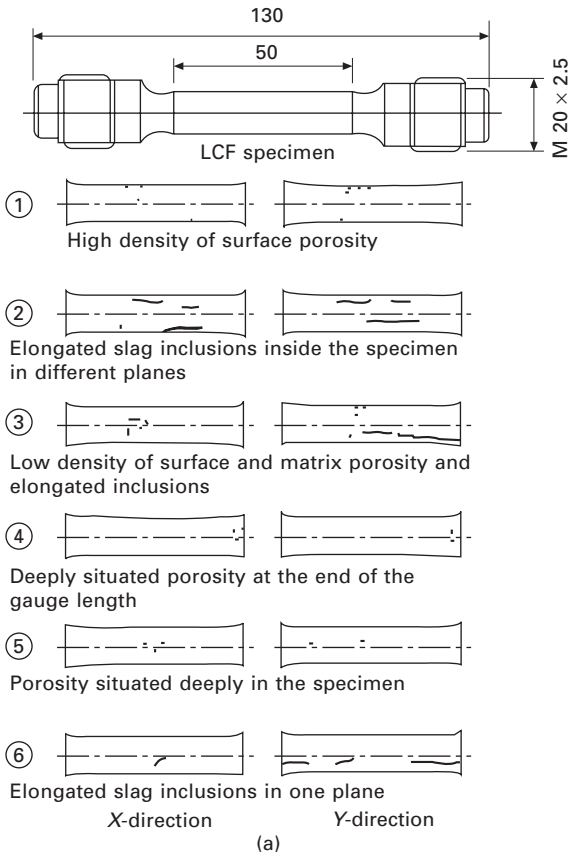

5.5 (a) Description and location of defects in LCF specimen of weld metal. (b) Strain-life plots of 304 SS base and 308 SS sound weld and defective weld metal. Numbers at data points refer to the samples shown in [14].

mechanisms that control life under creep–fatigue interaction conditions in base and welds are different. This necessitates comprehensive understanding of the factors controlling creep–fatigue interaction in welds and weld joints. Furthermore, relative creep–fatigue interaction resistance of base and weld metals depends on the material chosen for particular application. Creep–fatigue interaction tests are conducted by introducing hold at peak strain either in tension or compression alone or at both tension and compression peaks. The effect of hold-time on life depends not only on the material condition but also on the position of hold in a cycle (Table 5.1). Fatigue lives recorded for 308 SS weld metal in the 1 min hold-time tests are in the order: compression hold > continuous cycling > tension-plus-compression hold > tension hold. Fatigue lives of 304 SS base metal are in the order: continuous cycling > compression hold > tension-plus-compression hold > tension hold. A significant reduction in the life of weld metal is noted on increasing the duration of hold-time to 10 min (Table 5.1) though the time to failure increases. The damage behaviour in hold-time tests is generally described by characterising the stress relaxation as a function of time elapsed in hold-time tests. The mid-life stress relaxation response curves for the different hold-time tests are shown in Fig 5.6(a) and (b) respectively for 304 SS base and 308 SS welds. In the initial stages, rapid relaxation in stress occurs in less than 5 s. The inelastic strain rates associated with relaxation strain decrease continuously with increasing fraction of hold time. The inelastic strain rates associated with rapid relaxation period ($> 10^{-4}$ s^{-1}) correspond to those which are expected to cause matrix deformation while those observed in the slow relaxation period ($< 10^{-5}$ s^{-1}) are typical of creep deformation. The increase in inelastic strain occurring as a result of creep in a cycle (Table 5.1) under hold-time conditions would lead to a reduction in life.

Metallographic investigations on failed samples of 304 SS suggest that bulk creep damage effects are associated with tensile hold periods whereas the fracture modes associated with compression holds and continuous cycling are very similar in nature, being dominated by ductile fatigue striations. The large reduction in life under tensile hold results from the introduction of grain boundary creep damage during low strain rate tensile deformation, which modifies the failure process. Premature failure and reduced fatigue life result primarily because the reduced crack length at failure is effectively shorter than that in the absence of creep cavitation. Hales [18] proposed that a creep strain rate of less than $< 10^{-4}$ s^{-1} and an accumulated relaxation strain of ~ 7% are necessary to accumulate grain boundary damage at second-phase particles. As the process of initiation and early growth of internal grain boundary cavities which give rise to CFI failures require both shear and tensile stresses across a grain boundary, bulk damage is unlikely to occur during the period of compressive stresses. The longer lives under compressive holds result from healing effects of compressive creep. In general, intergranular

Table 5.1 Low cycle fatigue and creep–fatigue interaction properties of 304 SS base and 308 SS weld materials

Material	Wave shape*	Hold time (min.)	Strain Range		Creep (%)	Stress Amplitude		Number of cycles to separation	Duration of test(s)
			Total	Inelastic		First cycle	Half-life		
304 SS base	CC	0	1.0	0.73	0	127	266	900	6 000
	TH	1	1.0	0.76	0.03	111	255	555	37 000
	CH	1	1.0	0.75	0.02	123	250	880	58 670
	TCH	1	1.0	0.84	0.11	131	242	695	46 340
308 SS weld	CC	0	1.0	0.72	0	215	188	525	3 500
	TH	1	1.0	0.73	0.01	217	188	385	25 600
	CH	1	1.0	0.78	0.05	218	204	730	48 670
	TCH	1	1.0	0.86	0.14	223	185	415	52 570
	TH	10	1.0	0.83	0.11	245	210	160	97 070

*CC, continuous cycling; TH, tension hold; CH, compression hold; TCH, tension plus compression hold.

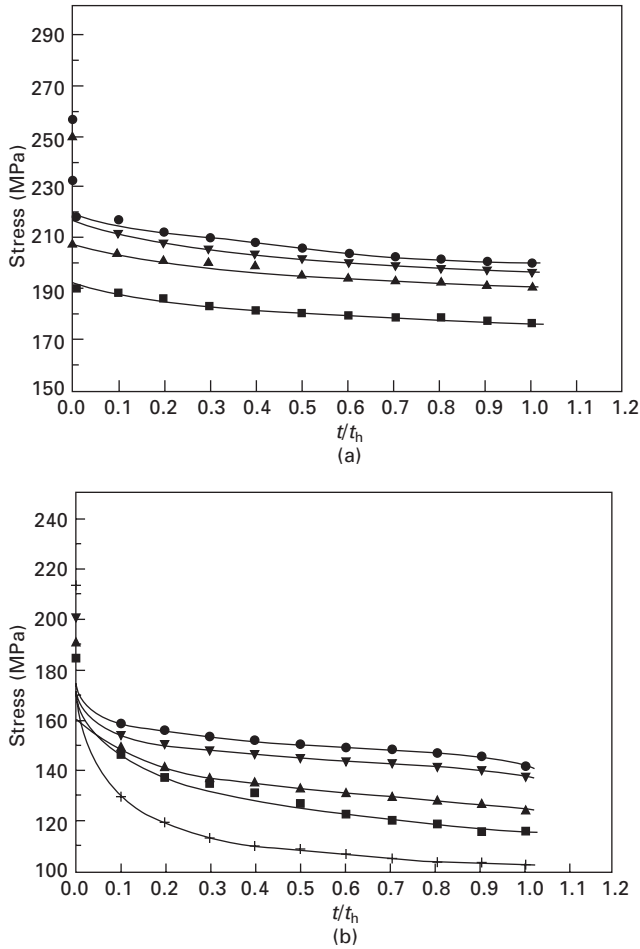

5.6 Stress relaxation response for (a) 304 SS base material (923 K, ± 0.5%; * 1 MTCH, ● MCH, ■ 1 MTCH-TH, ▲ 1 MTCH-CH) and (b) 308 SS all-weld material (923 K, ±0.5%; * 1 MTCH, ● MCH, ■ 1 MTCH-TH, ▲ 1 MTCH-CH) [14].

crack propagation occurs at a faster rate than transgranular cracking. Therefore the fatigue lives of the specimens tested with tension hold are shorter than those with symmetrical or compressive hold periods.

308 SS weld exhibits a shorter life than 304 SS under identical loading conditions during CFI tests. In weld metal, surface cracks initiate at austenite–ferrite boundaries. In the hold time tests extensive transformation of δ–σ phase occurs at gamma–delta interfaces, providing a variety of interface boundaries to serve as fracture paths. Extensive sigma phase formation might lower ductility locally and hence initiate cracks. A large number of microcracks

are developed in the tension hold specimens at gamma–sigma interfaces. The joining of these types of microcracks with the main crack shortens the crack propagation stage, leading to overall reduction in life. Weld specimens tested under compression holds does not reveal microcracks at the gamma–sigma interfaces. The process of crack initiation and early growth at interfaces require the normal tensile stresses across the interface. Thus for cycles containing compression holds, fatigue life would be dominated by fatigue striation mechanisms.

The creep–fatigue lives of 316L(N) base metal, 316 SS weld metal and 316L(N) weld joint as a function of the length of the hold time are shown in Fig. 5.7 [19]. At 873 K, in both continuous cycling and hold time tests, 316 weld metal shows higher endurance compared with 316L(N) base metal. The weld joint shows the shortest life.

The temperature dependence of fatigue life of 316L(N) base, weld metal and weld joints is shown in Fig. 5.8. Temperature dependence of fatigue life is similar for the base metal, weld metal and weld joints and shows a maximum in the intermediate temperature range [20]. The reduction in lifetime with increasing temperature beyond 573 K results from the combined effects of dynamic strain ageing and oxidation. The shorter lifetime at 300 K, compared

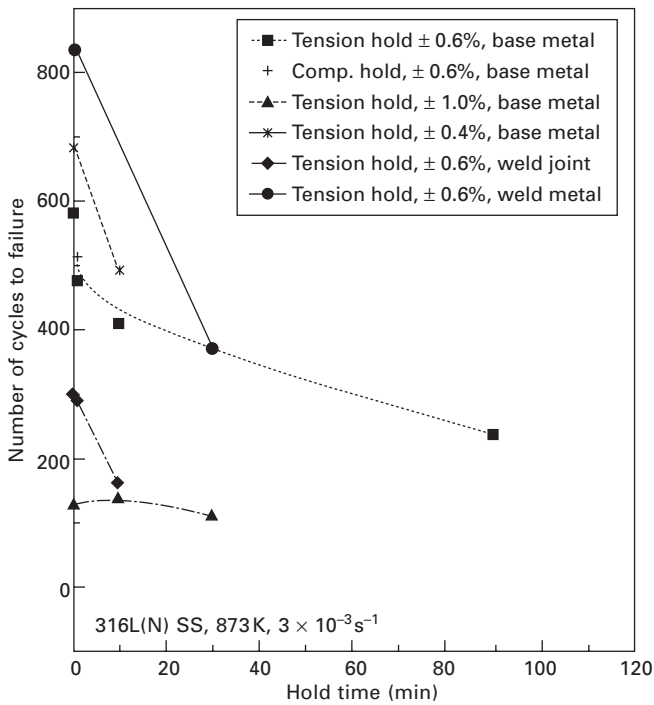

5.7 Fatigue life as a function of hold time [19].

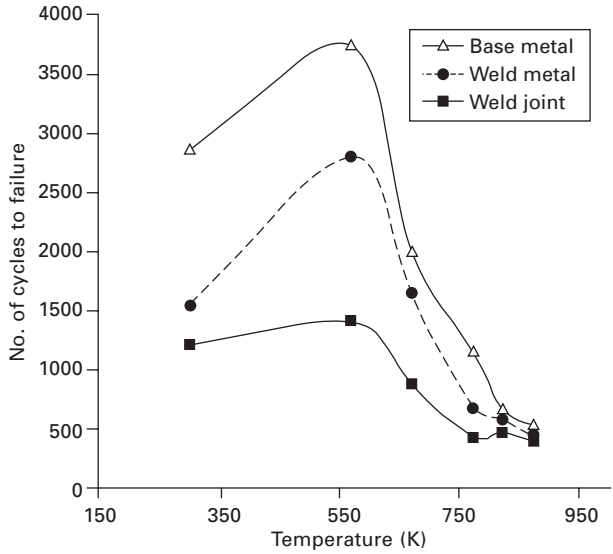

5.8 Temperature dependence of fatigue life of 316L(N) base metal, 316(N) weld metal and 316(N)/316(N) weld joint [20].

with that at 573 K occurs from the shortening of both crack initiation and propagation stages due to cyclic deformation-induced transformation of the austenite to martensite.

5.4 Creep behaviour of austenitic stainless steel welds

The creep properties of modified grade of type 316 SS and its welds (prepared using E316-15 basic coated electrodes with a ferrite number of 3 to 6) at 823, 873 and 923 K over a wide range of stress levels [21–25] are shown in Fig. 5.9. Chemical compositions of the base metal and the weld metal are given in Table 5.2. 316 SS weld metal creeps at a faster rate than the base metal by a factor of 10 at 823 K, and by a factor of 2 at 873 K. At 923 K, the minimum creep rates of the base and weld metals are similar at all stress levels. Higher creep rate of the weld metal is attributed mainly to the lack of precipitation of $M_{23}C_6$ in the weld metal matrix unlike in the case of base metal [26–28]. Creep being a diffusion-controlled process, it occurs at a faster rate in δ-ferrite than in austenite. Since δ-ferrite did not undergo total transformation at 823 and 873 K, the weld metal crept at a faster rate. Therefore, 316 SS weld metal shows lower rupture life than base metal. Strength reduction varied in the range of five to ten depending upon the test conditions. A comparison of the experimental weld metal data with the ASME design curves (also included in Figs 5.10a–c) reveal that (i) rupture strength of the

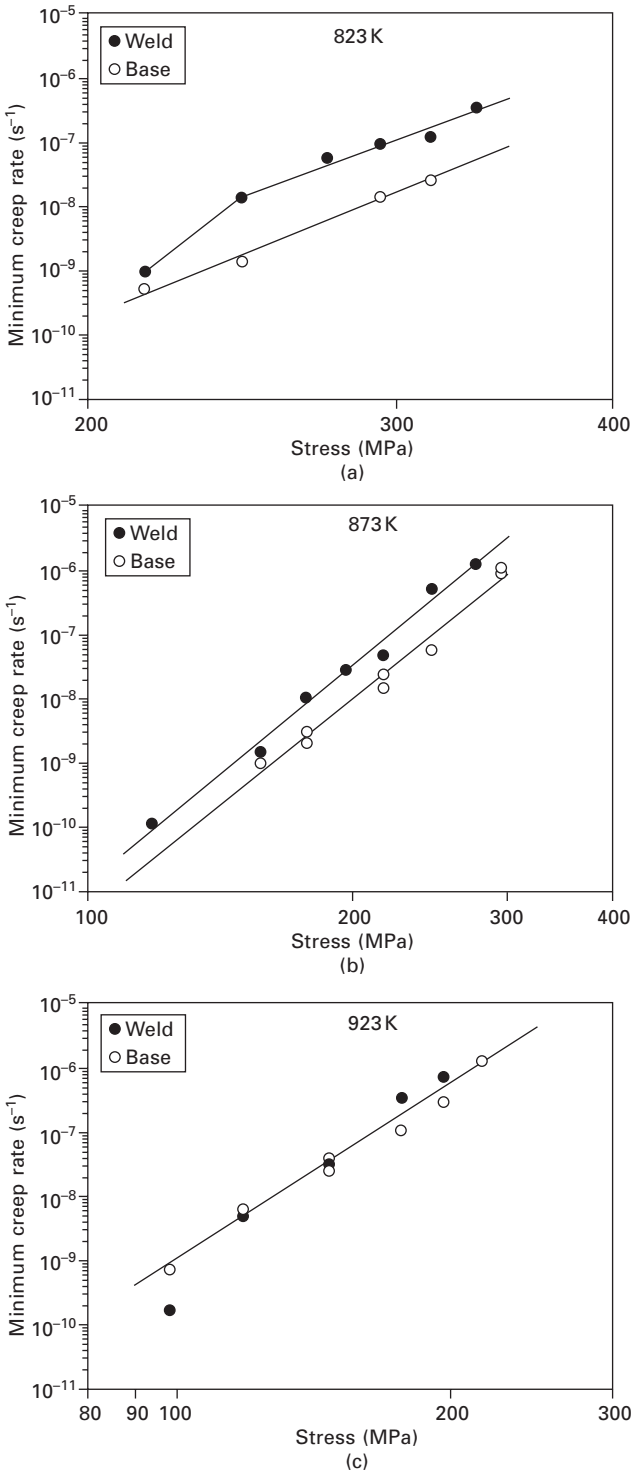

5.9 Comparison of steady state creep rates of 316 SS base and weld metals at (a) 823 K, (b) 873 K and (c) 923 K.

Table 5.2 Chemical composition of 316 SS and 316(N) SS (in wt%)

Material	C	Cr	Ni	Mo	Mn	Si	S	P	Fe	Nb	Ti	N
316 SS weld	0.06	18.8	11.9	2.06	1.42	0.58	0.01	0.01	bal.	0.01	0.01	
316LN SS base	0.023	17.1	12.2	2.31	1.65	0.29	0.003	0.024	bal.			0.03
316N SS weld	0.052	18.6	11.5	2.20	1.74	0.64	0.007	0.022	bal.			0.07

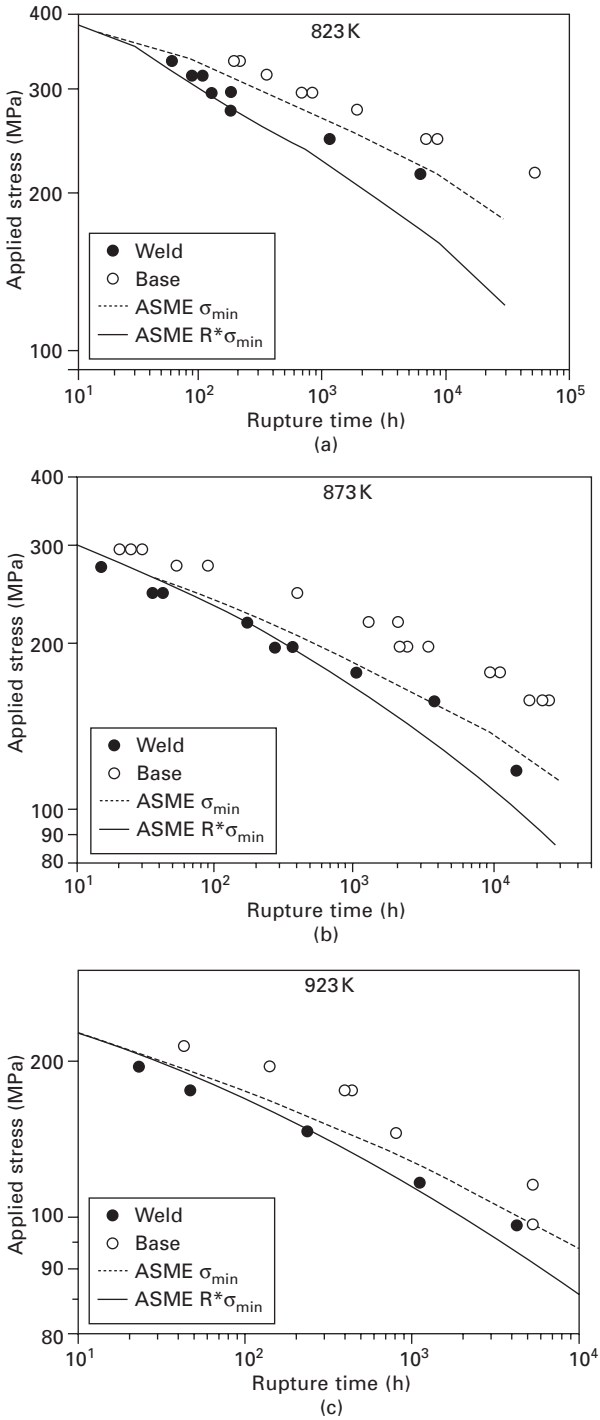

5.10 Comparison of rupture strengths of type 316 SS base and weld metals at (a) 823 K, (b) 873 K and (c) 923 K [22].

weld metal is lower than the expected minimum stress to rupture for the base metal and (ii) rupture strength of the weld metal is generally equal to or higher than the ASME values for expected minimum stress to rupture for the weld metal. Figure 5.11(a) shows the variation of rupture elongation with applied stress for the base and weld metals at 923 K. Weld metal ductility is considerably lower than that of the base metal. Difference in the ductility increases with decreasing stress level. At 823 and 873 K, ductility of the weld metal is more than that of the base metal at high stresses but less at low stress levels (Fig. 5.11b and c). In the base metal, creep damage has developed in the form of cracks at grain boundary triple points and the fracture mode is dependent on the test conditions. Low ductility creep failures of weld metal containing δ-ferrite at 923 K is attributed to the formation of brittle phase sigma, from δ-ferrite facilitating easy creep cavitation. This explains the observation that the difference between the ductility of base and weld metals depends on the rupture life and temperature.

5.4.1 Influence of nitrogen on creep properties of austenitic stainless steel welds

Nitrogen is known to be an effective solid solution strengthening element in wrought austenitic stainless steels over a wide range of cryogenic to high temperatures, without much concomitant loss of toughness, and at the same time it imparts better pitting corrosion resistance. The effect of nitrogen (chemical composition of 316 SS and 316(N) SS weld metals are shown in Table 5.2) on steady state creep rates of weld metals at 923 K is shown in Fig. 5.12. Alloying with nitrogen decreases the steady state creep rate up to two orders of magnitude depending upon the temperature and stress level. The creep behaviour of weld metals of the two steels could be described by a power law relationship between steady state creep rate ($\dot{\varepsilon}$)and stress (σ) at all the three temperatures. The stress exponent (n) in the power-law relationship varies in the range of 10 to 20. The high values of n suggest that dislocation creep is the rate-controlling mechanism of creep deformation in 316 and 316(N) SS weld metals.

The influence of nitrogen on creep rupture strength at 873 K is shown in Fig. 5.13. Rupture strength of 316(N) weld metal is substantially higher than that of 316 SS weld metal under all the test conditions. The beneficial effect of nitrogen would continue for rupture lives much beyond 20 000 h. The dashed line in these figures represents the expected minimum stress to rupture specified by the French nuclear design code RCC-MR used for the design of high temperature components of FBRs [29]. The RCC-MR creep rupture strength for the weld metal is established by scaling the expected minimum stress to rupture data of the base metal, employing appropriate weld strength reduction factors under various test conditions provided in the design codes.

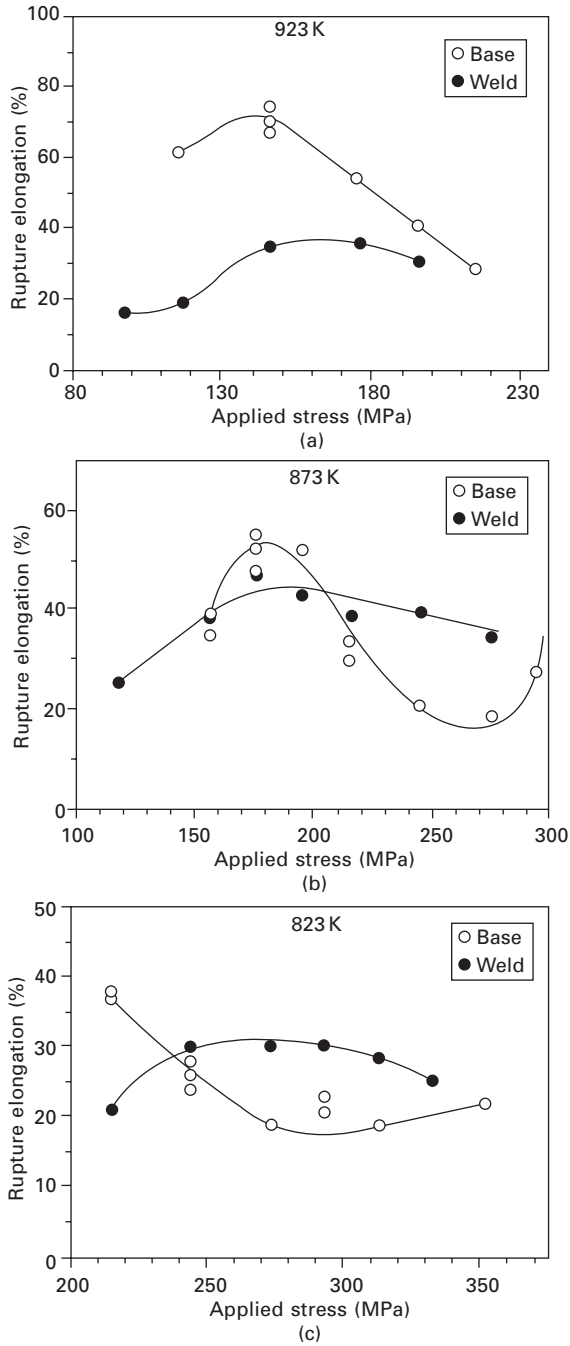

5.11 Comparison of rupture ductilities of type 316 SS base and weld metals at (a) 923 K, (b) 873 K and (c) 823 K [22].

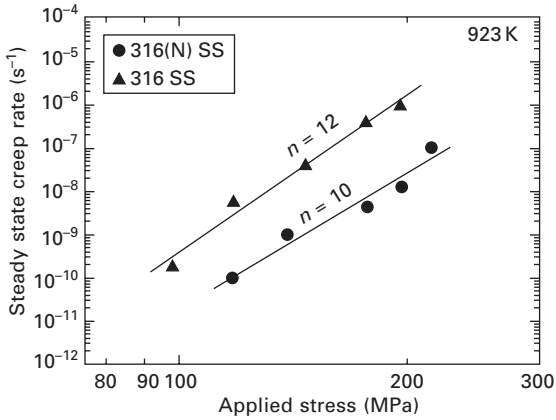

5.12 Comparison of steady state creep rates of 316 and 316(N) SS weld metals at 923 K [25].

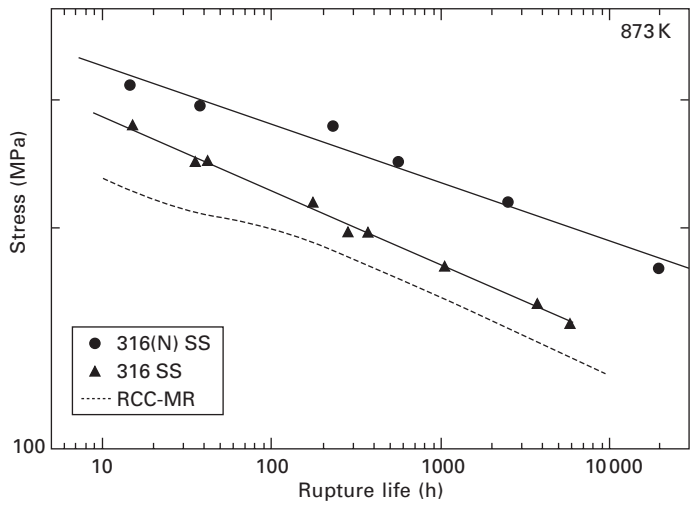

5.13 Comparison of rupture strengths of 316 and 316(N) SS weld metals at 873 K [25].

It is evident from Fig. 5.13 that rupture strength of 316(N) SS weld metal is much higher than the design code requirements. Both the nitrogen-bearing base metal and weld metals display lower ductility than nitrogen-free base and weld metals at 923 K. In general, the weld metals show lower ductility with increase in rupture lives (Figs 5.13 and 5.14).

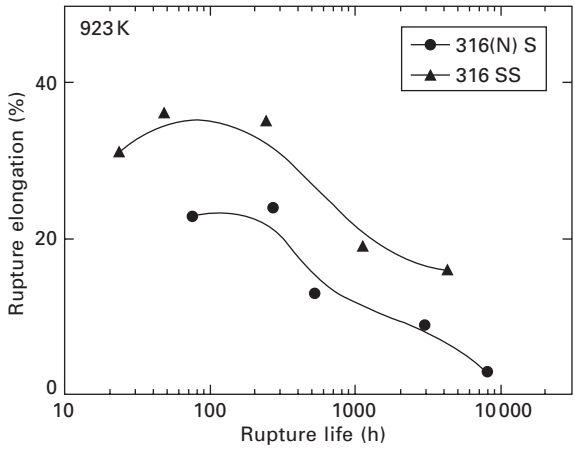

5.14 Comparison of rupture ductilities of 316 and 316(N) SS weld metals at 923 K [24].

5.4.2 Microstructural changes during creep deformation in austenitic stainless steel welds

The δ-ferrite transformation in 316(N) SS weld metal is found to take place in the following sequence: (i) initially the δ-ferrite network breaks down, forming continuous beads of carbides along delta/austenite (gamma) interphase boundaries, (ii) on prolonged exposure, the growth of carbides result in depletion of the ferrite stabilising elements in δ-ferrite and favours its transformation to austenite in regions adjacent to the carbides and delta/gamma interface advances into the ferrite leaving the carbide particles isolated in the austenite matrix. On further exposure, the remaining region of δ-ferrite continues to get enriched in ferrite stabilising elements and attains the chemical composition of sigma-phase, at which stage the δ-ferrite undergoes transformation to sigma phase. These sigma particles grow and agglomerate at the expense of the carbides so that the entire delta-ferrite has transformed into coarse sigma precipitates.

Several mechanisms have been reported for the increase in strength due to nitrogen, such as solid solution hardening, decrease in stacking fault energy (SFE), precipitation strengthening, formation of interstitial-substitutional solute complexes and order strengthening [30–32]. Generally, nitrogen shifts the precipitation of carbides to longer durations and also delays the rate of coalescence of carbides in austenitic stainless steels. Nitrogen in the carbides decreases the mismatch between the precipitate and the austenite matrix, thereby reducing the interfacial energy and inhibits precipitate coarsening. The comparative decrease in steady state creep rate and increase in rupture

life of 316(N) SS weld metal is attributed to the strengthening of the austenite matrix in the weld metal. The weld metal strength is always inferior to the strength of the base metal due to differences in chemistry, δ-ferrite network, columnar structure of grains, etc. The lower rupture elongation with 316(N) SS weld metal as compared with 316 SS weld metal is consistent with the lower ductility generally observed in nitrogen-bearing base metal, especially at long rupture lives.

5.5 Creep rupture strength of ferritic steel weld joints

Figure 5.15 describes schematically the formation of complex microstructure across a ferritic steel weld joint based on Fe–C phase diagram during welding and their subsequent modification into further complicated microstructures upon multipass welding. For a single weld bead on 2.25Cr–1Mo steel plate typical microstructures that can be obtained in the weld and HAZ are shown in Fig. 5.15(a) and Fig. 5.15(b) describes the microstructural modifications resulting from the deposition of weld metal in the subsequent passes. Since the peak temperatures attained and the subsequent cooling rates decrease with increasing distance from fusion boundary, welding results in a variety of non-equilibrium microstructures in the HAZ of 2.25Cr–1Mo steel as shown in Fig. 5.15(b).

During elevated temperature operations cracking can arise both in the weld metal and HAZ of the joint because of the highly heterogeneous microstructure across it. Different types of cracking that could occur in Cr–Mo ferritic steel weld joint are described in Fig. 5.16 [33]. The Type I and Type II cracking originate in weld metal, propagate either through the weld metal itself (Type I) or cross over into HAZ (Type II). The Type III cracking develops in the coarse-grain region of HAZ close to the weld interface. Type IV cracking occurs at the outer edge of HAZ (intercritical/fine-grain region) towards the base metal. Selecting the proper chemistry of the deposited weld metal and adopting the proper welding technique (refining the coarse-grain HAZ by multipass welding) the Type I, Type II and Type III cracking have been avoided in weld joints of ferritic steels. Type IV cracking at the outer edge of HAZ is the life-limiting linkage of ferritic steel weld joints and is predominant at higher operating temperature.

5.5.1 Creep behaviour of 2.25Cr–1Mo steel welds and weld joints

Creep behaviour of base, weld and weld joint of 2.25Cr–1Mo steel is shown in Fig. 5.17 [34]. The composite weld joint displays much lower creep rupture strength than both the base metal and weld metal. The creep behaviour of

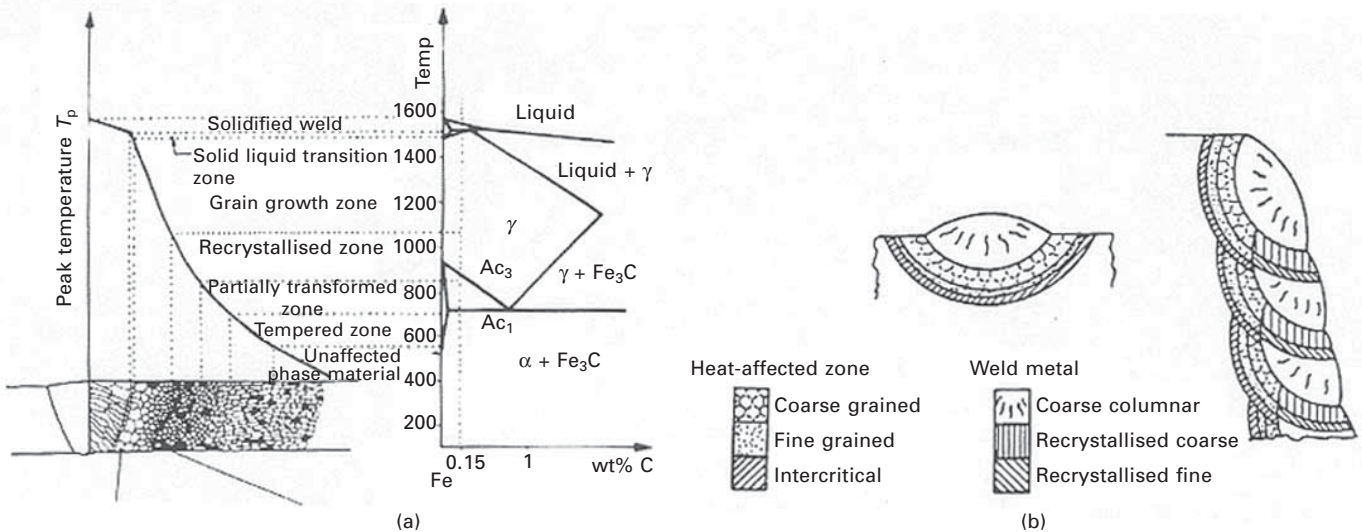

5.15 (a) Schematic description of HAZ formation in ferritic steel based on Fe–C phase diagram and (b) schematic description of refinement of weld and HAZ during multipass welding.

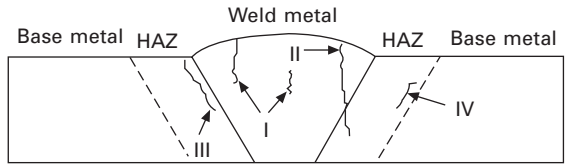

5.16 Schematic representation of different types of cracking in weld joint of ferritic steel on service exposure [33].

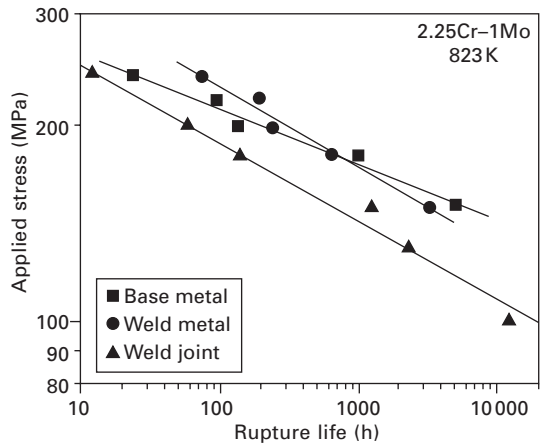

5.17 Creep rupture strength of 2.25Cr–12Mo steel weld joint compared with its base metal and weld metal [34].

weld joint is rationalised on the basis of initial microstructures across the joint during a weld thermal cycle (Fig. 5.15), and evolving microstructure during subsequent creep exposure. The microstructure of 2.25Cr–1Mo steel base metal in the normalised and tempered condition consists of 70% tempered bainite and 30% ferrite. The weld metal microstructure has a morphology characteristic of upper bainite and identifiable by its lath-like arrangement of ferrite. The HAZs of the weld joint consist of coarse-grain bainite close to the fusion boundary, which becomes progressively finer as the distance from the fusion boundary towards the base metal increases, terminating in a fine intercritical structure composed of uniformly distributed carbides in a ferrite phase (tempered bainite) surrounded by austenite transformation products. The grain sizes of coarse and fine-grain bainite regions are 120 and 15 μm, respectively. The rapid fall in hardness is seen as the distance from the fusion boundary in HAZ increases (Fig. 5.18). Within the HAZ, the intercritical region shows lowest hardness. Preferential creep strain accumulation in the intercritical region of HAZ (Fig. 5.19), leads to the cracking in this region and the premature failure of the weld joint. The 2.25Cr–1Mo steel derives its creep strength mainly from the intragranular precipitation of Mo_2C. The

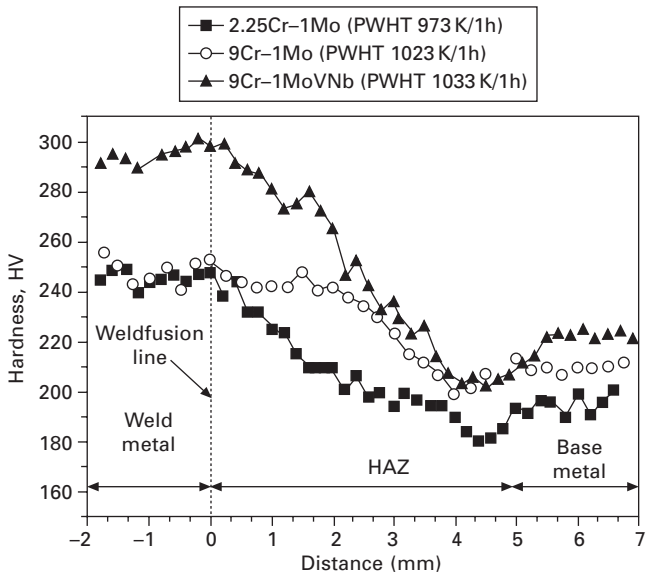

5.18 Hardness profile across the weld joint of 2.25Cr–1Mo, 9Cr–1Mo and modified 9Cr–1Mo steels weld joint.

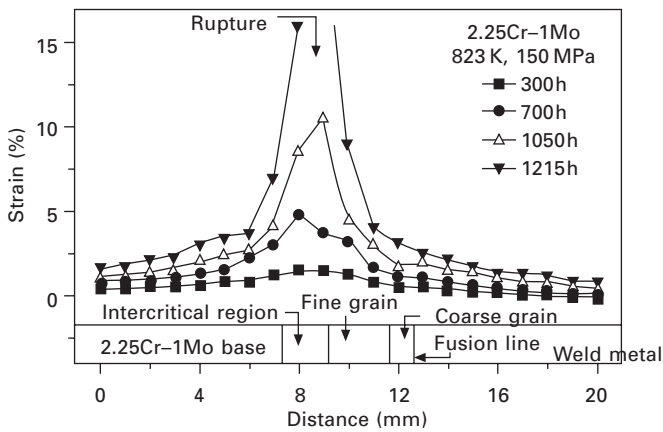

5.19 Creep strain accumulation across the different constituents of 2.25Cr–1Mo weld joint during creep test [34].

reduction in the number density of Mo_2C particles in the intercritical region of HAZ renders it soft and hence acts as a zone of preferential accumulation of creep deformation and creep cavitation.

In order to locate the exact region of HAZ responsible for premature failures, detailed investigations have been performed on the simulated microstructures present in the HAZ of the 2.25Cr–1Mo steel weld joint [35].

The simulated HAZ microstructures are developed by subjecting the base metal to appropriate iso-thermal heat treatments. The simulation was based on the detailed comparison of microstructure, prior-austenite grain size and hardness of the heat-treated base metal with those in the HAZ of the weld joint. The creep rupture strength of the various constituents of the joint differs considerably (Fig. 5.20). The intercritical HAZ exhibits poor strength while coarse-grain HAZ exhibits higher strength. This heterogeneity of creep strength across the weld zone induces extensive creep cavitation in the intercritical region of HAZ (Fig. 5.21), leading to the premature failure of the joint.

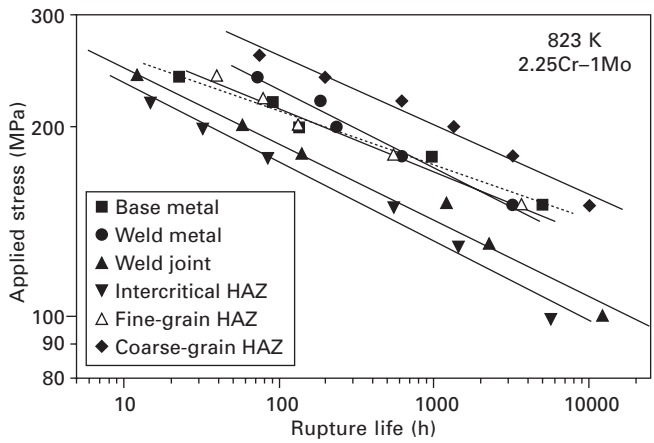

5.20 Creep rupture strength of different constituents of 2.25Cr–1Mo weld joint [35].

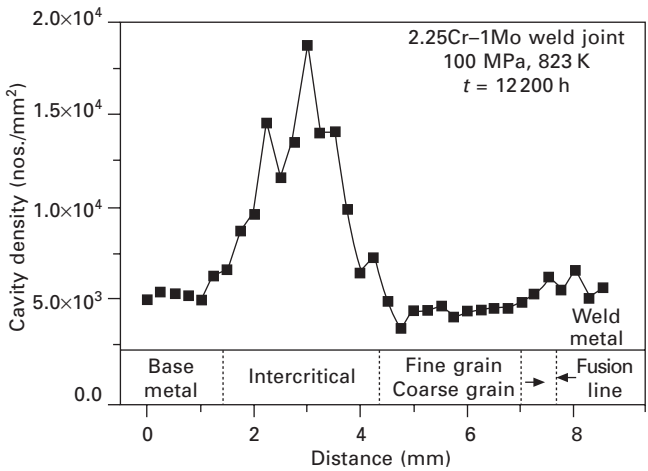

5.21 Creep cavity distribution across the HAZ of a 2.25Cr–1Mo weld joint, creep tested at 100 MPa, 823 K for 12 200 h.

5.5.2 Creep behaviour of modified 9Cr–1Mo steel weld joints

Modified 9Cr–1Mo acquires complete martensitic structure on normalisation and is used in tempered condition with tempered martensite structure. It derives its high temperature strength mainly from the complex microstructures consisting of a high dislocation density, sub-boundaries decorated with $M_{23}C_6$ precipitates and Nb–V carbonitride precipitates of MX type in the intragranular region [36,37]. Figure 5.22 shows the creep rupture strength of modified 9Cr–1Mo steel weld joint in comparison with its base metal. At relatively lower stresses and higher test temperatures, the weld joint shows lower creep rupture life than the base metal, and the difference in creep rupture life increases with decrease in stress and increase in test temperature. Preferential accumulation of creep deformation coupled with extensive creep cavitation in the intercritical region of HAZ resulted in failure of the weld joint in the intercritical region of HAZ. Strength reduction in the intercritical HAZ is associated with combined effects of coarsening of $M_{23}C_6$ and dislocation substructure. Constrained deformation of the soft intercritical HAZ sandwich between relatively strong constituents of the joint is responsible for the induced creep cavitation in the soft intercritical HAZ.

The type IV cracking susceptibility depends on the type of ferritic steel. The 2.25Cr–1Mo steel is most susceptible to type IV cracking, whereas the plain 9Cr–1Mo steel is the least susceptible (Fig. 5.23). The relative instability of Mo_2C from which the 2.25Cr–1Mo steel derives its creep strength, drastically

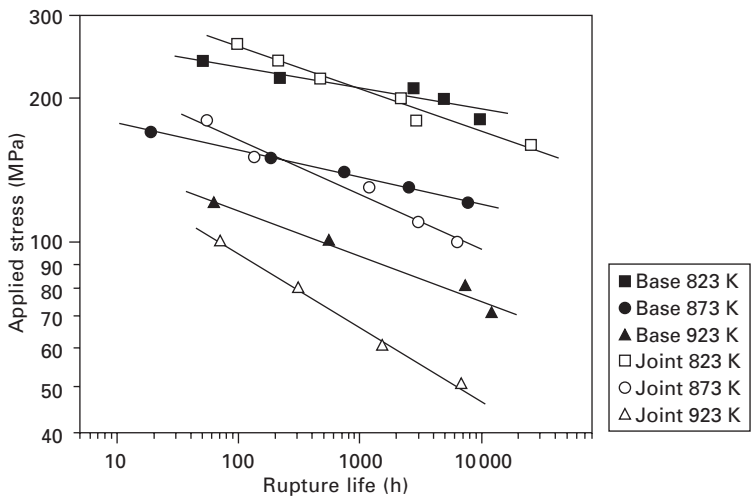

5.22 Variation of creep rupture life of modified 9Cr–1Mo base metal and weld joint with applied stress at different test temperatures.

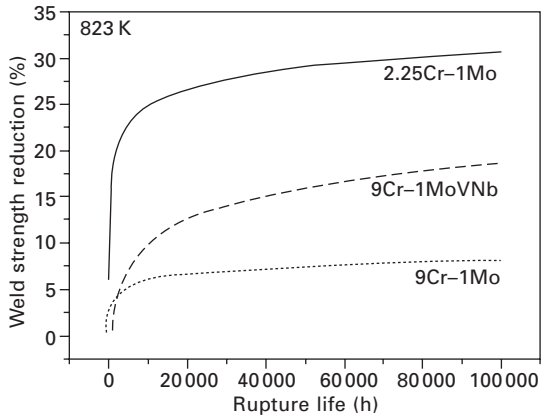

5.23 Variation of the weld creep strength reduction percentage of the steels with rupture life at 823 K.

reduces creep strength of the 2.25Cr–1Mo weld joint. The relatively higher type IV cracking susceptibility of modified 9Cr–1Mo steel compared with 9Cr–1Mo steel at higher test temperature is related to the precipitation of Z-phase, a complex Cr(V,Nb)N particle, in the former steel [38]. At elevated temperatures during long-term exposure, the Z-phase grows quickly by dissolving the beneficial MX type precipitates and accelerates the recovery in substructure with associated decrease in strength in the intercritical region of the HAZ.

Type IV cracking is difficult to avoid. Several methods are being adopted to minimise it in Cr–Mo steels [39–50]. Strength inhomogeneity across the weld joint can be eliminated by normalising the component after welding. Another approach may be the increase in width of the HAZ, which is expected to reduce the stress triaxiality so that the soft intercritical region deforms with less constraint with the consequence of reduced creep cavitation to minimise type IV cracking tendency. The width of the HAZ can be increased both by changing preheat and heat-input during welding. The resistance against intercritical softening can be improved by increasing the base strength of the steel with the addition of solid solution hardening elements such as W, Re and Co, and also by microalloying the steel with boron. Microalloying with boron retards coarsening rate of $M_{23}C_6$ on replacing some of its carbon. The added boron content is to be judiciously adjusted with the nitrogen content to avoid BN formation so that boron is available to achieve the desired function. Addition of Cu is also found beneficial. Copper, being almost completely insoluble in the iron matrix, precipitates as nano-size particles to impart creep resistance. A suitable adjustment of the chemical composition of steel within the specification range also reduces the large difference in creep strength between the softened HAZ, the base metal, and

the coarse-grain HAZ of the joint of modified 9Cr–1Mo steel. The weld joint of low carbon, nitrogen and niobium type modified 9Cr–1Mo steel has been reported to possess creep strength comparable to that of the base metal.

5.6 Creep of dissimilar weld joints

5.6.1 Ferritic/ferritic dissimilar weld joints

In practice, different grades of Cr–Mo steels are used in different parts of the same component to reduce the cost when differences in operating temperatures prevail. However, the use of different Cr–Mo steels (such as 9Cr–1Mo steel as header and 2.25Cr–1Mo steel as pipe in the steam generator) in the same circuit necessitates the fabrication of joints between different grades of Cr–Mo steels with the associated problem of the formation of decarburised soft zone in the low chromium steel and a carburised hard zone in the high chromium steel, with the consequence of an entirely different creep failure mode in dissimilar ferritic steel joints [51,52]. Highly localised creep deformation in the soft decarburised zone would lead to creep cavitation and reduced creep rupture strength in dissimilar weld joints of 2.25Cr–1Mo/9Cr–1Mo joints (Fig. 5.24) [52] welded with basic coated 9Cr–1Mo electrodes.

5.6.2 Ferritic/austenitic dissimilar weld joints

In several critical applications, welding of austenitic stainless steel to ferritic steels becomes a necessity, as different materials have to be chosen for different components operating under different service conditions. Differences in physical and mechanical properties and precipitation behaviour of base

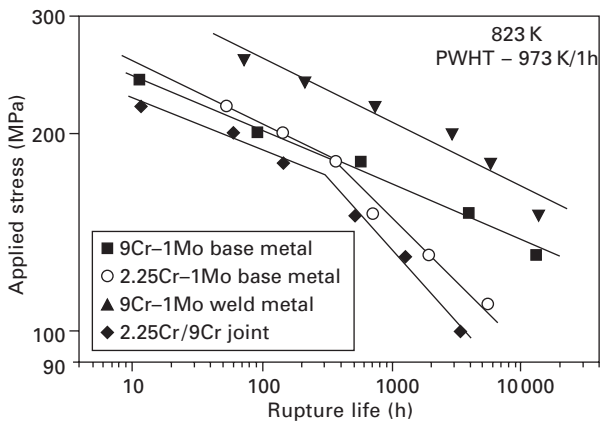

5.24 Creep rupture strength of 2.25Cr–1Mo/9Cr–1Mo dissimilar weld joint [53].

metals and their weld metal influence the service behaviour of the dissimilar weld joint. For example, in the steam generator circuit of fast breeder reactors, austenitic stainless steel 316L(N) pipes from the intermediate heat exchangers have to be welded to the modified 9Cr–1Mo steel pipes of the steam generators. These types of dissimilar welds are also anticipated in the piping circuits of fusion reactors. The dissimilar metal welds in steam generators are prone to large-scale premature service failures, leading to expensive plant outages, owing to the difference in thermal expansion coefficients between the ferritic steel and austenitic stainless steel base metal as well as weld metals. Failure occurs at the weld interface between austenitic weld metal and ferritic base metal due to nucleation of creep cavity [53]. The problem can be circumvented by engineering a gradient in the thermal expansion coefficients along the joint by using an Alloy 800 transition piece. For welding 316L(N) SS to Alloy 800 and Alloy 800 to modified 9Cr–1Mo steel, ER16-8-2 and Inconel 82/182 welding consumables, respectively, can be chosen. Thermal cycling performance tests have shown that this tri-metallic transition joint gives four times superior service life than the bi-metallic joints [54].

5.7 Acknowledgements

The authors wish to acknowledge Mr R. Kannan for many useful discussions and the help rendered in the preparation of the manuscript.

5.8 References

1. ASME Boiler and Pressure Vessel code Case N-47.
2. RCC-MR Design Code, 2002 ed., section 1, sub-section Z.
3. Shankar V, Gill T P S, Mannan S L and Sundaresan S, *Frontiers in Materials Science*: (eds). Raj B and Bhanu Sankara Rao K, The Indian Academy of Sciences, Bangalore, 359–382.
4. Slattery G F, Keown S R, and Lambert M E, *Met Technol* **10** (1983) 373.
5. Raghunathan V S, Seetharaman V, Venkadesan S, and Rodriguez P, *Metall Trans* **10A** (1979) 1683.
6. Kokawa H, Kuwana T, and Yamamoto A, *Weld J* **68** (1989) 92s.
7. Laha K, Bhanu Sankara Rao K, Chandravathy K S, and Mannan S L, *Trans Ind Inst Metals* **46** (1993) 77.
8. Chilton I J, Price A T, and Wilshire B, *Met Technol* **11** (1984) 383.
9. Smith E, Blanchard B E, and Apps R L, in *Proc. Conf. on Welding of Creep Resistant Steel*, The Welding Institute, Cambridge, (1970) p79.
10. Alberry P J, and Jones W R C, *Met Technol* **4** (1977) 360.
11. Lundin C D, Advances in welding science and technology in *Proc. Intl. Conf. on Trends in Welding Research*, Gatlinburg, TN, (1986) p475.
12. Nippes E F, *Welding J Res Suppl*. **38** (1959) 1s.
13. Bhanu Sankara Rao K, Valsan M, and Mannan S L, *Mater Sci Engng* **A130** (1990) 67.

14. Bhanu Sankara Rao K, Sandhya R, and Mannan S L, *Intl. J. Fat* **15** (1993) 221.
15. Valsan M, Bhanu Sankara Rao K, Sandhya R, and Mannan S L, *Mater Sci Eng A* **149** (1992) L9.
16. Valsan M, Sundararaman D, Bhanu Sankara Rao K, and Mannan S L, *Metal Mater Trans A* **26A** (1995) 1207.
17. Mannan S L, and Birla G D, Medal Lecture delivered during the National Metallurgists' day (1999).
18. Hales R, *Fatigue Eng Mater Struct* **3** (1980) 339.
19. Mannan S L, and Valsan M, *Intl J of Mech. Sciences* **48** (2006) 160.
20. Prasad Reddy G V, Sandhya R, Valsan M, and Bhanu Sankara Rao K, accepted for publication in *Materials Science and Technology*.
21. Mathew M D, Sasikala G, Mannan S L, and Rodriguez P, *Mater Sci Tech*, **7** (1991) 533.
22. Mathew M D, Sasikala G, Mannan S L, and Rodriguez P, *J Engng Mater Technol*, Transactions of ASME, **115** (1993) 163.
23. Mathew M D, Sasikala G, Gill T P S, Mannan S L, and Rodriguez P, *Mater Sci Tech*, **10** (1994) 1104.
24. Sasikala G, Mathew M D, Bhanu Sankara Rao K, and Mannan S L, *J. Nucl Mater*, **273** (1999) 257.
25. Sasikala G, Mathew M D, Bhanu Sankara Rao K, and Mannan S L, *Metal Trans*, **31A** (2000) 1175.
26. Morris D G, and Harries D R, *Met Sci*, **12** (1978) 525.
27. Mannan S L, and Rodriguez P, *Met Sci*, **17** (1983) 63.
28. Mathew M D, Sasikala G, Bhanu Sankara Rao K, and Mannan S L, *Mater Sci Engng*, **A148** (1991) 253.
29. RCC-MR, May 1983 Edition.
30. Sourmail T, *Mater Sci Tech*, **17** (2001) 1.
31. Schram R E, and Reed R P, *Met Trans A*, **11A** (1975) 1345.
32. Oda K, Kondo N, and Shibata K, *ISIJ Intl*., **30** (1990) 625.
33. Shüller H J, Haigh L, and Woitscheck A, *Der Machinenschaden*, **47**, (1974), 1–13.
34. Laha K, Bhanu Sankara Rao K, and Mannan S L, *Mat Sci Engng* **A129** (1990) 1380.
35. Laha K, Chandravathi K, Bhanu Sankara Rao K, and Mannan S L, in *Heat Resistant Materials*, (eds) Natesan K, *et al*., ASM, Gatlinburg, TN (1995) p399.
36. Vitek J M, and Kluch R H, *Metall Trans A* **14A** (1983) 1047.
37. Jones B W, Hills C R, and Polonis D H, *Metall Trans A* **22A** (1991) 1049.
38. Danielsen H K, and Hald J, *Energy Materials*, **1(1)** (2006) 49.
39. Rui Wu, Storesund J, and Sanstrom R, *Mater Sci Technol* **9**(1993) 773.
40. Nichnol S and Brook J C, *Heat Treatment Aspect of Metal Joining Process,* The Iron and Steel Institute (1972) p42.
41. Sikka V, U S Patent No. 4,018,070 Sept. 16,1986.
42. Francis J A, Mazur W, and Bhadeshia H K D H, *Trends in Welding Research*, Atlanta GA, 2005.
43. Albert S K, Tabuchi M, Hongo H, Watanabe T, Kubo K, and Matsui M, *Sci Technol Welding Joint* **10(2)** (2005) 149.
44. Arav F, Lentferink H J M, Etienne C F, and Wortal J C, *Proc 5th Int Conf Creep of Metal*, Lake Buena Vista, FL (1992) p117.
45. Shinozaki K, De-Jun Li, Kuroki H, Harada H, and Ohishi K, *Iron Steel Inst Jpn Int.* **42(12)** (2002) 1578.
46. Kojima T, Hayashi K, and Kajita T, *Iron Steel Inst Jpn Int* **35(10)** (1995) 1284.

47. Kobayashi S, Toshimori K, Nakai K, Ohmorio Y, Ashhi H, and Muraki T, *Iron Steel Inst Jpn Int Suppl* **42** (2002) S72.
48. Konda M, Albert S K, Tabuchi M, Tsukamoto S, Yin F, Okada H, and Abe F, *2nd Int Conf Integrity of High Temperature Weld*, London, 10–12 Nov IOM Communications Limited, London (2003) p123.
49. Iseda A, Natori A, Sawaragi Y, Ogawa K, Masuyama F, and Yokoyama T, *Thermal Nucl Power* **45(8)** (1994) 900.
50. Abe N, Kunisada Y, Sugiyama T, and Nagamine T, *Rivita Italian Delta Saldatura* **2** (1990) 44.
51. Cerjak H, *Proc Int Conf on High Temperature Materials for Power Engineering,* Liege, Belgium, Sept 1990 (eds) Bachelet *et al*., Kluwer, Dordrecht, (1990) p445.
52. Laha K, Latha S, Bhanu Sankara Rao K, Mannan S L, and Sastry D H, *Mat Sci Technol* **17** (2001) 1265.
53. Laha K, Chandravathi K S, Bhanu Sankara Rao K, Mannan S L, and Sastry D H, *Met Trans A* **32A** (2001) 115.
54. Bhaduri A K, Albert S K, Das C R, Vasudevan M, Srinivasan G, Ramasubbu V, Venugopal S (Jr), Sreenivasan P R, and Ray S K, *Proc. Seminar, Materials R&D for PFBR*, (eds) Mannan S L, and Mathew M D, 1–2 January, (2003) Kalpakkam, p263.

6

Fracture toughness in the design and operation of ferrous weldments

S K RAY and G SASIKALA, Indira Gandhi Centre for Atomic Research, India

Abstract: In this chapter, various approaches to fracture mechanics characterisation of ferrous weldments, consistent with the requirements of design and fabrication codes for fossil and nuclear power plants, are outlined. Both experimental and analytical approaches to describing fracture of welds, including innovations to characterise and also modelling to describe the behaviour of individual regimes of welds with metallurgical and mechanical gradients, are discussed. Crack growth and fracture in welds under dynamic and quasi-static loading conditions have been discussed in the framework of both linear elastic and elastic plastic fracture mechanics. Attempts to describe and characterise subcritical crack growth in welds under sustained and cyclic loading conditions have also been discussed.

Key words: fracture, welds, toughness, dynamic, quasistatic, crack growth, fatigue, creep.

6.1 Introduction: the importance of fracture properties

Welding is an integral part of modern component fabrication technology. It is well recognised that the fracture properties of weldments are inferior to those of the base materials, and therefore decisive in determining the integrity of the components: the majority of service failures in elevated temperature components occur at weld locations. Fracture and crack growth resistance of weld materials has been extensively studied from various perspectives. The present chapter adopts a 'practical' perspective, namely generating fracture property data generally consistent with the requirements of design and fabrication codes for fossil and nuclear power plants. Therefore, the materials referred to are the typical ferritic and austenitic steels joined by the fusion welding processes, as is common in power plant industry. There are several relevant design, fabrication and integrity assessment codes. There are similarities and dissimilarities in their approaches; they are also being continually evolved for improved assessment. Specific philosophies and provisions of these codes are not discussed; the codes cited [1–6] are only with respect to their material property data requirements. Also we make only passing reference to more 'theoretical' studies, for example, basic studies with bimetals, or micro-mechanical or continuum damage mechanics modelling

aimed at quantitative understanding of the interplay of various mechanical and metallurgical factors in determining component life.

In a strict sense, the term fracture toughness refers to the value of the appropriate crack tip characterising parameter at crack initiation. This chapter, however, briefly surveys the material property data requirements relevant for quasi-static and dynamic crack growth under monotonic loading conditions, and also discusses crack growth under fatigue and creep loading, within the limitations indicated above.

6.2 Fracture properties for materials qualification

Code requirements for weld fracture property data stem from two different requirements. The historic first reason is for materials qualification; the objective is basically to ensure the adequacy of the metallurgical microstructure for fracture resistance. Present day sophisticated experimental capabilities make it possible to generate strain rates in the wide range of 10^{-8} to $10^{3}\,s^{-1}$ [7]. Of these, the drop weight [8] and Charpy pendulum impact testing [9], encompassing strain rates of 1 to $10^{3}\,s^{-1}$, are widely used in routine fracture testing.

The Charpy V-notch (CVN) test is a standard procedure for characterising the ductile-to-brittle transition in steels, as has been discussed, e.g. in a book celebrating the hundredth anniversary of the test [10]. This test is also commonly used for welded joints. The notch may be in the base material, in the weld material, or in the heat-affected zone (HAZ). Usually, the specimen is oriented perpendicular to the weld, with the crack propagation direction oriented along the thickness or the width direction of the plate. The specimen may be cut at various depths below the surface of the welded material. A closely linked practice in the nuclear industry is the assessment of neutron irradiation-induced embrittlement by Charpy impact testing. In a ferritic material, irradiation embrittlement is reflected in reduction in the upper shelf energy, sharpening of the transition, and increase in the transition temperature. The main attraction for full-size ($10 \times 10 \times 55\,mm^{3}$) or sub-size Charpy specimens for this application is the small size of the specimen, because of the high premium on irradiation space. Replicate specimen testing is necessary because of the large statistical scatter of Charpy test data in the transition regime, reflecting the statistical nature of fracture in the brittle and quasi-brittle regimes. More recently, small punch tests have been used for characterising irradiation-induced embrittlement and changing ductile–brittle transition behaviour; see, e.g., Kim *et al.* [11].

For steels susceptible to ductile-to-brittle transition, the empirical approach for avoiding catastrophic brittle fracture in service aims at identifying the minimum temperature above which it will definitely fail in a ductile manner under the severest of constraints of stress triaxiality and strain rate. For the

ferritic/martensitic pressure vessel steels, drop-weight testing [8] is used to determine the nil-ductility transition temperature T_{NDT}, and CVN impact testing [9] is carried out to determine T_{CV}, the temperature corresponding to Charpy V energy $C_v \geq 68$ J and lateral expansion LE ≥ 0.89 mm. For materials under its purview, which includes pressure vessel steels in current use, ASME Boiler and Pressure Vessel Code [12,13] defines a 'reference NDT' (non-destructive test), designated RT_{NDT}, which is the higher of T_{NDT} and $T_{CV} - 33$ (all temperatures in K). A minimum temperature of $RT_{NDT} + 33$ K must be maintained during service (e.g., hydro-testing of pressure retaining components) to ensure upper shelf behaviour.

6.2.1 Fracture properties for damage-tolerant design

The data from the Charpy impact tests or drop-weight tests as described above cannot be directly used for assessing load-bearing capacity, or service life of a component with a measured or postulated crack. Fracture mechanics based approaches are required for this purpose. Linear elastic fracture mechanics (LEFM) formalism is appropriate for the case of limited crack tip plasticity, cleavage-induced failure at crack initiation or after a limited amount of crack extension. The appropriate crack tip characterising parameter here is the stress intensity factor K. The elastic plastic fracture mechanics (EPFM) approach can be considered to be a generalisation of the LEFM approach to the case of more extensive crack tip plasticity, with failure preceded by sizeable extent of ductile tearing. In EPFM, the variation of the path independent line integral J (or crack tip opening displacement, CTOD) with crack growth, called the J resistance (or CTOD resistance) curves, also called J–R or CTOD–R curves, defines the entire sequence, from crack initiation (physical crack growth by 0.2 mm), to crack growth, to eventual failure by instability when the 'applied' and material tearing modulus values (i.e, slopes of resistance curves) become equal. The EPFM is the philosophic basis of the assessment of cracked components in the various design codes. The failure assessment diagrams (FADs) described in various codes such as R-6, BS 7910 and API 579 [1,3,6] allow different simplified options (with added conservatism) depending upon the availability of relevant data for the specific material and structure. The fracture property data requirement for the codes depends upon the objective (category) of analysis, and ranges from K for cleavage initiation to J–R curve for extensive ductile tearing.

6.3 Dynamic and quasi-static fracture properties

For cleavage fracture in the brittle and transition regimes for non-austenitic steel with limited crack tip plasticity, the appropriate toughness parameter is the LEFM plane strain fracture toughness, designated K_{Ic} for quasi-static

conditions and K_{Id} for dynamic conditions. Cleavage fracture is initiation controlled. The inhomogeneity of orientation of individual grains, the difference in the properties of the grain boundaries from those of grains, and the random distribution of cleavage crack nucleation sites (carbides and non-metallic inclusions) with respect to the crack front, all lead to statistical variation in toughness in the non-austenitic steels in the lower shelf and transition regime. Theoretical reasoning based on weakest link statistics [14,15], backed by experimental data, suggests that a Weibull distribution with a fixed slope 4 can be applied to fracture with limited crack tip plasticity: the cumulative probability $P(K)$ for failure at or below stress intensity factor K (MPa m$^{0.5}$) is given by:

$$P(K) = 1 - \exp\left[-\left(\frac{B}{B_0}\right) \cdot \left(\frac{K - K_{min}}{K_0 - K_{min}}\right)^4\right] \qquad 6.1$$

where B is plate thickness, B_0 and K_0 are normalising factors, and $P(K) = 0$ for $K \leq K_{min}$. For ferritic steels tested in the transition regime under quasi-static loading conditions, the ASTM E1921 [16] adopts this concept to define a master curve that describes the shape and location of median K transition temperature fracture toughness for a 25 mm thick CT specimen. For ferritic steels for pressure vessels, a value of $K_{min} = 20$ MPa m$^{0.5}$ (for 25 mm thick specimens) is used. The master curve is positioned on the abscissa of K vs. T plot by the material parameter T_0 (the reference temperature).

$$K_0 = 31 + 77 \exp\,[0.019(T - T_0)]$$

T_0 is the transition temperature for a median fracture toughness (50th percentile) of 100 MPa$^{0.5}$ normalised to a 25 mm thick specimen in the master curve. Having established T_0, the material fracture toughness at a given temperature, specimen thickness B and cumulative probability level P_f can be obtained from

$$K_{mat} = 20 + (11 + 77 \exp[0.019\,(T - T_0)])\left(\frac{25}{B}\right)^{0.25} [-\ln(1 - P_f)]^{0.25}$$

The parameters K_0 and T_0 thus characterise the material behaviour in the transition regime. This concept is being increasingly used for characterising nuclear reactor pressure vessel (RPV) steels and their welds. In a weld joint, these properties for weld metal, HAZ and the parent material plate are of interest. Now, every specimen extracted from inhomogeneous materials such as weld metals and HAZ is unlikely to sample local brittle zones (LBZs) that may be present. At the same time, cost and material availability may prevent testing a large number of specimens. Therefore care is required to avoid non-conservative predictions of K_0 from a limited body of data.

Fracture mechanics assessment methods can be adopted for higher loading

rates as long as inertial loading can be ignored. The ASME Boiler and Pressure Vessel Code [12,13] prescribes an empirical universal relation between the lower bound (from static, dynamic, and crack arrest tests) critical stress intensity factor K_{IR} and $(T - RT_{NDT})$, where T is the service temperature, which can be used for the materials covered by this code. In this instance, materials are indexed by the parameter $T - RT_{NDT}$. Instrumented pre-cracked Charpy V (PCCV) testing has proved quite popular in dynamic fracture toughness testing, for the obvious reasons of simplicity and material economy. If the master curve concept developed for quasi-static conditions can be extended to dynamic loading conditions, then the corresponding reference temperature T_0^{dy} determined would be a more precise material index than RT_{NDT} and therefore the master curve would be more material-specific than the ASME K_{IR} curve. Limited attempts in this direction, with dynamic K-data determined from PCCV specimen testing, have yielded encouraging results (see Moitra and coworkers [17,18] and other reports cited therein). More importantly, it has been shown that RT_{NDT}-based ASME K_{IR} is unduly conservative compared with T_0^{dy}-based master curve, and T_0^{dy} is more sensitive to microstructural variations than RT_{NDT}.

Crack tip constraints in the specimens must be (nearly) identical to that in the component before the quasi-static or dynamic J–R or CTOD–R curve generated in the laboratory can be used for component assessment. This can be achieved by ensuring that specimen and component thickness are identical, and have sufficient ligament length.

6.3.1 Subcritical crack growth parameters

For integrity assessment of operating components, in addition to fracture toughness data, other fracture mechanics parameters characterising subcritical crack growth, namely under creep, fatigue and creep–fatigue loading conditions are to be considered. These properties are discussed in this section.

Fatigue crack growth

For fatigue crack growth (FCG) under high cycle conditions, the reversed crack tip plastic zone is small, and the cyclic crack growth rate da/dn is expressed as a function of the (elastic) stress intensity factor range ΔK, or more correctly ΔK_{eff}, the effective stress intensity factor range during which the crack is open. The parameters of interest are the threshold stress intensity factor range ΔK_{th} below which da/dn becomes negligibly small (operationally set as 10^{-10} m/cycle), and the Stage II or Paris regime of crack growth given by the equation $da/dn = C \cdot (\Delta K_{eff})^m$, C and m (Paris) constants. This regime covers da/dn in the range of, say, ~ 10^{-6} mm/cycle to ~10^{-3} mm/cycle. In stage III of FCG, static modes of fracture, namely intergranular fracture,

micro-cleavage, and micro-void coalescence, increasingly come into play. The slope of the plot gradually increases, approaching ∞, corresponding to maximum stress intensity during cyclic K_{max} approaching the critical stress intensity K_c. Both stages I and III are sensitive to microstructure and flow properties. However, while stage I is sensitive to environment, environment has little influence in stage III. Some authors have successfully used the ΔJ concept for characterising FCG when crack tip plasticity is to be taken into account. For example Appendix A16 of the French RCC-MR Code [4] recommends the use of a (elastic-plastic) ΔJ based FCG calculation, using

$$\Delta J = \Delta J_e \left[0.5 \frac{(\Delta\sigma_{ref})^2}{(\Delta\sigma_{ref})^2 + \sigma_0^2} + \frac{\Delta\varepsilon_{ref}}{(\Delta\sigma_{ref}/E)} \right]$$

where σ_{ref} and ε_{ref} are to be evaluated following a procedure laid out in this code. The effective stress intensity factor range is given by

$$\Delta K_{eff} = q\sqrt{E' \cdot \Delta J}$$

with q, the crack closure factor given by

$$q = \frac{1 - R/2}{1 - R} \quad \text{for} \quad R < 0, \quad q = \frac{1}{1 - R} \quad \text{for } R > 0$$

Creep and creep–fatigue crack growth

Creep crack growth (CCG) is significantly influenced by temperature, geometry and microstructure via their influence on the driving force for CCG, viz. the local elastic–plastic stress in the creep damage zone around a crack tip. The size and geometry effects on creep crack growth rate (CCGR) are related to plane stress/plane strain conditions and multi-axiality effects on the local stresses around a crack tip [19–22]. The effect of temperature on CCGR is dominated by local stress-dependent, thermally activated processes. In addition, cracking is found to be affected by microstructural degradation over time, e.g. by coarsening of the precipitates within the grains and on the grain boundaries [23]. Different parameters including K, that implicitly or explicitly incorporate the local elastic-plastic stress around a crack tip and temperature, have been proposed as correlating parameters for CCGR. Steady state CCG rates in creep-ductile materials, exhibiting extensive creep, are correlated with C^* [24]. Other parameters used are load line displacement rate $d\delta/dt$ [19,20] and Q^* which describes a thermally activated process dependent on local stress [21]. In the small-scale creep region, the parameter C_t [25] which allows transition from small-scale creep to extensive creep could also be used. Figure 6.1 schematically shows the crack tip process zone for small-scale creep – the Hui–Reidel creep zone is embedded in the Huchinson–

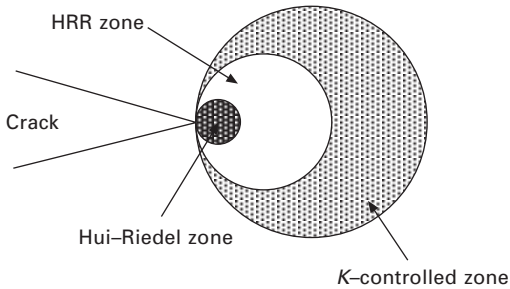

6.1 Stress fields around the crack tip.

Rice–Rosengren (HRR) plastic zone, which in turn is embedded in the elastic zone. The choice of specimens for CCG characterisation depends on many factors such as material availability, relevant crack orientation, component thickness, machine capacity, component geometry and loading, suitability for crack initiation and crack growth testing.

A reference stress-based method is adopted by the design code R5 [2] for conservatively estimating C^* from creep data. ASTM E1457 [26] describes the procedure to experimentally determine C^* for homogeneous materials using compact tension (CT) specimens. Dogan *et al*. [27] describe the procedure and expressions for determining C^* for a variety of standard fracture mechanics specimen geometries or for components using numerical and limit analysis methods. Under widespread, steady state creep conditions, C^* is analogous to J_p for a non-linear elastic material. Hence for a power law creeping material, C^* may be determined from the creep component of load-line displacement (LLD) record during a CCG test using the relation

$$C^* = \frac{P\dot{\Delta}_c}{BW} H\eta \qquad 6.2$$

In Eq. (6.2), the values of H and η for a power-law creeping material with Norton creep exponent n, are the same as those for a power-law plastic material with stress exponent, N, when it is assumed that $n = N$. Equation (6.2) is used in ASTM E1457 [26] to derive C^* for homogeneous materials. In using the same equation for weldments and inhomogeneous alloys it is assumed that instantaneous load-line displacement in each test is a measure of the overall response of the crack tip creep behaviour [28]. Hence, the variability in creep properties will give an average behaviour in displacement rate which directly affects the calculation of C^* in Eq. (6.2).

CCG data are generally correlated using the functional form

$$\dot{a} = A(C^*)^q \qquad 6.3$$

where A and q are constants. The French RCC-MR A16 code [4] incorporates

CCG data for low carbon nitrogen-bearing variant of AISI 316 stainless steel (SS 316LN) and its welds. For applying Eq. (6.3), it is necessary to meet two validity criteria [26]. Firstly, creep LLD rate must be at least half of the total LLD rate, i.e. $\dot{\Delta}_c^{LLD} \geq 0.5\,\dot{\Delta}^{LLD}$ This is meant to ensure that the material is 'creep ductile'. Otherwise, i.e. for creep-brittle situations, K may be used to describe the CCGR data. Secondly, CCGR data obtained prior to a crack extension $\Delta a = 0.2$ mm are assumed to represent a part or the whole of the crack initiation and transient region, during which the damage distribution ahead of the crack tip reaches a steady state. Therefore, these data are excluded from CCGR correlation against C^*. For plane strain and elastic or small-scale yielding conditions, this duration is given by

$$t_T = \max\left[\frac{K^2(1-\nu^2)}{E(n+1)\cdot C^*(t_T)}\right]$$

It has been suggested [29] that if there is significant plasticity on loading then K^2/E may be replaced by J. In design, it is conservative to assume that crack growth occurs on first loading, and ignore *creep crack incubation* time for 0.2 mm crack growth. Actually, the cause of cracking influences the incubation time. For example, a naturally occurring creep defect, such as a Type IV weld defect, may not experience an incubation period before macroscopic crack growth, unless the initial defect has extended across the region of extensive creep damage leading to its formation and thus has its tip in essentially undamaged material. t_i may be expressed in terms of K, and/or C_t or local CTOD, or for widespread creep conditions, by a relationship of the form $t_i(C^*)^\alpha = \gamma$, where α and γ are material constants [2]. While for creep ductile materials C^* is used for correlating CCG data, for creep-brittle conditions, K can be used.

CFCG rate is usually obtained as sum of the CCG and FCG components, determined from CCG and FCG data. For CFCG with dominant fatigue component, incubation period may be neglected. Alternatively, a creep–fatigue incubation time (or cycles) may be calculated using the failure assessment diagram [30] or the σ_d approach [31]. Experimental CFCG tests are usually carried out using cyclic loading with/without hold time at peak loads.

6.4 Metallurgical inhomogeneities

The weldment from a typical multiple-bead fusion welding process using a filler material represents variations of chemistry and microstructure from the fusion line to the base metal, and also through the thickness. Depending upon the thermal gradient, growth rate, solute concentration and partition coefficient, the morphology of the weld metal can be equi-axed dendrite, columnar dendrite, cellular dendrite, cellular or planar. Also, micro-segregation

of solutes at the dendrite/cell boundaries can be very severe because of high solidification rates during welding; this micro-segregation can considerably weaken the boundaries. Austenitic stainless steel welds usually contain a small amount of δ ferrite; δ ferrite, with higher solubility for these elements, prevents hot cracking during welding because of such segregation. However during extended service at elevated temperatures, δ ferrite transforms to the brittle σ phase, impairing creep and fracture properties. In a multi-pass weld metal of typical Cr–Mo ferritic/martensitic steels, the deposited weld beads undergo repeated tempering cycles; the HAZ in the base metal shows a gradient of microstructure that can be considered to comprise three bands from weld metal to base metal: coarse-grained HAZ, fine-grained HAZ, and inter-critical HAZ, each with different plastic flow, creep and fracture resistance properties.

6.5 Strength mismatch and residual stress

6.5.1 Strength mismatch

For a weldment, in general the crack tip plastic (or creep) zone has a heterogeneous microstructure, with variations in the yield and work hardening properties, creep rates, and the cleavage crack or micro-void nucleation site densities. Therefore, cracking resistance should depend strongly upon the location of the crack tip and the size of the crack tip plastic (or creep) zone, and the crack growth path should depend additionally upon variation in cracking resistance of the material in the proximity of crack tip. Weldments are conventionally designed primarily based on the strength mismatch factor M, the ratio of the yield stresses of the weld and the base metal, with $M > 1$ referring to material strength over-matching, $M < 1$ to under-matching and $M = 1$ corresponding to an even matching. Many researchers have investigated the effect of strength mismatch on the fracture toughness behaviour of weldments under bending and tension loading in quasi-static conditions; see Peñuelas *et al*. [32] for a brief review, and citations to the relevant literature. This two-material idealisation can be rationalised for an ‘ideal’ weld, with a crack contained within the weld material and running along the material’s centreline, parallel to the weld–base material interface, and where the effect of the HAZ is negligible. Using the finite element method and the slip-line field theory, it has been shown that constraint is not only a function of geometry, but also of material mismatching. It has been shown that even in absence of geometrical constraint, relative to those obtained in homogeneous weld material, the crack tip stress fields are lowered for over-matched welds, and raised for under-matched welds. The severity of this effect increases with increasing degree of mismatching and decreasing thickness of weld metal.

Different methodologies, based on that utilised for the quantification of geometrical constraint, have been developed for quantifying constraint due to material mismatching. It has been shown that fracture toughness for this kind of idealised over-matched welds is, in general, higher than that for under-matched specimens. Peñuelas *et al*. [32] applied a micro-mechanical model of damage growth to mismatched weld joints, and proposed a total constraint factor for ductile fracture. Experimental results were generally consistent with the model predictions. Micro-mechanical modelling of Charpy specimens with under-matched and over-matched weld joints in various orientations (see Tvergaard and Needleman [33] and references cited therein) has shown that the work of fracture in dynamic loading is strongly sensitive to the location of the notch relative to the weld, with the most brittle behaviour for a notch close to the narrow HAZ. For specimens with longitudinal axis rotated with respect to the plate axis such that the notch crosses a thin layer of HAZ, it strongly depends upon whether the location where the notch crosses the HAZ is near the centre of the specimen or near the free specimen edge. In the R5 code reference stress method for estimating C^*, the approach for defects lying within a single material region of a weldment is similar to that for a homogeneous material, but the reference stress for estimating C^* may be modified to account for stress redistribution between different microstructural zones, depending on the form of loading.

The elastic and elastic-plastic crack-tip fields for cracks lying in the interface between two dissimilar elastic or power-law plastic materials have been summarised by Shih [34] and Shih *et al*. [35] for large-scale yielding. Near the crack tip, the fields approximately scale by J but depend on a phase parameter related to the ratio of shear to opening stress on the crack line ahead of the tip. The crack tip field is no longer symmetric in the case of dissimilar materials and resembles the mixed mode field in a homogeneous material. The analogy between power-law plasticity and power law creep then enables estimates of crack-tip fields derived for widespread plasticity to be generalised to widespread creep situations. C^* remains well defined and creep crack growth can be correlated with C^*. It is expected that comparable values of the phase parameter occur between test specimen geometries and typical plant components. Hence, the specimen crack growth data can be simply transferred to component assessments. Numerically, the bi-material C^* integral can be evaluated by contour integration about the crack tip using methods similar to those for homogeneous materials.

The path independence of C^* (or J) follows from, for example, Smelser and Gurtin [36] provided the crack lies in the straight interface. Numerical solutions for J in power-law elastic-plastic bi-materials (with the same values of n) are given in O'Dowd *et al*. [37] for single edge notch tension (SENT) specimens and in O'Dowd and Budden [38] for externally circumferentially cracked cylinders under pressure, end load, and combined pressure and end

load. It was seen that for the SENT specimen, J was lower for the bi-material than for the corresponding homogeneous specimen consisting of the material with the larger plastic strain at a given stress level. This also held for the cracked cylinder, except perhaps for extremely short cracks where the free-surface interface singularity for the uncracked body interacts with the crack tip stress field. For the pressure and combined end load and pressure cases, the crack tip was found to be closed for some cases of high degrees of material mismatch, which would not be expected to lead to crack growth. Ainsworth [39] described a procedure for load-controlled situations in dissimilar metal weld (DMW), where C^* is estimated using reference stress method based on the creep properties of the faster-creeping, ferritic material. For application to real weldments, it is conservative to take this reference ferritic material to be the ferritic HAZ, as this tends to give a higher strain rate than the base ferritic steel. Validation of this approach for a test on a DMW tube specimen under global bend load is given in Curbishley and Hooton [40]. However, for highly constrained bend specimens, such as the CT specimen, deformation is not significantly affected by the thin HAZ and base ferritic material properties may also lead to conservative estimates of C^*. Crack growth data are derived from tests on welded specimens with the crack on the appropriate material interface using standard test procedures.

For crack assessment in welded structures using FADs in the codes, ideally representative tensile properties and fracture toughness of the weld metal and HAZ should be determined individually. However, evaluating HAZ properties is notably difficult because of its complex microstructural gradients; in addition, the HAZ is so narrow that standard specimens for mechanical property measurements cannot be produced. For these reasons, weld metal properties instead of HAZ properties may be recommended when flaws exist in the HAZ [1,3,6,41]. For example, the use of weld metal data for flaws in regions of twice the weld metal width is recommended [42]. However, the HAZ often has far different mechanical properties from weld metal because of such unfavourable microstructures as coarse-grained zones arising from welding process (for examples, see Ju *et al*. [43] and Jang *et al*. [44]). With API X65 line pipe steel welds, Lee *et al*. [45] showed that when flaws are found in the HAZ, for realistic assessment the properties of the HAZ itself and not those of weld metal must be used to construct the FAD.

6.5.2 Residual stresses

Welding introduces residual stresses in the fabricated components. Stress-relieving treatments are suggested for many critical components; in many situations, the components are pressed into service without any heat treatment. The presence of residual stresses can significantly influence the fracture behaviour of welded structures. For example, the J-integral in its original

form computed for welds with residual stresses will no longer be path-independent. Therefore, in principle, fracture mechanics parameters should be appropriately modified in order to take these effects into account [46]. The basic approach of the codes is to consider K from primary and secondary stresses, though they differ with respect to the details of how these two contributions are combined. Consider for example the treatment of primary and secondary stresses in the reference stress method in the R5 code [47]. Essentially, under combined loading, it is necessary to modify the reference stress to allow for the increased stress levels due to secondary thermal or residual stresses. This is achieved by setting

$$\sigma_{ref} = \sigma^{p}_{ref} (1 + K^{s}/K^{p}) \qquad 6.4$$

where the superscripts p and s pertain to primary and secondary stresses respectively. Under residual stress dominant conditions, stress intensity factor solutions have been used to characterise quasi-static crack growth behaviour in multi-pass girth welds [48,49] where detailed residual stress states were determined by finite element techniques [50–53].

Computations show that any presence of weld metal strength mismatch tends to introduce additional complexity in residual stresses. Basically, in absence of residual stresses, the weld strength mismatch effect may become noticeable only at high enough load levels. Dong and Zhang [54] discussed some of the general residual stress characteristics associated with mismatched welds in 5.1 mm thick Al–Li alloy panels, using two typical weld configurations, (i) a butt-welded plate with under-matched weld metal and (ii) a multi-pass girth weld with detailed residual stress results for under-matched, even matched and over-matched conditions. If residual stresses are not considered, weld strength mismatch effects become noticeable only at load levels high enough to cause the plastic zone at the crack tip to interact with base material [55–58]. Once welding-induced residual stresses are considered, weld metal strength mismatch can affect the fracture behaviour of welded structures for the entire loading spectrum. In the case of possible brittle fracture, at low load levels, these residual stresses could act as a sole driving force for crack growth, e.g. for some of the stress corrosion cracking cases [59]. Obviously, the weld residual stresses are strongly dependent on the weld metal mismatch conditions. At the upper end of the loading spectrum, it is typically assumed that the effects of the weld residual stresses should be insignificant. However, the presence of high residual stresses at an early loading stage could significantly alter the plastic zone development at a crack tip or even set off a different cross-section yielding mechanism at a later stage of the loading, as illustrated by Ainsworth [47] on repair welded wide panel specimens. Therefore, the combined effects of the strength mismatch and residual stresses on the fracture behaviour should be of critical importance in fracture mechanics analysis of welded structures.

Ravi *et al*. [60] studied the fatigue crack growth behaviour of undermatched, equal matched and over-matched weld joints in HSLA-80 steel and attributed the enhanced FCG properties of the over-matched joints to the superior mechanical properties (higher yield strength and toughness), ideal microstructure (more amount of acicular ferrite) and beneficial residual stress field (compressive residual stress) of the weld region. Saxena [61] also has observed that the creep–fatigue crack growth rates in undermatched welds were higher than the crack growth rates in the overmatched weld samples.

6.6 Characterisation of fracture properties: dynamic fracture properties

As mentioned in the introduction, there is a huge pool of literature on fracture and cracking resistance of weld materials. In this section, only a few examples are cited as illustrations.

CVN (and Charpy U notch (CUN) for austenitic steel materials) and drop-weight testing are used primarily for material qualification and temperature-based approach for avoiding brittle fracture. Instrumented impact testing PCCV specimens are being increasingly used for determining K_{Id} for cleavage/quasi-cleavage fracture, dynamic *J–R* curves for more extensive crack tip plasticity. Data analysis, and the subsequent verification as to whether the toughness determined is size-independent, follows the standard method for quasi-static fracture mechanics testing with three point bend specimens. Of course dynamic yield stress σ_{yd} must be used in data analysis. With increasing strain rates, inertial effects and adiabatic heating effects become increasingly important. For crack initiation within about three times the time period of inertial oscillations, (i.e. for brittle fracture), the fracture load is conservatively estimated from the load–time plot using reasonable empirical procedures. Beyond this regime, i.e. for more extensive crack-tip plasticity, the inertial effects become less important. Yet, graphical or numerical smoothing of load-time data is necessary. Adiabatic heating of the specimens during dynamic testing, which is ignored in data analysis, can give rise to apparently anomalous variations in the determined properties with temperature. Since CVN testing is much more common, simple and also considerably less susceptible to the problem of initial inertial oscillations, there is an abiding interest in developing reasonable estimates of fracture toughness and related properties using CVN test data. This aspect, including dynamic tear and tension impact testing, is being systematically studied in the authors' laboratory. Sreenivasan and Mannan [62] have summarised the available methods, and provided a comprehensive compendium of the relevant equations, and the relevant references.

In the authors' laboratory, routine determination of RT_{NDT} has provided crucial inputs during development of welding consumable for the modified 9Cr–1Mo (P91) steel. It was noted that synthetic electrodes, with major

alloying adjustments (beyond the levels permitted by American Welding Society specifications) in the weld metal through flux coating of the electrode, resulted in inordinately high RT_{NDT} (> 405 K); therefore, synthetic electrodes have not been allowed in the current specifications for electrodes for the P91 grade steel. For 9Cr–1Mo weld pads prepared with prescribed electrodes and post-weld heat treatment, RT_{NDT} varied over the range 273–302 K depending on the welding positions (1G, 2G and 3G), deposition technique (stringer bead, weave bead) and welding parameters, all of which influence the heat input; high heat input resulted in high RT_{NDT} [63]. Many similar applications, e.g. for optimising welding consumable, process or PWHT using CVN testing have been reported in the literature: CVN testing often proves to be the workhorse in such applications.

Sreenivasan *et al*. [64] demonstrated that instrumented drop weight tests can be used to determine K_{Id} at or below T_{NDT}. This is based upon two observations:

1. In a drop-weight test, the crack presented to the base metal is the boundary of the HAZ. This can be characterised as a semi-elliptic crack, and the crack profile can be measured on photographs of the fracture surfaces of broken specimens.
2. For tests at and below T_{NDT}, the corresponding brittle fracture load P_F can be identified as the point where load sharply drops to zero.

An application of this method for 9Cr–1Mo base and weld materials [64] is illustrated in Fig. 6.2. This figure shows the variation of different K_{Id} estimates from drop weight and impact tests for a 9Cr–1Mo weld and AISI 403 martensitic stainless steels. The corresponding ASME K_{IR} curves calculated using RT_{NDT} determined for these steels are also shown. The general agreement between K_{Id} from drop weight and PCCV impact tests may be noted.

Moitra *et al*. [65] reported an interesting extension of this concept for a 9Cr–1Mo base metal. For this material, in the drop weight tested specimen the three microstructural regions in HAZ (starting from the weld metal), viz. (i) coarse-grained, (ii) fine-grained and (iii) intercritical region, represent a steep positive toughness gradient (qualitatively corroborated by scanning electron microscopy (SEM) fractography). This resulted in three distinct peaks in the drop weight load–time traces, corresponding to initiation of brittle fracture in each of these three microstuctural regions. It thus became possible to determine K_{Id} values for the individual microstructural regions at or below nil ductility transition temperature (NDTT), Fig. 6.3. This result clearly illustrates the toughness gradient expected in ferritic steel HAZ.

Two important characteristics of cleavage fracture can be determined from instrumented impact testing of CVN specimens (see Sreenivasan *et al*. [66] for a review and also a compendium of relevant equations). The first is the brittleness transition temperature T_D: at T_D, the general yield load P_{GY}

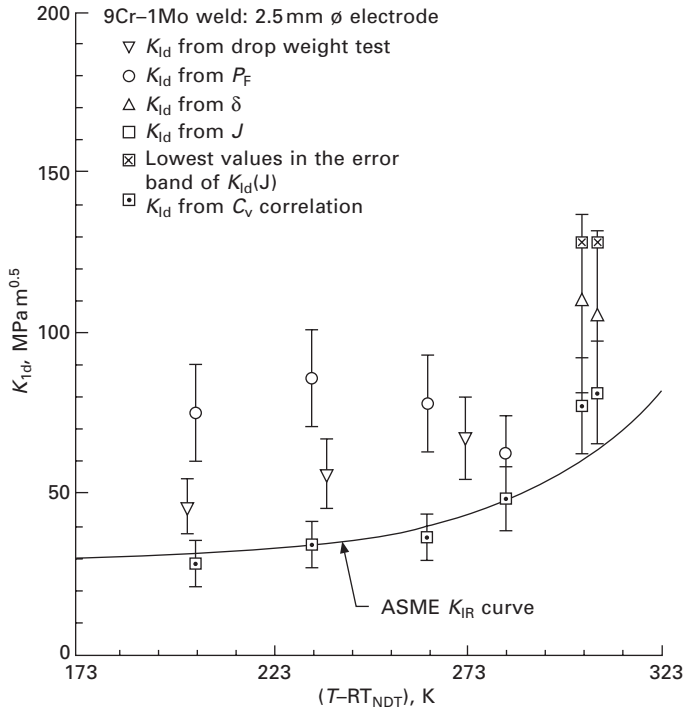

6.2 K_{Id} from 9Cr–1Mo weld and ASME K_{IR} curve.

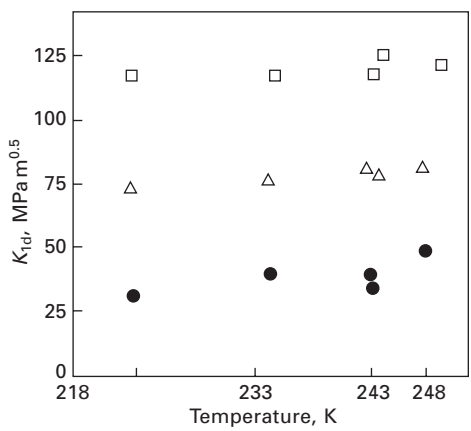

6.3 K_{Id} vs temperature for 9Cr–1Mo HAZ microstructural regions (□ intercritical, △ coarse grain, ● fine grain).

equals fracture load P_F. Dynamic yield stress σ_{yd} can be computed from the measured P_{GY} for temperatures $T \geq T_D$ using the expression $\sigma_{yd} = P_{GY}L/[kB(W - a)^2]$; the dimensionless constant k assumes the values 1.47 for standard CVN specimen, 1.18 for half-thick (= 5 mm) CVN specimen, 1.96

for standard (full-thickness = 10 mm) CUN specimen, and 1.40 for half-thick CUN specimen [66]. For $T < T_D$, σ_{yd} has to be estimated by back extrapolation. At T_D the local cleavage fracture stress can be estimated as $\sigma_f^* = C_F \sigma_{yd}$, with $C_F \approx 2.40$ to 2.57 for 10 mm thick CVN specimens. T_D and σ_f^* have been determined for a 9Cr–1Mo steel base metal, and also weld metal deposited with electrodes of different diameters [67]. σ_f^* values for the weld metals (2112–2160 MPa) were rather insensitive to electrode diameter, but lower than that for the base material (~ 2300 MPa). The poorer cleavage fracture resistance of the weld metal was more drastically reflected in the substantially higher T_D values (in the range 253–160 K) compared with 168 K for the base metal. T_D proved to be more sensitive to microstructure than RT_{NDT} (248 K for the base and 264–269 K for the welds).

For dynamic testing of PCCV specimens to fracture with more extensive crack tip plasticity, load line displacements for the various load values are computed from the corresponding time values using the hammer velocity corrected for the loss in hammer energy. Also, crack initiation point and growth must necessarily be estimated, as on-line crack length measurement is not possible, and the normalisation method, see Appendix A 15 of ASTM E1820 [68], cannot be adopted. For both quasi-static and dynamic conditions, the most direct method for determining initiation J is to measure stretch zone height (SZH) on fracture surfaces using SEM, which can then be used to determine the area under the load displacement curve up to crack initiation. An accurate method was developed for the measurement of SZH [69] without any *a priori* assumption as to the magnitude of the crack tip blunting angle θ. This method is too involved for routine adoption. Secant compliance-based essentially empirical methods [70] are usually adopted for identifying the crack initiation point from the graphically/numerically smoothened load-displacement data. Once J_{Id} for crack initiation is computed, K_{Id} can be computed from $J_{Id} E' = K_{Id}^2$ where E is Young's modulus, where ν is Poisson's ratio, where $E' = E$ for plane stress and $E' = E/(1 - \nu)^2$ for plane strain conditions. (Often however $E' = E$ is used irrespective of constraint, ignoring a possible error of maximum ~ 5%.)

Three methods have been proposed in the literature for $J - R$ curve estimation from such tests. The first of these proposed by Ray *et al.* [71] assumes $J = C\,(\Delta a)^n$ up to complete fracture (C and n constants); then it can be shown that

$$E/B(W - a_0) = [C/(1 + n)]\,(W - a_0)^n$$

where E is the energy absorbed to fracture. Thus C and n can be determined from double logarithmic plots of $E/B(W - a_0)$ against $(W - a_0)$ using fracture energy for four or five PCCV specimens with different initial $a_0/W \geq 0.5$. This method does not require the crack initiation point to be identified by the compliance method, but may prove unduly conservative for higher crack

growths. Sreenivasan and Mannan [72] assumed a power law key curve method, and determined the two constants in the power law function from the load displacement data between general yield and crack initiation identified by a compliance method. By this single specimen method, conservative *J–R* curves are obtained for AISI 308 SS weld at room temperature. More recently for ferritic steels, Schindler and co-workers (see [73], and references cited therein) attempted to predict the entire *J–R* curve from test data from a single PCCV specimen. This method essentially assumes a power law form for *J–R* curve for initial crack growth up to ~ one-tenth the initial ligament size, and a constant crack tip opening angle criterion thereafter, with a smooth transition between these two ranges. The total *J* is obtained as the sum of elastic and plastic components as for quasi-static testing; however their formulation allows use of specimens with relatively shallow cracks. The last two specimens are single specimen methods. Viability of each of these estimation methods depends upon the applicability of the underlying assumption for the specific material under consideration [74].

There are several reports in the literature using PCCV testing for characterising dynamic fracture with limited or more extensive crack tip plasticity. Only a few interesting examples are cited here, as illustrations of the range of application of instrumented impact testing of PCCV specimens for characterising weld materials. Recently Moitra *et al*. [75] characterised the dynamic fracture properties of modified 9Cr–1Mo welds in different welding positions by extending the master curve concept to dynamic conditions, and determining a dynamic reference temperature (T_0^{dy}). The fracture toughness data were generated at a reduced hammer velocity of ~ 1.12 m/s rather than the full capacity of 5.12 m/s; this significantly reduces the inertial oscillations, but only marginally affects the stress intensity factor rate. T_0^{dy} was computed from the test data following the procedure laid down by ASTM E 1921-05 for quasi-static conditions, and then corrected using an empirical procedure due to Schindler *et al*. [76] to determine T_0^{dy} for 5.12 m/s.

At a loading rate of ~ 5.12 m/s, the T_0^{dy} for the 1G position and 4G position welds have been evaluated to be 38 and 50.4 °C respectively. The SEM study of the 'process zone', that is, the fracture surfaces close to the fatigue crack front reveals that the lath boundary fracture is the predominating mechanism for brittle crack initiation in both the welds. A qualitative assessment of the concentration of probable crack initiation sites in the process zone, Fig. 6.4, indicates that the 4G weld is more vulnerable to the brittle failure than the 1G weld, consistent with its higher T_0^{dy} value. The effect of Weibull slope on the computed T_0^{dy} has also been assessed, Fig. 6.5, and it was shown that in this instance, the 'fixed slope of 4' concept yields slightly less conservative T_0^{dy} values compared to those obtained using the experimentally determined slope of 3.2. For these welds, the RT_{NDT} based ASME-K_{IR} curves

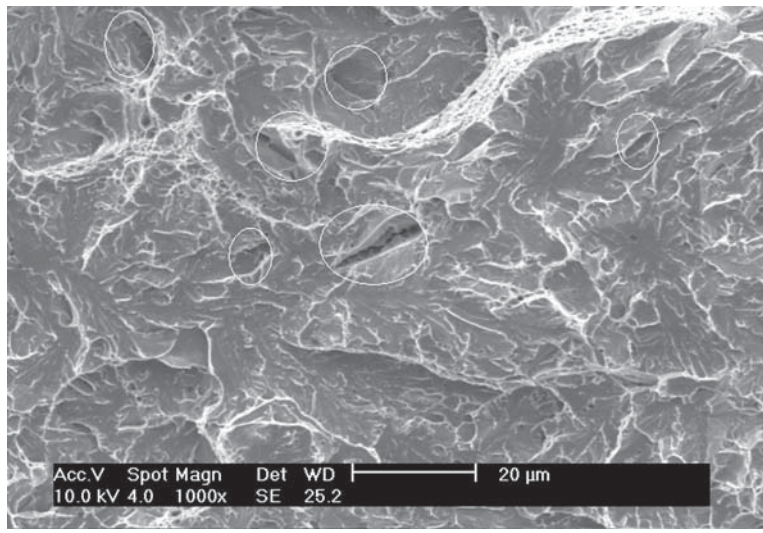

(a)

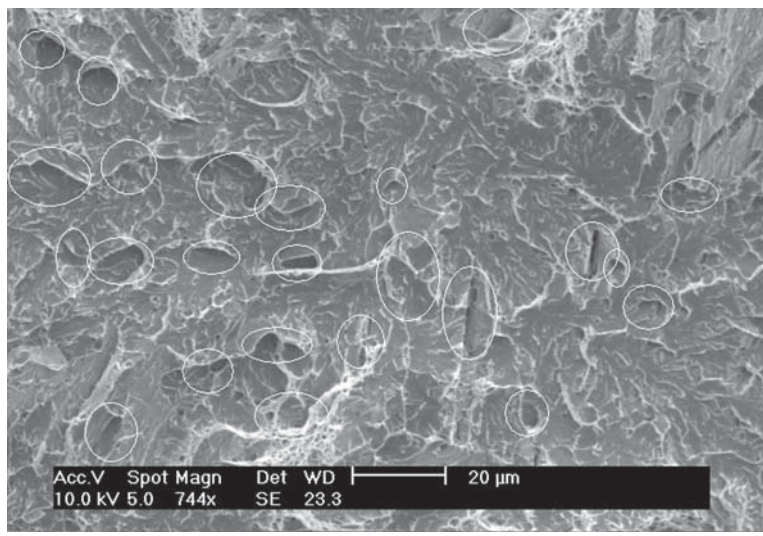

(b)

6.4 SEM of the process zone for (a) 1G and (b) 4G position weld (marked regions indicate lath boundary fracture).

have been proved to be ultraconservative as compared with the realistic dynamic fracture toughness variation described by the master curve indexed with T_0^{dy}.

Angamuthu *et al*. [77] studied the effect of weld strength mismatch on dynamic fracture toughness of a quenched and tempered steel (25 mm thick)

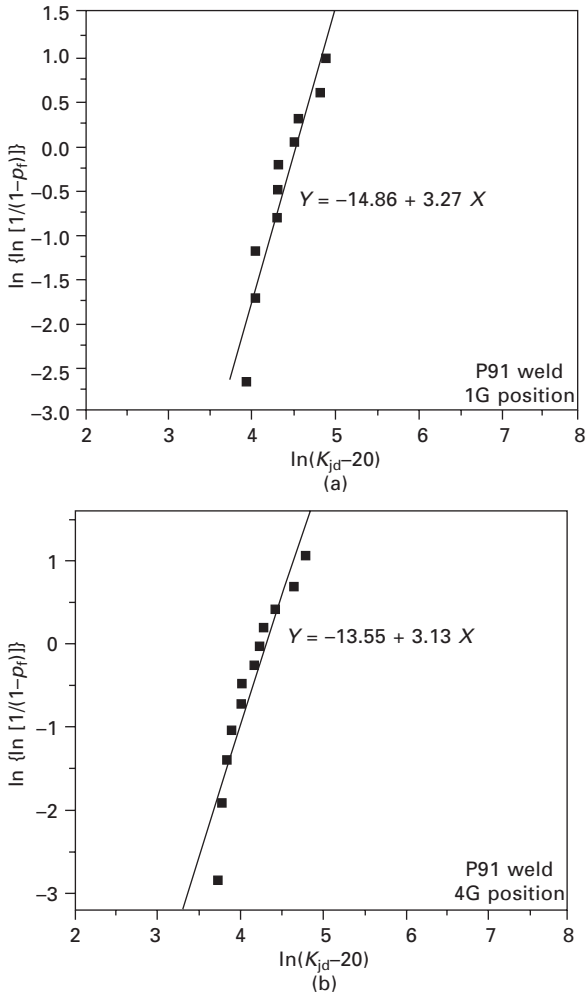

6.5 Weibull plot from modified 9Cr–1Mo weld (at 1.12 m/s): (a) 1G and (b) 4G positions.

using instrumented impact testing of PCCV specimens. Shielded metal arc welding (SMAW) with three different low-hydrogen welding electrodes was used to produce under-matched (M = 0.87), even matched (M = 0.98) and over-matched (M = 1.05) double bevel joints (K-joints). The V-notch in the HAZ specimen was cut in the coarse-grained region. Instrumented impact tests, at an initial hammer velocity of 4.85 m/s were carried out with PCCV base metal, weld metal and HAZ specimens fatigue pre-cracked with initial crack depth (a_0/W) ratio between 0.40 and 0.70, at different temperatures. The specimens tested covered both ductile fracture with dimple rupture, and brittle quasi-cleavage fracture. For ductile fracture, the secant compliance

change method was used to detect crack initiation, and a single-specimen power-law key-curve method (cf. Sreenivasan and Mannan [62]) was adopted to generate the ambient temperature J–R curves for Δa up to 2.5 mm. Because of relatively high scatter, five specimens were tested for each configuration and condition, and the most conservative results were chosen for comparison. SEM fractography was used to identify the fracture morphology and crack path. The under-matched HAZ showed the highest upper shelf J_{Id} values, followed by base metal; other HAZ and weld metals had lower J_{Id} values. J_{Id} values for the different materials were similar in the lower shelf region. For the ductile fracture in the under-matched HAZ specimen, the crack which was initially located in the coarse-grained HAZ, entered into the weld metal which had J_{Id} lower than those of both HAZ and base materials. In the even matched HAZ specimen, the crack ran entirely through the HAZ region which is flanked by base and weld metals of higher J_{Id} values. In some over-matched HAZ specimens, the crack in the HAZ region grew into the weld metal, while in some others it propagated entirely in the HAZ. In the case of weld metal specimens, the ductile crack propagation took place in the weld metal; however, in over-matched weld metal specimen after the ductile crack initiation the specimen failed by cleavage fracture. Because of these complexities, the values of J_d computed for 1 mm crack growth at ambient temperature were similar for the different specimens, with the exception of over-matched HAZ and weld metals for which the values were lower.

This example illustrates the complexities in elastic-plastic fracture toughness testing of weld materials for the dynamic loading condition. It is obvious that, in general, the computed J for initiation and particularly after crack growth is only an operational parameter, and its transferability from specimen to component must be independently assessed. The problem should be less severe with LEFM characterisation of crack tip restricted to crack initiation or a very small extent of crack growth, because of the considerably smaller plastic zone size. It must also be realised that the severity of this problem is material dependent. EPFM formalism can be adopted for integrity assessment of austenitic steel weld materials with more confidence (as is adopted in RCC-MR A16), because the variation of microstructure from weld material to parent material is considerably smaller.

6.6.1 Irradiation effects

Exposure of the structural materials to neutron irradiation is known to induce embrittlement arising from a variety of mechanisms, which can be classified in two categories, namely those which give rise to hardening of the matrix and those which are non-hardening, e.g. grain boundary embrittlement due to helium produced by (n, α) reactions (see, e.g., Odette *et al*. [78] and other references cited therein). The mechanism and extent of embrittlement is a

function of irradiation conditions, e.g. temperature, fluence. The increase in ductile-brittle transition temperature (DBTT) due to irradiation is a major problem in using ferritic steels in nuclear-irradiation environment. Fracture mechanics concepts can be used to establish an upper limit for brittle crack initiation and also maximum fluence of advanced reactors to avoid catastrophic failure for components being pressed into service and after neutron irradiation in-service.

As indicated earlier, CVN and PCCV testing are widely used in assessment of nuclear irradiation-induced embrittlement in steels. For example, Ray *et al*. [79] reported results from a campaign for an ASTM A 203D (3.5% Ni) steel and its weld using half-thickness CVN specimens. For the all-weld test specimens irradiated to a fast ($E > 1$ MeV) neutron fluence of 5.5×10^{18} neutrons cm^{-2}, $T_D = 232$ K and $\sigma_f^* = 1446$ MPa. These data may be compared with those for the base material irradiated to fast fluence of 3.5×10^{19} neutrons cm^{-2} ($T_D = 416$ K, $\sigma_f^* = 1360$ MPa), and annealed (15 days, 573 K) after irradiation to a fast fluence of 9×10^{19} neutrons cm^{-2} (T_D to 204.5 K, $\sigma_f^* = 1205$ MPa). The values for σ_f^* determined for the three conditions are in general agreement with the range of 1350–1450 MPa expected for this/similar steels in the un-irradiated condition. Irradiation-induced embrittlement in the base material, attributed primarily to the sharp increase in yield stress and also possibly a decrease in σ_f^*, is mitigated by post-irradiation annealing, resulting in decrease in T_D.

A material-specific fracture toughness curve based on fracture tests, rather than the ASME K_{IR} method based on RT_{NDT} from impact test data should be preferable for characterising the irradiation embrittlement. The master curve approach to characterising the transition behaviour based on the material fracture toughness data is being increasingly adopted. With data from a small number of pre-cracked Charpy specimens tested at several different fluence levels, the material specific reference temperatures can be shown as a function of fluence (see Yoon [80] for a specific case of welds, and other references cited therein). Extending this methodology to dynamic conditions and developing empirical correlations will prove useful in assessing the irradiation effects with minimum exposure to testing personnel.

6.7 Quasi-static fracture toughness

As indicated above, the master curve approach is being increasingly adopted to characterise non-austenitic grades in the transition regime. The experimental objective here is to determine K_0 and T_0. When a sufficiently large pool of valid (failure with limited crack tip plasticity) K data is available, K_0 can be determined, and indeed the viability of the Weibull distribution, or the value of the exponent can be directly determined, as illustrated in the preceding section for the case of dynamic fracture. This approach is adopted in BS

7910:1999 with more than 15 results available: a statistical distribution (e.g. log normal or Weibull, whichever fits best) should be fitted to the data and the mean minus one standard deviation should be used for the flaw assessment. The problem arises in determining a value of K_0 for conservative (but not unduly so) flaw assessment when the availability of data is restricted because of cost considerations, or lack of material. The British Standard adopts the minimum of three equivalent (MOTE) concept: when there are between 3 and 5 results, the minimum value is used; between 6 and 10 results, the second lowest; and between 11 and 15 results, the third lowest. These characteristic values represent the 20th percentile of the distribution with 50% confidence (approximately). In order to guard against excessive scatter, the BS procedures require the minimum to be not less than 70% of the average toughness (in terms of K) or the maximum to be no more than 1.4 times the average. If scatter is excessive, further testing is recommended. However, in many cases, this is not practical and the user must base his analyses on the data available.

A maximum likelihood (MML) estimation procedure based on the three parameter Weibull distribution has been incorporated in the SINTAP flaw assessment method [81]. Pisaraski and Wallin [82] described and illustrated the procedure for parent metal, weld metal and HAZ. The procedure uses K data 'censored' to ensure limited crack tip plasticity for fracture and then corrected to a reference specimen thickness of 25 mm using the relation $K_{25} = 20 + (K - 20)(B/25)^{0.25}$ (B is the thickness (mm) of the specimen on which K was determined). These data are used to derive an estimate of K_0 (the 'normal MML estimation') as would be applicable for a homogeneous material. For inhomogeneous materials, two more estimates of K_0 are obtained: (i) a 'lower tail MML estimate' that essentially accounts for the fact that not every specimen is likely to sample local brittle zones; and (ii) a 'minimum value estimate' $K_{0\min}$ derived using the minimum toughness value in the data set. Detailed prescriptions are provided for selecting the K_0 using the three estimates and also when to carry out further tests to examine if $K_{0\min}$ corresponds to an outlier. Finally, a further correction is made to adjust the estimate of K_0 for the sample size.

Once K_0 has been determined, the reference temperature can be determined, and then material fracture toughness for the reference thickness of 25 mm ($K_{\mathrm{mat}(25)}$) for a specific probability level can be determined using relations given earlier. Since weakest link theory is used for deriving K_{mat}, in application it must be adjusted for crack front length l in the component:

$$K_{\mathrm{mat}(l)} = 20 + (K_{\mathrm{mat}(25)} - 20)(25/l)^{0.25}$$

The SINTAP procedure recommends an upper cut-off value of $l = 2t$ when $l > 2t$; t is the thickness of the component being assessed. This approach differs from current codes, which requires fracture toughness data to be

generated with specimens of the same thickness as the component. The fracture toughness data for C–Mn steel parent metal, C–Mn steel weld metal (multipass submerged arc butt welds), and HAZ (X butt welds in thermo mechanically controlled processing (TMCP) steel welded with two different consumables corresponding to over match of ~ 24% and 41%) were generated using full thickness bend specimens (SE(B), $B \times 2B$, $B = 50$ mm, $a_0/W = 0.5$ for parent and weld metal; SE(B), $B \times B$, $B = 48$ mm, $a_0/W = 0.3$ for HAZ material). For the plate material, the crack was in LT (longitudinal transverse) orientation. For the weld metal, crack was along the weld centre line. The HAZ specimens were notched from the original plate surface into HAZ close to the weld fusion boundary. For the HAZ specimens, post-test metallography was conducted to establish the actual microstructures at the fatigue crack tip and at fracture initiation. Two data sets were examined for each HAZ: (i) the one that included all the results, and (ii) the set with data from specimens in which post-test metallography confirmed that the fatigue crack tip was located in, or fracture initiated from, the coarse-grained HAZ, the lowest toughness region of the HAZ. Results from specimens with the fatigue crack tip in weld metal were included, provided that fracture initiation took place in the grain coarsened HAZ no further than 0.5 mm from the crack tip. It turned out that for all the materials examined, K_0 obtained by the lower tail MML estimation step characterised each fracture toughness distribution. This is probably because the data sets were relatively large (the minimum data pool size was for the weld metal with 27 results, of which 21 specimens failed by cleavage) and the distributions were fairly even in the lower tail. With small data sets where scatter is high, the conclusion could be different and $K_{0\min}$ is likely to characterise the distribution.

As a whole, the normal MML procedure provided an overestimate of K_0. This indicates that the Weibull distribution shape parameter of 4 is not optimum. The lower tail MML estimate and $K_{0\min}$ appeared to provide a conservative description of the lower tail to the fracture toughness distribution. For both the HAZ, post-test metallographic censoring yielded lower K_0 values; clearly censoring provided by the MML procedure alone cannot be relied upon to provide a conservative, lower bound estimate of K_0. The authors recommended that the MML procedure should be only applied to HAZ data which have been confirmed by post-test metallography to test the HAZ correctly. Comparison of MOTE and MML procedures led the authors to conclude that the MML procedure reduces (but does not eliminate) the risk of overestimating fracture toughness compared with the MOTE procedure, especially for small data sets, e.g. 12 or less.

Lee *et al*. [83] in their study on the tensile and fracture properties of API X65 pipeline steel, have proposed and verified use of micro-tensile specimens of dimensions $12.5 \times 2 \times 0.5\,\text{mm}^3$ for determining the tensile properties of the HAZ. For determining fracture toughness, since K_{Ic} cannot be evaluated

directly due to the size requirement, CTOD tests were conducted according to ASTM E1290 [84] using single-edge-notched bend (SENB) specimens. While the notch tip for the weld metal specimens was centred in the weld region, for the HAZ specimen, it was near the fusion line. The fatigue pre-crack of HAZ specimens was located at the fusion line to evaluate the fracture toughness of the coarse-grained heat-affected zone (CGHAZ), known to be the weakest region within this HAZ. For use in the FAD, the CTOD data obtained were converted into K_{Ic} data using

$$K_{Ic} = \left(\frac{m\sigma_y \text{CTOD}E}{1 - \nu^2} \right)^{0.5}$$

where σ_y is the yield strength (MPa); CTOD, the critical crack tip opening displacement (m); E, Young's modulus (MPa); and ν, Poisson's ratio. The constant m depends on specimen geometry, crack size and work hardening. These authors used $m = 2$ because of the various equations for the conversion from CTOD to K_{Ic} available, this one being the least conservative for this API X65 grade pipeline steel; $m = 1.5$ is considered appropriate for deeply notched bend specimens made from low work hardening ferritic steels [82] . Formation of texture during thermo-mechanical processing enhancing dislocation slip and formation of plastic zone is found to result in directionality of toughness, a higher CTOD in the circumferential direction (L–S) than in the longitudinal direction (T–S). They showed that crack assessment results can be strongly affected by the representative mechanical properties used in constructing FAD. For a crack within the HAZ, FAD constructed using weld metal property data can be very non-conservative. They recommended using lower bound tensile and fracture properties of HAZ for this purpose.

For crack tip constraints beyond those permissible for the LEFM regime, $J_{0.2}$ (corresponding to 0.2 mm physical crack growth) and J–R curves are the relevant fracture mechanics parameters that characterise the material. The procedure for determining quasi-static $J_{0.2}$ and J–R curves is well established (ASTM E1820 [68]), and is applied for specimens from weld joints. As expected from the results illustrated for dynamic fracture property determination, complications can be expected for ferritic steels because of the graded microstructure of the HAZ. Another problem is that of pop-in crack extension. The ASTM standard prescribes that when it is small according to the criteria provided, it can be ignored in the multi-specimen data analysis method for determining $J_{0.2}$. In the context of applying the single specimen normalisation method (ASTM E1820-Appendix 15) when on-line crack length measurements are not available, the authors developed [85] an analysis scheme for treating data from such tests by considering two limiting cases of pop-in crack extension: (i) when it is small (continuous J_R curve, but for a localised disturbance in the J–R curve corresponding to pop-in) and (ii) when it is very

large (a shift in J_R curve parallel to the Δa axis by the extent of pop-in crack growth). The model to be adopted is chosen by matching single specimen J–R curves thus determined for a number of specimens.

For a 316(N) SS weld metal in severely aged condition (923 K/4000 h), $J_{0.2}$ was determined at 643 K [86] using 10 mm thick CT specimens with 20% side grooves. The multiple specimen method assuming a power-law form yielded $J_{0.2} \sim 250\,\text{kJ m}^{-2}$ (Fig. 6.6) considerably higher than the value ($40\,\text{kJ m}^{-2}$) indicated in the RCC-MR code [4], in Appendix A16. While a part of the difference could arise from specimen thickness effect, improved

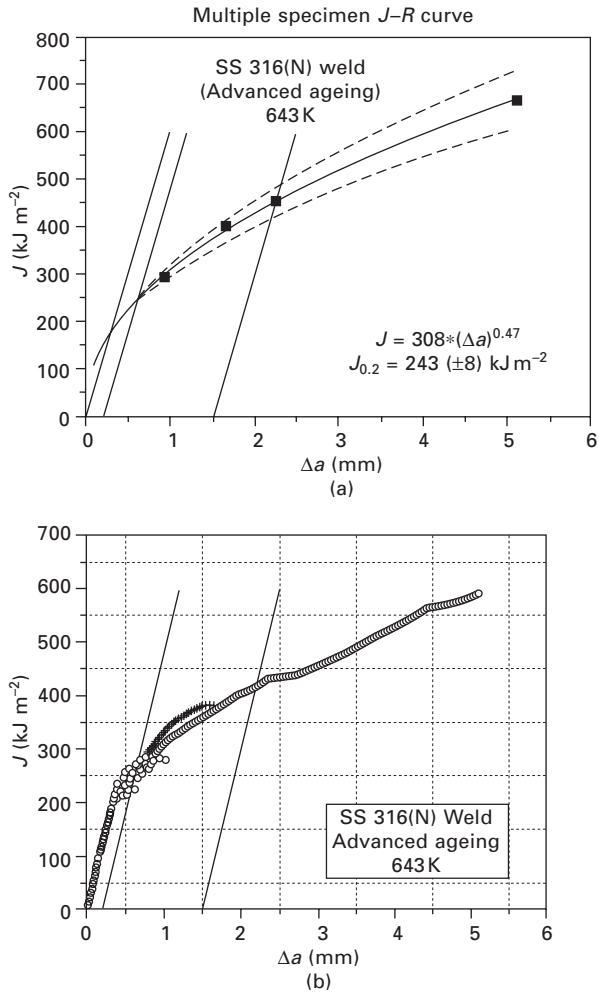

6.6 (a) Multiple specimen J–Δa curve for SS 316(N) weld metal; (b) single specimen J–R curves estimated using normalisation method with 'small pop-in' assumption.

toughness of this weld material was attributed to the high degree of cleanliness of the weld deposit prepared using the chosen consumable.

In experimental studies, the standard methods (e.g. ASTM E1820-01) developed for homogeneous materials are adopted for inhomogeneous materials also, ignoring material inhomogeneity or crack path veering towards regions with lower crack growth resistance. Obviously, as mentioned in the context of dynamic fracture testing, J values thus determined have only operational significance, and their transferability from specimen to component, particularly beyond a small amount of crack growth needs to be independently assessed. This problem may be expected to be serious in non-austenitic grades with strong gradient in microstructure. Saxena [61] reported the results for J–R curve testing at 565 °C of the base metal, weld metal and the weldment region for a nominally 1Cr–1Mo–0.25V (ASTM A356 Grade 9) steam turbine casing material in two different damage conditions labelled D1 and D2, after ~ 30 years in service. D2 material had a larger grain size and a higher level of inclusions, and the fracture appearance transition temperature (FATT) of the D2 condition was 128 °C compared with 88 °C for D1. Repair welds were simulated on these materials using two techniques labelled T1 (using a post-weld heat treatment (PWHT) that produced 10% under-matched welds) and T2 (using a temper bead technique that produced 30% over-matched welds) using filler material of the American Welding Society (AWS) designation A5.1-81. The six resulting material conditions were labelled as follows: (i) D1: damage condition 1; (ii) TC1: D1 welded using T1; (iii) TC2: D1 welded using T2; (iv) D2: damage condition 2; (v) TC4: D2 welded using T1, and (vi) TC5: D2 welded using T2. The scatter in the J–R curves from replicate tests of the base material D1 and D2 increased with increasing crack growth with no systematic dependence on the material condition and J_{Ic} for both D1 and D2 at the test temperature was 104 kJ m^{-2}.

The specimen-to-specimen scatter for the weldment data too was very high, with separate scatterbands for over-matched and under-matched welds (Fig. 6.7), and no reliable estimates for J_{Ic}. The scatter in the fracture toughness depends significantly on the crack path that varied within the fusion zone due to presence of microstructural gradients, and influenced by (i) the type of mismatch (over-match or under-match) and (ii) the location of the end of the fatigue pre-crack relative to the fusion line. Owing to concentration of the strain in the weaker material, mismatch in strength can be quite significant in determining the crack path in welds. Shih, and co-workers [34, 87–89], based on finite element method (FEM) analyses, had predicted that propagation of a ductile crack in a bimaterial with a transitional layer will follow the interface between the weaker material and the transitional layer. However, it was observed that the crack jumped the interface layer and microstructural or microhardness observations could not indicate any reason for the cracks to jump to that region. The FEM analyses of Shih and coworkers cited above

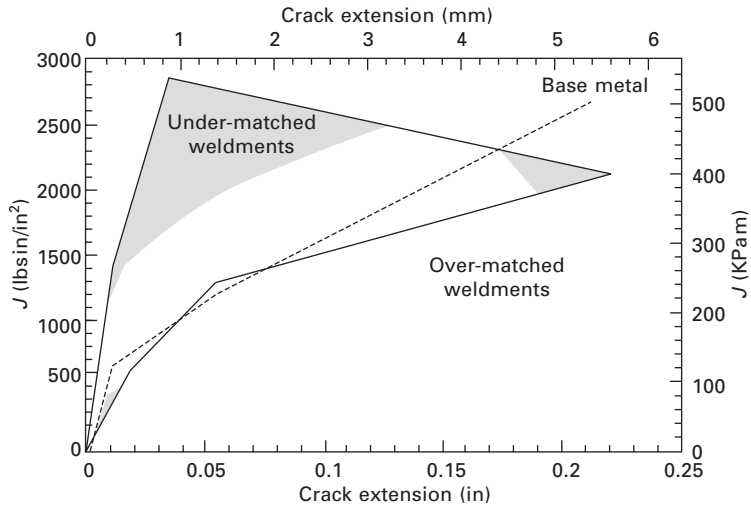

6.7 J–R curves for base metal in damaged condition, and undermatching and overmatching repair welds simulated using different procedures [61]. Reprinted from *Engineering Fracture Mechanics*, 74, 821–838, 2007, Ashok Saxena, 'Role of nonlinear fracture mechanics in assessing fracture and crack growth in welds', Copyright 2007, with permission from Elsevier.

do not account for inhomogeneous fracture properties which could be the case in these weldments. In addition, when the crack turns, mode-mixity begins to play an important role which is also not accounted for in the above analyses. Thus, it appears that a number of other factors contribute to the deviation of the precise crack path from the predicted trend.

Cretegny and Saxena [90] defined a parameter r to enable a comparison of apparent fracture toughness values between weldments with different widths of the HAZs: r = (distance from fusion line to fatigue pre crack)/(distance between fusion line to the end of stable crack). A plot of apparent fracture toughness as a function of r is shown in Fig. 6.8. r values close to 1 correspond to the region of lower fracture toughness, positive r values close to zero represent the zone near the fusion line in the HAZ, and negative r values refer to region in the weld metal. For $|r| >> 1$, the fracture toughness values approach those of the base metal and the weld metal. Saxena [61] showed that the data for all the specimens tested, follows the expected trend as seen in Fig. 6.8, indicating that the lower bound fracture toughness can occur in the base metal at the boundary of the base metal and the HAZ and rationalising the observed fracture behaviour of welds. The most important conclusion from these results is that fracture toughness of welds is not a single value and it depends on a number of factors that have not been accounted for in theoretical analyses. Also, more experiments must be performed with the end of the pre-crack located at different distances from the fusion line to verify this theory.

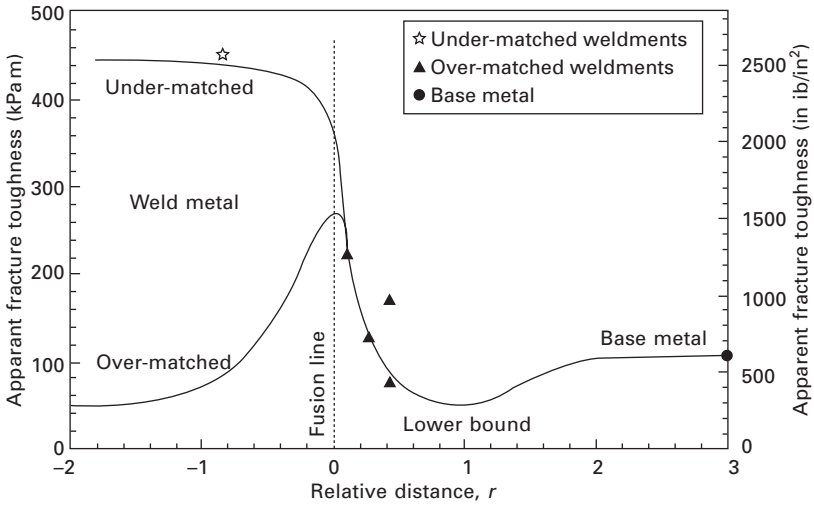

6.8 Variation of apparent fracture toughness with relative distance *r* for under- and over-matched weldments [90]. From *Int J Fracture*, vol. 92, 119–130, 1998, L. Cretegny and A. Saxena, 'Fracture toughness behavior of weldments with mis-matched properties at elevated temperature', with kind permission from Springer Science and Business Media.

6.8 Subcritical crack growth characterisation of welds

Subcritical crack growth at stress intensity factor values well below K_{Ic} levels, can take place under fatigue loading (FCG) or sustained loading (CCG) in benign environments, or in hostile environments by the mechanism of corrosion fatigue or stress corrosion cracking (SCC). Analysis of subcritical crack growth assumes importance in assessing service lives of components with flaws which are smaller than the critical size.

6.8.1 FCG

Under dominantly linear elastic conditions, the inhomogeneous microstructure of the weld region and the resulting gradients in inelastic properties such as resistance to plastic deformation and creep are of little consequence because the elastic properties are largely uniform and also isotropic. Thus, the stress intensity parameter approach for representing fracture and crack growth is directly applicable to the assessment of welds even if the crack meanders from one region of the weld to another within certain limits. Results from continuous cycling fatigue crack growth tests on specimens from D1, D2, TC1, TC2, and TC5 conditions at a cyclic frequency of 1 Hz plotted in Fig. 6.9 show that the FCG data for all the conditions can be described by a single

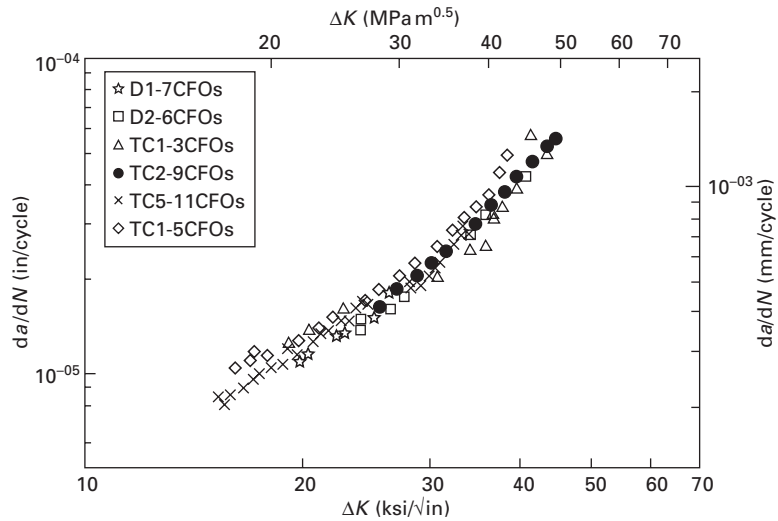

6.9 FCG behaviour of base metal and different weld metals of 1Cr–1Mo–0.25V steel [61]. Reprinted from *Engineering Fracture Mechanics*, 74, 821–838, 2007, Ashok Saxena, 'Role of nonlinear fracture mechanics in assessing fracture and crack growth in welds', Copyright 2007, with permission from Elsevier.

fit, $da/dN = 1.69 \times 10^{-6}\ (\Delta K)^{1.68}$, justifying the use of ΔK to characterise crack growth rate under dominantly linear elastic condition [91].

Ravi *et al*. [60] studied the FCG behaviour of under-matched, equal matched and over-matched weld joints of HSLA-80 steel and attributed the enhanced FCG properties of the over-matched joints to the superior mechanical properties (higher strength delaying crack initiation and toughness increasing the resistance to crack propagation), ideal microstructure (more amount of intragranular acicular ferrite offering additional barriers to cleavage) and beneficial residual stress field (compressive residual stresses) of the weld region.

6.8.2 CCG

Dogan *et al*. [27] have correlated the crack initiation time t_i (h) for P22 base and weld material at 823 K with K (MPa m$^{0.5}$) and C^* (N mm^{-1} h^{-1}), see Figures 7–10 in [27]. These are summarised in Table 6.1. DMW between austenitic Type 316 and ferritic 2.25Cr–1Mo steels, welded with Type 316 or a nickel-based Inconel alloy, are used in high temperature piping. Defects in DMW generally occur at or near the ferritic to weld metal interface. Budden and Curbishley [92] found that high temperature growth of such an interfacial crack follows the interface but is fully in the ferritic material. Correlating the CCG data with C^* and $C(t)$, they concluded that the data are bounded above by crack growth data for the ferritic steel. Also, data on transition welds

Table 6.1 Correlations of the crack initiation time t_i (h) for P22 base, HAZ and weld material at 823 K with K (MPa m$^{0.5}$) and C^* (N mm^{-1} h^{-1}), see Figs. (7–10) in [27]

	Δa = 0.2 mm (Figs 7 & 9)		Δa = 0.5 mm (Figs 8 & 10)	
Base metal	$K = 41.03\,t_i^{-0.11}$	$C^* = 35.96\,t_i^{-2.06}$	$K = 47.13\,t_i^{-0.12}$	$C^* = 53.56\,t_i^{-1.0043}$
HAZ	$K = 59.02\,t_i^{-0.23}$	$C^* = 34.80\,t_i^{-1.24}$	$K = 63.86\,t_i^{-0.21}$	$C^* = 53.75\,t_i^{-1.24}$
Weld metal	$K = 28.9\,t_i^{-0.06}$	$C^* = 0.91t_i^{-0.53}$	$K = 29.9\,t_i^{-0.06}$	$C^* = 9.04\,t_i^{-0.84}$

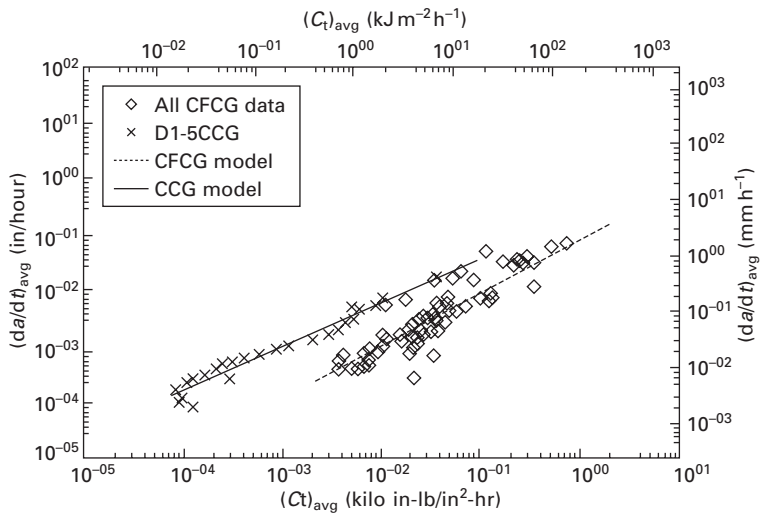

6.10 Creep–fatigue crack growth for base metal in different damage conditions and their repair welds using different procedures [61]. Reprinted from *Engineering Fracture Mechanics*, 74, 821–838, 2007, Ashok Saxena, 'Role of nonlinear fracture mechanics in assessing fracture and crack growth in welds', Copyright 2007, with permission from Elsevier.

containing Type 316 filler material as opposed to Inconel presented by Ainsworth [39], show that the 2.25Cr–1Mo:316 weld interface creep crack growth rate for that material combination was bounded by the 2.25Cr–1Mo upper bound line of Saxena *et al*. [93].

Saxena [61] reported the use of $(C_t)_{avg}$ to describe the crack growth under creep–fatigue conditions (FCG tests with different hold times) on base metals 1Cr–1Mo–0.25V steel, in two damage conditions and on their repair welds simulated using two procedures (Fig. 6.10), in comparison with the CCG behaviour of the base metal. The $(C_t)_{avg}$ values were obtained from load-line displacements measured during the hold time, and thus account for differences in creep deformation rates between the weld metals and the respective base

metals that are embedded in the measured load-line displacement rates. He has shown that CFCG rates are lower than the CCG rates, and the CFCG behaviour of over-matched weld using temper bead technique is better than the under-matched weld with PWHT. Also, he noted that the differences between the $(da/dt)_{avg}$ versus $(C_t)_{avg}$ behaviour between the various material conditions is small (approximately a factor of four or less) compared with the much larger differences in the creep deformation behaviour. However, calculating $(C_t)_{avg}$ using the measured load-line displacements normalises the effects of higher creep deformation rates and tends to consolidate the CCG and CFCG data into a much closer band, notwithstanding some differences between the under and over-matched weldments, and needs further attention. Despite the fact that crack growth was dominantly intergranular for long hold tests while it was mixed mode for short hold tests, the CFCG behaviour described by $(da/dt)_{avg}$ versus $(C_t)_{avg}$ was nearly identical. The $(da/dt)_{avg}$ versus $(C_t)_{avg}$ behaviour for the under-matched condition was higher than that for the others. The crack path under CFCG meanders from the fusion line to the weaker material, i.e. to the weld metal in the case of under-matched condition, and the base metal in the over-matched condition.

6.9 Conclusions

Fracture toughness is an important property to be considered in the material qualification as well as integrity assessment of components. Fracture and crack growth in weldments under dynamic and quasi-static loading conditions and under fatigue, creep and creep-fatigue conditions can be described in the framework of fracture mechanics. The choice of appropriate fracture mechanics parameters for fail-safe design depends on the service conditions that the component is subjected to, and on the materials and processes of fabrication.

In this chapter an attempt is made to outline the various approaches to fracture mechanics characterisation of ferritic weldments. These include both experimental studies, which produced many innovations to characterise the properties of individual regimes of welds with different metallurgical and mechanical conditions and also modelling, mainly using FEM, to describe the behaviour of complex combinations of microstructural and mechanical gradients. Also, different analytical approaches to describing fracture of welds have been discussed. Crack growth and fracture in welds under dynamic and quasi-static loading conditions have been discussed in the framework of both linear elastic and elastic plastic fracture mechanics. Attempts to describe and characterise subcritical crack growth in welds under sustained and cyclic loading conditions have been discussed. Crack growth assisted by environments has not been included in this chapter, since it is the subject matter of chapter 14.

6.10 References

1. *R-6, Assessment of the Integrity of Structures Containing Defects*, British Energy, R/H/R-6-Revision 3, 1998.
2. 'R5: Assessment procedure for the high temperature response of structures', Issue 3, British Energy Generation, Gloucester, UK, 2003; R. A. Ainsworth, R5 procedures for assessing structural integrity of components under creep and creep–fatigue conditions, *International Materials Reviews* 51 (2) (2006) 107.
3. *Guide on Methods for Assessing the Acceptability of Flaws in Metallic Structures*, BS7910: 1999 (incorporating Amendment No. 1), British Standards Institution, London, 2000.
4. *RCC-MR: Design and construction rules for mechanical components of FBR nuclear islands*, AFCEN, Paris, 2002.
5. *SINTAP, Structural Integrity Assessment Procedures for European Industry*. Project BE95-1426. Final Procedure, British Steel Report, Rotherham, 1999; *An overview of the European flaw assessment procedure SINTAP and its validation*, R. A. Ainsworth, A.C. Bannister, U. Zerbst, *International Journal of Pressure Vessels and Piping* 77 (2000) 869–876.
6. *API 579, Recommended Practice for Fitness for Service*, American Petroleum Institute, 2000.
7. P. R. Sreenivasan and S. K. Ray, Mechanical testing at high strain rates. *Encyclopedia of Materials: Science and Technology*, Elsevier Science Ltd. (2001) pp. 5269–5271.
8. ASTM E 208, Standard method for conducting drop-weight test to determine nil-ductility transition temperature for ferritic steels, *Annual Book of ASTM Standards* Vol. 03.01, American Society for Testing and Materials, Philadelphia, PA, 1990.
9. ASTM E23-07, Standard test methods for notched bar impact testing of metallic materials, *Annual Book of ASTM Standards* Vol. 03.01, American Society for Testing and Materials, Philadelphia, PA, 2007.
10. D. Francois, A. Pineau, editors, *From Charpy to Present Impact Testing*. Oxford: Elsevier, 2002.
11. M.-C. Kim, Y. J. Oh, B. Sang Lee, Evaluation of ductile–brittle transition temperature before and after neutron irradiation for RPV steels using small punch tests, *Nuclear Engineering and Design* 235 (2005) 1799–1805.
12. ASME Boiler and Pressure Vessel Code, Sec. III, Nuclear Power Plant Components, Div. 1, Appendix G, ASME, New York, 1980.
13. ASME Boiler and Pressure Vessel Code, Sec. XI, Rules for In-service Inspection for Nuclear Power Plant Components, Div. 1, Appendix A, ASME, New York, 1980.
14. K. Wallin, The Scatter in K_{Ic}-results, *Enging. Fract. Mech.* 19 (1984) 1085.
15. K. Wallin, in *Defect Assessment in Components – Fundamentals and Applications*, ESIS/EGF Publn 9, Mech Engng Publns, London, UK, 1991, p 415.
16. ASTM E 1921, Standard test method for determination of reference temperature T_0 for ferritic steels in the transition range, *Annual Book of ASTM Standards*, Vol. 03.01, American Society for Testing and Materials, Philadelphia, West Conshohocken, PA, 1997.
17. A. Moitra, P. R. Sreenivasan, S. L. Mannan and V. Singh, Ductile-brittle transition temperature and dynamic fracture toughness of 9Cr–1Mo steel, *Met and Mater Trans A* 36 A (2005) 2957.
18. S. Sathyanrayanan, A. Moitra, K. G. Samuel, G. Sasikala and S. K. Ray, Evaluation

of Dynamic Fracture Toughness Based Reference Temperature (T_0^{dy}) of Modified 9Cr-1Mo Steel in Phosphorous Embrittled and Cold Worked Condition, *Mater Sci Engg* A488 (2008) 519.
19. A. T. Yokobori Jr, T. Yokobori, T. Kuriyama, T. Kako and Y. Kaji, Characterization of high temperature creep crack growth rate in terms of independent parameters. In: *Proceedings of the International Confererence on Creep*, JSME, 1 Mech. E, ASME, 1986, pp. 135–140.
20. A. Saxena, B. Dogan and K.-H. Schwalbe, Evaluation of the relationship between C^*, $\delta 5$ and δt during creep crack growth. In: *Proceedings of the ASTM 24th Symposium on Fracture Mechanics*, ASTM-STP 1207, 1994, pp. 510–526.
21. A. T. Yokobori Jr and T. Yokobori, New concept to crack growth at high temperature creep and creep–fatigue. In: K. Salama, K. Ravi-chander, D. M. R. Taplin, P. Rama Rao, editors, *Advances in Fracture Research*, proc ICF7, vol. 2. Pergamon Press, 1989, pp. 1723–1735.
22. A. T. Yokobori Jr, R. Sugiura, M. Tabuchi, A. Fuji, T. Adachi and T. Yokobori, The effect of multi-axial stress component on creep crack growth rate concerning structural brittleness, 11th International conference on fracture, Turin (Italy) – March 20–25, 2005, Proceedings CD-Rom, Trading, Torino 2005, ISBN 978-88-903188-1-8.
23. K. Saito, A. Sakuma and M. Fukuda, Recent life assessment technology for existing steam turbines. In: *Proceedings of ICF*11: CDrom, 2005.
24. J. D. Landes and J. A. Begley, A fracture mechanics approach to creep crack growth. In: *Mechanics of Crack Growth*, ASTM STP 590, ASTM Philadelphia, 1976, pp. 128–148.
25. A. Saxena, Creep crack growth under non steady-state conditions. In: *Fracture Mechanics, Seventh Conference*, ASTM STP, vol. 905, 1986, pp. 185–201.
26. ASTM E 1457-00. Standard test method for measurement of creep crack growth rates in metals, *Annual Book of ASTM Standards* 3(1) (2001) 936–950.
27. B. Dogan, K. Nikbin, B. Petrovski, U. Ceyhan, D. W. Dean, Code of practice for high-temperature testing of weldments, *Intl J Pressure Vessels and Piping* 83 (2006) 784–797.
28. C. M. Davies, N. P. O'Dowd, D. W. Dean, K. M. Nikbin and R. A. Ainsworth, Failure assessment diagram analysis of creep crack initiation in 316 h stainless steel. *Int J Pressure Vessels Piping* 80(7–8) (2003) 541–551.
29. H. Riedel and A. R. Rice, *Tensile Cracks in Creeping Solids, Fracture Mechanics 12th Conference*. ASTM STP 700 (1980) 112–130.
30. R. A. Ainsworth, D. G. Hooton and D. Green, Failure assessment diagrams for high temperature defect assessment, *Eng. Fract. Mech*, 62 (1999) 95–109.
31. D. Moulin, B. Drubay and D. Acker, Proc. *ASME PVP 223, Pressure Vessel Fracture, Fatigue and Life Management*, 19–25, 1992.
32. I. Peñuelas, C. Betegón and C. Rodríguez, A ductile failure model applied to the determination of the fracture toughness of welded joints. Numerical simulation and experimental validation, *Engineering Fracture Mechanics* 73 (2006) 2756–2773.
33. V. Tvergaard and A. Needleman, 3D analyses of the effect of weld orientation in Charpy specimens, *Engineering Fracture Mechanics* 71 (2004) 2179–2195.
34. C. F. Shih, Cracks on bi-material interfaces: elasticity and plasticity aspects. *Mater. Sci. Eng*. A143 (1991) 77–90.
35. C. F. Shih, R. J. Asaro and N. P. O'Dowd, Elastic-plastic analysis of cracks on bimaterial interfaces: part III – large scale yielding, *J. Appl. Mech*. 58 (1991) 450–463.

36. R. E. Smelser and M. E. Gurtin, On the J-integral for bi-material bodies, *Int. J. Fracture* 13 (1977) 382–384.
37. N. P. O'Dowd, P. J. Budden and E. R. J. Griffiths, Finite element analysis of a bimaterial SENT specimen under elastic-plastic loading. In: J. R. Willis, (Ed.), *Proc. IUTAM Symposium on Nonlinear Analysis of Fracture*, Kluwer Academic Publishers, pp. 33–42, 1997.
38. N. P. O'Dowd and P. J. Budden, The effect of mismatch on *J* and *C** for interfacial cracks in plane and cylindrical geometries. In: K.-H. Schwalbe, M. Kocak, (Eds.), *Proc. 2nd. Intnl. Symposium on Mis-Matching of Interfaces and Welds*, GKSS, pp. 221–232, 1997.
39. R. A. Ainsworth, Characterisation of creep fracture at interfaces in weldments. In: *Proc. ICF9*, vol. 1. Pergamon, pp. 143–153, 1997.
40. I. Curbishley and D. G. Hooton, Assessment of creep and creep crack growth of 2.25Cr–1Mo:Inconel 182:Type 316 dissimilar metal weld features. In: *Proc. IOM: ImechE Conf. on Integrity of Welds at High Temperature*, Nottingham, November 1998, pp. 273–282.
41. *BS7910, Guide and Methods for Assessing the Acceptability of Flaws in Fusion Welded Structures*, British Standards Institution, 1999.
42. T. L. Anderson and D. A. Osage, APl 579: A comprehensive fitness-for-service guide, *Int. J. Pressure Vessel Piping*, 77 (2000) 953–963.
43. J.-B. Ju, J.-S. Lee, J.-i. Jang, W.-S. Kim and D. Kwon, *Proceedings of the Fourth International Pipeline Conference* (IPC2002), 2002, IPC02-27180 (published on CD-ROM).
44. J.-i. Jang, J.-B. Ju, B.-W. Lee, D. Kwon, W.-S. Kim, Effects of microstructural change on fracture characteristics in coarse-grained heat-effected zones of QLF processed 9% Ni steel, *Mater. Sci. Eng. A* 340 (2003) 68–79.
45. J.-S. Lee, J.-B. Ju, J.-i. Jang, W.-S. Kimc and D. Kwon, Weld crack assessments in API X65 pipeline: failure assessment diagrams with variations in representative mechanical properties, *Mater Sci Eng A* 373 (2004) 122–130.
46. F. W. Brust, Classical and emerging fracture mechanics parameters for history dependent fracture with application to weld fracture. In: *Proceedings of ASME Pressure Vessels and Piping Conference*, Boston, MA, 1–5 August 1999.
47. R. A. Ainsworth, R5 procedures for assessing structural integrity of components under creep and creep–fatigue conditions, *International Materials Reviews* 51 (2) (2006) 107–126.
48. J. Zhang, P. Dong, F. W. Brust and W. Shack, Analysis of residual stresses in a girth weld of a reactor shroud. In: *Approximate Methods in the Design and Analysis of Pressure Vessels and Piping Components, Proceedings of ASME Pressure Vessels and Piping Conference*, Orlando, Florida, 27–31 July 1997, 347, pp. 141–156.
49. F. W. Brust, P. Dong, J. Zhang and W. Shack, Crack growth behavior in residual stress fields of a girth weld in reactor shroud structures. In: *Fatigue and Fracture, Proceedings of ASME Pressure Vessels and Piping Conference*, Orlando, Florida, 27–31 July 1997, 350, p. 391–406.
50. F. W. Brust, P. Dong and J. Zhang, A constitutive model for welding process simulation using finite element methods. In: S. N. Atluri, G. Yagawa, editors, *Advances in Computational Engineering Science, Proceedings of ICES Conference*, 1997, pp. 51–56.
51. J. Zhang, P. Dong and F. W. Brust, A 3D composite shell element model for residual stress analysis of multi-pass welds in pressure vessels and pipes. In: *Proceedings of*

the 14th International Conference on Structural Mechanics in Reactor Technology (SMiRT 14), Lyon, France, 17–22 August 1997, pp. 335–344.
52. P. Dong, J. K. Hong and P. Roger, Analysis of residual stresses in Al-Li alloy repair welds and mitigation techniques, *Welding Journal* 17 (11) (1998) 439s–445s.
53. P. Dong, J. K. Hong, J. Zhang, P. Roger, J. Bynum and S. Shah, Effects of repair weld residual stresses on wide-panel specimens loaded in tension, *J Pressure Vessel Technol*, 120(2) (1998) 122–128.
54. P. Dong and J. Zhang, Residual stresses in strength-mismatched welds and implications on fracture behavior, *Engineering Fracture Mechanics* 64 (1999) 485–505.
55. P. Dong and J. R. Gordon, An investigation to determine the effect of under/overmatching on the accuracy of fracture prediction models. In: *Design and Fitness for Service of Welded Structures, Proceedings of Sixth Annual North American Welding Research Conference*, Columbus, OH, 8–10 October 1990, pp. 41–65.
56. P. Dong and J. R. Gordon, The effect of weld metal mismatch on the fracture behavior of center-cracked panels. In: *Fatigue, Fracture and Risk, Proceedings of ASME Pressure Vessels and Piping Conference*, New Orleans, LA, 21–25 June 1992 241, pp. 59–67.
57. P. Dong and J. R. Gordon, The effect of under and overmatching on fracture prediction models, *Welding-90: Technology, materials, fracture*, Kocak M, i.i.t.t. International, 363–370.
58. Y. Y. Wang and M. T. Kirk, A structural integrity assessment procedure for welded structures with weld metal strength mismatch. In: *Fatigue and Fracture, Proceedings of ASME Pressure Vessels and Piping Conference*, Montreal, Quebec, Canada, 21–26 July 1996, 324, pp. 133–141.
59. F. W. Brust, P. Dong, J. Zhang and W. Shack, Crack growth behavior in residual stress fields of a girth weld in reactor shroud structures. In: *Fatigue and Fracture, Proceedings of ASME Pressure Vessels and Piping Conference*, Orlando, FL, 27–31 July 1997, 350, pp. 391–406.
60. S. Ravi, V. Balasubramanian and S. Nemat Nasser, Effect of mis-match ratio (MMR) on fatigue crack growth behaviour of HSLA steel welds, *Engineering Failure Analysis* 11 (2004) 413–428.
61. A. Saxena, Role of nonlinear fracture mechanics in assessing fracture and crack growth in welds, *Eng Fracture Mechanics* 74 (2007) 821–838.
62. P. R. Sreenivasan and S. L. Mannan, Dynamic J-R curves and tension impact properties of AISI 308 stainless steel, *Int. J. Fracture* 101(3) (Feb. 2000) 215–228.
63. M. Gopalakrishnan, M. S. Sabhesan, B. S. C. Rao and P. R. Sreenivasan, Influence of welding parameters, deposition techniques and position of welding on RT_{NDT} of 9Cr–1Mo steel welds, in *Proc 9th Int Conf Pressure Vessel Technology* (*ICPVT-9*), Sydney, Australia, 9–14 April 2000.
64. P. R. Sreenivasan, S. K. Ray, S. L. Mannan and P. Rodriguez, Determination of K_{Id} at or below NDTT using instrumental drop-weight testing, *Int J Fracture* 55 (1992) 273.
65. A. Moitra, S. K. Ray and S. L. Mannan, Determination of dynamic fracture toughness of heat affected zones of 9Cr–1Mo steel from instrumental drop-weight loss, *Mater Sci Technol* 55 (1999) 137.
66. P. R. Sreenivasan, S. K. Ray and S. L. Mannan, An empirical relation between yield stress and general yield loaded for a Charpy U-notch specimen *Eng Fract Mechanics* 42(2) (1992) 1047.
67. P. R. Sreenivasan, A. Moitra, S. K. Ray, S. L. Mannan and R. Chandramohan,

Dynamic fracture toughness properties of 9Cr–1Mo weld from instrumental impact and drop-weight tests, *Int J Pressure Vessels and Piping* 69 (1996) 149.
68. *ASTM Standard Test Method for Measurement of Fracture Toughness*, ASTM E 1820-06, American Society for Testing of Materials, 2006, Philadelphia.
69. P. R. Sreenivasan, S. K. Ray, S. Vaidyanathan, and P. Rodriguez, Measurement of stretch zone weight and its relationship to crack tip opening displacement and initiation i-value in an AISI 316 stainless steel, *Fatigue Fract. Engng Mater Struct* 19 (1996) 855.
70. T. Kobayashi, I Yamamoto and M. Niinomi, Introduction of a new dynamic fracture toughness evaluation system. *J Testing and Evaluation, JTEVA*, 21 (3) (1993) 145–153.
71. S. K. Ray, P. R. Sreenivasan, K. G. Samuel and P. Rodriguez, Quality control for nuclear grade austenitic stainless steels using Charpy impact testing, in *Advances in Fracture Research*, *Proc ICF 6*, p. 3221, 1984.
72. P. R. Sreenivasan and S. L. Mannan, Plastic n-factor for three-point bend specimens analysis of instrumented Charpy impact test results for AISI 308 weld and AISI 316 stainless steels, *Int. J. Fracture* 101(3) (2000) 215.
73. H. J. Schindler, T. Varga, F. Loibnegger, and J. Noeggerath, Ageing and irradiation surveillance by means of impact testing of precracked Charpy specimens, *Proc Int Symp. Materials Ageing and Life Management*, B. Raj *et al*. (eds), Allied Publishers, Chennai, p. 837, 2000.
74. S. Sathyanarayanan, G. Sasikala and S. K. Ray, Evaluation of dynamic fracture toughness of cold worked 9Cr–1Mo steel, *Int. J. Pressure Vessel & Piping* 81 (2004) 419.
75. A. Moitra, S. Sathyanarayanan, S. K. Albert, V. Ramasubbu, G. Sasikala, K. G. Samuel, and S. K. Ray, A dynamic fracture toughness based reference temperature characterization of 1G and 4G weld metals of modified 9Cr–1Mo steel, *Int J Pressure Vessels and Piping*, 85 (2008) 478.
76. H. J. Schindler, T. Varga, D. H. Njo and G. Prantl, Key issues on instrumented precracked Charpy type testing in irradiation surveillance progranmes, in *Proc. Int. Symp. Materials Ageing and Component Life Extension*, V. Bicego *et al*. (eds), Milan, 10–13 Oct 1995, p. 1367.
77. K. Angamuthu, B. Guha and D. R. G. Achar, Investigation of dynamic fracture toughness (J_{Id}) behaviour of strength mis-matched Q & T steel weldments using instrumented Charpy impact testing, *Engineering Fracture Mechanics* 64 (1999) 417–432.
78. G. R. Odette, T. Yamamoto, H. J. Rathbun, M. Y. He, M. L. Hribernik and J. W. Rensman, Cleavage fracture and irradiation embrittlement of fusion reactor alloys: mechanisms, multiscale models, toughness measurements and implications to structural integrity assessment, *J Nuclear Mater* 323 (2003) 313–340.
79. S. K. Ray, P. R. Sreenivasan, K. G. Samuel and P. Rodriguez, Characterization of irradiation-induced embrittlement in an ASTM A 203 D steel using instrumented impact testing, *Int J Pressure Vessels & Piping* 54 (1993) 481–496.
80. K. K. Yoon, A direct fracture toughness model for irradiated reactor vessel weld material based on reference temperature, *Nuclear Engineering and Design* 198 (2000) 253–259.
81. *SINTAP, Structural integrity assessment procedures for European industry, Final Procedure*, European Union Brite-Euram Programme. Project no. BE95-1426, contact no. BRPR-CT95-0024, 1999.

82. H. G. Pisarski and K. Wallin, The SINTAP fracture toughness estimation procedure, *Engineering Fracture Mechanics* 67 (2000) 613–624.
83. J.-S. Lee, J.-B. Ju, J.-i. Jang, W.-S. Kimc, and D. Kwon, Weld crack assessments in API X65 pipeline: failure assessment diagrams with variations in representative mechanical properties, *Mater Sci Eng A* 373 (2004) 122–130.
84. ASTM Standard E1290, *Standard Test Method for Plane-Strain Fracture Toughness of Metallic Materials*, 1993.
85. S. K. Ray and G. Sasikala, *Fracture Toughness Evaluation of Modified 9Cr–1Mo Steel Plate*, Internal Report PFBR/33130/DN/1022, IGCAR, October 2002.
86. G. Sasikala, S. K. Ray and K. G. Samuel, Fracture toughness evaluation of indigenously developed SS 316 (N) weld, in *Proc Int Conf Pressure Vessels and Piping*, Chennai, 7–9 February 2006.
87. C. F. Shih and R. J. Asaro, Elastic-plastic analysis of cracks on bimaterial interfaces: Part I – small-scale yielding. *J Appl Mech*, 56 (1988) 299–316.
88. R. J. Asaro and C. F. Shih, Elastic-plastic analysis of cracks on bimaterial interfaces: Part II – structure of small-scale yielding fields, *J Appl Mech* **56** (1989) 763–779.
89. R. J. Asaro N. P. O'Dowd and C. F. Shih, Elastic-plastic analysis of cracks in bimaterial interfaces: interfaces with structure, *Mater Sci Engng* A162 (1993) 175–192.
90. L. Cretegny and A. Saxena, Fracture toughness behavior of weldments with mismatched properties at elevated temperature, *Int J Fracture* 92 (1998) 119–130.
91. P. S. Grover, Creep–fatigue crack growth in Cr–Mo–V base material and weldments. PhD dissertation, Georgia Institute of Technology, May 1996.
92. P. J. Budden and I. Curbishley, Assessment of creep crack growth in dissimilar metal welds, *Nuclear Engineering and Design* 197 (2000) 13–23.
93. A. Saxena, J. Han and K. Banerji, Creep crack growth behaviour in power plant boiler and steam pipe steels. *ASME J. Pressure Vessel Tech.* 110 (1988) 137–146.

7

Testing and evaluation of weld cracking in ferrous alloys

B RAJ, T JAYAKUMAR and P PALANICHAMY,
Indira Gandhi Centre for Atomic Research, India

Abstract: Ferrous alloys are extensively used as structural materials in various industries due to their widely different metallurgical and mechanical properties. Quality assurance programmes play a crucial role for ferrous alloys and ferritic steel welded components. In general, testing and evaluation of materials and components are an integral part of a quality assurance programme. For an effective quality assurance programme, integrated use of destructive, semi-destructive and non-destructive testing techniques is essential. In this chapter, the importance of the quality assurance programme for ensuring the integrity of ferritic steel welded components and the application of various destructive, semi-destructive and non-destructive testing techniques is discussed. Destructive techniques such as tensile testing and impact testing, semi-destructive techniques such as hardness, corrosion and metallography, and non-destructive testing techniques such as X-ray, ultrasonics and acoustic emission are discussed. Emphasis is given to testing techniques such as ultrasonics, X-ray and metallography due to their applicability in all stages of the ferrous alloy welded components, starting from the fabrication stage to plant maintenance and in the life extension programme. The importance of understanding the formation and quantitative estimation of residual stresses and distortion in welds is also included. Semi-destructive hole-drilling and non-destructive X-ray and ultrasonic techniques for the quantitative estimation of residual stresses are discussed in detail. The applicable codes and standards for welding of ferrous alloy components and destructive and non-destructive testing techniques for evaluation of welded components are also identified in this chapter.

Key words: quality assurance, ferrous alloys, welds, testing and evaluation, destructive testing, semi-destructive testing, non-destructive testing, defects, residual stresses, microstructures, codes, standards.

7.1 Introduction

Ferrous alloys consist of iron and other elements such as carbon, silicon, nickel, manganese and chromium. Various elements are incorporated in alloy steel in order to alter the material properties of the steel. The following are the important forms of ferrous alloys: carbon steels, stainless steels, low alloy ferritic steels, martensitic steels, duplex steels and precipitation hardening steels, etc. Carbon steel is composed mostly of iron and carbon and relies on these elements for its structure and properties. It is the most widely produced

steel. High carbon steels contain at least 0.6% carbon. If more carbon is added, the steel becomes hardened, and less malleable and difficult to utilise. Low-carbon steels contain less than 0.2% carbon. This steel is ductile and can be stretched or rolled for automotive parts.

Stainless steels are iron-based alloys with a minimum chromium content of 12 wt%, the amount necessary to form a 'passive film', a thin, transparent and adherent chromium-rich oxide film that prevents the formation of rust in the environment. The passive film automatically forms and regenerates (i.e, heals itself) in the presence of oxygen. Additional corrosion resistance depends on the alloying elements, e.g. nickel, molybdenum, copper, titanium, aluminium, silicon and niobium. The chromium content can vary significantly from grade to grade; some of the grades contain chromium as high as 30 wt%. Stainless steels contain carbon in a range of less than 0.03 wt% to over 1.0 wt%.

Austenitic stainless steels have high ductility, low yield stress and relatively high ultimate tensile strength, when compared with typical carbon steel. Austenitic steels have a face centred cubic (FCC) crystalline structure which provides more planes for the flow of dislocations, combined with the low levels of interstitial elements (elements that lock the dislocation chain), which confer good ductility to these steels. This also explains why this material has no clearly defined yield point, and so its yield stress is always expressed as a proof stress. Austenitic stainless steels have excellent toughness down to true absolute zero (–273 °C), with no steep ductile to brittle transition. This material has good corrosion resistance, but quite severe corrosion can occur in certain environments. The right choice of welding consumable and welding techniques can be crucial as the weld metal can corrode more than the parent material.

Ferritic stainless steels have a chromium content typically within the range 11–28%. Commonly used alloys include the 430 grade, having 16–18% Cr and 407 grade having 10–12% Cr. As these alloys can be considered to be predominantly single phase and non-hardenable, they can be readily fusion welded. The main problem when welding this type of stainless steel is a coarse-grained heat-affected zone (HAZ) with poor toughness. The excessive grain coarsening can lead to cracking in highly restrained joints and thick section material. However, when welding thin section material, less than 6 mm, no special precautions are necessary.

Martensitic stainless steels are also based on the addition of chromium as the major alloying element but with a higher carbon and generally lower chromium content (e.g. 12% in Grade 410 and 416) than the ferritic types. Grade 431 has a chromium content of about 16%, but the microstructure is still martensite because this grade also contains 2% nickel.

Duplex stainless steels such as 2304 and 2205 (these designations indicate compositions of 23% chromium, 4% nickel and 22% chromium, 5% nickel

respectively but both grades contain further minor alloying additions) have microstructures comprising a mixture of austenite and ferrite generally in equal volume ratio. Duplex ferritic-austenitic steels combine some of the features of each class: they are resistant to stress corrosion cracking (SCC), albeit not quite as resistant as the ferritic steels; their toughness is superior to that of the ferritic steels but inferior to that of the austenitic steels, and their strength is greater than that of the (annealed) austenitic steels, by a factor of about two. In addition, the duplex steels have general corrosion resistances equal to or better than 304 and 316, and in general their pitting corrosion resistance is considerably superior to 316. They suffer reduced toughness below about –50 °C and also when exposed to above 300 °C. Hence, duplex steels are used in the temperature range of –50 °C to 300 °C.

Precipitation hardening stainless steels are chromium and nickel containing steels that can develop very high tensile strengths. The most common grade in this group is '17-4 PH', also known as Grade 630, with the composition of 17% chromium, 4% nickel, 4% copper and 0.3% niobium. The great advantage of these steels is that they can be supplied in the 'solution treated' condition. In this condition the steel is just machineable. Following machining, forming, etc. the steel can be hardened by a single, fairly low temperature 'ageing' heat treatment which causes no distortion of the component.

It is clear from the above discussion that various ferrous alloys have widely different properties and hence these are the most exclusively used structural materials in various industries. It is essential to test and evaluate these steels and also the components made of these steels through fabrication routes including rolling, forging, casting and welding. A number of quality control procedures including non-destructive testing, destructive mechanical property evaluation and corrosion testing are employed for ensuring stringent quality of the raw material and semi-finished and finished products. In this chapter, the quality assurance procedures, non-destructive testing (NDT), destructive mechanical testing, residual stress measurements and corrosion testing methods and evaluation procedures are discussed, giving due emphasis to welded structures. Important standards for testing and evaluation of welded ferrous alloy components are also given.

7.2 Quality assurance and qualifications

The term quality can be defined as conformance of a material or product to drawings and specifications. This is an outdated definition and does not meet the objectives of the term quality. The product may conform to drawings and specifications but may not serve the purpose satisfactorily. Today, quality means the ability of a product to serve the purpose reliably with minimal maintenance. With the advent of quality movement in many countries in recent times, the most accepted definition of the term quality is 'the totality

of features and characteristics of a product or service that bears its ability to satisfy a given need' [1].

Quality assurance (QA) is a term related to the efforts of manufacturer/supplier in order to create confidence with the clients that the supplied product will perform the intended service satisfactorily over the period of design life. QA can be defined as all those well-planned and systematic actions taken by a supplier or service organisation to instill confidence in the minds of buyers that the product or service is made as per a standard and it serves the purpose well.

In pursuance of QA in the fabrication of welded structures, the following activities are typically to be carried out by the manufacturer.

- approval of detailed drawings by the client;
- tracability of materials and welding consumables;
- approval of raw materials and consumables by client;
- preparation of QA plan, manufacturing and NDT procedures [2];
- calibration of testing equipment;
- qualification of welding consumables, welding procedure and welders;
- qualification of NDT personnel;
- quality control during production welding;
- NDT of welds;
- quality control during post-weld heat treatment (PWHT);
- NDT after PWHT;
- hydraulic testing or load testing of welded structures;
- leak testing of welds; and
- documentation.

In the 'welding qualifications' programme listed above, the qualification of welding consumables, welding procedures and welders are most important steps which facilitate the quality of production welding.

7.2.1 Welding consumable qualification

Material selection for a component is one of the design criteria. The material is selected based on its physical characteristics such as strength, ductility, fatigue, resistance to service temperature, creep resistance, etc. and its compatibility and corrosion resistance to the fluids handled in service. Once the parent material is specified for a welded structure, selection of appropriate welding consumable to join the material is done such that the produced weld will be better than or equal to parent material in strength, with specified ductility, impact strength and corrosion resistance to fluids handled in service. Apart from the above factors, the weld metal should be sound and metallurgically compatible with parent material. Factors such as chemistry, coefficient of thermal expansion, dilution of elements and metallurgical

structure of parent metal and weld metal are considered while selecting the welding consumable. The welding consumable used should conform to a specified standard.

The manufacturer of the welding electrodes has to qualify each lot of welding electrodes produced with one set of production variables such as flux mix and core wire composition and issue a certificate with test results conforming to the standard. The covered electrode is qualified by depositing from each lot of electrodes to form weld pads for testing. Figure 7.1 indicates the testing scheme for qualifying steel weld metal as per the 2004 ASME Boiler and Pressure Vessel Code [3]. The tests performed on the deposited weld metal are (a) chemical analysis, (b) radiography to assess the soundness, (c) all-weld tensile test and impact test to assess mechanical properties and (d) fillet weld test to assess usability characteristics. All these tests should meet the acceptance criteria specified in the standard. For chromium, nickel

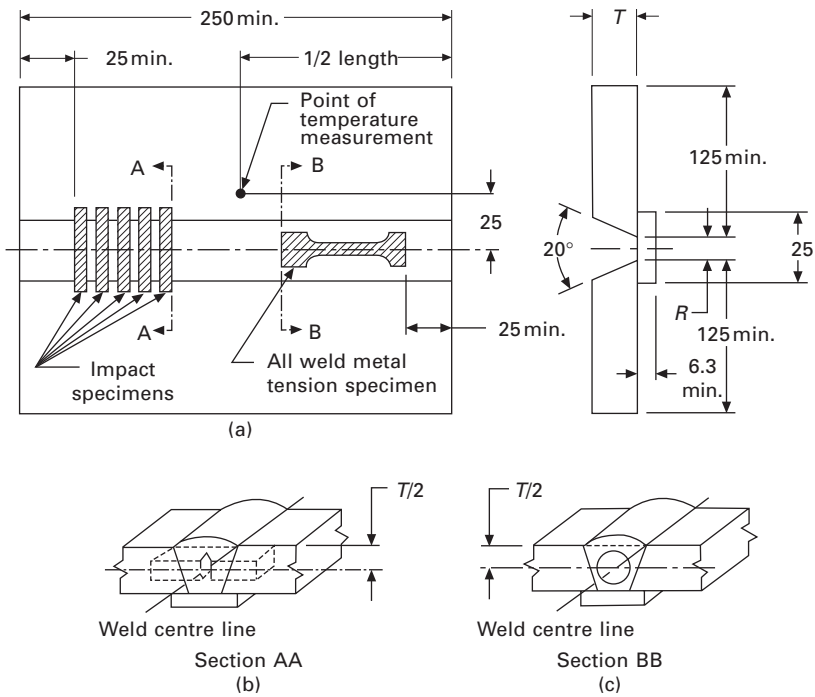

7.1 Typical details of test assembly for soundness and mechanical tests of welding consumables for steel: (a) test plate showing location of test specimens; (b) orientation and location of impact specimen; and (c) location of all-weld-metal tension specimen (Reprinted from ASME BPVC 2004, Section II-Part C, by permission of the American Society of Mechanical Engineers. All rights reserved). All dimensions are in mm.

and chromium–nickel bare electrodes and solid welding rods, the qualification is based on chemical analysis of the manufactured filler metal.

7.2.2 Welding procedure qualification

Though it is possible to make welds for the given set of materials and working conditions, in actual production welding, there are many factors which influence the weld metal quality. These are (1) joint configuration, (2) base metal chemistry, (3) filler metal chemistry, (4) position of welding, (5) pre-heating, (6) post-heating, (7) type of gas used for shielding and purging, (8) electrical characteristics and (9) welding process.

For the given set of conditions of welding on the shop floor, one should prove that the weld produced under fabricating conditions should at least meet the strength of the base metal and should have specified ductility and impact strength. This is done as part of the welding procedure qualification. For the given set of fabricating conditions, the manufacturer of welded structures should document the welding procedure specification before undertaking the procedure qualification. After preparing the welding procedure specification, the manufacturer should qualify the procedure by welding a plate or pipe test coupon. The tests performed on the weld test coupon are:

- transverse tensile tests (two) to meet the base metal minimum tensile value;
- transverse root bends (two) and transverse face bends (two) to prove the ductility and soundness of the weld; and
- one set of impact test at a specified temperature, where the base metal is specified for notch toughness in service.

The American Society for Mechanical Engineers (ASME) has specified in ASME Code section IX, the type and number of tests to be done and the range of thickness qualified for a given size of plate test coupon used for procedure qualification [2,3]. Procedure qualification for plate is valid for pipe of any diameter, and the range of thickness qualified is given in the ASME Code. Procedure qualification on pipe is valid for plate welding within the range of the qualified thickness. The procedure qualification on a groove weld is valid for fillet weld but not the vice versa. Groove weld procedure qualification on plate or pipe qualifies fillet welding of any size on plate or pipe without limitation on thickness or diameter. Fillet weld procedure qualification on plate or pipe qualifies only fillet welding on plate or pipe respectively.

Any procedure qualification is valid for a given set of parameters such as joint configuration, base metal composition, filler metal composition, position of welding, pre-heating, post-heating, type of gas used for shielding and purging, process of welding and electrical characteristics. When a welding

procedure is qualified by a manufacturer, it is necessary that the procedure details and test results in the Procedure Qualification Record (PQR) are also documented. Once a procedure is qualified and documented, the manufacturer need not re-qualify the same provided the procedure is only used within the allowable range of the essential or the supplementary essential variables.

7.2.3 Welder performance qualification

In welding performance qualification, the welder's ability and skill to make a sound weld, following a qualified procedure, is verified. This is done by giving a test to the welder on a pipe or plate as applicable to the job. The soundness of the weld made is checked by either radiography of test coupon or by two transverse bend tests, one on root side and the other on face side of the weld. The welder qualified on pipe welding is qualified to do plate welding but not vice versa.

Since varying degrees of the skill are required to make sound welds in different positions of welding, with different types of welding consumables, in different welding processes and techniques, with different electrical characteristics and different material configuration such as plate and pipe, all these variations form the essential variables which call for requalification of a welder. ASME section IX specifies the range of thickness and diameters qualified by a welder for groove and fillet welds in terms of thickness of the test coupon and diameter of pipe welded.

The welder who passes the welding procedure test is thereby qualified for the welding process and procedure. Other welders who are to be employed on the same job are separately performance tested and qualified. A qualified welder's skill will be consistent only if he or she is continuously employed on the welding process in which he or she is qualified. Renewal of qualification of a welder or welding operator is required in the following conditions:

- When the welder is not employed on the specific process, viz. metal arc, gas, submerged arc, etc. for a period of 6 months.
- When there is a specific reason to question his or her ability to make welds that meet the specification, the qualification which supports the welding being done is revoked.

The qualifications of the welding consumable, welding procedure and welder performance are the most important activities to ensure the quality of welds. It is much easier for the manufacturer to implement QA on welded structures once these activities are performed properly.

7.3 Testing and evaluation of welds

Present-day engineering industry relies heavily on the integrity of welds for adequate and reliable performance of components, structures and plants. Weld integrity is dependent on the base material, specifications and welding processes. Reliability of weld performance is evaluated by measurement and control of weld properties. It is accepted widely that testing, measurement and control of welds should be optimised based on the fitness-for-purpose (FFP) approach, taking into account the welding processes and economic aspects of ensuring the desired levels of reliability. Recent advances in test techniques for ensuring the desired quality have met high technological demands.

7.3.1 Weld imperfections and importance of their evaluation

Historically welding has replaced riveted construction in engineering structures. It is now scarcely possible to design an industrial structure without a welded joint. No weld is completely perfect [4]. Welds may be compared to small castings except that weld metal cools much more rapidly mainly because of heat sinks provided by the base metals. This results in thermal stresses that may lead to cracking and also due to the entrapment of gases or foreign materials within the weld. These and other defects may cause premature failure of the weld in service.

Defects in welded joints [5]

Defects can be of three types:

1. physical discontinuities;
2. microstructural defects;
3. defects related to residual stress and distortion.

The relevance and importance of defects are best understood through fracture mechanics concepts, wherein the following parameters are important: (a) defect size, (b) defect shape, (c) defect location and (d) loading, including both externally imposed and arising out of the presence of residual stresses. The objective of a good and effective testing programme is to detect defects as specified by the design based on FFP.

Choice of NDE technique to evaluate FFP

Mainly in highly stressed components, failure occurs in an elastic manner involving fast fracture. The ability to detect planar defects is the first of the

relative merits of various NDT techniques, since fracture mechanics concepts indicate the prime importance of detecting and measuring planar defects. Hence, the NDT techniques that are most appropriate for use in conjunction with an FFP approach are those that are:

- sensitive to planar defects, whatever their orientation and position;
- sensitive to surface breaking defects;
- capable of discriminating planar from non-planar defects.

7.4 Non-destructive tests

NDT is an integral and important constituent of the QA programme of any industry. The objectives of the QA programmes are safety, reliability and economy. Non-destructive evaluation (NDE) places due emphasis on characterisation of materials, including quantitative determination of the size, shape and location of a defect or abnormality, thus enabling evaluation of structural integrity of a component, particularly in the context of FFP. NDT[4], along with material properties and operational history, is vital for successful prediction of damage and residual life of welded components.

7.4.1 Visual inspection

Visual inspection is probably the most widely used among the nondestructive tests. It is simple, easy to apply, quickly carried out and usually low in cost. Even though a component is to be inspected using other NDT methods, a good visual inspection should be carried out first. A simple visual test can reveal gross surface defects, thus leading to an immediate rejection of the component and consequently saving much time and money, which would otherwise be spent on more complicated means of testing. It is often necessary to examine the weld joint for the presence of finer defects. For this purpose, visual methods have been developed to a very high degree of precision. With the advent of change coupled devices (CCD) based cameras, microprocessors and computers, visual examination can be carried out very quickly, reliably and with minimum cost. Image processing, pattern recognition and automatic accept/reject choices are used when large numbers of components are to be assessed.

Visual inspection has wide applications for inspection of wrought, cast and welded materials. However, for welds, this is all the more important as at various stages of welding, visual inspection gives useful information. Many characteristics of a weld can be evaluated by visually examining a completed weld, but much can be learnt by observing the weld as it is being made. For many non-critical welds, integrity is verified principally by visual inspection. Even when other non-destructive methods are used, visual inspection

still constitutes an important part of quality control. Visual inspection should be done before, during and after welding. Visual inspection is useful for assessing the following: (a) dimensional accuracy, (b) conformity of welds to size, fit up and control requirements, (c) acceptability of weld appearance with regard to surface roughness, weld spatter, undercuts and overlaps, and (d) imperfections and cracks on the observed surfaces. Although visual inspection is a very valuable method, it is incapable of detecting subsurface flaws. Therefore, judgement of weld quality must be based on information from bulk material in addition to that from surface indications. Capabilities of visual inspection can be enhanced considerably by using simple gadgets and instruments for viewing, dimensional measurements, etc. In spite of the developments in the field of visual aids, as yet there is no decision-making electronic computer that can emulate the human brain. The experienced eye is invaluable for an intelligent first inspection. Many visual aids are available to enhance the inspection ranging from a pocket magnifier to microscope and monochromatic illumination to CCD camera colour video presentation. Intra-scopes are available that enable entry and inspection of internal surfaces through access openings and the human inspector is equipped to supply a wealth of primary NDT results.

Optical aids used for visual inspection

The use of optical instruments in visual inspection is beneficial and is recommended to (a) magnify defects that cannot be detected by the unaided eye and (b) permit visual checks of areas not accessible to the unaided eye. In performing visual/optical checks, it is of utmost importance to know the type of defects that may develop and to recognise the areas where such failures may occur. Magnifying devices and lighting aids should be used wherever appropriate. The general area should be checked for cleanliness, presence of foreign objects and corrosion damage. In many cases, the area to be inspected should be cleaned before the visual examination.

- *Microscope:* An optical microscope is a combination of lenses used to magnify the image of a small object. Minute defects and details of fine structure on a surface can be detected more easily with the help of a microscope. The practical upper limit of the magnifying power of a simple microscope is in the region of 10×. Optical microscopes are used at a magnification of 2 to 20× to examine external cracks on unprepared surfaces. Observation of microstructural details alongside the crack location usually requires a magnification of 100–500× after metallographic preparation.
- *Borescope:* As the name implies, a borescope is an instrument designed to enable and observe to inspect the inside of a narrow tube, bore or

chamber. The borescope consists of a precision built-in illumination system having a complex arrangement of prisms and plain lenses through which light is passed to the observer with maximum efficiency. The light source located in front or ahead of the objective lens provides illumination for the part being examined. Borescopes are available in numerous models from 2.5 to 19 mm in diameter and a few metres in length. Optical systems are generally designed to provide direct, right-angle, retrospective and oblique vision. The choice of the inspection angle is determined by flaw type and location. In most borescopes, the observed visual area is approximately 25 mm in diameter and 25 mm from the object. The size of the visual field usually varies with the diameter for a given magnification system.

- *Endoscope:* The endoscope is much like a borescope except that it has a superior optical system and a high intensity light source. Various viewing angles, as discussed for the borescope, can be used. A unique feature of the endoscope is that objects are constantly in focus from about 4 mm to infinity. Endoscopes are available in diameters down to 1.7 mm and in lengths from 100 to 1500 mm.
- *Flexible fibre-optic borescope (flexiscope):* Flexible fibre-optic borescopes permit manipulation of the instrument around corners and through passages with several directional changes. Woven stainless steel sheathing protects the image-relaying fibre optic bundle during repeated flexing and manoeuvring. These devices are designed to provide sharp and clear images of parts and interior surfaces that are normally impossible to inspect. Remote end-tip deflection allows the viewer to thread the fiberscope through a complex series of bends. High resolution CCD camera-based fibroscopes are available for examination of the inner surface of the tubes.

7.4.2 Liquid penetrant inspection

Liquid penetrant inspection (LPI) is another NDT method to detect surface defects and also sub-surface defects open to surface in welded materials. This method is used in root pass and subsequent passes to detect surface defects so that repair work can be undertaken to remove the defects in the weld. In this method, a liquid penetrant is applied to the surface of the product for a certain predetermined time during which the penetrant seeps through the surface opening defects by capillary action. The excess penetrant is removed from the surface. The surface is then wiped with solvent or water, dried and a developer applied to it. The penetrant which remains in the discontinuity is absorbed by the developer to indicate the presence as well as the location, size and nature of discontinuity. The procedural sequence adopted for liquid penetrant inspection is shown in Fig. 7.2. Care should be taken so

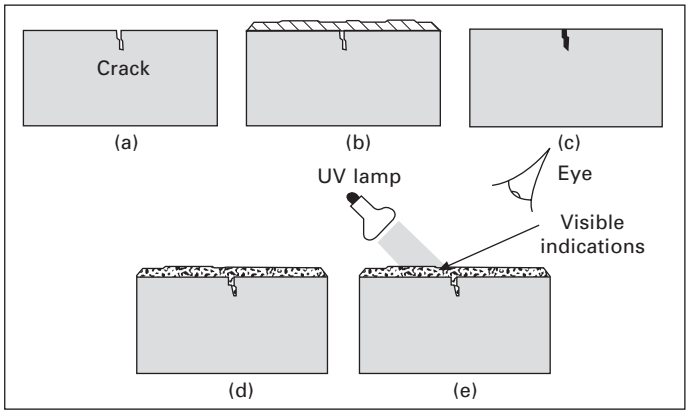

7.2 Sequence of liquid penetrant testing: (a) material with crack/discontinuity, (b) penetrant seeps into discontinuity, (c) excess penetrant removed, (d) developer applied and (e) developer absorbs residual penetrant that seeped into discontinuity during step (b). Examination by naked eye aided with UV lamp, in case of fluorescent penetrant.

that chemical contents in the liquid penetrant do not affect the material. This method may be adopted for inspection of all types of surface cracks, porosity, laminations and lack of bond at exposed edges or joined materials and leaks in welded tubes and tanks. It has been used with excellent success on ferrous and non-ferrous materials, ceramics, powder metallurgy products, weldments, glass as well as on some plastics and synthetic materials.

Types of penetrants and developers

Penetrants are either colour contrast (red dye) or fluorescent. Fluorescent dyes require viewing under UV light. Fluorescent penetrants have a higher sensitivity than normal penetrants. Liquids having good penetrating ability and potent coloured dyes are required to achieve the desired sensitivity. The amount of penetrant that can enter extremely fine surface discontinuities is quite minute. The visibility of the penetrant brought out of the flaw must be extremely high. The contrast between the penetrant and the developer or surface of the part should be as great as possible. Some penetrants are water-washable and can be removed from the surface by washing with ordinary tap water while others are removed with special solvents.

Types of developers

Two types of developers are employed:

1. A dry developer consists of a dry, light-coloured, powdery material. Dry

developer is applied to the surface of the parts after removal of the excess penetrant and drying of the part.
2. A wet developer which consists of a powdered material suspended in suitable liquid such as water or a volatile solvent.

Penetration time

The penetration time varies considerably depending upon (1) the type of penetrant used, (2) the type of materials to be inspected, (3) the sensitivity desired and (4) the type of defects to be found. The temperature also has a considerable effect on penetration time. The time may vary from as little as 1 minute to 1 hour.

Inspection

Inspection is carried out by viewing the part for colour contrast between the penetrant drawn out from a defect and the background surface. In the case of fluorescent dyes, viewing is done in a darkened area under ultraviolet light. The important thing is to look for very small amounts of penetrant that indicate discontinuities.

Post-emulsifiable fluorescent penetrant system

This is the most sensitive of all penetrant systems; it will locate wide and shallow flaws as well as tight cracks. Emulsification is time critical and must be mechanised. Emulsification requires an extra operation, which increases the cost. Also, it requires a water supply and facilities for inspection under black light (UV light).

Solvent-removable fluorescent penetrant system

This employs a procedure similar to that used for the post-emulsifiable fluorescent system, except that excess penetrant is removed with a solvent. This system is especially recommended for spot inspection or where water cannot be conveniently used. Sensitivity is similar to water wash.

Water washable fluorescent system

This is the fastest of the fluorescent procedures. It is also reliable and reasonably economical. It can be used for both small and large work pieces and is good on rough surfaces. However, it cannot reliably reveal open shallow flaws. Other limitations are that the inspection must be carried out where there is adequate water supply and where a black light (UV light) can be used.

7.4.3 Magnetic particle testing (MPT)

In order to detect surface defects in welded and other components, liquid penetrant testing or MPT is widely used. In the case of ferromagnetic materials, the magnetic particle technique has been preferred as it is quicker to apply. Because of this advantage over liquid penetrant, it has become customary to specify magnetic particle testing for all ferromagnetic materials.

This method is based on the principle that when a ferromagnetic material under test is magnetised, discontinuities that lie in a direction generally transverse to the field will cause a leakage field around the discontinuity. The procedure adopted for MPT is shown in Fig. 7.3. When finely divided ferromagnetic powder is applied to the surface, either as dry powder or as a suspension in a carrier fluid, some of these particles will be gathered and held by the leakage field. This magnetically held collection of particles forms an outline of the discontinuity and indicates its location, shape and extent.

Magnetising

Test pieces may be magnetised by flowing electric current through them by placing them near or within a coil with electrical current flowing within, or by causing a magnetic field to flow through the test piece. The test method consists of magnetisation of the component, applying magnetic powder or suspension (ink), examination of powder patterns and, if required, demagnetisation of the component. MPT is a sensitive means of locating surface-connected cracks and other discontinuities in ferromagnetic materials. With certain magnetic particle methods, sub-surface discontinuities that are near to the surface may be detected. Indications may be produced at cracks

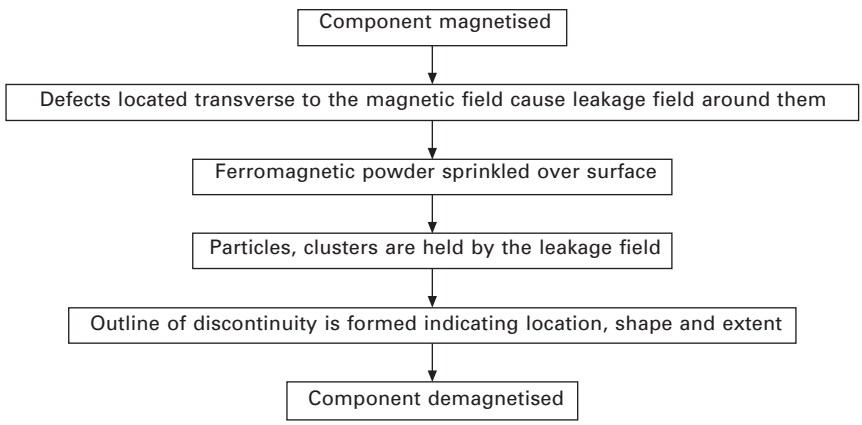

7.3 Sequence of magnetic particle testing.

that are large enough to be seen by the naked eye. Wide cracks will not produce a particle pattern if the surface opening is too wide for the particles to bridge. These discontinuities will be visually detected. If a discontinuity is fine and sharp and close to the surface, such as a long stringer type non-metallic inclusion, a sharp indication will be produced. If the discontinuity lies deeper, the indication is less distinct. Magnetic particle indications are produced directly on the surface of the part, and constitute magnetic pictures of actual discontinuities. There is little or no limitation on the size or shape of the part being inspected. The surface to be tested must be clean and cracks filled with foreign materials can be detected. Surface coatings will reduce the sensitivity of magnetic particle testing. If testing is to be carried out on coated surfaces, the procedure must be validated prior to use.

Magnetisation methods

In MPT, the magnetic particles may be applied to the part prior to magnetisation, while the magnetising current is flowing or after the current has ceased to flow, depending largely on the retentivity of the part. The first two techniques are known as the prior and continuous methods and the third is known as the residual method. The residual method can be used only on materials having sufficient retentivity. Usually, the harder the material, the higher the retentivity. The prior and continuous methods are used on low carbon steels or iron having little or no retentivity.

Magnetising current

Each direct current (DC) and alternating current (AC) is suitable for magnetising parts. The strength, direction and distribution of magnetic fields are greatly affected by the type of current that is used for magnetisation. Fields produced by DC generally penetrate the cross-section of the part, whereas the fields produced by AC are confined to the metal at or near the surface of the part which is commonly known as the skin effect. Therefore, AC should not be used in detecting sub-surface discontinuities. The most satisfactory source of DC is the rectification of AC. Configurations of the magnetisation of parts for inspection of pipe and rod geometries are shown in Figs 7.4 and 7.5, respectively.

Inspection of weldments

Many weld defects are open to the surface and are readily detectable by magnetic particle inspection using prods and yokes (Fig. 7.6). For detection of sub-surface discontinuities, such as slag inclusions, voids and inadequate joint penetration at the root of the weld, prod magnetisation is the best, using

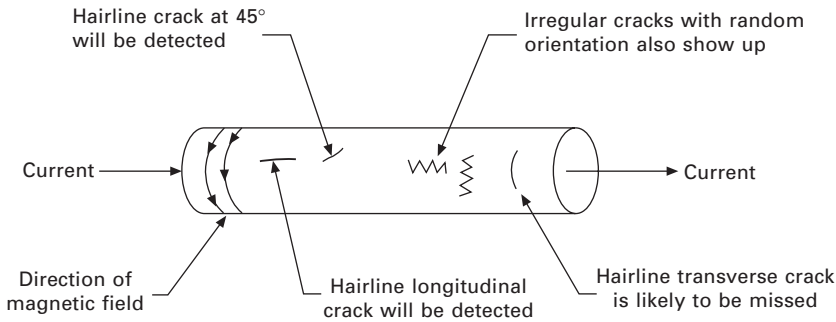

7.4 Circular magnetisation using single turn of coil.

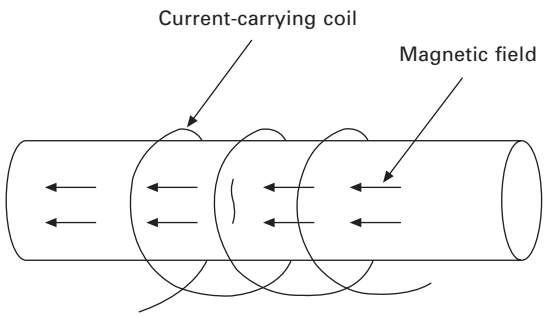

7.5 Longitudinal magnetisation using coil.

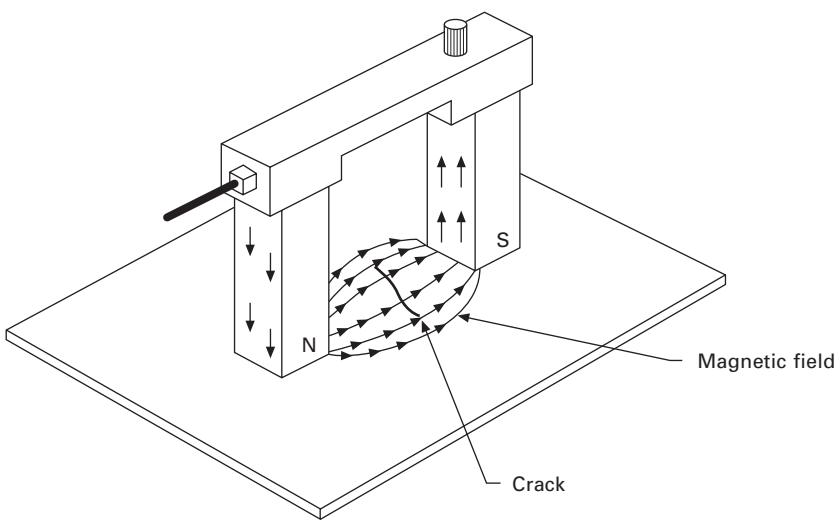

7.6 Use of yoke for magnetisation.

DC. For reliable detection of internal discontinuities, radiography testing (RT) or ultrasonic testing (UT) is preferred. The use of prods is not favoured owing to the possibility of an arcing problem.

Positioning of a yoke with respect to the direction of the discontinuity sought is different from the corresponding positioning of prods. Because the field traverses a path between the poles of the yoke, the poles must be placed on opposite sides of the weld bead to locate transverse cracks. Prods are spaced adjacent to the weld for parallel cracks and on opposite sides for transverse cracks.

For applications in which holding of prod contacts by hand is difficult or tiring, prods incorporating magnetic clamps or faces that hold the prods magnetically to the part to be tested are available. The prods carrying the magnetising current are held firmly to the part by an electromagnet. Both prods may be attached by the magnets, or one of the prods may be held magnetically and the other by hand.

The detectability of sub-surface discontinuities in butt welds made between relatively thin (≤ 4 mm) plates can often be improved by positioning a direct current yoke on the side opposite the weld bead. Magnetic particles are applied along the weld bead. An improvement is achieved because of the absence of extraneous leakage flux that normally emanates from the yoke's pole pieces.

AC yokes are preferred for detection of surface breaking discontinuities. The effectiveness of the DC and permanent magnet-based yokes is reduced on materials over 10 mm in thickness and doubtful on materials over 16 mm in thickness.

Demagnetisation after inspection

All ferromagnetic materials after having been magnetised will retain some magnetic field, which is known as the residual magnetic field. This field is negligible in magnetically soft materials. However, in magnetically hard materials, it may be comparable to the intense fields associated with the special alloys used for permanent magnets. The ease of demagnetisation depends upon the type of material. Metals having high coercive force are difficult to demagnetise. There are many reasons for demagnetising a part after magnetic particle inspection. For example, during subsequent machining of a part, chips may adhere to the surface being machined and adversely affect surface finish, dimensions and tool life. During electric arc welding operations, strong residual magnetic fields may deflect the arc away from the point at which it should be applied.

Methods of demagnetisation

- *Thermal method:* A ferromagnetic component can be demagnetised if it is raised above its Curie temperature (for example 1023 K for iron) but

often this is not practicable or convenient. This can be employed where post weld heat treatment (PWHT) to a temperature above the Curie temperature follows magnetic particle inspection.

- *AC circular field demagnetisation:* This is useful for large parts. This is similar to the AC coil method in that the field reversal is provided by the cyclic nature of the current. In this method, the desired field is obtained by passing current through the part where the current intensity is gradually reduced to zero. Parts magnetised with DC current require demagnetisation by DC current. The direction of the DC current must be reversed, and with each reversal, the magnitude of the current is marginally reduced. Most modern equipments automate this process.
- *AC or DC yoke method:* This is suitable for parts having very high coercive force. Some yokes are similar in operation to the AC coil method whereby the part is passed between pole faces and then withdrawn. A modified version of this uses a solenoid-type electromagnet.

7.4.4 Eddy current testing

The eddy current technique (ECT) is based on the principle of electromagnetic induction. The procedure is shown schematically in Fig. 7.7. It is a technique based on the induction of electrical currents in the material being inspected and observing the interaction between test currents and the material, and is used to identify or differentiate between a wide variety of physical, structural

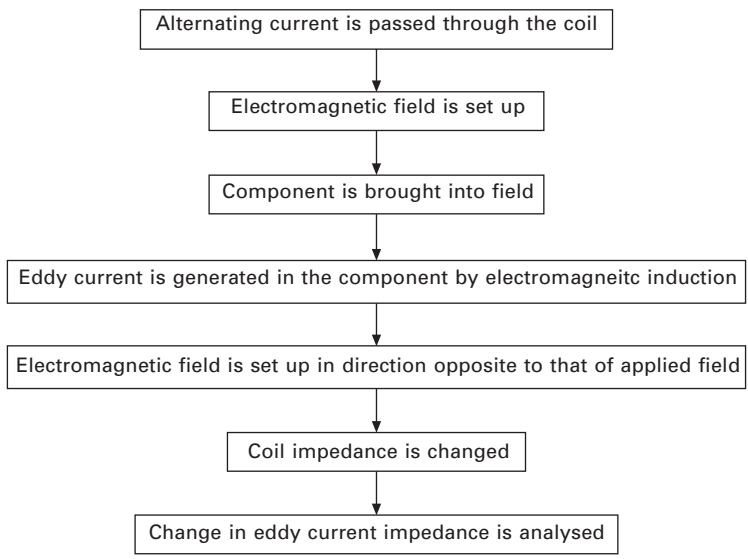

7.7 Sequence of events in eddy current testing.

and metallurgical conditions in electrically conductive materials and metal parts. Being based on the principle of electromagnetic induction, the technique does not require direct electrical contact with the part being tested. The eddy current method is adaptable to high speed inspection and, because it is non-destructive, it can be used to inspect an entire production run if desired. The method is based on indirect measurement and the correlation between the instrument readings and the structural characteristics and the serviceability of the parts being inspected must be carefully and repeatedly established. It is used extensively to identify or differentiate between a wide variety of physical, structural and metallurgical conditions in welded stainless steel tubes. It has also been successfully used to locate defects such as lack of fusion, incomplete penetration, cracks, oxidation and changes in chemical composition and hardness of welds. One of the difficulties in using electromagnetic testers is that the instruments must be made to measure the desired weld properties without interference from non-critical characteristics. Many improvements in the newest electronic instruments have made electromagnetic testing equipment more suitable for evaluation of production welds.

The test coil is the main link between the test instrument and the test object and serves two main functions, the first to establish a varying electromagnetic field, which induces eddy currents within the test objects, and the second to feed the response due to the electromagnetic field to a signal analysis system. The part to be inspected is placed within or adjacent to an electric coil in which an AC is flowing. This AC, called the exciting current, causes eddy currents to flow in the test specimen as a result of electromagnetic induction. These currents flow within closed loops in the test specimen, and their magnitude and timing depends on: (a) the electrical properties of the test specimen, (b) the original or primary field established by exciting currents, and (c) the electromagnetic fields established by currents flowing within the part.

The electromagnetic field in the part and surrounding the part depends on both the exciting current from the coil and eddy currents flowing in the part. The change in eddy current flow pattern in the inspected part with coil configuration is shown in Fig. 7.8. The flow of eddy currents in the part depends on the electrical characteristics of the part, the presence or absence of flaws or other discontinuities in the part and the total electromagnetic field within the part. Since eddy currents are induced by a varying magnetic field, the magnetic permeability of the material being inspected strongly influences the eddy current response. Consequently, the techniques and the conditions used for inspecting magnetic materials differ from those used for inspecting non-magnetic materials. However, the same factors that may influence electrical conductivity (composition, hardness, residual stress and flaws) also may influence magnetic permeability. Thus eddy current inspection can be applied to both magnetic and non-magnetic materials.

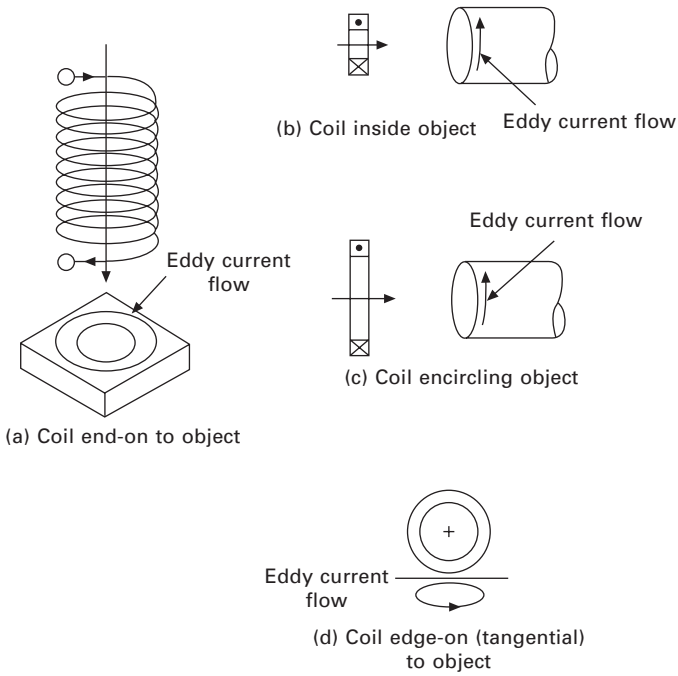

7.8 Variation of eddy current flow with different coil arrangements.

Basically, any discontinuity that appreciably alters the normal eddy currents can be detected by eddy current inspection. With encircling coil inspection of either solid cylinders or tubes, surface discontinuities having a predominantly longitudinal dimensional component are readily detected. When discontinuities of the same size are located beneath the surface of the part being inspected at progressively greater depths they become increasingly difficult to detect. The depth at which sub-surface discontinuities can be detected is dependent on material conductivities, test frequency and probe size.

Weld inspection

For complete evaluation of welds, it is essential to verify the alloy composition. There is always a possibility that the wrong welding rod or wire is accidentally used for a critical weld and this may cause a premature failure of the weld. Many types of ECT instruments are currently available for sorting various types of welding consumables and the weld metal, provided their electrical conductivity or magnetic permeability values are sufficiently different. This is possible; however, verification of welding consumables before and after welding is more accurately achieved with X-ray fluorescence alloy identification equipment.

Longitudinal welds in welded tubing and pipes can be inspected for discontinuities using ECT with an external encircling coil and a probe-type detector coil. The inspection is performed by passing the tube or pipe longitudinally through the primary energising coil, causing the probe-type detector coil to traverse the longitudinal weld from end to end. The primary coil is energised with AC at a frequency that is suitable for the part being inspected and induces eddy currents in the tube or pipe.

For the inspection of ferromagnetic products, a DC magnetic coil is located concentrically around the primary energising coil. The DC coil is energised at high current levels to magnetically saturate the tube or pipe. This improves the penetration of the eddy currents and cancels the effect of magnetic variables. Owing to circumferential orientation of the eddy current flow, this type of inspection is effective in detecting most types of longitudinal weld discontinuities such as open welds, weld cracks, penetrators and pinholes.

It is important that the longitudinal weld be carefully positioned under the detector coil before the pipe is passed through the tester. It is essential to provide good scanning equipment so that, as the pipe is propelled longitudinally, the longitudinal weld will always be located under the detector coil.

ECT of in-service welds is now common in all industries. The equipment and the methodology are described in BS 1711.

7.4.5 Ultrasonic testing

UT is an NDT method in which sound waves of high frequency (in MHz) are introduced into the material being inspected to detect internal flaws (defects) and to study the properties of the material. The sound waves travel into the material with some loss of energy due to attenuation and are reflected at interfaces. The reflected beam (in most of the applications) is detected and analysed to define the presence and location of defects and for quantitative evaluation.

The degree of reflection depends largely on the physical state of matter on the opposite side of the interface and on specific physical properties. The sound waves are almost completely reflected at metal–gas (air) interfaces, while partial reflection occurs at metal–liquid or metal–solid interfaces. The reflected energy depends mainly on the ratios of certain properties of the matter (e.g. impedance = density × velocity). Defects such as cracks, shrinkage cavities, lack of fusion, pores, and bonding faults can be easily detected by this method. Inclusions and other inhomogeneities in the metal can also be detected due to partial reflection or scattering of the ultrasonic waves. This widely used NDT method has many applications such as defining bond characteristics, measurement of thickness of components, measurement of corrosion and determination of physical properties, structure, grain size and elastic constants.

Ultrasonic inspection is mostly carried out at frequencies between 1 and 25 MHz. The inspection system includes:

- an electronic flaw detector having a sweep circuit, pulse, generator, clock circuit and a display (liquid crystal or other);
- a transducer, also called a probe or search unit, having a piezoelectric crystal that emits a beam of ultrasonic waves when bursts of alternating voltages are applied to it;
- a couplant to transfer energy of the ultrasonic waves to the test piece (material).

Ultrasonic inspection is used for quality control and materials inspection in many industries. In-service ultrasonic inspection for preventive maintenance is used for detecting impending failure of rail-road rolling stock axles, mill rolls, earth-moving equipment, mining equipment, welded pipelines in chemical and nuclear plants, boilers, pressure vessels, nozzle welds, etc.

For successful application of ultrasonic inspection, the inspection system must be suitable for the type of inspection being done and the operator must be sufficiently trained and experienced. If either of these prerequisites is not met, there is a possibility of gross error in the interpretation of the results.

- *Ultrasonic flaw detector:* The most common technique employed is the pulse echo technique. The basic equipment comprises an ultrasound pulse generator, a receiver, and its amplification and display system. Depending on the display of information, pulse echo equipment can be subdivided into three groups, A-scan, B-scan and C-scan.
- *Test techniques:* Techniques of ultrasonic testing are either of the contact type or the immersion type. In the contact type, the probe is placed in direct contact with the test system with a thin liquid film used as couplant for better transmission of ultrasonic waves into the test specimen. In the immersion method, a waterproof probe is used at some distance from the test specimen and the ultrasonic beam is transmitted into the material through a water path or water column. Contact techniques are normal beam techniques, angle beam techniques and surface wave techniques. Immersion testing techniques are mostly used in the laboratory and for large installations performing automatic ultrasonic testing.

UT of weldments

There are two aspects that distinguish UT of welds from UT of other products such as forgings, castings and pipes. They are that (a) the area of interest is well defined and limited (weld and HAZ) and (b) a specific set of defects is considered whose probable location and orientation is known. Most welds

fall into one of the following categories: (1) butt weld, (2) tee weld and (3) nozzle weld. Various butt weld configurations are shown in Fig. 7.9.

A typical UT procedure for the examination of weld root and weld body is shown in Fig. 7.10. A typical pattern of indications where a weld defect is encountered is shown in Fig. 7.11, while Fig. 7.12 gives the methods for angle beam examination of various locations in a single V weld joint. The method of examination for other joint configurations such as double 'V', nozzle and tee joints is detailed in Fig. 7.13.

Welds of certain materials such as austenitic stainless steel and nickel-based alloys pose serious problems for UT. These problems are primarily due to the acoustic anisotropy of these materials and the cast structure of the weld. Heavy scattering of the ultrasonic beam, false indications and wrong judgement of position and size of the defect can be encountered in these materials. These result from heavy attenuation of the beam as well as 'noise' signals reaching the probe. The combined effect results in loss of sensitivity and low signal to noise ratio. These problems are greatly minimised by the utilisation of low frequency and longitudinal angle beam probes for such applications.

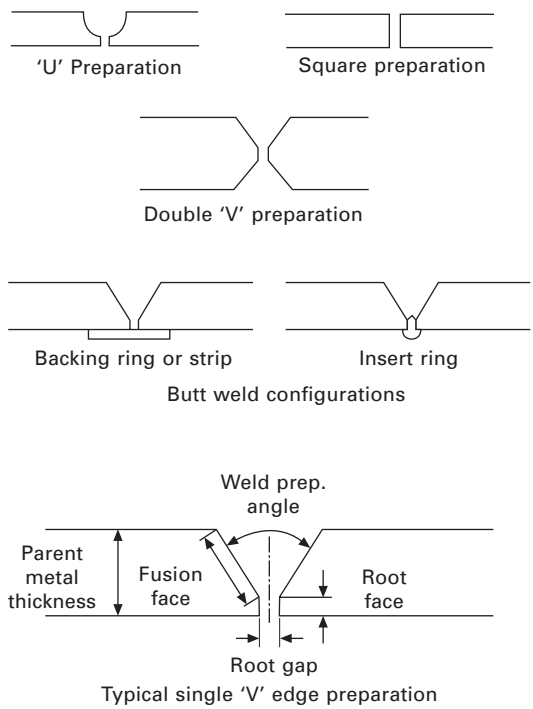

7.9 Various butt weld configurations and terminology.

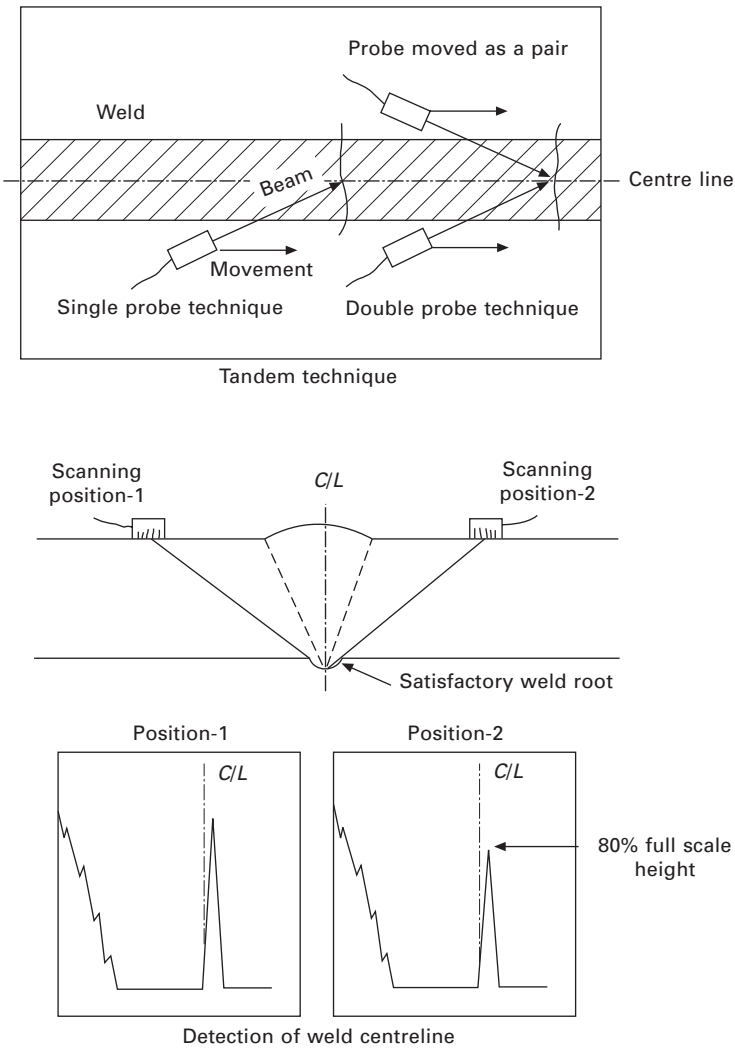

7.10 Ultrasonic test scanning methods for weld inspection.

7.4.6 Radiographic testing

Radiography is based on the differential absorption of short wavelength radiations such as X-rays and gamma rays on their passage through matter because of differences in density and variations in thickness or differences in absorption characteristics. The principle of radiographic examination is shown in Fig. 7.14. A shadow projection is obtained on a detector which is normally a grey level image with varying grey tones depending on the quantum of radiation received at that point. The source of radiation can be X-rays, gamma

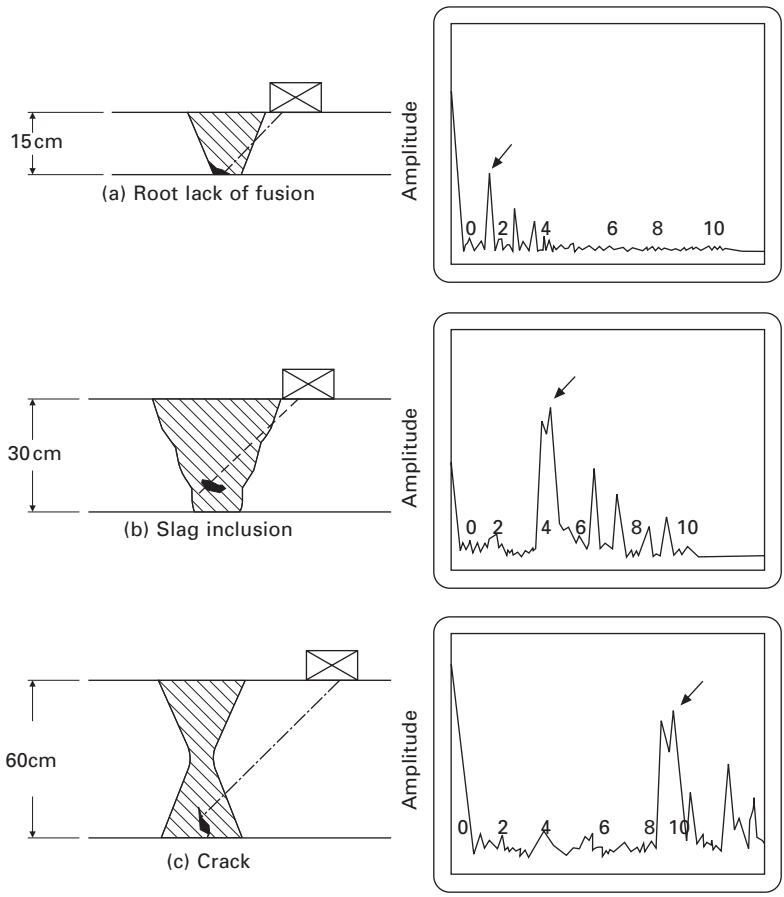

7.11 Typical cathode ray tube (CRT) patterns from weld defects.

rays, neutrons, protons or electrons. X and gamma rays are the most commonly used source of radiation. The detector can be radiographic films, image intensifiers or scintillator screens/counters. However, double-coated, fine-grain, high-contrast industrial X-ray films are the most widely used means of detecting the transmitted radiation. Conventional radiography is the most widely used method for the inspection of welds. Radiography is the best method for the detection of volumetric defects such as porosites, slag inclusions and other defects such as crater cracks, lack of penetration and incomplete fusion.

Geometric factors in radiography

Since a radiograph is a two-dimensional representation of a three-dimensional object, the radiographic images of most test pieces are somewhat distorted in

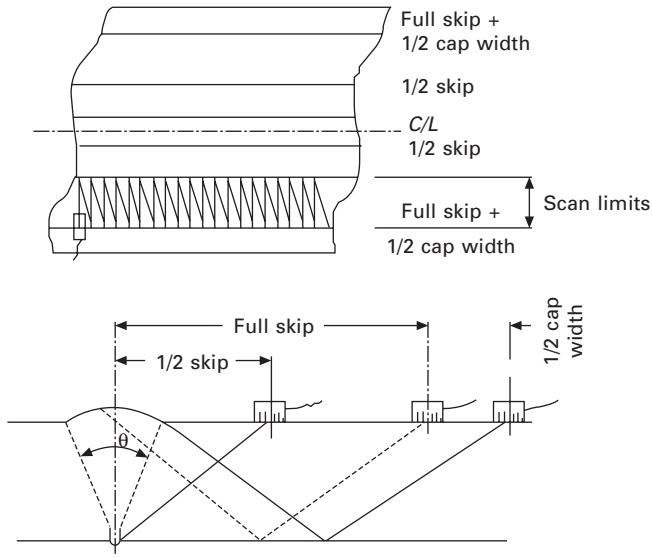

Selection of probe angle for the weld body examination depends upon the weld preparation angle
probe angle = 90° – θ/2
where θ is the weld preparation angle

7.12 Angle beam examination of a single 'V' joint weld.

size and shape as compared to the actual test piece. The severity of distortion depends primarily on source size (focal spot size for X-ray sources), source to object and source-to-film distances and position and orientation of the test piece with respect-to-source and film.

In conventional radiography, the position of a flaw within the volume of a test piece cannot be determined exactly with a single radiograph, since depth parallel to the radiation beam is not recorded. However, techniques such as stereo-radiography, tomography and double-exposure parallax methods can be used to locate flaws more exactly within the test piece volume.

Sources

Radiography has been used for years in evaluating welds and standard radiographic techniques have been well documented. Today we have X-ray machines with a maximum output voltage of 450 kV and 15 mA tube current. Such machines can be used for the examination of steel up to thickness of 120 mm. Apart from X-rays, isotopic sources emitting gamma rays also find extensive application. The main advantage of a gamma ray source is its simplicity of apparatus, compactness and portability. It does not require cooling of the power supply and is thus ideal for field applications. However,

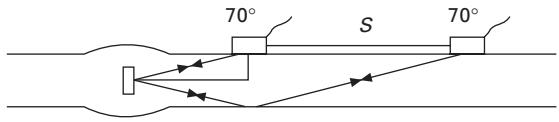

Root scan for double vee welds
$S = 2(t - d) \tan \theta$
where θ = probe angle, S = distance between probe indices, d = depth of aiming point and t = specimen thickness

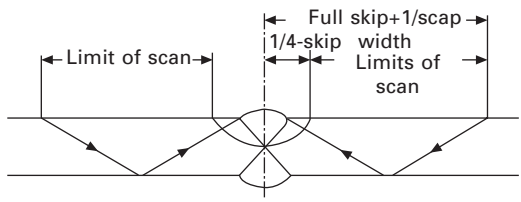

Scan limits for double vee-weld

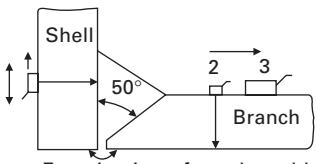

Examination of nozzle weld

Examination of nozzle welds
Scan 1 & 2 to determine thickness of the shell and branch, lamination in shell and branch, tack of fusion of shell wall and weld body defects
Scan 3 – lack of side wall fusion and weld body defects

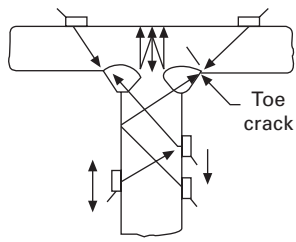

Examination of T-weld

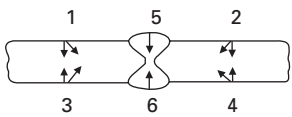

Scanning positions for double 'V' weld

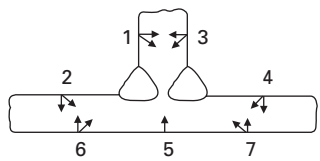

Scanning position for partial penetration nozzle weld

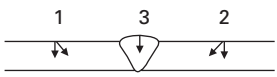

Scanning positions for single 'V' weld

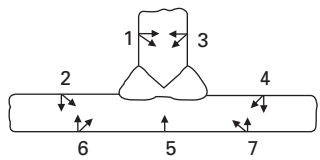

Scanning position for full penetration nozzle weld

7.13 Normal and angle beam examination of various weld configurations.

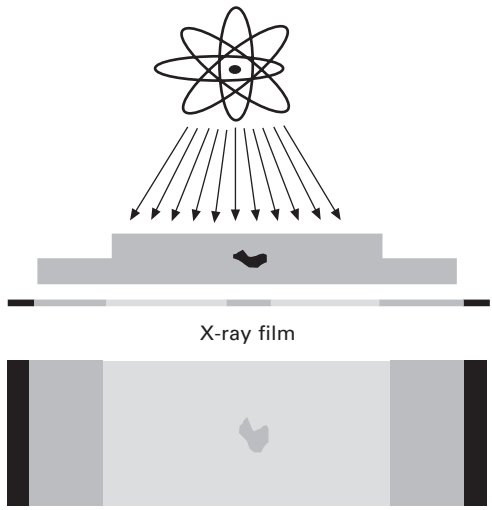

7.14 Principle of radiographic testing.

the main disadvantage of the gamma ray source is that it decays with time and hence requires replacement. Commonly used gamma sources are cobalt-60, iridium-192 and selenium-75.

Gamma ray sources are housed in protective containers made of lead, depleted uranium or other dense materials such as tungsten that absorb gamma rays, thus providing protection from exposure to radiation. Two types of containers are generally used. One type incorporates a conical plug that is swung away from the enclosed radioactive source to permit radiation to escape. This type is referred to as a radioisotope camera. The second type incorporates a remote controlled mechanical or pneumatic positioner that moves the encapsulated radioactive source out of the container and into a predetermined position where it remains until exposure is completed. The source is then returned to the container again by remote control. Remote control of the positioner allows the operator to remain at a safe distance from the source while manipulating the capsule out of and into the protective container.

Apart from improved equipment, far more is known today about the art of making good radiographs, the factors which control contrast and sensitivity and the limitations of radiography in what it can detect. Various codes have been evolved for the evaluation of radiographs. Sets of reference radiographs showing the appearance of weld and casting defects of different metal thicknesses are commercially available which are extremely valuable for instructional purposes also. ASTM E 390 deals with difference radiographs for steel welds. The International Institute of Welding has also brought out such reference radiographs for steel weldments up to 125 mm.

Radiographic sensitivity

The sensitivity and quality of radiographs is normally judged by image quality indicators (IQI). Both wire and plaque type indicators are available today. These IQIs are normally placed on the source side of the weld and should be of the same material as the weld. The quality of the radiographs is always quoted in terms of the amount of detail discernible in the image of the IQI. The sensitivity depends on the radiographic technique, the type of IQI used and the specimen thickness.

ASTM penetrameters of plaque and wire type are widely used, as shown in Fig. 7.15. In UK and other European countries wire type penetrameters are used. The plaque type penetrameters as per ASTM E-1032 have 2T, 1T and 4T diameter holes. In a wire type penetrameter, the wires are arranged by diameter ranging from 0.1 mm to 3.2 mm, and all wires are of the same length. The wire material is chosen to match the material to be tested. In normal use, specifications will indicate the minimum diameter of wire to be seen on a radiograph or a 2T hole, 1T hole or 4T hole depending on the application. Typical radiographic sensitivities to be achieved in various applications range from 0.5% to 4% of wall thickness.

Industrial X-ray films

In general, the films consist of an emulsion–gelatin containing a radiation-sensitive silver compound and a flexible transparent blue-tinted base. Emulsion on both sides (0.025 mm (0.001 inch) thick) doubles the amount of radiation-sensitive silver compound and thus increases the speed. Where highest visibility of detail is required, film with emulsion on one side is preferred. When X-

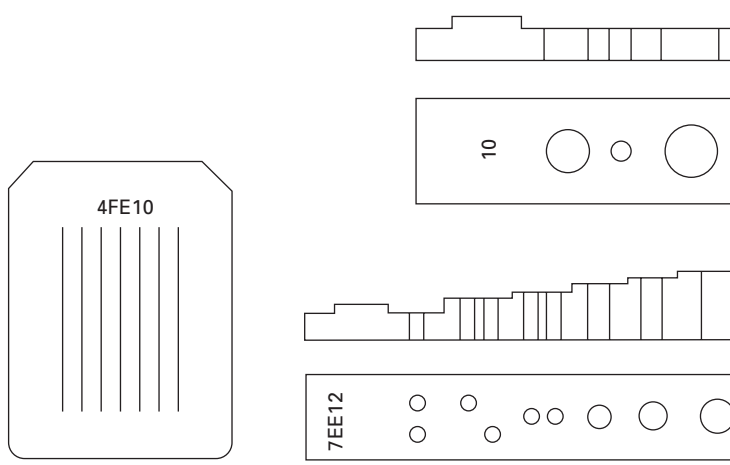

7.15 Designs for image quality indicator.

rays or gamma rays strike the grains of the sensitive silver compound in the emulsion, a change takes place in the physical structure of the grains. This change is of such a nature that it cannot be detected by ordinary physical methods. However, when the exposed film is treated with a chemical solution (called a developer), a reaction takes place, causing the formation of black metallic silver. It is this silver suspended in the gelatin on both sides of the base that constitutes the image of the object. The selection of a film for radiography of any particular part depends on the thickness and material of the specimen and on the voltage range of the available X-ray machine. In addition, the choice is affected by the relative importance of high radiographic quality or short exposure time.

If high quality is the deciding factor, a slower and hence fine-grained film should be used. If short exposure times are essential, a faster film (or film-screen combination) can be used. Direct exposure films can be used with or without lead screens depending upon kV, time and geometry of the object. Fluorescent intensifying screens must be used in radiography requiring the highest possible photographic speed.

Film viewing

To assess the radiograph and the sensitivity achieved, the radiograph is placed on an illuminated screen of appropriate brightness (luminescence) and the film is suitably masked to eliminate glare emanating from around the film or any part of the film having particularly low density. The diameter of the smallest wire or drilled hole which can be detected with certainty is taken as a measurement of the attained sensitivity. Good film viewing conditions are essential as it is possible to overlook information on the radiograph because of too high a film density or low illuminator luminance. The importance of relating illuminator luminescence to film density has been recognised by the International Institute of Welding (IIW) Commission V-A (Radiography) which has brought out a recommendation that an illuminated radiograph should not be less than 30 and whenever possible 100 cd m^{-2} or greater. This minimum value requires illuminator luminance of 300 for a film density of 1, 3000 cd m^{-2} for a film density of 2 and 30 000 cd m^{-2} for a film density of 3.

Radiographic defect evaluation

Generally, by radiography, one can recognise the nature of a defect and also measure its effective length and width parallel to the plane of the film but the through-thickness dimension (height) is less easy to determine. The distance of a defect from the surface can be found by stereometric methods. In principle, it is possible to measure the height of a defect from the density of the image on a radiograph using a microdensitometer. The densities determined from

the microdensitometer trace can be converted into thickness either by absolute calculations using the film characteristics and exposure curves, or by having an appropriate step wedge on the radiograph alongside the weld.

Halmshaw [6] has found that for general weld defects occupying 10–30% of the thickness, this method can be applied with an accuracy of 8%. However, this method has not been found suitable for planar defects such as cracks. While defects such as porosities, lack of fusion, lack of penetration, voids, inclusions, etc. in welds and hot tears, shrinkage cavities, etc. in castings can be easily detected, the detectability of cracks by radiography is influenced by the position and size of the crack, the incident angle of X-rays, the distance between the film and the crack, size of the focal spot, sensitivity of films, screens and so on. Conventional radiography is being widely used for the inspection of a variety of weldments, castings and complete assemblies in various industries.

Applications

Radiography is widely used in evaluating different types of weld joints and configurations for their integrity.

- *Butt weld:* Butt joints on the flat plates are usually made with edge preparation of single 'V', double 'V' or square. Inspection techniques for butt welds with ASTM penetrameter are shown in Fig. 7.16.
- *Fillet welds:* Fillet welds are generally made with square or level edge preparation. The exposure set up for different fillet joints are shown in Fig. 7.17.
- *Fusion welds on pipes and cylindrical objects:* Depending upon the size and accessibility on either side of the pipe, the following techniques are recommended:
  - *Single wall penetration:* Single wall penetration method with source inside and film outside or vice versa is shown in Fig. 7.18. The ideal position to locate the source is the centre of the pipe which enables coverage of the entire circumferential weld in a single panoramic exposure.

    Butt welds of thick-walled pipes are radiographed with source located either in the centre or eccentrically. To facilitate radiographic inspection of thick-walled steam pressure pipe welds, usually a hole is provided adjacent to the circumferential weld for the insertion of radioisotope inside the pipe (Fig. 7.18d).
  - *Double wall penetration:* Both film and the source are placed external to the pipe when there is no access to the inside of the pipe. Here the radiation beam passes through both the walls but only the bottom weld image is evaluated (Fig. 7.19).

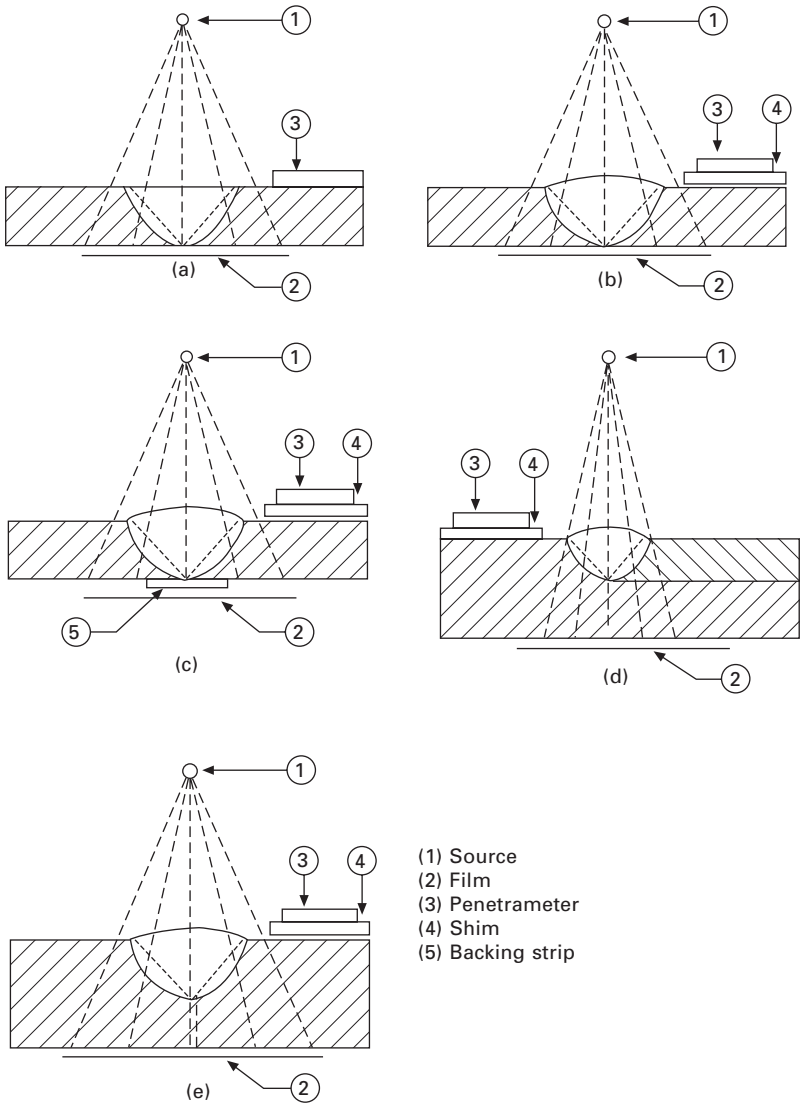

7.16 Radiography configurations of butt welds.

- *Double wall single image:* This technique is used for pipes with an outer diameter > 89 mm. The source is either placed on the top of the weld (superpositioned technique) or it is slightly offset. Degree of offset depends on the source–film distance (SFD) chosen. The radiation source is placed at a minimum SFD compatible with source size and wall thickness of the pipe. The film is wrapped on the portion further from the radiation source. Overlapping of the images is avoided by

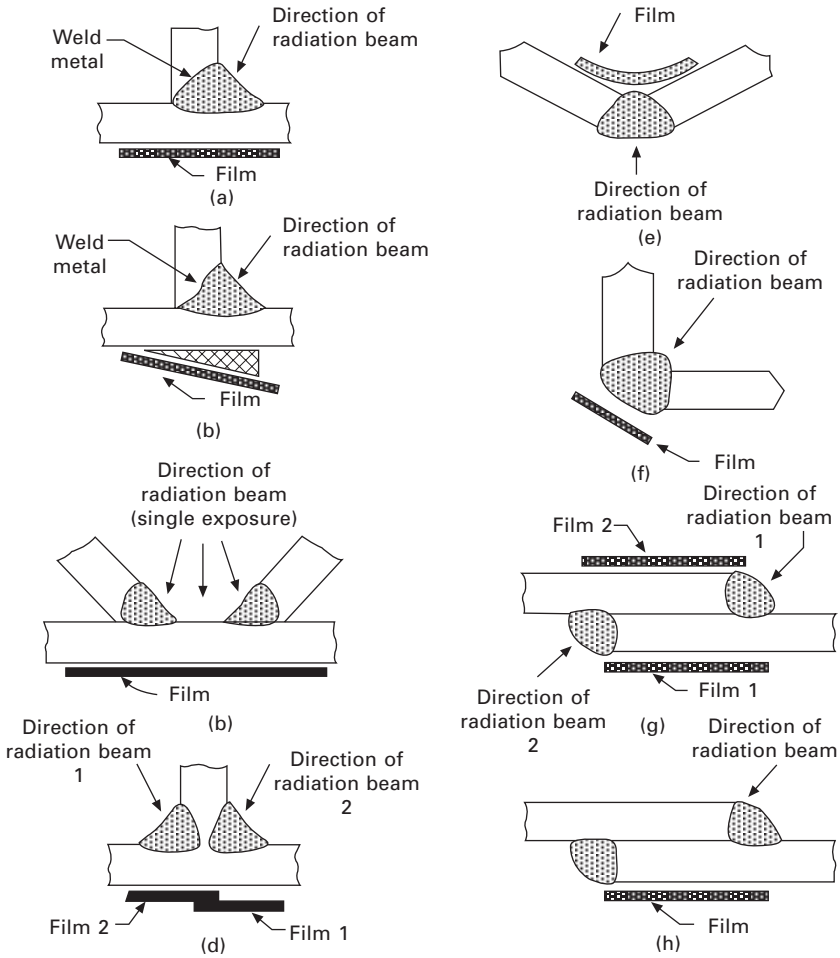

7.17 Direction of radiographic exposure for various fillet weld configurations: (a) single-fillet T joint, (b) single-fillet T joint with equalising wedge, (c) two adjacent single-fillet T joints radiographed simultaneously, (d) double-fillet T joint, (e) corner joint with film positioned at the inside surface, (f) corner joint with film positioned at the outside surface, (g) and (h) alternative views for double welded lap joint.

placing the source offset by about 10° from the plane of the weld.

- *Double wall double image:* This technique is specially suited for smaller pipes up to 89 mm diameter. The source is placed offset to the weld, the inclination being 10 to 15° to avoid the overlap of top and bottom weld images. A minimum of two exposures are taken, the second one after rotating the weld through 90°. Both the top and bottom images are recorded on film with suitable separation.

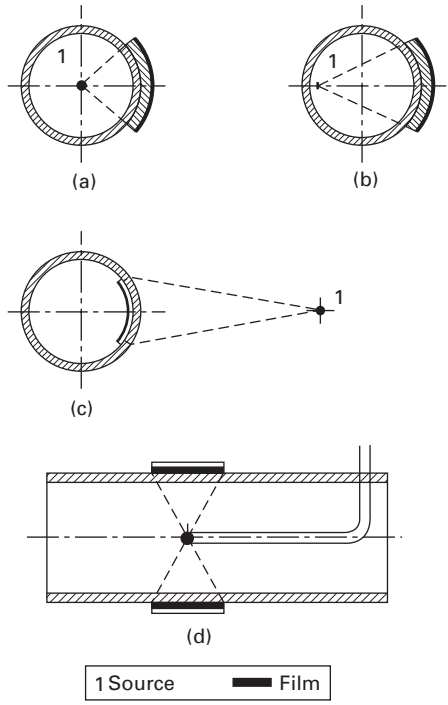

7.18 Single wall penetration.

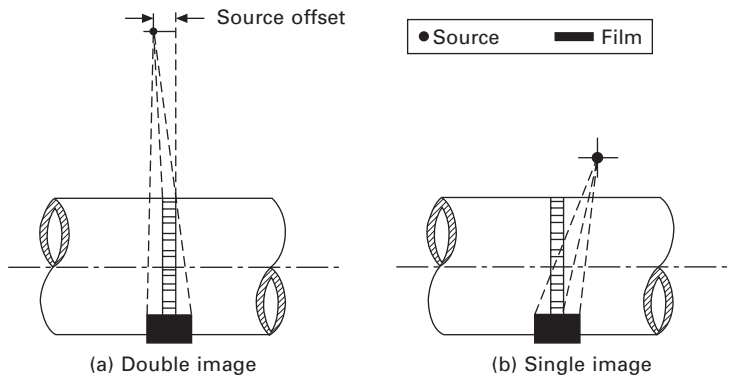

7.19 Double wall penetration.

7.4.7 Leak testing

Leaks are special types of flaw that can have tremendous importance where they influence the safety or performance of engineering systems. Leak testing is performed for three basic reasons:

1. To prevent material leakage loss, which interferes with system operation.
2. To prevent environmental contamination hazards caused by accidental leakage.
3. To detect unreliable components and those whose leakage rates exceed acceptance standards.

The end purpose of leak testing is to ensure reliability and serviceability of components and to prevent premature failure of systems containing fluids under pressure or vacuum.

The term 'minimum detectable leak' refers to the smallest hole or discrete passage that can be detected and 'minimum detectable leakage rate' refers to the smallest detectable fluid-flow rate, generally known as sensitivity of the test system. The sensitivity of the instrument is the amount of leakage required for a leak testing instrument to give a minimum detectable signal. The instrument sensitivity is independent of test conditions, but when an instrument is applied to a test, the sensitivity of the test depends on the existing conditions of pressure, temperature and fluid flow.

Leak testing SI units

The leak is measured by how much leakage it will pass under a given set of conditions, as leakage will vary with conditions. At a given temperature, the product of pressure and volume of a given quantity of gas is proportional to its mass. Therefore, leakage rate is often expressed as the product of some measure of pressure and volume per unit of time. The basic SI units used in leak testing are: pressure – pascal (1 N/m^2), volume in m^3 and time in seconds.

The fluid quantity can thus be expressed as pascal cubic metre (Pa m^3) and the fluid leakage rate as pascal cubic metre per second (Pa m^3/s) or in terms of Std. cc/s (0.1 Pa. m^3/s). The SI unit for vacuum is the pascal (132 Pa is 1 mm of Hg = 1 torr).

Types of leak

There are two basic types of leak – real leaks and virtual leaks. A real leak is an essentially localised leak – that is, a discrete passage through which fluid may flow. Such a leak may take the form of a tube, a crack, an orifice, etc. The flow can be of permeation type or diffusion type. Virtual leaks are leaks that involve the gradual desorption of gases from surfaces or components within a vacuum system.

Helium leak testing

Among various leak testing methods, helium leak testing plays an important role for weld inspection especially in thin structures [7].

- *Classical helium spray test:* A helium spray test involves evacuation of the part to be tested, connection to the helium leak detector and spraying of helium around the outer surfaces of the part. Helium will penetrate through leaks in the wall and be transported to the analyser (Fig. 7.20). Modern leak detectors combine vacuum pumps with a gas analyser in a compact unit.

  The response time of the analyser is dependent on the volume of the part to be tested and the effective helium pumping speed of the test set up. The effective helium pumping speed depends upon the helium pumping speed of the leak detector and the conductance of the part and the pipework connecting it to the leak detector. A typical commercially available leak detector has its maximum sensitivity at comparatively low pressures of less than 10^{-2} mbar.

  When long thin tubes are pumped down to the ultimate pressure of the leak detector, gas flow is in the molecular flow regime. In this flow regime the conductance of the tube is much smaller than for laminar flow which results in extended measuring times. Signal intensity can be drastically reduced by a very broad gas velocity distribution.
- *Spray test with carrier gas:* In order to achieve a fast response time and high sensitivity the leak test is best performed in the laminar flow regime. Introduction of a carrier gas provides a fast and active gas transport through the gas line to the leak detector. A typical test set up is shown in Fig. 7.21.
- *Spray test with and without carrier gas – a comparison:* Figure 7.22 shows the response time differences between a free volume of 1 litre and two gas lines with an internal diameter of 4 mm and a length of 7 m or 20 m respectively. In all measurements the shut-off valve of a calibrated leak was opened when the background of the leak detector reached a value of 10^{-9} mbar l/s. Transport of the calibration gas was very fast through the open volume and showed almost instantaneous signal response. In contrast the signal response time with the gas line was comparatively long.

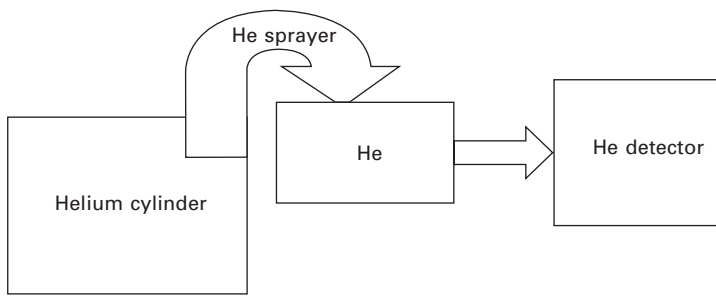

7.20 Helium spray test.

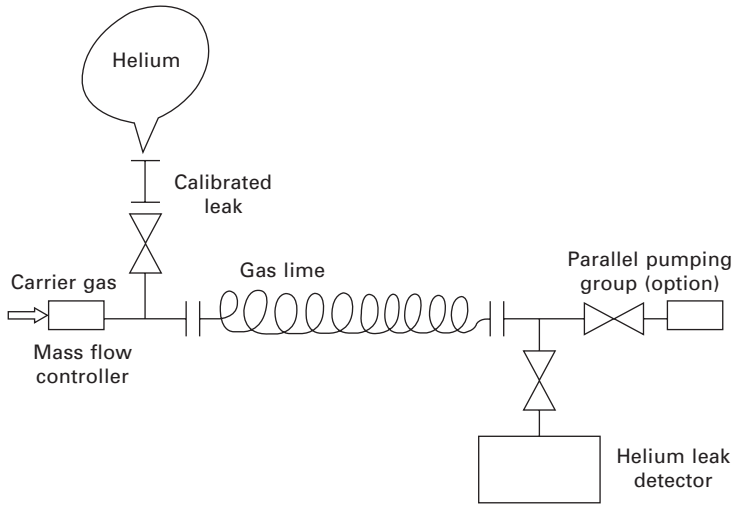

7.21 Helium spray test using carrier gas.

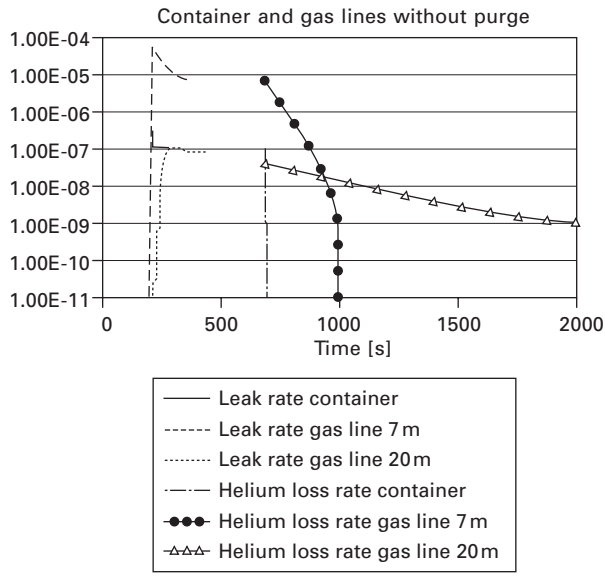

7.22 Signal response time and signal decay time of a 1 litre volume compared with two gas lines.

7.5 Semi-destructive testing: metallography

Metallography is the science and art of preparing a metal surface for analysis by grinding, polishing and etching to reveal microstructural constituents. After preparation, the sample can easily be analysed using optical

or electron microscopy. A skilled technician is able to identify alloys and predict material properties, as well as processing conditions by metallography alone. Capabilities include surface evaluation, grain size determination, intergranular attack, intergranular oxidation, macro-examination, micro-examination, solderability evaluation, weld examination, fractography examination, inclusion counts, eutectic melting examination and phase volume fraction determination.

7.5.1 Preparing metallographic samples

Metallographic samples are cut in required size and typically 'mounted' in a phenolic or epoxy resin. Mounting a sample provides a safe and ergonomic way by which to hold a sample during the grinding and polishing operations.

After mounting, the sample is wet sanded to reveal the surface of the metal/weld. The sample is successively ground with finer and finer grades of sandpaper to remove scratches from the sample surface. After grinding the sample with 1000 grit or finer sandpaper, polishing can begin. Typically, a sample is polished with slurry of alumina silica, or diamond on a low cloth to produce a scratch-free mirror finish. After polishing, the microstructural constituents of the sample are revealed by using a suitable chemical or electrolytic etchant. The ideal etchant is dependent on sample composition, and the microstructural feature(s) of interest.

Analysis

Prepared samples are most often inspected using an inverted metallographic microscope. This type of microscope is sufficient for magnifications less than 1000×. If a sample must be observed at higher magnification, it will be examined by a scanning electron microscope (SEM). When equipped with energy dispersive spectrometry, SEM analysis is able to determine the composition of the sample.

7.6 Hardness testing

Hardness is the characteristic of a solid material, not a fundamental physical property, expressing its resistance to permanent deformation [8,9]. It is determined by measuring the permanent depth or width of a test indentation. When using a fixed force (load) and a given indenter, the smaller the indentation, the harder the material. While the concept is extremely simple, the indentation hardness value is obtained by using one of over 12 different test methods. Hardness can be measured on the Mohs scale or various other scales.

There are three principal operational definitions of hardness: scratch hardness, rebound, dynamic or absolute hardness, and indentation hardness.

7.6.1 Scratch hardness

In mineralogy, *hardness* commonly refers to a material's ability to penetrate softer materials. An object made of a *hard* material will scratch an object made of a *softer* material. Scratch hardness is usually measured on the Mohs scale of mineral hardness. Pure diamond is the hardest known natural mineral substance and will scratch any other material. Diamond is therefore used to cut other diamonds; in particular, higher-grade diamonds are used to cut lower-grade diamonds.

Estimates from proposed molecular structure indicate the hardness of beta carbon nitride should also be greater than diamond. This material has not yet been successfully synthesised.

7.6.2 Rebound hardness

Also known as *dynamic* or *absolute hardness*, rebound hardness measures the height of rebound of an indenter dropped onto a material using an instrument known as a scaleroscope. One scale that measures rebound hardness is the Bennet Hardness Scale. The LEEB hardness scale as used by various devices (EQUOTIP) is also popular and leaves a smaller underestimation than the scaleroscope. Conversion tables are available to convert LEEB hardness to other common scales. Newer equipment does this electronically.

7.6.3 Indentation hardness

Primarily used in engineering and metallurgy, indentation hardness seeks to characterise a material's hardness, i.e. its resistance to permanent and, in particular, plastic deformation. It is usually measured by loading an indenter of specified geometry onto the material and measuring the dimensions of the resulting indentation.

There are several alternative definitions of indentation hardness. The most common and industrially important methods of measuring hardness are:

- Rockwell hardness test (HR), principally used in the USA;
- Brinell hardness test (HB); and
- Vickers hardness test (HV), which has one of the widest scales.

There is, in general, no simple relationship between the results of different hardness tests. Though there are practical conversion tables for hard steels, for example, some materials show qualitatively different behaviours under the various measurement methods.

7.6.4 Rockwell hardness

The Rockwell test method measures a permanent depth of indentation produced by the preliminary and total test forces. First, a preliminary test force (preload or minor load) is applied. This is the zero or reference position. Then, an additional test force (or major load) is applied to reach the total required test force. This additional force is held for a predetermined amount of time and then released, but with the preliminary test force still applied. The indenter reaches the final position at the preliminary force and the distance travelled from the major load position is measured and converted to a value into one of the many scales for Rockwell hardness. Preliminary test forces range from 3 kilograms (superficial Rockwell) to 10 kilograms (regular Rockwell) to 200 kilograms (macro Rockwell scale). Total test forces range from 500 grams (micro) to 15–150 kilograms (superficial and regular) to 500–3000 kilograms (macro). Figure 7.23 shows the details of the hardness testing by Rockwell hardness tester.

7.6.5 Brinell hardness

Widely used on castings and forgings, the Brinell method applies a predetermined test force (F) to a hard steel or carbide ball of fixed diameter (D) which is held for a predetermined time and then removed. The resulting indentation is measured across at at least two diameters – usually at right

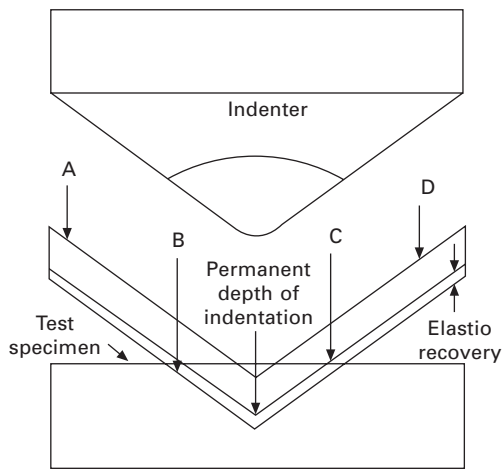

7.23 Rockwell hardness test: A, depth reached by indenter after application of preliminary test force (minor load); B, position of indenter under total test force; C, final position reached by indenter after elastic recovery of the material; and D, position at which measurement is taken.

angles to each other and averaged (d). A chart is then used to convert the averaged diameter measurements to a Brinell hardness number. Test forces range from 500 to 3000 kilograms. Figure 7.24 shows the details of the Brinell hardness testing method.

7.6.6 Vickers hardness (micro and macrohardness) and Knoop hardness

Mostly used for small parts, thin sections or case depth work, Vickers (Fig. 7.25) and Knoop (Fig. 7.26) methods are based on an optical measurement system. PC-based systems are now available for the improved productivity, accuracy and repeatability of these labour-intensive methods. To perform a test, a predetermined test force is applied with a pyramidal shaped diamond indenter. After a dwell time, the force is removed. Then, in the Vickers method, the indentation length of vertical and horizontal axis is measured

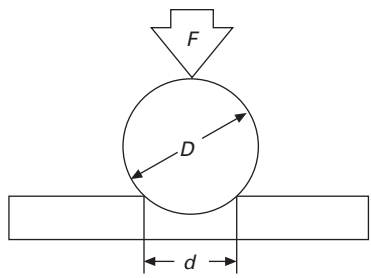

$$HB = \frac{2F}{\pi D(D - \sqrt{D - d})}$$

7.24 Brinell measurement calculation: D = ball diameter; d = impression diameter; F = load; HB = Brinell result.

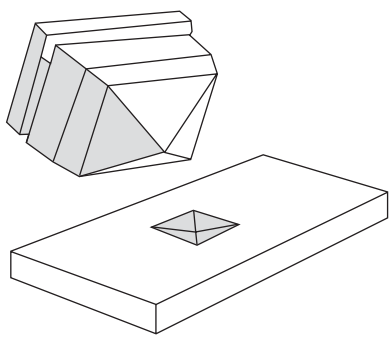

7.25 Vickers test: opposing indenter faces are set at a 136° angle to each other.

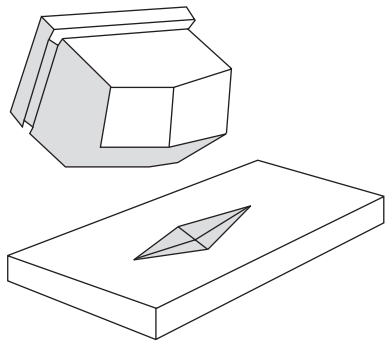

7.26 Knoop test: long side faces are set at a 172° 30′ angle to each other. Short side faces are set at a 130° angle to each other.

and averaged. In the Knoop method, only the long axis is measured (Fig. 7.26). A chart is used to convert the measurements to corresponding Vickers or Knoop hardness numbers. Test forces range from 0.001 to 1 kg. Vickers does offer higher force capabilities – up to 150 kg – but is not frequently used in North America.

7.6.7 Micro-hardness testing

Where specific information is required on the hardness of sub-structures within the HAZ zone (e.g. 'coarse grain', 'fine grain', 'inter-critical' and 'sub-critical' regions) it is necessary to carry out micro-hardness testing with loads in the 0.5–2 kg range. For these applications purpose-built micro-hardness testers are available using either the Vickers or Knoop test method. With these techniques, the area of interest is identified under a microscope and a hardness measurement made directly on the area of interest.

Such techniques are applied to critical welding applications such as temper bead welding where a primary basis of acceptance of the welding technique is the hardness test. Such testing is beyond the scope of standards such as ASTM E-384/AS 2205.6.1 and requires a technician or engineer with metallurgical experience to undertake such work.

7.6.8 Hardness testing of welds and HAZ

Vickers hardness is the predominant measurement technique for welds and HAZs. The diamond indentation can be made using a range of loads from 1 to 100 kg. The higher the load the larger the impression the diamond makes on the surface of the steel made and the more of an average the hardness reading becomes.

For weld testing there is specific interest in the HAZ that is in the order

of 1 or 2 mm thick. Thus it is necessary to use low loads, 1, 2 or 5 kg, in order to accurately assess the hardness in such cases. Australian Standard AS 2205.6.1 – 2003 provides a method for carrying out hardness testing and recommends use of a 5 kg load with traverses carried out 2 mm below the surface of the weldment.

The aim of weld and HAZ hardness testing is to identify: (a) the hardness of the parent metal and make an approximate determination of the material's tensile strength to assure the correct material is being welded, (b) the hardness of the weld to ensure the weld metal meets or exceeds the strength requirements of the parent metal, (c) the hardness of the HAZ to ensure the welding heat input, preheat and interpass temperature have been controlled sufficiently to produce a HAZ with the appropriate strength and toughness and (d) areas for fracture toughness testing when such testing is required.

7.7 Destructive testing

In destructive testing, sample portions of the welded structures are required. These samples are subjected to loads until they actually fail. The failed pieces are then studied and compared with known standards to determine the quality of the weld. The most common types of destructive testing are known as tensile test, free bend, guided bend, nick-break, impact, fillet welded joint, and etching. The primary disadvantage of destructive testing is that an actual section of a weldment must be destroyed to evaluate the weld. This type of testing is usually used in the certification process of the welder such as ASME Certification, as per AWSD1.1, etc. Some of the testing requires elaborate equipment that is not available for use in the field. Three tests that may be performed in the field without elaborate equipment are the free-bend test, the guided-bend test and the nick-break test.

7.7.1 Tensile test

The term tensile strength may be defined as the resistance to longitudinal stress or pull and is measured in kilograms per square millimetre of cross-section. Testing for tensile strength involves placing a weld sample in a tensile testing machine and pulling on the test sample until it breaks. The essential features of a tensile testing machine are the parts that pull the test specimen and the devices that measure the resistance of the test specimen. Another instrument, known as an extensometer or strain gauge, is also used to measure the strain in the test piece. Some equipment comes with a device that digitally records and plots the stress–strain curve for a permanent record and software for acquiring the data to get desired tensile properties.

The tensile test is classified as a destructive test because the test specimen must be loaded or stressed until it fails. Because of the design of the test

machine, weld samples must be machined to specific dimensions. This explains why the test is made on a standard specimen, rather than on the part itself. It is important that the test specimen represents the part. Not only must the specimen be given the same heat treatment as the part but it also must be heat-treated at the same time.

There are many standard types of tensile test specimens, and Fig. 7.27 shows one standard type of specimen commonly used. The standard test piece is an accurately machined specimen. Overall length is not a critical item, but the diameter and gauge length are important. The 12.5 mm diameter cross-section of the reduced portion provides an easy factor to manipulate arithmetically. The 50 mm gauge length is the distance between strain-measuring points. This is the portion of the specimen where the extensometer is attached. In addition, the gauge length is used to determine percentage elongation.

The tensile test amounts to applying a smooth, steadily increasing load (or pull) on a test specimen and measuring the resistance of the specimen until it breaks. Even if recording equipment is not available, the test is not difficult to perform. During the test, the behaviour of the specimen is observed and the extensometer and gauge readings at regular intervals are recorded. After the specimen breaks and the fracturing load is recorded, the percentage elongation and reduction in area of the specimen are determined using a calliper. In addition, a stress–strain curve is plotted. From the data strength, yield point, elastic limit, modulus of elasticity, and other properties of the material are determined.

7.7.2 Free-bend test

The *free-bend test* is designed to measure the ductility of the weld deposit and the heat-affected area adjacent to the weld. It is also used to determine the percentage of elongation of the weld metal. Ductility is the property of a metal that allows it to be drawn out or hammered thinly.

The first step in preparing a welded specimen for the free-bend test is to

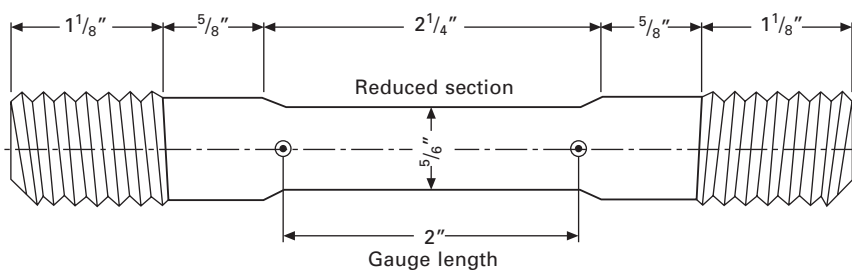

7.27 Standard tensile test specimen (1 inch = 25.4 mm).

machine the welded reinforcement crown flush with the surface of the test plate. When the weld area of a test plate is machined, as is the case in the guided-bend as well as in the free-bend test, perform the machining operation in the opposite direction to that the weld was deposited.

The next step in the free-bend test is to scribe two lines on the face of the filler deposit. Locate these lines 1.5 mm from each edge of the weld metal, as shown in Fig. 7.28, view B. Measure the distance, in mm, between the lines to the nearest 250 µm and let the resulting measurement equal *X*. Then bend the ends of the test specimen until each leg forms an angle of 30° to the original centerline. With the scribed lines on the outside and the piece placed so all the bending occurs in the weld, bend the test piece by using a hydraulic press or similar machine.

When the proper precautions are taken, a blacksmith's forging press or hammer can be used to complete the bending operation. If a crack more than 1.5 mm develops during the test, stop the bending because the weld has failed; otherwise, bend the specimen flat. After completing the test, measure the distance between the scribed lines and call that measurement *Y*. The percentage of elongation is then determined by the formula:

$$\frac{Y - X}{X} \times 100 = \% \text{ elongation}$$

or

$$\frac{\text{Change in length}}{\text{Original length}} \times 100 = \% \text{ elongation} \qquad 7.1$$

Requirements for a satisfactory test area are a minimum elongation of 15% and no cracks greater than 1.5 mm on the face of the weld.

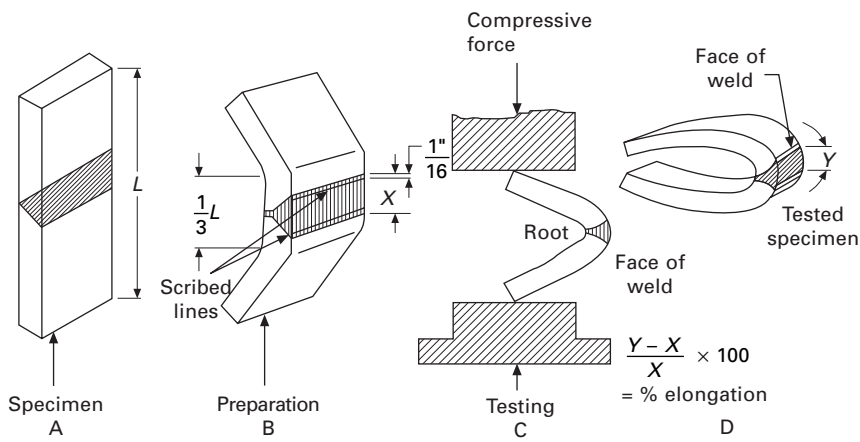

7.28 Free bend test.

7.7.3 Guided-bend test

The guided-bend test is used to determine the quality of weld metal at the face and root of a welded joint. This test is made in a specially designed jig. An example of one type of jig used is shown in Fig. 7.29.

The test specimen is placed across the supports of the die. A plunger, operated from above by hydraulic pressure, forces the specimen into the die. To fulfil the requirements of this test, the specimen must be bent through 180° – the capacity of the jig. No cracks should appear on the surface greater than 3 mm. The face-bend tests are made in this jig with the face of the weld in tension (outside), as shown in Fig. 7.30. The root-bend tests are made with the root of the weld in tension (outside), as shown in Fig. 7.30.

Figure 7.31 shows the actual machine used for making the guided-bend test. It is used in many welding schools and testing laboratories for the daily testing of specimens. Simple in construction and easy to use, it works by hydraulic pressure and can apply a direct load up to 20 tonnes, and even more on small specimens. During the test, the specimen is positioned in the machine and the pumping is carried out. The indicator has two pointers, one for indicating the maximum load applied and other (auxiliary) for indicating the instantaneous applied load. During increase in load, care is taken to monitor the large gauge indication which corresponds to the maximum load applied to the specimen. After removing the load, the larger hand

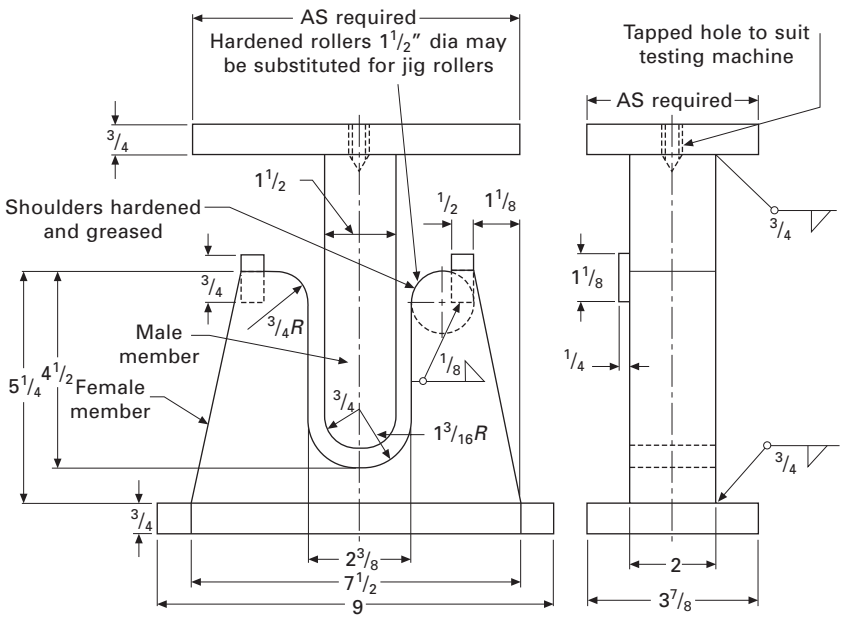

7.29 Guided bend test rig. All dimensions are in inches.

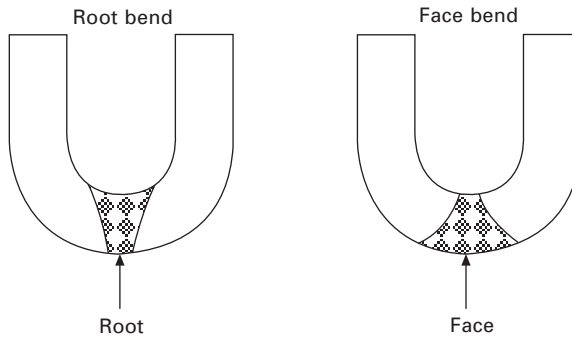

7.30 Guided-bend test specimen.

7.31 Testing machine for making guided bend test.

remains at the point of maximum load whereas the auxiliary pointer returns to zero.

7.7.4 Nick-break test

The nick-break test is useful for determining the internal quality of the weld metal. This test reveals various internal defects (if present), such as slag inclusions, gas pockets, lack of fusion, and oxidised or burned metal. To accomplish the nick-break test for checking a butt weld, the test specimens

are flame cut from a sample weld (Fig. 7.32). Make a saw cut at each edge through the centre of the weld. The depth of cut should be about 6 mm.

Then, the saw-cut specimen is placed on two steel supports, as shown in Fig. 7.32. Using a heavy hammer, break the specimen by striking it in the zone where the saw cuts were made. The weld metal exposed in the break should be completely fused, free from slag inclusions, and contain no gas pockets greater than 1.5 mm across their greatest dimension. There should not be more than six pores or gas pockets in 25 mm^2 of exposed broken surface of the weld.

7.7.5 Impact test

The impact test is used to check the ability of a weld to absorb energy under impact without fracturing. This is a dynamic test in which a test specimen is broken by a single blow, and the energy used in breaking the piece is measured

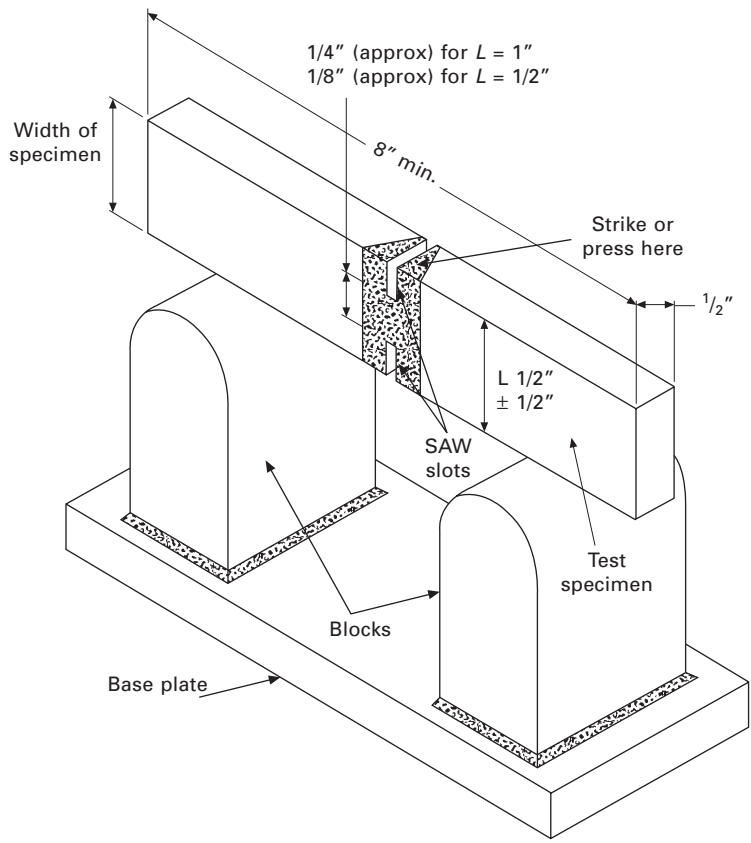

7.32 Nick-break test of a butt weld (SAW, submerged arc weld).

in joules. This test is used to measure the toughness of the weld metal or base metal. It is useful to find out if any of the mechanical properties of the base metal were destroyed by the welding process.

The two kinds of specimens used for impact testing are known as *Charpy* and *Izod* (Fig. 7.33). Both test pieces are broken in an impact testing machine. The only difference is in the manner that they are anchored. The Charpy piece is supported horizontally between two anvils and the pendulum strikes opposite the notch, as shown in Fig. 7.34, view A. The Izod piece is supported as a vertical cantilever beam and is struck on the free end projecting over the holding vice (Fig. 7.34, view B).

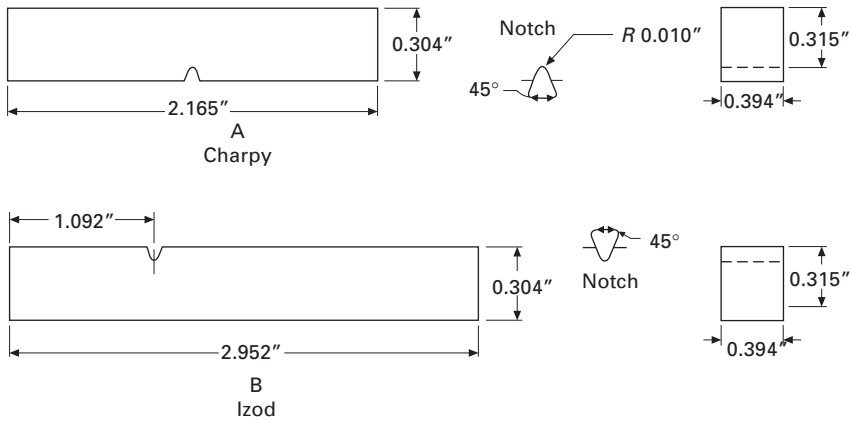

7.33 Test pieces for impact testing.

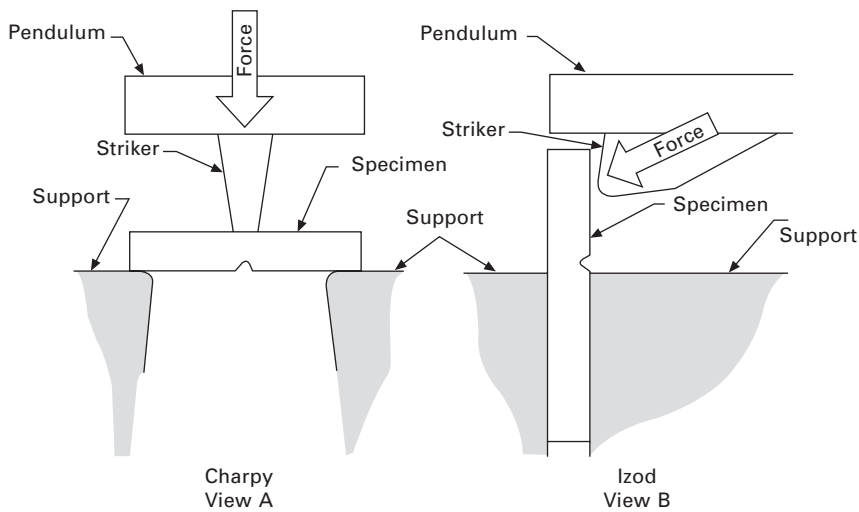

7.34 Performing impact test.

7.7.6 Etching test for macro-assessment

The macro-assessment test is used to determine the soundness of a weld and also make visible the boundary between the base metal and the weld metal. To accomplish the test, a test piece must be cut from the welded joint so it shows a complete transverse section of the weld. Cutting can be done by sawing or flame cutting. File the face of the cut and then polish it with grade 00 abrasive cloth. Then place the test piece in the etching solution.

The etching solutions generally used are hydrochloric acid, ammonium persulphate, iodine and potassium iodide, or nitric acid. Each solution highlights different defects and areas of the weld. The hydrochloric acid dissolves slag inclusions and enlarges gas pockets, while nitric acid is used to show the refined zone as well as the HAZ and parent metal zone. Further polishing would be required to obtain acceptable micrographs.

7.8 Testing methods for corrosion assessment

A welded joint is required to perform either equal to or better than the base metal it joins under the given operating conditions. However, in practice, this objective is never achieved since the welding process itself introduces features that degrade the mechanical and corrosion properties of the welded joints as compared with the wrought base metal. Despite shielding by a gas or by slag, the weld metal can get contaminated by slag inclusions, tungsten inclusions, etc. The fast cooling rates associated with weld metal cause the formation of dendrite structures besides the straining of the weld metal. In fact, the majority of the corrosion failures in components could be directly or indirectly related to the corrosion of the weld metal or HAZ. Both uniform and localised corrosion attacks can take place in the base metal as well as the weldments. Weldments, because of their microstructural and compositional heterogeneities, are inherently more prone to corrosion than the unaffected base metal, though the basic corrosion mechanisms may be the same.

The various regions of a weldment are schematically illustrated in Fig. 7.35. Visual examination of the welds is often a satisfactory method of judging the degree of preferential corrosion, but this is not always the case. Many test methods are suitable for weld performance evaluation and are performed for qualifying the weld. The immersion test is the preferred method for ascertaining the susceptibility of welds in steels to preferential corrosion.

7.8.1 Immersion tests

Historically, immersion tests have been extensively used to generate uniform corrosion data for alloys used in the process industries under immersion conditions. Typical immersion tests can be as per ASTM D1141 with seawater

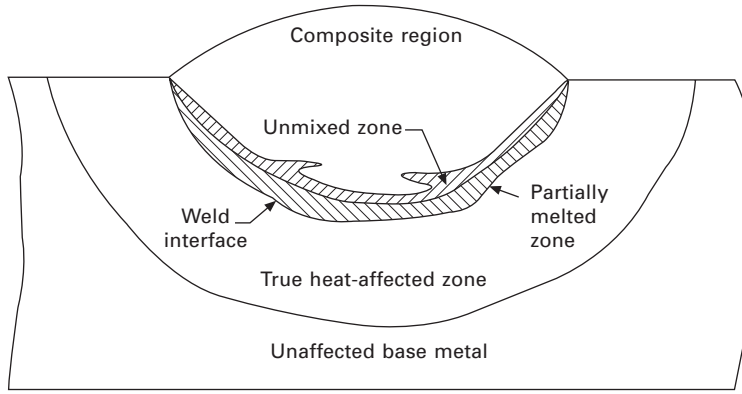

7.35 A schematic illustrating the various regions of a weldment.

under freely corroding conditions using the weld specimens with dimensions 150 mm × 50 mm × sample thickness. The specimens are suspended in the solution, with the longest side vertical, by the connecting wires used to measure the potential. The specimens are glass-bead blasted to remove any pre-existing corrosion product and washed with acetone and alcohol prior to testing. The solution is changed every 4 days to maintain the pH between 7.9 and 8.2. The total exposure time is 9 months. The electrode potential of one specimen of each weld type is monitored on a daily basis using a saturated calomel electrode (SCE) for the entire duration of the exposure. The solution temperature is between 19 °C and 22 °C for all the tests.

After removal from solution, the specimens are rinsed in distilled water. Profiling of the sections is then carried out to determine which areas of the originally flat cross-section are corroded preferentially. A stylus-based instrument with a stylus radius of 1 mm, a load of 2 mN and a scanning speed of 5 mm s^{-1} could be used without filtering.

A wide variety of other corrosion test methods are often used for testing weldments, including the following:

- intergranular corrosion (IGC) test as per ASTM A262 Practice A, B, C, E & F;
- corrosion test as per ASTM G35 specification;
- SCC test;
- sulphide stress corrosion test (SSCC) as per NACE TM0177;
- sulphide SCC, ASTM G35;
- pitting corrosion test as per ASTM G48 specification;
- hydrogen-induced cracking (HIC) test as per NACE TM0284;
- humid sulphur dioxide tests (ASTM G87, DINS0018, BS EN ISO 3231: 1998)
- sour service corrosion testing;

- cyclic corrosion testing;
- passivation testing.

7.8.2 Intergranular corrosion test as per ASTM A262 practices A, B, C, E & F

Intergranular corrosion in stainless steels may result from precipitation of carbides, nitrides or intermetallic phases. Only in the most highly oxidising solutions can intergranular attack be caused by intermetallic phases. When a test is to be restricted to carbides, in a material containing nitrides or intermetallic phases, a less oxidising solution is chosen.

Oxalic acid test, ASTM A262, practice A (oxalic acid etch)

The oxalic acid etch test is a rapid method of screening those specimens of certain stainless steel grades for intergranular attack associated with chromium carbide precipitates. The test is used for acceptance but not rejection of material.

Ferric sulphate–sulphuric acid, ASTM A262 – practice B (Streicher test)

This test is based on weight loss determinations and provides a quantitative measure of the relative performance of the material evaluated. The procedure includes subjecting a specimen to a 24 to 120 hour boil in ferric sulphate–50% sulphuric acid. This procedure measures the susceptibility of stainless steels and nickel alloys to intergranular attack associated with the precipitation of chromium carbides at grain boundaries.

Nitric acid, ASTM A262, practice C (Huey test)

The specimens are boiled for five periods, each of 48 hours, in a 65% solution of nitric acid. The corrosion rate during each boiling period is calculated from the decrease in the weight of the specimens. Properly interpreted, the results can reveal whether or not the steel has been heat treated in the correct manner. The customer must specify the maximum permissible corrosion rate.

The Huey test environment is strongly oxidising, and is used only as a check on whether the material has been correctly heat treated. This test is suitable for the detection of chromium-depleted regions as well as intermetallic precipitations, like the sigma phase, in the material. The Huey test is also used for materials that come into contact with strongly oxidising agents, e.g. nitric acid. This procedure may also be used to check the effectiveness of

stabilising elements and of reductions in carbon content in reducing susceptibility to intergranular attack in chromium–nickel stainless steels.

Copper–copper sulphate–16% sulphuric acid, ASTM A262 – practice E (Strauss test)

This procedure is conducted to determine the susceptibility of austenitic stainless steel to intergranular attack associated with the precipitation of chromium-rich carbides. Once the specimen has been subjected to the boiling solution, it is bent through 180° and over a diameter equal to the thickness of the specimen being bent. This test is based on a visual examination of the bent specimen, by looking for the presence of any microfissures/cracking.

Copper–copper sulphate–50% sulphuric acid, ASTM A262 – practice F

This test is based on weight loss determination which provides a quantitative measure of the relative performance of the material evaluated. It measures the susceptibility of 'as-received' stainless steels to intergranular attack.

7.8.3 Corrosion test as per ASTM G35 specification

The polythionic acid (sulphurous acid and hydrogen sulphide) environment provides a way of evaluating the resistance of stainless steels and related alloys to intergranular SCC. This practice can be applied to wrought products, castings, weld metal of stainless steels or other materials to be used in environments containing sulphur or sulphides.

7.8.4 SCC test

The objective of this test is to predict the service behaviour or to screen alloys for service in a specific severe environment for an accelerated time. Stress corrosion specimens can be smooth, or pre-cracked or notched. Smooth SCC specimens allow for the evaluation of the total SCC life, which includes crack nucleation and propagation. The use of pre-cracked or notched specimens is based upon the engineering concept that all structures contain crack-like flaws. Pre-cracking can contribute to the susceptibility of SCC of alloys such as titanium which may not be evident from smooth specimens.

- *C-Ring specimens (ASTM G38 C-Rings).* These are commonly used to determine the susceptibility to SCC of alloys in different product forms such as tubing, rods and bars in the short transverse direction.
- *Tensile specimens, as per ASTM G49.* This is one of the most versatile methods of SCC testing because of the flexibility permitted in the type

and size of the test specimen, the stressing procedures and the range of stress level. It allows the simultaneous exposure of unstressed specimens with stressed specimens and subsequent tension testing to distinguish between the effects of true SCC and mechanical overload.

7.8.5 SSCC, NACE TM0177

SSCC is a form of hydrogen embrittlement cracking which occurs when a susceptible material is exposed to a corrosive environment containing water and H_2S at a critical level of applied or residual tensile stress. The SSCC tests are performed routinely for customers using tensile and bent beam specimens. For each stress level and temperature, the following sample size is required: (i) plate – 16 mm thick × 160 mm long, (ii) pipe – 160 mm long pieces irrespective of diameter, cut strip of 16 mm width and (iii) bar – 160 mm long piece irrespective of diameter.

Test details

Method A: Tensile Test (Proof Rings) and Method B: Bent Beam Test (3 or 4 Point Bends). NACE TM0177 specifies Solution A (acidified), Solution B (acidified and buffered) and Solution C (for martensitic stainless steel). Solution A is used in Method A unless the properties of Solution B or C are specified. In any case, H_2S is bubbled through the solution constantly throughout the test period.

Testing is performed in NACE solutions A and/or B, saturated with H_2S at 24° and 90 °C. Stressed samples are exposed to a sour environment for a predetermined time, after which they are removed and analysed for crack detection. NACE TM0177 specifies test duration of 30 days (720 hours) for Method A or B test.

7.8.6 SSCC, ASTM G35

The polythionic acid (sulphurous acid and hydrogen sulphide) environment provides a way of evaluating the resistance of stainless steels and related alloys to intergranular SCC. This practice can be applied to wrought products, castings, weld metal of stainless steels or other materials to be used in environments containing sulphur or sulphides.

7.8.7 Pitting corrosion test, ASTM G46

ASTM G46 procedure is used to assist in the selection of test methods that can be used to identify and examine pits and to evaluate pitting corrosion to determine the extent of its effect. The importance of this evaluation is to be

able to determine the extent of pitting, either in a service application where it is necessary to predict the remaining life in a metal structure, or in laboratory test programs that are used to select the most pitting-resistant materials for service. ASTM G48 Method A and ASTM A923 Method C are other typical pitting corrosion tests performed.

7.8.8 HIC test, NACE TM0284

This test method evaluates the resistance of pipeline and pressure vessel plate steels to HIC caused by hydrogen absorption from aqueous sulphide corrosion. An unstressed test specimen is exposed to a solution at ambient temperature and pressure and after a specified time, the test specimen is removed and evaluated.

7.8.9 Humid sulphur dioxide tests (ASTM G87, DIN50018, BS EN ISO 3231: 1998)

This test consists of exposing parts to the environment of a cabinet operated at an elevated temperature and high humidity with the addition of sulphur dioxide. There are variations in the test conditions made to adjust the severity of the conditions. These variations include the concentration of sulphur dioxide added and either leaving the test pieces in the cabinet for 82 hours and in the ambient laboratory atmosphere for 16 hours (most common) or leaving the test pieces in the cabinet continuously. In both approaches the water in the bottom of the cabinet and the SO_2 are changed daily. The number of cycles performed usually varies between 5 and 25.

7.8.10 Sour service corrosion testing

A variety of corrosion problems can be encountered in industries such as oil and gas production, oil and gas transmission, energy conversion systems, and nuclear power systems. Such problems include weight loss corrosion, pitting corrosion, corrosion fatigue, SCC, SSCC and HIC.

7.8.11 Cyclic corrosion testing

The purpose of cyclic corrosion testing is to provide an accelerated laboratory test which will simulate the results of actual outdoor activities by the changing of environments inside the exposure zone which contains the test samples. Testing can be done to various specific automotive specifications. The cycles typically include salt spray, humidity and drying periods.

7.8.12 Passivation testing, ASTM A380, F86, A967

The practice of passivation is used on metallic surgical implants and stainless steel parts, equipment or systems. Passivation is the process by which a stainless steel will spontaneously form a chemically inactive surface when exposed to air or other oxygen-containing environments. Passivation is the removal of exogenous iron or iron compounds form the surface of a stainless steel by means of a chemical dissolution, most typically by a treatment with an acid solution that will remove the surface contamination but will not significantly affect the stainless steel itself. There are a number of methods used to test for passivation. As per ASTM A967, there is practice A, which is a water immersion test. Practice B is a High Humidity Test. Practice C is a salt spray test. Practice D is a copper sulphate test, and practice E is a potassium ferricyanide–nitric acid test.

7.9 Measurement of residual stresses in weldments

Residual stresses are self-balancing internal system of stresses arising from non-uniform mechanical deformation or non-uniform thermal distribution with some measure of plastic flow. These stresses exist in a body even when all external forces are removed.

During welding a weldment experiences complex temperature changes that cause transient thermal stresses and non-uniform distribution of elastic strains that are produced in the weld and in the regions near it. Because of this, both distortion and residual stresses result in the welded part. These stresses are elastic in nature and exist in a body without any external force. Hence, they are self-equilibrating, i.e. the summation of the forces and moments about any point in the cross-section of the body is equal to zero.

The most obvious manifestation of the mechanism producing residual stress is distortion, which cannot be considered in isolation from residual stress. In simple terms, high conditions of restraint during welding limit distortion but impose large local strains at the welded joint, giving rise to higher stress, which greatly increases the risk of failure. Conversely, low restraint does not inhibit the local contractions which result in larger displacements or distortion and lower levels of residual stress.

7.9.1 Basic mechanisms of generations of residual stresses

Residual stresses in welded components arise directly from the local shrinkage associated with the cooling of the hot weld metal which is restrained, either internally or externally, by the cold sections of the fabrication surrounding

the weldment. But this does not accurately describe the true mechanism, which in reality is a highly transient condition, being modified continually, depending on the nature of the joint, the number of passes involved, and to some extent the welding parameters themselves. At any moment any one of the influencing parameters could be different, making study of the mechanism an extremely complex exercise.

A better understanding of the process each incremental element of material experiences can be obtained from Fig. 7.36, which illustrates a typical thermal stress cycle for an element of material with yield strengths in tension and compression decreasing with temperature. The cycle starts at room temperature, O, and the initial thermal expansion is restrained by the surrounding cold material, thus generating plastic compressive stresses until the yield strength is reached at position A. With further increase in temperature, plastic strains occur following the material's characteristic tensile yield strength curve, AB. On cooling, the response is once again elastic, but opposite in sense to the heating cycle, until the tensile yield strength is achieved at position C. Cooling back to room temperature then follows the material's characteristic tensile yield strength curve, thus generating yield magnitude residual stresses at room temperature, position D. In addition, Fig. 7.36 illustrates clearly that the magnitude of residual stress is also a function of the temperature difference experienced. In the case considered, any temperature rise exceeding T on Fig. 7.36 will always generate yield magnitude elastic residual stresses, whereas at lower temperatures the shrinkage strains are not sufficient to reach the tensile yield limit and will result in less than yield magnitude

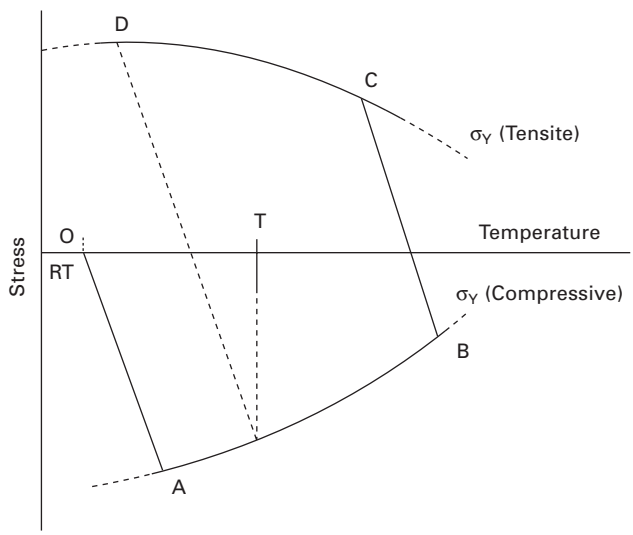

7.36 Schematic illustration of the origin of residual stresses during heating and cooling of welds.

elastic residual stress. The critical temperature difference is a function of material yield strength, which for typical mild steel is of the order of 175 °C, with reference to room temperature.

Figure 7.37 illustrates the commonly observed classical distribution of residual stresses arising from this simple construction and reaction mechanism. These are produced in three directions, viz. longitudinal, transverse and in the thickness directions during welding of thick low carbon ferritic steel plates. The peak magnitude of the longitudinal residual stress is usually of the order of yield stress level. The magnitude of the transverse residual stress is much lower than the magnitude of the longitudinal stress component. Often a ratio of 1:4 to 1:3 is reported for the magnitude of both residual stress components.

7.9.2 Types of residual stress

Residual stresses are commonly classified into two groups: macro and micro. Macro-residual stresses, or residual stresses of the first kind, are those of an

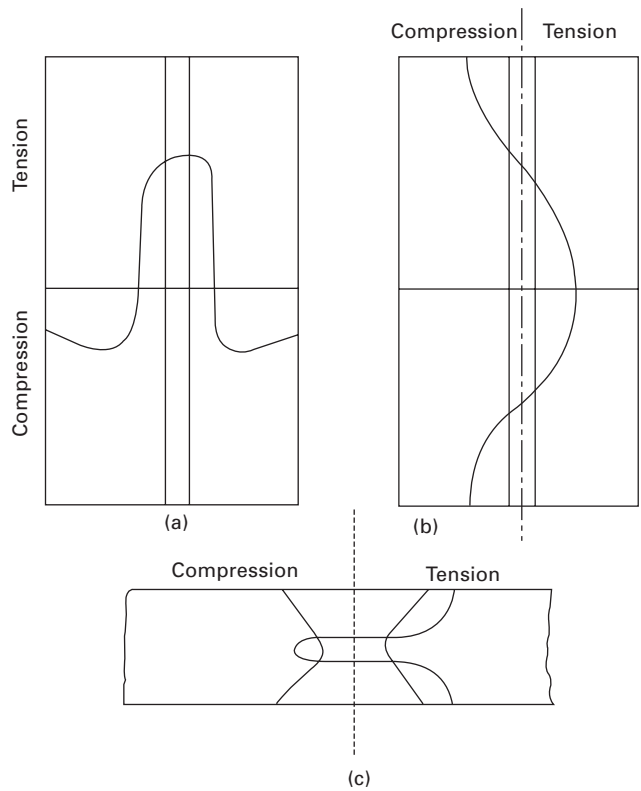

7.37 Typical 'traditional' residual stress distributions in plates without fixed ends: (a) longitudinal, (b) transverse and (c) through thickness.

engineering nature and which are measured over a gauge length that encompasses several grains. Micro-residual stresses, or residual stresses of the second kind, relate to stress systems set up by microstructural inhomogeneities which can be confined within either a single grain or a particular set of grains of the same preferred orientation.

Though doubts do exist over which of these mechanisms is to be considered important to SCC – brittle fracture or fatigue initiation – it is likely that both types can contribute depending on the situation. However, it is suggested that for all mechanisms it is the first kind that is of fundamental interest. The two measurement techniques used in this study, namely the strain relaxation technique and X-ray diffraction technique, measure macro-residual stresses.

7.9.3 Factors influencing residual stresses

Among the various factors influencing residual stress magnitude and distribution, the material properties, specimen dimension, heat input, welding process and welding sequence are considered to be the most important.

Material properties

The magnitude of residual stresses is affected by:

- the temperature distribution in the weldment characterised by thermal conductivity and diffusivity;
- the thermal expansion characteristics of the material; and
- the mechanical properties of the material at elevated temperature.

Specimen dimension

Reports indicate that the specimen length in the case of steel butt welds should be at least longer than 457 mm to produce high enough tensile stresses in the longitudinal direction. Longitudinal residual stresses become uniform in the central region of the welds longer than 457 mm. Specimen lengths seem to have little effect on the transverse residual stresses. The effect of specimen width is negligible as long as it is several times the width of the residual stress zone.

As far as the plate thickness is concerned, it is found that if weldments are made in plates thicker than 25 mm, residual stresses in the thickness direction can become significant. However, the lack of a simple and reliable measuring technique appears to limit the studies conducted so far.

Welding processes

It is generally believed that similar residual stresses are produced in welds made by various arc processes including the shielded metal arc, submerged arc, gas metal arc and gas tungsten arc processes.

Welding sequence

As far as residual stresses along the weld are concerned, the effect of welding sequence is minor. High tensile longitudinal stresses are found in all welds tested. Block welding sequences generally produce less shrinkage, less strain energy and less reaction than multilayer sequences.

7.9.4 Different sources of residual stresses

Welding residual stresses arise not only because of the variation in shrinkage of differently heated areas but also as a result of a surface quenching effect and transformation of austenite.

Residual stresses owing to the shrinkage process of the seam and HAZ

An important source of residual stress is the difference in shrinkage of differently heated and cooled arms of a welded joint. The weld metal subjected to the highest temperature tends to contract more than all other areas, but this contraction is hindered by the cooler parts of the joint. Thus the weld metal is subjected to tensile stresses in the longitudinal direction. Stress increases with higher yield strength of the material as a result of decrease in temperature. Owing to the shrinkage effect, stresses also arise in a direction perpendicular to the seam. The final stresses, remaining after cooling, are residual stresses due to the shrinkage process. The magnitude of the transverse stress component at the centreline of the seam ($Y = 0$) is much lower than the longitudinal stress component (Fig. 7.38). Comparing different materials, higher residual stresses brought about by welding should be found in materials with a larger product of Young's modulus and coefficient of linear thermal expansion.

Residual stresses owing to the more rapid cooling of the surface

During the cooling process, the surface layers of the weld and the highly heated areas close to it may cool more rapidly – even with air cooling – than the interior of the weld. Because of this, temperature differences are present not only over the width of the joint but also across the thickness. As time progresses an increasing temperature difference develops between the surface

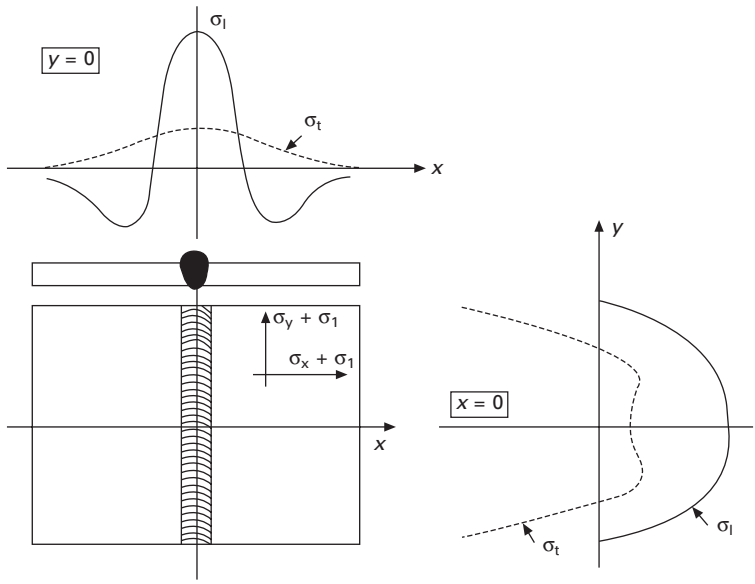

7.38 Longitudinal (σ_l) and transverse (σ_t) residual stresses showing shrinkage along lines parallel (*y*-axis) and perpendicular (*x*-axis) to seam.

and the interior. Thus, thermal stresses arise over the cross-section, which can lead to inhomogeneous plastic deformation and eventually to residual stresses. The more rapid cooling of the surface is called a quenching effect, and the residual stresses resulting from this process are quenching residual stresses.

Plastic deformation at elevated temperatures is necessary for the formation of quenching residual stress. If the surface quenching effect were to be the only source of residual stresses, compressive residual stresses would be obtained at the surface of the highly heated areas, especially the seam, and would be in equilibrium with the tensile stresses in the inner part of the seam.

Residual stresses owing to a phase transformation

During cooling of welded steel plate phase transformation from austenite to ferrite, bainite or martensite will occur, either at a certain temperature or over a temperature range. Owing to transformation there is an increase in specific volume and so the material in the seam and the HAZ which is being transformed tends to expand. But the expansion is hindered by the cooler material not being transformed. Thus the area being transformed is subject to compression, if the transformation temperature is sufficiently low, so that the material has marked yield strength after transformation. Therefore compressive residual stresses parallel to the seam should be expected in this area and, for reasons of equilibrium, tensile residual stresses should exist in

the region not being transformed. However, the transformation will occur with different heating temperature at different times. Therefore only a narrow strip of the weld material being transformed would be subjected to compressive residual stresses. In all areas being transformed occurs mainly at low temperature after the weldment has attained strength. Transformation residual stresses will appear, especially if bainite or martensite is formed. These transformation stresses diminish as the area being transformed becomes wider.

Superimposition of residual stresses owing to shrinkage, quenching and transformation

In reality the various stress sources are not independent from one another. At least two or even three different kinds of stress in a cooling welded joint are superimposed, leading to a complicated total state of stress. Therefore, statements concerning the finally resulting residual stress state can be made only on distinct assumptions. The most simple is that a linear superimposition of residual stresses owing to different sources can describe the total residual stress state. Figure 7.39 schematically illustrates the linear superimposition

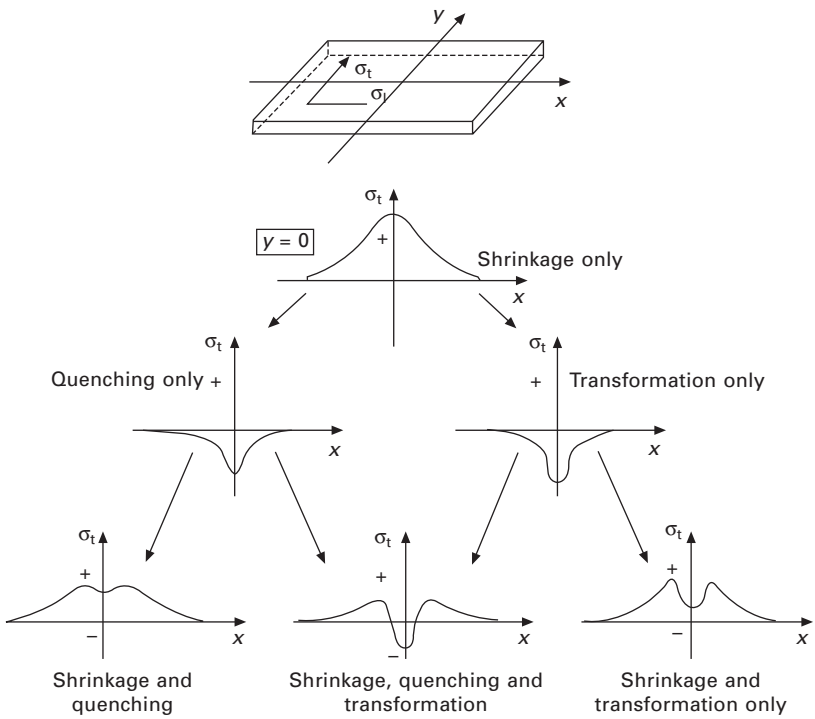

7.39 Schematic representation of superposition of transverse residual stresses owing to shrinkage, quenching and transformation.

of residual stresses owing to shrinkage, quenching and transformation. All diagrams show the transverse stress components as a function of the distance from the centreline of the weld. In all instances maximum tensile residual stresses are not present at the centreline of the seam but at the top. These tensile stress maxima represent the residual stresses owing to shrinkage. The difference between the maximum tensile stress and the stress value at the centreline represents either the surface quenching type of residual stress, the transformation type or both together.

7.9.5 Effects of residual stresses on performance

Effect of residual stress on fatigue strength and structural behaviour

Residual stresses have a serious and usually deleterious effect on fatigue failure, brittle fracture and structural behaviour. Fatigue strength (the number of cycles at fracture under a given load) increases when a specimen has compressive residual stresses, especially on the specimen surface. Many investigations have reported that the fatigue strength increased when specimens had compressive residual stresses, whereas tensile residual stresses increased fatigue crack propagation rate.

Residual compressive stresses can cause premature buckling of structural members loaded in compression such as struts, columns and stiffened diaphragms. More recently they have also been thought to interfere with the detection of sub-surface flaws, using ultrasonic methods, by holding the flaw together and making it transparent to the ultrasound.

Fracture under tensile loading

Figure 7.40 shows the residual stress distribution in the longitudinal direction in a butt weld in the as-welded condition and also the stress distribution when an external tensile load is applied. The figure also shows the resulting residual stress distribution after the release of the externally applied tensile load. It can be seen from the figure that as a result of tensile loading the peak stress has become more even and has also decreased.

The following basic effects of residual stresses have been revealed by investigations:

- The effect of residual welding stresses on the performance of welded structures is significant only on phenomena which occur under low applied stress, such as brittle fracture and SCC.
- As the level of applied stress increases, the effect of residual stress decreases.
- The effect of residual stress is negligible on the performance of welded structures under applied stresses beyond yielding.
- The effect of residual stress tends to decrease after repeated loading.

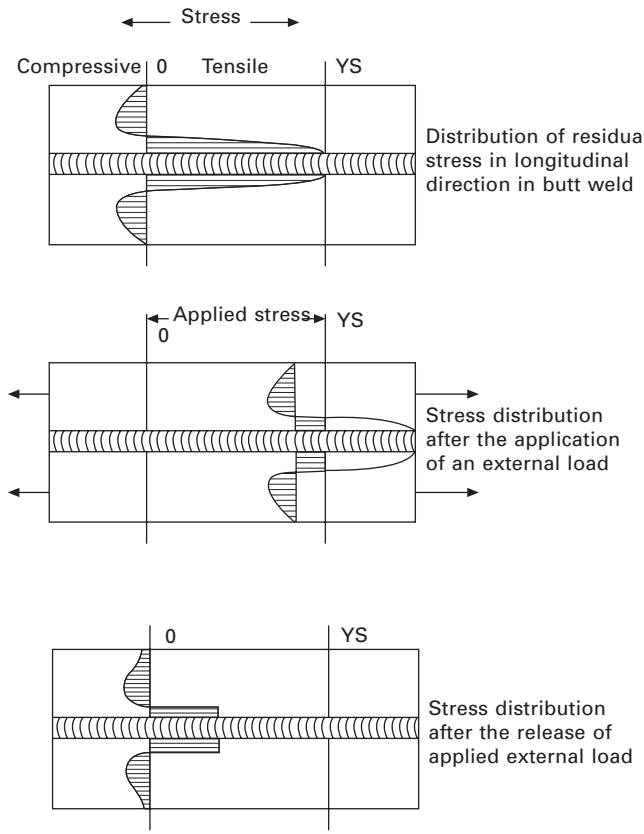

7.40 Effect of proof stressing on residual stresses in a weldment.

Effects of environment

Cracking can occur in weldments, even without external loading, when the material is embrittled by exposure to certain environments and residual stresses are present. Stress corrosion cracking is a brittle-type fracture and has been observed in a number of ferrous and non-ferrous alloys exposed to certain sensitive environments containing nitrates, chlorides, hydroxides, hydrogen sulphide, etc.

7.9.6 Techniques of residual stress measurement

The methods of residual stress measurement available at present fall into the following three categories [10, 11]:

1. Mechanical or stress relaxation methods.
2. X-ray and neutron diffraction methods.
3. Methods using stress-sensitive properties.

Mechanical methods

Mechanical methods are based on the fact that cutting or removal of part of an internally stressed body results in stress redistribution in both the removed portion and the remainder of the body. This redistribution is accompanied by change in strain distribution whose magnitudes are related to the magnitude of stresses. Measurement of strain distribution is complicated, since the stresses are generally triaxial in nature. In many cases, however, measurement of the strains in one direction either longitudinal or transverse is sufficient. Linear, biaxial and rosettes are readily available for the measurements of strains using mechanical or stress relaxation methods. Most important methods in this category are the dissection method and the hole-drilling strain gauge method.

Dissection method

The dissection method is one of the oldest methods but is still extensively used to measure residual stresses. The method is best applied to structures having uniaxial stress or to specimens in which the stress along one particular direction alone is important. The following steps are followed in the dissection method:

- strain gauges are bonded along maximum expected stress direction;
- initial strain gauge readings are taken before cutting by strain measuring equipment;
- cutting the part along maximum and minimum stress directions;
- strain readings are taken after each cutting;
- calculation of residual stress values using stress strain relations.

If it is intended to determine the residual stress along the welding direction (longitudinal stress) at the weld centre, strain gauges are bonded on the weldment with their grid length oriented along the weld direction. The size of the strain gauges are chosen depending on the type of spatial resolution desired. After bonding the strain gauges, cutting must be made transverse to the welding direction. Strain released is usually measured after every stage of cutting. If stresses transverse to the welding directions are desired, then the strain gauges are bonded transverse to the weldment, and the cutting is done along the weldment.

This method is suitable for measuring uniaxial stresses such as longitudinal or transverse stresses in welded components. It is, however, tedious, time consuming and often analytically difficult. The serious disadvantage of the dissection technique is that it is destructive to the part being analysed. It can, however, be used on mock-up weld pads and to calculate other techniques of residual stress measurements.

Hole-drilling technique

The hole-drilling technique or hole-drilling strain gauge technique is a widely used mechanical method for the measurement of residual stresses. It can be taken as 'semi-destructive', if the size of the hole is small in relation to the thickness of the component. In many cases, the presence of a small hole may not noticeably impair the integrity of the weldment. The drilled hole also can be plugged, if necessary, after the residual stresses are measured if the plugging operation does not introduce residual stresses.

Owing to circular geometry, the drilled hole does not releve stresses in a unidirectional direction as is introduced by cutting in the dissection technique. At the region of interest, a special purpose strain gauge rosette (Fig. 7.41) is attached to the welded component. A small hole is drilled into the component through the rosette centre. The measured relieved strains in three directions determine the stresses in the principal directions. The size of the hole may be varied. The hole diameter is often 1.6 m. The hole is usually drilled to a depth of 2 mm.

The rosettes are bonded on weldments usually with the grid length of strain gauge 1 parallel to the welding axis and grid 2 perpendicular to the weld axis (Fig. 7.41). Then the hole is drilled at the centre of the rosette. If ε_1, ε_2 and ε_3 are the strains measured through strain gauges 1, 2 and 3, respectively, then maximum and minimum principal stresses, their directions and residual stresses acting parallel and perpendicular to the welding direction could be known using the standard relations involving the measured strains in the three rosettes.

Ultra-high speed drilling technique (approximately 35 000 rpm) is generally employed for drilling holes. Commercial apparatus for alignment and drilling holes is available. The other techniques available for producing holes in the

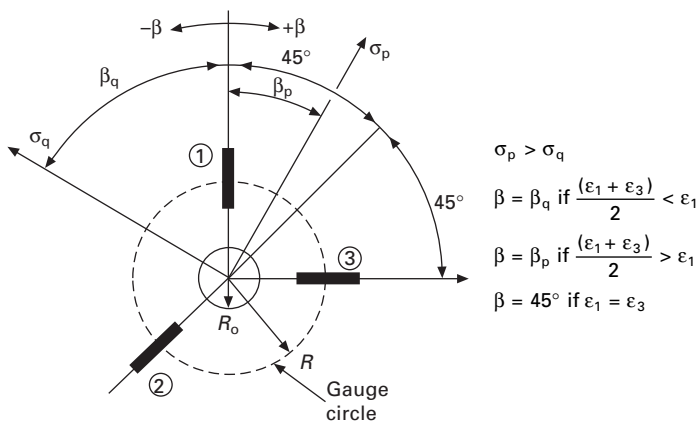

7.41 Strain gauge rosette arrangement.

components are electro-chemical milling and air abrasive techniques. The selection of the hole drilling technique is related to the material of the weldment and the amount of residual stress present. For example, electro-chemical milling is limited to electrically conducting materials, ultra-high speed drilling technique is not suitable for extremely hard materials, etc.

The hole drilling strain gauge method is a standard method recognized for the measurement of residual stresses in weldments. It measures residual stresses in a very small area which can be approximated as a point. Thus spatial resolutions are good. Rosettes and milling guides are available commercially, and the procedures for calculating the residual stresses from the measured strains are reasonably well established. The method is capable of measuring through thickness–residual stress gradients by incrementing the hole depth and recording the strains after each increment.

The main limitations of this method are:

- measurement of the residual stresses at a large number of points can be time consuming;
- size of the drilling set-up, rosette dimension and accessibility, etc. impose restrictions in obtaining residual stress results in closure steps and therefore gradients may be missed;
- the method is capable of measuring only surface/sub-surface macro residual stresses;
- the method is of destructive nature in thin sections.

X-ray and neutron diffraction methods

Diffraction methods are based on the phenomenon that when a metal is under stress, applied or residual, the resultant elastic strain causes the atomic planes in the metallic crystal structure to change their spacing. Diffraction methods measure this inter-planar spacing to arrive at the stresses present in the crystalline material. The method is made possible by the fact that wavelengths of the electromagnetic radiations used for investigations are of the same order of magnitude as the atomic spacing in metallic crystals (a few angstroms). The X-ray diffraction method is very widely used [12]. Portable equipment is commercially available which permits the use of the method on large objects and carries out the measurements in field and quickly. The method is versatile in the sense that it can be used for quantitative analysis of macro and micro-stresses separately.

The neutron diffraction method is similar to X-ray diffraction, but its penetration in most of the materials is up to several orders of magnitude greater than that found with X-rays. Neutrons differ from X-rays in interacting weakly with matter, thus penetrating several centimetres in most materials. The penetration depth may be varied by changing the energy of the neutrons

using suitable filters. Because of the neutrons' ability to penetrate inside the bulk materials, it is an important method for internal stress measurement. This important advantage is also driving the development of reference standards for ultrasonic methods calibrated with the help of the neutron diffraction method. However, this application requires improvements in the precision attainable with the neutron diffraction method. Neutron sources are relatively weak when compared with conventional X-ray and coarse collimation has been used to increase intensity at the expense of the resolution. Neutron beams of sufficient intensity are only available at the site of reactors or accelerators. To date, the most powerful and widely used physical method of stress measurement in engineering components is X-ray diffraction. It is the only means presently available for the measurement of residual stress in ball bearings, in gear teeth, and in material surfaces after machining or grinding.

Methods using stress-sensitive properties

When stress exists in a metal, some of the physical or mechanical properties, such as the propagation velocity of elastic wave, magnetic properties and hardness, are changed. Many stress measuring methods of this type, in recent years, have been proposed and developed. The most important methods in this category such as (i) ultrasonic and (ii) Barkhausen noise methods have attracted more attention.

Ultrasonic methods

Ultrasonic methods of residual stress measurements are based on the influence of stress on the propagation velocity of elastic waves. When a material deforms in response to mechanical stress, a small shift in ultrasonic velocity occurs. Mechanisms of this shift include density changes, changes in interatomic forces, etc. But it is found that the velocity change depends on the state of deformation and hence the state of stress in the solid. This dependence is known as the acousto-elastic effect. The stress-induced velocity shift is generally linear and can be described by the simplified relation:

$$V = V_0 + A\,\sigma \qquad 7.2$$

where V is the ultrasonic velocity in the presence of stress, V_0 is the stress-free velocity, A is the acousto-elastic constant (AEC) and σ is the stress. However, determination of stress from the above equation involves the prior determination of an AEC. For this purpose a standard specimen having the same composition as that of the component for which residual stress has to be determined (welded or rolled plates) is tested in a Universal Testing Machine (UTM). Specimens used are fabricated as per ASTM standards for tensile testing.

The change in ultrasonic velocity due to stress, in general, is very small, usually less than 1%. Of the several electronic methods proposed to measure this small change in velocity, the pulse-echo overlap (PEO) method is the easiest and least sensitive to variations in the quality of ultrasonic echo train. Commercial instruments of these types are not generally available and have to be built indigenously. The principal steps followed in the measurement of residual stress by ultrasonics are the following [13]:

- Determination of the AEC of the material or component using standard tensile specimen with applied loads.
- Ultrasonic velocity measurements in the material or component of interest.
- Determination of residual stresses using AEC.

Several such methods have been tried with varying degrees of success. For example:

- Longitudinal waves can be used in a continuous-wave reflection mode to excite a resonant frequency in a member. The resonant frequency, in turn, depends upon the ultrasonic wave inducing the deformation and the ultrasonic velocities in the member, both of which are influenced by stress.
- Changes in ultrasonic velocity of longitudinal wave across the thickness can be related to the stress present in the material.
- Polarised shear waves can be used to evaluate the stress-induced birefringence in a member in a manner analogous to optical birefringence techniques.
- Changes in the velocity of surface waves between two points on the surface of a member can be related to the deformation and stress between the points.

After X-ray diffraction, ultrasonics is clearly the most advanced of the non-destructive approaches for evaluating residual stresses. A specific advantage of ultrasonics over X-ray diffraction is that it could be used to measure surface as well as bulk residual stresses.

- Ultrasonic velocity measurement methods are truly non-destructive methods for the estimation of bulk as well as surface cold rolled, welded pads, etc.
- Ultrasonic methods are fairly quick for quantitative determination of residual stresses over strain gauge methods.
- The use of surface waves offers possibilities of measuring surface residual stresses by ultrasonic NDT method.
- Development of suitable electromagnetic acoustic transducers (EMATs) for the generation and detection of bulk and surface waves will be a considerable undertaking.

Ultrasonic methods, however, are not free from limitations. Higher order elastic constants are generally required in order to relate the ultrasonic velocity measurements to stresses. These constants are not generally available and must be experimentally determined for the particular material being tested. Unfortunately, these constants are influenced by metallurgical texture, so that interpretation of the results in many cases is questionable. The value resulting from particular measurement is an average of the stresses along the path traversed by the ultrasonic beam. There is, thus, only a limited possibility of detecting sharp stress gradients.

The usefulness of the ultrasonic approaches is obviously reduced in highly attenuating materials such as plastics, composites and certain inorganic non-metallic components. Though the ultrasonic methods are self-calibrated, it is necessary to compare the results with those of standard methods such as dissection and hole-drilling strain gauge methods, for reliable applications.

Barkhausen noise analysis

This method is applicable to ferromagnetic metals and alloys and depends on the Barkhausen effect which takes place when a magnetic field is swept in a ferromagnetic specimen along a hysteresis loop. Two types of high frequency signals are thereby generated. One – the magnetic Barkhausen noise (MBN) signal – is due to irreversible change in magnetic moments during the hysterisis. The second, the magnetomechanical acoustic emission (MAE) is due to elastic deformations associated with magnetic domain activities during irreversible changes in magnetisation. MBN signals are detected by a sensor coil or by a Hall-type probe and MAE signals by a piezoelectric transducer.

Both MBN and MAE signals are strong functions of microstructures and stress (deformation) conditions. Several practical applications are therefore possible from MBN and MAE. Although the use of MAE for residual stress determination has been found in laboratory investigations, commercial equipment is still not available. On the other hand, commercial equipment based on MBN is available for the determination of residual stresses. In such a measurement, the maximum amplitude of the MBN signal is taken as the measuring parameter. Figure 7.42 shows the schematic sketch of the probe for the measurement of residual stresses using MBN signals. In this probe, the magnetisation is affected by the yoke. The sensor coil positioned between the pole pieces senses the MBN signals. Use of MBN signal for residual stress on welded joints is now possible.

The disadvantage of the Barkhausen noise technique is its surface specificity, reduced spatial resolution and unreliability. Surface specificity is not a problem in many cases because it is the surface residual stress that is more important. The reduced spatial resolution is because of the need to use a sensor coil whose sizes cannot be reduced very much. The reliability of the method is

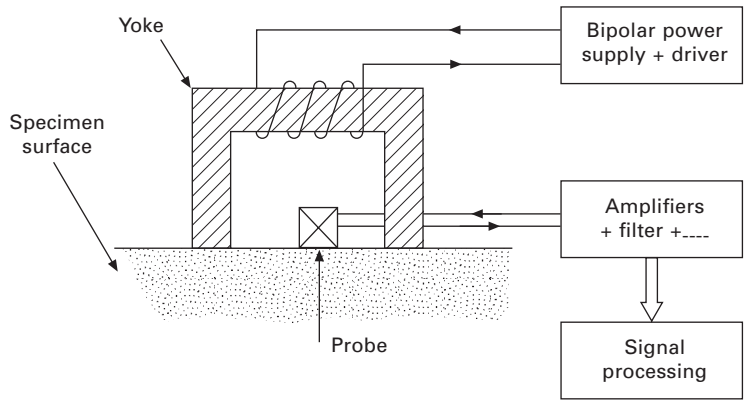

7.42 Schematic diagram of the probe for Barkhausen noise analysis.

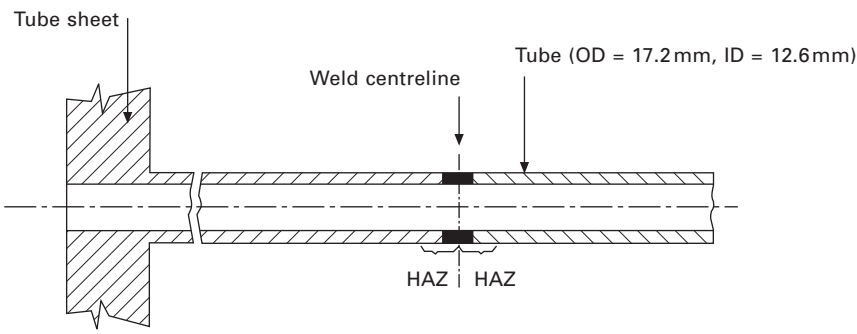

7.43 Tube to tube sheet weld joints in the steam generator.

being improved by extensive studies with respect to various types of microstructures which also influence the nature of the signals apart from the stress conditions inside the specimen. It is hoped that the use of the MBN signal will find widespread application in weld joints in those cases where high spatial resolution is not important. The method is simple, cheap and quick.

Case study: MBN analysis for residual stress measurements

MBN analysis has been developed and used for the assessment of residual stresses in weld joints. The MBN technique is simple to employ compared with other techniques such as strain gauge hole drilling and X-ray diffraction techniques. This type of simplicity was demonstrated for the field application involving a residual stress measurement for a large number of tube to tube sheet weld joints in a steam generator (Fig. 7.43). For example, the total numbers of tube to tube sheet weld joints in the steam generator modules (42) of the proposed prototype fast breeder reactor (500 MWe) in India are:

evaporator, 7084; reheater, 1708; superheater, 2380. The results of the MBN analysis have been correlated with those obtained by micro-hardness and X-ray diffraction measurements. This is the first time that an assessment of the residual stresses before and after PWHT in such a joint has been demonstrated using the MBN technique.

Magnetic flux perturbation and acoustic emissions are generated when an induced magnetic field in ferromagnetic materials is swept in a hysteresis loop. The former is referred to either as MBN or BN (Barkhausen noise). MBN signals are produced as a result of discrete changes in magnetisation caused mainly by the motion of the 180° domain walls as the magnetic field is varied. Since MBN is related to the nucleation and movement of magnetic domain walls which get influenced by presence of residual stresses in addition to different microstructural features, MBN measurements can be used to assess residual stresses and for characterisation of microstructural features. MBN measurements were made at the weld centre, 5, 15 and 25 mm from the weld centre on both sides of the weldment. The measurement positions were selected in such a way as to cover weld, HAZ and base metal regions. Micro-hardness measurements were made at these positions using a Vicker's hardness tester with a load of 5 kg for the purpose of correlating with MBN data. After the measurements in the as-welded condition, the tubes were post-weld heat treated at 973 K for 1 h followed by air cooling. Again the measurements were repeated at the same locations after removing the oxide layer.

The results (Fig. 7.44) showed that, in the as-welded condition, there is maximum MBN peak height at both ends (parents' metal region) and there

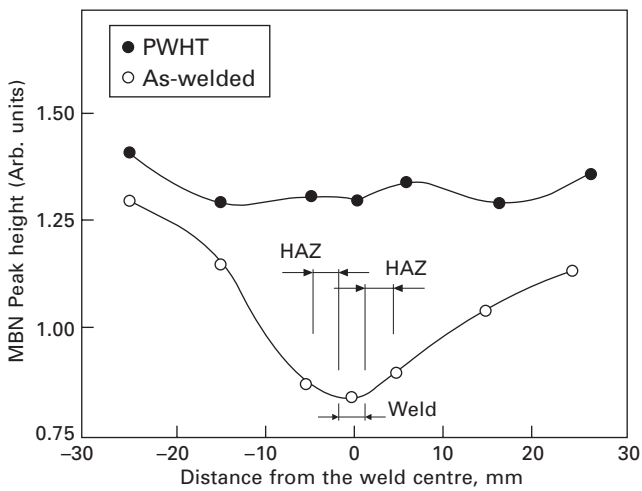

7.44 MBN response as function of distance from weld centre.

is gradual reduction in peak height with decreasing distance from weld. The weld shows the minimum MBN peak height. The difference in the peak height and peak position at the two ends is attributed to the difference in the heat transfer during welding due to the presence of a thick carbon steel support block on one side and the free end on the other side. The carbon steel block acts as a heat sink in one side and the free end is subjected to slow cooling. The large variation in MBN peak height indicates significant differences in the hardness in the weld, HAZ and base metal regions. This is supported by the corresponding variation in the hardness values. After the PWHT, the MBN peak height becomes more or less the same at all locations. This is also supported by the narrow variations in the hardness values after PWHT. In the as-welded condition, the results showed an inverse linear relationship between MBN and hardness. There is a large increase in the MBN peak height in the weld and HAZ regions after PWHT compared with the base metal regions. This is attributed to the removal of residual stresses and reduction in dislocation density in the weld and HAZ during PWHT. The MBN peak height values in the weld and HAZ regions differ significantly before and after PWHT and were found to be complementary to the hardness values. It is possible to evolve an acceptance criterion based on MBN peak height values to ensure the effectiveness of PWHT.

7.9.7 Selection of residual stress measuring method

A few basic criteria are useful in identifying a suitable residual stress measuring method for weldment. These criteria are particularly important, since present-day manufactured structures include weldment of various types, shapes and sizes. They are made not only of metallic materials but also of plastics, composites and structural ceramics. The basic criteria are: (i) non-destructibility, (ii) applicability, (iii) resolution, (iv) sensitivity, (v) depth of penetration, (vi) versatility, (vii) reliability, (viii) stress direction, (ix) portability, (x) cost and (xi) speed. Comparison of six residual stress measurement methods is made in Table 7.1. This table will be of use in selecting a suitable residual stress measuring method once the area of measurement, accessibility, type of stress to be known, etc. of the job are identified.

7.10 On-line weld monitoring and intelligent welding [14,15]

The reliability and consistency of welds produced can be enhanced through the use of real-time (in-time) monitoring. This approach enables assessment and control of the welding process. Presently, success of automatic/robotic welding systems has been confined to repetitive and large-scale fabrication jobs. The present day automatic welding systems do not have the adaptive

Table 7.1 Selection of residual stress measurement method

Method	Non-destrctive	Reliability	Bulk stress	Surface stress	Stress direction	Resolution	Cost*	Portability	Speed
Dissection	No	Good	No	Yes	Yes	– 4 mm^3	1–10	Yes	Poor
Hole-drilling	Partially	Good	No	Yes	Yes	> 30 mm^3	1	Yes	Poor
X-ray diffraction	Yes	Good	No	Yes	Yes	< 1 mm^3	0.1–1	Yes	Poor to excellent
Neutron diffraction	Yes	Good	Yes	Yes	Yes	< 1 mm^3	1–10	No	Poor to excellent
Ultrasonics	Yes	Poor	Yes	Yes	Yes	> 5 mm^3	< 0.1	Yes	Excellent
Barkhausen noise	Yes	Poor	No	Yes	Yes	> 10 mm^3	> 0.1	Yes	Excellent

*These estimated costs per reading are mainly for labour and do not include cost of equipment. They are normalised against the cost per reading of hole-drilling method.

features of welding process control, unlike manual welding wherein the welder alters the welding parameters utilising his experience and depending on visual observations during welding. An approach to the adaptable and automatic welding systems lies in the development of on-line sensing techniques capable of giving precise information about the appearance of defects. Two such techniques for on-line sensing are discussed. They are thermography and acoustic emission (AE). On-line techniques are particularly useful and cost effective for high technology industries such as nuclear and aerospace, where welds with stringent specification for defects acceptance are a must for higher reliability.

Thermography and AE techniques give real-time information regarding weld quality and defect formation, thus offering an on-line possibility of rectification of the welding procedure, resulting in reduced scrap and repairs. Thus the need for post-weld NDT techniques for examination is reduced. This helps in timely completion and also reduces financial and personnel requirements. The advantage is particularly important for thicker weldments as rectification and repair costs are significantly reduced by an on-line monitoring approach. On-line monitoring can be utilised for a welder's qualification/training for specialised jobs as the welder gets additional information about his of her capabilities and inadequacies. In the case of resistance spot welding, weld quality can be immediately known without the necessity for destructive testing of samples. In the following sub-sections, advantages of the real-time monitoring of different weld joints have been exemplified with appropriate case studies.

7.10.1 Thermography to monitor welding process [16]

Thermography refers to the mapping of temperature profiles on the surface of an object. This technique utilises the infrared spectral band of the electromagnetic spectrum. With the aid of a suitable detector, infrared (IR) radiation can be converted into an image and visualised for interpretations. The temperature distribution over plate surface and weld profile is monitored. For a good weld, these gradients should show repeatable and regular patterns. However, imperfections arising due to weld perturbations are expected to cause a discernible change in the thermal profiles. Experiments were conducted in the authors' laboratory to assess the possibility of the use of thermal imaging as a real-time device for monitoring the defects arising during the welding process. A set of experiments was conducted in which six plates were butt welded by manual metal arc welding process and gas tungsten arc welding process. The plate material used in all the cases was austenitic stainless steel (AISI type 316).

Four plates were welded in the 1G position while two plates were welded in the 3G position. Surface temperature distributions were measured using

the IR scanning camera placed both at the front (i.e. the same side as the welding torch) and at the rear of the plate. One of the objectives of the investigations was the detection of arc misalignment during the welding process. It was observed that with the arc being aligned with the centre of the weld, the heat input to the plate by the welding torch is equally distributed on either side of the joint. This balanced thermal distribution results in isotherms that are symmetric about the weld torch centre. In the case of an off-seam weld, where the torch has been offset from its centre, the heat input is unequally distributed on either side of the joint, resulting in the asymmetry of thermal profiles. A variety of defects were introduced during the welding process. The thermal profiles were recorded and analysed so as to identify the presence and nature of the defects. The defects introduced included porosities, lack of side wall fusion, lack of root penetration, undercut and blow holes. Thermal images were recorded for each pass of the weld. The results obtained from thermography were then correlated with those obtained by radiographing the plates subsequently after welding. It was observed that thermography can be used for on-line detection of lack of penetration, lack of fusion and undercuts. Thermal profiles obtained during on-line weld monitoring provide an excellent data bank to model residual stresses in the weldments. Thus, stresses and defects, determined with the help of thermographic technique can pave the way for reliable fabrication of weld joints in situ.

7.10.2 AE studies for monitoring welding process [17]

The acoustic emission technique (AET) can be utilised for detection and location of dynamic defects (i.e. as and when they form or grow) as a welding process progresses. The generation of elastic waves due to strain energy released during the formation of the above defects and consequent detection of these elastic waves using piezoelectric-based transducers is the main principle of AET. The defects that can be detected, located and qualitatively evaluated by AET are (i) nucleation and growths of cracks during welding and cooling (delayed cracking), (ii) slag inclusions (iii) micro-fissuring (iv) cold and hot cracking, (v) reheat cracks and (vi) weld cracking associated with phase transformations. Once these defects are detected and located by AET, other NDT methods can be used for detailed analysis, if needed. AET has been successfully used for on-line monitoring of welds prepared by tungsten inert gas (TIG), submerged arc, electro slag welding, etc. However, non-slag forming welding processes are particularly suitable for AE monitoring. The main problem in AE monitoring of welding process is the elimination of unwanted signals due to slag cracking and electromagnetic influence from the arc. The methodologies have been developed to eliminate noise by proper signal conditioning and advanced digital signal processing techniques.

7.10.3 Intelligent welding process

A real-time ultrasonic system (Fig. 7.45) has been being developed for on-line monitoring and control of multi-pass arc welding process. Experimental results show that it is possible to detect and locate the liquid/solid weld pool interface. The measurements enable understanding the influence of high temperature gradients near the molten zones on the ultrasonic wave propagation. Artificial defects are introduced in the already completed weld pass. The detection and location of these defects during welding of subsequent passes by accounting for the beam propagation behaviour in the complex weld pool zone are in progress. The ultimate aim is the detection of the formation of defects during the welding process itself so that corrective action can be taken immediately by feedback control intelligent algorithms.

Under the Department of Science and Technology (DST) project on Intelligent Process Monitoring (IPM), work has been carried out on the use of NDT techniques such as AE and thermography for the study of resistance spot welding and narrow gap welding, and also for end cap welding, spacer pad welding and bearing pad welding processes employed for critical nuclear fuel sub-assembly components, in collaboration with the Welding Research Institute (WRI), Tiruchirapalli, and the Nuclear Fuel Complex (NFC), Hyderabad.

Narrow gap welding

In this study, carbon steel plates of length 1000 mm, width 100 mm and thickness 40 mm were machined to have a 'U' groove. CO_2 welding was

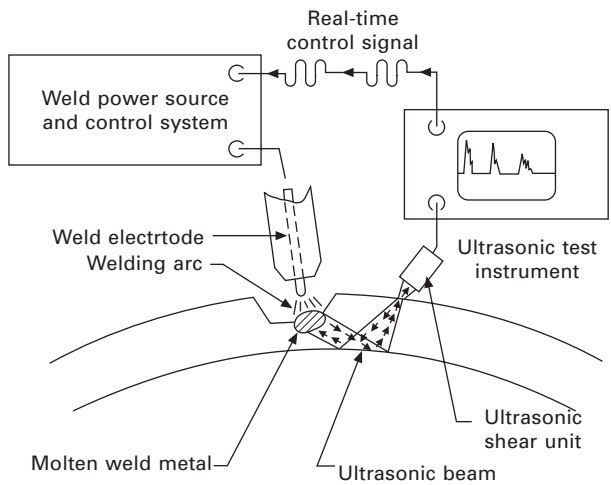

7.45 Conceptual ultrasonic system for intelligent welding process.

carried out inside the groove. AE and thermography techniques have been used to monitor the process. Analysis of the AE signals during the three phases of welding indicated that it should be possible to monitor the welding process. Analysis of thermal images indicated that it is feasible to map the thermal wave fronts from isothermal contour movements as the arc moves along the gap. The thermal distribution and its variation with time provides the required input for model-based evaluation of residual stresses, which in turn helps in optimising the welding process for obtaining weldments with minimum residual stresses.

Evaluation of resistance spot welds by acoustic emission, thermography and fuzzy logic assessment

In this study, AE and thermography techniques were used for on-line monitoring of the resistant spot welding process. In addition, other online approaches such as the use of the variations in dynamic resistance with a fuzzy logic approach have been attempted on the data of resistance spot welding generated at the WRI, Tiruchirapalli.

A number of carbon steel sheets of approximately 1.6 mm thickness were spot welded by making use of a 45 kVA capacity portable spot welding machine. Spot welding trials were carried out at different welding conditions (representing struck weld, good weld and splash weld conditions) by adjusting the phase shift setting and the weld time. Figure 7.46 shows the variation of root mean square (RMS) voltage of the AE signal with time for good welds and poor welds. Analysis of a number of welds indicated that the heat distribution in a good weld is uniformly and symmetrically distributed about the centre of the weld, whereas poor welds have an irregular thermal pattern.

To implement the fuzzy logic control, both nugget diameter and dynamic resistance were graded as small, medium and large with triangular membership function. The quality was assessed as very poor, poor, good and very good. Based on the software developed at the Indian Institute of Technology (IIT), Madras (Chennai), a fuzzy estimator for the above experimental data has been arrived at. Systematic studies showed that the experimental value of quality index is in agreement with that predicted by the fuzzy estimator.

Artificial neural networks applied to evaluation of resistance spot welding process

The process variables considered are the dynamic resistance, nugget diameter and the percentage load. From the data generated, a database of 20 points was screened during the training process. The first 15 points were used for training and the remaining 5 points were used for prediction. The optimum network architecture was achieved with 20 hidden nodes. The number of

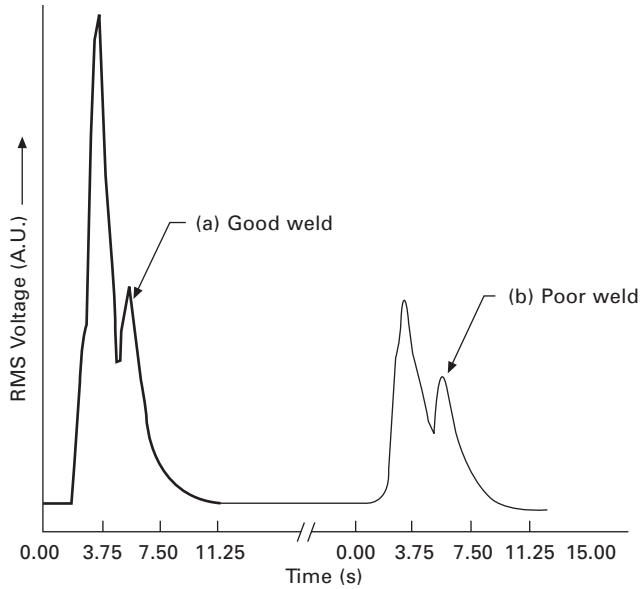

7.46 Variation in AE RMS voltage with time for (a) good weld and (b) poor weld.

cycles required was 30 000. The optimum value of learning rate is 0.000 13 and momentum rate is 0.5. The maximum deviation in the percentage error is about 5% for the trained data and 3.23% for the predicted data.

7.10.4 Weld monitoring of nuclear fuel element components

End cap welding

End cap welding is used for welding of nuclear fuel elements. The AE signals generated during the welding stage as well as during the post-weld stage were also found successful to discriminate normal welds from welds with defects. Higher acoustic activity was generated for tubes welded with various defects as compared with the AE generated during welding of tubes without any defects, i.e. normal weld (Fig. 7.47). The AE signals generated during the welding stage as well as during the post-weld stage were also successful in discriminating normal welds from welds with defects. It has been observed that two separate clusters (normal welds and welds with defects) are formed corresponding to the two weld categories. Thermal imaging carried out on these elements after the welding process indicated that it is possible to detect most of the imperfections very confidently. In general good welds are characterised by uniform isothermal widths and symmetrical

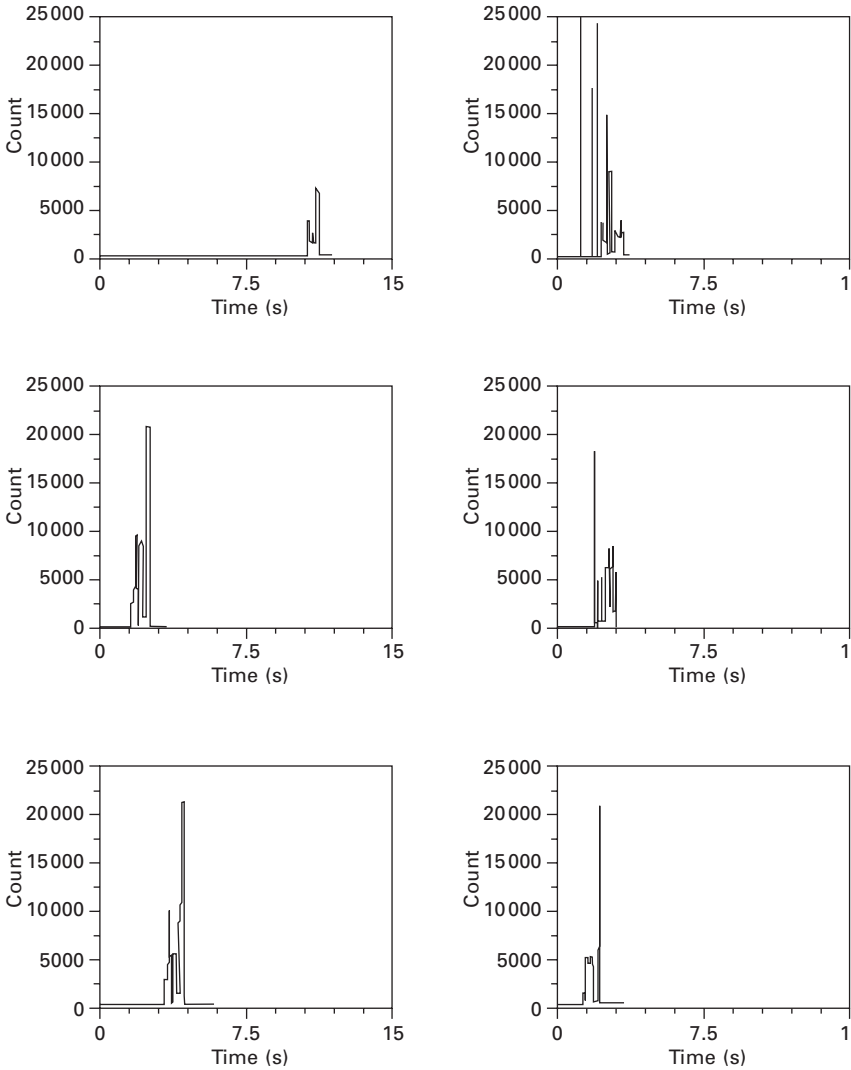

7.47 AE counts observed during end cap welding with various defects and variation of weld parameters.

isothermal patterns while poor welds are characterised by uneven isothermal widths and patterns. By thermography, the circumferential location where the defect had occurred could also be indicated.

Spacer pad welding

AE generated during the spacer pad welding was correlated with weld quality. A combination of AE parameters such as (a) initial counts and energy upon

start of welding, (b) cumulative counts and energy for the complete weld cycle including their values, and (c) counts and energy generated only during the welding stage, were identified. Figure 7.48 shows the master plot ((cumulative energy – initial energy) vs. (initial energy/cumulative energy)) for different types of welds. It can be seen that normal double coin welds form clusters in both the upper and lower regions of the plot while the single coin welds fall in the central region. The low pressure welds form clusters in the central region. It is also seen that the defective welds comprising both single coin welds and welds made with low pressure fall in the high side of the energy ratio. Thus, the different categories of welds, namely normal double coin weld, single coin weld and welds made with low pressure, can be clearly distinguished using different parameters of the AE signals.

Bearing pad welding

AE activity generated during bearing pad welding of the normal welds and welds with high current have shown that higher AE counts are generated during welding of the bearing pads with high current compared with normal weld. The variation of total counts generated with total strength values of the welds has also indicated the feasibility of distinguishing normal welds and welds with high current (Fig. 7.49).

7.11 Welding codes and standards

7.11.1 Codes

A code is a comprehensive document relating to all aspects such as design, material, fabrication, construction, erection, maintenance, quality control as well as documentation for specific industrial sectors such as pressure vessels, aircrafts, etc. Codes are prepared by professional bodies or government agencies on a specific subject. For some activities like design calculation, material qualification, NDT, semi-destructive testings, etc., codes may refer to standards which are independent and parallel documents. As for NDT, the codes should clearly indicate when and what NDT methods should be applied, what is the intent of NDT and what are the acceptance limits.

7.11.2 Standards

The codes will often refer to standards while more specific documents give the details of how a particular operation is to be carried out. These standards take into account the available technological levels and operational skills of the operators. To take an example, with regard to radiographic testing or any other NDT, test results are greatly dependent on the person's skill. Hence,

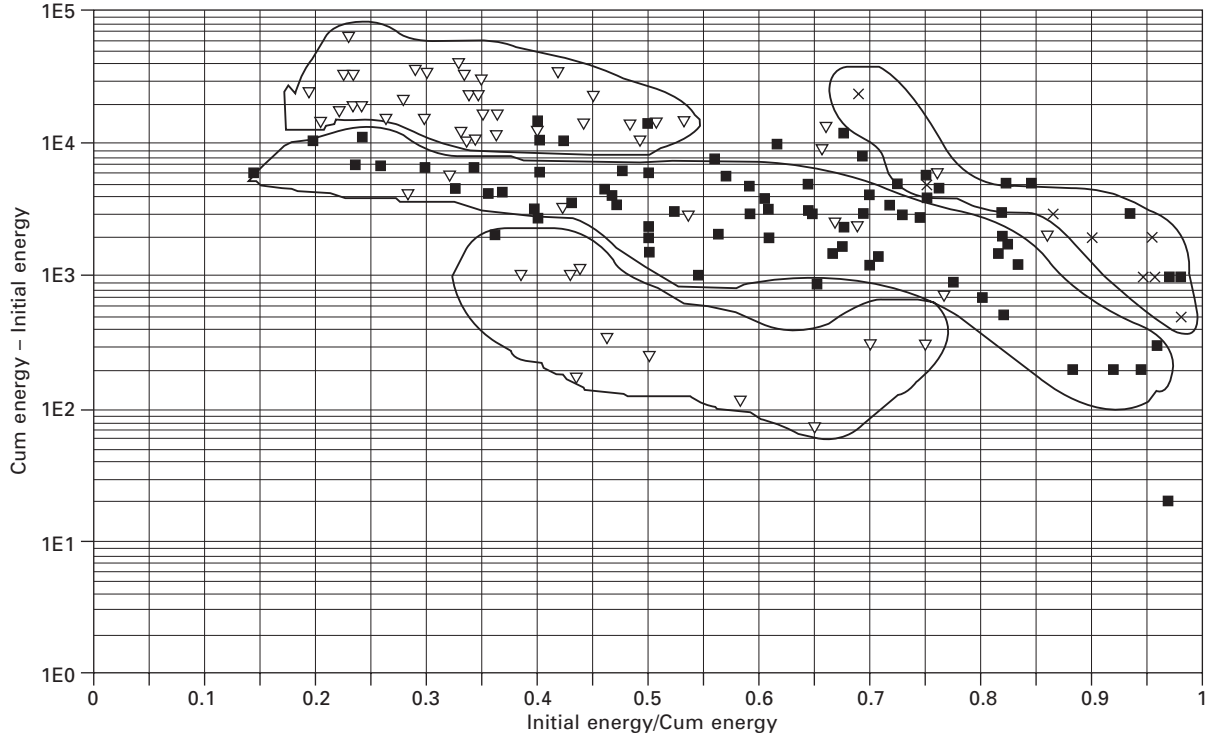

7.48 Variation in (cumulative – initial AE energy) with AE energy ratio for spacer pad welding (■ coin removed; ▽ double coin; × low press).

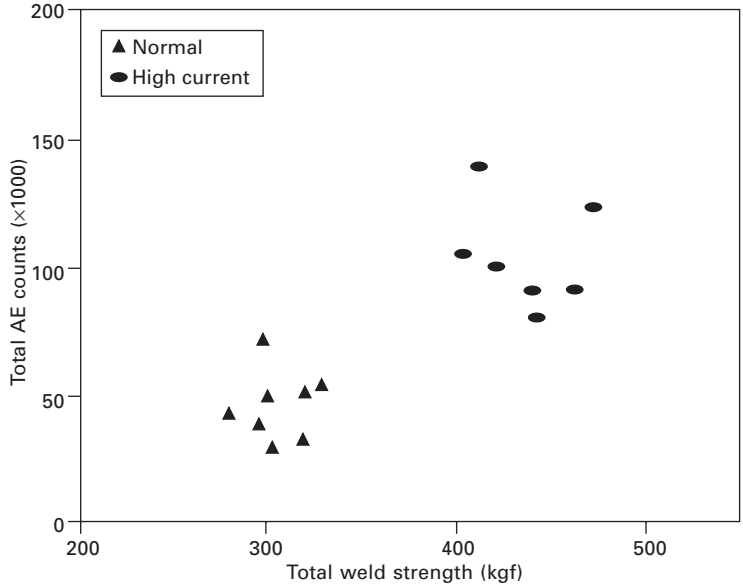

7.49 AE during bearing pad welding.

the procedures for testing and evaluation must be standardised in detail so that the test results will be least affected when the differences in the personnel skill exist.

Standards are documents prepared by a body of professionals or a government agency in a specific subject. As the name implies, standards attempt to standardise material or activity. The standards-making body takes into account industrial requirements and prepares standards in such a way that a few standards can fit in for a large variety of industrial applications. Codes in turn find it convenient to make use of these ready-made standards. Standards relating to NDT of welds are given in Appendix 7.1.

7.11.3 Specifications

The document that prescribes in detail the requirements with which the product or service has to comply is the specification. The specifications are of paramount importance in the achievement of quality. They may be written either by national bodies or by the manufacturer from their own experience. Appendix 7.2 gives the list of ASTM materials specifications where NDT is mandatory/non-mandatory. Appendix 7.3 gives the list of important standards available for hardness measurements, metallography, corrosion studies and destructive tests.

7.12 Conclusions

The qualifications of the welding consumable, welding procedure and welder performance are the most important activities to ensure the quality of welds. Once these activities are performed properly by the manufacturer it greatly facilitates the manufacturer to implement QA on welded structures. Destructive, semi-destructive and non-destructive testing play crucial roles of different kinds in each stage of the welding process of the components and structures. However, NDT techniques are the most preferable, starting from the qualifications of welding consumables and all stages of fabrication process of the welded structures. Also NDT plays key roles at the early detection of defects and the subsequent remedial measures during various inspection stages of welded components to assess their structural integrity. On-line monitoring of welds is another important subject matter for quality industrial productions and maintenance.

7.13 Acknowledgements

The authors are thankful to many colleagues at IGCAR and outside IGCAR whose work has been referred in this chapter and also for many useful discussions.

7.14 References and further reading

1. *Tool and Manufacturing Engineering Hand Book*, Eds. Raymond F. Veilleux and Louis W Petro, Publication of Society of Manufacturing Engineers, Vol. 5, p. 22–23, 1998.
2. *Welding Handbook*, Vol. 1, Chapters 11, 12 and 15, American Welding Society, Miami, USA.
3. ASME BPVC 2004, section IX, Qualification standards for welding and brazing procedures, welders, brazers and welding and brazing operators.
4. *American Society of Metals Handbook*, Vol. 6 and Vol. 11, ASM International, The Materials Information Society, Materials Park, OH, USA.
5. T.K. Kanazawa and A.S. Koayashi, Significance of defects in welded structures, *Proceedings of the Japan–U.S. Seminar*, University of Tokyo Press, 1974.
6. R. Halmshaw, *Non-destructive Testing*, Metallurgy and Materials Science Services, 1987.
7. W.J. Sperko, Exploring Temper Bead Welding, *Welding Journal*, July 2005, pp. 37–40.
8. AS 2205.6.1 – 2003 Methods for destructive testing of welds in metal Method 6.1: Weld Joint Hardness Test.
9. TWI, Hardness Testing Part 1 and Hardness Testing Part 2, www.twi.org.uk ('Information & know-how: Join IT technical information: Job Knowledge').
10. P. Palanichamy, A. Joseph, D.K. Bhattacharya and B. Raj, Residual stresses and their evaluation in welds, *Welding Engineering Hand Book*, Eds. S. Soundararajan,

S. Vijaya Bhaskar and G.C. Amarnath Kumar, Radiant Publications Pvt. Ltd, Secundrabad, India, 1992, Vol. 1, pp. 269–296.

11. P. Palanichamy, A. Joseph, S.K. Rai, T. Jayakumar and B. Raj, Evaluation of Residual Stresses in Weldments using NDT Techniques, *Proc. Symp. Joining of Metals (SOJOM 96*), Tiruchirapalli, India, Sept. 1996, pp. H021–H028.
12. S.K. Rai, T. Jayakumar, C. Babu Rao, D.K. Bhattacharya and B. Raj, Residual stress measurement in ferritic steel tube welds using X-ray diffraction technique, *Science and Technology of Welding and Joining*, Vol. 3, 1998, pp. 204–207.
13. B. Raj, T. Jayakumar and P. Palanichamy, Ultrasonic non-destructive evaluation for defects, microstructures and residual stresses, *Proc. National Symposium on Ultrasonics (NSU-96*), Sivakasi, Sept. 1996.
14. B. Raj, B. Venkatraman, C. Mukhophadyay, T. Jayakumar and A. Lakshminarayana, Intelligent Welding Using NDE Sensors, *7th European Conference on Non-Destructive Testing*, Copenhagen, 26–29 May 1998.
15. S. Nagarajan, W.H. Chen and B.A. Chin, 'Infrared sensing for adaptive arc welding', *Welding Journal*, Nov. 1989, pp. 462S–466S.
16. B. Venkatraman, S. Kanmani, C. Babu Rao, D.K. Bhattacharya and B. Raj, On-line monitoring of welds by infrared imaging, Presented in *7th Asian–Pacific Conference on Non-Destructive Testing*, October 1993, China.
17. P. Mclntire and R.K. Miller, *Non-Destructive Testing Handbook*. Vol. 5 on Acoustic Emission Testing, American Society for Testing and Materials, 2nd Edition, 1987, p. 276.

Appendix 7.1: compilation of standards on weld testing

Radiographic testing

Organisation	Standard No.	Title
ASTM	E 390	Reference radiographs for steel fusion welds.
	E 1032	Method for radiographic examination of weldments.
ASME	Sec. I/PW II	Radiographic and ultrasonic examination of boilers fabricated by welding.
	Sec. II/PW 51	Acceptance standards for radiography of boilers fabricated by welding.
	Sec. III (1)/NB 2553	Radiographic examination of seamless and welded (without filler metal) tubular products and fittings.
	Sec. III (1)/NB 2560	Examination and repair of tubular products and fittings with filler metal.
	Sec. III (1)/NB 5320	Radiographic acceptance standards for welds.
	Sec. VIII (1)/UW 11	Radiographic and ultrasonic examination of pressure vessels fabricated by welding.
	Sec. VIII (1)/UW 51	Radiographic examination of welded joints in pressure vessels fabricated by welding.
	Sec. VIII (1)/UW 52	Spot examination of welded joints in pressure vessels fabricated by welding (spot radiography).
BSI	BS 499/Part 3	Terminology and abbreviation for fusion weld imperfections as revealed by radiography.
	BS 2600	Methods for radiographic examination of fusion welded butt joints in steel.
	BS 2910	Methods for radiographic examination of fusion welded circumferential butt joints in steel pipes.
BIS	IS 1182	Recommended practice for radiographic examination of fusion welded butt joints in steel plates.
	IS 2953	Glossary of terms used in radiographic inspection of castings.
	IS 4853	Recommended practice for radiographic inspection of castings.
	IS 7810	Code of practice for radiographic examination of resistance spot welds of aluminium and its alloys.
ISO	ISO/R 947	Recommended practice for radiographic inspection of circumferential fusion welded butt joints in steel pipes up to 50 mm wall thickness.

Organisation	Standard No.	Title
	ISO/R 106	Recommended practice for radiographic inspection of fusion welded butt joints for steel plates up to 50 mm thick.
	2407	Recommended practice for radiographic inspection of fusion welded butt joints for steel plates of 50 to 200 mm thick.
	2437	Recommended practice for X-ray inspection of fusion welded butt joints for aluminium and its alloys and magnesium and its alloys of 5 to 50 mm thick.
	3777	Recommended practice for radiographic inspection of resistance spot welds for aluminium and its alloys.
DIN	DIN 54/11/Part I/II-73	Testing of welds of metallic materials by X-rays or gamma rays.

Ultrasonic testing

Organisation	Standard No.	Title
ASTM	E 164	Recommended practice for ultrasonic contact examination of weldments.
	E 273	Ultrasonic inspection of longitudinal and spiral welds of welded pipe and tubing.
ASME	Sec. I/PW 11	Radiographic and ultrasonic examination of boilers fabricated by welding.
	Sec. I/PW 52	Acceptance standards for ultrasonic examination of boilers fabricated by welding.
	Sec. III (1)/NB 2552	Ultrasonic examination of seamless and welded (without filler metal) tubular products and fittings.
	Sec. III (1)/NB 2560	Examination and repair of tubular products and fittings welded with filler metal.
	Sec. III (1)/NB 5330	Ultrasonic acceptance standards for welds.
	Sec. VII (1)/UW 11	Radiographic and ultrasonic examination of pressure vessels fabricated by welding.
	Sec. VIII (1)/W 53	Technique for ultrasonic examination of welded joints in pneumatically tested pressure vessels.
	Sec. VIII (1) Appendix U	Non-mandatory appendix, ultrasonic examination of welds.
	Sec. VIII (2) Appendix 9, Article 9-3	Mandatory appendix–Non-destructive ultrasonic examination welds.
BSI	BS 3923	Methods for ultrasonic examination of welds.
	Part 1	Manual examination of fusion welded butt joints in ferritic steels.

Organisation	Standard No.	Title
	Part 2	Automatic examination of fusion welded butt joints in ferritic steels.
	Part 3	Manual examination of nozzle welds.
BIS	IS 4260	Recommended practice for ultrasonic testing of butt welds in ferritic steels.
	IS 7343	Code of practice for ultrasonic testing of ferrous welded pipes and tubular products.
ISO	ISO 2400	Reference blocks for the calibration of equipment for ultrasonic testing of welds in steel.

Eddy current testing

Organisation	Standard No.	Title
ASTM	E 426	Recommended practice for electromagnetic (eddy current) testing of seamless and welded tubular products of austenitic stainless steel and similar alloys.
	E 1033	Recommended practice for eddy current examination of Type F-continuously welded ferromagnetic pipe & tubing above Curie temperature.
ASME	Sec. III (1) NB 3554	Eddy current examination of seamless and welded (without filler metal) tubular products and fittings.
BSI	BS EN 1711	Non-destructive examination of welds. Eddy current examination of welds by complex plane analysis

Magnetic particle testing

Organisation	Standard No.	Title
ASME	Sec. III (1) NB 2555	Magnetic particle examination of seamless and welded (without filler metal) tubular products and fittings.
	Sec. III (1) NB 2560	Examination and repair of tubular products and fittings welded with filler metal.
	Sec. III (1) NB 5340	Magnetic particle acceptance standards for welds.
BSI	BS 4397	Methods for magnetic particle testing of welds.
BIS	IS 5334	Code of practice for magnetic particle flaw detection of welds.

Liquid penetrant testing

Organisation	Standard No.	Title
ASME	Sec. III (1) NB 2556	Liquid penetrant examination of seamless and welded (without filler metal) tubular products and fittings.
	Sec. III (1) NB 2560	Examination and repair of tubular products and fittings welded with filler metal.
	Sec. VIII (2) AF 228	Liquid penetrant examination of welding joints.
BSI	BS 4416	Methods for penetrant testing of welded or brazed joints in metals.

Appendix 7.2: ASTM material specifications for welded components with NDT requirements

No.	Reference	Description	NDT Requirements	
			Mandatory	Non-mandatory
1.	A 381	Specification of metal arc welded steel pipe for high pressure transmission systems.	RT	
2.	A 422	Specification for butt welds in steel tubes for refinery service.	RT	
3.	A 557	Specification for electric resistance welded carbon steel feed water heater tubes.	UT/ECT	
4.	A 587	Specification for electric welded low carbon steel pipe.	UT/ECT	
5.	A 672	Specification for electric fusion welded steel pipe for high pressure service at moderate temperatures.	RT	UT/LPI/MPI
6.	A 688	Specification for welded austenitic stainless steel feed water heater tubes.	UT/ECT	
7.	A 691	Specification for carbon and alloy steel electric fusion welded pipes for high pressure service at high temperatures.	RT	UT/LPI/MPI

Appendix 7.3: standards for semi-destructive and destructive techniques

Metallography

	Standard no.	Description
1	ASTM E3	Practice for Preparation of Metallographic Specimens
2	ASTM E7	Terminology Relating to Metallography
3	ASTM E45	Test Methods for Determining the Inclusion Content of Steel
4	ASTM E112	Test Methods for Determining Average Grain Size
5	ASTM E92	Test Method for Vickers Hardness of Metallic Materials
6	ASTM E407	Practice for Microetching of Metals and Alloys

Corrosion tests

	Standard no.	Description
1	ASTM G 1-90	Practice for Preparing, Cleaning, and Evaluating Corrosion Test Specimens
2	ASTM G 4-95	Guide for Conducting Corrosion Coupon Tests in Field Applications
3	ASTM G 30-97	Practice for Making and Using U-Bend Stress-Corrosion Test Specimens
4	ASTM G 31-72	Practice for Laboratory Immersion Corrosion Testing of Metals
5	ASTM G 36-94	Practice for Evaluating Stress-Corrosion-Cracking Resistance of Metals and Alloys in a Boiling Magnesium Chloride Solution
6	ASTM G 31	Standard Practice for Laboratory Immersion Corrosion Testing of Metals
7	ASTM G 60-95	Test Method for Conducting Cyclic Humidity Tests

Hardness

	Standard no.	Description
1	ASTM-E10-01	Standard Test Method for Brinell Hardness of Metallic Materials
2	ASTM-E18-05	Standard Test Methods for Rockwell Hardness and Rockwell Superficial Hardness of Metallic Materials
3	ASTM-E92-82(2003)	Standard Test Method for Vickers Hardness of Metallic Materials

	Standard no.	Description
4	ASTM-E103-84(2002)	Standard Test Method for Rapid Indentation Hardness Testing of Metallic Materials
5	ASTM-E110-82(2002)	Standard Test Method for Indentation Hardness of Metallic Materials by Portable Hardness Testers
6	ASTM-E140-05	Standard Hardness Conversion Tables for Metals
7	ASTM-E384-06	Standard Test Method for Microhardness of Materials
8	ASTM-E1842-96	Standard Test Method for Macro-Rockwell Hardness Testing of Metallic Materials
9	ASTM-E384-06	Standard Test Method for Microhardness of Materials
10	TWI-Hardness	Testing Part 1 and Hardness Testing Part 2, www.twi.org.uk
11	AS 2205.6.1 – 2003	Methods for destructive testing of welds in metal. Method 6.1: Weld joint hardness test

Destructive tests

	Standard no.	Description
1	BS ISO 22826:2005	Destructive tests on welds in metallic materials. Hardness testing of narrow joints welded by laser and electron beam (Vickers and Knoop hardness tests)
2	BS EN ISO 14323:2006	Resistance spot welding and projection welds. Destructive testing of welds. Specimen dimensions and procedure for impact shear test and cross-tension testing
3	BS EN ISO 17642-3:2005	Destructive tests on welds in metallic materials. Cold cracking tests for weldments. Arc welding processes. Externally loaded tests
4	BS EN ISO 17653:2003	Destructive tests on welds in metallic materials. Torsion test of resistance spot welds
5	BS EN ISO 14329:2003	Resistance welding. Destructive tests of welds. Failure types and geometric measurements for resistance spot, seam and projection welds
6	BS EN ISO 14324:2003	Resistance spot welding. Destructive tests of welds. Method for the fatigue testing of spot welded joints
7	BS EN ISO 17654:2003	Destructive tests on welds in metallic materials. Resistance welding. Pressure test on resistance seam welds

Residual stress measurements

	Standard no.	Description
1	ASTM-E837-01e1	Standard Test Method for Determining Residual Stresses by the Hole-Drilling Strain-Gage Method
2	ASTM-E915-96(2002)	Standard Test Method for Verifying the Alignment of X-Ray Diffraction Instrumentation for Residual Stress Measurement

NACE – National Association of Corrosion Engineers
ASTM – American Society for Testing of Materials
ASME – American Society of Mechanical Engineers
AWS – American Welding Society
BIS – Bureau of Indian Standards
BSI – British Standards Institution
CSA – Canadian Standards Association
DIN – Deutsches Institute for Normung
ISO – International Organization for Standardization
NIST – National Institute of Standards and Technology

8

Lessons learnt from failures of ferrous weldments

B RAJ, K V KASIVISWANATHAN, N RAGHU, N G MURALIDHARAN and V KARTHIK,
Indira Gandhi Center for Atomic Research, India

Abstract: Iron-based alloys are widely used in the engineering industries due to their ease of fabrication and ability to meet the desired properties. A variety of ferrous alloys with varying chemical composition have been developed in the recent years for achieving desired results. Among the known fabrication techniques, welding is a reliable, cost-effective and efficient metal joining process. A number of welding processes have been developed over the years to meet industry's stringent specifications and requirements. However, most of the industrial failures have been weld related. In spite of utmost care in design, selection of materials and fabrication route and judicious choice of operating conditions, degradation of the fabricated components takes place in service leading to failures at times. Weld defects that occur during fabrication can be avoided by careful selection of welding process. The defects formed during fabrication or during service can be detected by a variety of non-destructive testing methods. This chapter discusses the various aspects of welding related degradation of commonly used ferrous alloys with an aim to reduce their failures.

Case studies to elucidate the different kinds of failures and a summary of a few important failure investigation campaigns undertaken at the authors' laboratory are highlighted. Recommendations to avoid such failures are brought out in this chapter.

Key words: ferrous alloys, stainless steel, sensitisation, design, fabrication, testing, failure analysis, non-destructive test, heat-affected zone, condenser tube, transition joint, residual stress, reducer, dished end, ball valve, stainless steel bellows, bellow sealed valve, electric resistance welding, insulation, stress corrosion cracking, hydrogen embrittlement, fatigue, hardness.

8.1 Introduction

Welding is a reliable, cost-effective and efficient metal joining process for a wide range of metallic components in most engineering activities. Presently, in addition to conventional welding methods such as arc welding, energy beam welding methods using lasers and electron beam with concentrated heat source have come into existence. High speed automated welding of metals and alloys is commonly practised to produce superior quality welds for critical applications in aerospace, defence and nuclear industries. However, the quality of the welding chiefly depends on the design of the joint, type of

process, chemistry of base metal and welding consumables and also on the skill of the welding personnel.

Iron-based metals and alloys are widely used as materials of construction for a variety of applications due to their consistent, uniform and predictable properties. The properties of the metal can also be customised by addition of different alloying elements. Welding is a commonly used fabrication technique for these classes of alloys owing to their easy weldability with adequate mechanical and corrosion-resistant properties of weldments. However, most industrial failures have been weld related. Investigation of weld failures and their detailed analyses have given valuable feedback for the development of welding technology of ferrous alloys. A host of welding processes and consumables have been developed for iron-based alloys to mitigate the problems of weld failure. This chapter will discuss some of the fundamental aspects of welding of various ferrous alloys, focusing on avoiding weld failure and the lessons learnt from the failure analysis as feedback. Case studies of some failure analysis carried out in the authors' laboratory and the related illustrations are also presented.

8.2 Welding processes for ferrous alloys

Ferrous metals and alloys such as carbon steels, alloy steels, stainless steels and cast iron are used in a wide variety of industrial applications. These ferrous alloys are classified according to their chemical composition. The processes used for welding of ferrous alloys are either fusion or solid state welding methods. The three most important characteristics of a fusion welding process are the intensity of the heat source, heat input rate per unit length of the molten weld metal and the type of shield of the weld from the atmosphere during welding. Fusion welding relies on the use of a heat source to melt the edges of a joint to produce the weld. Heat sources for welding can be obtained either by electrochemical, electrical or radiation means. The popular methods using electrochemical heat source are the gas welding and thermit welding methods. Arc welding and resistance welding methods use an electrical heat source. Fusion welding techniques that use radiant heat sources are electron beam welding and laser welding, which have a very high energy density, achieving deep weld penetration and thereby minimising the size of the weld area.

The type of heat source used to create a ferrous weld has a profound effect on the properties of the joint, in addition to the welding consumables used. Fusion welds can be associated with various defects such as cracks, lack of fusion, porosity, undercut, lack of penetration, segregation, non-equilibrium phase transformation and solidification cracking. These defects are produced due to processes that commonly take place during fusion and re-solidification. In addition to this, the parent metal adjacent to the fusion zone undergoes

thermal cycling leading to the formation of heat-affected zones (HAZ) with microstructural variations. Solid state welding methods such as forge welding, friction welding, explosive welding and diffusion bonding are also employed to join ferrous alloys and have the advantage of being able to weld ferrous alloys to other non-ferrous materials with varying melting points and properties.

8.2.1 Microstructural and welding defects arising out of design, fabrication and service

Operating conditions and application requirements are essential elements in the design of a weld joint to give a reliable, stable and useful service life. The life of the joint chiefly depends upon tension, bending, torsional and thermal stresses experienced by the joint both during fabrication and in service. Hence, operating conditions and service requirements have to be primarily considered during the design of a weld joint.

If welded components are likely to undergo cyclic loadings during service, sufficient design features to avoid fatigue failure also have to be considered. Apart from the nature and frequency of loading, the strength of the joints in fatigue is largely dependent on the geometry and surface contours. Discontinuities such as sharp angles, corners and notches cause stress concentration and can generate stress intensities of greater magnitude than the designed value, leading to premature failures. Also, the changes in chemical composition and microstructure of the component during service exposure can cause considerable degradation in material properties. Most components are not uniformly susceptible to such ageing degradation. Factors that affect vulnerability to degradation include localised chemical or metallurgical variations, geometry, stresses and chemical potential gradients. The change in the initial microstructure arises basically due to metallurgical instability, viz. transformation of metastable phases to different stable phases, precipitation of new phase and changes in the grain size. Such changes take place when the component is exposed to high temperatures for long durations.

Hence, it is important to understand the mechanisms of ageing and particularly the changes that take place with time during service in the chemical composition of the material and its microstructure. Most of the damage processes are microstructure-related changes, which cause degradation in the mechanical properties and consequent reduction in the residual life of the component. An important factor to be considered is the synergism between the various damage mechanisms. The damage caused by an individual mechanism is much less than that caused by the combination of mechanisms such as creep-fatigue damage, corrosion fatigue and hydrogen stress cracking.

To manage the degradation process, a thorough knowledge of material behaviour is essential in design and operation, and for developing quality

assurance methods, plant inspection, condition monitoring and maintenance schedules. Therefore a multi-pronged strategy based on state of the art techniques is essential to extract information on the material performance for the safe, reliable and efficient operation of the plant component.

8.2.2 General failure mechanisms related to weldments

An ideal weld joint is required to match the properties of the base material and perform like the base material it joins. This is, however, rarely achieved in practice as the process of welding itself introduces certain features which degrade the mechanical and corrosion properties of the weld joint. The weld metal is an *in situ* casting and may contain discontinuities which may weaken it either during fabrication or in service. The weld metal is generally regarded as a weak link in the structure as the majority of the component failures take place in this region either during welding or during service. The discontinuities present in a weld metal can be categorised as a planar or volumetric defect. The planar defects are crack-like in nature, such as hot cracks, cold cracks, lack of bead penetration and lack of side wall fusion, and can be treated as two-dimensional discontinuities. The volumetric defects have rounded geometries such as porosities and slag inclusion. In general, the planar defects are more harmful to weldment than the volumetric defects.

Critical design properties of a weldment such as creep, low cycle fatigue and creep–fatigue interaction depend on the type, distribution and location of the discontinuity. The formation of welding defects is dictated by the type of material, its weldability, welding process, welding parameters, joint design and the welding consumables used. A strict control on these parameters minimises the formation of defects. Moreover, knowledge of the behaviour of a defect in a given service environment increases the confidence in the design and performance of a component. Therefore, to increase reliability of the components, it is essential to understand the various phenomena affecting the weldability of a material.

8.3 Major failure mechanisms associated with ferrous weldments

The contents of sub-sections 8.3.1 to 8.3.4 provide summaries of these topics. Elaborate descriptions can be found in other chapters of this book.

8.3.1 Low alloy carbon steels

Plain low alloy carbon steels contain 0.10–0.25% carbon, 0.25%–1.5% Mn and silica. These steels are found to be readily weldable by fusion welding methods without any danger of cracking. However, low alloy steels such as

low manganese steels, nickel–chromium steels and, chromium–molybdenum steels having a small amount of alloying elements are sometimes associated with welding defects. Fusion welding of these alloys requires selection of low hydrogen-covered consumable electrodes to match the mechanical properties and chemical composition of the base metal. For welding of thicker sections, preheating of the components in the range of 423–533 K is required when the carbon content is more than 0.15% to minimise the danger of hydrogen embrittlement. Also, post-weld heat treatment (PWHT) is necessary to relieve residual stresses caused due to rapid cooling.

During the process of welding, the HAZ and the weld metal are subjected to phase transformation caused by the weld thermal cycle. However, the heating and cooling rates in the weld thermal cycle are much faster and hence the final transformation products formed in the HAZ and the weld metal are different from those present in the unaffected base metal. These transformations, coupled with the presence of residual stresses and segregation of deleterious elements (e.g. P and S) in the weld metal, make the steel susceptible to cracking. The most significant cracking problems in steels are the hydrogen-assisted cracking (HAC) and PWHT cracking during the fabrication. HAC commonly occurs in the grain-coarsened HAZ. It is also known as delayed cracking or cold cracking because cracking usually occurs after an incubation period, which may vary from a few hours to days. The weldability of such steels has been improved by (i) the introduction of steels with lowered carbon contents and thus lower carbon equivalent, (ii) the application of various thermo-mechanical treatments to enhance strength and toughness by grain size and micro-structure control, (iii) lower sulphur content and inclusion shape control and (iv) the availability of high quality low hydrogen consumables.

8.3.2 Chrome–molybdenum steels

The Cr–Mo ferritic steels are widely employed in the fabrication of steam generators for power plants, which are capable of withstanding higher service temperatures. The most popular variety of these steels is the 2.25Cr–1Mo ferritic steel whose applications are limited to service temperature not exceeding 773 K. For applications at temperatures higher than 773 K, 9Cr–1Mo and 12Cr–1Mo steels and their modified versions are used.

Ferritic steels are prone to HAC in the HAZ and weld metal during the fabrication process. Three factors are of paramount importance in defining the HAC problem: (i) susceptible microstructure, (ii) diffusible hydrogen content ($[H]_D$) and (iii) restraint. Control of any of these parameters can greatly reduce the risk of HAC. The microstructure and restraint essentially depend on the composition of the steel and joint design respectively, and therefore are less amenable to control. However, the amount of $[H]_D$ in a

weld can be controlled by judicious choice of welding consumables and their pretreatment. The practice of baking the welding electrodes and preheating the work piece is usually employed to minimise the amount of $[H]_D$ in the weldments. For a given set of welding parameters, the preheat temperature depends on the steel composition and diffusible hydrogen content. The Cr–Mo ferritic steels show a variety of microstructures in the weld and the HAZs which depend on the chemical composition and heat input of the welding process. The 9Cr–1Mo steel is fully hardenable steel and the weld microstructure is essentially independent of the heat input employed, whereas the weld metal microstructure in the low Cr alloys depends on heat input.

The PWHT is carried out (i) to relieve residual stresses and (ii) to temper the hard microstructure. However, some steel compositions are prone to PWHT cracking in the HAZ. The crack propagates along the prior austenite grain boundaries in a brittle manner and manifests itself often in the coarse-grained HAZ and occasionally in the weld metal also. The tendency of PWHT cracking primarily depends on the material composition. Low alloy Cr–Mo steels are more prone to cracking than the high alloy steels. The Cr–Mo composition with Cr < 1 wt% and Mo < 0.5 wt% is insensitive to PWHT cracking. The composition with Cr contents 0 to 1 wt% but Mo > 0.5 wt% is very sensitive to cracking and the tendency to cracking increases as the Mo content is increased. However, the alloys with Cr > 2 wt% and 0.5–1 wt% Mo show decreasing sensitivity to cracking with increasing Cr content. The precipitation of M_2C type of carbides is responsible for PWHT cracking and precipitation of M_7C and $M_{23}C_6$ type carbide precipitation does not influence cracking. The presence of V, Al, B, Cu and tramp elements are also found to increase the crack susceptibility of Cr–Mo steels [1].

Traditionally, Cr–Mo steels are used in the power plant headers and boilers that are exposed to high temperature oxidative atmospheres. The service life of these parts is limited by creep, fatigue and oxidation. In the fabrication of steam generators for power plants, steels with different Cr contents are used depending on the service temperature experienced by the different parts of the steam generators (superheater, reheater). This results in the dissimilar metals welds at selected locations. PWHT of such dissimilar weldments results in the formation of a soft region near the weld interface on the low Cr side and a hard zone on the high Cr side of the weldments. The presence of the soft zone and an adjoining hard zone near the weld interface of the weldment adversely affect the properties of the joint, although no major failure has been reported. This is in contrast to a number of failures that have been observed in the case of dissimilar welds between ferritic steels and austenitic stainless steels where fracture has been attributed to the formation of precipitate bands in the weld metal and recrystallised soft zones near the weld interface in the ferritic steel.

Trimetallic joints

Dissimilar welding between austenitic stainless steels and Cr–Mo ferritic steels that are used in power plants are found to suffer premature failures. The difference in the coefficients of thermal expansion (CTE) between the base metals and the weld metal generates thermal stresses during the numerous start-ups and shut-downs. These cyclic stresses superimposed on the residual stresses due to welding, external loads and internal pressure of the process fluids result in the service failure of these joints. These failures take place in the ferritic steel HAZ immediately adjacent to the weld fusion line. To circumvent such problems associated with the dissimilar joint, a trimetallic transition joint with an intermediate piece (having a CTE between that of the ferritic steel and the austenitic stainless steel) is used. In case of Cr–Mo steel–AISI 316 stainless steel weld, Alloy 800 is used as a transition piece. Alloy 800 is welded to stainless steel by 16-8-2 consumable and to Cr–Mo steel by using Inconel 182 consumable [2]. There is a gradual reduction in CTE from the stainless steel side of the joint through the Cr–Mo ferritic steel side, leading to significant reduction in the magnitude of thermal stresses. Accelerated laboratory studies have demonstrated a four-fold increase in the life of the trimetallic joint over the conventional bimetallic joint.

8.3.3 Stainless steels

Stainless steels are highly corrosion-resistant ferrous alloys that contain chromium with or without nickel additions. There are three basic types: austenitic, ferritic and martensitic stainless steels, and a host of modified varieties of stainless steels to suit particular applications.

Austenitic stainless steels are used as a major structural material, particularly in the nuclear industry where reliability and long service life are the major considerations. The desirable properties of austenitic stainless steels include excellent corrosion resistance, absence of ductile-to-brittle transition phenomenon, good resistance to radiation damage and attractive high temperature properties including oxidation resistance. The primary joining method for components made of stainless steel is fusion welding.

The austenitic stainless steel welds tend to crack in the weld deposit if they are fully austenitic and are prone to solidification cracking in the weld deposit and liquation cracking in the base metal HAZ and in the weld metal HAZ. The presence of a certain minimum amount of δ-ferrite in the weld metal is essential to obtain a crack-free joint. This is achieved by intentionally balancing ferrite formers and austenite formers in the welding consumable. The ferrite formers are Cr, Mo, Si, Nb and Ti and are represented by Cr_{eq}, while the austenite formers are C, N, Ni, Mn and Cu and are represented by Ni_{eq}. The ratio of Cr_{eq}/Ni_{eq} is an important indictor with respect to (a) primary

solidification mode of the weld metal, (b) δ-ferrite amount and its morphology and (c) susceptibility of weld metal to hot cracking. The amount of ferrite can be determined by constitution diagrams such as the Delong diagram and WRC–92 diagram. The WRC–92 diagram also provides additional information about the primary mode of solidification since it is a function of Cr_{eq}/Ni_{eq} ratio. When this ratio is less than 1.48 the weld metal solidifies in the primary austenitic mode and the room temperature microstructure may not contain δ-ferrite. However, if the Cr_{eq}/Ni_{eq} ratio is greater than 1.48, the weld metal solidifies in primary ferritic mode and the room temperature microstructure may contain varying amounts of δ-ferrite. Resistance of the weld metal to hot cracking depends on the amount of δ-ferrite and the amount of trace element content of (P + S). The small addition of Ti to stainless steel makes it less susceptible to the hot cracking phenomenon. However, when a duplex microstructure containing δ-ferrite is exposed to elevated temperatures, the ferrite transforms to various secondary phases. The rate of transformation of δ-ferrite and the nature and amount of secondary phases formed depend on ageing temperature, exposure time and chemical composition of the weld metal. These secondary phases can sometimes be hard, leading to loss of ductility.

8.3.4 Sensitisation in stainless steel

Stainless steel is a family of iron–base alloys that contains at least 12% chromium. Chromium is an essential element that makes steel corrosion resistant by forming a protective chromium oxide film on its surface. Stainless steels have excellent corrosion resistance as chromium rapidly oxidises and repairs the damaged oxide film due to self-healing property. During heat treatment or weld thermal cycles, stainless steel experiences a temperature range of 550–850 °C. Chromium and carbon react to precipitate as chromium carbides along the grain boundaries. This process leads to the depletion of chromium in the adjacent narrow region along the grain boundaries. The chromium-depleted region has poor resistance to corrosion compared with the normal grains where chromium content is not affected. A stainless steel is said to be sensitised when chromium carbides form in its microstructure. Sensitisation is a condition where the protective chromium in the material is reduced to levels below the minimum level necessary for effective corrosion protection. The temperature range for sensitisation to occur varies for different grades of stainless steels. If sensitised stainless steel is placed in an environment favourable to corrosion, then intergranular corrosion (IGC) occurs. The rate of intergranular corrosion is hard to predict and is based on a complex relationship involving time, temperature and environment. Weld decay is a form of IGC in stainless steel with a sensitised microstructure at the HAZ formed during welding. Weld decay can be prevented by (i) selection of low

carbon grade stainless steel, (ii) stabilized grade of stainless steel which contains titanium or niobium and (iii) adoption of proper PWHT methods. Another form of intergranular corrosion is knife line attack, which occurs in stabilised stainless steel along an extremely narrow line close to the fusion zone.

Nitrogen steels

The structural integrity of stainless steel components is affected by various types of material degradation processes such as IGC, pitting corrosion, wall thinning, creep and fatigue damage. Most of these failures have been attributed to sensitisation of austenitic stainless steels. The problem of sensitisation can be overcome by decreasing the carbon content, which would cause drastic reduction in mechanical properties. Replacing much of the carbon with nitrogen can offset this deterioration in mechanical properties. Nitrogen in solid solution is the most beneficial alloying element in promoting high strength in austenitic stainless steel without sacrificing its good ductility and toughness as long as the solubility limit of nitrogen in austenite is not exceeded. The addition of nitrogen to stainless steel also improves the corrosion properties of the base metal and has been found to be beneficial in retarding the precipitation of embrittling phases in the welds. Together with chromium and molybdenum, nitrogen additions to austenitic stainless steels improve resistance to pitting and crevice corrosion, IGC and stress corrosion cracking (SCC). Therefore, high-nitrogen stainless steels have become an increasingly important new class of engineering materials for wide-ranging applications.

8.4 Reducing failures in weldments

Sub-sections 8.4.1 through to 8.4.4 provide summaries of these topics. Elaborate descriptions can be found in other chapters of this book.

8.4.1 Design

The weld joint is designed to ideally give the assembly the required structural strength and integrity for its intended function. The welding design should also take into consideration various factors such as (i) ease of fabrication, (ii) reliability, (iii) cost and (iv) ease of inspection using non-destructive examination (NDE) techniques during periodic repair and maintenance.

The joint design is determined primarily on the basis of the load requirement and the method of welding. Joint design also takes into account the thickness, geometry of the parts to be welded and the restraint of the weld joints. The required thickness for the load-carrying members is commonly determined

by an allowable design stress, which is based on a fraction of the yield strength at the intended elevated temperature and stress-to-rupture strength parameter used for high temperature design.

8.4.2 Choice of welding processes, parameters and consumables

The welding process is selected on the basis of the thickness of the material, joint design, physical characteristics such as strength, ductility, fatigue, creep resistance, corrosion resistance and compatibility with the fluids handled in service. Welding consumables are the filler metals employed in different forms for the various welding processes. A welding consumable is selected on the basis of its compatibility with the base material to ensure that no brittle intermetallics are formed. The weld metal should have adequate toughness at the given design temperature. The weld metal should also have the ability to resist some amount of dilution of the base metal and should be acceptable under the expected service condition. The corrosion resistance of the weld metal has to be superior to that of the base metal to prevent preferential corrosion by galvanic coupling. PWHT operations such as normalising and stress-relieving treatment are found to produce desired results.

During welding there is an intense concentration of heat and hence the regions near the weld line undergo severe thermal cycles. These thermal cycles cause non-uniform heating and cooling in the material, thus generating inhomogeneous plastic deformation and residual stresses in the weldment. The presence of residual stresses can be detrimental to the performance of the welded products. Tensile stresses are generally detrimental in increasing the susceptibility of a weld to fatigue damage, stress corrosion cracking and fracture. The magnitude of residual stresses depends on the temperature distribution in the weldments which is chiefly determined by its thermal conductivity, and the CTE. Suitable mechanical treatment such as proof stressing, peening, vibratory conditioning and thermal treatment such as pre-heating and PWHTs are carried out to minimise the effects of these residual stresses, leading to service failures.

8.4.3 Welding process optimisation

In fusion welding, the melting of metal causes shrinkage when the liquid metal solidifies. Shrinkage of metal introduces residual stresses and distortion. Distortion can be minimised by offsetting the work to produce the desired configuration and by tailoring the welding sequence and by carrying out welding in different segments.

In welding process optimisation, the size of the weld is estimated by stress–strain formulas based on mechanics of materials and various yield/

failure theories. ASME section VIII division 1 code 5 based on maximum principal stress theory is generally used for design purposes.

The welding process is optimised after taking into consideration the following:

- Selection of the joint design that requires least amount of weld metal. An excess weld reinforcement may lead to distortion and also affects the performance of the joint.
- Use of fillet welds instead of groove welds if fatigue is not a design criterion.
- Use of double groove welds instead of a single groove weld on thick plates to reduce the amount of weld metal and to control distortion.
- Use minimum root opening and included angle in order to reduce the amount of filler metal requirements.
- For corner joints in thick plates where fillet welds are not adequate, bevelling both members should be considered to reduce tendency for lamellar tearing.
- Design of joint for easy accessibility for welding.

The welding design plans for joints that are essentially free from discontinuities but this is not realistic as welded joints generally contain some discontinuities. Welded components are at times subjected to cyclic loading during service. This leads to fatigue loading and fatigue failure of joints has to be considered. Apart from the nature and frequency of loading, the strength of the joints in fatigue depends on the physical shape and contours. All kinds of discontinuities such as sharp corners, notches, angles and weld beads can create stress concentration sites. These stress concentration sites lead to initiation of cracks whose propagation results in service failure [3].

8.4.4 Quality assurance and quality control methods

Weldability testing

Weldability is defined as the capacity of a material to be welded into a specific, suitably designed structure under the imposed fabrication conditions and to perform satisfactorily in the intended service. Weldability testing is intended to demonstrate the suitability of a particular material combination to form a weldment for a particular service. This involves testing under specific conditions of fabrication or of service, which is intended to reveal the metallurgical behaviour of the weld metal. No single weldability test or a combination of tests can exactly duplicate the conditions present in an actual structure. Standard weldability tests provide a means to compare different metals, processes and procedures with respect to their suitability.

Destructive testing of weldments

The direct way to assess the performance of a welded joint in service would be to test it in actual service conditions. However, this is impractical, and therefore standardised tests and testing procedures are necessary. The standardised testing methods of weldments provide specific information on the serviceability. The tests are used for qualifying the welding procedure, for establishing the properties of welded assembly and for determining whether it is capable of imparting the required properties for the intended application. The uniaxial tension test is a very popular method for evaluation of strength and ductility of the material. In tensile tests for base metal, either longitudinal or transverse section of the sample is chosen. The engineering parameters such as yield strength, tensile strength and percentage elongation and percent reduction in cross-sectional area are determined. In the guided bend test, the weld is bent or wrapped around test jigs to evaluate ductility and soundness of welded joints. This test is commonly used in welding procedure and welder performance qualification. The variants of the tests are root bending (weld root in tension), face bending (weld face in tension) or side bending (weld cross-section in tension). Thus, the ductility and soundness of the welded joints are evaluated. Presence of weld defects drastically reduces the ductility and non-uniform properties along the length of the specimen cause non-uniform bending. The drop weight test determines the nil-ductility transition temperature, the temperature above which a dynamic crack will be arrested for gross elastic deformation in the specimen. The Charpy V-notch impact test is also a common method to characterise this transition behaviour. The test data are represented as a plot of the absorbed energy or percentage of shear fracture with test temperature. The data are used to predict the minimum service temperature so as to avoid the possibility of brittle fracture in carbon steel structures. Current practice, however, calls for data from Charpy and drop weight tests to arrive at this temperature.

Plain strain fracture toughness (K_{IC}) is the resistance to crack extension under conditions of plain strain (highest restraint to plastic flow) at a crack tip. For welded material, compact tension (CT) specimens are made in standard geometries. The initial crack is obtained by fatigue pre-cracking a machined notch. Once the desired crack length is obtained, the specimen is tested in tension and the load corresponding to failure is determined. Standard procedures are used to estimate the value of K_{IC}. The fracture toughness properties of weld metal, HAZ or the base metal in the welds are evaluated for their susceptibility to cracking. Fatigue testing of weldments is used to develop design data when the material is subjected to cyclic loading. Fatigue properties depend on the component design and the state of stress, mean stress and stress range. In fatigue tests, the data are represented in the form of *S–N* plots, i.e. a double logarithmic plot of stress range to the number of cycles

to failure. The creep test is a crucial property for structural components operating at high temperatures [4].

Non-destructive testing of weldments

In spite of best efforts to design, fabricate and inspect the welded components for their high quality and reliable performance, many of the industrial failures are related to weld and HAZ. These failures can be attributed to the improper design of weld joint, selection of base materials and filler materials, welding processes, inspection procedures and/or operating parameters. The use of non-destructive testing (NDT) to inspect welded components immediately after fabrication and also during service helps in minimising weld failures.

Defects can be classified as physical discontinuities, microstructural defects and defects related to residual stress and distortion. The objective of the testing method is to detect defects as specified in the design based on fitness-for-purpose. Many advanced NDT techniques have now emerged for detecting defects with improved sensitivity and also with the capability to quantify the defects.

Visual inspection techniques play an important role in the quick assessment of the quality of welds and to identify defects. Many characteristics of a weld can be evaluated by visually examining a weld. For non-critical welds, integrity is verified principally by visual inspection. Visual inspection is also useful for assessing the dimensional accuracy, conformity of the welds to size, fit up and control requirements, weld appearance with regard to surface roughness, weld spatter, undercuts and overlaps and other imperfections. Geometrical imperfections such as improper weld ripple, convexity and concavity formed in tubular components can also be visually detected. Capabilities of visual inspection technique can be enhanced by using simple gadgets and instruments.

Liquid penetrant testing (LPT) is a popular NDT method to detect surface defects and sub-surface defects open to surface in welded components. This method is adopted for inspection of all materials and to detect leaks in welded tubes and tanks. LPT is also used in root pass and subsequent passes to detect surface defects so that repair work can be undertaken to remove the defects in the weld. In the case of inspection of ferromagnetic materials, the magnetic particle testing (MPT) technique is preferred since this facilitates detection of sub-surface detects that are not open to the surface.

The eddy current testing (ECT), based on the principle of electromagnetic induction, is used to identify and differentiate among a wide variety of physical, structural and metallurgical conditions in electrically conductive materials. A discontinuity that appreciably alters the normal flow of eddy current is detected in this technique. ECT is used to locate defects such as lack of fusion, incomplete penetration, cracks, oxidation and changes in

chemical composition and variation in hardness of welds. This method is adaptable for high speed inspection, and the improvement in sensor development and electronic instruments has paved the way for automation.

In ultrasonic testing (UT) high frequency sound waves are introduced into the material to detect the presence of internal defects. The sound waves travel into the material and the reflected beam is detected and analysed to locate the presence of defect. Defects such as cracks, shrinkage cavities, lack of fusion, porosity and bonding faults are easily detected by UT. Inclusion or other material inhomogenities can also be detected due to partial reflection or scattering of the ultrasonic waves.

Radiography testing (RT) is based on the differential absorption of short wavelength radiation such as X-rays and gamma rays on their passage through matter due to the difference in density and variation in thickness and/or differences in absorption characteristics. Radiography is best suited for the detection of volumetric defects such as porosities, slag inclusions, crater cracks, lack of penetration and incomplete fusion.

Advanced NDT methods

High resolution X-radiography has an edge over conventional radiography to detect small defects such as microcracks in components having a thin section with complex geometries, especially when it is welded using a laser beam or an electron beam.

Imaging-based techniques play an important role in non-destructive evaluation. In the eddy current imaging (ECI) technique, the components are inspected by scanning the surface of an object in a raster fashion, and the impedance measured at all points is converted into grey levels. This technique has the potential for automation and can estimate defect sizes from the image data. Advanced ultrasonic techniques such as the synthetic aperture focusing technique (SAFT) and time of diffraction (TOFD) technique are also gaining popularity for the inspection of weldments. The acoustic emission technique (AET) is another useful tool for on-line inspection of welded vessels and pipelines both during fabrication and in service.

For residual stress measurements of weldments, various non-destructive methods such as ultrasonic testing, X-ray diffraction (XRD), acoustic Barkhausen noise (ABN) and magnetic Barkhausen noise (MBN) can be employed. In ultrasonic testing, the evaluation of residual stress is based on the measurement of changes in the velocity of ultrasonic waves caused by stress after establishing the acousto-elastic constant. The XRD technique for residual stress measurement is based on the changes in the interplanar spacing of the lattice caused by residual stresses. The direction of the shift in the diffraction beam indicates the nature of the stresses, i.e. tensile or compressive. MBN and ABN techniques, which are based on Barkhausen effects, are

applicable only for ferromagnetic materials and alloys. Barkhausen effect occurs when a magnetic field is swept through the material along a hysteresis loop. MBN is due to irreversible change in magnetic domain movements during hysteresis and ABN is due to elastic deformation associated with magnetic domain rotation during irreversible changes in magnetisation. MBN signals are acquired by sensor coil or Hall-type probe and ABN signals are acquired by piezo-electric transducers. Both MBN and ABN signals are strong functions of the stress condition and hence residual stresses can be estimated by analysing the MBN and ABN signals.

8.4.5 Plant operational practices

The operating practices of a plant play a vital role in mitigating the failure of welded components. These include strict adherence to the stipulated design limit both by operating and maintenance personnel. The plant parameters such as operating temperature, flow parameters and process chemistry should be monitored and controlled during operation. Any unavoidable excursion should be properly recorded and proper logic/safety systems should be incorporated in the plant to avoid failure. Proper records of regular maintenance repair and replacement carried out should be available for future reference. Periodic inspection of the weld joints should be carried out to ascertain for any damage to weldments due to unplanned excursion or activities/conditions.

A periodic in-service inspection (ISI) programme has to be planned and an ISI document covering various inspection schedules for critical weld areas has to be formulated. A proper corrosion protective coating such as painting and chemical inhibitors should be applied to protect the welds from failure. Similarly, insulation materials used in pipelines should be free from leachable chlorine. While supports/stiffeners need to be regularly monitored for slackness, pipelines have to be checked for vibrations. Whenever *in situ* repair welds are carried out, the configuration of weld joints, material and process of welding should be similar to that of the original weld design. It is also equally essential to document these parameters and have them available during periodic inspection.

8.5 Case studies in failure investigation

The first inspection of the failed component is normally carried out at the site where the failure has taken place. The evidence in and around the failed location has to be preserved until the failure investigation begins. The following stages are generally involved during the failure investigation:

- *Collection of background data*. Before starting the failure analysis of any failed component, it is important to collect the basic background data about the failure. A visit to the site of failure and observation should

be made in and around the failed component. This will give some valuable important information such as normal operating condition and environmental details as well as operating conditions prevailing during the failure. Also interaction with plant and operational personnel is very important to understanding the reason for failure. The collection of data from the records or log book will give more valuable information to find out the root cause of the failure.

- *Preliminary examination of the failed part*. The preliminary inspection of the component can immediately give some details about the failure and mode of the failure. Visual examination of the fracture surface, corrosion deposits, etc. can give an idea about the type and mode of failure. This will also help in identifying parts to be extracted for detailed analysis. The results of the preliminary examination will assist in the decisions for urgent repairs to be carried out and to put the plant back into operation.
- *Preservation of the fracture surface*. Preservation of fracture surface is very important to carry out the failure analysis. The two fracture surfaces should be preserved without contamination and further damage. For ferrous components, oil or grease is applied to avoid corrosion of the fracture surface. Often matching both the fracture surfaces is not advisable as it can damage them. The chemical composition of the inclusion/precipitates/corrosion products present in the fracture surface also plays a vital role in failure analysis.
- *NDT/NDE.* NDT techniques such as X-ray, dye penetrant testing, MPT and UT are carried out on the failed components to identify the possible defective location in the failed component. This will help in selecting the area of interest for further investigations.
- *Mechanical testing*. Mechanical tests using specimens extracted from the failed component provide another useful method for evaluating the mechanical properties in and around the failed location. The data of the mechanical tests can be verified for conformity to the design code requirements and also in estimating the degradation of the properties caused due to service exposures.
- *Macroscopic examination/microscopic examination*. Examination of the failed components at micro- and macro- levels is an important stage of the failure analysis. The macroscopic examinations include visual inspection at low/high magnification, photography, dimensional measurements, weld penetration, and hardness testing. Metallographic examinations and micro-hardness measurements provide details of the microstructure, phases present, grain size and inclusions at the microscopic level.
- *Fractographic examination*. Examination of the fracture surface under stereomicroscope/scanning electron microscope (SEM) gives magnified

details of the failed surface. The type and mode of failure and the initiation sites of the crack or failure location of the component can be ascertained during this examination.

- *Chemical analysis*. The chemical analysis of the failed component is used for confirming the chemical composition as per design specifications and to detect any deviation in the material specification that could have caused the failure.
- *Determination and analysis of failure mechanism*. With all above details collected during the investigation, it is possible to determine the failure mechanisms or the combination of several factors leading to failure.
- *Testing under simulated conditions*. Sometimes, simulation and testing full size or sub-size test coupons of the component under plant condition will help in analysing the behaviour under service conditions. This may help in further confirming the cause of the failure.
- *Analysis and synthesis of all the evidence and formulation of conclusion*. After conducting all the above tests during the failure analysis, a systematic analysis of all the results is crucial. Failure analysis is multidisciplinary in nature. Using the data available from the systematic and stage-wise analysis of the failed component, the root cause of the failure can be arrived at through the synthesis of evidences gathered from the analysis.
- *Preparation of detailed failure analysis report*. Preparation of the final report is very important. The report should be self-explanatory, giving details about the various steps carried out during the failure analysis and results, with sufficient evidence or proof for the cause of failure. The final report may sometimes be used as a document for claiming insurance or settling legal disputes. The report will also be useful for adopting appropriate safety standards to minimise the loss of production and to avoid accidents.

The root cause of the failure will be immensely beneficial as a feedback for improved design, material selection, fabrication procedures and operating practices to avoid repetition of similar failures. This will also fuel our quest for the development of new engineering materials with improved properties and in understanding the basic science behind these failures.

A few case studies of the failure analysis of welded components carried out at the authors' laboratory are now presented.

8.5.1 Case I: Failure of a condenser tube in a fertiliser plant

Component

Ammonia refrigerant condenser tube, 370 mm diameter, 11 mm wall thickness welded to a hemispherical dished end [5].

Material of construction

A 106 Gr.B (0.3% C (max.)/0.3–1% Mn).

Life of component

Catastrophic failure within 3 h of start up. Figure 8.1 shows the failed component in as-received condition.

Fabrication

Pipe welded to dished end by submerged metal arc welding (SMAW) using AWS E 6013 electrode. Welded pipe passed hydrostatic test at 3.2 MPa.

Operating history

Component was filled with liquid ammonia. The temperature dropped from –3 ° to –32 °C. The Pressure reduced from 0.1 to 0.04 MPa.

Cause of failure

- Weld region was associated with lack of penetration (LOP) almost throughout the length of the weld.

8.1 The failed condenser tube.

- Hydrogen absorbed at the time of welding helped in crack initiation from LOP during storage of welded component. Figure 8.2 shows crack emanating from the base of lack of penetration and extending into the material.
- Poor weld toughness at low temperature facilitated easy crack growth during start up and culminated in a catastrophic failure.
- SEM examination revealed blisters around inclusion (Fig. 8.3) and decohesion of inclusions from the matrix (Fig. 8.4).

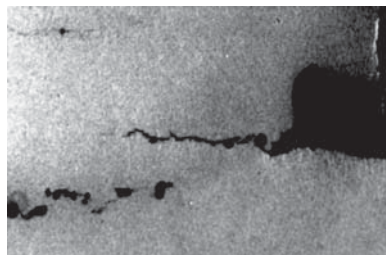

8.2 Crack emanating from the base of LOP.

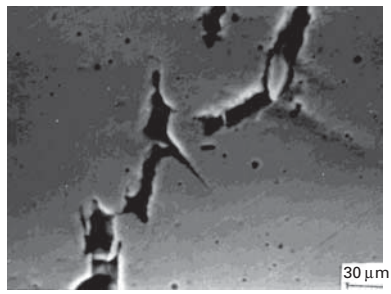

8.3 Blisters around inclusions.

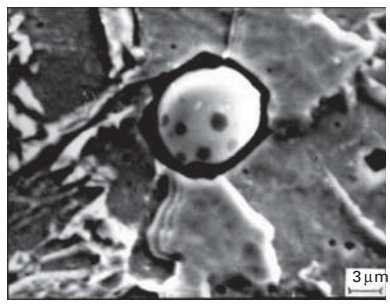

8.4 Decohesion of inclusion/matrix.

Recommendations

- Improvement in fabrication procedure.
- Use of low hydrogen electrodes (e.g. AWS E 6016 & 6018) for pipe to dished end welding.
- Radiographic examination of welded components.

8.5.2 Case II: Failure of a pipeline reducer

Component

Bimetallic transition joint in a steam pipeline reducer. The pipeline reducer was welded between ferritic steel pipeline and a stainless steel header [6].

Material of construction

The material of construction of the reducer pipe was AISI A335 P22 grade material, with a thickness of 30 mm. This material, which conforms to 2.25Cr–1Mo ferritic steel, was welded to the AISI 347 type stainless steel header.

Life of component

Weld failure was noticed after being put into service for 2200 h. Figure 8.5 shows the failed component in as-received condition.

Fabrication

To make the dissimilar joint, the edge of reducer was buttered with Inconel 82 for a length to 12 mm. PWHT was given for 2 h at a temperature of 973–

8.5 The failed steam reducer.

1013 K after the buttering for the pipeline. This pipeline was welded to the stainless steel header using Inconel 192 electrodes by gas tungsten arc weld (GTAW) and SMAW processes.

Operating history

The pipeline reducer carries steam at a nominal pressure of 115 MPa and at a temperature of 788 K.

Cause of failure

The cause of failures in bimetallic weld joints is attributed to the difference in thermal expansion coefficient between the base metal and the weld metal, which generates thermal stresses, due to thermal cycling experienced by the joint, during a number of start-ups and shut-downs.

Failures occur in the ferritic steel HAZ by propagation of low ductility circumferential cracks along a planar array of globular carbides. The welding characteristics of Inconel/Nickel due to poor flow properties give rise to defects (Fig. 8.6). Factors such as oxide notches and carbon migration that lead to formation of narrow regions of carbon-depleted zone during the welding process can also contribute to failure for such joints [6].

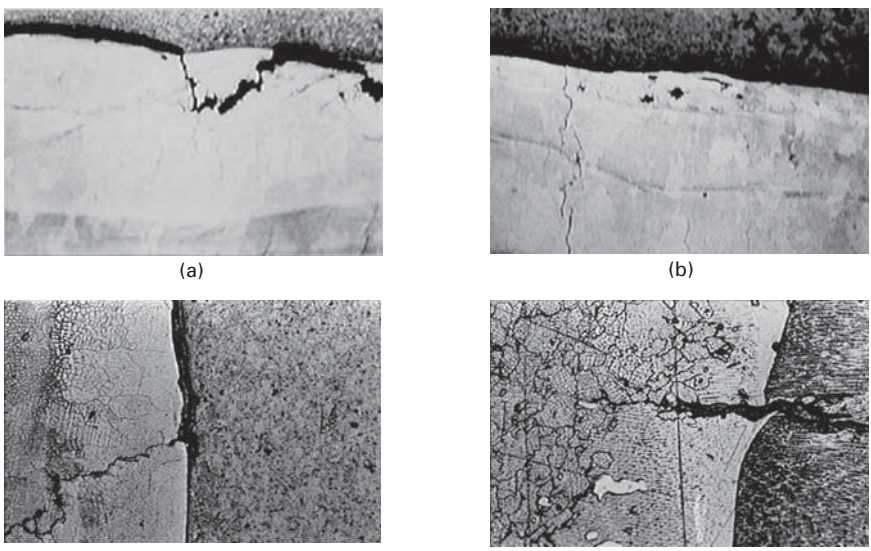

8.6 Steromicrographs showing weld defects at the weld interface.

Recommendations

- Such critical joints should be made only employing qualified welding procedures and welders.
- Proper PWHT procedure should be followed. The recommended procedure is PWHT at 973 K (+0/–15 K) for 1 h per 25 mm thickness.
- During buttering increase the current, decrease the speed and increase the inter-pass/pre-heat temperature.
- Ultrasonic inspections to detect weld defects, at the weld interface.
- Use of trimetallic joints with Alloy 800 as a transition piece.

8.5.3 Case III: Failure of a stainless steel dished end

Component

Dished end for cylindrical vessels (Fig. 8.7) [7].

Material of construction

AISI type 304L stainless steel.

History

The dished ends were manufactured by cold spinning. No stress relieving was specified for the formed dished ends. All dished ends were procured from the same manufacturer and belong to the same batch. Dished ends developed extensive cracking during storage.

Cause of failure

- The formed dished ends were stored in a hot and humid coastal climate with high concentration of corrosive chloride ions.
- During storage, surface of the formed dished ends came in contact with

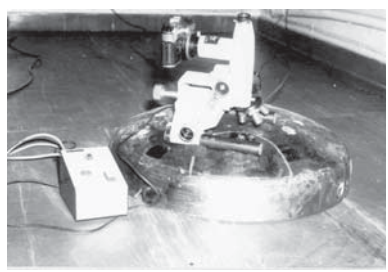

8.7 The failed stainless steel dished end.

iron contaminants, which subsequently underwent rusting. The rusted iron particles absorb moisture and chloride ions from the humid atmosphere.

- The presence of locked up residual stresses (arising from fabrication fit-up). Figure 8.8 shows the effect of re-shuffling of the residual stresses between two hacksaw cuts at locations A and B.
- The presence of high level of residual stresses along the availability of corrosive environment led to transgranular stress corrosion cracking (TGSCC) (Fig. 8.9).

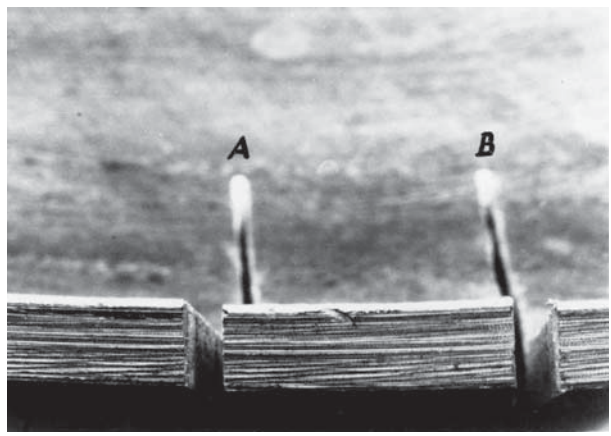

8.8 Photograph revealing reshuffling of residual stresses between two hackshaw cuts at location A and B.

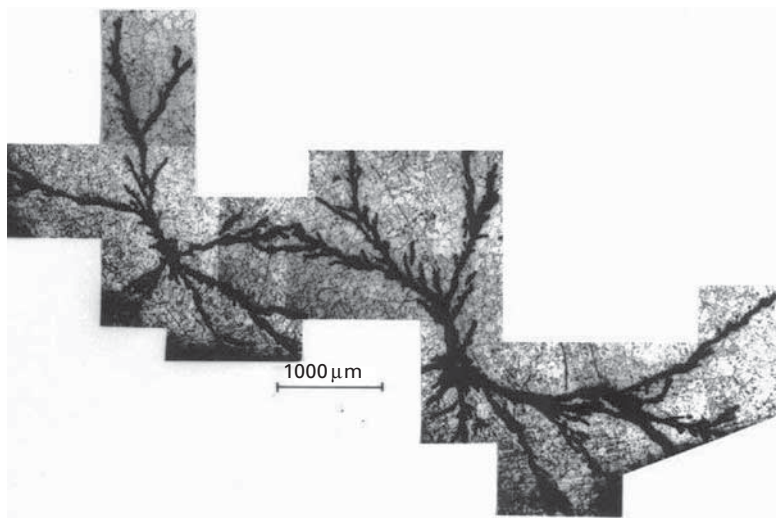

8.9 Mosaic photomicrograph revealing extensive transgranular stress corrosion cracking (TGSCC) on the dished end.

Recommendations

- Proper storage conditions to avoid pickup of iron contaminants by the stainless steel components.
- Stress relieving of formed dished ends.
- Pickling and passivation of components prior to despatch.

8.5.4 Case IV: Failure of a ball valve

Component

Ball valves failed after about 8 months of operation. The failure was noticed at the junction of the ball and stem (Fig. 8.10) [8].

Material of construction

The ball valve was made of martensitic grade stainless steel – AFNOR Z30C13.

Operating history

The ball valve in the chemical plant controlled the flow of dry synthetic gas (mixture of nitrogen and hydrogen). During operation, the ball valve operated at a pressure of 25 MPa in the temperature range of 278–453 K.

Testing

The failed ball valve exhibited a typical brittle fracture appearance as shown in Fig. 8.10. Fracture surfaces were associated with radial lines that point back toward the crack nucleation site at the circumferential weld. The ball valve steam had 27 mm long austenitic stainless steel sleeves starting from the junctions of ball and stem. The sleeves were welded to the stem at their two ends. The location of one of these welds coincided with the fracture location (Fig. 8.11). Metallography on the sleeve exhibited a typical sensitised microstructure with the hardness of 250 VHN.

Cause of failure

- Welding of martensitic stainless steel body with austenitic stainless sleeve without proper pre- and post-weld heat treatments was mainly responsible for the cracks in the weld (Fig. 8.12).
- The presence of the weld at the stress concentration site facilitated easy crack propagation and the failure of the component.

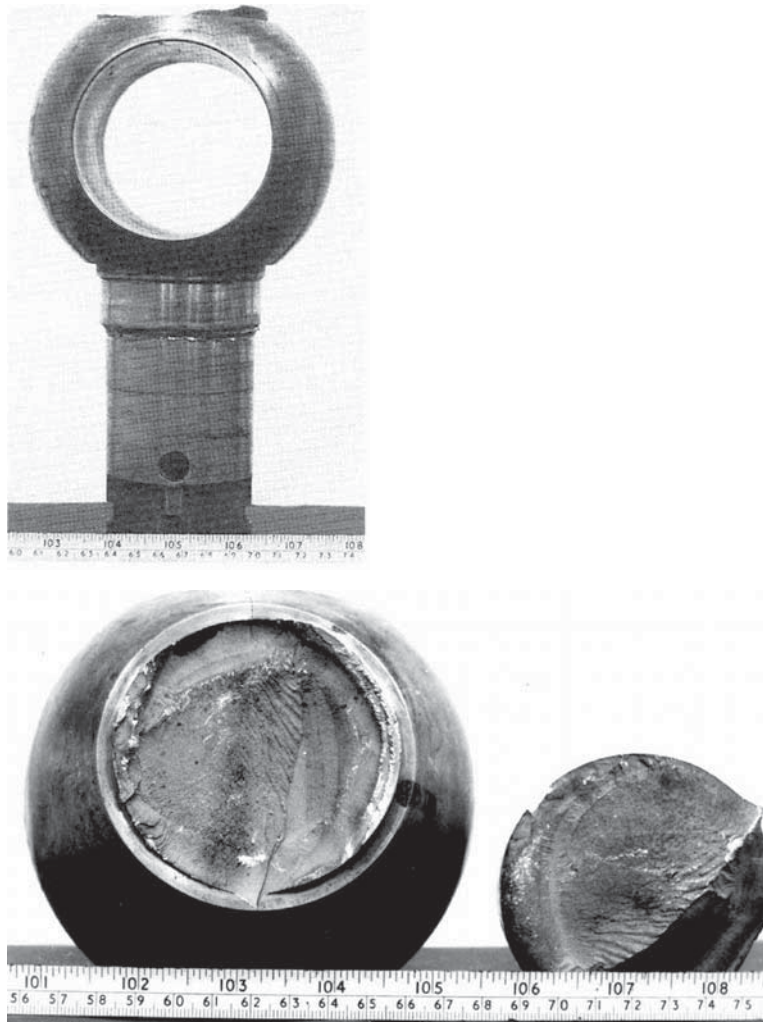

8.10 The failed ball valve at the stem.

- Failure of the component was due to improper fabrication procedure for welding different types of materials.

Recommendations

- Use of proper weld heat treatment schedule while welding austenitic stainless steel sleeve to the martensitic stainless steel stem.
- Design modification to avoid abrupt change in cross section near the weld.
- Periodic dye penetrant test at ball/stem junction as an in-service inspection procedure to detect any defect developed during operation.

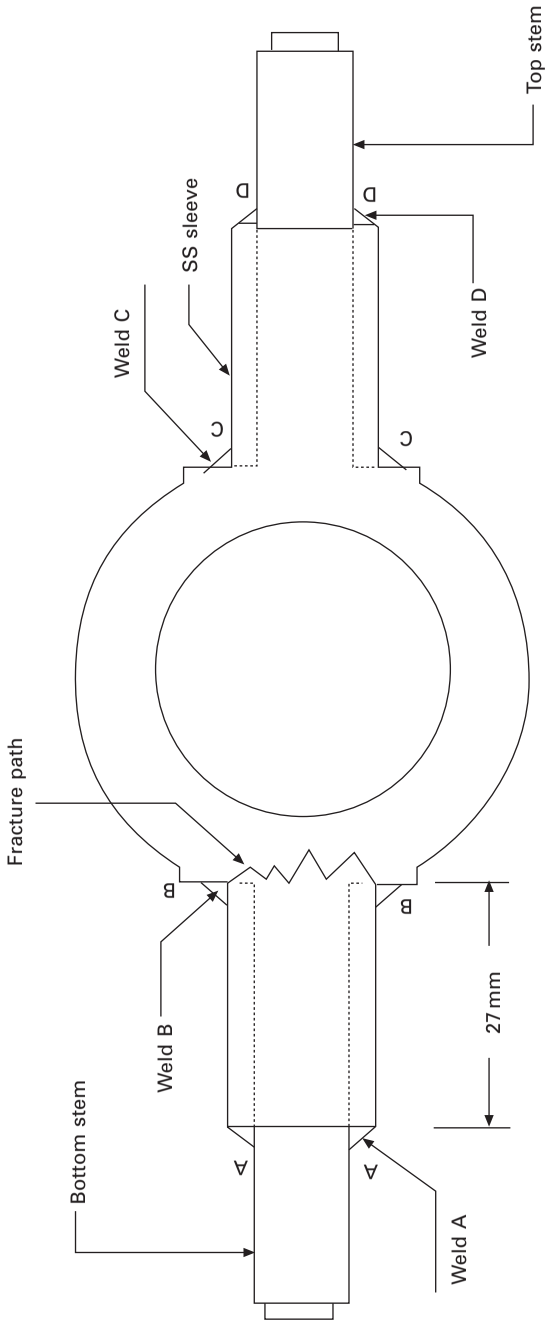

8.11 Schematic sketch showing failed region and location of various welds.

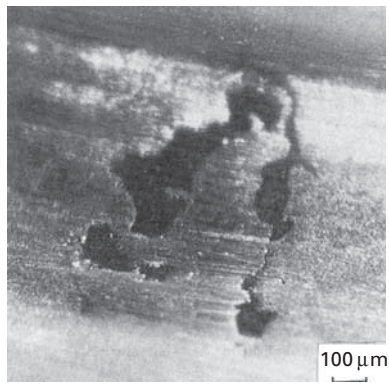

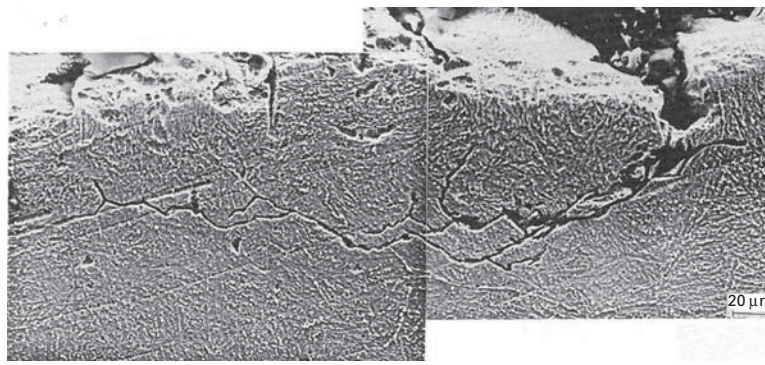

8.12 Photomicrograph of The blow holes and the origin of the crack.

8.5.5 Case V: Failure of a bellow sealed valve

Component

Bellow in the bellow sealed valve (Fig. 8.13) [9].

Material of construction

The material of construction of the bellow was specified as AISI 316L type stainless steel. The bellow is 56 mm long with inside and outside diameter being 24 and 35 mm respectively.

Life of component

The bellow sealed valves are used to control the flow of liquid sodium in the fast breeder nuclear reactors. These valves are generally not frequently operated. The bellow failure was suspected when high torque was required to open the valve. The bellows provide adequate leak tightness across the valve stem

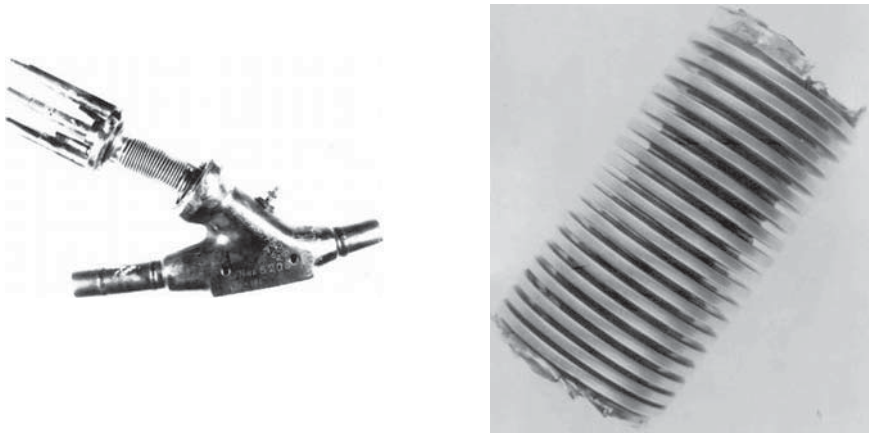

8.13 The failed bellow sealed valve and the stainless steel bellow inside the valve.

and at the same time allow movement of the spindle to control flow of liquid sodium. The outside surface of the bellow during operation would be in contact with molten sodium at 573 K while the inside surface of bellow is in contact with argon cover gas.

Fabrication

The stainless steel bellow is made of two plies, each 0.150 mm thick, and is welded to the end flanges.

Operating history

The bellow sealed valve was stored in the hot and humid coastal climate for about 3 years before putting it into operation. After about 8 years of smooth operations, the concerned valve was found to be quite difficult to operate.

Testing

The microstructure at the HAZ of the bellow to end flange weld joint exhibited a sensitised microstructure. Several intergranular cracks and grain boundary carbide precipitation were noticed in a much localised area near the weld (Fig. 8.14). Microhardness measurements revealed a hardness of about 290–320 VHN in these locations. The chemical analysis revealed that the carbon content of the bellow material was high and not conforming to AISI type 316L specifications.

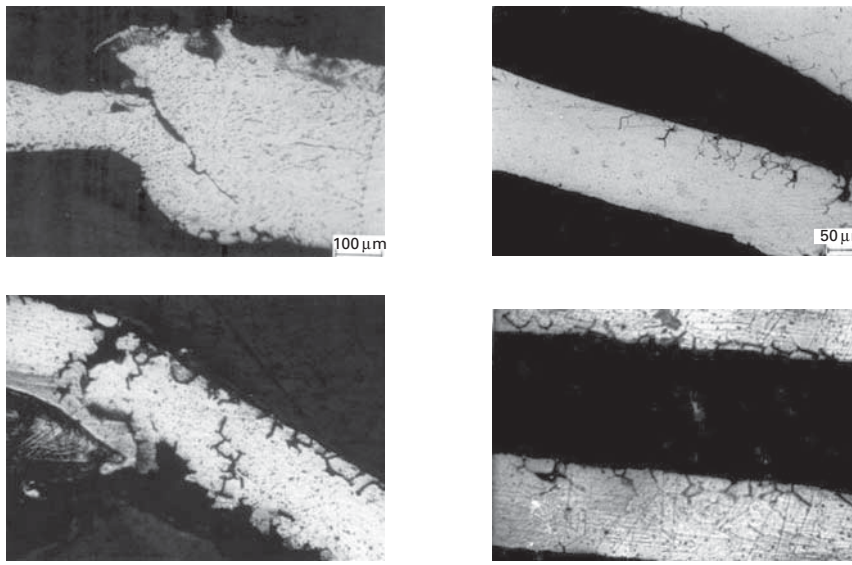

8.14 Photomicrographs showing intergranular cracking and carbide precipitation on the bellow convolutes near the weld.

Cause of failure

The cause of the failure of the bellow in the bellow sealed valve was attributed to the sensitisation of the material during welding and subsequent corrosion of the material during storage and operation. High carbon content of the material assisted the sensitisation of material during welding

Recommendations

To avoid such failures it was recommended that the bellow material chosen should have been a low carbon stainless steel material like AISI 316L as specified. Welding parameter should also be optimised to avoid sensitisation during welding. During storage, the valves should be sealed in double PVC cover with dehumidifying agent to avoid direct contact with the coastal environment.

8.5.6 Case VI: Failure of a pipeline in a fire-fighting system

Component

Electric resistance welding (ERW) pipeline in the ring header of the fire-fighting system as shown in Fig. 8.15.

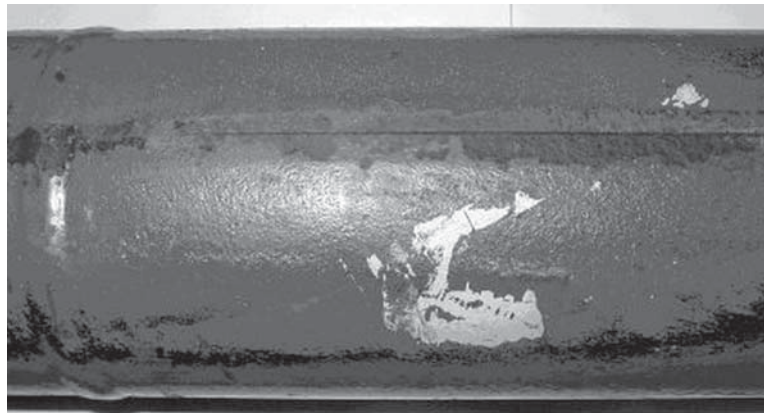

8.15 The failed fire hydrant pipeline.

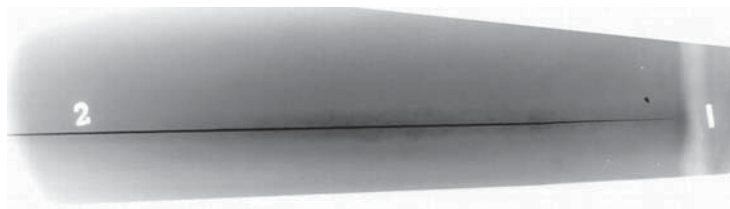

8.16 Radiograph showing cracking along the long seam weld in the ERW pipe.

Description of component

Visual examination revealed that the pipes are manufactured by ERW process. The length of crack was found to be in a straight line on the long seam. The ring header pipeline was 114 mm in diameter, 5.8 mm wall thickness and about 1.2 m in length.

Life of component

The ERW pipeline was in service for about 30 years.

Testing

Lack of fusion in the root of the long seam weld was clearly observed during radiographic inspection (Fig. 8.16). Metallographic studies on the weld cross-section using SEM revealed that the weld lacked penetration as shown in Fig. 8.17 and was also associated with presence of inclusion/impurities. The energy dispersive analysis of X-rays (EDAX) shows these impurities were typically associated with silica and alumina and the grain boundaries where

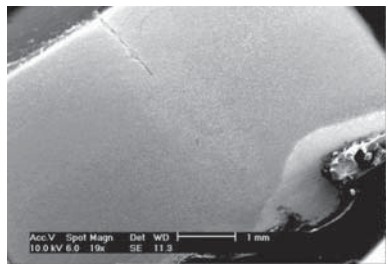

8.17 SEM micrograph showing presence of LOP on the weld.

the observed cracking revealed presence of Cl and Si. The micro-hardness of the pipe was found to be in the range of 144–156 VHN. The hardness on the weld region varied from 130 to 165 VHN.

Cause of failure

ERW pipes suffer selective seam corrosion (SSC) cracking on the weld bond line. SSC is a localised corrosion attack along the weld bondline that leads to the development of a wedge-shaped groove that is often filled with corrosion products. SSC is affected mainly by the degree of exposure to corrosive conditions, ineffective cathodic protection and the presence of non-metallic inclusions in the weld bondline region (mainly due to contaminants present during the manufacturing process).

Recommendations

To avoid such failures ERW pipeline to be replaced with new pipe seamless construction for longer life. Use of cathodic protection system to protect the pipeline from SSC. Annual survey of the pipeline and applying proper coating over pipeline will help in prevention of failure. During the annual inspection, the hydrostatic pressure tests to be carried out to avoid sudden failures.

8.5.7 Case VII: Failure of pipe fittings

Component

Carbon steel pipe fittings of high pressure carbon dioxide line tappings (branch line) in a fertiliser plant [10].

Material of construction

A 105 grade steel.

Life of component

Premature failures were detected within 2 years of commissioning in the form of leakage of carbon dioxide.

Operating history

In the fertiliser plant, carbon dioxide gas is passed to urea reactor through a pipeline at a pressure of 15.6 MPa. The main pipeline has been provided with 19 mm ($^3/_4''$) or 13 mm ($^1/_2''$) tapping line for pressure and flow measurements. The temperature and flow rate of the gas in the pipeline are 377 K and 29 000 –33 000 N m^3/h respectively.

Fabrication

Branch line fittings are socket welded to the main line by using SMAW process. Additional supports were provided to the valve to reduce vibrations on the branch line as shown in Fig. 8.18.

Causes of failure

- Weld defect was noticed on the outside surface of the socket weld (Fig. 8.19).
- The weld defect was filled with corrosion products.
- Evidence of crack nucleation from the outer surface was observed. Beach marks were observed on the fracture surface.
- Corrosion underneath the weld defect in the support weld deposit was primarily responsible for crack initiation.
- The cracks thus nucleated had propagated by fatigue loading (Fig. 8.20) as the pipe was experiencing high flow-induced vibration transmitted from the main pipe through the supports.

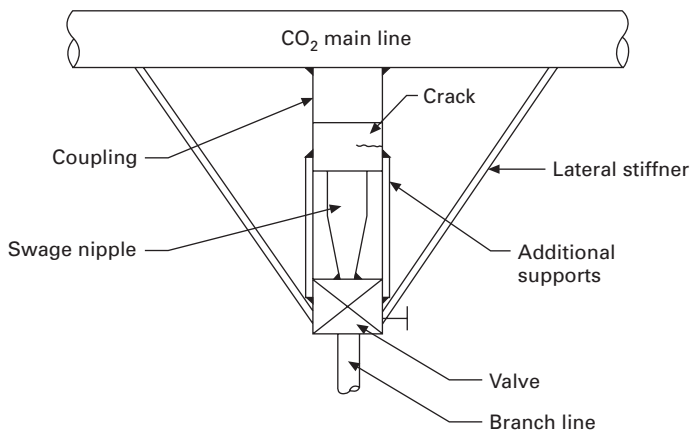

8.18 Schematic arrangement of the branch line from the main pipeline.

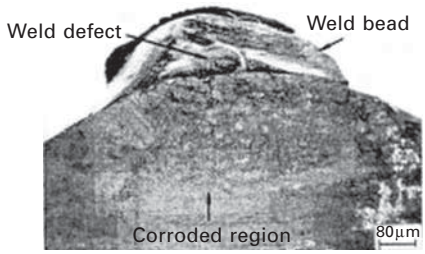

8.19 Photomicrograph showing weld defects.

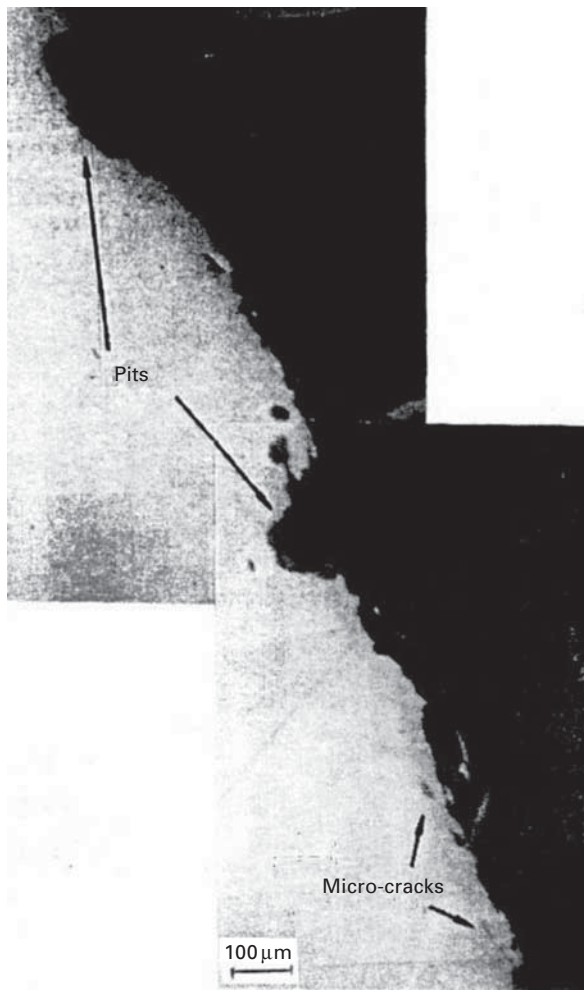

8.20 Photomicrograph showing corrosion pits and microcracks inside weld defects.

Recommendations

- Support to the branch pipe line should be given from a separate base and not from the main pipeline.
- Proper welding procedure to avoid defects during welding.
- Proper NDT method to check the quality of the weld.

8.5.8 Case VIII: Failure of conical inlet

Component

Conical inlet of a waste heat boiler was in service for 20 years in a chemical plant (Fig. 8.21)

Material of construction

ASTM A 182 GRF1 (carbon steel).

Type of insulation

The conical inlet had insulation and a stainless steel sleeve over it to minimise heat loss due to conduction. The normal temperature of operation was 393 K above insulation.

Operation condition

The pipeline carried cracked ammonia and synthesis gas (N_2 and H_2) flow through the conical inlet to waste heat boiler, at a pressure of 125 kg/mm^2 and at 803 K.

8.21 The conical inlet that suffered damage.

Abnormality observed

The surface temperature at the inlet end of the cone was found to be 623 K above the insulation during routine inspection.

Problems envisaged

As the component got exposed to a higher temperature than the designed limits for a long time, material degradation was suspected.

Testing and observations

Ultrasonic normal beam examination carried out on the areas affected by temperature, revealed heavy scattering and attenuation for about 300 mm on the affected region with a complete loss of back wall echo signal. Angle beam ultrasonic examination revealed defect up to a depth of 4.2 mm on the affected areas.

Hardness measurements at the affected area indicated hardness in the range of 100–110 BHN, whereas it was 132–136 BHN in the areas away from the affected areas.

In–situ metallographic investigation revealed normal ferrite–pearlite microstructure (Fig. 8.22a) on the outer surface of the pipeline where the insulation was intact. In the affected areas, the microstructure was found to have degraded as the pearlite colonies were seen to have been transformed to ferrite and spheroidal carbides (Fig. 8.22b). Micro-cracks and micro-fissures (Fig. 8.23) were also seen at a few locations of the affected area.

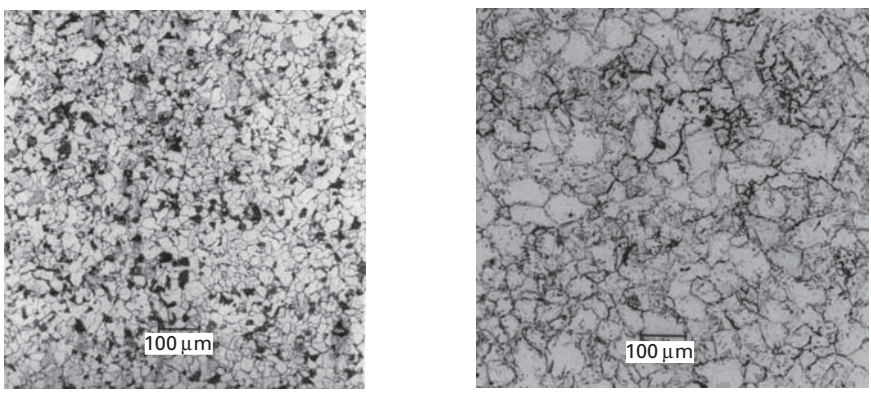

(a) (b)

8.22 (a) Microstructure of conical inlet at the unaffected region; (b) microstructure of conical inlet at the heat-affected area.

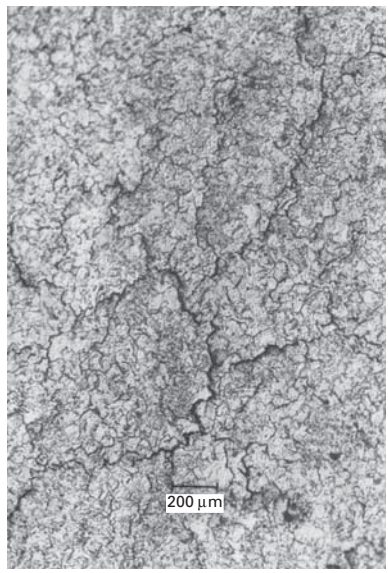

8.23 Microstructure of conical inlet showing cracks and fissures.

Conclusion

The conical inlet is affected by hot hydrogen damage due to over-temperature exposure for a long duration. The scattering and attenuation of ultrasonic signals indicated hydrogen damage which has been confirmed metallographically.

Recommendations

The surface of the pipeline was ground to a depth of 4 mm and equivalent thickness of material was weld deposited and the plant operation continued.

8.5.9 Case IX: Failure of stainless steel tubes under insulation

Component

Seamless stainless steel tubes were found to be leaking at several locations in a single length of the tube in a pressurised heavy water reactor.

Material of construction

AISI 304L stainless steel tubes in the delayed neutron monitoring (DNM) system were insulated with mineral wool. The heavy water flowing inside

the tube was continuously analysed to monitor the presence of certain elements in the heavy water circuit of the reactor system. The failed tubes had outside diameter of 9.6 mm and wall thickness of 1.4 mm.

History

After a service of about 10 years, the tubes were found to be leaking at several locations in one of the tubes. The mineral wool insulation cover was found to be damaged at some locations. The insulation was also found to be soaked with heavy water to a considerable length near the leaking tubes.

Testing

Visual examination of the DNM tubes revealed pit marks at several locations. Dye penetrant testing revealed several branched micro-cracks. A circumferential weld was found in the middle of this seamless tube. *In situ* metallography was carried out inside a fume hood, due to the presence of radioactivity inside the tubes. Cracks emanating from the pits were found to be branching (Fig. 8.24). The metallographic examination on the cut cross-section of the tube revealed failure due to TGSCC (Fig. 8.25a). The presence of a long seam weld with welding defects was also observed as shown in Fig. 8.25(b), even though the tubes were supposed to be seamless as per design drawings. Residual stress measurement by XRD revealed tensile stresses on the circumference of the tube. The extent of residual stresses was not uniform and was found be varying. Hence, a quantitative estimation of the stress was difficult. Chemical analysis of the insulation material to determine the amount of leachable chlorine content revealed higher amount of chlorine content than specified.

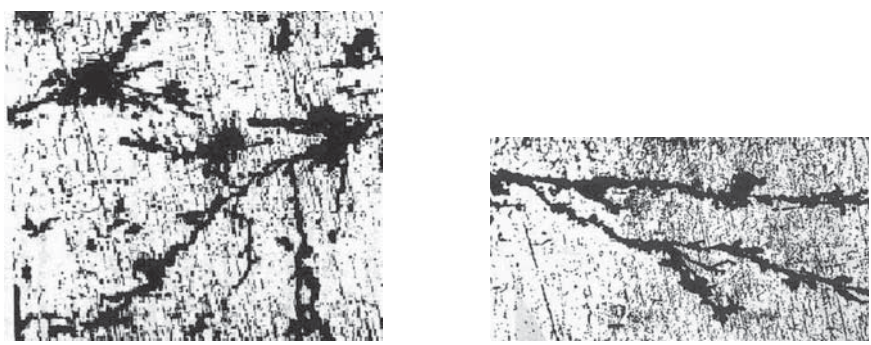

8.24 Branched TGSCC initiation from corrosion pits on the stainless steel tube.

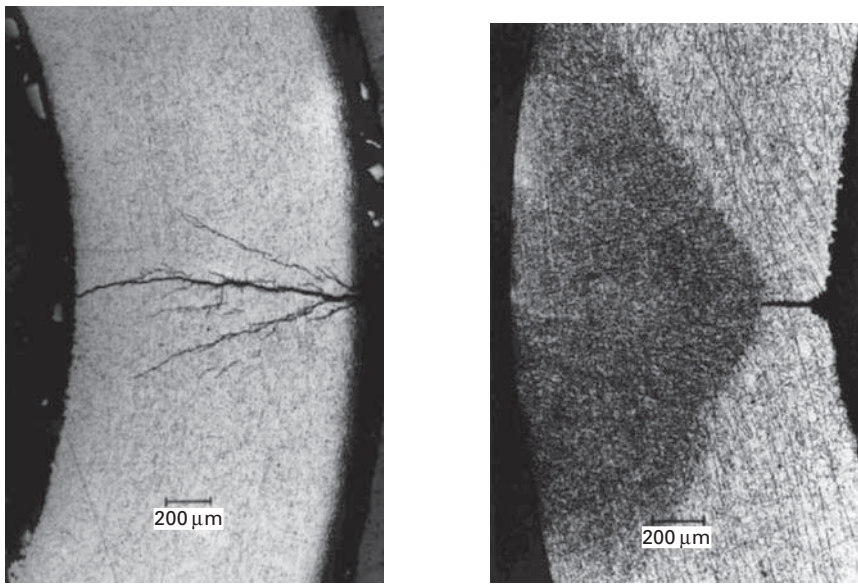

8.25 (a) Microstructure at the tube cross-section revealing propagation of TGSCC; (b) cross-section of the tube revealing welded tube construction associated with welding defects.

Cause of failure

The failure of the AISI type 316L stainless steel tubes was due to TGSCC originating from surface pits. The potent corrosive medium was due to chloride ion leached from the insulating material due to the condensation of moisture coming in contact with the insulating material. The leached chloride ion in combination with residual stress resulted in TGSCC.

Recommendations

Careful selection of the insulating material is quite important for avoiding such failures. The chloride content should be less than that specified in the appropriate standards. Quality control and inspection procedure during fabrication to be strictly monitored to avoid mix up of seamless tubes and seam welded tubes.

8.6 References

1. P. Rodriguez and T.P.S. Gill, 'Alloy Steels for Fast Breeder Reactors and their Weldability Demands', Workshop on Steels for Engineering Industries - Trends in Weldability (TWS-98), Trichy, January 19–20, 1998, pp. 203–209.

2. A.K. Bhaduri, S. Venkadesan, P. Rodriguez and P.G. Mukunda, 'Transition Metal Joints for Steam Generators – An overview', *Int. J. Pres. Ves. & Piping* **58** (1994) pp. 251–265.
3. T.K. Mitra, 'Weld Joint Design', *Welding Technology for Engineers*, Narosa Publishing House, 1996, pp. 289–303.
4. S.K. Ray, 'Mechanical Testing of Welding', *Welding Technology for Engineers*, Narosa Publishing House, 1996, pp. 355–367.
5. N.G. Muralidharan, R. Kaul, K.V. Kasiviswanathan and B. Raj, 'Failure Analysis of an Ammonia Refrigerant Condenser Tube', *J. Materials Engg. and Performance* **5**, 1996, pp. 241–246.
6. N. Raghu, C.N. Venkiteswaran, N.G. Muralidharan and K.V. Kasiviswanathan, 'Failure Analysis of Dissimilar Weld Failure on a Steam Pipeline Reducer', *Proceedings in the International Symposium on Material Ageing and Life Management (ISOMALM)*, IGCAR, Kalpakkam, 2000, pp. 1534–1538.
7. D.K. Bhattacharya, 'Failure of AISI Type 304L Stainless Steel Dished Ends During Storage', *Handbook of Case Histories in Failure Analysis*, ASM International, Vol. 2, pp. 135–137.
8. R. Kaul, N.G. Muralidharan, K.V. Kasiviswanathan and B. Raj, 'Failure of a Martensitic Stainless Steel Ball Valve due to Improper Weld Heat Treatment', *ASM Handbook of Case Histories in Failure Analysis*, Vol. 2, 1992, pp. 262–266.
9. R. Kaul, N.G. Muralidharan, N. Raghu, K.V. Kasiviswanathan and B. Raj, 'Failure of Stainless Steel Bellow in a Critical Bellow Sealed Valve', *Practical Metallography* **33** (1996) 6 pp. 315–321.
10. R. Kaul, N.G. Muralidharan and K.V. Kasiviswanathan, 'Failure of Carbon-dioxide Branch Line in a Urea Plant', *Practical Metallography* **32** (1995) 12, pp. 633–639.

9

Cracking in high performance superduplex stainless steel welds

A COMER, Dublin City University, Ireland

Abstract: This chapter addresses corrosion fatigue cracking in high performance superduplex stainless steel welds. Superduplex alloys are employed in critical applications such as in the offshore oil and gas industries, and weld joints are critical locations for structural integrity with most failures occurring in the vicinity of such joints. Sections 9.2–9.4 review the microstructure, mechanical properties and corrosion resistance of superduplex stainless steel welds. Sections 9.5–9.8 address the corrosion fatigue cracking of superduplex weld metal in both laboratory air and seawater with cathodic protection. Crack propagation resistance in seawater under high electrochemical potential is also examined in Section 9.7.

Key words: corrosion-fatigue, weld metal, superduplex stainless steel, cathodic protection, seawater.

9.1 Introduction

This chapter addresses cracking in high performance superduplex stainless steel welds in both a benign and an aggressive environment. Superduplex stainless steels emerged only in the 1980s. Up to this point duplex stainless steels were employed in medium to severe corrosion-resistant applications such as chemical, petrochemical, on/offshore, pulp and paper and chemical tanker applications (Charles *et al*., 1999). Superduplex stainless steel alloys are appropriate structural materials for service in *extremely aggressive* environments and are increasingly employed in sub-sea oil and gas developments (Gunn, 1997). This is mainly due to the long life cycles and weight savings achievable by using high strength corrosion-resistant alloys.

The main focus of this chapter is on the resistance of superduplex stainless steel weldments to crack propagation while functioning in seawater, since offshore installations are a major application area for superduplex stainless steels. It is widely appreciated that weld joints are critical locations for structural integrity and most failures occur in the vicinity of such joints. Often, fatigue cracks initiate at the edge of the root bead and propagate through the weld metal (Maddox, 1991). This chapter is divided into two parts. Sections 9.2–9.4 look at the microstructure, mechanical properties and corrosion resistance of superduplex stainless steel welds. Sections 9.5–9.8 address the corrosion fatigue cracking of superduplex weld metal.

9.2 Microstructure of superduplex stainless steel welds

Stainless steels are often divided into five families: (1) austenitic, (2) ferritic, (3) martensitic, (4) precipitation hardened and (5) duplex. Situated mid-way between the austenitic and ferritic grades, duplex stainless steels are a family combining the best aspects of both (Charles, 1991). Crucially, duplex stainless steels in general are no longer perceived as exotic alloys but as 'industrial steels'. In the future, owing to their cost and maintenance-free nature, they are likely to be considered as materials for buildings and bridges in hot, wet and coastal locations (Gooch, 1991). Their yield stress (Table 9.1) is double that of austenitic steels, therefore regarding strength to weight ratios, potential exists for economic saving (Charles, 1991). Similar thermal expansion and conductivity make them compatible with low alloy or plain carbon ferritic steels.

Table 9.2 lists selected duplex and superduplex stainless steels. The main difference between the superduplex and duplex grades is that the superduplex grades have higher chromium, nickel, molybdenum and nitrogen contents. The superduplex grades also contain small amounts of other alloying elements typically not present in duplex grades such as tungsten and copper. However, the effective use of highly alloyed superduplex stainless steels requires extensive knowledge of the properties and capabilities of the alloy (Charles, 1997). Presently, superduplex alloys are used in thickness up to 100 mm, and with design temperatures as low as –50 °C (Johansson, 1994; Charles *et al*., 1999). They are always cathodically protected when utilised offshore.

Modern superduplex stainless steels are characterised by a two-phase structure, generally consisting of an optimum mixture of about 50% by volume face-centred cubic (FCC) austenite and 50% by volume body-centred cubic (BCC) ferrite. Mutual interactions take place between the phases, resulting in the aggregate having a greater strength than either of the

Table 9.1 Mechanical property ranges for the various stainless steel classes

Alloy type	Ultimate tensile strength (UTS) (MPa)	Yield strength (MPa)	Elongation (%)	Hardness (HRB)
Austenitic 200–300 series	485–655	170–260	40	88–96
Ferritic 400 series	380–515	170–275	21	88–96
Martensitic	415–485	205–275	21	89–96
Precipitation hardening	895–1620	655–1520	6–16	105–116
Austenitic/ferritic (duplex/superduplex)	600–750	450–550	15–25	105

Table 9.2 Unified numbering system (UNS) designation for selected duplex and superduplex stainless steels

UNS	Trade name	Superduplex	Manufacturer
S32520	Uranus 52N+	*	Creusot-Loire Industrie
S32750	SAF 2507	*	Avesta Sheffield Ltd
S32760	Zeron 100	*	Weir Materials Ltd
S39274	DP3W	*	Sumitoto Metal Industries
S31260	DP3		Sumitoto Metal Industries
S32550	Ferralium		Haynes International
S32900	329		Various
S32404	Uranus 50		Creusot-Loire Industrie
S31803	SAF 2205		Avesta Sheffield Ltd

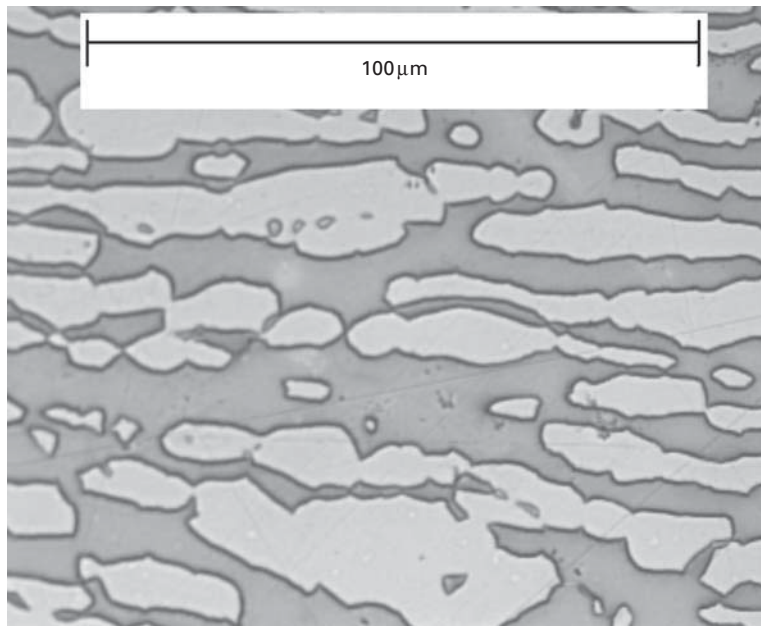

9.1 Base metal microstructure (Comer and Looney, 2006a), showing the aligned austenite colonies (bright) in a ferrite matrix.

constituents. Wrought forms contain a rolling texture obtained by hotworking followed by solution anneal and quench. The two-phase structure consists of austenite colonies (or islands) in a ferritic matrix (Fig. 9.1).

Obtaining an effective duplex microstructure depends on having good control over both alloy composition and temperature. This is relatively easily achievable for the base alloy, which is produced under controlled factory conditions. However, welds are seldom made under such conditions and

consequently grain structures prevalent in base and weld metals are significantly different.

Duplex stainless steel fusion welds with corrosion resistance close to that of the parent metal are achievable (Gooch, 1991). Many different welding processes can be chosen for welding superduplex stainless steels, but gas tungsten arc (GTA) welding and shielded metal arc (SMA) welding are regarded to be the most practical in a large number of applications. GTA is usually chosen for root passes due to its clean spatter and inclusion-free beads. Good quality weld profile is typically achievable. However, welding with GTA requires good skill and a sheltered environment. Deposition rates are relatively low. SMA is the easiest all-weather method. Relative to GTA-type welding, higher deposition rates are possible, but weld toughness and profile are often poor. In addition, slag on the weld surface must be removed during each weld pass. Subsequent to a welding operation, weld metal with a 50/50 phase balance similar to the surrounding base alloy is desirable. This must be achieved without deleteriously affecting the microstructure of the surrounding alloy (heat-affected zone/HAZ) by submitting these regions to prolonged periods at high temperatures.

As previously discussed, the base metal is supplied in a solution annealed and quenched condition to give an optimum duplex microstructure with correspondingly high corrosion resistance and good mechanical properties (Stevenson *et al*., 1986). In contrast, welds are put into service 'as deposited'; it is usually impractical to solution anneal completed weldments (Stevenson *et al*., 1986). Therefore, welding consumables and procedures must combine to ensure weldments perform similar to base metal in the as-welded condition.

The weld metal structure differs from the parent material because of variations in chemical composition and its total thermal history. Superduplex stainless steel weld metal solidification involves epitaxial growth of primary ferrite grains from the parent material at the fusion boundary (Atamert and King, 1991). Figure 9.2 depicts the primary ferrite grains and their direction of growth. Initial growth is orientated in relation to the thermal gradient (Nassau *et al*., 1991) and produces a columnar ferritic structure. This provides the starting conditions for further solid state transformations (from ferrite to austenite) upon cooling, which dominate the final weld metal structure (Fig. 9.3).

The ferrite content, grain size and orientation are well known to influence weld metal properties. Early attempts at welding duplex stainless steels yielded weld metal with high ferrite contents and very coarse grain structures (Lippold *et al*., 1991). High temperatures and rapid cooling rates experienced by the weld metal promoted dissolution of austenite on heating and retardation of austenite reformation on cooling (Lippold *et al*., 1991). Highly ferritic microstructures promoted extensive precipitation of Cr-rich nitrides such as Cr_2N. These factors produced weld metal with reduced fracture toughness,

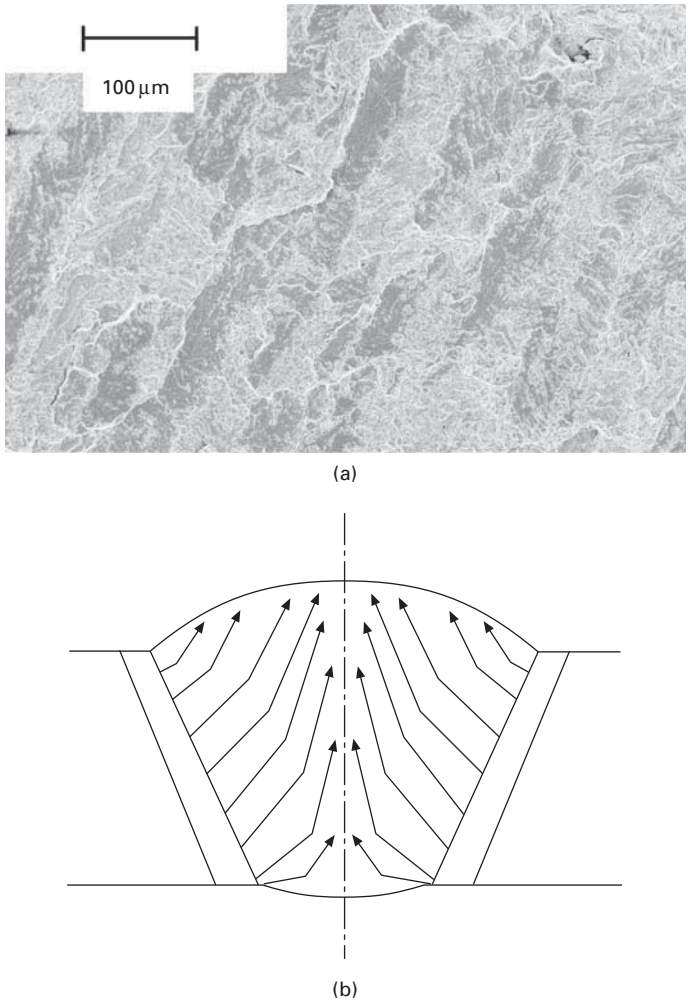

9.2 (a) Fractograph showing macrostructure of weld metal (Comer and Looney, 2006a), (b) Schematic showing the growth pattern of the columnar weld grains (Comer and Looney, 2006a).

localised corrosion resistance and hydrogen embrittlement resistance (Lippold *et al*., 1991).

However, advances have been made. The relatively sophisticated metallurgy of super duplex stainless steel welds has demanded a degree of refinement of standard stainless steel welding procedures (Stevenson *et al*., 1986). The key to the achievement of corrosion-resistant welds in duplex stainless steels is via control of the ferrite–austenite phase balance, and of nitrogen level (Gooch, 1991). The importance of nitrogen content in superduplex base and weld metals cannot be underestimated. Nitrogen is well known to have beneficial

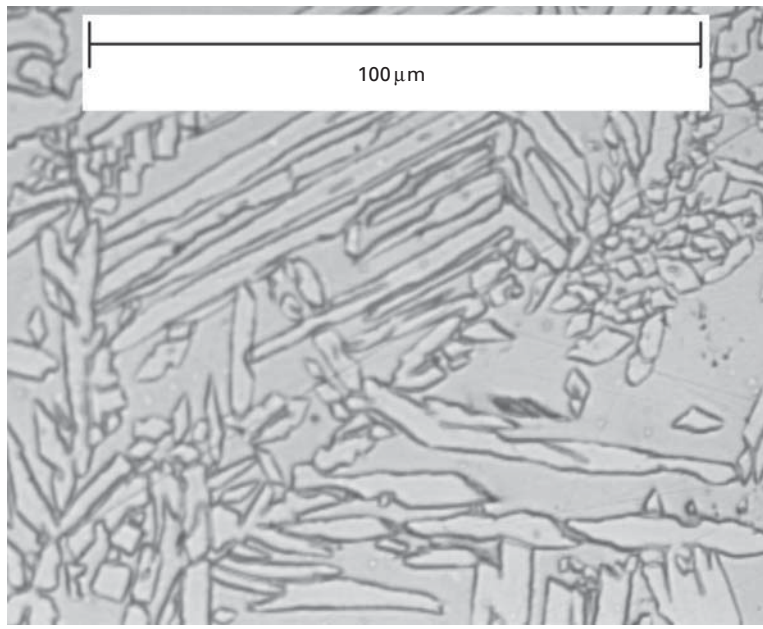

(a)

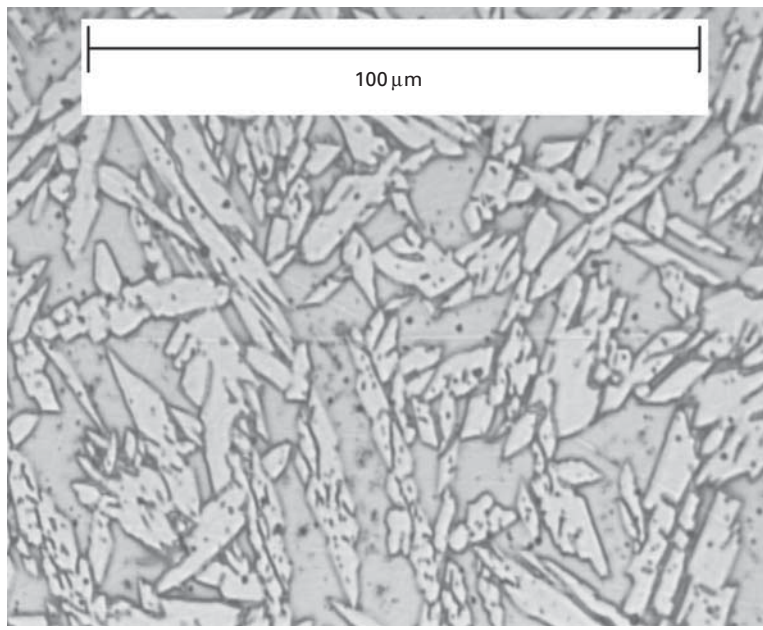

(b)

9.3 (a) GTA weld metal microstructure (Comer and Looney, 2006a). The random austenite colonies in a ferrite matrix are evident. (b) SMA weld metal microstructure (Comer and Looney, 2006a).

and detrimental effects on the properties of duplex stainless steels in general. Nitrogen is an interstitial solution-strengthening element and mainly dissolves into the austenitic phase (Hertzman *et al*., 1986; Wahlburg and Dunlop, 1986). Consequently, nitrogen preferentially hardens and strengthens the austenitic phase, but simultaneously decreases its ductility.

It is well known that arc energy must be high enough to ensure adequate austenite reformation. However, arc energies which are too high will cause intermetallic precipitation. Arc energies of 1–2 kJ/mm for 10 mm thick butt welds, given a maximum interpass temperature of 150 °C, have been recommended (Gooch, 1991). A limit of 1.2 kJ/mm for 15 to 20 mm thick plate has been suggested elsewhere (Gunn, 1994).

Tests have been carried out on Zeron 100 weld metals formed with Zeron 100X consumables (Stevenson *et al*., 1986). Satisfactory basic mechanical and corrosion resistance similar to the base metal were found. Further research was carried out to find the most important factors, which must be controlled in order to achieve satisfactory mechanical and corrosion properties for duplex and superduplex weld metals (Rouault and Bonnet, 1997). A sufficient level of nitrogen in the weld metal was found to be fundamental for adequate localised corrosion resistance: minimum contents of 0.14 wt% and 0.22 wt% are recommended for duplex and superduplex stainless steels respectively. If the chemistry is mainly controlled by the consumables, the second fundamental parameter for achieving good weld metal properties is the cooling time since it governs the occurrence of deleterious precipitation such as intermetallics and nitrides (Rouault and Bonnet, 1997).

In a study on welded joints of 25%Cr (UNS S31260, 32550) and superduplex stainless steels (UNS S32750 and 60) using GTA root and SMA fill welding processes (Gunn, 1994), corrosion resistance decreased at high arc energies. Weld metal consumables with a composition at least equal to and preferably above the base steel were recommended to maximise corrosion properties. However, it was noted that increased contents of alloying elements promote intermetallic formation.

Dilution of the weld metal with parent metal was found to be directly related to the amount of precipitate formed in weld metal (Karlsson *et al*., 1997). Precipitates compromise weld metal toughness through a decrease in ductility. Joint geometry also has an effect on dilution. For example, X joints have lower toughness than V joints at the centre of the weld. In addition, avoiding excessive heat inputs is essential in achieving good toughness and ductility. Limiting the interpass temperature (from 150 to 100 °C) while welding thicknesses over 25 mm allow the time spent at temperatures where embrittling phases can precipitate to be reduced (Doyen and Niset, 1991).

Duplex and superduplex weld metals have ultimate tensile strengths (UTS) and yield strengths greater than their respective base metals (Table 9.3). However, ductility of the weld metal is usually lower than the base metal.

Table 9.3 Mechanical properties for two superduplex stainless steels base plate and weld metals (Wiesner, 1997)

	Yield strength (MPa)	UTS (MPa)
SAF 2507 Base plate	518	787
SAF 2507 Weld metal (GTAW root/SMAW fill)	767	955
Zeron 100 Base plate	552	801
Zeron 100 Weld metal (SMAW)	744	947
Zeron 100 Weld metal (GTAW)	722	922

Percentage elongations down to 10% for a GTA weld metal compared with up to 40% in the base metal have been reported (Comer, 2004).

During the fabrication of a multipass weld a steep temperature gradient exists initially between the weld beads and the cooler surrounding material. Consequently, as the weld beads cool and contract, the restraining action of the surrounding material leaves a portion of the weld metal in tension. The tensile stresses are balanced by compressive stresses in other portions of the weld metal. These *residual* stresses, which are generally considered of yield magnitude, lead to distortion in weldments. For example, the contraction associated with the cooling of individual weld beads can result in angular distortion. In addition, tensile/compressive residual stress fields influence mean stress levels locally, which can influence crack growth rates.

A study was carried out on Zeron 100 weldments to assess the detrimental effect of residual stresses (Baxter *et al.*, 1993). Weld zone hardening was attributed to strain hardening caused by high local (residual) stresses. The extent of strain hardening is related to the thickness of the joint. The thicker the weld joint, the higher the hardness of the weld metal relative to the base metal. This results in weld metal with high strength and reduced ductility. Metallurgical factors were found not to contribute. In order to increase weld metal ductility, it was deemed important to minimise weldment distortion. This results in lower local stresses and consequently minimal strain hardening in the weld metal.

In summary, obtaining an effective superduplex microstructure depends on having good control over both alloy composition and temperature. Fusion welds have a coarse columnar macrostructure, which is not present in the base metal. Nitrogen, an interstitial element, governs austenite reformation and can strengthen the austenitic phase. For adequate localised corrosion resistance, a nitrogen level of 0.22 wt% is required for superduplex welds. Nickel contents must be at least greater than 7 wt% to guarantee adequate toughness. Arc energies of 1–2 kJ/mm for 10 mm thick butt welds given a maximum interpass temperature of 150 °C are recommended. When welding

superduplex stainless steels to approved guidelines, the only degree of freedom available to the welder is the arc energy/welding speed. Duplex and superduplex weld metals have UTS and yield strengths greater than their respective base metals. However, ductility is reduced. This is thought to be due to strain hardening of the weld metal caused by the welding process.

9.3 Toughness and corrosion resistance of superduplex stainless steel welds

It is now well known that alloys become stronger but also brittle at low temperatures. Reduced ductility at stress concentrations inhibits blunting by plastic deformation. In other words, the material loses its ability to accommodate cracks. Rapid, unstable crack propagation from a stress concentration may result in catastrophic brittle fracture. A material's resistance to crack advance is commonly referred to as toughness, which is of critical importance in any crack propagation study.

With regard to weldments, lowest toughness is most often found at the centre of weldments (Dhooge and Deleu, 1994; Deleu and Dhooge, 1997). In this way, the welding process can have a major bearing on weld metal toughness. Through a combination of exceptionally low filler wire oxygen content and fully inert gas shielding, acceptable weld metal toughness down to –70 °C is possible with the GTA method (Gough and Farrar, 1997). As such, the method is invariably used for initial root passes; higher deposition methods are generally preferred for the fill, in all but the most critical applications. SMA electrode types predominantly have a basic flux coating for two reasons; maximum toughness potential and positional operability. Deposition rates are relatively high but protection of the molten metal is inferior to the GTA method. Electrodes with rutile-type coatings are confined to applications where sub-zero toughness is not a critical factor.

Extensive tests have been carried out to assess the toughness of superduplex base and weld metals (Charles and Bonnefois, 1986; Hertzman *et al*., 1986; Dhooge and Deleu, 1994; Dupoiron *et al*., 1994b; Gunn, 1994; Deleu and Dhooge, 1997; Gough and Farrar, 1997; Wiesner, 1997; Byrne *et al*., 2000). Overall, the toughness of a given welded joint is always less than base metal toughness at a given temperature. However, the actual reduction in toughness depends largely on the welding process. If high deposition rates are required such as those achievable by SMA welding, a sacrifice in toughness is inherently involved.

9.3.1 Corrosion resistance

In general, the resistance of duplex stainless steels to various types of corrosion is excellent (Bernhardsson, 1991). This can be considered as resistance to

either general (corrosion of bulk material in acids and caustics) or localised corrosion (pitting, crevice corrosion, stress corrosion cracking (SCC)) and intergranular corrosion in chloride environments.

The exceptional resistance to corrosion is partly due to the very low inclusion content, which is a characteristic of the argon oxygen decarburisation melting route employed for producing duplex stainless steels (Charles and Bonnefois, 1986). Laboratory investigations and field tests have shown that superduplex stainless steels perform better than austenitic stainless steels in many situations: polluted inorganic acids (sulphuric, phosphoric), hot organic acids, chloride containing media and abrasion corrosion (Dupoiron *et al*., 1994a). For these reasons, duplex stainless steels find several industrial applications, particularly chemical industries that include: pulp and paper, hydrometallurgy, fertiliser, petrochemical, organic products and pollution control equipment.

Offshore installations are another major application of duplex stainless steels. Seawater is considered as a neutral chloride-containing solution. Chloride ions (Cl^-) are well known for their ability to destabilise the protective passive film inherent on stainless steels (Olsson and Landolt, 2003). Seawater has a surprisingly homogeneous composition around the world. The salinity is about 3.5% by weight. The pH ranges between 7.9 and 8.1 (Kivisakk, 1999). Synthetic seawater containing manganese chloride, calcium chloride and sodium chloride can be used to simulate natural seawater. However, since the concentration of sodium chloride is relatively high compared with the other salts, 3.5% by weight sodium chloride (NaCl) is used in the majority of laboratory tests.

Localised corrosion phenomena such as pitting and crevice corrosion are acknowledged to be the most deleterious corrosion mechanisms with regard to stainless steels (Kain, 1997). Crevice corrosion begins when discrete areas on a passive surface are physically isolated or occluded from the bulk material such as in a crack enclave. The occurrence and extent of crevice corrosion damage are highly dependent on a number of interrelated factors. Alloy composition, material surface finish, crevice geometry, bulk environment chemistry and temperature may all influence resistance to crevice corrosion (Kain, 1997).

In contrast to crevice corrosion, pitting is a plane surface phenomenon. Pitting corrosion occurs when discrete areas of a material undergo rapid attack while the vast majority of the surface remains virtually unaffected. However, it is generally agreed that for stainless steels in seawater, crevice corrosion is more potent than pitting.

Stainless steels are often protected from corrosion in aqueous solution by, for example, electrically connecting an alloy with a relatively lower electrochemical potential (ECP) to the stainless steel (Roberge, 1999). Zinc, which corrodes in preference to the stainless steel, is often employed for this

purpose. However, even if stainless steels are cathodically protected in seawater, local regions can assume different ECPs from the bulk material. Therefore, local dissolution can still occur. Local variations in ECP can arise from a number of reasons including local metallurgy (in the case of pitting) and geometry (in the case of crevice corrosion) (Roberge, 1999). In addition, local ECP depends on the condition of the seawater (oxygen content, chlorine level) (Francis, 2001b). This is shown in Table 9.4.

The local corrosion resistance of stainless steel is largely dependent on metallurgy and thus composition (Olsson and Landolt, 2003). The effect of alloying content is commonly calculated by an index termed the 'pitting resistance equivalent' (PRE). PRE values essentially indicate the effectiveness of individual alloying elements in a particular stainless steel and therefore indicate its effective resistance to the initiation of localised corrosion (Haynes, 1986). Superduplex grades have a pitting resistance equivalent number (PRE_N) greater than 40, which ensures relatively good resistance to pitting corrosion, where:

$$PRE_N = \%Cr + 3.3 \times (\%Mo) + 16 \times (\%N) \qquad 9.1$$

However, a modified form of the PRE relationship is used for grades such as superduplex stainless steels which contain both nitrogen and tungsten:

$$PRE_W = \%Cr + 3.3 \times (\%Mo + 0.5 \times 5\%W) + 16 \times (\%N) \qquad 9.2$$

Critical pitting temperature (CPT) tests are typically employed to experimentally rank alloys with regard to pitting resistance and validate the theoretical PRE relationship. As such, the pitting resistance of superduplex stainless steels is controlled in the foundry through the alloying content. In neutral, chloride-containing environments, the corrosion resistance of duplex stainless steels is determined by the phase with the poorer corrosion resistance rather than by the corrosion resistance of the bulk (Weber and Uggowitzer, 1998; Perren *et al.*, 2001).

In contrast to the base metal, it is often difficult to control the corrosion

Table 9.4 ECPs of high alloy stainless steels as a function of seawater condition (Francis, 2001b)

Seawater condition	Electrochemical potential (mV, SCE)
Chlorinated seawater	+600
Natural aerated	+300
Hot seawater	+100
Seawater with 200 ppb oxygen	–100
De-aerated seawater	–450

SCC, saturated calomel electrode

resistance of weld metal due to microstructural changes caused by the weld thermal cycle, which affects compositional makeup of the phases and phase proportions. Therefore, the corrosion resistance is largely dependent on the welder, his/her experience and technique. The weakest areas of a weld with regard to corrosion are the stop/start areas where the welder rests the arc while repositioning (Scully, 1995). Overheating in these locations implies cooling rates are slow and the probability of intermetallic precipitation is high.

Numerous tests have been carried out on superduplex base and weld metals in order to glean an insight into their resistance to both localised and general corrosion mechanisms (Dupoiron *et al*., 1994b; Gunn, 1994; Kivisakk, 1999; Byrne *et al*., 2000). For example, extended immersion tests carried out on SAF 2507 base material in natural seawater that lasted for 8 years revealed no corrosion attack even though biological species, which aid the initiation of localised corrosion were present (Kivisakk, 1999). Welds were also tested for a minimum of 6 years. SAF 2507 weld metal formed by the GTA root and fill method showed some pitting attack (0.03 mm in depth) in the root pass. SMA root and cap weld metals exhibited no attack. In other work, corrosion tests were carried out on welded joints of 25%Cr (UNS S31260, 32550) and superduplex stainless steels (UNS S32750 and 60) using GTA root and SMA fill welding processes (Gunn, 1994). The parent steels showed high pitting resistance compared with 316L and 22% Cr steels. The relative behaviour depends on composition and relates to the PRE_w. Weldment corrosion resistance was below that of the parent steel in all cases, often as a result of use of underalloyed consumables.

In summary, superduplex stainless steels derive their corrosion-resistant properties from a stable, durable passive film. Corrosion behaviour depends mainly on composition. Composition influences the stability of the passive film. Localised corrosion resistance is critical for stainless steels. Localised corrosion mechanisms such as crevice corrosion are oxygen supported, indicating a dissolution-type mechanism. Duplex and superduplex stainless steels and weld metals are highly resistant to pitting and crevice attack in seawater and are more resistant than austenitic alloys. Corrosion resistance is always lower for the weld metal compared with the base metal.

9.4 Hydrogen embrittlement

Similar to other steels, hydrogen may be introduced into superduplex stainless steels by cathodic protection (Francis *et al*., 1997), galvanic coupling to less noble materials, from hydrogen sulphide during handling of crude oil or during welding processes (Wessman and Pettersson, 2000). It is well known that once inside the metal, hydrogen can cause embrittlement, leading to reduced crack propagation resistance and premature failure. There are no

known favourable effects of hydrogen in steel. The hydrogen embrittlement mechanism involves the following key stages:

- generation of hydrogen;
- transport of hydrogen through the lattice;
- embrittlement and failure of the lattice.

Much research has been carried out into the resistance of superduplex stainless steels and their weld metals to hydrogen embrittlement (Fang *et al*., 1994; Francis, 1994; Francis *et al*., 1997; Ollson *et al*., 1997; Byrne *et al*, 2000; Wessman and Pettersson, 2000; Kivisakk and Holmquist, 2001; Woolin and Murphy, 2001). The basic aim of the various tests is to assess the effect of hydrogen on fundamental mechanical properties. A reduction in ductility is a typical consequence of exposure to hydrogen. Stress at failure is reported most often. In addition, the effect of metallurgical variables such as the austenite/ferrite phase balance is often assessed (Francis *et al*., 1997).

Data are often compiled using a range of test methods including constant load, constant displacement and slow strain rate (SSRT) tests. However, displacement control has been found to be less severe for duplex stainless steels due to low temperature creep, which allows stress relaxation (Woolin and Murphy, 2001). The most common method of charging the specimens with hydrogen is cathodic protection in aqueous solution. However, exposure to a hydrogen gas environment is sometimes used.

Under constant load tests on UNS S31803 and UNS S32750 base alloys, cracking only occurred after stresses corresponding to 90% of the tensile strength (UTS) of the alloy when cathodically protected by zinc in chloride-containing solution (Olsson *et al*., 1997; Kivisakk and Holmquist, 2001). Precharging had no influence (Kivisakk and Holmquist, 2001). SSRT testing of stainless steel base material (duplex SAF 2205 and superduplex SAF 2507) and weld metal (2205 SMA, GTA and 2507 SMA) was performed under cathodic hydrogen charging conditions in 3.5% NaCl at $-1000\,mV_{Ag\text{-}AgCl}$ (Wessman and Pettersson, 2000). SAF 2507 had the highest resistance to cracking (90% UTS) followed by SAF 2205 (75% UTS). Weld metals showed lower resistance and data scatter was large. Values ranged from 47 to 77% of UTS. The importance of maintaining adequate austenite content in the weld metal was highlighted by the poor resistance (30% UTS) of a weld metal that was heat treated to give a high ferrite content of 67%. Highest hydrogen levels were observed in the SMA welds. Austenite essentially hinders crack propagation. As such, HE is reduced by a fine grain size and a phase balance with 50% or more austenite (Francis *et al*., 1997).

In summary superduplex grades show better resistance to HE than duplex grades. Stresses at failure by hydrogen embrittlement approach 90% of UTS for superduplex base metals. Weld metals are much more susceptible to hydrogen embrittlement; stresses below 50% UTS can cause failure. Alloys

with a high ferrite content and high hydrogen levels are most susceptible to embrittlement. Ferrite contents below 45% are recommended. Hydrogen decreases ductility, leading to brittle crack propagation. Austenite impedes hydrogen diffusion and hinders crack propagation from embrittled ferrite regions.

9.5 Corrosion fatigue cracking of stainless steel welds

The author has recently carried out an in-depth study on the corrosion fatigue cracking of superduplex stainless steel weld metal in both a benign (air) and an aggressive environment (Comer and Looney, 2006a,b, 2008). The author's work is described and compared with other recently published work in the field. This section briefly describes the sample types used in the corrosion fatigue experiments along with the experimental procedures employed. In Section 9.6, the performance of superduplex weld metal operating in a benign environment (laboratory air) is addressed. An insight into the intrinsic crack propagation resistance of commercial superduplex weld metals formed by different welding methods is sought. Aspects such as the threshold stress intensity factor range, crack propagation resistance, relative fracture toughness and influence of residual stresses on superduplex weld metal formed by different welding procedures are addressed. Section 9.7 investigates the resistance of superduplex weld metal to dissolution under the specific condition of high positive electrochemical potentials. Of critical concern is the crack propagation resistance under such circumstances. Data on corrosion fatigue crack propagation at high electrochemical potentials in commercial duplex or superduplex weld metal are scarce and this subsection aims to address the area in detail. Section 9.8 addresses the crack propagation resistance of superduplex weld metals in synthetic seawater under cathodic overpotential. In order to mitigate general corrosion of structures functioning in seawater, it is common practice to employ cathodic protection to control the ECP of a component. However, environmentally aided crack propagation can occur, especially in medium to high strength steels under cathodic protection (Francis *et al*., 1997). Commonly referred to as hydrogen embrittlement (HE), it is widely documented as having catastrophic consequences, namely rapid crack propagation and fast brittle fracture. The performance of superduplex stainless steels under such conditions is discussed.

9.5.1 Experimental details

Two types of weld process were used to fabricate the single V butt type weldments tested. The first was a GTA weld and the second type of weld consisted of a GTA weld root and a SMA weld fill. Table 9.5 shows the base

Table 9.5 Base metal and welding consumable composition (wt%) of alloy Zeron 100: remainder Fe (WMF, 2004a)

Element	Cr	Ni	Mo	Cu	Mn	W	Si	N	C	P	S
Base	24–26	6–8	3–4	0.5–1	1	0.5–1	1	0.2–0.3	0.03	0.03	0.01
GTA	24.8	9.35	3.8	0.61	0.69	0.6	0.39	0.225	0.018	0.03	0.001
SMA	25	9.5	3.6	0.8	0.7	0.7	0.5	0.2	0.03		

metal and consumable composition as documented by Weir Materials and Foundries (WMF, 2004a). Welding parameters and experimental composition analysis are detailed in WMF (2004b).

A summary of the basic mechanical properties and microstructural properties of the weldments is shown in Tables 9.6 and 9.7. The values compare well with those reported in the literature (e.g. Dhooge and Deleu, 1994; Wiesner, 1997 and acceptance standards, BS 7910, 1999). Thus, adequate weldment integrity was ensured.

The fatigue crack propagation tests discussed in subsequent sections were carried out on a computer controlled closed-loop servo-hydraulic fatigue-testing machine. A fracture mechanics approach was employed for the tests. Figure 9.4 depicts a standard single edge notch four point bend (SENB4) sample. This sample was employed in the majority of crack propagation tests discussed in this section.

Centre cracked tension (CCT) samples (Figs 9.5a, 9.5b) were employed in addition to SENB4 samples for tests carried out in laboratory air. These samples were necessary in order to establish if significant residual stresses were present perpendicular to the propagating crack.

Table 9.6 Summary of experimental base and weld metal mechanical properties. Q1 is the highest quality category for butt welds (Comer and Looney, 2006a).

	Base metal	GTA weld metal	SMA weld metal
Misalignment (°)	N/A	SENB4 5.5 CCT 2	6.5
Misalignment Assessment (BS 7910)	N/A	Q1 in bending	Q1 in bending
Yield/UTS (MPa)	750/910	700/825	700/830
Ductility (%)	23	9	18
Toughness (J)	172	69	47
Average hardness (HV)	315α /310γ	335α/310γ	328α/355γ

Table 9.7 Microstructural data for base and weld metals investigated (Comer and Looney, 2006a)

	Base metal	GTA weld metal	SMA weld metal
Inclusion content (%)	Negligible	Negligible	0.3
Intermetallic content (%)	Negligible	Negligible	Negligible
Weld flaw assessment (BS 7910)	Not applicable	Q1	Q1
Phase balance (%)	48α/52γ	35α/65γ	30α/70γ

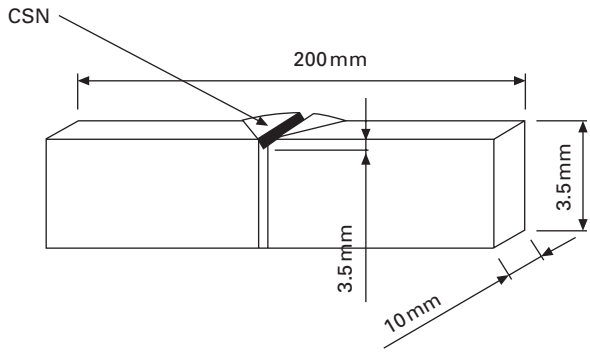

9.4 SENB4 fracture mechanics weldment sample showing dimensions, crack starter notch (CSN) (Comer and Looney, 2006a).

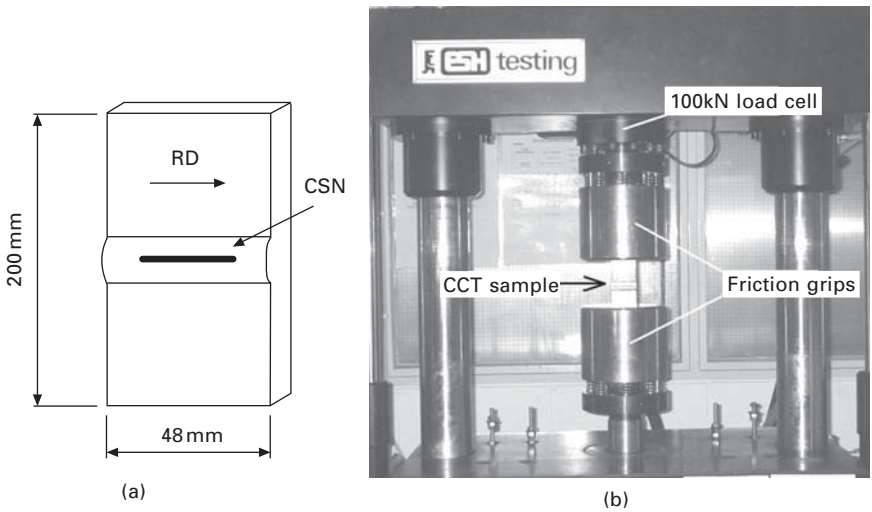

9.5 (a) CCT sample (RD, rolling direction) (Comer and Looney, 2006a), (b) CCT sample set-up in laboratory air. Loading is by a 100 kN hydraulic actuator (Comer and Looney, 2006a).

Residual stresses perpendicular to the crack growth direction could influence crack propagation rates. For both the CCT and SENB4 samples, the crack starter notch coincided with the centre of the weld metal. In this way, crack propagation rates could be determined in the regions of assumed tensile (CCT) and compressive (SENB4) residual stress fields (Fig. 9.6).

In the case of tests performed in a benign environment, constant load range, ΔK increasing and decreasing, crack propagation tests were carried out in accordance with BS 6835-1 (BS 6835-1, 1998). The majority of tests

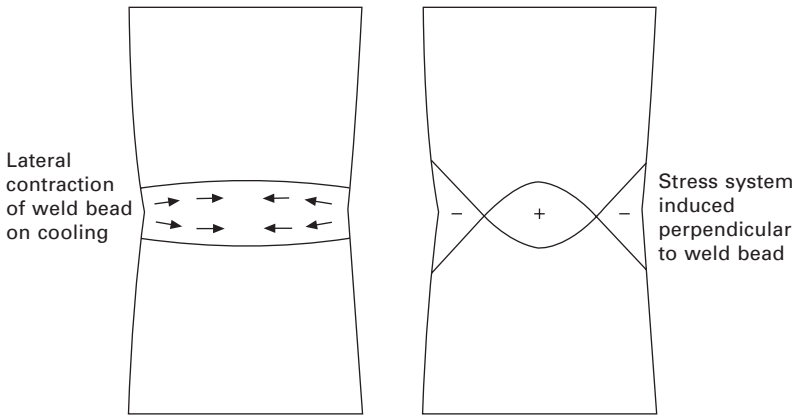

9.6 Schematic of residual stress system induced transverse to weld bead by weld bead contraction on cooling (Comer and Looney, 2006a).

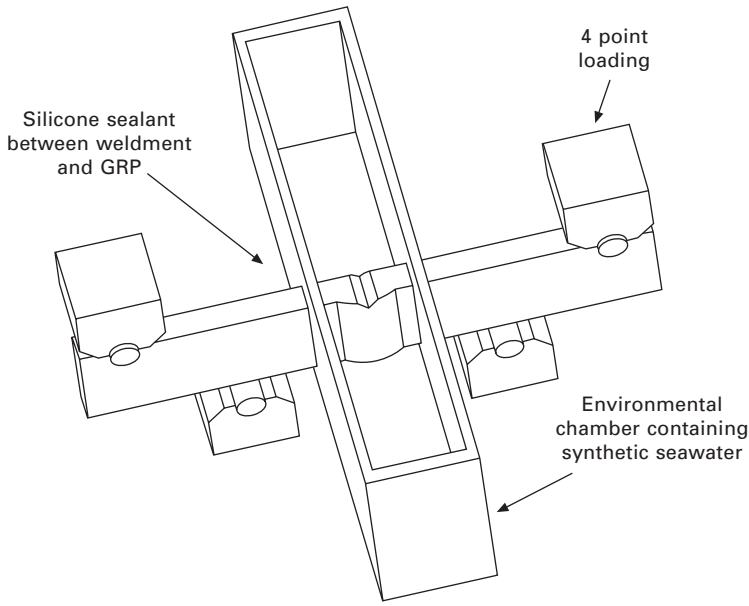

9.7 SENB4 sample with environmental chamber attached (Comer and Looney, 2006b).

in laboratory air were carried out with a loading frequency of 5 Hz. However, some were carried out at 25 Hz. An *R*-ratio of 0.5 was employed. This value is often employed in such tests to simulate the presence of residual stresses which are inherently present in weldments.

The servo-hydraulic fatigue-testing machine was subsequently modified to allow corrosion fatigue tests to be performed. A glass reinforced polymer/

plastic (GRP) environmental chamber was fitted between the innermost loading points (Fig. 9.7).

A fluid circulation system was employed to ensure optimum solution corrosivity over time. Oxygen was bubbled into the environmental chamber for the duration of the dissolution-type tests. The composition of the synthetic seawater used in the tests is given in Table 9.8.

The SENB4 sample was polarised by a counter electrode with reference to a saturated calomel electrode (SCE). A potentiostat was employed for this purpose. A noise reduction probe (NRP) connected to the potentiostat was also placed in the seawater for the duration of the tests. The SCE was situated in a remote reservoir. The corrosion fatigue set up can be seen in Fig. 9.8.

Table 9.8 Synthetic seawater composition (Francis, 2001a)

Chemical	Weight per litre (g)
Sodium bicarbonate	0.2
Calcium chloride	2.3
Magnesium chloride	6.0
Magnesium sulphate	7.7
Sodium chloride	28.0

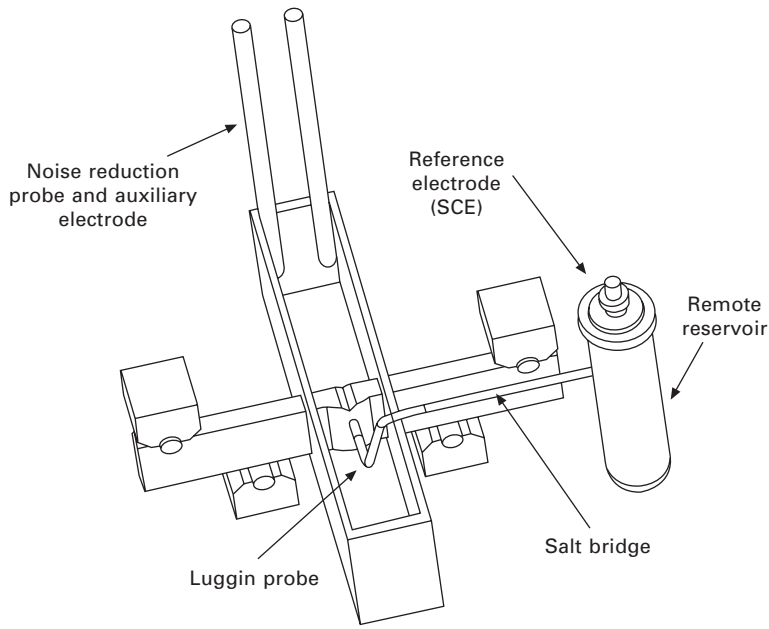

9.8 Corrosion fatigue set up showing reference, auxiliary, noise reduction electrodes, remote reservoir and salt bridge (Comer and Looney, 2006b).

Tests performed in synthetic seawater were constant load range, ΔK increasing crack propagation tests with reference to BS ISO 11782-2 (1998) and ASTM E 647-95a (1995). Loading frequency of tests in synthetic seawater was 0.1 Hz in order to maximise dissolution time at the crack tip. An R-ratio of 0.5 was again chosen for these tests.

Before starting a test, the region immediately in front of the crack starter notch was given a metallographic finish in order to aid crack visualisation and measurement as described in Comer and Looney (2006b). Each sample was then pre-cracked in air using either the traditional load shedding technique (ASTM E 647-95a, 1995; BS 6835-1, 1998) or the novel cyclic compression technique as described by Suresh (1998) and Forth *et al*. (2003). Post-test, investigation of the fracture surface was carried out using a scanning electron microscope (SEM). Local crack growth rates were determined by striation spacing measurements carried out in the SEM at different crack lengths, which correspond to different ΔK values between 20 and 60 MPa m$^{0.5}$.

9.6 Crack propagation in a benign environment

In this section, the results pertaining to a series of tests carried out in laboratory air are presented and discussed with reference to relevant literature. The first set of results relates to crack propagation in the threshold regime. Figure 9.9 is a schematic depicting the significant influence of the chosen test method on the threshold for crack propagation. Table 9.9 lists the threshold values

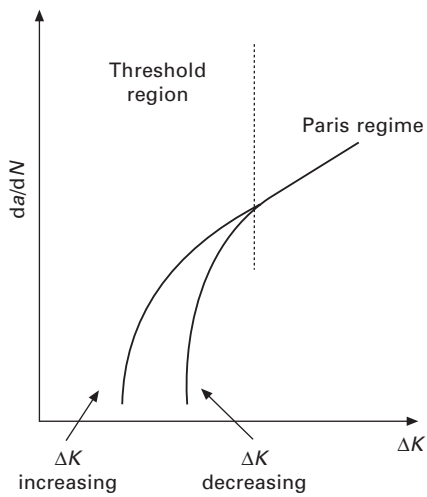

9.9 Schematic showing variation in crack propagation data and dependence on ΔK increasing/decreasing test method. (Comer and Looney, 2006a).

Table 9.9 Threshold and fast fracture values for base and weld metal samples (Comer and Looney, 2006a)

	ΔK_{th} (ΔK increasing) (MPa $m^{0.5}$)	ΔK_{th} (ΔK decreasing) (MPa $m^{0.5}$)	ΔK_C (fast fracture) (MPa $m^{0.5}$)
Base	3.5	8.5	94
GTA	3.5	9.0	56
SMA	3.1	6.7	41

for the base and weld metals when tested in laboratory air using different test techniques.

Thresholds for the onset of crack propagation obtained using the ΔK increasing technique were more conservative for two reasons. First, a cyclic compression technique was necessary to precrack the samples. This technique has two main consequences. First and perhaps most importantly, the precrack is relatively short. Therefore, contact between fracture surfaces is minimised for the ΔK increasing technique whereas closure due to contact between the fracture surfaces in the wake of the crack tip was significant for the ΔK decreasing technique. The low loads required to obtain threshold exacerbated the closure effect for the ΔK decreasing technique. Therefore, ΔK effective was reduced, and relatively high non-conservative threshold values were obtained.

Secondly, unlike precracking using positive load cycling, a zone of residual tension remains after cyclic compression as opposed to a zone of residual compression (load shedding technique). Therefore, it is likely that the crack will propagate easier than through a zone of residual compression. In support of these observations is the fact that it has recently been concluded that constant load range ΔK decreasing type tests generate artificially high threshold values when compared to data from ΔK increasing type tests, (Forth *et al*., 2003). With regard to the Paris regime, the slope of the Zeron 100 base and weld metal data found in laboratory air was on average 3.0, which is the generally acknowledged value for alloys fatigue tested in benign environments such as laboratory air (Fig. 9.10).

Each data set is made up of three ΔK increasing tests performed at 5, 10 and 25 Hz. As such, frequency independence in laboratory air is noted. The Paris law constants (C and m) and the coefficient of determination calculated using the accumulated data from the three individual (SENB4) tests on each sample are shown in Table 9.10.

The current crack propagation data were then compared with other researchers' data on superduplex: Uranus UR52N+ and SAF 2507 (Coudreuse and Charles, 2000; Linder, 1994), duplex: SAF 2205 (Linder, 1994), SUS 329 (Misawa, 1989; Komai *et al*., 1990), X6 (Makhlouf *et al*., 2003) and super austenitic stainless steels: SMO 654 (Linder, 1994). Good agreement

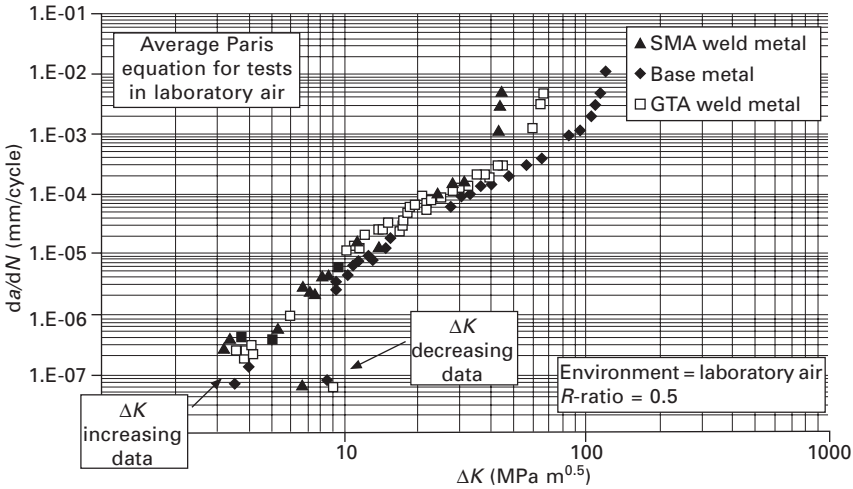

9.10 Fatigue results for SENB4 samples tested in laboratory air. Loading frequency varied from 5 to 25 Hz (Comer and Looney, 2006a).

Table 9.10 Paris equation coefficients and the coefficient of determination for data obtained in laboratory air (Comer and Looney, 2006a)

Sample	C	m	R^2
Base metal	4E-9	3.0	0.96
GTA weld metal	6E-9	3.0	0.97
SMA weld metal	5E-9	3.1	0.97

between the data for the superduplex stainless steels considered was obtained. The relatively higher UTS and yield strength of the superduplex stainless steels appears to have little benefit with regard to resistance to crack propagation in the range ΔK = 10–40 MPa m$^{0.5}$. This observation is commonly acknowledged (Maddox, 1991).

Results from the tests on CCT samples can be seen in Fig. 9.11. It is evident that any possible tensile residual stresses present did not increase average crack growth rates above those found for the SENB4 type samples. Since the data for SENB4 and CCT samples is coincident, it appears likely that residual stress fields possibly present had little effect on crack propagation rates. This is to be expected considering the relatively short length of weld bead involved (< 50 mm).

Therefore, the crack propagation data shown in Figs. 9.10 and 9.11 are thought to represent the intrinsic crack propagation resistance of the GTA and SMA weld metals. Also evident from Fig. 9.11 is the fact that both sample types (SENB4 GTA and CCT GTA) yielded the same crack growth

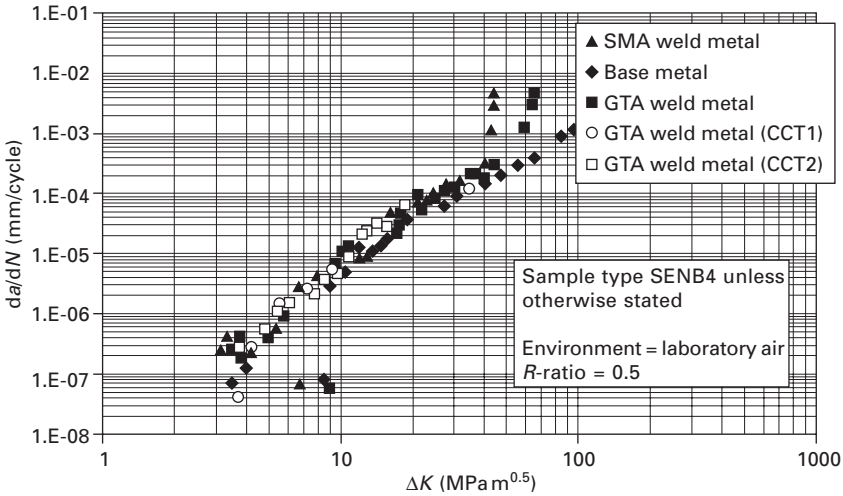

9.11 Fatigue results for SENB4 and CCT samples tested in laboratory air (Comer and Looney, 2006a).

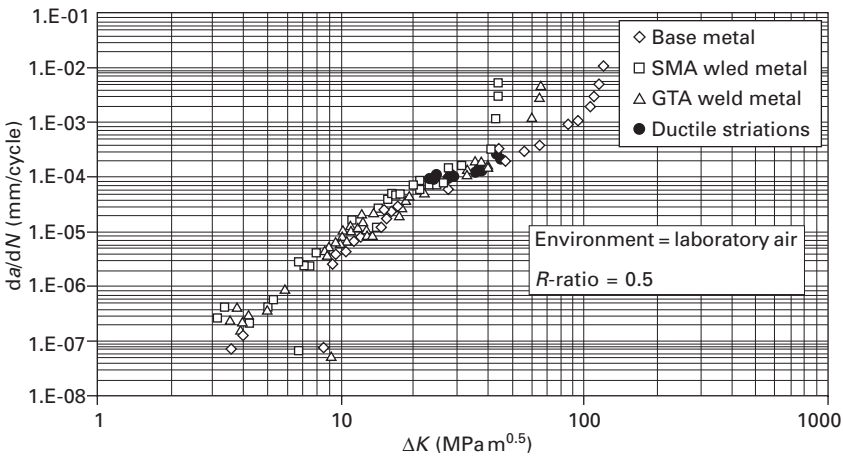

9.12 Ductile striation spacing compared with macrocrack growth rates in laboratory air (Comer and Looney, 2006a).

threshold value of 3.5 MPa $m^{0.5}$. It is in the threshold region where one would expect residual stress effects on crack growth rates to be significant.

In order to comprehensively assess the intrinsic resistance of the base and weld metals, the fracture surfaces of each sample was examined. As expected, striations were ductile in nature on samples tested in laboratory air. Good correlation was obtained between the striation size and macro-crack growth rate for the ΔK domain (23–50 MPa $m^{0.5}$) analysed (Fig. 9.12). A ductile striation was formed on each load cycle (Fig. 9.13). Therefore, a subcritical ductile mechanism controlled the rate of crack propagation.

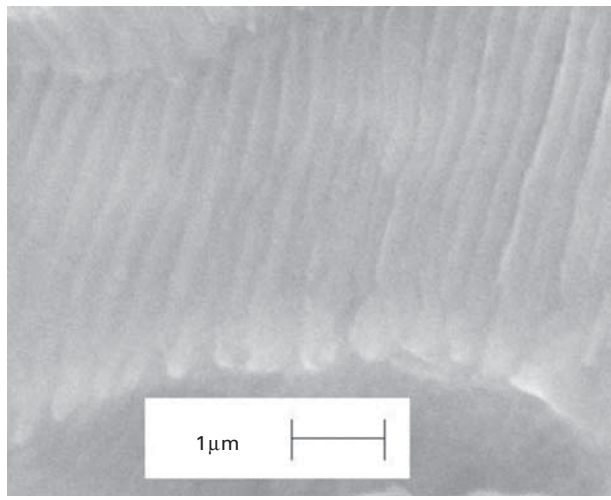

9.13 Ductile striations at 45 MPa $m^{0.5}$ (Comer and Looney, 2006a).

Perhaps the most important intrinsic factor in the crack propagation resistance of the weld metals is the prior macrostructure (Fig. 9.2). In multipass welds, a through thickness notch is known to coincide with both the weakest planes of the coarse columnar solidification structure and the greatest concentration of weak grain boundary segregates (Dawes, 1971). In both SENB4 (GTA and SMA) and CCT (GTA) samples, the macrocrack regularly followed what is thought to be the grain boundaries of the columnar grain macro-structure at least up to a ΔK of 10 MPa $m^{0.5}$. It is thought that the columnar grain boundaries provide a path of least resistance to crack growth at low ΔK. The macrocrack path is thought to highlight the columnar weld grains (Fig. 9.14). The average width (30 μm) of the columnar weld grains agrees with measurements recorded from Fig. 9.2. A similar phenomenon (reported as mode II type crack propagation) has been reported for the weld metal of an SAF 2304 duplex stainless steel under high cycle *S–N* type fatigue tests (Beretta and Boniardi, 1996).

With regard to fracture toughness, it has been observed that the centre of the weld metal, as opposed to the HAZ, exhibits the lowest toughness with regard to superduplex stainless steel weldments (Charles and Bonnefois, 1986; Dhooge and Deleu, 1994; Gunn, 1994; Deleu and Dhooge, 1997). In general, low toughness at the centre of weld metals has been attributed to the highly restrained conditions under which solidification and cooling take place (Dawes, 1971). A study was carried out on Zeron 100 weldments to assess the mechanisms responsible for low weld metal toughness (Baxter *et al*., 1993). Strain hardening caused by high local (residual) stresses induces weld zone hardening. This results in weld metal with reduced ductility and thus low toughness. Reduced ductility may also result from the presence of

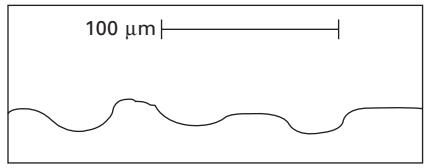

(a)

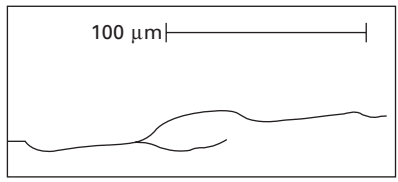

(b)

9.14 Macrocrack propagation around columnar weld grains at $\Delta K <$ 10 MPa $m^{0.5}$ (Comer and Looney, 2006a).

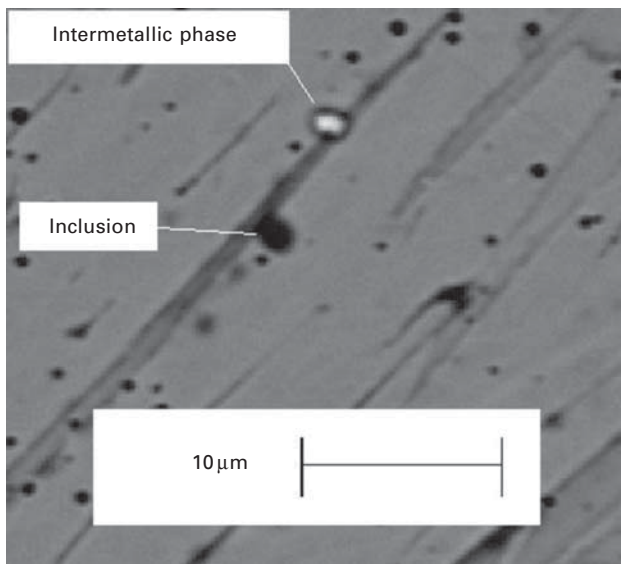

9.15 Intermetallic (bright spot) at ferrite/austenite grain boundary in SMA weld metal. Image obtained using back-scattered electrons (Comer and Looney, 2006a).

hard brittle intermetallic phases. However, even though illuminated spots (Fig. 9.15), which correspond to intermetallic phases, were located after scanning systematically around both weld metals, the intermetallic content was negligible. Highest estimates obtained using image analysis software were in the region of 0.03%.

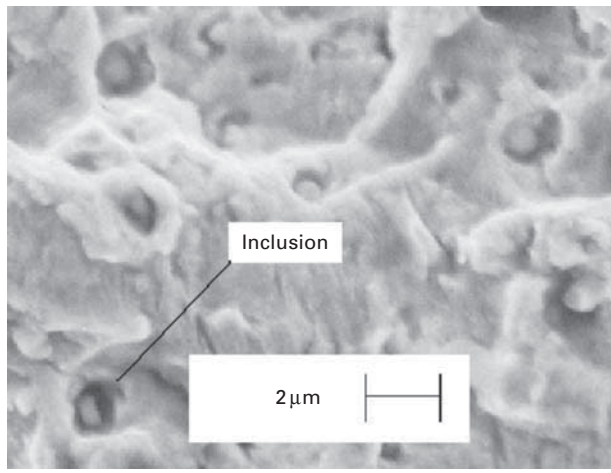

9.16 Inclusions on SMA weld metal fracture surface (Comer and Looney, 2006a).

However, as seen in Fig. 9.14 the grain boundaries of the weld macrostructure appear to be preferred paths for crack growth and are probably at least a contributory factor to the low toughness observed in the weld metal. Appreciable inclusion content (0.3%) was observed in the SMA weld metal (Fig. 9.16), which caused a significant reduction in toughness compared with the GTA method (negligible inclusion content).

9.7 Crack propagation in seawater under high electrochemical potential

Superduplex stainless steels are typically cathodically protected in seawater. However, local regions can assume different electrochemical potentials from the bulk material. Local variations in electrochemical potentials can arise due to a number of reasons including local metallurgy (in the case of pitting) and geometry (in the case of crevice corrosion) (Roberge, 1999). Local electrochemical potential is also influenced by the condition of the seawater, for example, aerated and chlorinated seawater induces high local electrochemical potentials when in contact with highly alloyed stainless steels (Francis, 2001b). Non-uniform organic biofilms often create preferential sites for fast oxygen reduction (Roberge, 1999).

The generation of negative hydroxyl ions (OH^-) by the cathodic reaction is counterbalanced electrostatically by the creation of iron cations (Fe^{2+}) as shown respectively in Eqs. 9.3 and 9.4:

$$4e^- + O_2 + 2H_2O \rightarrow 4OH^- \qquad 9.3$$

$$Fe \rightarrow Fe^{2+} + 2e^- \qquad 9.4$$

It is important to highlight that adequate oxygen levels must be present in the seawater. This is typically the case in the splash/spray zone. In this section, the resistance of Zeron 100 weld metal to dissolution in the specific case of high positive electrochemical potentials is assessed.

Firstly, the Paris coefficients (Table 9.11) for the base and SMA that were comparable for samples tested in air are also comparable in seawater tests. However, the crack growth rates are significantly greater in seawater than in air over the ΔK range investigated (Fig. 9.17). In this way, the significant microstructural variation between the base and weld metal does not appear to have been a significant factor in terms of crack propagation resistance in seawater. The crack growth rate for the SMA weld metal in synthetic seawater was 2.3 times greater than rates in air at $\Delta K = 30\,\text{MPa}\,\text{m}^{0.5}$. The performance of the base metal in synthetic seawater was at least as good as the SMA weld

Table 9.11 Paris equation coefficients and the coefficient of determination for data obtained in laboratory air and seawater (Comer and Looney, 2006b)

Sample	Environment	C	m	R^2
Base metal	Laboratory air	4E-9	3.0	0.96
Base metal	Seawater	1E-7	2.0	0.94
SMA weld metal	Laboratory air	5E-9	3.1	0.97
SMA weld metal	Seawater	1E-7	2.2	0.96
Ferralium 255 weld metal (Tavara *et al.*, 2001)	Seawater	2E-9	3.1	–

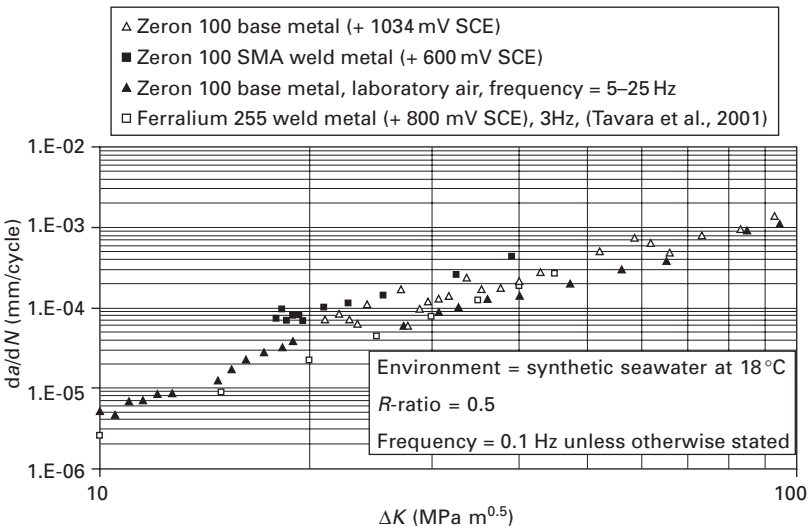

9.17 Base and weld metal at high potential in synthetic seawater at 18 °C (Comer and Looney, 2006b).

metal and converged with the data for the base metal tested in air at 85 MPa $m^{0.5}$. Fast fracture levels were the same as in air.

Tavara observed negligible influence of a high positive potential on a duplex weld metal (Fig. 9.17) (Tavara *et al*., 2001). However, it must be noted that a relatively high loading frequency (3 Hz) was utilised. The *m* coefficient for Tavara's data (Table 9.11), which is similar to the *m* coefficient for the base metal tested in laboratory air, indicates that the seawater had little effect on crack propagation rates. Marrow and King (1994) carried out tests on Zeron 100 superduplex base metal at a frequency of 0.1 Hz in 3.5% NaCl solution at free corrosion potential. The maximum enhancement in crack growth rate was recorded at ΔK = 26.5 MPa $m^{0.5}$. Here, the crack growth rate was 1.8×10^{-4} mm/cycle. Similarly, a crack growth rate of 1.7×10^{-4} was recorded at 27 MPa $m^{0.5}$ (Comer and Looney 2006b). Marrow observed an increase in crack growth rates over a ΔK range from 24 to 40 MPa $m^{0.5}$. This is in contrast to the results shown in Fig. 9.17 where enhancement in crack growth rates is evident below 24 MPa $m^{0.5}$ in both the base and weld metal. Moreover, enhancement continues in the base metal up to 60 MPa $m^{0.5}$. The weld metal fractured at 41 MPa $m^{0.5}$. Enhancement in crack growth rates over a wider ΔK range in the current tests is probably due to the imposed high electrochemical potential which allows the seawater to influence the intrinsic crack propagation resistance of the alloy over a wider ΔK range. Intrinsic crack propagation resistance is discussed below with reference to the fractography.

The appreciable inclusion content in the SMA weld metal (+600 mV) may have contributed to the increase in crack propagation rates by a factor of 2 (at ΔK = 30 MPa $m^{0.5}$) over rates in air (Fig. 9.17). However, it is more likely that dissolution at the crack tip was the key factor with regard to increased crack propagation rates at 0.1 Hz in seawater. Marrow and King (1994) concluded that the frequency with which ferrite/austenite grain boundaries are encountered by the crack tip is a key factor governing the intrinsic resistance of duplex stainless steels to crack growth. In this way, a medium which can selectively attack grain boundaries could influence crack growth rates. With regard to the base metal sample, it was evident that dissolution selectively attacked the grain boundaries (Fig. 9.18) and that this phenomenon was independent of ΔK. However, it is also possible that a significant portion of the dissolution in Fig. 9.18 occurred in the wake of the crack tip.

Girones carried out corrosion fatigue tests in aerated seawater at free potential on a superduplex stainless steel, SAF 2507 (Girones *et al*., 2005). A significant reduction in fatigue life was observed in base metal samples tested at low, intermediate and high plastic strain amplitudes. It was concluded that at relatively high strain amplitudes, the seawater enhanced microcrack initiation within the active ferritic phase and aided crack crossing of microstructural boundaries such as grain boundaries. Perdriset *et al*. (1994)

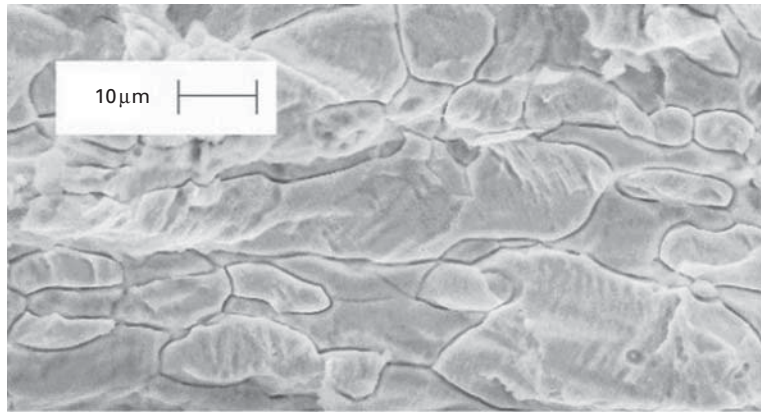

9.18 Dissolution of grain boundaries evident on unetched base metal fracture surface tested in synthetic seawater (+1034 mV SCE). Crack growth is from left to right (Comer and Looney, 2006b).

also reported that dissolution facilitated cracks crossing ferrite–austenite phase boundaries, increasing crack propagation rates. Further, selective dissolution of boundary regions between ferrite and austenite phases and of ferrite grains was clearly observed when testing duplex stainless steel 2205 and 2507 in acidic chloride solutions (Femenia *et al.*, 2000). Preferential dissolution in boundary regions was much less on 2507 than 2205. A well-balanced high content of alloying elements (Cr, Mo and N) appeared effective in minimising selective dissolution.

9.8 Crack propagation in seawater under negative imposed electrochemical potential

First of all, a brief study has been made into the threshold for the onset of environmentally assisted cracking (Comer and Looney, 2008). Initially, ΔK_{EAC} values were obtained from ΔK decreasing type tests in synthetic seawater (Table 9.12). Here, there is a high probability that ΔK_{EAC} is not conservative. First, the test methodology in ΔK decreasing type tests ensures that the crack is relatively long even before load shedding is employed. For example, the crack length was 12.6 mm at ΔK_{EAC} for the base metal. As such, the likelihood of contact between crack surfaces in the wake of the crack tip is high. Secondly, calcareous deposits form in the crack enclave in the presence of synthetic seawater and cathodic protection. This further increases the likelihood of contact in the crack enclave and reduces ΔK at the crack tip. In order to obtain conservative ΔK_{EAC} values, ΔK increasing type tests were carried out in 3.5% NaCl solution (Table 9.12). 3.5% NaCl solution is widely used as a seawater substitute in laboratory tests. Using this method there is much less chance of premature crack closure because ΔK_{EAC} values are obtained when

Table 9.12 EAC thresholds obtained in synthetic seawater (ΔK decreasing) and 3.5% NaCl (ΔK increasing) at –1040 mV SCE (Comer and Looney, 2008)

Sample	Threshold in seawater (ΔK_{EAC})	
	ΔK decreasing (synthetic seawater) (MPa $m^{0.5}$)	ΔK increasing (3.5% NaCl) (MPa $m^{0.5}$)
Base metal	15.4	11
GTA weld metal	15.2	–
SMA weld metal	–	11

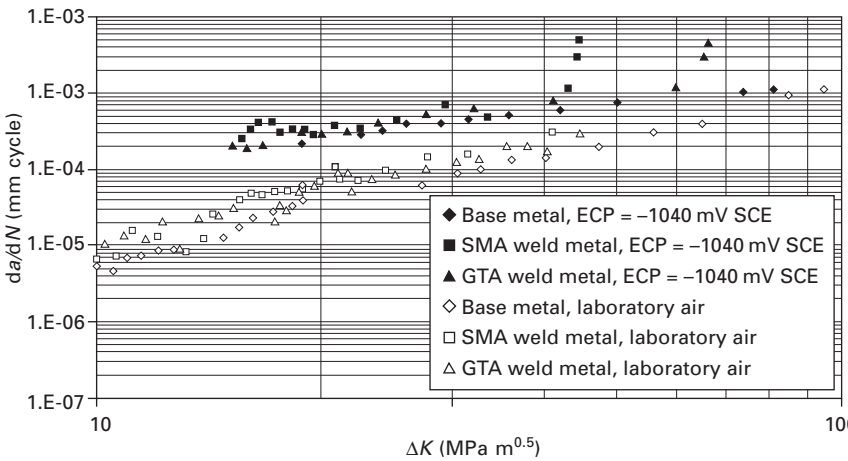

9.19 Test results in synthetic seawater at –1040 mV SCE (Comer and Looney, 2008). Loading frequency = 0.1 Hz, *R*-ratio = 0.5.

the crack is relatively short (5.4 mm on average in the tests conducted) and calcareous deposits cannot form in 3.5% NaCl solution.

With regard to the Paris regime, crack growth rates were obtained from ΔK increasing type tests carried out on the base, GTA and SMA samples. Samples were precracked using the traditional load shedding technique and polarised at –1040 mV SCE. The results were comparable, exhibiting a linear trend on a log–log scale (Fig. 9.19).

The fast fracture values obtained were the same as those obtained in laboratory air (Comer and Looney, 2006a). However, crack propagation rates were greater than those obtained in laboratory air by a factor of 5 at $\Delta K = 20$ MPa $m^{0.5}$, reducing uniformly to a factor of 3.5 at $\Delta K = 40$ MPa $m^{0.5}$. Woolin (Woolin *et al.*, 2006), carrying out crack growth tests through the HAZ/parent metal of a superduplex weldment under cathodic protection in seawater, reported a step change in crack growth rates by a factor of 3 at

$\Delta K \sim 19\,\text{MPa}\,\text{m}^{0.5}$. The significantly lower increase in crack growth rates is probably due to the higher loading frequency (0.5 Hz) employed. *R*-ratio was 0.5 in both cases. Clearly, the lifetime of a component can be dramatically reduced in the presence of hydrogen and on the attainment of a specific stress intensity factor range. The environmental effect initially occurred at $\Delta K = 11\,\text{MPa}\,\text{m}^{0.5}$ in the current tests which agrees quite well with the value ($12.6\,\text{MPa}\,\text{m}^{0.5}$) reported by Woolin *et al.* (2006). The lowest ΔK at which hydrogen contribution to subcritical failure processes is maximised is approximately $15\,\text{MPa}\,\text{m}^{0.5}$ in the results shown in Fig. 9.19. The Paris law coefficients for the linear portion of the data for environmentally assisted tests along with the coefficients of determination and the corrosion cell data are given in Table 9.13.

It is well known that hydrogen diffusion is usually more rapid in BCC metals such as ferrite than in FCC metals such as austenite (Fukai, 1993). Austenite is also known to have a higher hydrogen solubility level than ferrite and can act as a hydrogen sink. These are key reasons why ferrite, unlike austenite, is particularly susceptible to hydrogen embrittlement. Krishnan (1997) concluded that corrosion fatigue crack propagation in duplex stainless steels is due to hydrogen cracking in ferrite. Fracture surfaces exhibited brittle steps in ferrite and tearing and ductile striations in austenite. Classic features (such as fanned cleavage facets, riverlines and brittle striations) (Brookes and Choudhury, 2001) are clearly evident on the fracture surfaces of the tested samples, indicating that hydrogen contributed to the failure process (Figs 9.20–9.22).

The common consensus is that hydrogen embrittles a percentage of the ferrite present along the crack front. Marrow *et al.* (1990) postulated that the degree of embrittlement reflected the rate of hydrogen entry to the crack tip.

It is evident from the fractographs the effect of the structure of the weld metal on the distribution of cleavage. Columnar-type grains are embrittled preferentially in the weld metal. This shows that the primary ferritic structure of the weld metal, initially formed on cooling, dominates even after the formation of austenite in the columnar grains. Perhaps austenite reformation

Table 9.13 Paris law coefficients (*C* and *m*), coefficients of determination (R^2) and corrosion cell data for tests in synthetic seawater (–1040 mV SCE), *R*-ratio = 0.5, load frequency = 0.1 Hz (Comer and Looney, 2008)

Sample	*C*	*m*	R^2	Average Corrosion Cell Data			
				pH	ECP v SCE (mV)	Current density (mA/mm^2)	Solution temp (°C)
Base metal	2E-5	0.9	0.97	8	–1045	3.1×10^{-4}	22
GTA weld metal	5E-6	1.3	0.96	8	–1044	3.0×10^{-4}	21
SMA weld metal	1E-5	1.1	0.72	8	–1024	2.5×10^{-4}	20

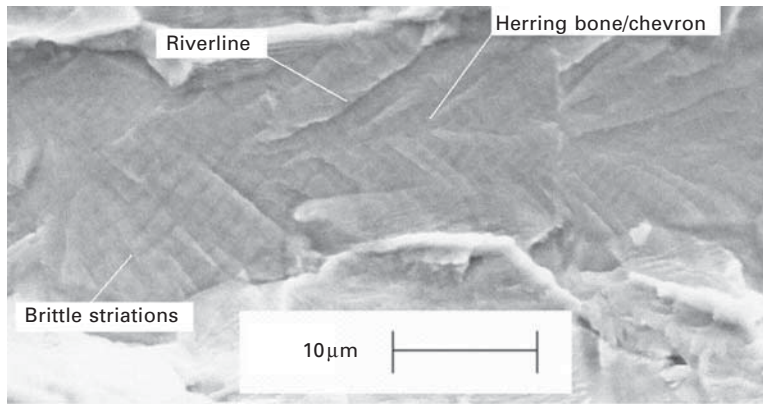

9.20 Riverlines and brittle striations evident on base metal fracture surface tested in synthetic seawater (–1040 mV SCE). Propagation direction, left to right (Comer and Looney, 2008).

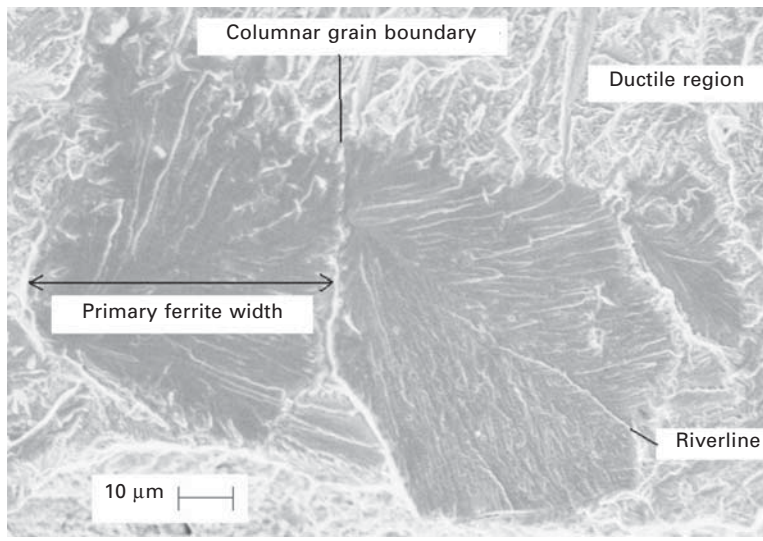

9.21 Brittle cleavage facets fanning out in the direction of crack propagation (left to right) on the fracture surface of SMA weld metal tested in synthetic seawater (–1040 mV SCE) (Comer and Looney, 2008).

was suppressed in some columnar grains due to an absence of austenite promoting alloying elements such as nitrogen. Columnar grains with low austenite contents would be more susceptible to embrittlement as austenite is known to act as a hydrogen sink.

Bulloch established that the degree of environment-assisted crack growth, under ambient conditions is uniquely related to the extent of static failure mode and not the failure type (intergranular, cleavage, etc.) (Bulloch, 1994). Therefore, the distribution of embrittlement is insignificant. The percentage

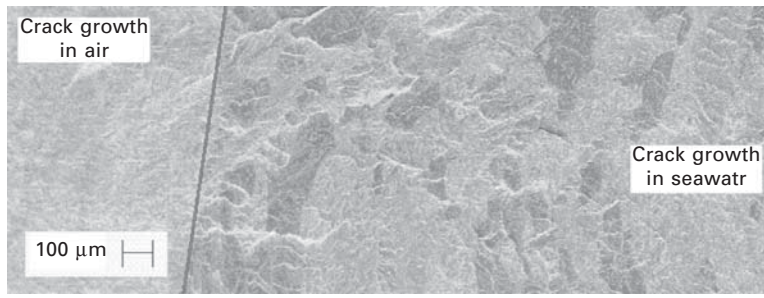

9.22 GTA weld metal fractograph showing precrack grown in laboratory air and brittle facets, which occurred in synthetic seawater (–1040 mV SCE). Crack propagation direction, left to right (Comer and Looney, 2008).

cleaved is the critical variable. The area fraction cleaved ranged from 24 to 36% for the base and two weld metals. There was no significant dependence on ΔK. As such, the average cleavage was 30%. Implicit in Bulloch's model is the assumption that the crack growth rate is controlled by the remaining ductile ligaments. Support for this point is evident in the reviewed work, where reasonable agreement exists between the ductile striations measured on the fracture surfaces of the base and GTA weld metal samples and the macrocrack growth rates (Fig. 9.23). Therefore, crack growth rates increase owing to embrittled ferrite fracturing prematurely on the positive portion of a load cycle. This serves to increase the effective ΔK acting on the remaining ligaments, leading to faster crack growth rates than those obtained in benign environments such as laboratory air.

The fact that the crack propagation rates of the base and weld metals are comparable shows that the effect of relative phase content (ferrite/austenite, base 48/52, GTA 35/65, SMA 30/70 reported in Comer and Looney, (2006a) on crack propagation rates was negligible. The percentage cleaved had the dominant effect.

Even though the crack propagation rate is controlled by ductile deformation and hence ductile striation spacing, it is important to consider the brittle striations present, as these could take on added significance if embrittlment was more severe, i.e. occupied a greater percentage of the fracture surface. Marrow (1991) carried out tests on Zeron 100 in brine (3.5% NaCl, $R = 0.5$, $f = 0.1$ Hz) with cathodic overcharging and in high purity water ($R = 0.5$, $f = 5$ Hz) over a ΔK range of 20 MPa $m^{0.5}$ to failure. Crack growth rates in both cases were similar to the current results in synthetic seawater under cathodic overpotential. The average cleavage fraction in high purity water in the ΔK range 20–28 MPa $m^{0.5}$ was approximately 30%, which is the same as the average percentage found in Comer's work (Comer and Looney, 2008). Brittle striation spacing averaged at 1 μm at $\Delta K = 30$ MPa $m^{0.5}$ and ΔK dependence was low at 0.4 (Marrow, 1991).

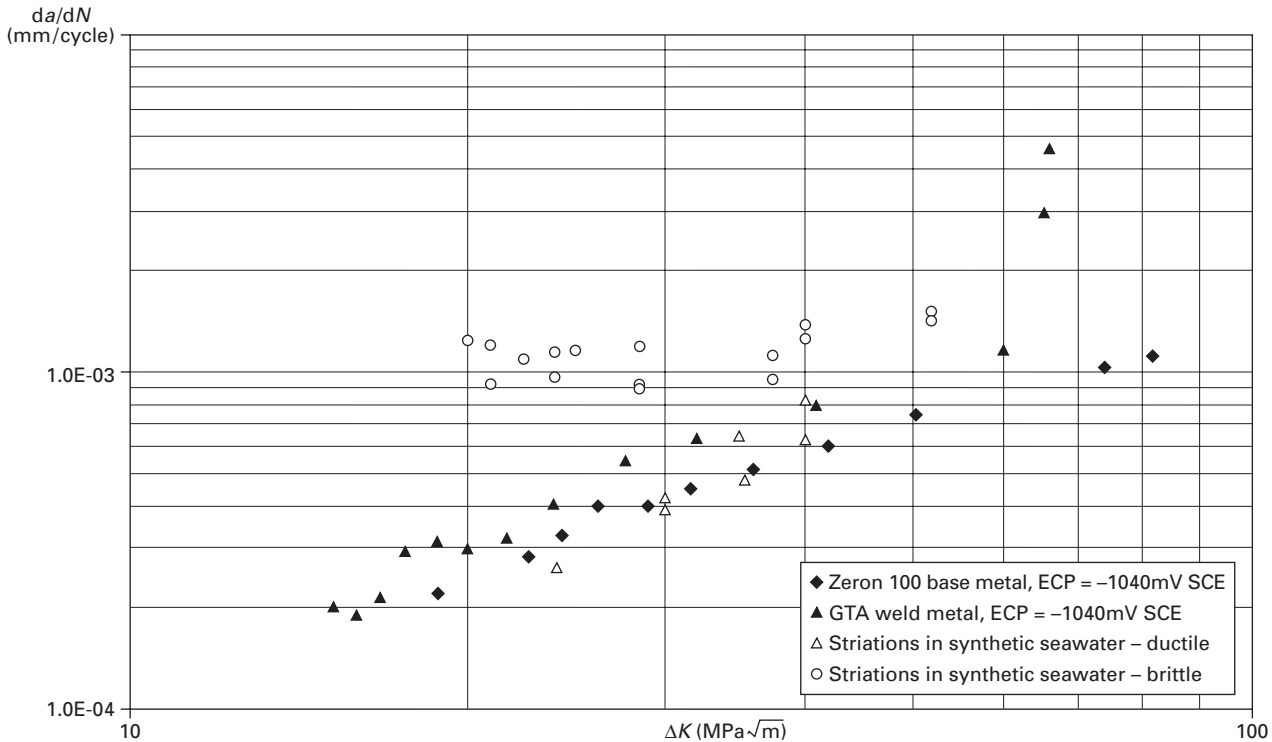

9.23 Ductile and brittle striations relative to macrocrack growth rates (Comer and Looney, 2008).

A similar phenomenon was found in Comer's research (Comer and Looney, 2008) where the brittle striation spacing measured on the base and GTA weld samples ranged between 1 and 1.5 μm over a ΔK range of 28–52 MPa $m^{0.5}$ (Fig. 9.23). This implies that the macroscopic crack growth rate was 3.3 times less than the brittle striation spacing at $\Delta K = 20$ MPa $m^{0.5}$. As such, 3.3 ductile striations were formed to every one brittle striation at $\Delta K = 20$ MPa $m^{0.5}$. This reduced to 1.5 ductile striations at approximately $\Delta K = 40$ MPa $m^{0.5}$. Therefore, a conditioning period probably took place after the formation of a brittle striation.

Another key factor on the severity and extent of hydrogen embrittlement is the tendency for atomic hydrogen adsorption as opposed to hydrogen gas evolution. Olive observed that the quantity of adsorbed and absorbed atomic hydrogen is lower than gaseous hydrogen by an order of magnitude (Olive *et al*., 1999). Therefore, the reaction shown in Eq. 9.5 where hydrogen gas is produced is typically dominant:

$$2H_2O + 2e^- \rightarrow H_2 \uparrow \text{(hydrogen gas)} + 2OH^- \qquad 9.5$$

The hydrogen gas does not enter the alloy but bubbles out of the crack enclave (Olive *et al*., 1999). Production of atomic hydrogen is maximised when hydrogen recombination poisons such as sulphide (perhaps in the form H_2S) are present (Cohen *et al*., 1987; Francis, 2001a). These poisons minimise the occurrence of the reaction described by Eq. 9.5 maximising atomic hydrogen adsorption into the lattice.

9.9 Future trends

It is apparent from the above discussion the fact that more research into superduplex stainless steel welds operating in seawater is required. Many gaps still exist in the knowledge base which must be addressed before the full potential of superduplex stainless steel can be realised. Below are some suggested areas where it is believed future work will proceed.

S–N type curves for superduplex stainless steel weldments fabricated by different welding processes would complement existing ΔK–da/dN type data and fatigue resistance benefits relative to structural steel could easily be identified. Further, *S–N* type data is readily understandable to the non-specialists and is in widespread use throughout the offshore industry. Such tests could quite easily be carried out in seawater under cathodic overprotection at a representative low frequency. These tests could initially be performed on smooth weldments to assess crack initiation resistance in air and in seawater. However, it is suggested that further tests should be carried out where a crack is introduced into the weldment samples pretest, by means of a machined notch and subsequent cyclic compression loading. The resulting number of load cycles to failure at a particular initial remote stress level would be

conservative. Every effort should be made to ensure that distortion and residual stresses in the fabrication are minimised.

Short crack growth tests need to be carried out on polished smooth welded samples to establish if the threshold data obtained for the base and weld metals in air with the aid of the cyclic compression technique is conservative or whether long crack growth is actually possible at lower ΔK. Examination of the fractography post-test could lead to an improved understanding of the interaction of the crack tip with the duplex microstructure under very low loading. In addition, it has been established that the onset of hydrogen assisted crack growth requires a critical stress level. Therefore, it would be pertinent to assess the effect of high positive ECPs on crack propagation around the threshold ΔK for the onset of crack growth as it is thought that dissolution mechanisms have their greatest effect at low ΔK where the hydrogen mechanisms are least effective.

9.10 Sources of further information and advice

9.10.1 Selected standards

ASTM E 647-95a, Standard Test Method for Measurement of fatigue Crack Growth Rates. This standard also contains an annex concerning 'special requirements for testing in aqueous environments' (1995).
BS ISO 11782-2:1998, Corrosion of metals and alloys – Corrosion fatigue testing – part 2, Crack propagation using pre-cracked specimens (1998).
BS 6835-1: 1998, Method for the determination of the rate of fatigue crack growth in metallic materials – part 1 (1998)

9.10.2 Selected professional bodies

The Welding Institute (TWI)
www.twi.co.uk
NACE international (National Association of Corrosion Engineers)
www.nace.org

9.10.3 Selected superduplex producers

The Weir Group PLC – Zeron 100
<www.weirmaterials.co.uk>
Sandvik Materials Technology – SAF 2507
<www.smt.sandvik.com>

9.10.4 Selected publications

Comer AJ, Corrosion–fatigue of a Superduplex Stainless Steel Weldment, PhD thesis, Dublin City University (2004).

Marrow TJ, Fatigue mechanisms in an embrittled duplex stainless steel, PhD thesis, Cambridge (1991).
Andresen PL, Corrosion fatigue testing, in *ASM Corrosion tests and standards Hand book, application and interpretation*, Baboian R ed. (1995).
Gunn RN, *Duplex stainless steels, Microstructure, properties and applications*, Abington Publishing (1997).

9.11 References

ASTM E 647-95a (1995), Standard Test Method for Measurement of fatigue Crack Growth Rates. This standard also contains an annex concerning 'special requirements for testing in aqueous environments'.
Atamert S, King JE (1991), Elemental partitioning and microstructural development in duplex stainless steel weld metal, *Acta Metal Mater*, **39**, 3, 273–285.
Baxter CFG, Irwin J, Francis R (1993), The weld zone hardness and serviceability of Zeron 100 Super Duplex Stainless Steel, *Proc International Offshore and Polar Engineering Conference*, Singapore, 401–407.
Beretta S, Boniardi M (1996), Microstructure and fatigue properties of a welded duplex stainless steel, *Fatigue fracture Eng Mat Structures* **19**, 6, 647–654.
Bernhardsson S (1991), The corrosion resistance of duplex stainless steels, *Proc Duplex Stainless Steels*, Beaune, France, 185–209.
Brookes CR, Choudhury A (2001), Failure Analysis of Engineering Materials, McGraw-Hill.
BS ISO 11782-2, (1998), Corrosion of metals and alloys – Corrosion fatigue testing – part 2, Crack propagation using pre-cracked specimens.
BS 6835-1 (1998), Method for the determination of the rate of fatigue crack growth in metallic materials – part 1.
BS 7910 (1999), Guide on methods for assessing the acceptability of flaws in metallic structures.
Bulloch JH (1994), Fatigue fracture surface features prevalent in steels at ambient temperatures, *Theoret Appl Fracture Mech*, **20**, 133–140.
Byrne G, Francis R, Warburton G (2000), Variation in mechanical properties and corrosion resistance of different alloys within the generic designation UNS S32760, *Proc Duplex America*, Houston, USA, 113–125.
Charles J (1991), Super duplex stainless steels: structure and properties, *Proc Duplex Stainless Steels*, Beaune, France, 3–48.
Charles J (1997), Why and where duplex stainless steels, *Proc Duplex Stainless Steels*, 5th world conference, Maastricht, Netherlands, 29–42.
Charles J, Bonnefois B (1986), Superduplex stainless steels: properties & weldability, *Proc Duplex Stainless Steels*, The Hague, Netherlands, 1108–1121.
Charles J, Verneau M, Audouard JP, Demars S (1999), Some duplex applications-test results and practical experience, *Proc Stainless Steel World*, The Hague, Netherlands, 473–485.
Cohen LJR, Charles JA, Smith GC (1987), Influence of cathodic hydrogen on microstructure of duplex stainless steels, *Proc Stainless Steels*, York, UK, 363–374.
Comer AJ (2004), Corrosion–fatigue of a superduplex stainless steel weldment, PhD thesis, Dublin City University.
Comer AJ, Looney L (2006a), Crack propagation resistance of Zeron 100 weld metal

fabricated using the GTA and SMA welding processes, *Theoret Appl Fracture Mechs*, **45**,139–147.

Comer AJ, Looney L (2006b), Corrosion and fatigue characteristics of positively polarised Zeron 100 base & weld metal in synthetic seawater, *Int J Fatigue*, **28**, 826–834.

Comer AJ, Looney L (2008), Crack propagation resistance of Zeron 100 GTA and SMA weld metal in synthetic seawater under cathodic overpotential, *Int J Fatigue*, **30**, 3, 444–452.

Coudreuse L, Charles J (2000), Fatigue and corrosion fatigue behaviour of duplex stainless steels, *Proc Duplex Stainless Steels*, Venice, Italy, 629–638.

Dawes MG (1971), Fatigue pre-cracking weldment fracture-mechanics specimens, metal, *Construction Br Welding J* **3**, 2, 61–65.

Deleu E, Dhooge A (1997), Fracture toughness of welded thick walled stainless steels, *Proc Duplex Stainless Steels*, 5th World Conference, Maastricht, Netherlands, 387–394.

Dhooge A, Deleu E (1994), Weldability and fracture behaviour of duplex and superduplex stainless steels, *Proc Duplex Stainless Steels*, Glasgow, Scotland, paper 77.

Doyen R, Niset M (1991), Welding of duplex and superdulex stainless steels, *Proc Duplex Stainless Steels*, Beaune, France, 1043–1051.

Dupoiron F, Verneau M, Audouard JP, Charles J (1994a), Industrial experience of duplex and superduplex stainless steels in the chemical, mineral and petrochemical industries, *Proc Duplex Stainless Steels*, Glasgow, UK, paper 92.

Dupoiron F, Bonnefois B, Verneau M, Charles J (1994b), Superduplex stainless steels for offshore applications: high performance welded joints, *Proc Duplex Stainless Steels*, Glasgow, UK, paper 129.

Fang PJ, Kirkwood D, Power LJ, Baxter CFG (1994), The resistance of superduplex stainless steel to hydrogen cracking, *Proc Duplex Stainless Steels*, Glasgow, UK, paper 51.

Femenia M, Luukkonen P, Pan J, Leygraf C (2000), *Situ* electrochemical STM study of dissolution behaviour of duplex stainless steels in aggressive solutions. *Proc Duplex Stainless Steels*, Venice, Italy, 261–270.

Forth SC, Newman JC, Forman RG (2003), On generating fatigue crack growth thresholds, *Int J Fatigue*, **25**, 9–15.

Francis R (1994), Environmental cracking and embrittlement of duplex stainless steel, *Proc Duplex Stainless Steels*, Glasgow, UK, paper KIV.

Francis R (2001a), Corrosion services manager, Weir Materials, Manchester, UK (private communication).

Francis R (2001b), *Galvanic Corrosion – A Practical Guide for Engineers.* National Association of Corrosion Engineers (NACE) International.

Francis R, Byrne G, Warburton GR (1997), Effects of cathodic protection on duplex stainless steels in seawater, *Corrosion, NACE*, **53**, 3, 234–240.

Fukai Y (1993), *The Metal Hydrogen System*, Springer-Verlag.

Girones A, Llanes L, Anglada M, Mateo A (2005). Influence of artificial seawater on the cyclic response of superduplex stainless steels, *Int J Fatigue*, **27**, 197–201.

Gooch TG (1991), Corrosion resistance of welds in duplex stainless steels, *Proc Duplex Stainless Steels*, Beaune, France, 325–346.

Gough PC, Farrar JCM (1997), Fracture toughness of duplex and superduplex stainless steel welds, *Proc Duplex Stainless Steels*, 5th World Conference, Masstricht, Netherlands, 483–490.

Gunn RN (1994), Comparison of the corrosion and mechanical properties of weldments

in wrought 25%Cr and superduplex stainless steels, *Proc Duplex Stainless Steels*, Glasgow, UK, paper 32.

Gunn RN (1997), *Duplex Stainless Steels, Microstructure, Properties and Applications*, Abington Publishing.

Haynes AG (1986), Some influences of composition on the corrosion resistance of duplex and higher alloyed austenitic steels and alloys, *Proc Duplex Stainless Steels*, The Hague, Netherlands, 415–435.

Hertzman S, Roberts W, Lindenmo M (1986), Microstructure and properties of nitrogen alloyed duplex stainless steels after welding treatments, *Proc Duplex Stainless Steels*, The Hague, Netherlands, 257–267.

Johansson KA (1994), Duplex stainless steels in offshore applications – experiences from projects and operations, *Proc Duplex Stainless Steels*, Glasgow, UK, paper KVII.

Kain R (1997), Crevice corrosion resistance of duplex stainless steels in chloride containing waters, *Proc Duplex Stainless Steels*, 5th World Conference, Maastricht, Netherlands, 627–638.

Karlsson L, Andersson SL, Rigdal S (1997), Welding superduplex stainless steels with Ni-base consumables, *Proc Duplex Stainless Steels*, 5th World Conference, Maastricht, Netherlands, 433–443.

Kivisakk U (1999), SAF 2507 in seawater, 10 years of experience, *Proc Stainless Steel World*, The Hague, Netherlands, 519–528.

Kivisakk UH, Holmquist M (2001), Influence of cathodic protection on hydrogen embrittlement on annealed and cold worked duplex stainless steels, *Proc Corrosion*, NACE, Houston, USA, paper 01019.

Komai K, Minoshima K, Kim G, Irifune K (1990), Corrosion fatigue crack growth characteristics of duplex stainless steel weldment in synthetic seawater, *J Soc Mater Sci, Japan*, **39**, 439, 343–349.

Krishnan KN (1997), Mechanism of corrosion fatigue in super duplex stainless steel in 3.5% NaCl solution, *Int J Fracture*, **88**, 205–213.

Linder J (1994), Corrosion fatigue of duplex and austenitic stainless steels in 3.5% NaCl at 80 °C and room temperature, *Proc Duplex Stainless Steels*, Glasgow, UK, paper 47.

Lippold JC, Varol I, Baeslack WA (1991), Microstructural evolution in duplex stainless steel weldments, *Proc Duplex Stainless Steels*, Beaune, France, 383–391.

Maddox SJ (1991), *Fatigue Strength of Welded Structures*, second ed., Abington Publishing.

Makhlouf K, Sidhom H, Triguia I, Braham C (2003), Corrosion fatigue crack propagation of a duplex stainless steel X6 Cr Ni Mo Cu 25-6 in air and in artificial seawater, *Int J Fatigue*, **25**, 2, 167–179.

Marrow TJ (1991), Fatigue mechanisms in an embrittled duplex stainless steel, PhD thesis, Cambridge.

Marrow TJ, King JE (1994), Microstructural and environmental effects on fatigue crack propagation in duplex stainless steels, *Fatigue Fract Eng Mater Struct*, **17**, 761–71.

Marrow TJ, King JE, Charles JA (1990), Hydrogen effects on fatigue in a duplex stainless steel, *Proc Fatigue 90*, Hawaii, USA.

Misawa T (1989), Effects of cathodic protection potential on corrosion fatigue crack growth for a duplex stainless steel in synthetic sea water, *Corrosion Eng*, **38**, 315–318.

Nassau LV, Meelker H, Hilkes J (1991), Welding duplex and super-duplex stainless steels. A guide for industry, *Proc Duplex Stainless Steels*, Beaune, France, 303–323.

Olive JM, Cweik J, Desjardins D (1999), Quantification of the hydrogen produced during corrosion fatigue crack propagation, *Corrosion Sci*, **41**, 1067–1078.

Olsson COA, Landolt D (2003), Passive films on stainless steels – chemistry structure and growth, *Electrochim Acta* **48**, 1093–1104.

Olsson P, Bauer AD, Eriksson H (1997), Hydrogen embrittlement of duplex grades UNS S32750 and UNS S31803 in connection with cathodic protection in chloride solutions, *Proc Duplex Stainless Steels*, 5th World Conference, Maastricht, Netherlands, 607–618.

Perdriset F, Magnin T, Cassange T, Hoch P, Dupoiron F (1994), Environmental effects on low cycle fatigue behaviour of Z3 CND 2205 duplex stainless steel, *Proc Duplex Stainless Steels*, Glasgow, UK, paper 13.

Perren RA, Suter TA, Uggowitzer PJ, Weber L, Magdowski R, Bohni H, Speidel MO (2001), Corrosion resistance of superduplex stainless steels in chloride ion containing environments: investigation by means of a new microelectrochemical method I. Precipitation free states, *Corrosion Sci* **43**, 707–726.

Roberge PR (1999), *Handbook of Corrosion Engineering*, McGraw Hill.

Rouault P, Bonnet C (1997), Make the duplex and superduplex welding easier through metallurgical and practical simple recommendations!, *Proc Duplex Stainless Steels*, 5th World Conference, Maastricht, Netherlands, 297–304.

Scully JR (1995), Electrochemical, in Baboian R, *Corrosion Tests and Standards, Application and Interpretation*, ASM Handbook.

Stevenson AW, Gough PG, Farrar JCM (1986), The weldability of superduplex alloys – welding consumable and procedure development for zeron 100, *Proc Duplex Stainless Steels*, The Hague, Netherlands, 290–306.

Suresh S (1998), *Fatigue of Materials*, second ed., Cambridge University Press.

Tavara SA, Chapetti MD, Otegui JL, Manfredi C (2001), Influence of nickel on the susceptibility to corrosion fatigue of duplex stainless steel welds, *Int J Fatigue*, **23**, 619–626.

Wahlburg G, Dunlop GL (1986), Nitrogen strengthening of duplex stainless steels, *Proc Stainless Steels*, The Hague, Netherlands, 291–295.

Weber L, Uggowitzer PJ (1998), Partitioning of chromium and molybdenum in super duplex stainless steels with respect to nitrogen and nickel content, *Mater Sci Eng*, **A242**, 222–229.

Wessman SM, Pettersson RFA (2000), Hydrogen cracking of cathodically polarised duplex stainless steels and weld metals, *Proc Duplex Stainless Steels*, Venice, Italy, 279–287

Wiesner CS (1997), Toughness requirements for duplex and superduplex stainless steels, *Proc. Duplex Stainless Steels*, 5th World Conference, Maastricht, Netherlands, 979–990.

WMF (2004a), Zeron 100 technical information, Weir Materials & Foundries, Manchester, UK, www.weirmaterials.co.uk

WMF (2004b), Zeron 100 welding guidelines, Weir Materials & Foundries, Manchester, UK, www.weirmaterials.co.uk

Woolin P, Murphy W (2001), Hydrogen embrittlement stress corrosion cracking of superduplex stainless steel, *Proc Corrosion*, NACE, Houston, USA, paper 01018.

Woolin P, Maddox S, Baxter D (2006), Corrosion fatigue of welded stainless steels for deepwater riser applications, *Welding and Cutting*, **5**, 4, 204–209.

10

Weld metal cracking in cellulosic girth welds of pipelines

D D U N N E, University of Wollongong, Australia and
D N O L A N, BlueScopeSteel, Australia

Abstract: Cellulosic welding consumables are widely used for shielded metal arc (manual) welding of pipeline steels. The hydrogen present in the plasma promotes a forceful arc that results in deep penetration and allows one-sided girth welding. However, the high hydrogen environment enhances the potential for development of the weld defects: hollow bead, solidification cracking and cold cracking. This chapter examines the effect of welding conditions on formation of these defects with the aim of elucidating operative mechanisms and defining strategies to minimise or eliminate their occurrence. Special attention is paid to the role of hydrogen in the generation of these weld metal defects.

Key words: pipeline girth welding, cellulosic manual welding, hollow bead defect, solidification cracking, hydrogen-assisted cold cracking.

10.1 Introduction

Shielded metal arc welding (SMAW) with cellulosic electrodes is a widely used manual welding process for steel because of its favourable operating characteristics. The forceful arc provides deep penetration and allows tolerance to variable fit-up. However, the good handling characteristics are achieved largely because of the generation of copious volumes of hydrogen in the arc plasma by decomposition of the electrode coating.

SMAW has become a core process for field girth welding of oil and gas pipelines, at least for thin walled, small diameter pipeline steels with strengths equivalent to, or less than, X80 (550 MPa minimum yield stress). Lincoln engineers have identified the formation of a 'small keyhole' during cellulosic root pass welding of pipeline steels as a requirement for effective penetration of the weld root (Lincoln Electric, 1993). The keyhole welding phenomenon is treated in Section 10.2 and is also discussed in Section 10.3 on cellulosic welding and in Section 10.5.1, in relation to the formation of the peculiar root pass 'hollow bead' defect observed in pipeline girth welds.

Besides modification of the arc plasma, a significant amount of hydrogen dissolves in the molten steel. The equilibrium concentration at the melting point and 1 atmosphere pressure is 25 ppm hydrogen, but superheating above the melting point and the higher than atmospheric pressure of the plasma should ensure a much higher concentration of solute hydrogen during welding.

In the cooling and solidification phase of the welding process, hydrogen will be lost by effusion into the atmosphere and re-distributed by diffusion. The low solubility of hydrogen in delta-ferrite (δ-ferrite or δ) will result in its rejection of, and concentration in, the remaining liquid, thus increasing the danger of gas porosity and liquid metal rupture due to the 'negative pressure' created in the liquid by dissolved gas and by thermal contraction (Cross, 2005). The contribution of hydrogen to solidification cracking, together with other weld processing factors, is addressed in Section 10.6.

At low temperatures, <150 °C, excess hydrogen present in the weld bead and the heat-affected zone (HAZ) can lead to the extensively researched phenomenon of hydrogen-assisted cold cracking (HACC). The high potential for this type of defect arises directly from the use of cellulosic electrodes. HACC in cellulosic welds of pipeline steels is discussed in detail in Section 10.7.

Since hydrogen can simultaneously be hero and villain in root pass girth welding, the challenge is to take advantage of its benefits while suppressing its capacity to produce dangerous defects.

10.2 Keyhole welding

Certain welding processes and processing conditions that are characterised by a high energy beam (HEB), or a constricted arc, can produce a 'keyhole' in the molten weld bead. Electron beam welding (EBW) and laser beam welding (LBW) are examples of high energy beam welding processes (10^{10}–10^{13} W/m^2) in which the high energy beam can produce a deep crater in the liquid puddle. The crater or keyhole is a result of the beam pressure (P_b) and the vapour (P_v) and recoil (P_r) pressures arising from vaporisation of the melt. The balance of these pressures against opposing pressures due to gravity (liquid head, ρgh) and surface tension determines the depth of the keyhole (Quigley, 1986).

Keyholes can also form in lower energy density processes (10^8–10^{10} W/m^2), such as high current gas tungsten arc welding (GTAW) and plasma arc welding (PAW). Although vaporisation is less significant in these cases, the momentum of the electrons and/or gas atoms in the arc plasma is sufficiently high to generate a keyhole in the molten weld pool. It is generally accepted that the 'drilling' of a hole or surface crater in the liquid results from the interaction of the high energy plasma column with the molten puddle. Nevertheless, Eagar and Lin (1984) have proposed that, at least for high current GTAW, plasma jet momentum may not be the main factor causing the formation of the keyhole. They claim that convective flow, driven by electromagnetic force in the transition current range, together with surface tension, is responsible for rapid circumferential flow and vortex formation in the weld pool. Although it is possible that the mechanism can differ for

different welding processes, the end result is the same: the formation of a deep, narrow surface crater or keyhole in the liquid immediately below the arc or the beam source.

The major advantage of keyhole welding is deep penetration and the formation of a narrow weld bead. The keyhole is, of course, both a dynamic and a transient phenomenon – as the keyhole moves, molten metal at its front and sides flows to its rear to back-fill space, maintaining a steady state surface contour which, in cross-section, is slightly elongated in the direction opposite to keyhole motion (Quigley, 1986). However, steady state conditions are likely to be difficult to maintain because of variations in the welding control variables that affect the keyhole size and shape and the thermo-physical properties of the melt. One serious ramification of this instability is that porosity can occur when the rate of solidification of the weld bead exceeds the rate at which liquid metal can back-fill the void associated with the moving keyhole (Zhou and Tsai, 2007).

It is well established that the addition of hydrogen to the plasma generating gas used in constricted arc PAW promotes keyhole formation. The arc energy can drive endothermic dissociation of hydrogen molecules into atomic and ionic forms that re-combine at the metal surface to release significant enthalpy, thereby increasing the melting efficiency (Suban *et al*., 2001). Further, hydrogen has a very high thermal conductivity and acts to constrict and concentrate the arc, producing deeper penetration. It is therefore possible, under appropriate processing conditions, for a keyhole welding mode to develop during cellulosic SMAW of steel, because of the copious volume of hydrogen formed by decomposition of the electrode coating. The formation of a 'small keyhole' during cellulosic root pass welding of pipeline steels has, in fact, been identified as a requirement for effective penetration of the weld root (Lincoln Electric, 1993).

Cellulosic SMAW is treated in more detail in Section 10.3 and its role in the development of weld metal defects is covered in Sections 10.5 to 10.7.

10.3 Cellulosic welding

Cellulosic electrodes typically contain about 25 wt% cellulose ($C_6H_{10}O_5$) in the form of purified wood pulp which volatilises and combusts in the arc to produce carbon dioxide, carbon monoxide, hydrogen and water vapour. According to Linnert (1994) a typical covering for a cellulosic EXX10 electrode consists of 21 wt% cellulose (gas former); 10 wt% titania (slag former and arc stabiliser); 13 wt% asbestos (hydrated magnesium silicate, binder and slag former); 1.5 wt% ferrosilicon and 3.5 wt% ferromanganese (alloying elements and de-oxidisers); and 51 wt% waterglass (sodium silicate, binder). After drying, the dominant oxides are SiO_2 (47 wt%) and TiO_2 (10 wt%).

Volatile matter and moisture constitute 29 wt% and provide gases for shielding the weld pool and modifying the arc plasma.

Despite the potential for substantial hydrogen pick-up in the weld metal, cellulosic electrodes are highly favoured for the manual SMAW process because of the forceful arc, the deep penetration and the spray deposition of the weld metal (Linnert, 1994). A particular advantage cited by the pipeline industry is that the deep penetration achieved in the root pass allows one-sided girth welding. The cellulosic SMAW process is also favoured because of its outstanding capacity to accommodate poor pipe fit-up and changing terrain during pipe welding (Nicholson, 2003). Although vertical-down DC welding is employed, the recommended polarity can be electrode negative, DCEN (e.g. Thyssen Bohler) or electrode positive, DCEP (e.g. Lincoln, ESAB, Hobart, Cigweld). The latter polarity typically produces deeper penetration, but a lower electrode melting rate than DCEN (*ASM Metals Handbook*, 1984). In either case a power source with a drooping voltage–current characteristic is used so that the current increases with decreasing arc length. Operating currents are normally in the range 50–210 A, depending on the electrode diameter, and welding is performed vertically down, This so-called 'stovepipe' technique requires specialised welding skills and one important practice is to 'bury the arc' by forcing the electrode into the groove, shortening the arc length and increasing the current. This technique increases the melt temperature and allows root penetration through keyhole formation.

All electrode manufacturers are conscious of the potential dangers of high weldment hydrogen contents and recommend preheats of up to about 180 °C prior to root pass welding of thicker wall (>10 mm) and higher strength pipes (X80 and above). In addition, it is recommended that the delay time before hot pass welding is sufficiently short to slow the cooling rate and allow significant hydrogen effusion from the weldment. The maximum delay time specified by Lincoln Electric (1993) is 5 min, whereas Bohler recommend hot pass welding as soon as possible after root pass completion and at least within 10 min. The precise welding conditions need to be decided on a case by case basis.

Electrode manufacturers also recommend completion of the root pass before lifting of the pipe to enable set up of the next pipe length (see Fig. 10.1). This procedure is designed to minimise the potential for cracking in the hot stringer bead region due to mechanical (bending) stress. Nevertheless, since the productivity of pipeline construction is dependent on the elapsed time between lifts, there is a trend to lift before completion of the root pass (see Section 10.4).

10.4 Pipeline construction

This contribution draws heavily on experience and research related to Australian oil and gas pipeline manufacture, which is dominated by relatively small

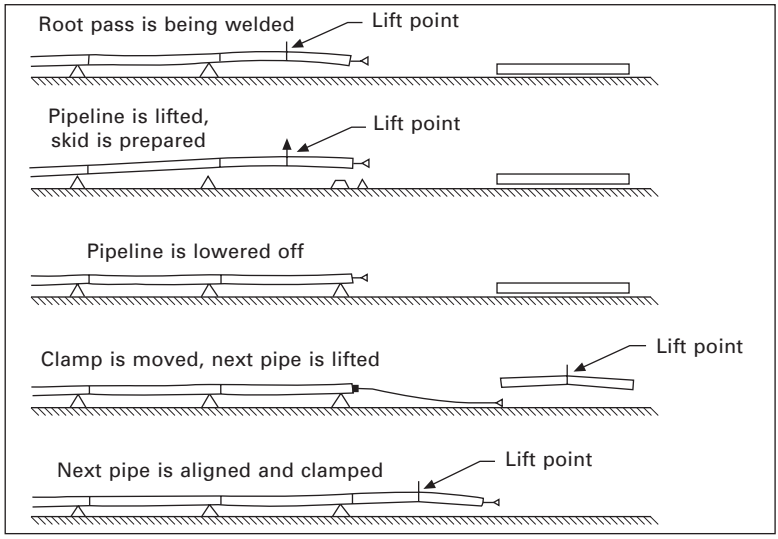

10.1 Sequence of operations during pipeline construction (after Smart and Bilston, 1995).

diameter, thin-walled pipelines. Nevertheless, the procedures that have evolved are in accord with best international practice and the principles underlying the occurrence and control of defects have universal relevance.

The historical, strong preference in Australia for cellulosic SMAW for field girth welding of oil and gas pipelines, is based on established cost and productivity advantages. Although HACC is a potential problem because of the high hydrogen content of cellulosic weld metal, the weld fabrication techniques used for typical thin walled, small diameter, long distance pipelines have, at least up to X70 grade, minimised the risk of hydrogen cold cracking even in the absence of preheat.

Current Australian practice for land-based pipeline constructions, illustrated schematically in Fig. 10.1, involves lifting and lowering on to a supporting skid after 50–70% completion of the root pass. This lifting action imposes tensile stresses/strains at the bottom-dead-centre (6 o'clock position) of the root weld. As welding of this joint is continuing, a new pipe length is lifted into place and aligned with the free end of the previous pipe length using an internal clamp. When the pipes are properly aligned and wedges are in place to set the root gap, welding of the next root pass is commenced. Welding of the root pass is usually undertaken by two welders; one starting at about the 11 o'clock position and welding through the top-dead-centre (12 o'clock position) to approximately 2 o'clock and the other welder beginning at about 8 o'clock and welding through the bottom-dead-centre (6 o'clock position) to 5, as illustrated in Fig. 10.2. Early clamp release and lifting after 50–70% completion of the root pass substantially increases productivity.

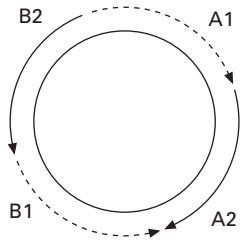

10.2 A typical welding sequence for root pass pipeline girth welds. Welders A and B weld sections A1 and B1 concurrently. The pipe is then lifted and lowered during preparation pf the next pipe joint and the welders then complete the root pass by welding sections A2 and B2 (after Smart and Bilston, 1995).

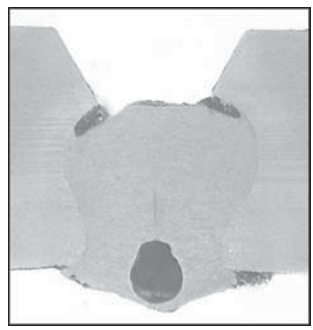

10.3 Macrograph of cross-section of cellulosic root pass weld in 8.9 mm thick X80 pipe, showing hollow bead defect in the root reinforcement region. Undercut of the base steel has occurred on each side of the weld face and centreline solidification cracking is present above the hollow bead defect.

The face of the completed root pass weld normally has a central convex profile with 'shoulder' regions on each side (see Fig. 10.3). Slag usually deposits on these two shoulders, resulting in slag stringers that are described as 'wagon tracks'. Grinding of the root pass is recommended to eliminate the central hump and expose the slag tracks so that they can be floated off during the hot pass. This procedure prevents slag entrapment, re-melts part of the root bead, eliminates undercut and extends the cooling time.

10.5 Hollow bead defect

10.5.1 Characteristics

Hollow bead (HB) defect occurs in the root pass of pipeline girth welds and takes the form of an elongated void aligned in the direction of welding. The pore is in the shape of a channel or tunnel, typically with a circular cross-

section and located in the weld centreline. Hollow bead defect is usually limited in length and forms sporadically around the circumference of the weld. It is most frequently found at the bottom of the weld bead, often in the reinforcement region, with only a thin layer of solidified weld metal at its base (Fig. 10.3). Sometimes a fissure extends through this layer, connecting the defect to the external environment. Although confined to the weld bead centreline the defect can also be located near the top face, near the centre of the bead and, occasionally, at both the top and bottom surfaces of the bead simultaneously (Cantin and Bee, 1994; Nolan *et al*., 2003). An extensive microstructural study by Cantin and Bee (1995) revealed that the internal surfaces of hollow bead defects can be largely covered by a thin oxide layer and can include larger oxide inclusions containing Si, Fe, Ti and Mn. In clear regions of the inner surface, topographical features consistent with cellular-dendritic structure were observed.

10.5.2 Effect of processing conditions

Hollow bead defect is not unique to cellulosic SMAW stovepipe welding of steel pipelines. According to Wright (1993), it has been encountered in SMAW vertical-down welding of steel plate components in the shipbuilding and fabrication industries. Moreover, similar elongated pores have been observed for EBW, LBW and high current GTAW welding, and have been related to keyhole formation. In the case of SMAW the common processing condition appears to be vertical-down welding using cellulosic electrodes. Although these factors may be necessary, they are not sufficient, as hollow bead is a relatively infrequent defect. A widely held view is that HB is operator-induced and depends on the welding procedures and practices of the welder (Barkow, 1973). In particular, welding too fast is commonly implicated and Barkow concluded that, because of reduced heat input (HI) at a fast welding speed, there is insufficient molten metal to fill the root, resulting in the formation of linear porosity. However, a welder operating at higher speed is likely to increase the welding current to maintain the heat input and to increase the rate of electrode melting in order to produce a continuous root bead with satisfactory penetration. Nevertheless, HB defect is still observed, and is more pronounced, for high speed, high current welding.

Cantin and Bee (1995) have conducted systematic experiments on the effect of speed, current and heat input on the incidence of HB defect, using automatic stick welding of 8.3 mm X70 plate. 4 mm diameter Lincoln 5P+ electrodes were used. The plate was set vertically and butt welded under force control with a vee preparation conforming to AS 2885 or API 1104 (30° bevel angle, 1.6 mm root face and 1.6 mm root gap). The electrode was set at a trailing angle of 15° and the work carriage containing the test plates was driven upwards at constant speed past the fixed electrode and its feed

system to simulate vertical-down welding. A 170 mm long weld run was produced for each set of welding conditions.

The test results showed that the incidence of hollow bead increased substantially on increasing the welding current from 120 to 240 A at a constant welding speed selected from the range, 250–600 mm/min. For an approximately constant voltage, an increase in current at a given speed results in an increase in HI and therefore, %HB increases with increasing HI, contrary to the hypothesis by Barkow. Further, Cantin and Bee demonstrated, by welding tests at a constant HI in the range 0.4–0.7 kJ/mm, that %HB increased with increasing speed and, therefore, with increasing current. For higher heat inputs of 0.9 and 1.1 kJ/mm the incidence of hollow bead peaked and then decreased marginally with increasing speed (or current). This trend reversal occurred with increasing welding speed over the relatively low range of 250–450 mm/min., accompanied by an increasing current, which was in the relatively high range (>200 A).

It has been shown that the volume and shape of the molten pool can vary substantially at a constant nominal heat input, depending on the values of the control variables. For example, Ahmed and Jarvis (1998) showed that for bead-on-plate submerged arc welding (SAW) at a constant heat input, the weld bead volume and penetration increased significantly with increasing welding speed (and current). Therefore, despite a nominally constant heat input, the effective heat input can increase with increasing welding speed. In relation to the observation of Cantin and Bee that %HB can decrease with increasing speed at high heat input, it is plausible that an increase in bead volume allows more effective back-filling of pores, reducing the incidence of HB. For lower heat inputs, they observed that %HB increased continuously with increasing speed or current over the range examined. It is likely that for these conditions, the bead volume and the bead volume increase are too small to counteract the increasing trend in %HB with increasing welding speed/current. Mechanistic models for this trend are presented and discussed in Section 10.5.3.

The effect of base metal composition on HB is controversial and has not been the subject of detailed and systematic study. Barkow suggested that hollow bead defect might be promoted in higher Si, fully killed pipeline steels because of increased weld pool fluidity and welder compensation by increasing the welding speed. In addition, reports by consumable manufacturers in the 1970s suggested that base steel Si contents higher than 0.1 wt% can promote HB defect. However, the base plate composition is not likely to be a significant factor per se since root pass dilution is typically about 50% and therefore the composition of the diluted weld metal should be considered. Recent work by Nolan *et al*. (2003) showed that %HB in root pass pipeline welds was not sensitive to variations in Si content from 0.14 to 0.28 wt% in the diluted weld metal for a base steel with 0.27%Si. Further, other reports

indicate HB-free root pass welding of 'high' Si pipeline steels with up to 0.4 wt%Si (Hart, 1969). Therefore, this factor should be discounted.

An aluminium content higher than 0.04% has been identified by Bohler as promoting HB defect. However, this level is much higher than that typical of a range of diluted weld metals produced with X80 pipe using commercial cellulosic E6010 and E9010 electrodes (Nolan *et al.*, 2003). In this case, the maximum Al content of the welds was 0.01 wt%, yet HB defect was detected and, furthermore, there was no correlation with Al content.

Oxygen and sulphur are known to reduce the surface tension of molten steel and promote radially inward flow (the Marangoni effect) and deeper weld penetration. Therefore, the rationale behind the maximum Al and Si limits might be avoidance of excessive deoxidation of the melt. In a similar way, the claim that very low S steels promote HB defect may be based on the occurrence of a reversed melt flow pattern as a result of higher surface tension and, consequently, less effective back-filling of pores. This type of radially outward flow (with a negative temperature coefficient of surface tension) is claimed to occur for S < 30 ppm (0.003 wt%), whereas the more favourable, radially inward convection (with a positive temperature coefficient) occurs for S > 0.006 wt% (Mills *et al.*, 1998). Typically, the S levels of diluted cellulosic root pass welds are higher than 0.003 wt%.

The work by Nolan *et al.* (2003) was concerned primarily with solidification cracking in the root pass weld bead, but HB was also observed. The test welds were made using DCEP on short pieces ('pups') of X80 pipe, 406 mm in diameter and 8.9 mm thick. The ends were bevelled to produce the AS 2885 standard pipeline preparation defined above. Two pups were tack-welded together at four equidistant points around the circumference leaving a 1.6 mm gap. The welder held the electrode at the 2 o'clock position, approximately normal to the pipe surface while the pipe was rotated at a constant speed. Again, this procedure was used to simulate vertical-down welding, but without a trailing angle. Each welding test consisted of a quadrant of the 406 mm diameter pipe (~ 315 mm). E6010 and E9010 electrodes (4 mm diameter) were used from five different manufacturers. The ranges of heat input and welding current were: 0.44–0.70 kJ/mm and 135–200 A. Two welding speeds (300 and 500 mm/min) were used. The results confirmed those of Barkow (1973) and Cantin and Bee (1995): %HB was higher for a higher current and welding speed.

Partly because of the normalising effect of the base plate composition on the weld bead, the compositions of the root pass weld beads were very similar for the E6010 electrodes sourced from four different manufacturers. The E9010 weld bead compositions varied slightly more because of the different alloying strategies used to achieve the higher strength level. In one case, Mo was used as the main strengthening agent (~0.40%Mo), whereas two other manufacturers relied on increased V content (~0.03%V). This

difference apart, the remaining elemental compositions of the diluted weld metals were again surprisingly similar.

The E6010 consumables showed a slightly higher propensity for HB defect than the E9010 electrodes. Moreover, there was a slightly different susceptibility to HB defect for the E6010 electrodes obtained from four different manufacturers (identified as A to D in Fig. 10.4). Since the differences in composition were minor and no systematic trends were apparent that could explain the observed variations in %HB, the differences are likely to be associated with aspects of the coating formulations that are not reflected in the weld bead composition. Moisture content and the nature and quantity of shielding gas generated, particularly the hydrogen content, are the most obvious factors.

Overall, for the composition ranges typical of diluted root pass weld metal for up to X80 pipeline steel, composition appears to have little effect on HB formation and is certainly insignificant compared with the effect of welding speed and current.

10.5.3 Mechanisms

The investigations discussed above indicate that high weld travel speed and high current are the main causative factors of HB. These variables cannot be varied independently without changing the heat input; and to maintain heat

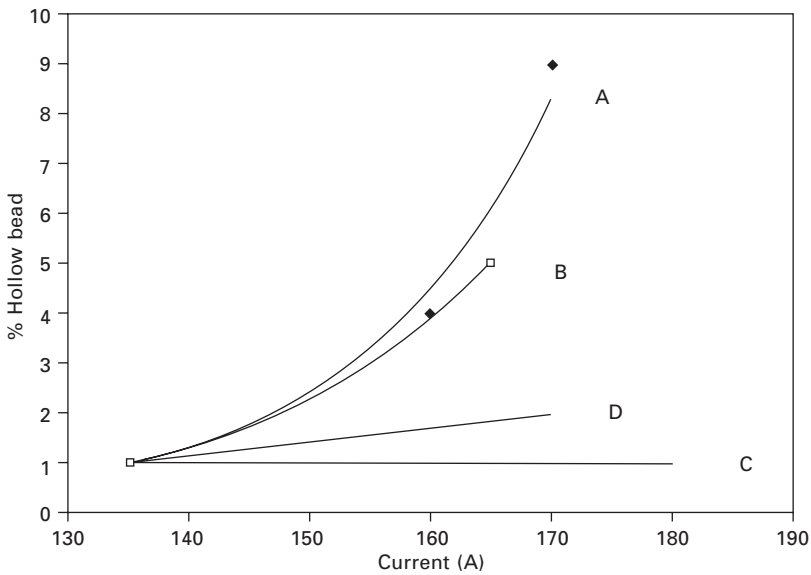

10.4 Effect of welding current on incidence of hollow bead for four different E6010 welding electrodes.

input within the recommended range an increase in speed requires an increase in current. In general therefore, operating at high welding speed is associated with a high current, which, combined with copious hydrogen in the arc plasma, produces a forceful arc and keyhole formation in the molten weld pool. It is proposed that the main factors for HB porosity are keyhole formation, a high content of dissolved gases in the weld pool and fast freezing that prevents back-filling of pores. The last factor is promoted by a high welding speed which produces an elongated ('tear-drop') shaped weld pool and rapid dissipation of thermal energy.

Cantin and Bee (1995) used optical and scanning electron microscopies to study the morphology of hollow bead defects sectioned both parallel to the surface and transversely in the welding direction. The defects were typically 1–15 mm long and 1–2 mm in diameter. In general, the HB defect showed an initiating bubble-like 'cusp', an increase in bead diameter with length and a deposit of Ti–Si rich slag at the terminating end. Although slag was also scattered along the walls of the cavity, the relatively smooth nature of the internal surfaces of HB defects indicates that the voids were gas-filled, serving as reservoirs for bubbles of gas liberated from the molten pool.

Since the slag deposit at the terminating end of the hollow bead was commonly found to be perforated by bubble-shaped pores, Cantin and Bee (1994) proposed that an initiating gas bubble is formed in the melt by slag out-gassing. This slag particle continues to out-gas as it is pushed forward by the solidification front, resulting in an extended pore that terminates when gas evolution ceases. Cantin and Bee (1995) rationalised this mechanism with the strong effect of welding current on HB by pointing out that melt pool temperature and volume will increase with increasing welding current, resulting in increased gas absorption. Further, flux drying will be promoted, resulting in less effective shielding and increased entrainment of atmospheric gases. This last proposition is consistent with evidence that the total length of HB increases as the flux moisture content decreases. However, such a mechanism would be expected to apply more universally to the SMAW process and the pores should be more randomly located instead of predominantly in the root reinforcement region at the weld centreline. Furthermore, it does not account for the strong association of HB with the specific process of vertical-down cellulosic welding of pipeline root passes.

In cellulosic root pass welding, the shielding gas atmosphere, including the keyhole would be expected to contain a complex mixture of gas molecules, atoms and ions based on hydrogen, oxygen, nitrogen, CO and CO_2. As little as 250–300 ppm of nitrogen from entrained air can cause weld metal porosity (Bailey, 1994). In addition, the presence of a keyhole and rapid fluid circulation in the weld pool would be expected to facilitate entrainment and dissolution of these and other gases from the plasma column. Absorbed nitrogen is likely to be more significant with decreasing flux moisture content and 'poor

electrode handling characteristics', because of less effective shielding and increased entrainment of air. Moreover, there is ample evidence that nitrogen and hydrogen are the main contributors to elongated pores in GMAW and GTAW processes. For example, Lancaster (1999) reported that tunnel pores (also called wormholes) can occur because of nitrogen absorption in GMAW of ferritic and stainless steels and Willgoss (1980) observed tunnel pores in GTAW of 316 stainless steel as a result of weld metal hydrogen and a low surface area/volume ratio of the weld bead, which limits hydrogen effusion. The last point is relevant to the American Petroleum Institute (API) joint configuration for root pass pipeline girth welding which involves a 60° included angle, a narrow root gap and a significant land. Any narrowing of the gap during field welding is likely to encourage the welder to increase the welding current and arc force to obtain root penetration, thus increasing the keyhole depth, the melt temperature and weld pool gas absorption.

The tunnel pore defects discussed above can follow the solidification pattern or nucleate near the centre of the weld bead and extend along its axis (Lancaster, 1999). The distribution of the similar hollow bead defect in cellulosic welds is somewhat different, with the pore normally being located in, or close to, the reinforcement region of the weld root. A feasible model consistent with this characteristic is as follows. For cellulosic vertical-down welding, especially at the recommended 15° trailing angle, upward deflection of the plasma column could occur as shown schematically in Fig. 10.5,

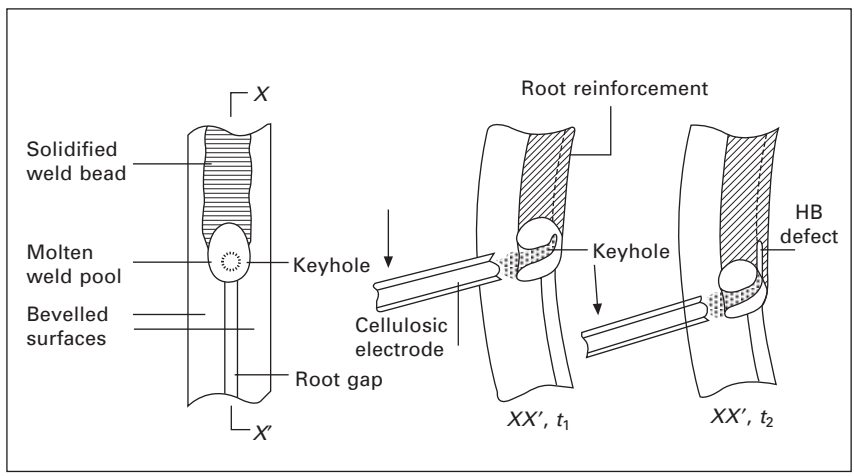

10.5 Schematic diagrams showing (from left to right) a plan view of the weld bead surface and cross-sections at times t_1 and t_2 (where $t_2 > t_1$) during vertical-down welding with a 10–15° trailing angle. The presence of a keyhole is depicted, together with the development of an elongated pore by keyhole deflection and filling with gas bubbles evolved from the weld pool.

introducing a cavity ('cusp') that is kept open by gas pressure from both the plasma and dissolved gases effusing from the molten weld pool. In terms of this model, freezing occurs around the gas pressurised cavity rather than back-filling with liquid, leaving an elongated pore in the wake of the moving keyhole. In principle, variations in the depth of the keyhole or perturbations in its surface shape could lead to pore development at other positions along the weld centreline. However, the most frequently observed location is near the weld root, presumably in association with the presence of a relatively deep keyhole, which is the weld pool condition favoured to ensure full penetration of the joint.

This model assigns a major role to hydrogen, because it constricts the arc and promotes keyhole formation, particularly under DCEP conditions. With the workpiece electronegative, hydrogen ions produced by dissociation in the plasma will be accelerated to the weld pool, where they can recombine, with release of considerable exothermic energy: 422 kJ/mole (Suban *et al*., 2001). Thus high temperatures are generated at the weld pool surface, vaporising elements from the pool and producing vapour and recoil pressures that contribute to the depth and shape of the keyhole. Furthermore, the absorption of hydrogen into the weld metal as ions, atoms or in molecular form results in a supersaturated melt that will reject hydrogen with falling temperature, as gas bubbles that rise to external surfaces or fill internal gas pockets. Hydrogen will also be rejected into the liquid phase from the delta-ferrite that forms as solidification begins and progresses. Other dissolved gases, such as nitrogen, are expected to act in the same way.

Cantin and Bee (1995) discounted a contribution by hydrogen to the development of HB because the presence of oxide on the internal surfaces of the pores reflects oxidising rather than reducing conditions. However, the gaseous atmosphere of the pores is likely to be complex and even in the presence of hydrogen the net result could still be an oxidising environment because of the presence of CO_2, H_2O and O_2. Entrained nitrogen is also to be expected. Moreover, any exposure of the pore to the external environment, while the weld is still hot, will result in rapid dissipation of hydrogen, ingress of air and oxidation of the surface. As most HB defects lie in the reinforcement region, only a thin membrane separates the pore from the ambient environment and any channel or crack, such as a solidification crack or hot tear, connecting the pore to the external surface will allow oxidation of the internal surfaces of the pore. The thin uniform cover of oxide reported by Cantin and Bee could arise in this way. In relation to the observation of slag on the surface of the terminating end of the pore, de-oxidation of the melt, particularly by Ti and Si, will produce oxide slag particles that circulate through the melt within convection currents. These particles eventually rise to and deposit at free surfaces of the weld bead. The pore interface also constitutes a free surface and it is conceivable that slag particles could collect in the end pocket.

10.5.4 Prevention

The presence of HB in the upper centreline region is not detrimental to pipeline girth welding, as the combination of root grinding to expose slag entrapped in the wagon tracks and re-melting of part of the root run in the hot pass will normally eliminate any HB porosity. HB in the root region, including the reinforcement, is more problematic and, if detected by radiography, it usually requires repair welding of the affected region.

Preventative measures are therefore called for to avoid HB formation and the expense of repair welding. Since HB is sensitive to welding speed and current, lower speeds and currents within the recommended ranges would be expected to reduce the depth of the keyhole and reduce the melt cooling rate. Back-filling of pores generated by keyholing should thereby be promoted. Cantin and Bee (1995), for example, did not observe HB for welding currents ≤130 A for a welding speed of 600 mm/min; even higher currents, up to 140 A, produced HB-free welds at lower welding speeds. However, welding at too low a current could promote fast freezing because of a low weld metal volume and a 'cold' weld metal. These effects will militate against gas evolution and back-filling of pores and increase the probability of significant, non-HB types of porosity.

Welding with a lower current would be expected to decrease keyhole depth and could even eliminate keyhole formation. The potential consequence of incomplete root penetration at lower current can be countered by a wider root gap and the use of DCEN welding to allow root penetration without substantial keyhole formation. This latter strategy is recommended by Lincoln Electric (1993) in the event of persistent HB formation using DCEP welding. The wider, shallower weld pool facilitates discharge of gas bubbles from the melt surface and the higher electrode melting rate delivers a higher mass of weld metal per unit time. However, this strategy requires a significant change in welding technique, resulting in reduced welding speed and process productivity. There is a clear industry preference for DCEP; and, provided welding is carried out within the specified limits, HB is not normally a significant problem.

10.6 Solidification cracking

10.6.1 Characteristics

Solidification cracking (SC) is a common, but complex, weld metal hot cracking phenomenon, which has defied the development of a robust unifying theory because of the multiplicity of influential compositional and processing factors. SC usually occurs in the weld centreline, but it can also be intercolumnar, at a large angle to the centreline – and is described as 'flare' or 'dove-wing' cracking. In both cases, the cracks are typically wide and

'blunt-ended' and often do not break the surface. SC is common in the weld crater formed at the end of a run, because of solidification shrinkage and the absence of a reservoir of molten metal to feed the weld bead. In this case the crack is surface-breaking.

Another typical characteristic is a fracture surface which, at least in part, consists of a relief solidification pattern of cells or cellular-dendrites. This morphology confirms that cracking involves rupture of a liquid film and subsequent solidification of the liquid walls of the cavity. In addition to solidification cracking, hot (solid state) cracking may also occur at high temperatures below the solidus by tearing or extension of existing SC. This type of fracture depends on the hot ductility of the solidified weld metal and the presence of tensile stress and a localised stress concentration that exceeds the hot fracture strength of the weld metal.

Solidification cracking occurs most commonly in the weld centreline, where solidification fronts from either side of the weld preparation meet in the final stages of weld metal solidification. Partitioning of elements to the remaining liquid can result in a lowered freezing point (widening the solidification temperature range). As the weld metal cools and solid bridges begin to form, contraction strains develop in the liquid and solid phases, leading to the potential for rupture of liquid films. A schematic illustration of this general mechanism for solidification cracking (Baker, 1975) is shown in Fig. 10.6(a), while Fig. 10.6(b) is an example of centreline cracking in an actual root pass pipeline weld (Ohshita *et al*., 1983). In the case of centreline cracking, shrinkage strains occur during cooling in a direction normal to the solidification fronts. In general, SC will develop if the tensile stress arising from shrinkage exceeds the fracture strength of the semi-solid weld bead at any temperature in the solidification range. The tensile ductility of the semi-solid weld bead is limited because, in the absence of adequate liquid feeding, the liquid films can rupture at relatively low strains.

More detailed treatment of mechanisms proposed for SC is presented in Section 10.6.3, but the fundamental causes of this phenomenon are the development of a coarse weld metal microstructure and/or an adverse weld bead shape; segregation of elements that extend the freezing range and/or adverse freezing conditions; and generation of high strain across the weld bead due to thermal contraction and phase change. These factors will obviously be influenced by the welding conditions.

10.6.2 Effect of processing conditions

There are numerous welding process variables that control the bead shape and the weld metal composition and microstructure, and therefore exert an influence on the susceptibility to SC. The welding conditions include the specific welding process; base metal; joint type and preparation; restraint

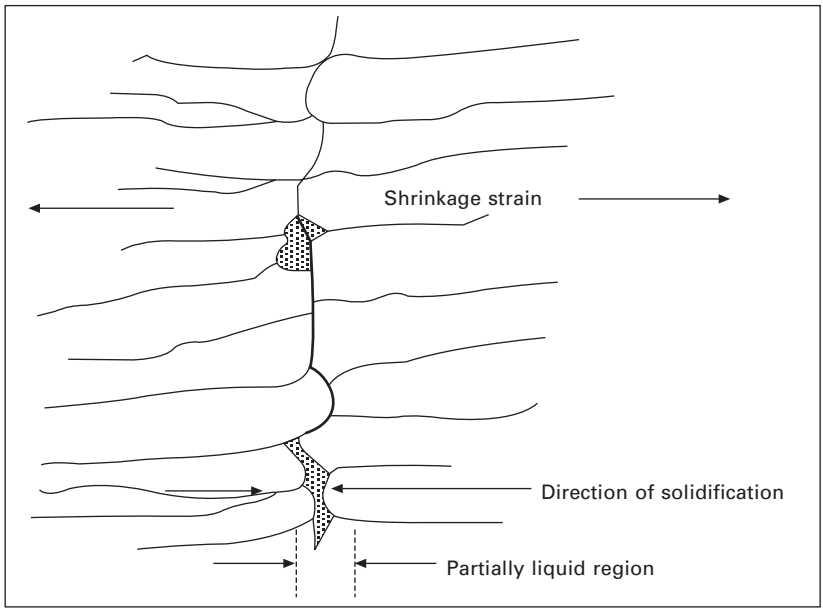

(a)

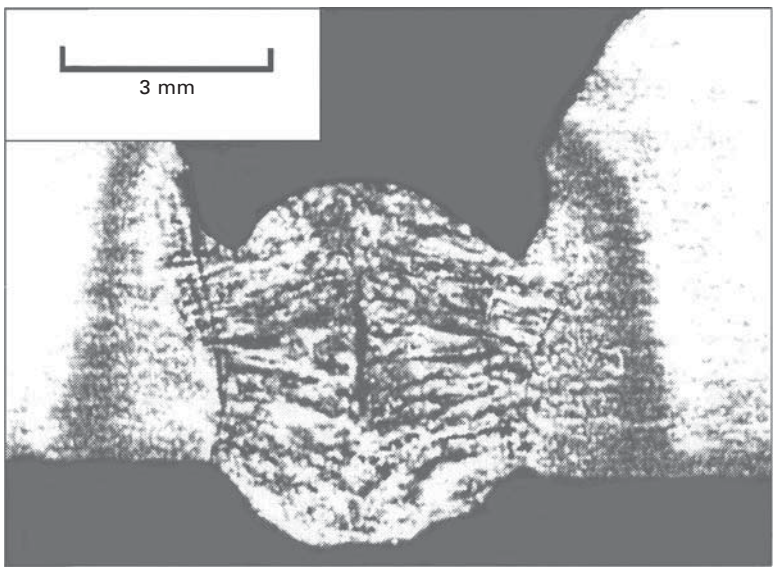

(b)

10.6 (a) Schematic diagram illustrating the conditions leading to solidification cracking (after Baker, 1975) and (b) an example of centreline solidification cracking in a cellulosic root pass weld bead (Ohshita *et al.,* 1983).

conditions; consumable type; welding position; pre-, interpass- and post-weld heating; operating voltage; welding current; and travel speed. The influence of welding process variables on SC is covered in detail in reviews by Bailey (1994) and Cross (2005) and only a brief summary is presented below.

For a given process and type of weld, the most important variables are the operating voltage, current and travel speed, which together determine the weld heat input. The heat input dominates in determining the total weld thermal cycle, including the cooling rate experienced by the solidifying weld bead and the accompanying evolution of the microstructural and stress states. The welding conditions also determine the weld metal composition and bead shape and volume, which are important factors in weld metal solidification cracking. The effect of weld metal composition on susceptibility to SC is discussed in Section 10.6.3, in the context of proposed mechanisms.

Welding process

High heat input, high dilution processes such as SAW and electroslag resistance welding (ESRW) are prone to SC because of the formation of coarse microstructures and slow freezing rates that allow pronounced segregation.The high energy, deep penetration processes, LBW and EBW, produce high weld bead depth to width (D/W) ratios which are associated with end-on collision of growing columnar grains at the weld centreline; with enhanced susceptibility to SC. In contrast, gas metal arc welding (GMAW) and GTAW generally have a medium to low susceptibility for normal welding conditions; and SMAW has a low susceptibility for typical low speed, low dilution conditions. An exception is root pass butt welds using cellulosic electrodes, as discussed in Section 10.6.3.

Welding speed

The propensity for solidification cracking can be increased by increasing the welding speed, reducing the weld pool volume and promoting fast freezing. These factors limit feeding of molten metal during solidification and increase the likelihood of liquid rupture because of failure to accommodate the shrinkage strain. Further, an increase in welding speed leads to a tear drop-shaped molten weld bead, which results in head-on collision of solidification fronts at the centreline of the weld behind the arc. Decreasing the travel speed allows an elliptical molten pool and the solidification front(s) can turn and follow the molten pool in the direction of travel, thus avoiding a sharply defined centreline with a high degree of segregation.

Even if an increase in welding speed is accompanied by an increase in current to ensure satisfactory penetration, weld pool volume and bead

uniformity, SC can still be a problem if the *D*/*W* ratio increases. According to Bailey (1994), an increase in welding current in SMAW usually leads to an increase in the bead *D*/*W* ratio; and Ahmed and Jarvis (1998) have demonstrated that, for bead-on-plate submerged arc welds deposited at constant heat input, an increase in current associated with an increase in travel speed produces a deeper weld bead. However, this effect may not be significant in the case of root pass girth welds, since they are full penetration welds and an increase in current is likely to simultaneously increase the breadth and depth of a larger weld bead volume, with little effect on *D*/*W* ratio. Ohshita *et al.* (1983) concluded that for SMAW of pipe girth welds using cellulosic electrodes, a critical travel speed (~330 mm/min) exists below which solidification cracking does not occur for any weld carbon level in the range 0.04–0.16 wt% (see Fig. 10.7).

Weld bead shape

As well as the *D*/*W* ratio, the shape of the weld bead can have a significant effect on SC. A concave-shaped weld bead surface profile generally creates a higher sensitivity to cracking than a convex profile (Bailey, 1994), probably

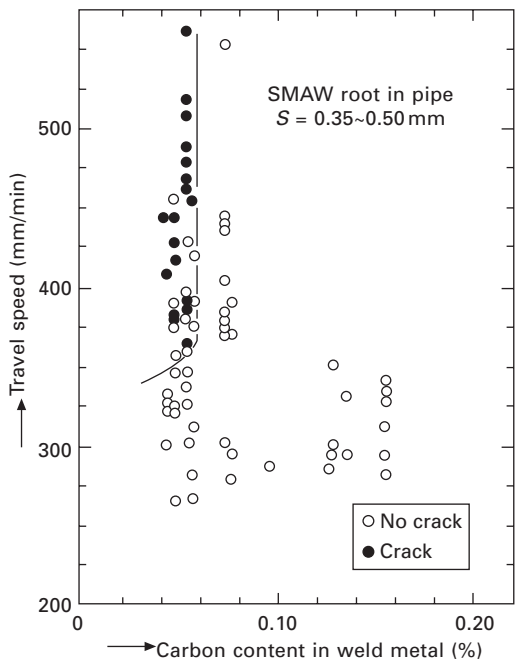

10.7 The critical welding speed and carbon content for solidification cracking in cellulosic SMAW root welds in pipes (after Ohshita *et al.*, 1983). *S* represents the joint shrinkage measured by strain gauge.

because of the capacity of convex beads to accommodate shrinkage by feeding from a larger reservoir of molten weld metal.

Heat input

Since the solidification microstructure is related by epitaxial growth to the grains in the grain-coarsened HAZ at the fusion boundary, large HAZ grains generated by a high heat input will result in large weld metal grains. A coarser cellular-dendritic structure is associated with more pronounced segregation and increased susceptibility to SC.

Stress

In general, SC can develop if the tensile stress caused by shrinkage exceeds the fracture strength of the semi-solid weld bead at any temperature in the solidification range. Below the coherence temperature T_c at which a continuous solid network is established, the tensile restraint stress experienced by the solidifying network is $xE\alpha'$, where E and α' are respectively the Young's modulus and coefficient of thermal contraction at a given temperature, and x is a process-dependent restraint factor which is a function of the type of joint, the weld gap, the plate thickness, the plate and weld metal strengths and the relative thicknesses of the weld bead and the plate (Lancaster, 1999). This factor increases for small bead/plate thickness ratio and a rigid joint set-up. In the case of steel welding, the restraint stress is also increased by the delta-ferrite (δ) to austenite (γ) transformation (0.82% volume contraction). Therefore, the stress developed across the solidifying weld bead is sensitive to the weldment materials and the welding conditions. The development of restraint force during a Gleeble simulation of the melting and re-solidification of an X80-diluted E9010 weld metal is shown in Fig. 10.8 (Dunne *et al*., 2000). During the initial heating stage, compressive force developed because of thermal expansion and the force was offset progressively by increasing the stroke. The blip at **a** corresponds to the effect of volume contraction associated with ferrite (α) to austenite transformation. On melting (plateau region labelled as **b**), the force became zero. Before starting the cooling cycle, the stroke was fixed to simulate a fully restrained weld and the force was monitored during cooling. A rapid increase of tensile restraint force occurred at **c** with the onset of solid bridging (at T_c). The force is amplified by a volume contraction of 0.82% associated with polymorphic transformation of δ to γ. It subsequently rises at a lower rate consistent with the thermal contraction of the γ phase before the onset of γ to α transformation starting at **d**. The volume increase results in almost complete stress relaxation before thermal contraction of the α phase causes a substantial rise in tensile force. The significant tensile force that develops on cooling to room temperature is

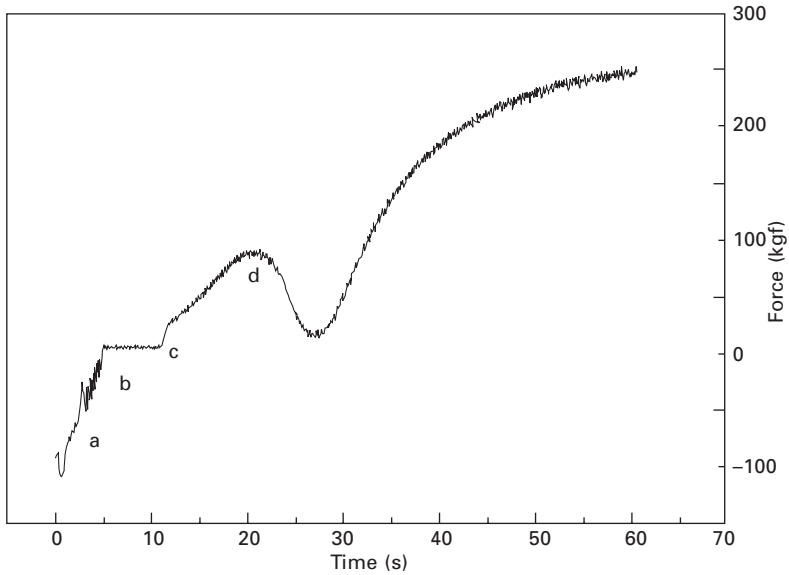

10.8 Restraint force developed with time during melting and solidification of Gleeble sample containing a central diluted weld metal zone of E9010-X80. See text for explanation of labels **a**–**d**.

highly relevant to cold cracking, but only the stress evolution around region **c** is of importance in SC.

10.6.3 Mechanisms

Since SC originates by rupture of liquid films during the weld freezing process, much attention has been focused on the mechanism of initiation and propagation of liquid rupture. A model by Fisher (1948) considers homogeneous nucleation of a single pore in a liquid, thereby initiating the rupture process. The critical 'negative' pressure (P_c), or tensile stress, increases with increasing liquid–solid surface tension and decreasing temperature, but the predicted pressure is orders of magnitude higher than experimental measurements. More appropriate approaches might be calculation of the pressure to cause growth of existing gas bubbles, or to take account of dissolved gases which contribute an internal gas pressure P_g and to embrace heterogeneous nucleation on substrates such as inclusions or oxide films (Cross, 2005). Pressure build-up in the liquid can, of course, be relieved by adequate feeding of liquid metal into the solidification zone and so the welding conditions and particularly the weld geometry have important bearings on the likelihood of solidification cracking. Further, extension of the freezing range by solute segregation will increase the vulnerability to SC as the magnitude of the restraint stress (negative pressure) rises rapidly as the temperature falls (Fig. 10.8).

Therefore, the segregation of alloying elements at the solid/liquid interface is regarded as one of the most important factors influencing the development of solidification cracking, and the presence of the peritectic reaction in carbon steel weld metals results in complex solidification behaviour with significant implications for the effect of alloying elements.

Consider the partial Fe–C phase diagram and the solidification paths illustrated in Fig. 10.9 (Dunne *et al.*, 2000). An alloy containing ≤0.1%C

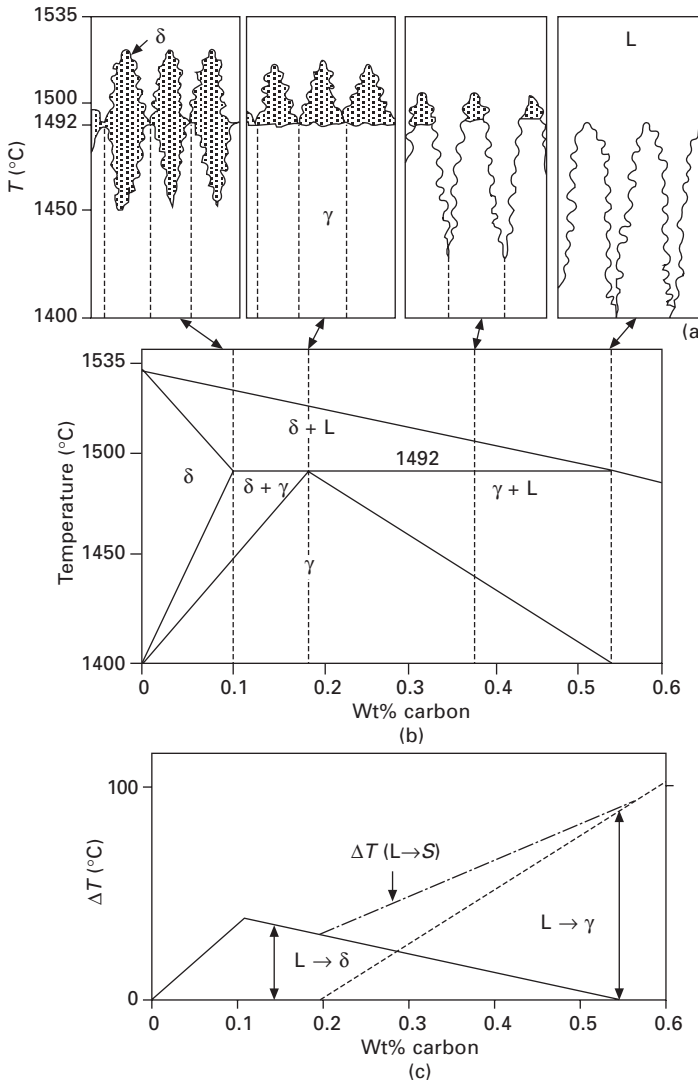

10.9 Partial phase diagram for Fe–C showing the peritectic reaction (b); schematic diagram showing microstructural development with temperature for alloys of selected C contents (a); and the freezing range ΔT as a function of C content (c).

will solidify completely as delta-ferrite, over a temperature range which decreases with decreasing carbon content. Between 0.10% and 0.18% carbon, solidification occurs firstly as δ, but at the peritectic temperature of 1492 °C (1767 K), the remaining liquid reacts with δ to form γ phase. For hyper-peritectic alloys (0.18–0.55%C), solidification occurs initially as δ, but at the peritectic temperature, peritectic γ forms and the excess liquid solidifies to γ as the temperature falls. The weight fraction of γ formed at the peritectic temperature decreases with increasing carbon content and, therefore, the extent of γ solidification increases. Although the freezing paths described here are based on equilibrium freezing, the high temperature of the solidification reaction should ensure a close approach to equilibrium conditions.

The freezing temperature range ΔT as a function of C content is shown in Fig. 10.9(c). The upper envelope shows the liquid → solid freezing range, which has two components: δ solidification and γ solidification between the peritectic composition (0.18%C) and 0.55%C. The freezing range shows a peak at 0.1%C and then increases again for alloys in excess of the peritectic composition. Further, since the critical elements phosphorus and sulphur are far less soluble in austenite than in δ-ferrite, the risk of SC would be expected to increase as a result of enhanced partitioning of these elements to the remnant liquid in alloys solidifying at least partially as austenite (hyper-peritectic alloys). Therefore, SC susceptibility might be expected to be relatively high at 0.1%C and to increase with %C beyond the peritectic composition due to a wider freezing range, exacerbated by increased solute partitioning, particularly of S and P. A similar trend based on γ solidification has been predicted by Bailey (1994) based on solidification to γ at the expense of δ phase. He argues that since more than about 0.1%C is needed for γ to form on solidification and >0.18%C leads to an increase in the freezing range, carbon contents greater than 0.1% are therefore likely to degrade resistance to SC. Garland and Bailey (1973) have also proposed that carbon is detrimental, with a linear effect between 0.08 and 0.19%. However, this trend is not supported by recent experimental results, as discussed below.

Ohshita *et al.* (1983) observed that solidification cracking in cellulosic SMAW root pass butt welds occurred for welds with C contents of 0.04–0.065% for welding speeds in excess of 330 mm/min (Fig. 10.7), with no SC for carbon levels between 0.065 and 0.2%. It was suggested that this behaviour might be a result of the additional contraction strains which accompany the solid state δ to γ transformation at high temperatures in alloys with <0.1%C, rather than as a result of segregation effects.

Tamaki *et al.* (2000) investigated solidification cracking in GMA welds using the circular groove method and reported a complex effect over the range 0.2–0.9%C (see Fig. 10.10). Cracking sensitivity was found to be negligible for ≤ 0.15%C, to increase above 0.2% to a maximum at 0.4%C, followed by a relative minimum at 0.65%C. Beyond 0.65%C, cracking

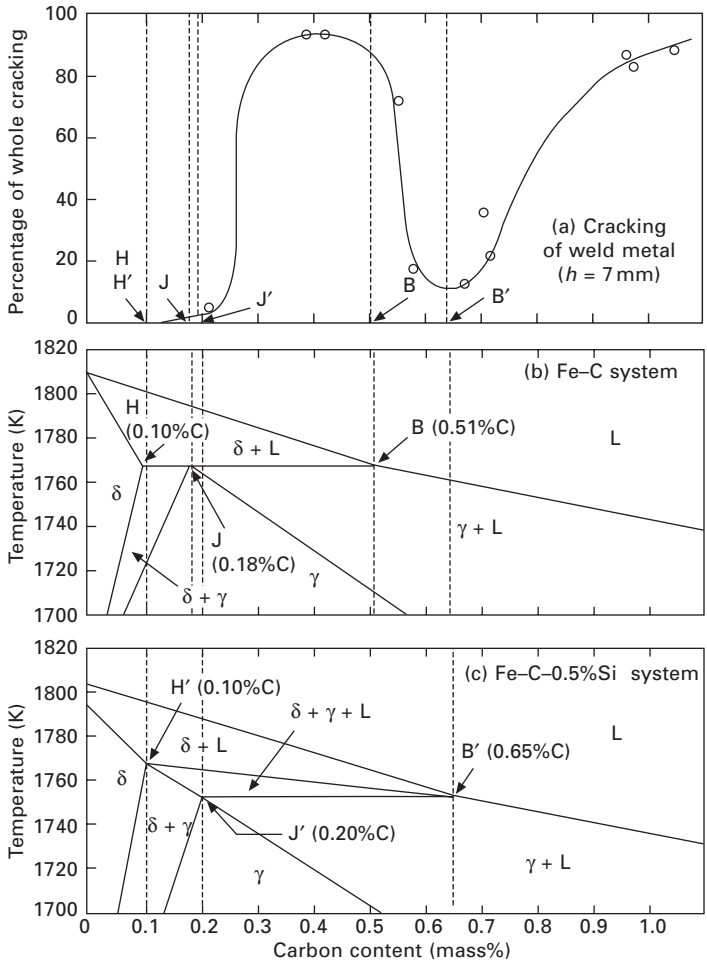

10.10 Diagram showing the relationship between hot cracking sensitivity of ferrous weld metals and carbon content (top) and with the Fe–C and Fe–C–0.5%Si phase equilibrium diagrams (after Tamaki *et al.,* 2000).

sensitivity increased. This behaviour was explained in terms of the influence of solidification mode on the segregation of impurities, particularly P and S. During the peritectic reaction, γ is formed at the interface of δ and liquid. If the solubility of an alloying element is lower in γ than in δ, the element will partition from the γ to the remaining liquid. If the quantity of liquid is small, then solute enrichment may be relatively large, and if the solute results in a low freezing point liquid, then progressive enrichment of the liquid fraction will occur with falling temperature. Referring to Fig. 10.10, the steep rise in %SC from 0.2 to 0.4%C was attributed to solute enrichment of the relatively

small amount of liquid remaining after the peritectic transformation. The decline in sensitivity between 0.5 and 0.65%C was correlated with a larger volume fraction of less highly solute-enriched liquid. For alloys containing more than 0.65%C, the risk of cracking increases again because of complete solidification to γ and a significantly lowered solidus temperature. However, strong solute partitioning should also occur in alloys containing 0.5–0.65%C and therefore, the reason for the observed lower SC susceptibility over this range remains obscure.

Phosphorus is generally considered to promote solidification cracking in ferritic steels (see, for example, Baker, 1975 and Bailey, 1994). Sulphur is also thought to exert a similar effect. However, the SC susceptibility in both cases appears to be closely related to the carbon content of the alloy. The observed effect of phosphorus is usually attributed to the formation of low melting point liquid films that solidify at about 1050 °C to the Fe + Fe_3P eutectic. This extreme extension of the solidification range is thought to be responsible for increased cracking sensitivity.

Tamaki *et al*. (2000) reported the effect of P and S on solidification cracking in their circular groove test for weld metals containing between 0.07 and 0.95%C. As shown in Fig. 10.11, the critical content required to produce solidification cracking varied with carbon content, with a sharp decrease in the critical concentrations at carbon contents close to the peritectic composition (0.18%C) which is a threshold value for γ solidification. The critical P and S contents for a hyper-peritectic alloy with 0.35%C were found to be <0.01%. However, in relation to the lower C steels used in pipeline girth welds the critical concentrations are relatively high (>0.1% for P and >0.2% for S, Fig. 10.11) and are well above the concentrations of P and S found in typical weld metals. For example, research by Nolan *et al.* (2003) on E6010 and E9010 root pass welds in X80 pipe showed that the total P + S content of the weld metals was <0.03%. Moreover, no SC was observed in weld metal with a deliberately increased P+S content of 0.052%. Therefore it was concluded that the usual concentrations of P and S in cellulosic root pass weld metal are unlikely to promote SC.

Root pass girth weld metal compositions are strongly hypo-peritectic and therefore γ solidification is not likely to be a significant factor. However, solidification to δ-ferrite can still result in significant segregation of alloying elements. The degree of segregation of a solute element from δ-ferrite to liquid during solidification can be estimated from the partitioning coefficient, *k*, which is the ratio of the solubility of the element in the solid and liquid phases. A lower value for *k* indicates a higher tendency for segregation from δ-ferrite to liquid and, on this basis, the elements most likely to segregate during solidification of low carbon steels are S, O, B, P, C, Ti, N and H, in decreasing order (Kumar, 1968).

The observations of Ohshita *et al*. (1983) and Tamaki *et al.* (2000) indicate

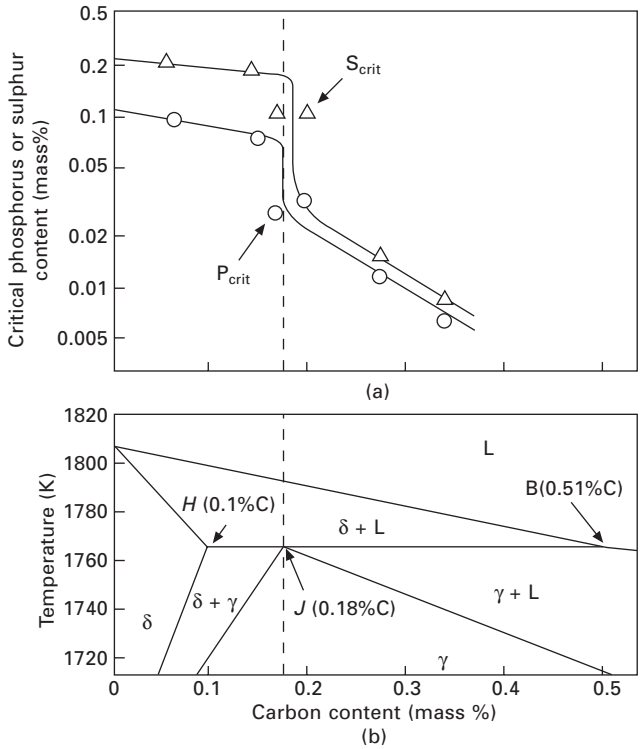

10.11 Diagram showing the influence of carbon content on the critical phosphorus and sulphur contents required to produce solidification cracking in ferrous weld metals (after Tamaki *et al.,* 2000).

that SC would not be expected for the carbon ranges typical of root pass weld metals (0.08–0.12%C). The results of Ohshita *et al.* differ insofar as SC was observed for 0.04–0.06%C weld metals for welding speeds > 350 mm/min. They conducted SMAW girth weld tests on pipe pups with the standard vee preparation, rather than using a simulated SC testing technique. The same kind of testing was conducted recently by Nolan *et al.* (2003) and the results confirmed that SC was promoted by increased welding speed and current. Points of difference were, however, that SC was observed for levels of about 0.1%C and a small amount of SC (about 1%) was recorded for 'low' speed welding at 300 mm/min. Research on HACC in root pass welds using the Welding Institute of Canada (WIC) test also confirmed the occurrence of SC (Dunne *et al*., 2000), as discussed in Section 10.7.

In summary, the evidence suggests that solidification cracking in root pass girth welds is more common than is normally assumed. Root pass pipeline girth welds deposited by SMAW with cellulosic consumables are full penetration welds with a tendency for solidification fronts from either

side of the weld preparation to meet at the weld centreline, as illustrated in Fig. 10.6(b). This geometry is unfavourable for SC resistance. In addition, solute segregation to the remnant liquid along the centreline is likely to extend the solidification range, increasing susceptibility to SC.

Another factor, which has been given scant attention, is the effect of hydrogen in promoting SC. The use of cellulosic electrodes guarantees a hydrogen saturated melt and accumulation of hydrogen in the liquid phase as solidification progresses. While the liquid phase extends to the free surface, supersaturation will be relieved by discharge of hydrogen as bubbles formed in the liquid, but when channels to the external surface become closed, hydrogen will be trapped in the remnant liquid. The build-up of hydrogen in the liquid will be enhanced by partial rejection of hydrogen trapped in the δ phase as solidification progresses. The gas pressure within the liquid will contribute substantially to the negative pressure developing in the liquid because of thermal contraction and phase transformation (region **c**, Fig. 10.8). It is therefore proposed that the formation and linkage of high pressure gas bubbles provide the initiating flaw for liquid metal rupture. The bubbles are likely to nucleate heterogeneously on refractory particles circulating in the melt, e.g. oxides and/or nitrides. The above argument also applies to other gases, particularly oxygen and nitrogen, which are trapped in the weld metal. Cellulosic SMAW provides a gas-rich arc atmosphere and only limited protection from entrainment of air. Gases liberated from the molten weld metal during cooling are therefore likely to be mixtures of hydrogen and other gas species.

Susceptibility to SC may be further exacerbated during pipeline construction, because lifting of the pipe to prepare for joining of the next pipe length results in additional tensile strains across the weld bead. Current Australian practice for land-based pipeline constructions, illustrated schematically in Fig. 10.1, involves lifting and lowering on to a supporting skid after 50–70% completion of the root pass. This lifting action imposes tensile stresses/strains at the bottom dead centre (6 o'clock position) of the root weld. During lifting and lowering, the weld metal at the bottom of the pipe (6 o'clock position) will still be at very high temperature, perhaps even partially molten, during the lifting procedure. If this were the case, the tensile strain applied at the 6 o'clock position, superimposed on the shrinkage strains experienced by the solidifying weld bead, would be expected to increase the risk of solidification cracking. The imposed tensile strain (~5%) is of lower magnitude than the overall shrinkage strains experienced by the solidifying weld bead (10% to 25%) (Henderson *et al.*, 1997). However, it is the incremental strain near the solidus temperature that is important and so the bending stress applied by lifting is likely to be significant if liquid phase is still present.

10.6.4 Prevention

Even though SC is a possible defect in the root pass, practices developed for field stovepipe welding are effective, perhaps inadvertently, in eliminating SC. Grinding of the root to expose the slag deposit in the wagon tracks removes a significant volume of the root pass bead, along with at least some of any centreline SC. The subsequent hot pass remelts part of the remnant root bead and again will serve to eliminate any residual SC either by fusion or crack filling. The shape and position of the hot pass weld bead ensure that the solidifying columnar grains are oriented upwards towards the weld face (see Fig. 10.12), so that the liquid/solid interface is concave upwards, providing a liquid well to feed the liquid/solid regions. Therefore solidification is likely to occur last at the free surface and the bead configuration is not prone to trapping of solute-enriched films of liquid at the centreline or in inter-columnar pockets.

Rather than relying on post-root pass weld procedures to eliminate any solidification cracking that may occur, however, greater security would follow from procedures that minimise the probability of SC occurring in the root pass. The basis of this argument is that a small, but significant, risk resides in dependence on grinding and hot pass remelting to remove solidification cracks. If the crack is too deep, its complete elimination may not occur, leaving a residual defect that can act as a powerful stress concentrator for subsequent cold cracking (see Section 10.7).

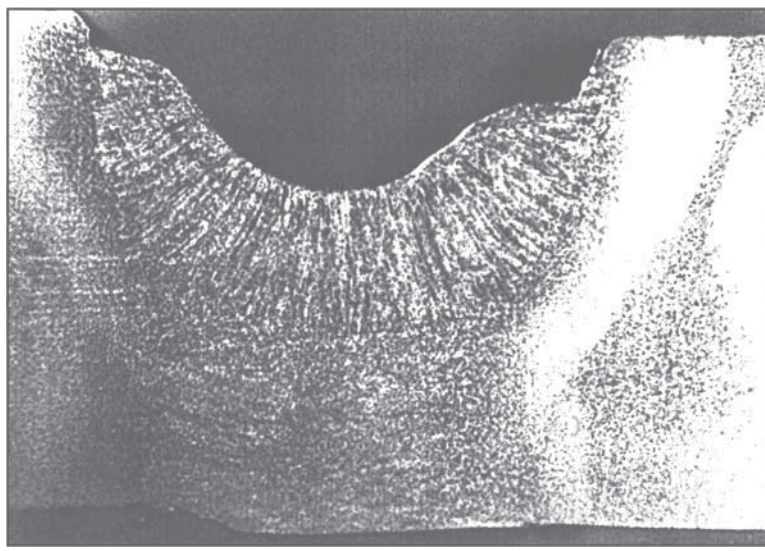

10.12 Macrograph showing a hot pass superimposed on the root bead pass in 8.6 mm thick X80 pipe.

The experimental data obtained by Nolan *et al.* (2003) from solidification cracking tests using 4.0 mm diameter E6010 and E9010 electrodes indicate that the probability of root pass solidification cracking is minimised by:

- careful alignment and fit-up of the pipe ends;
- welding at speeds lower than 500 mm/min; and
- welding at currents below 160 A.

Field welding practices in Australia can exceed these recommended speed and current limits. Furthermore, lifting is commonly performed after 50–70% root pass completion, despite the recommendation of 100% completion by electrode manufacturers. Whether the root pass is 50% or 100% complete, welding test results (Alam *et al.*, 1999; Dunne *et al.*, 2000; Nolan *et al.*, 2003) suggest that lifting of pipe of ≤10 mm thickness should be delayed by at least 10 seconds to ensure complete solidification of the root pass before additional tensile (bending) stress is imposed on the weld bead. This recommendation is conservative, but is based on the argument, detailed below, of a slightly increased risk of solidification cracking as a result of 'early' lifting. Moreover, even if solidification is complete, the restraint stress and a superimposed bending stress could exceed the hot strength of the weld metal, generating solid state hot cracking along planes such as the centreline that have been weakened or embrittled by segregation.

Data on cooling rates of the weld bead during WIC tests and during girth welding of 8.6 mm thick pipe have been obtained by plunging thermocouples into the molten weld pool behind the arc (Alam *et al.*, 1999). WIC tests were conducted without pre-heat, with a pre-heat of 100 °C and with a pre-cool to –10 °C, at a heat input in the range 0.5–0.8 kJ/mm (Fig. 10.13). The cooling

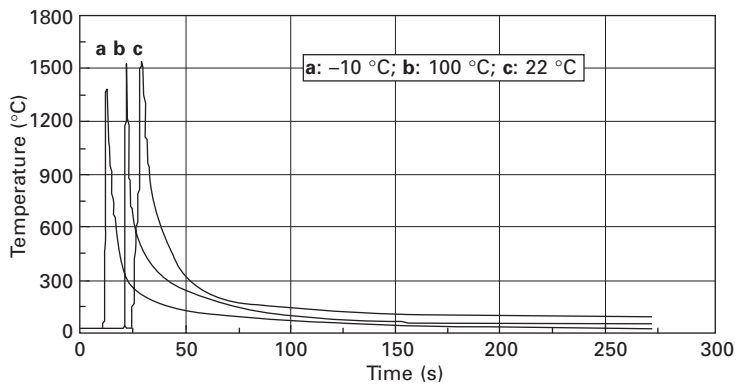

10.13 Temperature profiles of weld metal during weld metal solidification in WIC tests. Curves **a**, **b** and **c** represent temperature profiles for the specified pre-heat temperatures (Alam *et al.*, 1999).

curves indicated that it took less than 2 seconds from the indicated peak temperature to reach 1300 °C and the Δt_{8-5} times were about 5–7 seconds. Given that the response time from deposition of weld metal, to deployment of the thermocouple and measurement of the actual weld bead temperature is approximately 5 seconds, it is estimated that the total time for the bead to cool to 1300 °C is about 7 seconds. Since the 6 o'clock position is close to the end of weld run B1 (see Fig. 10.2), it is possible that the weld metal at 6 o'clock remains at a susceptible temperature for solidification cracking for up to 7 seconds. Therefore, a delay of 10 seconds before lifting should ensure that there is little risk of lifting-enhanced solidification cracking. Too long a delay, on the other hand, is undesirable since hydrogen-induced fracture could occur if lifting takes place after cooling below about 150 °C. Figure 10.13 indicates that for the no pre-heat WIC test (curve **c**), the time to cool to 100 °C was about 75 seconds. For actual girth welds of 8.6 mm thick X80 pipe, the cooling time to 100 °C was found to be about twice as long (Alam *et al*., 1999), suggesting a maximum delay time before completion of lifting and hot pass welding of about 150 s. Therefore, as well as not lifting 'too hot', it is also important to lay down the hot pass weld before the root pass weld cools to temperatures below about 150 °C, in order to avoid cold cracking, as discussed in the next section.

10.7 Cold cracking

10.7.1 Characteristics

Hydrogen-assisted cold cracking of weldments of ferritic steels is also referred to as hydrogen-induced cold cracking (HICC). This type of cracking is a form of hydrogen embrittlement (HE) that requires a temperature below about 150 °C, critical levels of hydrogen and stress concentration and a susceptible microstructure.

HACC has been a major problem in the HAZ of the base steel and various composition-based carbon equivalent (CE) formulae have been developed to enable prediction of the HACC susceptibility of the HAZ. The CE formulae are effectively estimators of hardenability, since the hard, low temperature transformation products, martensite and bainite, have generally low resistance to HACC. Therefore, CE values can be calibrated against pre-heat treatments and weld heat inputs that avoid the formation of hard, HACC-susceptible microstructures.

With the introduction of low carbon, fine-grained, microalloyed steels, the incidence of HACC in the HAZ has diminished and the problem has been transferred largely to the weld metal. Since the weld metal is a combination of a melted consumable or filler and fused base steel, its composition is less well defined than the base steel. In addition, the weld metal usually contains

a relatively high volume fraction of non-metallic inclusions and is characterised by significant compositional and structural variations.

HACC in the HAZ generally occurs in the weld toe, the weld root or in under-bead regions. In weld metal, it is frequently observed as root cracking running in the weld direction, or as transverse cracks perpendicular to the weld direction or at ± 45° (chevron cracking). HACC originates in regions of stress concentration and is a time-dependent process, appearing within minutes, hours or even days after arc extinction. Cracking also propagates intermittently. The time-dependence of cracking is one of the main defining characteristics of HACC and implies that hydrogen diffusion to the stress field of the crack is rate controlling. As little as a few ppm of mobile hydrogen atoms can produce HACC in susceptible microstructures containing critical stress concentrations; and it can also occur at higher hydrogen levels in microstructures normally considered to be 'safe'. The mechanism of cracking is not specific and can involve any or all of the mechanisms: microvoid coalescence (MVC), quasi-cleavage (QC) and intergranular (IG) fracture.

Solute hydrogen in steel is attracted to sites of high stress intensity and if the local hydrogen concentration reaches a critical level, cracking can be initiated which causes failure at strains that are markedly lower than for hydrogen-free steel tested under identical conditions (Christenson *et al*., 1981). The reduction in ductility can be expressed (Pussegoda and Tyson *et al*., 1981) in terms of an embrittlement index (EI):

$$\mathrm{EI} = \frac{\varepsilon_u - \varepsilon_c}{\varepsilon_u}$$

where ε_u is the true fracture strain for uncharged or hydrogen-free steel and ε_c is the true fracture strain for hydrogen charged steel.

In general, low carbon, high strength structural steels show the reduced ductility regime over a temperature range between about –150 °C and 100 °C. At higher temperatures the mobility of the hydrogen atoms prevents concentration at sites of stress concentration and at very low temperatures (< –150 °C), the reduced mobility of hydrogen atoms prevents segregation to potential crack sites.

The results of embrittlement tests are strongly dependent on the strain rate, with differences between true fracture strains of charged and uncharged samples at a given temperature decreasing markedly with increasing strain rate. The tensile test data of Brown and Baldwin (1954) show a maximum EI value > 85% for a strain rate of $8 \times 10^{-4}\,s^{-1}$, about 15% for a rate of $80\,s^{-1}$, and zero for $3 \times 10^{2}\,s^{-1}$.

As the strength of a steel increases, the susceptibility to hydrogen cracking also increases and much lower concentrations of hydrogen can induce embrittlement. In higher strength quenched and tempered steel, such as AISI 4340, delayed fracture testing is often employed. Sustained loads during

hydrogen charging can eventually induce fracture at stresses well below the yield stress (Ishikawa *et al*., 1994).

In the case of weldments, the stresses are internal rather than externally applied and result from restraint of thermal and transformation strains developed on cooling (see Fig. 10.8). Therefore, even for a diffusible hydrogen concentration of a few ppm, delayed cracking can occur in higher strength weld metal by progressive build-up of hydrogen at regions of stress concentration at an initiating defect site and subsequently, near the crack tip during propagation.

10.7.2 Effect of processing conditions

There have been several excellent reviews on the mechanisms of HACC and the welding conditions that promote it (see, for example, Yurioka and Suzuki, 1990). Therefore, only a brief summary is presented here on the general effect of process variables.

Processing conditions that generate and maintain significant hydrogen in the weld metal and HAZ enhance the risk of HACC. Although hydrogen-controlled consumables are available, SMAW is generally regarded as a 'high' hydrogen process because shielding from the atmosphere is inefficient. Moreover, the use of cellulosic SMAW electrodes exacerbates the problem of hydrogen pick-up. In contrast, inert gas shielded GTAW and SAW with a basic flux are considered to be intrinsically low hydrogen processes.

Given the pick-up of hydrogen, the thermal and restraint conditions imposed by welding become important factors in preventing HACC. Slow cooling allows time for hydrogen effusion and can be effected by a relatively high heat input, as well as by pre-heat and/or post-weld heat treatment. Minimising high residual stress and stress concentrations in the completed weld requires close attention to the weld configuration and the welding procedure, including the restraint conditions; and the production of sound welds without stress-concentrating defects. The effect of processing variables on the incidence of HACC in cellulosic root pass welds is addressed in Section 10.7.4.

10.7.3 Mechanisms

HACC is a weldment-specific form of hydrogen embrittlement. One of the most compelling proposals for HE in ferritic steels is due to Beachem (1972) who rationalised the effect on the basis of two assumptions: (i) hydrogen migrates to regions of triaxial stress; and (ii) local concentration of hydrogen facilitates plastic deformation in that region. The first assumption is supported by evidence that the solubility of hydrogen is increased by the application of tensile stress. The second assumption is based on the observation that the cracking mechanisms that can occur at the crack tip (MVC, QC and IG) all

require microscopic plastic flow. The essential idea underpinning Beachem's 'slip softening' model is that hydrogen assists or facilitates those deformation and fracture modes favoured by the local stress intensity and microstructure.

Although Beachem's model appears to be able to explain many of the reported aspects of hydrogen cracking, it is only one of several theories. Hirth (1980) summarised the concept underlying each of the major mechanisms as follows:

(a) internal hydrogen gas pressure in microvoids (Zapfee and Sims, 1941);
(b) decreased surface energy due to hydrogen absorption (Petch, 1956);
(c) decohesion of atoms in lattice regions with high hydrogen concentration (Troiano, 1960);
(d) hydride cracking near the crack tip (Westlake, 1969); and
(e) slip softening due to enhanced dislocation mobility (Beachem, 1972).

Beachem's model (e) and the decohesion model (c) are generally most favoured, but there is little doubt that precipitation of molecular hydrogen in microvoids (a) can exert sufficiently high pressures to enlarge the pores or to cause 'blisters' if the effect occurs close to the surface.

In addition to theories about the cracking mechanism, another theoretical framework, so-called 'trap theory' has been developed to address the distribution of hydrogen in the metal matrix and hydrogen atom migration to stress concentrations. As a small interstitial solute atom, hydrogen can migrate to and be trapped by structural heterogeneities such as grain boundaries, particle–matrix interfaces, dislocations and vacancies. Hydrogen traps are separated into two types: irreversible (strong or deep) and reversible (weak or flat). Reversible traps can exchange hydrogen atoms with their environment, whereas irreversible traps bind hydrogen strongly and require a significant temperature increase for its liberation. Free hydrogen is referred to as mobile or diffusible hydrogen, which can migrate to (and be trapped by) regions of stress concentration.

The division of traps into two categories is a convenient simplification since there will be a spectrum of binding energies, E_b (Pressouyre *et al.*, 1981). The heat of solution of hydrogen in iron (E_S = 29 kJ/mole) serves as a convenient marker and weak traps can be regarded as those with $E_b < E_S$. For moderate traps $E_b = E_S$ and for strong traps $E_b > E_S$. Strong traps in steels are features such as grain boundaries and incoherent interfaces between the matrix and carbide and nitride precipitate particles (Gibala and DiMiglio, 1981). The various hydrogen traps can modify the diffusivity of hydrogen at temperatures near and below ambient.

A basic assumption of trap theory is that irreversible traps can act as crack initiation sites if there is sufficient diffusible H available to raise the H concentration in the trap C_H to a critical concentration, C_K. C_H is time-dependent and the H content of a deep trap can be increased by lattice

diffusion, sweeping-in of H atmospheres by dislocation motion, and short circuit diffusion along dislocation cores and grain boundaries.

Higher strength hot rolled, normalised and heat-treated steels can contain large concentrations of deep traps in the form of alloy carbide/nitride particles. In the case of ferritic weld metals, high densities of non-metallic inclusions can also be present, which act as effective H traps. These traps can take H atoms out of circulation at low temperatures, thus reducing the susceptibility to HACC. However, if the diffusible hydrogen content is sufficiently high that C_H can be increased to C_K, the 'benign' traps can become 'malignant' and act as crack initiators. Incoherent particles are often prominent in HACC fracture surfaces, interacting with hydrogen to promote microvoid formation, quasi-cleavage or intergranular cracking. Hydrogen accumulation in the stress field surrounding incoherent particles can promote decohesion and microplasticity, effectively lowering the local 'lattice strength' until it falls to the magnitude of the stress concentration at the crack tip. Crack extension will then occur, allowing hydrogen effusion from the crack surface. Further cracking occurs discontinuously after the accumulation of hydrogen atoms to a critical concentration in the stress field ahead of the crack tip.

10.7.4 Prevention

The relatively high diffusible hydrogen content of cellulosic root pass welds is a major concern to the pipeline industry, particularly with the application of X80 (550 MPa YS) and higher strength pipeline steels. Figures quoted for weld metal hydrogen content immediately after cellulosic SMAW are usually in the range 30–50 ml H/100 g of deposited weld metal and depend on the measurement method (Yurioka and Suzuki, 1990; Grong, 1994). After normal post-weld cooling, the actual level of hydrogen remaining in the weld bead below 100 °C is considerably lower because of effusion from free surfaces and diffusion into the base plate. In this respect the pipeline joint preparation is significant since the root pass girth weld has a bead–air interfacial area similar to the weld bead–base plate interfacial area (see Fig. 10.6b) and, given the expected steeper temperature gradient into the base plate compared with that towards the free surfaces, loss of H by effusion is likely to be highly significant. The thin-walled nature of Australian pipelines is also expected to be favourable in restricting heat loss into the base plate and extending the cooling time from 800 to 100 °C (t_{100}), and promoting the effusion of the highly mobile (diffusible) H atoms from the weldment. In addition, a hot pass is laid down before the root pass cools into the critical range (<150 °C), increasing the thermal load and slowing the rate of cooling of the weldment. The current fabrication practices therefore provide built-in safety factors that reduce the risk of hydrogen cold cracking. The maintenance of security for X80 and X100 steels using strength-matching cellulosic

electrodes without pre-heat is an issue that stimulated an extensive laboratory testing programme in Australia using the WIC test to assess the susceptibility of root pass welds to HACC (Barbaro *et al*., 1998; Alam *et al*. 1999).

A diagram of the WIC test set-up is shown in Fig. 10.14. The restraint conditions can be varied by changing the free (restraint) length of the joined plates, measured between the ends of the opposing fillet welds to the rigid base plate. According to Graville (1994), the standard WIC test (restraint length = 25 mm), approximates the restraint and bending stresses occurring across the weld face at the 6 o'clock position during field root pass welding and lifting. The corresponding restraint factor (R_F) for 8.6 mm thick plate is 16 400 N mm^{-1}mm^{-1}, which, according to an equation by Suzuki (1979), is equivalent to a restraint stress of 656 MPa (well above the nominal yield stress of the weld metal).

Barbaro *et al*. (1998) reported lifting strains for X60, X70 and X80 full-length pipes with diameters of 219–457 mm and thicknesses of 5.7–8.6 mm, for 300 and 600 mm lifts after 50% completion of E6010 root pass welds. Tensile strains up to 5% were recorded at the bottom dead centre (BDC) or 6 o'clock position. Although these strains are well into the plastic range, they are reversed by lowering and no lift-induced cracking was observed. The lifting procedure imposes a transient bending stress, typically at a

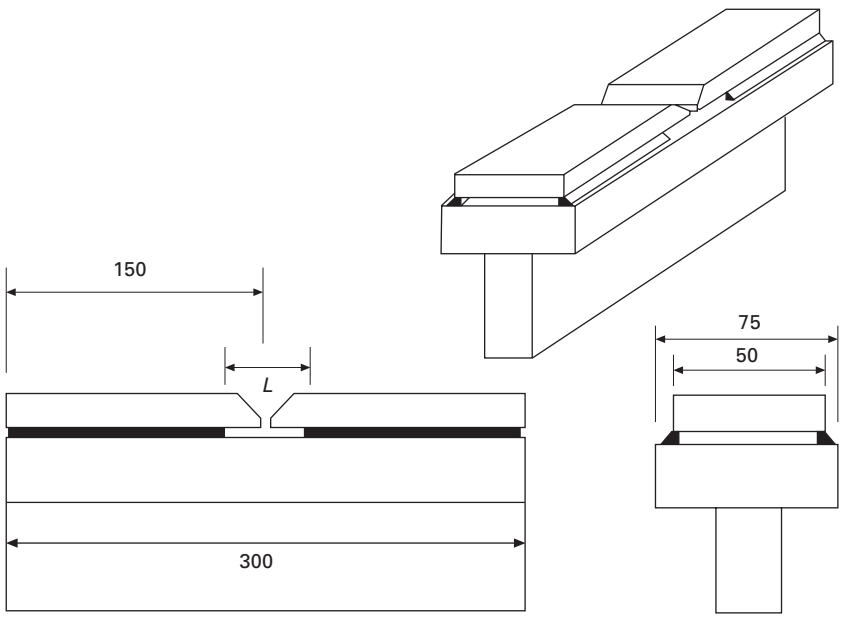

10.14 Diagrams showing the WIC test set-up. The distance *L* is the restraint length. Run-on and run-off tabs are used in making the root weld pass. All dimensions are in mm.

temperature too high for HACC, whereas the WIC test applies and *maintains* a high restraint stress as the weld cools to the critical range for HACC.

Internal clamps were used in the pipeline welding trials, as in actual string welding in the field, but the joint region contracted by up to 0.38 mm as a result of thermal and transformation strains, indicating that the restraint intensity is relatively low and similar to levels present in other structural steel welding applications. In such cases the restraint intensity is often estimated by the formula: $R_F \leq 400\,h\,\mathrm{N\,mm^{-1}mm^{-1}}$ (Yurioka and Suzuki, 1990), where h is the plate thickness. For an 8.6 mm plate the equivalent restraint stress is 138 MPa and a stress concentration factor of 3.2 gives a localised concentrated stress σ_c of 440 MPa. Although it is difficult to quantify the restraint stress in actual field welding, it is likely that the restraint factor R_F and restraint stress σ_r implied by the standard 25 mm restraint length in the WIC test are well in excess of those that apply to field welding. However, for a 100 mm restraint length in the WIC test, R_F, σ_r and σ_c ($\times$ 3.2) are, respectively, 4.1 kN/mm^2, 164 MPa and 525 MPa, much closer to the estimates for structural steel welding. Nevertheless, even these lower estimates may be excessive since the pipes are restrained only by line-up clamps, with wedges to prevent gap closure after the welding of the initial segments.

WIC testing with a 25 mm restraint length established that, without preheat, significant weld metal HACC occurred for an E9010 consumable on X80 plate (see, for example, Fig. 10.15). However, for a pre-heat of 60 °C, which substantially increases t_{100}, cracking was completely eliminated. The WIC

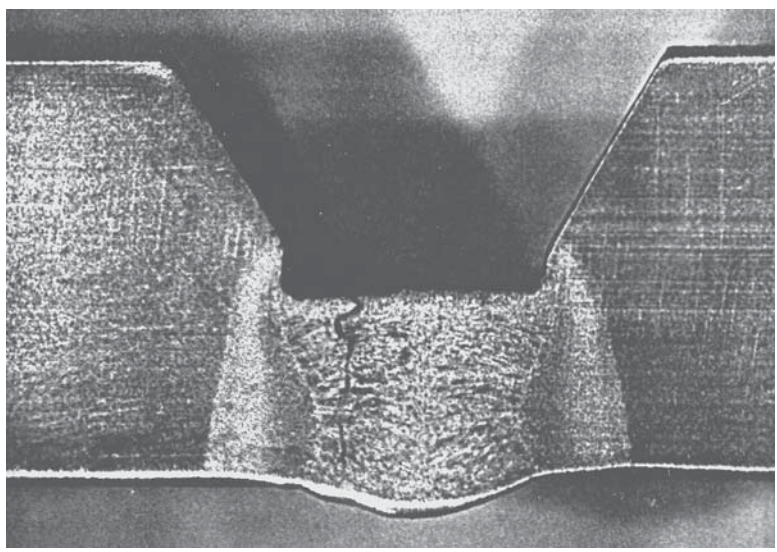

10.15 Macrograph of transverse section of E9010 weld pass in 8.6 mm thick X80 plate. Weld metal cracking (HACC) has occurred across the weld bead.

test set-up allows faster cooling than that occurring in practice and calibration of the test cooling conditions with field root pass welding showed that a test preheat of 80 °C was equivalent to ambient temperature field welding. For testing with a 100 mm restraint length, which introduces a restraint stress that is likely to be closer to that of field welding, no HACC was observed. As well as the reduced restraint, the cooling time t_{100} was significantly increased because of the longer thermal path to the sink provided by the thick base plate of the test rig (Fig. 10.14). Therefore, WIC testing at 100 mm restraint length is considered to more accurately simulate field welding. Nevertheless, the standard 25 mm test has been recommended by Graville (1994) on the basis that it results in a root face stress higher than yield, consistent with the lifting stress. However, it should be noted that the lifting strain is transient and reversed by lowering and that it is likely to occur at a temperature above the critical temperature range for HACC. Therefore, it is concluded that the standard WIC test is conservative because the cooling rate and restraint intensities exceed those expected in root pass girth welding in the field (Alam *et al*., 1999). Moreover, the established practice of laying down the hot pass within a few minutes of completing the root pass provides added security against HACC. It was demonstrated by WIC testing (Alam *et al*., 1999) that a hot pass delay of 5 minutes prevented HACC, whereas after a 15 minute delay, root pass cracking occurred before hot pass welding and the crack subsequently extended through the hot pass after re-cooling to a temperature below 150 °C. Overall, the results indicate that for a thickness ≤ 8.6 mm, X80 can be safely welded with E9010 cellulosic consumables without preheat.

This conclusion must be qualified in terms of the ambient temperature and plate thickness. Under low temperature ambient conditions (zero or below) and for plate thicknesses greater than 10 mm, preheat would be necessary to prevent HACC. Moreover, for security against HACC, consumable manufacturers recommend preheat for strength-matching consumables on X80 and higher strength steels.

Non-cellulosic low hydrogen electrodes are an alternative solution, but if the favourable features of cellulosic electrodes and manual welding are to be retained, pre-heat to a minimum temperature is required for thicker pipe and higher strength pipeline grades to extend t_{100} to a figure which allows the H concentration to fall below the critical level for the welding and service conditions. Mechanised low hydrogen processes are also gaining favour, particularly for thicker, larger diameter pipes.

10.8 Conclusions

The above analysis demonstrates that hydrogen plays a central role in all three of the major defects possible in cellulosic welds: HB, SC and HACC.

The first two cracking mechanisms involve the hydrogen saturated molten metal. However, they differ insofar as HB is a product of the high arc force and deep penetration associated with keyhole production, whereas SC develops in a small volume fraction of remnant liquid when solidification is nearly complete. Nevertheless, the work by Nolan *et al*. (2003) showed that HB and SC can be associated, probably because of solid state cracking (hot cracking or HACC) across the membrane of centreline material separating the two defects.

HACC is a solid state phenomenon resulting from residual hydrogen in the weld metal after cooling to near ambient temperatures and the development of restraint stresses that are concentrated at flaws or discontinuities. HB and SC can be eliminated or minimised by controlling the welding speed and welding current, whereas HACC can be prevented, at least for strength levels up to those of E9010-X80 weld metals, by appropriate pre-heating and/or control of the thermal cycle to ensure significant effusion of hydrogen on cooling to the susceptible temperature range.

A root pass testing programme for 8.6 mm X80 pipeline steel using both E6010 and E9010 electrodes (Dunne *et al*., 2000) established that SC and HACC can also be associated. If SC is present in the root pass weld and is not eliminated by grinding and hot pass re-melting, it constitutes a serious centreline flaw that can promote subsequent HACC. WIC test samples often showed diagonally oriented cracks, with one link between a wagon track on the weld face and the upper tip of a centrally located crack and another from the lower tip of the central crack to the opposite side of the root (see Fig. 10.16). The

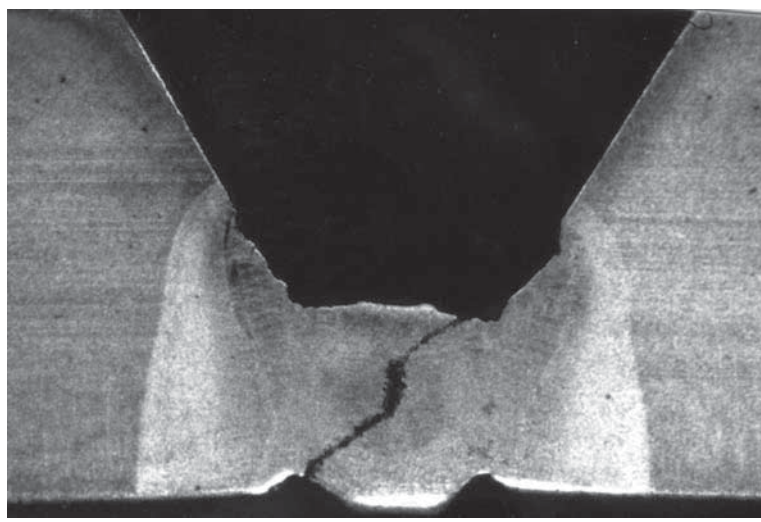

10.16 Macrograph of transverse section of E9010 root pass weld in WIC test sample for 8.6 mm X80 plate. Cracking has occurred 'diagonally' across the weld bead.

surface of the central crack showed cellular-dendritic regions, indicating that the crack propagated, at least in part, as SC.

Cellulosic electrodes are clearly attractive in SMAW because of their handling characteristics and the high arc force that they generate. However, hydrogen control is essential to prevent dangerous weld defects. During solidification, control of HB and SC is best achieved by limiting the welding speed and current. For avoidance of HACC, sufficiently slow cooling is required to allow effusion of hydrogen to levels that are safe relative to the microstructure of the weld metal and the restraint stress inherited from the welding process.

10.9 Acknowledgements

The authors would like to acknowledge the support of the CRC for Welded Structures and particularly the advice and encouragement of Mr Leigh Fletcher and Dr Colin Chipperfield, who were successive directors of the CRC. Other research colleagues whose contributions are gratefully acknowledged are Dr Frank Barbaro (BlueScopeSteel), Professor John Norrish (University of Wollongong), Paul Grace (WTIA), Dr Nazmul Alam (CSIRO), Dr Huijun Li (ANSTO) and Dr Liang Chen (University of Wollongong).

10.10 References

Ahmed N.U. and Jarvis B.L., (1998), 'The effect of welding conditions on the thermal cycles in single electrode submerged arc welding', *Australasian Welding Journal*, **43**, 40–47.

Alam N., Dunne D. and Barbaro F., (1999), *Proc. 1st Int. Conf. on 'Weld Metal Hydrogen in Pipeline Girth Welds'*, Wollongong, Australia, ed. by N. Yurioka, APIA-CRC for Welded Structures.

ASM Metals Handbook, Desk Edition, (1984), Chapter 30, 'Joining', p. 30–32.

Baker R.G., (1975), *Proc. Rosenhain Centenary Conf.*, London, The Royal Society, p. 129.

Bailey N., (1994), *Weldability of Ferritic Steels*, Cambridge, UK, Abington Publishing, pp. 54–87.

Barbaro F., Henderson I., Dunne D., Painter M., Norrish J. and Harrison R., (1998), *Proc. International Pipeline Conf. IPC'98*, ASME Intl., Calgary, Alberta.

Barkow A.G., (1973), 'Hollow bead: problem', *Oil and Gas Journal*, 40–47.

Beachem C.D., (1972), 'A new model for hydrogen-assisted cracking (hydrogen "embrittlement")', *Met. Trans.*, **3**, 437–451.

Bohler Technical Publication, 'Welding Consumables for Pipeline Construction', www.boehler-welding.com/.

Brown I.T. and Baldwin W.M., (1954), 'Hydrogen embrittlement of steels', *Trans. AIME*, **200**, 298–303.

Cantin G.M. and Bee J.V., (1994), 'An investigation of the formation of hollow bead defects,' *WTIA, 42nd National Welding Conference*, Melbourne, Australia, Paper 1.

Cantin G.M. and Bee J.V., (1995), 'The causes and control of hollow bead in pipeline

girth welds', WTIA/APIA Panel 7 Research Seminar, '*Welding High Strength Thin-walled Pipelines*', Wollongong, Australia, October, pp. P12-1 to P12-25.

Christenson D.J., Bernstein I.M., Thompson A.W., Danielson E.J., Elices M. and Gutierrez-Solana F., (1981), in '*Hydrogen Effects in Metals*', edited by I.M. Bernstein and A.W. Thompson, Met. Soc. AIME, pp. 997–1004.

Cross C.E., (2005), 'On the origin of weld solidification cracking,' in *Hot Cracking Phenomena in Welds*, ed. by T. Bollinghaus and H. Herold, Springer, Berlin, pp. 3–18.

Dunne D.P., Alam N., Li H. and Chen L., (2000), 'Cracks – running hot and cold. A tale of weld metal integrity', *Proc. IIW Asia-Pacific Int. Congress*, Melbourne, Australia, Paper 18.

Eagar T. and Lin M.L., (1984), 'Puddle surface depression and weld pool geometry', *Proc. 65th AWS Annual Meeting*, Dallas, Texas, pp. 184–185.

Fisher J.C., (1948), 'The fracture of liquids', *J. Appl. Physics*, **19**, 1062–1067.

Garland J.G. and Bailey N., (1973), 'Solidification cracking during submerged arc welding of C-Mn steels', *The Welding Institute Report M/75/73*, TWI Abington, Cambridge.

Gibala R. and DeMiglio D.S., (1981), 'Hydrogen in irons and steels: interactions, traps and crack paths', in *Hydrogen Effects in Metals*, edited by I.M. Bernstein and A.W. Thompson, Met. Soc. AIME, pp. 113–122.

Graville B.A., (1994), *Interpretive Report on Weldability Tests for Hydrogen Cracking of Higher Strength Steels and Their Potential for Standardisation*, Welding Research Council, Canada.

Grong O., (1994), *Metallurgical Modelling of Welding*, Institute of Materials, London, pp. 128–141.

Hart P.H.M., (1969), *Hydrogen Induced Delayed Cracking in the Site Welding of Line Pipe*, TWI Members Report M35/69.

Henderson I., Krishnan K.N. and Cantin G.M.D., (1997), *Investigation of Field Welding Limits for Girth Welding of Thin-Walled High Strength Pipes*, CRC for Materials Welding and Joining, Australia, Final Report on Project 96.32.

Hirth P., (1980), 'Effect of hydrogen on the properties of iron and steel', *Met. Trans A*, **11A**, 861–890.

Ishikawa M., Nakatani Y. and Yamada K., (1994) 'Mechanistic aspects of hydrogen cracking in high strength steels', in *Hydrogen Transport and Cracking in Metals*, edited by A. Turnball, IOM Pub., pp. 95–102.

Kumar R., (1968), *Physical Metallurgy of Iron and Steel*, Asia Publications, Bombay.

Lancaster J.F., (1999), *Metallurgy of Welding*, Sixth Edition, Abington Publishing, Abington, UK, pp. 185–192.

Lincoln Electric (1993), Technical Guideline: 'Welding Pressure Pipelines and Piping Systems', http://content.lincolnelectric.com/.

Linnert G.E., (1994), *Welding Metallurgy, Vol. 1, Fundamentals*, AWS Pub., 4th Edition, Miami, Florida.

Mills K.C., Keene B.J., Brooks R.F. and Shirali A., (1998), 'Marangoni effects in welding', *Phil. Trans. R. Soc*., **356**, 911–925.

Nicholson P.L., (2003), 'Challenges and solutions for the retention of field production rates in high strength pipe', *Exploration and Production: Oil and Gas Review*, **2**.

Nolan D., Dunne D. and Norrish J., (2003), 'Root pass solidification cracking in low carbon pipeline girth welds deposited by cellulosic manual metal arc welding,' *Sci. Tech. Welding and Joining*, **8**, 102–112.

Ohshita O., Yurioka N., Mori N. and Kimura T., (1983), 'Prevention of solidification cracking in very low carbon steel welds', *Weld. J.,* **63**, 129S–136S.

Petch N.J., (1956), 'The ductile fracture of polycrystalliner α–iron', *Phil. Mag*., **1**, 331–357.

Pressouyre G.M., Fidelle J.P. and Arnould-Laurent M., (1981), 'Trap theory of hydrogen embrittlement: experimental investigations', in *Hydrogen Effects in Metals*, edited by I.M. Bernstein and A.W. Thompson, Met. Soc. AIME, pp. 27–36.

Pussegoda L.N. and Tyson W.R., (1981), 'Relationship between microstructure and hydrogen susceptibility of same low carbon steels', in *Hydrogen Effects in Metals*, edited by I.M. Bernstein and A.W. Thompson, Met. Soc. AIME, pp. 349–360.

Quigley M.B.C., (1986), 'High power density welding,' Chapter 8, *The Physics of Welding*, 2nd edition, ed. by J.F. Lancaster, IIW, Abington Publishing, Abington, UK, pp. 306–323.

Smart R. and Bilston K., (1995), *WTIA/APIA Panel 7 Research Seminar, 'Welding high strength thin-walled pipelines*', Wollongong, Australia, October, Paper 6.

Suban M., Tusek J. and Uran M., (2001), 'Use of hydrogen in welding engineering in former times and today', *J. Mater. Proc. Technol*., **119**, 193–198.

Suzuki H., (1979), *Cold Cracking and Its Prevention in Steel Welding*, IIW Doc. IX-1074-79.

Tamaki K., Kawakami H. and Suzuki J., (2000), *Effect of Carbon Content and Peritectic Reaction on Hot Cracking of Weld Metal of High Carbon Steel*, IIW Commission IX Doc.1967-00, International Institute of Welding Congress, Vienna.

Troiano A.R., (1960), 'Role of hydrogen and other interstitials in the mechanical behaviour of metals', *Trans. ASM*, **52**, 54–80.

Westlake D.G., (1969), 'A generalized model for hydrogen embrittlement', *Trans. ASM*, **62**, 1000–1006.

Willgoss R.A., (1980), 'Weld pool profile and porosity in TIG-welding of BS 1501, Type 316 stainless steel', *Proc. Int. Conf. on 'Weld Pool Chemistry and Metallurgy*', The Welding Institute, London, pp. 133–145.

Wright M., (1993), 'Hollow bead – a question of technique?', *TWI Bulletin*, May/June 1993.

Yurioka N. and Suzuki H., (1990), 'Hydrogen assisted cracking in C-Mn and low alloy steel weldments', *Int. Mat. Reviews*, **35**, 217–249.

Zapfee C.A. and Sims C.E., (1941), 'Hydrogen embrittlement, internal stress and defects in steels', *Trans. AIME*, **145**, 225–237.

Zhou J. and Tsai H., (2007), 'Effects of electromagnetic force on melt flow and porosity prevention in pulsed laser keyhole welding', *Int. J. Heat and Mass Transfer*, **50**, 2217–2235.

11

Repair of weld cracks

R IBRAHIM, Monash University, Australia

Abstract: Cracks are the most important factor in the welding quality and can be located at different areas after the welding process. The main problem is that, in most cases, the cracked area is the weakest section in the welded parts and it is the point of stress concentration. Cracks are affected by three main factors: the thermal history of the welded parts; the chemical composition of the welded parts; and the conditions of the welding process. This type of crack can be avoided by slowing the cooling rate. In some cases, the joint can be pre-heated to minimize the heat impact of the welding process.

Key words: cracks, heat treatment, stress concentration, chemical composition, thermal history.

11.1 Introduction

Like any manufacturing process, the welding process has several advantages and some disadvantages. It achieves highly efficient structural joints with high strength that is similar to or higher than the parent material [1]. The welding process is associated with extreme heat. Heat is required to create a local melting region, or welding pool, of the joint components, the parent material or the base metals. Melting of the welding electrode or the filler metal depends on the type of welding process. The solidification of the melted part of the electrode (if it is included) and the melted parts of the parent materials together form the weld bead and the penetration of the welding into the parent material. The final quality of the welding is affected by three elements: the thermal history of the joint parts; the chemical composition of the parent material or the base metal and the welding electrode (if it is included); and the welding process conditions. The thermal history of the joint parts depends on the preheating, the heating rate, the cooling rate and the maximum temperature of each point in the joint parts. The chemical composition of elements such as carbon, manganese and sulphur affects the tendency of the parent material to cracking, as will be explained later. Welding process conditions depend on the surrounding environment such as the moisture and hydrogen presence and the appropriate welding parameters, such as welding voltage, welding current or shielding gas, if it is required. Welding quality is evaluated according to the ability of the weld to carry out the requirements of the joint during its lifetime.

11.2 Weld defects

Poor quality welding is of two types: firstly, defects appear due to applying an external load, and secondly defects appear after welding without applying an external load. In both cases, the most important defect is the crack and its location in the joint. Some other defects in addition to cracks appear and affect the welding quality, such as lack of fusion, lack of penetration, excessive amount of spatters around the weld bead, inclusion and porosity. Cracks are highlighted here because of their importance.

11.3 Weld cracks

Cracks are the most important factor in the welding quality and can be located at different spots after the welding process. The main problem is that, in most cases, the cracked area is the weakest section in the welded parts and it is the point of stress concentration. Cracks are affected by three main factors: the thermal history of the welded parts; the chemical composition of the welded parts; and the conditions of the welding process [2, 3].

11.3.1 Effect of thermal history on cracks

In any arc welded joint, the thermal history of the fusion zone and heat-affected zone (HAZ) in the parent material of the welded parts shows that a fast heating rate and fast cooling rate have occurred. Owing to the fast cooling rate in the presence of carbon, the two zones could transform to martensite microstructure. Martensite is not a favourable microstructure because it has high hardness and low ductility. Also, it is highly susceptible to cracking owing to the tensile stresses generated by volume expansion. This type of crack can be avoided by slowing the cooling rate. In some cases, the joint can be pre-heated to minimise the heat impact of welding. Low carbon steels (less than 0.3%C) can be welded without preheating. Preheating is required for medium carbon steels (0.3–0.7%C, 200–320 °C) and high carbon steels (250–320 °C) only.

11.3.2 Effect of chemical composition on cracks

The percentage of some elements such as sulphur, manganese and carbon together affect the susceptibility to cracking. The presence of sulphur in the steel as iron sulphide at the grain boundaries contributes to the cracking tendency. This tendency can be neutralised by adding manganese because it has higher affinity to iron than sulphur. Also, manganese produces manganese sulphide. The tendency to crack depends on the percentage of carbon and sulphur, as shown in Fig. 11.1. Also, the increase in carbon content increases

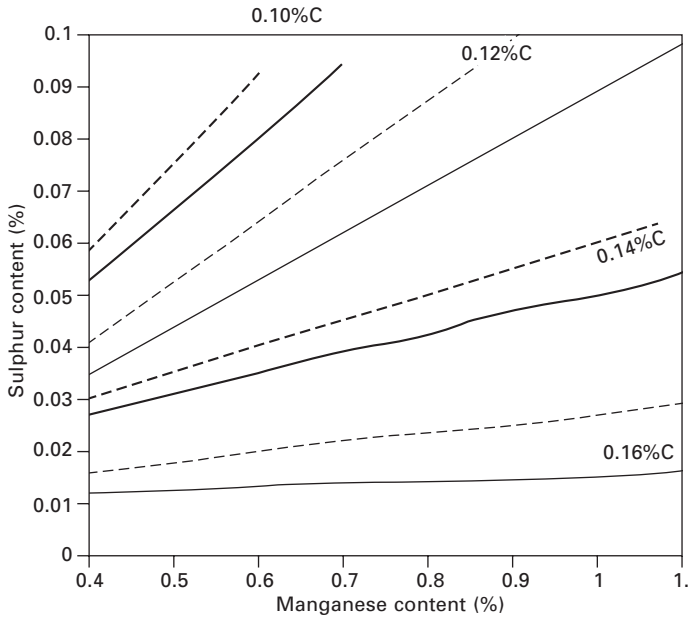

11.1 The influence of sulphur on the cracking of welds, as a function of the carbon and manganese content of the steel.

the possibility of cold cracking (hydrogen cracking). Crack susceptibility increases with an increase in material thickness. The material thickness has two effects: it works as a heat sink and the thick material has a higher cooling rate than that of thin material. Also, the thickness has a restraining effect. The thick material has higher degree of restraint than that of thin material. Such cracks can be avoided in low hydrogen welding procedures.

Figure 11.1 shows the influence of sulphur, manganese and carbon on the cracking of welds. For each different percentage of carbon content, the area above the dashed lines represents a cracked area, the area under the solid line represents the crack-free area and the area between represents a mixed area [3].

11.3.3 Effect of welding process conditions on cracks

Welding process conditions include both basic conditions of all welding processes and conditions particular to each type of welding process. The basic welding conditions are: clean and dry surfaces; moisture-free welding atmosphere; and dry welding electrodes. The particular welding conditions are: welding voltage; welding current; shielding gas or mixed gases and the gas flow rate; welding traverse speed; wire feeding rate; welding electrode type; and welder skills.

11.4 Crack locations

Cracks are located mainly in two areas: the weld metal and the HAZ of the parent material. The cracks situated in the weld metal are related to either wrong selection of the welding electrode or inappropriate welding conditions. The cracks situated in the parent material appear in the HAZ or the adjacent area and these are related to welding conditions, the parent material chemical composition and its weldabilty [3].

11.4.1 Cracks in weld metal

There are different types of cracks which can appear in the weld metal area. The most common types are: 'centreline' crack; traverse crack; 'vertical' crack and the 'under-bead' crack. These types are shown in Fig. 11.2. These cracks are developed in the weld metal due to expansion and contraction during the solidification at high temperature. There are two types of factors that affect the development of cracks: technical factors and metallurgical factors.

The technical factors include wrong choice of welding electrode (not suitable for the parent material or the operation of the joint); wrong welding conditions (lower or higher welding voltage, lower or higher welding current, too slow or too fast welding traverse speed); and presence of welding defects such as porosity and oxide inclusions. Such factors or crack causes can be easily avoided by making sure that the welding process is run in proper conditions and the surfaces to be welded are prepared carefully and clean before and during the welding process.

The metallurgical factors are the main factors in the development of weld metal cracks. Those factors are the cooling conditions from the molten state to the solid state; structural transformation in the weld metal; and the high temperature properties of the weld metal.

Cooling condition from molten to solid state

Owing to the contraction of the weld metal as it passes from the molten state to the solid state, cracks can form. These types of cracks most likely occur in the end of the run, especially when the electrode is removed suddenly.

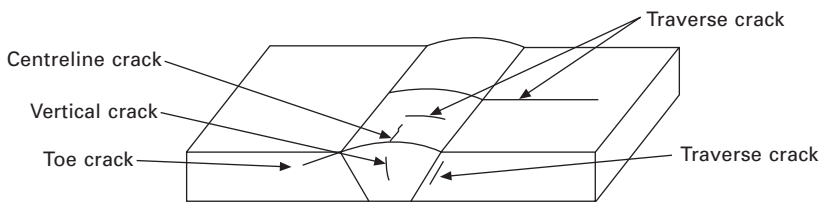

11.2 Common types of crack.

This gives the end of the weld bead a crater of variable depth which forms a tiny pipe that is susceptible to cracking due to tensile stress in different directions around the crater [3]. Figure 11.3 represents the crater in the end of the welding run.

In Fig. 11.3, point **a** is on the top surface of the parent material, point **b** is the bottom end of the weld bead and point **c** is the top end of the weld bead. Molten weld metal passes through three stages, depending on the phases of the material, until the solidification is complete. These stages are: all liquid; liquid and solid; and all solid, as shown in Fig. 11.4. It is well known that the solidification process is associated with an increase in density and a decrease in volume. This decrease in volume in the end of the weld bead forms the crater shape and creates a pipe. The previous section of the bead is in the advanced cooling stage, which causes contraction stresses in the molten metal. The parent material, under the end of the bead, is still in thermal expansion so that the bead end starts to open. This area has three reasons for cracks: cavity shrinkage; contraction stresses due to different cooling stages; and expansion stresses in the parent material under the end of the run. The crack in the crater could be longitudinal, traverse or a star crater crack [4, 5]. This type of crack can be avoided by applying a slower cooling rate, feeding the crater with more molten material and restraining the welded plate to reduce the opening of the weld bead end. Owing to the contraction during the solidification stage, vertical cracks can form in the weld metal. This type of crack is very dangerous because it is internal and not visible. It needs a penetrated inspection method such as ultrasonic or X-ray. It dramatically affects the weld metal strength and is a point of very high stress concentration.

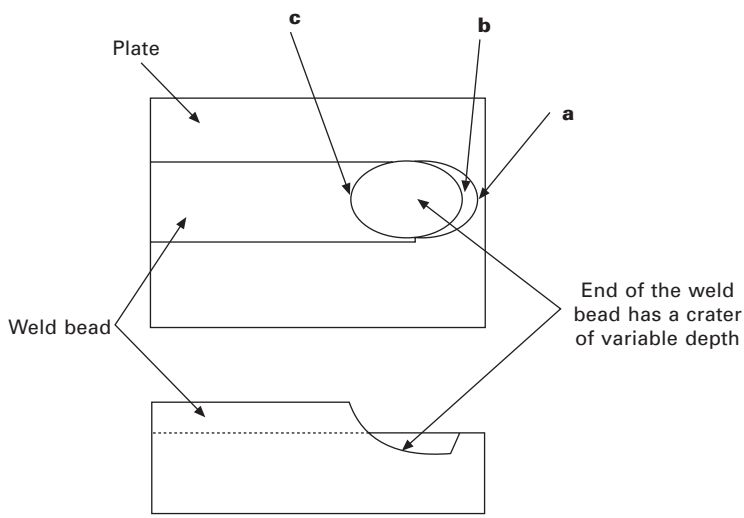

11.3 Schematic drawing of the development of a crater of variable depth in the end of the weld bead.

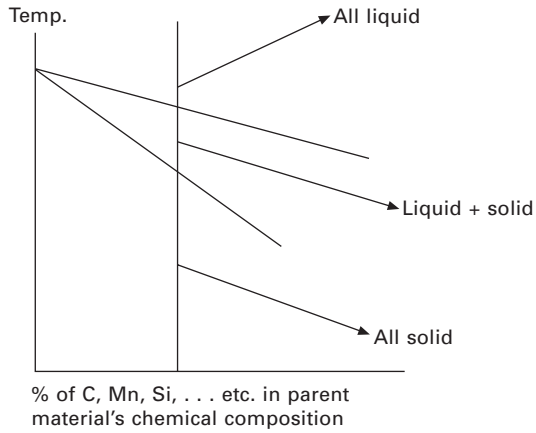

11.4 Different phases of weld metal during solidification.

Structural transformation in weld metal

Chemical changes during welding are too hard to investigate because of the different aspects of chemical composition effects. However, depending on the chemical composition of the welding electrode and the type of welding process parameters, the final microstructure and the susceptibility to cracking can be predicted. During solidification, the weld metal transforms from γ phase to α phase. This transformation can cause internal stresses because of the different grain sizes of the two phases and different crystal structures. The γ phase is face-centred cubic (FCC) crystal structure and the α-phase is body-centred cubic (BCC). The amount of this stress depends on the cooling rate and the peak temperature reached [6, 7]. This internal stress could lead to cracking in the weld metal. This type of crack is formed in different directions: longitudinally, in the direction of welding, centreline crack; or transversely, across the weld bead, traverse crack. The longitudinal cracks could be along the weld bead (continuous) or only in some positions along the weld bead (discontinuous) [4]. The transverse cracks could extend to the parent material also, as shown in Fig. 11.2.

High temperature properties of weld metal

The possibility of weld metal cracking can be determined according to its high temperature properties. Some austenitic steels and heat-resisting steels do not have adequate high temperature ductility. That causes inter-dendrite micro-cracks. Also, one of the reasons for the hot crack is the amount of transformation to the second ferritic phase [3]. This is because of the different

density of each phase. Owing to the mobility of hydrogen and consequently its segregation, the ductility of the junction area is reduced and leads to cracks in the weld metal side, under-bead cracks. These cracks appear on the fusion line between the welding metal and the HAZ of the parent material.

11.4.2 Cracking in parent material

There are different types of cracks in the parent material. The HAZ is the area of the parent material adjacent to the weld metal. It has a very high susceptibility to cracking. The common types of cracks in the parent material are traverse crack, under-bead crack and the toe crack as shown in Fig. 11.2. The main causes of cracks in the parent material are the chemical composition of parent material, the presence of hydrogen, and/or the development of internal stress.

Chemical composition of parent material

Steel is iron mixed with carbon and other elements. The percentages of carbon and other elements play a very important role in the tendency to crack after welding in the HAZ because some of these elements form hardened structures and some elements are sensitive to the cooling rate. For example, high carbon steel is highly susceptible to cracking if the weld cools in air without proper insulation. Also, in high manganese steel, during the welding process, carbon diffuses which can cause a hardened structure. Many researchers have proved that certain levels of carbon, silicon, phosphorus and nickel cause under-bead cracking due to the high temperature and a high cooling rate. Sulphur may form iron sulphide FeS at the grain boundaries. This increases the tendency for cracking. Pogodin has plotted the tendency to cracking and the percentages of sulphur, manganese and carbon in steel, as shown in Fig. 11.1 [3].

Presence of hydrogen

The presence of hydrogen is one of the causes of under-bead or root cracking. This type of crack is parallel to the weld bead and located at the hardest area in the HAZ. During the welding process, there is a very high temperature gradient between the molten pool, which has very high temperature, and the parent material, which has very low temperature. This temperature gradient in the presence of the hydrogen can give rise to parallel dissolved hydrogen in the parent material. The dissolved hydrogen tends to penetrate the crystal lattice when the parent material has cooled completely. The hydrogen atoms recombine to form hydrogen molecules in the parent material. This recombination causes very high stress in the crystal lattice and if these

stresses exceed the breaking load, cracks can be formed. The new electrodes of shielded metal arc welding (SMAW), flux-cored arc welding (FCAW), gas metal arc welding (GMAW) and gas tungsten arc welding (GTAW) have very low diffusible hydrogen levels [8].

Development of internal stresses

There are many different reasons for internal stresses. However, the main reason is the thermal cycle of the welding process. Most of these stresses are formed owing to the transformation during the cooling time. Also clamping or self-restraining in the presence of hydrogen increases the internal stresses. The appearance of martensite in the HAZ makes this area partially brittle and hard. Also the cooling conditions, as explained on page 436, can cause internal stresses.

11.5 Other welding defects

Some other defects apart from cracks may appear and affect the welding quality such as porosity, slag inclusion, lack of penetration and lack of fusion, undercut and excessive amount of spatter around the weld bead.

11.5.1 Porosity

Porosity is a cavity formed by gas entrapment as the molten weld solidifies. It can be pockets or bubbles. The common reasons for porosity are that: the base metal is contaminated with hydrocarbons which burn and produce gases; the welding electrode has condensation on it which can introduce hydrogen; the shielding gas flow rate may be too high and causing turbulence; the shielding gas is insufficient to protect the molten weld metal, owing to low gas flow rate or welding in wind; and inappropriate welding parameters lead to insufficient heat input. Porosity can be avoided by making sure that the welded joint and welding electrodes are clean, dry and not contaminated; providing enough shielding gas to the molten weld metal; running the welding process in reasonable atmosphere; and using proper welding process parameters.

11.5.2 Slag inclusions

Slag inclusions are pockets of trapped welding flux and are one of the causes of degradation fractures [9]. They appear between the parent material and the weld metal or inside the weld metal. They can be avoided by cleaning the weld metal carefully after each pass, increasing the welding current and ensuring proper joint design.

11.5.3 Lack of penetration and lack of fusion

Lack of penetration happens when the weld metal does not penetrate partially or totally into both sides of the joint. Lack of fusion is similar to lack of penetration; however it is in only one side of the joint. Both appear due to an excessively thick root face, a small root gap, a small bevel angle or a large welding electrode. These can be avoided by applying proper welding conditions and suitable joint design.

11.5.4 Undercut

An undercut is a groove at the weld toe parallel to the weld bead. It can be continuous or discontinuous and forms due to high welding traverse speed, high welding current, high welding voltage or improper welding torch angle. It can be avoided by applying proper torch angle, adjusting the electrical stick-out distance and reducing the welding traverse speed [10].

11.5.5 Excessive spatter

Spatters are very small metal balls separated from the melting welding electrode. These balls form due to large arc length or high welding voltage. Excessive spatter can be avoided by adjusting the arc length and welding voltage [11].

11.6 Resultant welding process microstructures

After the welding process, there are different zones in the joined steel. Each zone has a different microstructure, depending on its thermal history. The thermal history is the change in temperature against time and it is affected by the welding thermal conditions such as pre-heating before welding, arc welding heat input, the cooling rate after welding and the location of each zone relative to the welding process heat source [12]. The resultant welding process microstructures are the crystal rearrangements and recombination of the chemical composition elements of the steel after the welding process. They include three main zones: welding zone, HAZ and the parent material zone. The welding zone includes the weld metal zone and the fusion zone. It comprises the melted part of the parent material and the melted welding electrode (according to the welding process type). Depending on the steel alloying elements, if a point has been heated to 1450 °C (the melting point of the steel), this point has melted then resolidified. This is what occurs in the welding zone. The microstructure of the welding zone in most cases is dendritic. Curve 1 in Fig. 11.5 represents the thermal history of this point in the welding zone of low carbon steel.

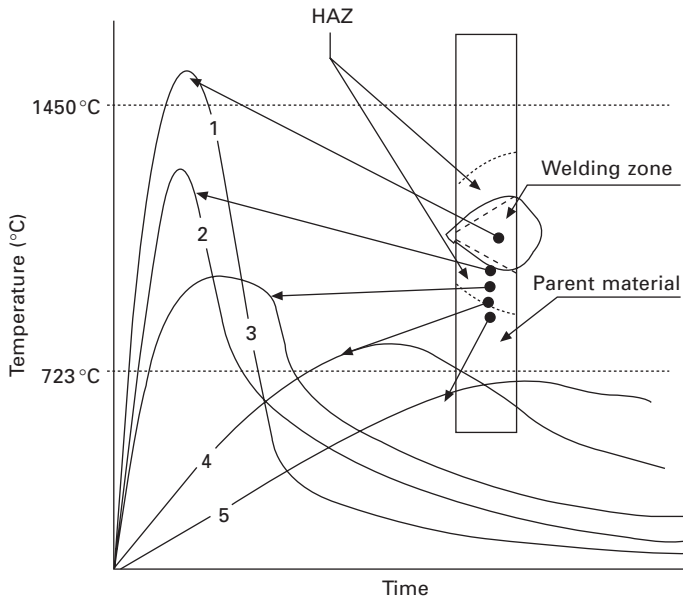

11.5 The thermal history of the different points during the welding process.

The HAZ is the zone adjacent to the welding zone. It is heated to a temperature that leads to changes in the microstructure of that part of the parent material to another microstructure without melting. The HAZ has three regions: coarse-grained heat-affected zone (CGHAZ); fine-grained heat-affected zone (FGHAZ) and inter-critical region. The coarse-grained region is the region adjacent to the welding zone. This region is heated to a temperature between 1100 and 1450 °C; it has a combination of two microstructures. The first microstructure is a pro-eutectoid ferrite and Widmanstätten side plates. This microstructure is located in the top half of the CGHAZ region close to the welding zone. The second microstructure is pro-eutectoid ferrite on the grain boundaries and the microstructure of the grain is bainite structure and/or a ferrite–bainite structure [2].

This microstructure is located in the bottom half of the CGHAZ region, close to the next HAZ region. However, the final microstructure depends on the cooling rate. If the cooling rate is fast, this region forms a martensite microstructure. Formation of the martensite increases the degradation fractures [13, 14]. Curve 2 in Fig. 11.5 represents the thermal history of the CGHAZ.

The next region in the HAZ is the FGHAZ. This region has a lower peak temperature (<1100 °C) and a slower cooling rate than the coarse-grained region. This temperature does not allow the austenite to develop properly. The $\alpha \rightarrow \gamma$ transformation during cooling produces a fine-grained ferrite–

pearlite structure. The ferrite is transformed from the grain boundary and the pearlite is transformed from the remaining austenite in the grains when it is rich in carbon. Therefore, the microstructure of the FGHAZ is fine-grained pearlite–ferrite, depending on the steel chemical composition and the welding conditions. Curve 3 in Fig. 11.5 represents the thermal history of the FGHAZ.

The inter-critical region is a narrow region between the fine-grained region and the parent material. It has a very characteristic structure. This region is heated to a temperature about 730 °C. This region has small portion of the $\alpha \rightarrow \gamma$ transformation. The lamellar pearlite of the parent material transforms to spheroidal particles of Fe_3C. Curve 4 in Fig. 11.5 represents the thermal history of the inter-critical region.

The parent material zone is the part of the welded joint which its microstructure did not change due to the welding process and this is called material as-received. Curve 5 in Fig. 11.5 represents the thermal history of the unaffected region of the parent material. However, in some research, the HAZ is considered as only the CGHAZ and FGHAZ [15].

In Fig. 11.5 curves 2, 3 and 4 represent the thermal history of the different regions of the HAZ and have been heated between 723 and 1450 °C. These regions are in the austenite (γ) area of the iron–carbon diagram and depending on the cooling rate, the final microstructure can be predicted. The austenite (γ) under 723 °C is unstable and it transforms to martensite in the case of a fast cooling rate or to a mixture of ferrite (α) and cementite (Fe_3C) in the case of a slow cooling rate. By following the temperature time transformation (TTT), the final microstructure could be martensite, bainite, pearlite or a mixture depending on the cooling rate. The martensite microstructure appears in the fusion area according to the cooling rate. Curve 5 in Fig. 11.5 was heated below 723 °C so this area will not form austenite [12].

After the welding process has been completed, different microstructures have been formed, with different mechanical properties [2, 16]. The most undesirable microstructure is martensite. The martensite is hard and stronger than the parent material; however, it is brittle and has minimal plastic capacity. Formation of martensite in the fusion zone can cause cracking due to the residual stresses that are associated with the welding process. Also, the HAZ has different grain sizes, coarse and fine grains. Coarse grains are closer to the fusion zone while the fine grains are closer to the parent material. In the case of loading of the welded parts, those different zones act as different materials and will have different load limits and failure points. The welding process should be monitored to avoid the appearance of undesirable microstructure in any zone. There is more than one method to achieve desirable microstructure from the welding process, such as controlling the thermal history of the welded joint, applying the temper bead welding (TBW) technique during the welding process or applying post weld heat treatment (PWHT).

11.7 Repair welding

Malin and Field [17] determined the guidelines for repair of large components and Bhaduri *et al*. [18] verified them in their paper about repair welding. These guidelines can be summarised as follows:

- Repair of a large component is typically of an urgent and critical nature since the failure of the component may have a devastating effect on industrial or financial activity, may jeopardise human safety and may have serious economic impact.
- In most cases, the only alternative to repair is replacement of a substantial portion of the component or even the entire component.
- In contrast to fabrication of a new component, repair is performed in the field under unfavourable conditions, such as a compressed time frame and poor environment.
- Many large components can only be repaired once without facing the risk of significant damage to the component.

Steel welded components which operate in circumstances that could lead to different types of cracking should be inspected frequently. In the case of a cracked component the decision must be made as to whether to replace or repair the part. The replacement costs are: the cost of disassembling the cracked component; the cost of the new component; and the cost of the assembly of the new component. Therefore, replacement in some cases is expensive and time consuming, especially in the case of a large and heavy component.

If the decision is made to repair the cracked component, then the organisation should investigate the availability of on-site repair. If the component cannot be repaired on-site, then it should be disassembled and moved to the workshop. In such cases, the cost of repair includes: the cost of disassembling the cracked component; the cost of the repair; and the cost of the reassembly of the component. However, if the repair period is longer than the scheduled shut-down time, then the company should have a spare of the cracked component.

All the above problems can be easily eliminated if there is a possibility of on-site repair. Therefore, on-site repair welding is a method of prolonging the equipment life and saving time and money. Repair welding is similar to any other welding processes. It needs preheating, certain welding procedures and PWHT, which is the main problem of the repair welding. The PWHT process is necessary after welding or repair to improve the internal microstructure and consequently the mechanical properties of the repair. However, PWHT is not possible for all on-site repairs. Sometimes, it is very expensive or impractical. In some cases, TBW can be applied. This chapter discusses welding heat treatment for stress relieving and the process of controlled tempering during repair welding.

11.8 Welding heat treatment

Welding heat treatment is a thermal process for relaxing the internal stresses of the weld metal and the HAZ due to the welding process. Also, it is applied to improve the microstructure of the welding zone and the HAZ, and to improve the impact and fracture properties of the welding zone and the HAZ to meet the requirements of the welding joint [19]. The heat is used for tempering or refining the microstructure grains of the welded joint especially the CGHAZ. It includes different methods. If it is applied before the welding process it is called pre-heat; if it is applied after the welding process, it is called PWHT. One or both can be applied for an improved welding microstructure, if heat treatment is required. TBW can also be considered as a welding heat treatment method.

11.8.1 Weld pre-heating method and inter-pass temperature control

The weld pre-heating method is simply heating the steel before applying the welding process. The heating could be done by putting the welded parts in a furnace, using oxy-acetylene torches, electrical strip heaters or induction heaters. Inter-pass temperature refers to the temperature of the material in the weld area immediately before the second and each subsequent pass of a multiple pass weld [20]. Pre-heating and controlling the inter-pass temperature do not change the microstructure of the parent material or the weld material before depositing the next bead; however they affect the changes in the microstructure after the welding process. The inter-pass temperature is the required temperature of the welded part at which the next bead can be deposited. Weld preheating and inter-pass temperature control are recommended for minimising the risk of cracking, for decreasing the level of diffusible hydrogen and for decreasing the cooling rate of the weld metal in the transformation range 800–500 °C as well as in the low temperature zone [21]. Applying weld pre-heating and inter-pass temperature control can minimise the risk of brittle fracture in the welded joint [22, 23]. Weld pre-heating is not necessary for all welding cases. It is recommended, for example, for the case of C–Mn steel only if the carbon equivalent exceeds 0.4% and the steel thickness is above 20 mm [19, 24]. Pre-heating should be applied uniformly because local pre-heat produces undesirable metallurgical structures away from the weld rather than eliminating them. Also, there is a limit to the pre-heating temperature to restrict the grain growth and coarsening which affects the mechanical properties of the welded joint [25, 26]. Pre-heat and inter-pass temperatures depend on: parent material chemical composition, parent material thickness, the potential for hydrogen-induced cracking (HIC) and welding heat input.

11.8.2 PWHT

PWHT is any heat treatment process which is applied to the welded joint or component of the welding process in order to achieve certain microstructure and mechanical properties for the welding and HAZ. Provost [27] classified the PWHT techniques in three groups:

1. Global heat treatments.
2. Local uniform heat treatments.
3. Local progressive heat treatments.

In global heat treatments the complete structure is uniformly heated and each point reaches the same temperature at the same moment. They are performed by using either a permanent or temporary furnace. The global treatment distributes temperature uniformly so that it has the lowest residual stress level.

In local uniform heat treatment, only the welds and the HAZ are uniformly heated and each point of the weld and the HAZ reaches the same temperature at the same moment. They are performed by using gas torches with multi-flame tips, indirect gas heating, electrical resistance heating, induction heating or exothermic heating. The major advantages of this method are: that it is cheaper than global heat treatment; it has lower energy consumption; the equipment can also be used for pre-heating and PWHT; and it can be applied during the manufacturing of the part without interruption of the manufacturing process.

In local progressive heat treatments, only the weld and the HAZ are heated with a moving heat source, resulting in different temperatures at each point of the weld. Although, the local progressive heat treatments are cheaper and use less energy than global heat treatment, it is not recommended in most cases because the temperature differences and the residual stress level will not be significantly decreased. However, it is used in limited applications in manufacturing.

The importance of PWHT encouraged a lot of researchers to investigate its positive and negative effects. Shiga *et al*. [28] reviewed the effects of PWHT on the properties of welded steel. The review, which covered the published papers from 1981 to 1994, included different steels: C–Si–Mn, micro-alloyed steels, low alloyed steels and low alloyed heat-resistant steels. The effect of PWHT on mechanical properties, tensile strength, creep strength, toughness, and fatigue strength of each steel were reported, as well as the change in the residual stress of the welded joints after PWHT.

The HAZ has two types of grain structure, coarse grains and fine [2]. The coarse-grain structure has inferior mechanical properties and is more susceptible to forming cracks than the fine-grain structure, which has superior mechanical properties, such as lower hardness and higher ductility. PWHT is required

mainly to refine the grain size of the coarse-grain area. PWHT has two procedures: post-heating and stress relieving. The welding process causes internal stresses, hardening and reduction in the ductility of the HAZ so that the PWHT is recommended. The main purposes of PWHT for the welded joints are: stabilising and improving the tensile properties at elevated temperatures; improving the resistance to deterioration with age; improving the ductility and toughness of the joint; relaxing the residual stresses in the welded joint; and minimizing the potential for HIC [19, 29–31].

One or both of the PWHT procedures can be conducted after the welding process is completed. The post-heating procedure involves heating up the steel up to 290 °C, and holding that temperature for a certain period of time. It helps to minimise the potential for HIC. The stress-relieving procedure involves heating the steel to 650 °C just below the eutectoid temperature, holding that temperature for a certain period of time and then cooling slowly. It reduces the residual stresses and consequently improves the elasticity, ductility and strength in some steels.

The PWHT process also tempers and refines the grains of the HAZ and improves the fracture toughness [6] at a certain temperature and cooling rate. The PWHT process is recommended for carbon steel components of thickness greater than 25 mm to achieve satisfactory mechanical properties and reasonable reduction of the residual stresses in the weld and the HAZ [24, 27, 30]. However, the PWHT method has some disadvantages. It can be complicated and in some cases impractical, such as in the case of very large components. It is an expensive process based on the site arrangement and the labour cost. Some steels, when heated to the required PWHT temperature suffer considerable loss of mechanical properties and as a result new supports are required to the welded structure [24, 29, 32]. In some cases, PWHT needs a long time (a few days) to be completed and should be supervised around the clock, which makes the process expensive.

11.9 Techniques for tempering and grain refinement of the HAZ without PWHT

There are three techniques for tempering and grain refinement of the HAZ without PWHT. These techniques are: the conventional buttering technique, the half-bead technique and temper bead technique [25, 33]. These techniques are alternative processes to PWHT [34]. The mechanism of bead tempering and grain refinement is adding heat at a certain rate, maintaining the heat for a certain time and then cooling to room temperature at a certain rate. A similar result to the PWHT mechanism can be achieved by using the two-layer deposition approach [24, 25].

These tempering and grain refinement techniques came from the two-layer approach. This approach is used to produce repair welding without

PWHT [33, 35–37]. The main concept of the two-layer approach is using the associated heat of the deposition of the second layer of welding to treat the microstructure of the HAZ of the first layer [24, 33, 38], as shown in Fig. 11.6 [33].

11.9.1 Buttering technique

In the buttering technique, after laying the first layer of the repair welding, this layer is removed totally. The steps of the buttering technique are shown in Fig. 11.7. The coarse grain structure of the removed layer (the first layer) will be refined by the heat input of the second deposited layer. The buttering method is time and material consuming. The removal of the first layer should be done carefully to avoid any removal of the parent material. Also, deposition of the second layer needs to be applied carefully so as to avoid over-penetration from second layer HAZ to the first layer HAZ.

11.9.2 Half-bead technique

The half-bead technique is similar to the buttering technique except that instead of removing the first welding layer totally, only half of it is removed. In the case of using manual metal arc welding (MMAW), for the first layer the electrode diameter is smaller than that of the second layer, pre-heat is applied, inter-pass is applied and 50% overlapped beads. The values of the electrode sizes and these temperatures depend on the chemical composition of the parent material, the weld metal and the welding process conditions. The welding deposition process is continued layer after layer until the repair welding area is full. An additional layer should be deposited carefully to the top of the welding repair layers. This additional layer should not touch the parent material surface [25, 31, 39–41].

Figure 11.8 shows the steps of the half-bead technique. The disadvantages of this technique are that it is time and material consuming (as with the buttering technique) and it is not easy to control the removal of only half of the first layer [25].

11.9.3 TBW technique

The TBW technique employs the main concept of the two-layer deposition technique for more than two layers. It has been used successfully for a number of repairs in the United States, Canada and Germany [24, 42, 43], by using the MMAW process or the SMAW process, and its use is accepted and specified by the ASME Boiler and Pressure Vessel codes [44]. The refinement reaches 100% in some cases [38], and 85% in other cases of the CGHAZ of the first layer [24, 33].

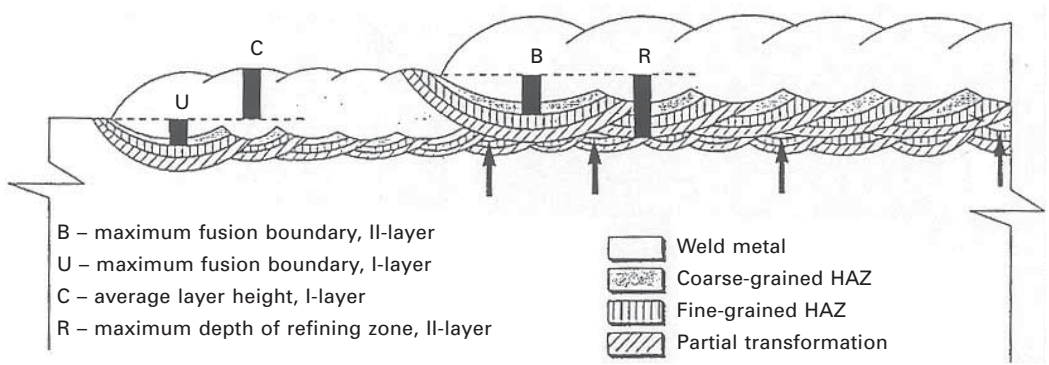

11.6 Two-layer section shown schematically exhibiting approximately 85% refinement of the first layer coarse-grained HAZ by the second layer.

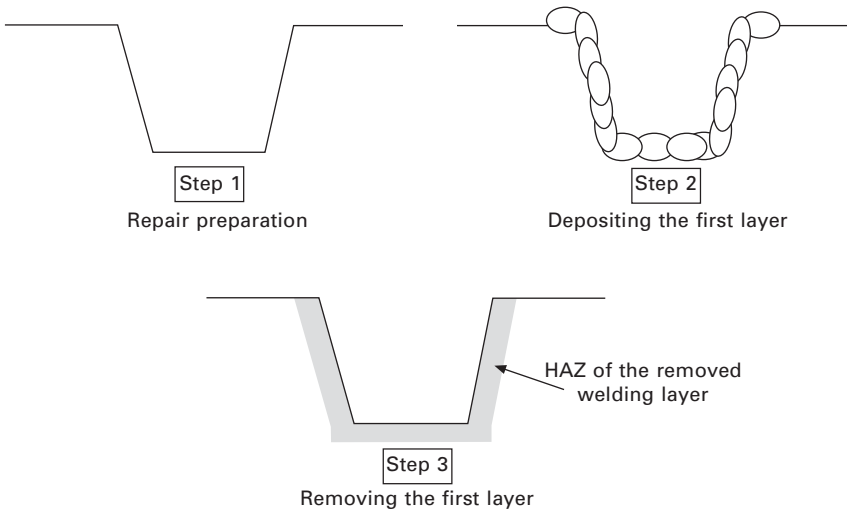

11.7 Steps of buttering technique.

11.9.4 Earlier work using the TBW technique

Must of the earlier work was done using MMAW with different electrode sizes for each layer according to the resultant bead geometry. The material of the repaired components was C–Mn or Cr–Mo–V steels.

Alberry [38] performed a simple test to reveal the level of two-layer refinement. This test applied the MMAW process and the base material was mild steel. A series of two-layer weld deposits was produced by four welders. The first layer was deposited using 3.25 mm electrodes whereas 4 mm electrodes were used for depositing the second layer. Three welders achieved 100% refinement for the HAZ of first layer and the fourth welder achieved 96%. The HAZ's grain size greater than 50 μm is classed as coarse grain. The mathematical relationship between the bead geometry of the first layer and the second layer to achieve 100% refinement for the HAZ of the first layer and avoiding any overpenetration has been summarised as follows:

Maximum fusion boundary depth bead 2	<	Maximum fusion boundary depth bead 1 + Average layer produced by bead 1	<	Maximum depth of refining zones of bead 2

The average layer height produced by bead 1 was estimated depending on the bead geometry of the single bead and the percentage of the overlap between the passes of the first layer.

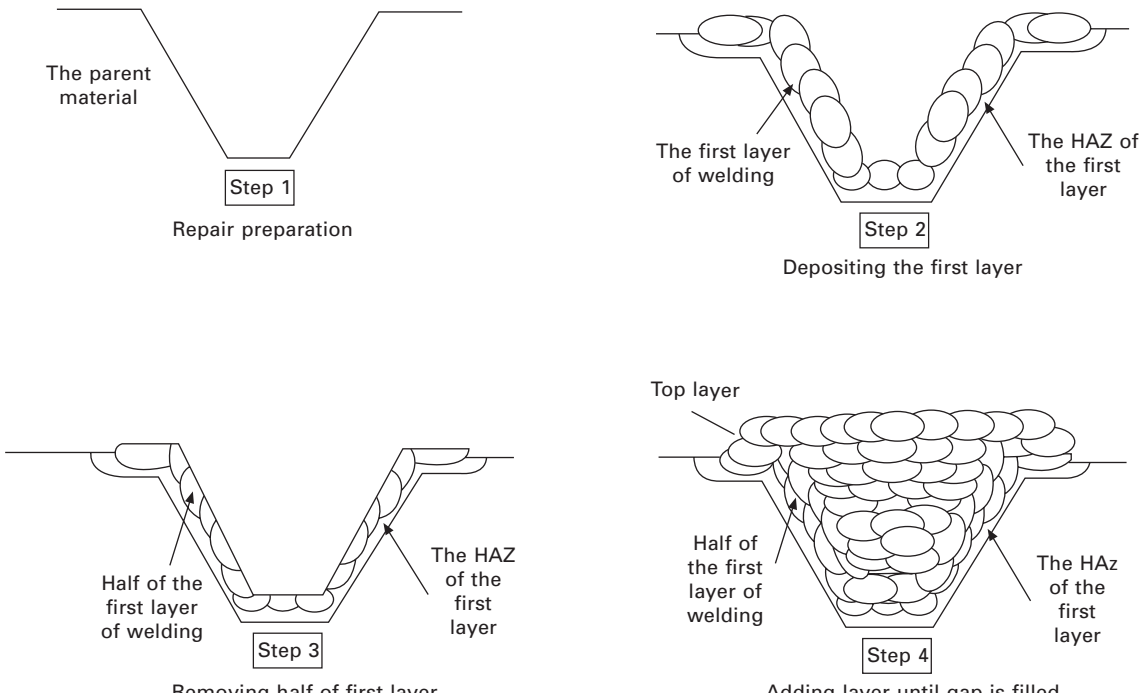

11.8 Steps of half-bead technique.

Kussmaul *et al*. [45] reported that the depression at the nozzle corner (Reactor Pressure Vessel of decommissioned HDR (Heissdampfreaktor) near Frankfurt) caused by the trepan removal had been repaired by TBW without stress relief heat treatment, similar to the half-bead technique of the ASME Boiler and Pressure Vessel Code [46]. At that time, they considered their positive experience would be helpful in the future of dealing with any cases of cracking in thick-walled diameter vessels which require repair welding when a post-weld stress relief heat treatment is not possible.

The repair was performed using the SMAW process. The repair region was pre-heated to 160 °C. The first layer was applied using a 2.5 mm diameter electrode, then half of the thickness of this layer was removed similar to the half-bead technique. The filler layers were performed using a 4 mm diameter electrode. Jones [33] showed that the importance of applying repair welding without PWHT comes from the necessity of repair or modification of thick steel components where it is not possible to repeat the original PWHT. This report depends on Alberry's previous work [38] in the two-layer approach and describes an application of that approach to achieve HAZ microstructure refinement in positional MMAW in welding of thick sectioned C–Mn steel plate. Two types of MMAW process electrodes were used, E7016 and E 7018. Two sizes of electrodes of each type were used, viz. 2.5 mm or 3.25 mm electrode for the first layer and 4 mm for the second layer. Pre-heating 100–150 °C and inter-pass 150 °C were applied to extend the depth of the refined zone. In this work, the refinement level of the HAZ reached 65–90%. The refinement of 100% was not achieved because welding conditions used to deposit the second layer did not penetrate sufficiently to overlap the first layer HAZ.

Edgley and Pitrun [24] reported the TBW repair of the Hazelwood steam drums in Victoria, Australia. Hazelwood power station has eight 200 MW generating units. Each boiler has a 21 m long cylindrical pressure vessel; the outer diameter is 1.7 m and it is made of 0.34%C–steel (similar composition to ASTM A105). MMAW was used in this repair. Preliminary welding tests were conducted to find out the weld bead geometry of 2.5 mm and 3.25 mm electrode diameter. Subsequently, the two-layer approach was applied with bead overlap of 50%. The results showed that 90–95% of HAZ grain refinement had been achieved. The maximum value of the hardness in the isolated unrefined areas was 328 HV using 5 kg load and typically HAZ hardness was 200–220 HV using 5 kg load in the fully refined area (according to ASME XI criteria the maximum acceptable hardness is 350 HV).

Allen [47] described the weld repair carried out by PowerGen to a cracked steam drum downcomer nozzle weld in coal-fired 500 MW at Cottam Power Station, UK. Depending on previous work on Cr–Mo–V steel for applying the two-layer approach [36, 48], a repair to remove a large lamellar tear defect in the drum shell adjacent to a set-on downcomer nozzle weld was

carried out successfully. The MMAW process was used. The drum outer diameter is 1.74 m and 108 mm thickness.

The Pressure Vessel Research Council (PVRC) and Welding Research Council (WRC) publish the *WRC Bulletin 412* [49]. This bulletin can be considered as the best source of information about controlled deposition and temper bead techniques. The controlled deposition technique uses the idea of distributing the welding heat in a controlled way to achieve proper mechanical properties and reasonable microstructure for the HAZ. *WRC Bulletin* 412 contains 14 papers covering some examples of repairs using controlled deposition and TBW technique, including the following.

Doty [34] showed that the support data from several major research programmes resulted in revised National Board Inspection Code (NBIC) rules permitting additional ferritic materials to be repair welded without PWHT. He showed the codes and their changing of alternatives to PWHT of different types of steel (C, C–Mn, C–Mn–Si, C–0.5Mo and 0.5Cr–0.5Mo steels) since 1977.

Ibarra [31] reviewed the experience of repair welding of pressure vessels in the petroleum industry. The TBW technique was used successfully to repair carbon steel (P-1), C–0.5Mo steel (P-3), 1.25Cr–0.5Mo steel (P-4) and 2.25Cr–1Mo steel (P-5A).

Lundin [43] overviewed the results from PVRC and WRC on temper bead technique. This study investigated the improvement in mechanical properties (hardness and fracture toughness) and the HAZ's microstructure (the percentage of refinement in the CGHAZ) in the case of weld repair without PWHT. This study was conducted on three different steels (C–Mn, 1.25Cr–0.5Mo and 2.25Cr–1Mo steels).

Friedman [50] demonstrated in his paper the work done by Edison Welding Institute (EWI) and The Welding Institute (TWI), Cambridge, in the application of controlled deposition repair welding technique in repair of 1.25Cr–0.5Mo and 2.25Cr–1Mo steels using SMAW. It was concluded that using SMAW with this technique could lead to a high level of refinement (92.9–96.8%) in the CGHAZ and the mechanical properties of the HAZ are comparable with the parent material (as suggested in the Charpy results).

Higuchi *et al*. [51] applied the TBW technique to dissimilar welded joints without PWHT. They showed that the maximum hardness of the HAZ of TBW was 340 HV and the maximum hardness of the HAZ of PWHT was 360 HV. The histograms of the comparison between the HAZ of the TBW technique and the HAZ of the PWHT are shown in Fig. 11.9. It is shown that the hardness of the HAZ of TBW technique was between 260 and 340 HV whereas the range of the HAZ of the PWHT was between 230 and 360 HV. The highest frequency of the HAZ of the TBW technique was 20 at 300 HV where for the PWHT it was 14 at 305 HV (the ASME recommendation is that it does not exceed 350 HV). They also concluded that the impact properties

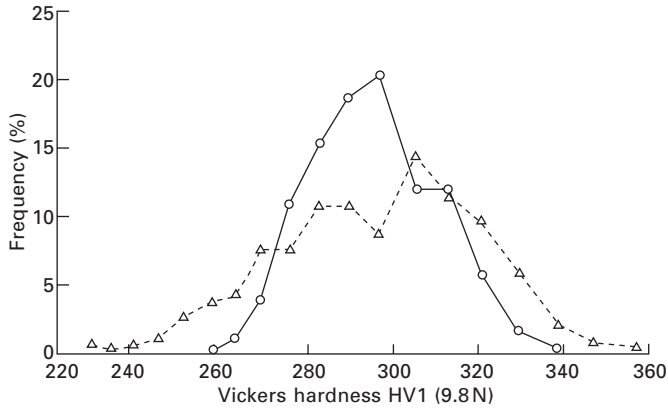

11.9 Comparison of hardness histograms in HAZ produced by TBW technique and normal welding with PWHT (○, temper bead welding, △, PWHT).

of the HAZ of the TBW technique were superior to that of the HAZ of the PWHT. The base metals were low alloy steel and austenitic stainless steel and TIG welding process was applied.

Hirano *et al*. [52] established a method for TBW repair using Inconel 82 filler material for as-quenched low alloy steel plate (SQV2A). The chemical composition percentages of the steel plate were: C 0.17, Si 0.23, Mn 1.42, P 0.005, S 0.003, Ni 0.64 and Mo 0.51. They plotted the relationship between the bead geometry, the heat input and the hardness along the different associated zones.

Gandy *et al*. [53] examined TBW using the SMAW process without using grinding between passes from both a metallurgical and a mechanical standpoint. The material used in this study was nuclear-carbon and low-alloy steels. Data were collected from several industry testing programmes such as Ontario Power Generation, Alliant Energy Group, Electric de France EPRI and TU Electric. The study demonstrated that the measured toughness of the HAZ is greater than the base material at the same temperature and excellent mechanical properties are obtained in the HAZ of SMAW temper bead repair. Also the study showed a greater improvement occurred in the toughness of the HAZ in the case of no grinding (TBW) compared with the half-bead case on the same parent material.

Lant *et al*. [25] prepared a review of weld repair procedures for low alloy steels designed to minimise the risk of fracture cracking. In this review the authors showed that the preparation of the weld repair area should be clear from any previous HAZ or residual stresses. The weld repair electrodes should be selected carefully because in most cases of the weld repair process MMAW is used while the manufacturing could be done using another welding

process. Then they expressed the importance of pre-heat and PWHT. They emphasised the significant cost and time advantages in the case of performing weld repair procedure which has the required microstructure and mechanical properties without PWHT. This study showed the advantage of the successful combination of the TBW technique and automated welding in repairs which had to be conducted remotely, for example in the nuclear industry (based on previous work by Babcock & Wilcox [54] and Gandy *et al*. [55]).

11.9.5 Nickel-based welding

Some researchers have demonstrated the application of the nickel-based welding technique (using an electrode with high nickel content) as a type one of repair welding without PWHT. Nickel-based welding is known as cold welding. Lant *et al*. [25] explained that the high nickel weldment is free from HIC; it has a high fracture toughness and low residual weld stresses [56–58]. High fracture toughness and low residual weld stresses have been reported in references [57–59] for nickel-based welding using a small electrode size and low heat input. This technique was used successfully for ferritic material and dissimilar metal welds [51].

Mitchell [59] reported the use of nickel-based wire for FCAW for cold welding. It was used for Cr–Mo–V and 2.25Cr–1Mo components. He predicted that the repair applications for cored wires in the power industry will grow significantly and the use of cored wires will provide clear benefits in terms of cost and time. This study was continued [22, 60].

11.10 Conclusions

Great savings in time, money and heat energy can be achieved by applying the TBW procedure which provides high degree of refinement of microstructure in the HAZ. This technique therefore allows weld repair without PWHT. The welding process which is most widely employed for TBW is MMAW. The FCAW process achieves further improvement in welding repair due to the significant reduction in repair time and higher quality due to better shielding in field conditions.

The merging of the benefits of the TBW technique and the FCAW process in the repair of carbon steel components provide a more cost-effective method of weld repairs to the industry than the other commonly known TBW using MMAW process. Also, applying the TBW technique using the FCAW process has a lot of benefits economically and environmentally. These benefits, without going into any detail, are wide and varied. They are an added bonus to the TBW technique and FCAW process.

11.11 References

1. Robert W, Messler J. *Principles of Welding Processes, Physics, Chemistry and Metallurgy*: USA: Wiley-Interscience; 1999.
2. Lancaster JF. *Metallurgy of Welding*. 6th ed. Cambridge, UK: Abington Publishing; 1999.
3. Seferian D. *The Metallurgy of Welding*: London: Chapman and Hall; 1962.
4. American Welding Socity, *Welding Inspection*. New York: AWS; 1968.
5. What's ailing that weld? *Welding Journal* 1997; **76**(8): 45–48.
6. Easterling KE. *Introduction to the Physical Metallurgy of Welding*. 2nd ed. Oxford; Boston: Butterworth Heinemann; 1992.
7. Radaj D. *Heat Effects of Welding*. New York: Springer-Verlag; 1992.
8. Doty WD. Keynote address challenges and solutions in repair welding of ferritic materials. *WRC Bulletin* 1996; **412**: 1–2.
9. Knott JHT. Effect of reheating on microstructure and toughness of C–Mn weld metal. *Material Science* 1983; **17**: 45–54.
10. Hicks J. *Welded Design, Theory and Practice*. Cambridge, UK: Woodhead Publishing Ltd; 2000.
11. Cullison A. Get that spatter under control. *Welding Journal* 1999; **78**(4): 43–45.
12. Beddoes J, Bibby MJ. *Principles of Metal Manufacturing Processes*; Bristol: Arnold; 1999.
13. Zhang LP, Davis CL, Strangwood M. Effect of TiN particles and microstructure on fracture toughness in simulated heat-affected zones of a structural steel. *Metallurgical and Material Transactions A* 1999; **30**: 2089–2096.
14. Kim BC, Kim NJ, Lee DY. Microstructure and local brittle zone phenomena in high-strength low-alloy steel welds. *Metallurgical and Material Transactions A* 1991; **22A**: 139–149.
15. Soboyejo WO, Crompton J, McGaughy T, Orth F. An investigation of the fracture behavior of coarse-grained heat-affected zones in A707 steel welds. *Metallurgical and Material Transactions A* 2001; **32A**: 533–545.
16. Patchett BM. Control of microstructure and mechanical propeties in SA and GMA weld metals. *Proceedings of an International Symposium on Welding Metallurgy of Structural Steels*, Colorado 1987: 189–199.
17. Malin V, Field SF. A balance approach to repair of large structures by welding. *Welding Journal* 1992; **71**: 63–72.
18. Bhaduri AK, Albert SK, Ray SK, Rodriguez P. Recent trends in repair and refurbishing of steam turbine components. *Sadhana* 2003; **28**(3 & 4): 395–408.
19. Hrivnak I. A review of the metallurgy of heat treatment of welded joints. *International Journal of Pressure Vessels and Piping* 1985; **20**: 223–237.
20. Funderburk RS. The importance of interpass temperature. *Welding Innovatio* 1998; XV (1).
21. Kuebler R, Pitrun M, Pitrun I. The effect of welding parameters and hydrogen levels on the weldability of high strength Q&T steel welded with FCAW consumable. *Australasian Welding* 2000; **45**(First Quarter): 38–47.
22. Mitchell KC, Brett SJ. Review of 'Cold Weld' Repair Applications. *3rd international HIDA and Integrity Conference*, 2000.
23. Funderburk RS. Fundamentals of preheat. *Welding Innovatio* 1997; XIV (2).
24. Edgley JS, Pitrun M. The temper bead weld repair of the Hazelwood steam drums. In: *Pressure Vessels and Pipework, Failures, repairs & life Assessment II*; 1993 27–28 April, 1993; Sydney, Australia; 1993.

25. Lant T, Robinson DL, Spafford B, Storesund J. Review of weld repair procedures for low alloy steels designed to minimise the risk of future cracking. *International Journal of Pressure Vessels and Piping* 2001; **78**: 813–818.
26. Allen DJ. Cold repair – development and application. *2nd International EPRI Conference and Vendor exposition*; May 21–24; Dayton Beach, Florida; 1996.
27. Provost W. Local uniform heat treatment and its effects on the toughness of welded C–Mn presure vessel steel. *International Journal of Pressure Vessels and Piping* 1984; **16**: 81–99.
28. Shiga C, Gotoh A, Kojima T, Horii Y, Fukada Y, Ikeuti K, *et al*. State of art review on effect of PWHT on properties of steel weld metal: *IIW Section IX working program*; 1995.
29. Smith C, Pistorius PGH, Wannenburg J. The effect of a long post weld heat treatment on the integrity of a welded joint in a pressure vessel steel. *International Journal of Pressure Vessels and Piping* 1997; **70**: 183–195.
30. Funderburk RS. Postweld heat treatment. *Welding Innovatio* 1998; **XV**(2).
31. Ibarra SJ. Weld repairs without PWHT in the petroleum industry. *WRC Bulletin* 1996; **412**: 12–15.
32. Nawrocki JG, DuPont JN, Robino CV, Marder AR. The stress-relife cracking susceptibility of new ferritic steel – Part 2: Multiple-pass heat-affected zone simulations. *Welding Research Supplement* 2001: 18-s–24-s.
33. Jones RL. *Development of Two-layer Deposition Techniques for the Manual Metal Arc Repair Welding of Thick C–Mn Steel Plate Without Post Welding Heat Treatment*. Welding Institute; 1987. Report No. 335.
34. Doty WD. History and need behind the new NBIC rules on weld repair without PWHT. *WRC Bulletin* 1996; **421**: 3–8.
35. Alberry PJ, Rowley T. *Repair Of Ince 'B' Power Station Reheat Pipework*. CEGB; 1978. Report No. R/M/N 982.
36. Alberry PJ, Meyers J, Chew B. An improved welding technique for HAZ refinement. *Welding and Metal Fabrication* 1977; **45**(9): 549–553.
37. Alberry PJ, Jones KE. Two layer refinement techniques for pipe welding. *Second International Conference on Pipe Welding*; November; London, UK: The Welding Institute; 1979.
38. Alberry PJ. Simple test reveals level of two-layer refinement. *Welding and Metal Fabrication* 1981; **49**(9): 543–547.
39. United States National Board Inspection Code. National Board of Boiler and Pressure Vessel Inspectors, Columbus, Ohio. 1989–1995.
40. ASME Boiler and Pressure Vessel code. Section XI Rules for service inspection of nuclear power plant component, Paragraph IWA-4513. Repair welding procedures A-SMA; 1992.
41. Gandy DS. Temper bead welding of P-Nos 5 and 5. *International Conference on Integrity of High Temperature Welds*; 3–4 November; Nottingham, UK; 1998.
42. Lau TW, Lim, G.C P. Development of controlled deposition repair welding procedures at Ontario Hydro. *WRC Bulletin* 1996; **412**: 35–42.
43. Lundin CD. Overview of results from PVRC program on half-bead/temper-bead/controlled deposition technique for improvement of fabrication and service performance of Cr–Mo Steel. *WRC Bulletin* 1996; **214**: 16–26.
44. Lampman S, ASM International. *Weld Integrity and Performance: A Source Book Adapted from ASM International Handbooks, Conference Proceedings, and Technical Books*. Materials Park, OH: ASM International; 1997.

45. Kussmaul K, Blind D, Jansky J. Influence of repair welding on cyclic thermal shock behaviour of a RPV nozzle corner. *International Journal of Pressure Vessels and Piping* 1986; **25**: 89–109.
46. ASME. ASME Boiler and Pressure Vessel Codes, Section XI, Repair Procedures, IWB-4000. New York; 1983 edition.
47. Allen DJ. Weld repair of steam drum downcomer nozzle cracking in coal-fired power plant. *Welding and Metal Fabrication* 1995: 226–228.
48. Allen DJ. Modelling and control of weld structure in power plant repair. In: International conference on modelling and control of joining processes; 1993 December; Orlando, Florida: AWS; 1993: 281–289.
49. Pressure Vessel Research Council and Welding Research Council. *WRC Bulletin 412* 1996.
50. Friedman LM. EWI/TWI controlled deposition repair welding procedure for 1.25Cr–0.5Mo and 2.25Cr–1Mo steels. *WRC Bulletin* 1996; **412**: 27–34.
51. Higuchi M, Umemoto T, Matsusita A, Shiraiwa T. Development of temper bead technique applied to dissimilar welded joints of nuclear pressure vessels. *WRC Bulletin* 1996; **412**: 77–86.
52. Hirano T, Hasegawa F, Sakamoto H, Kishida K. Temper-bead welding without pre- or post-heat treatment. *ASME, Pressure Vessels and Piping Division* 1999; **395**(Operations, Applications and Components): 47–53.
53. Gandy D, Smith R, Lau M. SMAW Temperbead Weld Repair Without Grinding. *Transactions, SMiRT 2001*; **16**: paper no. 2052.
54. Babcock & Wilcox. *Repair Welding of Heavy Section Steel Components in LWR*. EPRI Report NP-3614, volume 1 and 2; 1984.
55. Gandy GW, Findlan SJ, Childs WJ. Repair welding of SA-508 class2 steel using 3 layer temper-bead approach. *ASME Conference on Fatigue Fracture and Risk*; San Diego; 1991: 117–220.
56. Brett SJ. Methodology for the use of weld repairs without post-welding heat treatment on creep resisting steels. *BALTICA III*; June 6–8; Helsinki, Finland; 1995: 63–78.
57. Zemzin VN, Bagramova TI, Boyeva AV, Titner ZK, Dimetrieva GK, Biryukov MV. *Using High Nickel Electrodes for Repair Welding of Defects in Cast Casing Components for Steam Turbine*. Leningrad: Leningrad Organisation of the Znanie Association; 1974.
58. Schron RZ, Zemzin VN, Ehrenburg BS, Bukin YA, Titner ZK. An analysis of the damage to cast turbine casing components and the effectivness of repair welds to them. *Teploeneretica* 1987: 7–16.
59. Mitchell KC. Repair welding in power industry using cored wires. *Power Station Maintenance: Profitability through Reliability*, paper no. 452, IEE; 30 March – 1 April; United Kindom; 1998: 138–143.
60. Mitchell KC, Brett SJ. Review of 'cold weld' repair applications. *OMMI, Innogy, Operations and Engineering* 2003; **2**(1).

12

Measurement of residual stresses in weld repairs in steels

J PRICE, Monash University, Australia, A M PARADOWSKA, Rutherford Appleton Laboratory, UK and T FINLAYSON, University of Melbourne, Australia

Abstract: Welding residual stresses have important consequences on the performance of engineering components. Residual stresses are more likely to be significant in repair welds since they are small, more highly constrained and faster cooling than large construction welds. In repair welds the loss of integrity due to residual stress can be even more important that in welds in general since the area being repaired has already failed probably due to high loadings.

In the research presented in this chapter the neutron diffraction technique was used to investigate the residual stress distributions in carbon steel components with weld repairs. Two full penetration weld repairs were made using (a) the stringer bead and (b) the temper bead weld techniques in 25 mm thick plate. The welds were not post-weld heat treated. The focus of the measurements is on the values of the sub-surface and through-thickness strain/stress variations near the middle and the toe of the weld. The measurements were compared with current fitness-for-purpose approaches, such as BS7910 and R6, showing that these approaches underestimated and overestimated the stresses in various regions. The experimental results showed that both processes had high residual stresses particularly through the thickness. From the point of view of residual stress the temper bead weld appears no better than the stringer bead weld.

Key words: residual stress, neutron diffraction, repair welds, fitness-for-purpose codes, temper bead welding.

12.1 Introduction

In welding, residual stresses (RS) are formed in the structure as the result of differential contractions which occur as the weld metal solidifies and cools to ambient temperature [1]. The tensile stresses can have significant effects on the susceptibility of a material to degradation mechanisms such as fatigue, corrosion, fracture resistance and creep.

Assessment of the integrity of pressure and structural components is becoming increasingly important for both economic and safety reasons. In particular, welding repairs have increasingly become a structural integrity concern for ageing pressure vessel and piping components. The need for an effective welding technique is vital and becomes more evident as welding repairs are increasingly used in ageing pressure and structural components.

As such, both the repair procedure and the subsequent safety assessment, such as BS 7910 [2] and R6 [3], require a better understanding of the welding effect on structural components, which was reported by Zinn and Scholtes [4]. It has been demonstrated by Dong and Brust [5], Veiga *et al*. [6] and Dong *et al*. [7] that the residual stress distribution of repair welds can be drastically different from that of an original weld. Reduction of continuously applied stresses is desirable [8]. Residual stresses in weld joints can be reduced by heat treatment [9] or by mechanical stress relieving [10]. A survey presented by Gandy *et al*. [11] on repair of thick-walled structures in industry indicated that only 30% of the organisations covered by the survey appeared to use post-weld heat treatment (PWHT). The review also highlighted that 40% of all repairs cracked again after return to service.

The welding-procedure-related parameters and restraint condition appear to be more important in analysing repair welds than in initial fabrication welds. In many cases, repair welds are highly restrained and rapidly cooled and are thus likely to have high residual stresses.

Stringer welding (SW) and temper bead welding (TBW) techniques are commonly used in industry. SW represents a conventional repair where the cavity is filled up following an appropriate number of passes (stringers), and then when required by code, PWHT treatment is applied. TBW involves placing a layer of smaller beads on the parent metal and then welding with the intention of tempering earlier passes with late passes. The top crown (or reinforcement), where the last passes are made, is ground off. It is claimed that the TBW technique can be used when PWHT cannot be applied. In effect, the strategic sequencing and placement of the weld beads provides localised PWHT of preceding passes, thus achieving substantial tempering of the total weldment. Recent research [12–14] has shown that the TBW technique can provide the required properties of the weld without PWHT. However, detailed non-destructive measurement of the residual stresses in either SW or TBW has as yet not been reported.

As pointed out by Bouchard and Withers [15], in order to assess and predict the influence of residual stresses on integrity it is essential to quantify accurately the residual stress field. The direct measurements of residual stress [16] can be either semi-destructive (e.g. hole drilling and indenting [17]), non-destructive (X-ray (laboratory or synchrotron) or neutron diffraction (ND) [18] and ultrasonic [19]). However, ND is outstanding in its ability to obtain RS non-destructively deep within the interior of components, in three dimensions, in small gauge volumes and in thick specimens.

Numerical techniques have been developed to estimate residual stresses and good correlation between theory and experiment can now be obtained even on complex weld geometries [9,11]. However, a major review still determined that weld RS need more detailed investigation to develop the required knowledge, particularly for highly constrained repair welds [20]. In

recent work, the authors of this paper with others have examined the detailed comparison of experimental measurement [21] with theoretical estimates at the fine level [22].

Non-destructive measurement is a key issue in the confirmation of the theoretical work. In this study, ND has been used to establish the residual stress in full-penetration, butt-weld repairs carried out by SW and TBW techniques. The measurements were taken in the as-welded condition. The focus of the measurements is on the values of the sub-surface and through-thickness strain/stress variations near the middle and the toe of the weld. The RS are discussed and compared with the current safety assessment procedures, BS 7910 [2] and R6 [3].

12.2 Experimental procedure

12.2.1 Materials properties

The parent material used in this study was a carbon steel (AS 1548-7-460) [23]. The chemical compositions of the material and weld metal are shown in Table 12.1. Two weld repairs were manufactured. The dimensions of the parent metal plates were: length 250 mm, width 150 mm and thickness 25 mm.

Tensile properties of the parent material were examined in accordance with Australian Standard AS 1391 – 1991 [24] and the weld metal tensile properties were examined in accordance with Australian Standard AS 2205.2.2 – 1997 [25]. Materials were tested at ambient temperature. The test specimens were taken from each weld in the longitudinal direction (y), i.e. parallel to the weld. The average mechanical properties of the materials used in investigation are shown in Table 12.2.

Table 12.1 Chemical compositions of the parent and weld metal (in wt%)

	Parent metal Max.	Weld metal Max.
C	0.15	0.10
Mn	1.35	1.70
Si	0.2813	0.68
S	0.01	0.02
P	0.02	0.02
Ni	0.02	0.05
Cr	0.02	0.03
Mo	0.002	0.04
V	<0.01	0.04

Table 12.2 Measured room temperature mechanical properties (two for each case)

	Mechanical properties (according to ASTM A370 and AS 1391)					
	Yield stress 0.2% proof stress (MPa)		Tensile strength (MPa)		Elongation (%)	
Parent metal AS 1548-7-460	430	430	530	520	30	30
Weld metal (tested)	470	460	600	580	29	30

12.2.2 Welding procedure

Experimental work was carried out on two different repairs manufactured using SW (Sample I) and TBW (Sample II) techniques. A schematic illustration of the preparation and experimental procedure is shown in Fig. 12.1. The welds were produced using a flux-cored arc welding (FCAW) process. The specimens were mounted (tack-welded to achieve a restrained condition) under an automatic-speed-controlled welding torch. The welding parameters are shown in Table 12.3.

Both samples comprised a 60° preparation butt weld with a 3 mm gap between the plates (Fig. 12.1a). In the first sample, Sample I, 14 beads were deposited to fill the weld. The root bead had a heat input of 0.70–0.81 kJ/mm and the filling beads received 1.04–1.26 kJ/mm. The sequence of deposited beads is shown in Fig. 12.1(b).

The second sample, Sample II, contains two layers (Figs 12.1c and 12.2) to achieve TBW. The procedure has been proven as an appropriate one to achieve a tempering effect and this was confirmed by investigation of microstructure, hardness and impact [13,14].

The first layer was deposited manually with the lower heat input of approximately 0.70–0.81 kJ/mm and containing 18 beads, as shown in Figs 12.1(c) and 12.2(a). The heat input of the filling layers was 1.04–1.26 kJ/mm. After successive welding, attempts were made to remove the extensive reinforcement in the middle of the samples by grinding them flat, as is shown in Fig. 12.2(b). The welding parameters are shown in Table 12.3. There was pre-heat of 100 °C and an inter-run temperature of less than 150 °C was applied to both samples. There was no PWHT.

12.3 Residual stress measurement

Under tensile (or compressive) stress, the lattice spacing, d_{hkl}, for lattice planes *hkl* in individual grains, expands (or contracts). At constant wavelength,

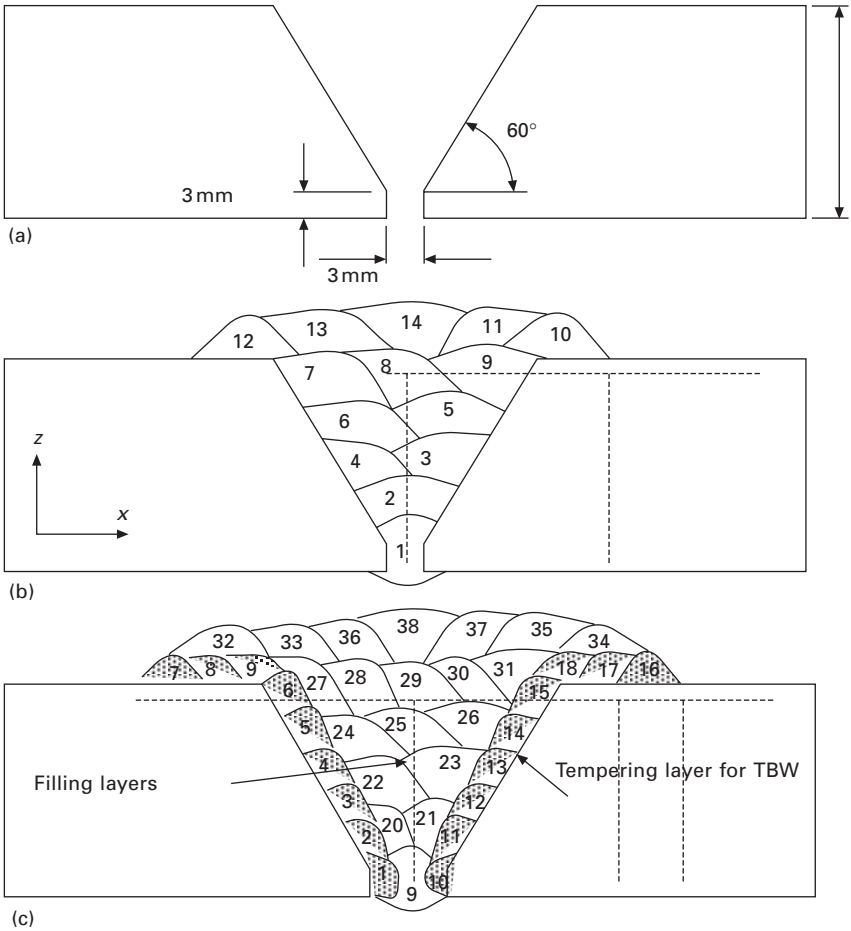

12.1 Schematic illustration of: (a) preparation for full penetration repairs using (b) stringer weld (Sample I) and (c) temper bead (Sample II) techniques. (The dotted line represents the line scans for ND measurements.)

Table 12.3 Parameters used in the experimental work

Sample I	Root run (1)	Runs (2–14)
Sample II	Temper beads runs (1–18)	Runs (19–38)
Electrode diameter (mm)	1.6	1.6
Current range (A)	260–280	260–280
Voltage range (V)	28–30	28–30
Traverse speed (mm/min)	480	360
Wire feeding speed (mm/min)	3600	3600
Electrode stick-out distance (mm)	20	20
Gas flow rate (l/min)	20	20

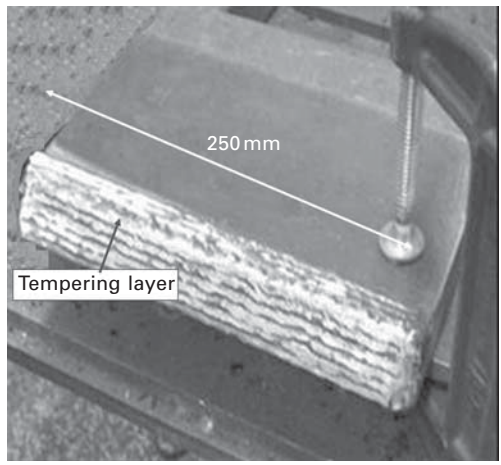

(a)

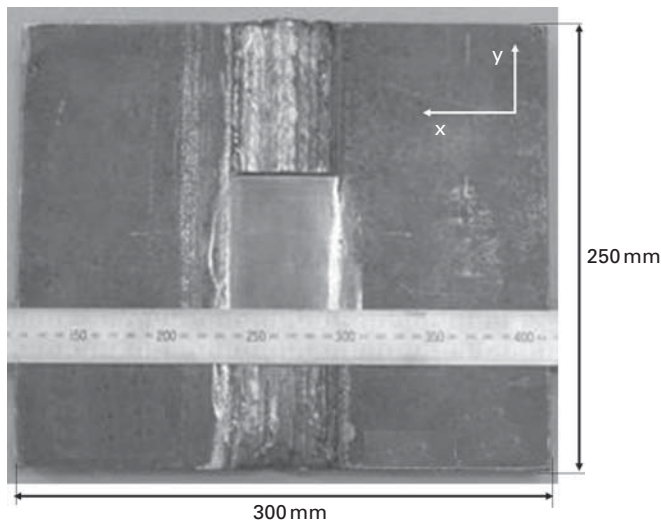

(b)

12.2 Sample II (TBW): (a) first tempering layer on one side of the joined plates and (b) overview of the completed sample. (The crown or reinforce is ground off in the centre of the weld.)

this change in lattice spacing is detected as a shift, $\Delta\theta_{hkl}$, in the *hkl* diffraction peak. From the Bragg equation the strain, ε_{hkl}, is given by

$$\varepsilon_{hkl} = \frac{d_{hkl} - d_0}{d_0} = -\cot\,\theta_{hkl}\Delta\theta_{hkl} \qquad 12.1$$

where d_0 is the strain-free lattice spacing for the *hkl* planes.

The orientation of the principal strains in any specimen is determined by specimen geometry. The strains (ε_{xx}, ε_{yy}, ε_{zz}) convert to the three-dimensional stress (σ_{xx}, σ_{yy}, σ_{zz}) state. For an isotropic solid, equations of the form:

$$\sigma_{xx} = \frac{E}{(1+\nu)(1-2\nu)}\left[(1-\nu)\varepsilon_{xx} + \nu(\varepsilon_{yy} + \varepsilon_{zz})\right] \qquad 12.2$$

give stresses in three directions, using σ_{xx} as an example, where E is Young's modulus (207 GPa) and ν is Poisson's ratio (0.3).

The incident and diffracted beam slits for measurements in the transverse and normal directions were 2 mm wide and could be 20 mm high. For measurements of strains in the longitudinal direction the slits can only be 2 mm in width and 2 mm high. In the authors' previous work [26] the problem of the local d_0 of the weld metal, HAZ and parent metal was discussed. The data suggest that for this particular alloy and weld, there is no significant effect on d_0 in the welded region resulting from microstructural and/or chemical compositional changes. Therefore, the average of the base and weld metal stress-free lattice parameters was used to determine the strains/stresses at all the measurement points in the weldment. The slits for the stress-free parameters were the same as those for longitudinal measurements ($2 \times 2\,\text{mm}^2$).

Scans were made along the surface (Fig. 12.3) across the weld, HAZ and parent metal ($x = 0$ is the centre of the weld). The centre of the gauge volume was 1.6 mm below the top surface. ND was carried out on the L3 diffractometer at the National Research Universal (NRU) reactor located at Chalk River Laboratory, Canada.

This reactor was chosen because the thermal neutron flux is relatively high, offering the potential to achieve reliable measurements of the residual strain/stress in a relatively small gauge volume of $2 \times 2 \times 2\,\text{mm}^3$ in 25 mm thick steel in short time intervals (3–20 minutes per point). The (115) planes of a Ge monochromator crystal were employed to produce a neutron beam of fixed wavelength $\lambda = 1.53$ Å. At this wavelength the αFe (211) reflection was detected at a detector angle, 2θ, of approximately 81.7°. The overview of the sample environment on the L3 diffractometer is shown in Fig. 12.3. Several surface and through-thickness scans of the weld were made. At each measurement point, the x, y and z components of strain (as indicated in Fig. 12.3) were measured by appropriately orienting each of the weld specimens.

12.4 Residual stress estimation

In this research the residual stresses were compared with two codes: BS 7910 [2] and R6 [3]. In these codes the residual stress distribution is proposed for several weld geometries and different types of materials. In this research only butt weld geometry in ferritic steel will be discussed. The details of the procedures are described in the following sections.

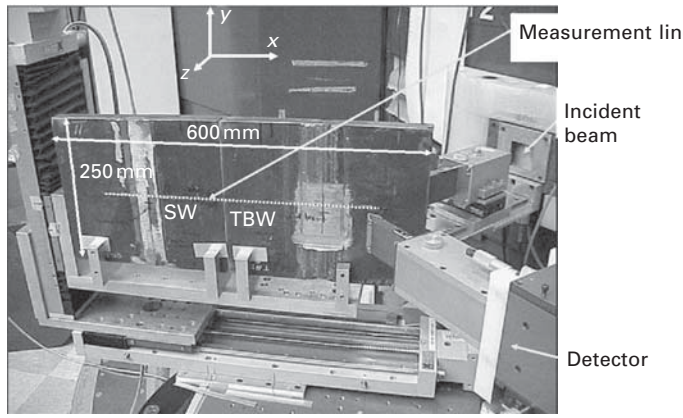

12.3 The strain scanning diffractometer at the Chalk River facility, showing Samples I (SW) and II (TBW) in position to measure the strain in the transverse (*x*) direction. The dotted line represents the locations of the surface scan using ND on both samples. The gauge volumes were centred 1.6 mm below the surface of the plate.

12.4.1 BS 7910

Estimates of the distribution of the weld transverse and longitudinal residual stresses are given in the current safety assessment procedure, BS 7910 [2]. According to Section 7.2.4 of BS7910 for 'a structure in the as-welded condition, with a flaw lying in a plane transverse to the welding direction, the tensile longitudinal residual stress is to be assumed to be a uniform membrane stress … equal to the room temperature yield strength of the material in which the flaw is located'. For a flaw parallel to the welding direction, the transverse residual stress 'should be assumed to be the lesser of the room temperature yield strength of the weld or parent material'.

12.4.2 Procedure R6

Three approaches for determining the as-welded residual stress distribution at room temperature are provided in R6 [3]. Simple estimates, Level 1, enable an initial conservative assessment of a defect to be made: '… a simple assumption is that the longitudinal and transverse components of residual stresses are tensile and uniformly distributed in both the through-thickness and transverse directions, with a magnitude equal to the material yield strength at room temperature'. This level is equivalent to the safety assessment procedure described in BS 7910. The second approach, Level 2, identifies published compendia that characterise a bounding profile for a range of structures. The third approach, Level 3, entails the use of analysis coupled with experimental measurements to define the detailed spatial

distribution of residual stress. Note that residual stress distributions in the BS 7910 or R6 (Levels 1 and 2) are upper bound distributions and they do not satisfy equilibrium.

Previous work by Wimpory *et al*. [27] has shown that the extent of the 'plastic zone', PZ, (or according to R6 'yield zone') can be used to determine the position from the weld toe, at which the magnitude of residual stress becomes compressive. This estimation of plastic zone size is very useful in predicting the residual stress distributions for welded joints. Parameters r_0 and y_0 (measured in mm) define the dimensions of the PZ. Based on R6, the PZ varies with the thickness of the parent material. For a ferritic steel weld in the longitudinal direction, PZ_{Long} is estimated by r_0 or y_0 which are based on the recommendation of Leggatt (R6 [3]) for the surface residual stress profile (Equations 12.3 and 12.4).

If $r_0 \leq t$, where t is a plate thickness (in mm)

$$r_0 = \sqrt{\frac{K}{\sigma_{YP}} * \frac{\eta q}{v}} \tag{12.3}$$

If $r_0 > t$,

$$y_0 = \frac{1.033\,K}{\sigma_{YP}} * \frac{\eta q}{vt} \tag{12.4}$$

where q is the arc power (in J/s), ($q = I*V$, I is the current (in A) and V is the voltage (in V)), K is a material constant (in N mm/J), v is the weld travel speed (in mm/s), η is the process efficiency (fraction of the arc power entering the plate as heat) and σ_{YP} is the yield strength or 0.2% of proof strength of the parent metal (in $N/mm^2 = 10^6$ Pa). Taking the typical value of process efficiency, $\eta = 0.8$, gives a value of $K\eta$ for ferritic steels of 122 N mm/J.

In the transverse direction the plastic zone, PZ_{Trans}, is estimated by thickness, and for a fully restrained sample,

$$PZ_{Trans} = 2t \tag{12.5}$$

The through-thickness longitudinal profile, σ_L, is assumed to be equal to the yield stress of the weld metal. For the transverse direction, transverse σ_T, the profile can be determined by the Equation 12.6:

$$\sigma_T/\sigma_y^*(z/t) = 1 - 0.917(z/t) - 14.533(z/t)^2 + 83.115(z/t)^3 - 215.45(z/t)^4 + 244.16(z/t)^5 - 96.36(z/t)^6 \tag{12.6}$$

where σ_y^* is the yield strength of the lesser of the weld or parent material, and z is the depth in the parent metal.

The schematic comparison of BS 7910 and R6 Level 2 profiles for the surface residual stress is shown in Fig. 12.4 and for the through-thickness case in Fig. 12.5.

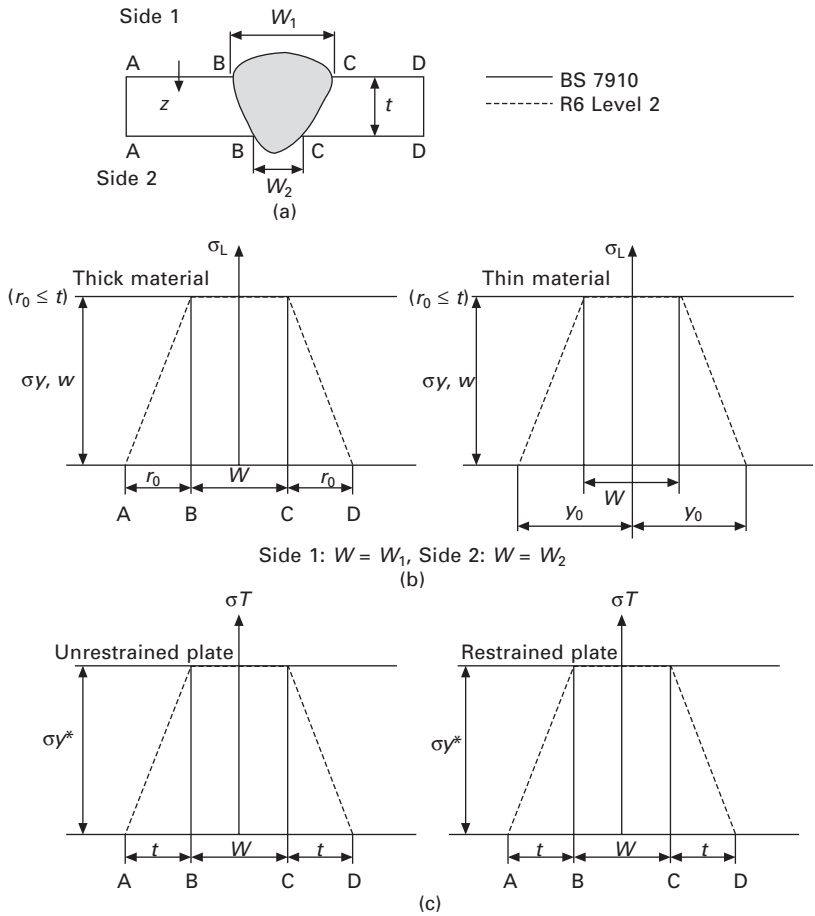

12.4 Comparisons of surface residual stress distributions in BS 7910 and R6 Level 2 (a) for a ferritic butt weld, for the longitudinal (b) and transverse (c) directions. (*W* is the width of observable weld.)

12.5 Results and discussion

To enable comparison of the results with BS 7910 and R6, the measured values of residual stress were normalised with respect to the material yield stress of the weld metal in the weld area and with respect to the yield stress of the parent metal outside the weld area (Table 12.2). This is termed normalised residual stress (NRS).

Figures 12.6 and 12.7 show the surface residual stress distributions for Samples I and II, respectively, together with the estimates BS 7910 and R6. Figure 12.8 shows comparisons of the through-thickness distributions for Samples I and II in the middle of the weld, as well as at the weld toe.

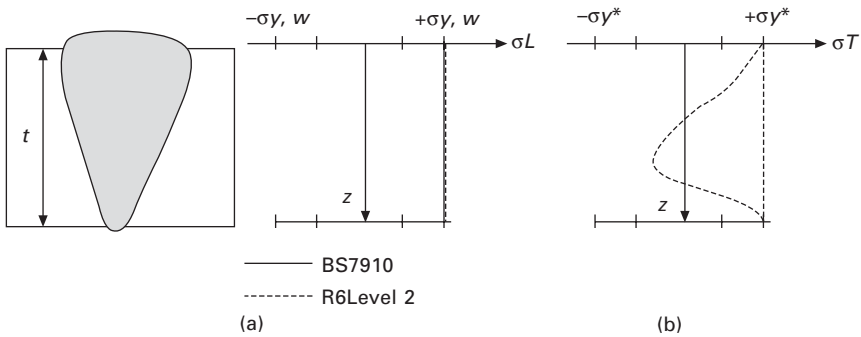

12.5 Comparisons of through-thickness distributions of residual streses in BS 7910 and R6 Level 2 for the longitudinal (a) and transverse (b) directions.

12.5.1 Distribution of stresses

Comparing the experimental results with the estimates in BS 7910 [2] and R6 [3] (Figs 12.6 and 12.7) shows that these codes underestimate the longitudinal surface stress within the weld and HAZ. High residual stress values were found in the longitudinal direction, reaching or even exceeding the uniaxial yield value of the parent and weld metal within the weld as well as the weld toe.

The transverse surface stresses are by contrast overestimated by both codes. The highest residual stresses in the transverse direction were found within the weld at approximately 40% for Sample I (Fig. 12.6b) and 60% for Sample II (Fig. 12.7b). At the surface, a stress distribution value below the yield was achieved in the longitudinal direction at the toe and the HAZ (Figs 12.6a and 12.7a).

Figure 12.8 shows comparisons of the through-thickness residual stress distributions in representative locations (at the weld centre, x = 0 mm, and 20 mm from the weld centre (x = 20) for Sample I and at x = 0, 20 and 30 mm positions for Sample II.

- The longitudinal residual stresses at the centreline (x = 0) of both samples exceeds the uniaxial tensile yield stress through the thickness for both samples. BS 7910 and R6 estimates are both exceeded.
- There is little decrease in the longitudinal residual stresses at the centreline (x = 0) of both samples and in fact there is an increase in measured stress for the temper bead sample II near the base of the plate.
- At x = 20 and 30 the longitudinal residual stresses in both samples fall away through the thickness. As can be seen from Fig. 12.1 these scans are both outside the fused areas below the surface.
- Transverse residual stresses in both samples are generally well below

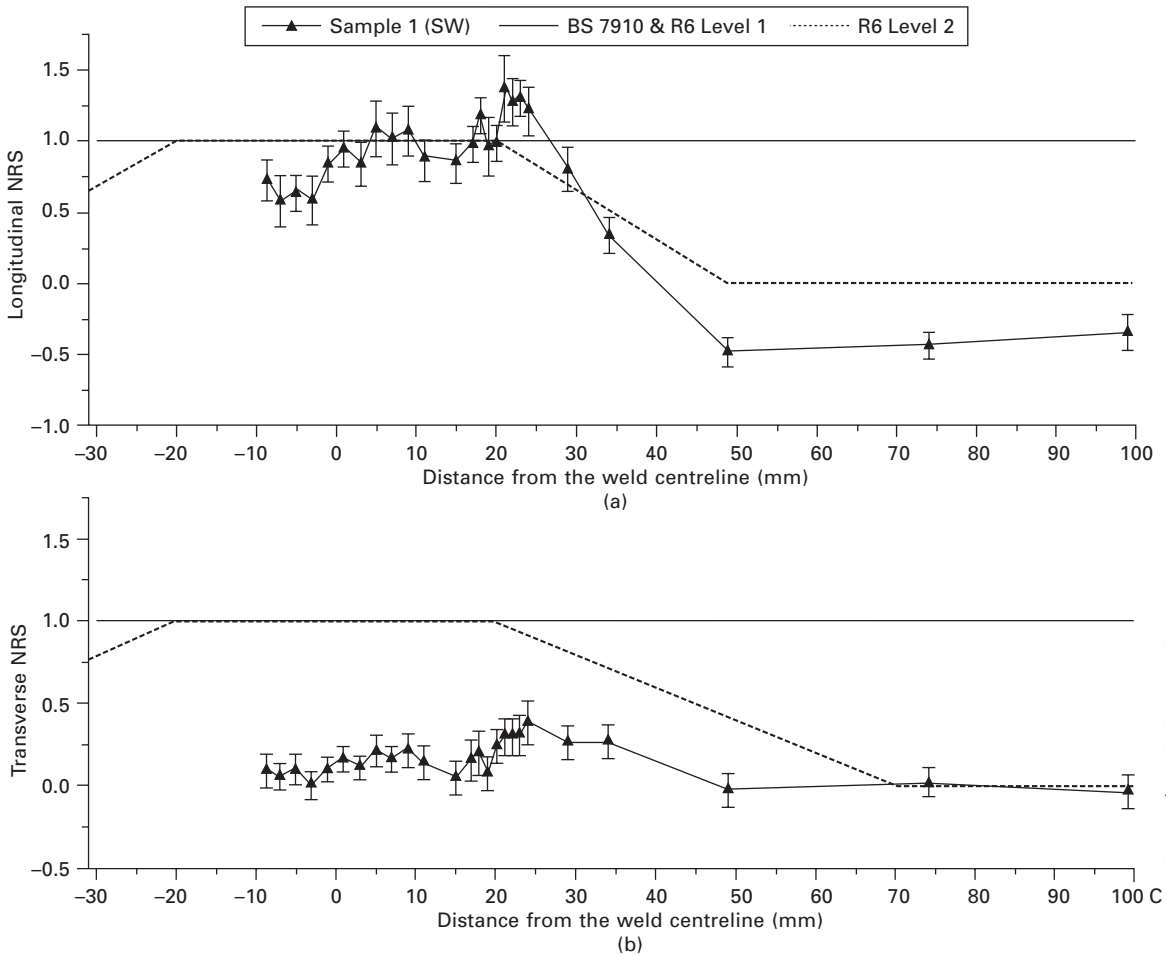

12.6 Comparison of normalised residual stress (NRS) distributions for Sample I (SW) with the estimates of BS 7910 and R6 for the longitudinal (a) and transverse (b) directions (1.6 mm below the surface).

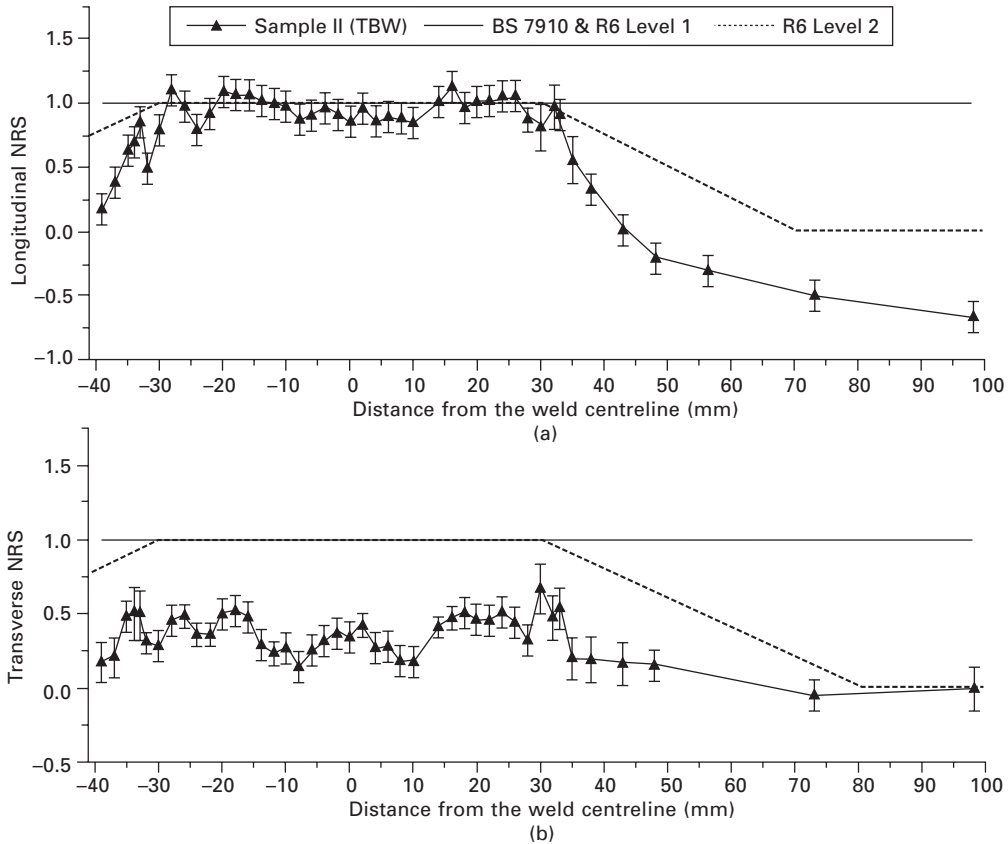

12.7 Comparison of normalised residual stress (NRS) distributions for Sample II (TBW) for the longitudinal (a) and transverse (b) directions (1.6 mm below the surface).

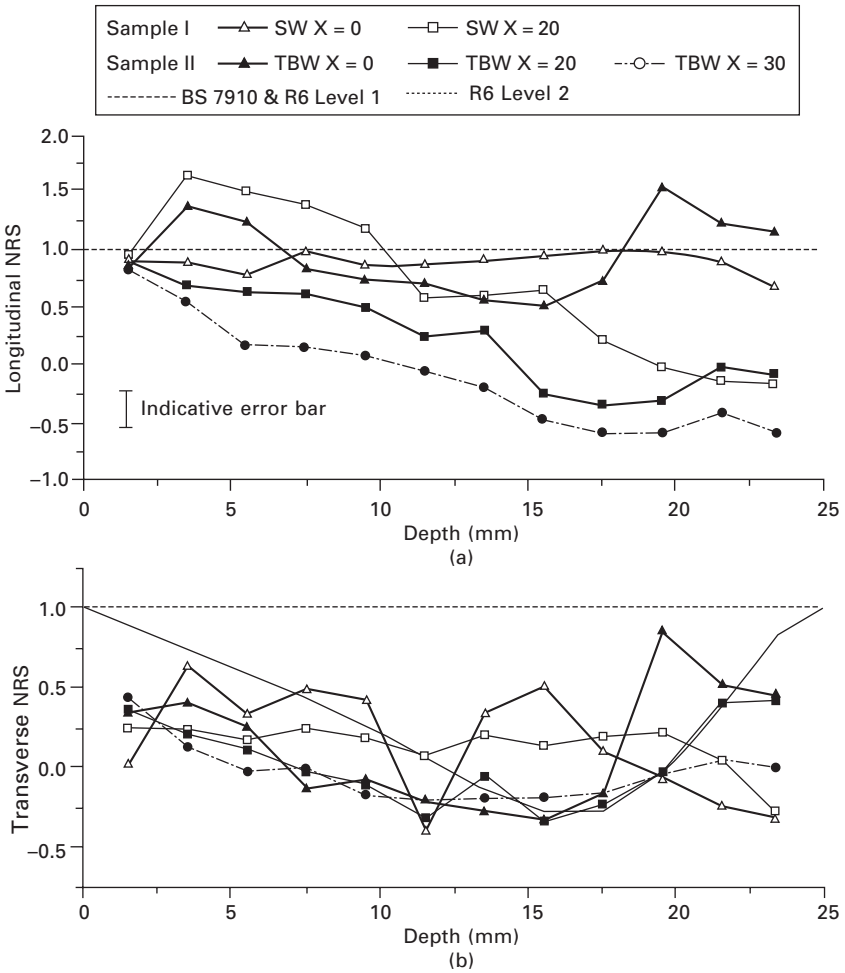

12.8 Comparisons of through-thickness normalised residual stress (NRS) distributions for Samples I (SW) and II (TBW) for the longitudinal (a) and transverse (b) directions. (Depth = 0 is the top surface of the welded plate and $x = 0$ is the centre of the weld.)

the uniaxial tensile yield stress, but there is little drop off with depth or distance from the centre line.

- For transverse residual stresses, the R6 Level 2 concept is exceeded. However BS 7910 and R6 level 1 are conservative.

12.6 Conclusions

The use of a neutron beam as a non-destructive method of measuring residual stress due to repair welding has been explored. Two types of full penetration

butt weld repairs on 25 mm ferritic steel were examined. The main research findings are:

- High values of the longitudinal residual stress occurred in both types of repairs within the fused region of the repair. Outside the fused region the longitudinal residual stress starts high but then drops through the thickness.
- Transverse residual stresses of approximately half the uniaxial yield strength were found within and near the fused region of the repair and the weld toe.
- BS7910 was conservative for transverse residual stresses. However, R6 Level 2 underestimates residual stresses through the thickness.

From the findings of this research in terms of residual stress, TBW repair may not be better than SW. PWHT may be still advisable for TBW repairs on ferritic steel.

12.7 Acknowledgements

This work was conducted with the assistance of an Australian Research Council grant supported by the Welding Technology Institute of Australia (WTIA). Other assistance has been received from the Monash University Research Fund and the Australian Nuclear Science and Technology Organisation (ANSTO). We acknowledge financial support from the access to Major Research Facilities Programme (Award No. 06/07-N-02) which is a component of the International Science Linkages Programme established under the Australian Government innovation statement, Backing Australians' Ability. Special thanks to Richard Blevins (ANSTO), Dr Rafaat Ibrahim (Monash University), Dr R.B. Rogge, R.L. Donaberger and Dr R. Hutanu from the Canadian Neutron Beam Centre (CNBC) for their input and assistance during this experiment. Anna Paradowska would like to thank the Australian Institute of Nuclear Science and Engineering (AINSE) for financial assistance during her PhD (Award No. AINSTU1604) at Monash University.

12.8 References

1. Withers, P.J., Bhadeshia, H.K., *Mater Sci Technol*, 2001; **17**: 366–375.
2. BS 7910: Guide on methods for assessing the acceptability of flaws in fusion welded structures, 1999, London: BSI, British Standards.
3. Milne, I., Ainsworth, R.A., Dowling, A.R., Stewart, A.T., 2001, *Assessment of the Integrity of Structures Containing Defects*, Nuclear Electric, Gloucester, UK Report R/H/R6-Rev. 4.
4. Zinn, W., Scholtes. B., *Handbook of Residual Stress and Deformation of Steel*, ASM International, 2002, pp. 391–396.
5. Dong, P., Brust, F.W., *J Pressure Vessel Technol*, 2000; **122**: 329–338.
6. Veiga, C., Loureiro, A., Dias, A., *Strain*, 2003; **39**: 57–63.

7. Dong, P., Hong, J.K., Bouchard, P.J., *Int. J. Pressure Vessel and Piping*, 2005; **84**: 258–269.
8. Price, J.W.H., Kerezsi, B., *Int. J. Pressure Vessels and Piping*, 2004; **81**: 173–180. doi:10.1016/j.ijpvp.2003.11.007
9. Sedek, P., Brozda, J., Wang, L., Withers, P.J., *Int. J. Pressure Vessels and Piping*, 2003; **80**: 705–713.
10. Cheng, X., Fisher, J.W., Prask, H.J., Gnäupel-Herold, T., Yen, B.T., Roy, S., *Int. J. Fatigue*, 2003; **25**: 1259–1269.
11. Gandy, D.W., Finland, S.J., Viswanathan, R., *ASME J Pressure Vessel Technol*, 2001; 123; 157–160.
12. Blackburn, J.M., Kirk, M., Brand, P., *et al*., *An Overview of Some Current Research on Welding Residual Stresses and Distortion in U.S. Navy*, 1998, IIW Doc. Nos. X–1359–96.
13. Shehata, T., Application of Flux Cored Arc Welding Process to the Temper Bead Repairs of Carbon Steel Components, Ph.D. Thesis, Monash University, Clayton, Australia, 2005.
14. Aloraier, A.S., Ibrahim, R.N., Ghojel, J., *J Materials Processing Technol*, 2004; **153–154**: 392–400.
15. Bouchard, P.J., Withers, P.J., *Journal Neutron Res*., 2004; **12** (1–3): 81–91.
16. Withers, P.J., Bhadeshia H.K., *Mater Sci Technol*, 2001; **17**: 355–365.
17. Jang, J., Son, D., Lee, Y.H., Choi, Y., Kwon, D., *Scripta Materialia*, 2003; **48**: 743–748.
18. Owen, R.A., Preston, R.V., Withers, P.J., Shercliff, H.R., Webster, P.J., *Mater Sci Eng A*, 2003; **346**: 159–167.
19. Duquennoy, M., Ouaftouh, M., Qian, M. L., Jenot, F., Ourak, M., *NDT & E International*, 2001; **34**: 355–362.
20. Dong, P., *J. Pressure Vessel Technol*, 2000; **123**: 207–213.
21. Paradowska, A.M., Price, J.W.H., Ibrahim, R., Finlayson, T.R., *Trans ASME J Pressure Vessel Technol*, 2008; **130**, 1: 1–7.
22. Price J.W.H., Ziara-Paradowska A.M, Joshi S., Finlayson T., Semetay C., Nied H., *Int J Mechanical Sci*, 2008; **50**, 3: 513–521. doi:10.1016/j.ijmecsci.2007.08.008
23. AS/NZS 3678:1996. Grade 250, Structural steel-hot-rolled plates, floor plates and slabs.
24. AS 1391-1991. Methods for tensile testing of metals. Standards Australia, Sydney, Australia.
25. AS 2205.2.2 – 1997. Methods for destructive testing of welds in metal – All-weld-metal tensile test Standards Australia, Sydney, Australia.
26. Paradowska, A., Finlayson, T., Price, J.W.H., Steuwer A., Ibrahim, R., Ripley, M., *Physica B: Condensed Matter*, 2006; **385–389**: 904–907. doi: 10.1016/j.physb.2006.05.245
27. Wimpory, R.C., Stefanescu, D., Smith, D.J., O'Dowd, N.P., Webster. G.A., May, P.S., Kingston, E., *J. Neutron Res*, 2003; **11**: 201–207.

13

Corrosion issues in ferrous weldments

R K DAYAL, H SHAIKH and
N PARVATHAVARTHINI, Indira Gandhi
Centre for Atomic Research, India

Abstract: The properties of weld metal in a specified environment should be equal to or better than those of the base metal. However, in most cases that is not the case. The main cause for the degradation of steel (austenitic or ferritic) weld joint is the formation of many regions with widely differing microstructures, which respond differently to the environment. The microstructure of a weldment depends on the chemical composition of the filler material, welding process and heat input, which controls the cooling rates in the various regions. These microstructural features deteriorate the general and localised corrosion properties of the weldment. Residual stresses add up to the service stresses and enhance the environment cracking susceptibilities of the weld joint besides increasing susceptibility to other forms of localised corrosion. The influence of microstructural variations in weld metal, sensitisation in heat-affected zone, residual stresses, etc., on general, localised and environmentally assisted cracking behaviour in austenitic stainless steels and ferritic steels are reviewed in this chapter.

Key words: weldment, austenitic stainless steel, ferritic steels, corrosion, heat input, localised corrosion, sensitisation, heat-affected zone.

13.1 Introduction

A welded joint is required to perform either equal to or better than the base metal it joins. However, in practice, this objective is never achieved since the welding process itself introduces features that degrade the mechanical and corrosion properties of the welded joints compared with the wrought base metal. Despite shielding by a gas or by slag, the weld metal can get contaminated by slag inclusions, tungsten inclusions, etc. The fast cooling rates associated with the weld metal cause the formation of a dendritic structure besides straining of the weld metal. Also, several metallurgical transformations can take place in the weld metal during this cooling. Apart from weld contamination and metallurgical changes, improper welding procedures can leave behind a host of defects, such as porosities, undercuts and microfissures, in the weld metal. All these detrimental features do not augur well for the mechanical and corrosion properties of the weld joint. In fact, a majority of the corrosion failures in components could be directly or indirectly related to the corrosion of the weld metal or the heat-affected zone (HAZ). Uniform and localised corrosion attacks can take place in the base metal as well as the weldments. Weldments, because of their microstructural and compositional heterogeneities,

are inherently more prone to corrosion than the unaffected base metal, though the basic corrosion mechanisms are the same. The various regions of a weldment are schematically illustrated in Fig. 13.1.

The composite zone, also known as mixed zone or fusion zone, is the conventionally fused region in the weldment where the filler material has been diluted with material from the base metal. The composition of this zone depends on the compositions of filler and base material. The extent of dilution is a function of heat input, joint geometry, position and the welding process. In an autogenous weld metal, where no filler metal is employed, the solidified material composition is very close to that of the base metal. However, in the case of welding using a 'matching' consumable, the composition of the weld metal tends to be different from the base metal. It is often mandatory to weld a joint with a consumable with composition entirely different from the base metal it joins, thereby resulting in additional problems of galvanic corrosion. Next to the mixed zone is the narrow region of unmixed zone where the base metal is melted but not fused with the filler metal and its composition is close to the base metal. In fact, the mixed zone can be considered to be the equivalent of an autogenous weld. The occurrence of an unmixed zone depends on a number of factors such as welding process, welding parameters, composition of filler metal and its physical properties. The extent of unmixed zone in a gas tungsten arc welding (GTAW) weld is less than in submerged metal arc welding (SMAW), gas metal arc welding (GMAW) and submerged arc welding (SAW) welds, thus indicating that metal transfer from the filler rod, and the weld pool motion play a very significant role in the formation of unmixed zones. The width of the unmixed zone varies with distance from the surface to the root of the weld [1]. The difference in the width and extent of unmixed zone with location is because the surface of the weld pool is more turbulent than that at the root, thus causing differences in mixing of filler and base materials. The HAZ in a weldment is situated in the base

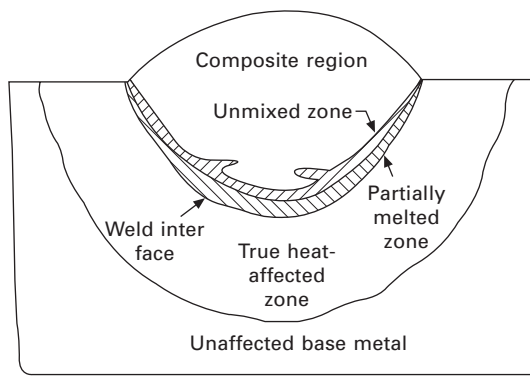

13.1 A schematic illustrating various regions of the weld joint.

metal adjacent to the fusion line. It experiences different thermal cycles depending on the distance from the fusion line. Each thermal cycle is characterised by a heating and cooling cycle and a peak temperature. The following sections discuss different manifestations of corrosion and their occurrence in weld joints of ferrous alloys.

13.2 Different forms of corrosion

A corroding metal is considered to consist of anode and cathode areas (local cell). The anode is the area at which chemical oxidation (corrosion) occurs and in which the current leaves the metal and enters the electrolyte (e.g. $M \rightarrow M^{n+} + ne$; $Zn \rightarrow Zn^{2+} + 2e$; $Al \rightarrow Al^{3+} + 3e$; $Fe^{2+} \rightarrow Fe^{3+} + e$). The electrons generated pass to the cathodic area through the bulk of the metal. The cathode is the area at which the reduction reaction occurs and the electrons are consumed. At the cathode areas practically no corrosion occurs and through this the current enters the metal (e.g. $Cu^{2+} + 2e \rightarrow Cu$; $Fe^{3+} + e \rightarrow Fe^{2+}$; $2H^{+} + 2e \rightarrow H_2$; $O_2 + 2H_2O + 4e \rightarrow 4OH^{-}$). Galvanic cells are formed due to two dissimilar metals in contact. In the presence of an electrolyte one metal becomes anodic and therefore gets corroded. For example iron pipe carrying water is anodic to copper pipe.

13.2.1 Uniform corrosion

The most commonly observed corrosion of metals and alloys is uniform or general corrosion, which is characterised by uniform thinning and corrosion attack of the surface. Technically this does not pose an unexpected threat since necessary allowances can be made in thickness to account for metal loss during service. The usual solutions to general corrosion involve the choice of more suitable materials, inhibitors, protective coatings, or combination of them.

13.2.2 Galvanic corrosion

Two different metals electrically connected in a corrosive solution set up an electrochemical cell with the more reactive metal acting as the anode and the less reactive metal (noble metal) as the cathode. The relative reactivity of one metal to another is listed with respect to the hydrogen electrode in an electromotive force (EMF) series or galvanic series. Galvanic corrosion is highly dependent on the ratio of areas of anode and cathode. An unfavourable area ratio, i.e. a large cathode and a small anode, can cause high rate of corrosion at anode.

13.2.3 Dealloying or selective leaching

In certain environments, one element of an alloy may dissolve with respect to the others, because of the differences in the corrosion rate of the various elements in the specific environment. Dezincification of high zinc brasses is a classic example of this type of corrosion. Both Zn and Cu corrode, but Cu immediately plates back on the metal because it is much more noble than Zn. Selective leaching also occurs in grey cast iron embedded in soil. Iron corrodes, leaving the graphite flakes in place.

13.2.4 Pitting corrosion

This type of corrosion occurs at discrete sites on a metal surface confined to a point or smaller area. Pitting refers to the formation of small cavities/holes on the surface of the material that is otherwise protected by an adhesive, tenacious and self-healing thin film. The formation of pits is attributed to the interaction of the aggressive ions with the film at the locations where it is defective or weak in nature. The pits may be visible to the naked eye in some cases but in general they are invisible, and dangerous to the extent they can allow the formation of stress corrosion cracking (SCC) or fatigue cracks which can catastrophically fail the component in service. Depending on the metallurgy of the alloy and chemistry of the environment, pits may be shallow, elliptical, deep undercut or sub-surface and may follow metallurgical features.

A change in the kinetics of electrochemical reactions arising as a result either of lower concentration of oxygen or of higher concentration of hydrogen ions, brings a change in the open circuit potential of metals in the localised area. As the concentration of oxygen diminishes, the potential of most of the metals is shifted to a more active value. Since the potential of the metal in the pit differs considerably from the potential of the metal freely exposed to the electrolyte, favourable conditions are created for the formation of a macro-galvanic couple (active–passive macro-couple) in which the region of the pit acts as anode.

13.2.5 Crevice corrosion

Crevice corrosion is defined as local destruction of metal surface at, or immediately adjacent to, an area that is shielded from full exposure to the environment because of close proximity between the metal and the surface of another material. Crevice corrosion refers to the formation of selective corrosion attack at local or shielded regions of metal to metal or metal to non-metal joint, where stagnation of electrolyte is possible. The differences in the concentration of corroding species and of oxygen between the local region and the bulk causes the selective attack at this local region called the

'crevice' which is defined by its size, gap and area. A crevice is called so when it is capable of generating such concentration cells inducing corrosion attack. In crevice corrosion also, the state and the stability of the passive film formed at the crevice and the remaining region play a vital role in the severity of the attack.

The general mechanism of crevice corrosion in chloride solutions can be classed into four steps: (1) oxygen is consumed within the crevice at a faster rate than can be supplied from outside, thus forming an oxygen concentration cell; (2) the cathodic reaction is slowly moved to the freely exposed external surface, and the pH decreases; (3) the concentration of chloride ions within the crevice solution increases, and in order to maintain charge neutrality, the crevice solution becomes sufficiently aggressive for the passive film to break down; and (4) in the final stage, the metal within the crevice continues to dissolve actively and crevice corrosion propagates in a self-sustaining manner.

Crevice corrosion can be prevented by adopting designs and fabrication procedures that eliminate crevices, e.g. elimination of rivet or threaded joints or avoid undercuts during welding, etc. In case crevices cannot be avoided, cathodic protection and inhibitors could provide adequate corrosion control.

13.2.6 Intergranular corrosion

The intergranular corrosion (IGC) or intergranular attack (IGA) of metal is the phenomenon when there is an increased corrosion rate of the material along the grain boundaries and reactively lower or negligible corrosion of the material at the grain interior in certain environments. The increased corrosion rate could result either from the dissolution of segregated impurities or precipitate at the grain boundaries or from the dissolution of material adjacent to the grain boundaries due to different alloy composition from that of the bulk matrix. The localised attack at grain boundaries becomes possible because grain boundaries are high-energy areas and preferred sites for segregation of impurity atoms and for precipitation of deleterious secondary phases, which could lead to enrichment, or depletion of alloying elements there. Stainless steels are highly susceptible to IGC when they pass through a specific temperature range (sensitisation) and then exposed to corrosive environment.

The IGC in austenitic stainless steels has long been explained by the chromium depletion theory in which carbon diffuses to the grain boundary and reacts with chromium to form chromium carbides, thereby depleting the adjacent areas of chromium. Since in stainless steels the corrosion resistance depends on Cr content, the areas adjacent to the grain boundaries become less resistant to corrosion and therefore more susceptible to localised attack. The stainless steels get sensitised when subjected to heat treatment between 723 and 1123 K. The precipitation of chromium carbide occurs when the

material is exposed to high temperature service or cooled slowly during welding. IGC in non-sensitised stainless steel can also occur in a highly oxidising medium. This has been explained due to solute segregation at the grain boundaries, particularly of P, Si and S.

13.2.7 Filiform corrosion

Filiform corrosion occurs on metallic surfaces coated with a thin organic film. The pattern of attack is characterised by the appearance of fine filaments emanating from one or more sources in semi-random direction. The source of initiation is usually a defect or mechanical scratch in coating. The filaments are fine tunnels composed of corrosion products underneath the bulged and cracked coatings. The filiform has an active head and a filamentous tail, and has been observed on many steels, tin plate steel, Al, and Mg subjected to high humidity. The fluid in the leading heads of a filiform is typically acidic. In all cases oxygen and water are the main media to sustain filiform. This indicates that the filiform corrosion is a specialised differential aeration cell. The filiform attack occurs when the relative humidity is typically 65–90%.

13.2.8 Impingement corrosion/attack

Impingement corrosion is a form of erosion corrosion generally associated with the local destruction of metal by the abrasive action of a high-velocity flowing fluid containing solid particles in suspension against the metal surface. This results in thinning or removal of material by flowing environment. Rapidly flowing environments can often disrupt adherent surface films that would otherwise offer protection against corrosion. It often occurs at locations in the plant where there are sudden changes in flow conditions, such as flow direction or flow velocity, in the plant. For example, nozzles or locations where tube constrictions exist can be the most susceptible areas in the plant where erosion corrosion could occur. Erosion corrosion takes the form of grooves, waves, gullies, teardrop-shaped pits and horseshoe shaped depressions on the surface. Erosion corrosion can be controlled by designing to reduce surface velocity and turbulence, and by careful material selection. In general, stainless steels and Ti and Ni–base alloys are resistant to erosion corrosion because of their tenacious surface film. Hard and strong metals, though resistant to wear, are not necessarily resistant to erosion corrosion, particularly if their corrosion resistance is low or if they have a weak passive film.

13.2.9 Cavitation damage

Cavitation is a form of erosive attack, which results from collapsing bubbles created by pressure changes across surfaces exposed to high velocity liquid

flow. Flow across a curved surface produces a pressure drop that causes local boiling when pressure is reduced below the vapour pressure of the liquid. When the bubbles land on the surface and collapse, the repeated pressure impacts are sufficient to erode or cavitate the surface. Once the surface has been roughened at a point, this serves as a nucleus for the new cavitation bubbles to form. A protective film on the metal surface is not necessary for cavitation damage to occur. Cavitation damage is a well-known cause of problems in ships' underwater fittings, especially propellers and rudders and in pumps and pipework circulating water. The fundamental remedy of cavitation damage is change in design, which stops the cavitation. Pressures may be raised, abrupt changes in section removed to eliminate severe turbulence and vibration reduced. Cathodic protection is sometimes beneficial, not because of reduced corrosion rate but because of the cushioning effect of hydrogen evolved on the surface. Removal of dissolved air is often beneficial because dissolved gases more easily nucleate cavitating bubbles.

13.2.10 Fretting corrosion

Fretting corrosion is an accelerated deterioration at the interface between contacting surfaces as the result of corrosion and slight oscillating movement between the two surfaces.

13.2.11 Corrosion cracking processes

Corrosion cracking processes, i.e. SCC, hydrogen embrittlement (HE) and corrosion fatigue (CF), account for almost half of the corrosion related failures in industries. This is to be expected because most of the components have some amount of residual stresses present in them due to fabrication processes involved. In many cases, these stresses cannot be relieved and they get added on to service stresses, leading to premature failure of the components. Thus, corrosion cracking processes assume significant importance with respect to mitigation of corrosion problems in industries.

Stress corrosion cracking

SCC is the process in which a metal fractures prematurely under condition of simultaneous corrosion and tensile loading at a lower stress level than would be required in the absence of the corrosion environment. SCC is the degradation of the material under the combined action of a load and a corrosive medium, neither of which when acting alone would cause considerable damage. The degradation in the material property includes loss in ductility and tensile strength. SCC occurs only in a specific medium, in which a critical balance between passivation and corrosion exists. SCC is a brittle failure that occurs

even in ductile materials [2]. It can also occur below yield stress. Crack morphology is transgranular, intergranular or mixed. SCC occurs in a definite range of strain rates and strain rates lower than this range cause general corrosion or no failure will occur. Above this range of strain rates, the material will fail by pure mechanical failure. SCC is a complex phenomenon and involves five important factors: stress, environment, temperature, alloy structure and composition. The stress has to be necessarily tensile in nature for SCC to occur. The stresses could be either residual or service induced. These could also act together and induce a very premature failure. Environmental factors that contribute to SCC failure include: concentration of aggressive species; temperature; pH; and dissolved oxygen. Metallurgical factors, which have a significant influence on SCC, are cold working, welding, sensitisation, grain size, stacking fault energy, segregation, etc. Two main mechanisms have been proposed for SCC: dissolution-based mechanism and hydrogen embrittlement mechanism.

Hydrogen embrittlement

HE is a process resulting in a decrease of the toughness or ductility of metal due to the presence of atomic hydrogen. It is a form of environment-assisted failure caused by the combined action of hydrogen and residual or applied stress. Generally, small quantities of hydrogen are sufficient to cause delayed failures because hydrogen has the ability to magnify its effect by migrating to regions of high triaxial stress. Hydrogen may be made available to a metal surface from various sources including the cathodic reduction of hydrogen ion from water. The cathodic reactions could occur during corrosion, cathodic protection, pickling and electroplating. Hydrogen may also enter the material from hydrogen-bearing atmospheres during heat treatment, welding and other manufacturing processes.

Hydrogen damage could occur in a number of ways, viz. creation of internal flaws, hydride formation and hydrogen embrittlement. Internal flaws such as blisters, shatter cracks, fish eye and flakes are formed owing to pressure build-up at metallurgical defects as a result of recombination of hydrogen atom to hydrogen molecules there. When steel structures are exposed to high-pressure hydrogen, hydrogen molecules dissociate on the steel surface to form nascent hydrogen atoms which readily diffuse into the steel. At the high temperatures this hydrogen can react with carbon in solid solution at grain boundaries, dislocations, inclusions and laminations to form methane gas. This results in high internal pressure to cause either blisters or intergranular fissures. This is called hydrogen attack. If the temperature is high enough, dissolved carbon diffuses to the surface to combine with hydrogen gas, causing overall embrittlement and loss in strength. Hydrogen can also get adsorbed on the free surface adjacent to the crack-tip and decreases the

surface energy required for crack growth. In many applications, a lower strength material will function better than high strength material and use of such material will eliminate HE. Lowering the applied load to values below threshold value for HE and/or decreasing the residual stresses can prevent HE.

Corrosion fatigue

CF is a process in which a metal fractures prematurely under condition of simultaneous corrosion and repeated cyclic loading at a lower stress level or fewer cycles than would be required in the absence of the corrosion environment. Corrosion fatigue is defined as a deleterious effect of corrosive environment on one or more of the progressive stages of damage accumulation, which constitute fatigue behaviour of materials, as compared with behaviour in inert surroundings. Damage results from synergistic interaction of cyclic plastic deformation and local chemical and electrochemical reactions. In addition to the material parameters (chemical composition, microstructure, yield strength) and solution parameters (pH, temperature, potential), loading parameters, viz. ΔK range (stress intensity factor range), stress ratio, K_{max} (maximum stress intensity factor), frequency and wave form, can have a large influence on the crack growth behaviour. The fatigue propagation rates in metals and alloys depend on alternating stress intensity factor, ΔK, and vary over a wide range of crack growth rates from 10^{-8} to 10^{-2}mm/cycle. Frequency too has a strong influence on the corrosion fatigue behaviour of a material. Maximum effect is felt at low frequencies; however, very low frequencies have no influence.

13.2.12 Oxidation

When a metal is exposed at elevated temperature to an aggressive gas (e.g., oxygen, sulphur or halogen), corrosion may occur in the absence of liquid electrolyte. This is sometimes called dry corrosion. In this a solid reaction product film or scale forms on the metal surface through which the metal, the environment or both must diffuse in order for the reaction to continue. Various steps in oxidation process are adsorption of oxygen; formation of oxide nuclei and growth of continuous oxide film. At a critical thickness, the stresses set up in the oxide may cause it to crack and detach (called spalling) and as a result the oxidation rate increases irregularly. For certain metals (Cu, Zn, Ni) metal ions migrate through the oxide to the outer oxide surface, reacting there with oxygen. Oxidation reaction product films are usually brittle and lack ductility. A surface film formed in tension favours fracture. Oxidation resistance is related to the ratio of volume of oxide scale and the volume of metal from which the oxide is formed per gram atom of the metal

(known as the Pilling–Bedworth ratio): Md/nmD; M = mol. wt of scale, m = mol. wt of metal, D = density of scale, d = density of metal, n = number of metal atoms in the molecular formula of scale. If this volume ratio is less than 1, it produces insufficient oxide to cover the metal and is unprotective. Also if this ratio is much greater than 1, it tends to introduce large compressive stresses in the oxide which also causes cracking and spalling and poor oxidation resistance. The ideal ratio should be close to 1. The oxide scale should also possess good adherence, high melting point, a low vapour pressure, good high temperature plasticity to resist fracture and low electrical conductivity or low diffusion coefficient for metal ions and oxygen.

13.2.13 Microbiologically influenced corrosion (MIC)

When deterioration of metals occurs at discrete sites as a result of metabolic activity of microorganism, the type of corrosion is known as MIC. Such corrosion is caused by the chemical/electrochemical changes at the metal–biofilm interface. When microorganisms colonise engineered surfaces and interfere with fluid flow over the surface or heat transfer across the surface, the phenomenon is called biofouling (micro-bialfouling).

13.3 Effect of defects on the corrosion properties of weld metal

Welding defects such as slag and other entrapments, cracks, microfissures, porosities, inclusions, lack of penetration and fusion, oxide and other scales, deteriorate the corrosion properties of a weld metal. These defects contribute to reduce the localised corrosion resistance of weld metal. These defects normally cause early pitting and crevice attacks in the weld metal [3]. A number of investigators have shown that sulphide inclusions are most susceptible sites for pitting and crevice attack; however, others suggest that other non-metallic inclusions are also capable of causing pit nucleation. Also, these defects act as regions of stress concentration which aid in faster initiation of the SCC. Non-metallic inclusions, such as sulphides, are undesirable from SCC point of view. Influence of non-metallic inclusions in reducing the SCC life is directly related to the easy initiation of pitting corrosion at inclusion sites [4]. In acid solutions, and hence in occluded cells, sulphide inclusions dissolve to form H_2S, which has an accelerating effect on corrosion of steel [5]. H_2S is reported to accelerate both the anodic and cathodic processes [4].

In many service applications, SCC initiates from pits which act as stress raisers [6,7]. In these cases, the induction times for SCC were longer than those for pitting [6]. Apparently, the non-metallic inclusions do not participate directly in crack nucleation, but their presence is undesirable, as they give

rise to pitting. However, Clarke and Gordon [8] reported a strong effect of secondary phases and inclusions on crack nucleation. They described how cracking nucleated from the crevice corrosion attack around the included particle. Non-metallic inclusions also play a role in HE of stainless steel welds. Surface inclusions facilitate entry of hydrogen into the weld and thus induce cracking [4]. Bulk inclusions may act as trap sites for hydrogen and thereby assist in nucleation and development of internal crevices and cracks. The shape of the sulphide inclusion influences the crack initiation time. Elongated sulphide particles may increase hydrogen entry into the metal six-fold compared with spherical inclusions. The non-metallic inclusion also causes stress concentration in the material. The extent of stress concentration would depend on the shape of the inclusion. Sharp-edged inclusions act as more effective notches than spherically or elliptically shaped inclusions. Apart from the shape, the ratio of thermal expansion coefficients and modulus of elasticity of the inclusion to that of the matrix also contribute to a lesser extent in determining the magnitude of stress concentration. In addition to sulphide inclusions, weld metals can contain other inclusions resulting from the oxidation and deoxidation reactions in the molten weld metal. Welds may also contain slag inclusions, which could result from slag entrapment in the solidified weld bead. The extent of slag entrapment is dictated by the nature of the flux coating on the welding consumable. Rutile coatings give ease of slag detachment and good bead shape. Out-of-position welding can also cause slag entrapment.

In designing welding consumables, it is a common practice to adjust weld metal composition by adding alloying elements in the flux. During welding, these elements may not get mixed well in the molten pool, thus leaving regions rich in these elements which may act as nucleation sites for localised corrosion attacks. For example, in offshore applications, the electrode coating contains ferromanganese particles, which if not homogeneously mixed in the weld metal leaves areas harder than the adjoining matrix [9]. These hard areas provide sites for initiation of SCC in service. Certain measures during welding, such as increase in welding current, reducing travel speed or the width of weaving, may help in mitigating the problem.

Porosities can lead to faster initiation of pitting attack or SCC since they act as sites for stress concentration [10]. The appropriate choice of heat input could reduce the amount of porosities in the weld metal. Cracks and micro-fissures also contribute to reduction in localised corrosion resistance of weld metal. The weldment may undergo cracking during welding, or immediately after welding, or during service or during post-weld heat treatment (PWHT) in the solidified weld metal HAZ. These cracks may act as sites for crack initiation or as crevices. In stainless steels and Ni–base alloys, micro-fissuring and hot cracking are major problems. C–Mn steels and low alloy steels normally undergo cold cracking and reheat cracking. Places where there are

undercuts, lack of fusion and lack of penetration are preferential sites for corrosion attacks. Judicious selection of the weld joint design, welding parameters, consumables and welding process may avoid corrosion problems associated with such faulty joints. Certain joint designs, such as lap and stake joints, may result in crevice corrosion attack and should be avoided; instead, full penetration butt joints should be preferred [11]. In some applications, it is a common practice to use welding inserts, which may not get properly fused in the weld metal and leave areas that may become prone to crevice attack. In addition to crevice corrosion problems, the crevices thus formed will act as stress raisers and cause SCC. In welding of steels, if the electrodes are over-baked, the amount of hydrogen, which increases bead penetration, is reduced, thus leading to lack of penetration defects in the weld metal. Some of the alloys, like Ni–base alloys, show poor fluidity, which is a common cause for lack of fusion and associated corrosion problems.

13.4 Effect of residual stresses on the corrosion properties of weld joints

During welding, residual stresses are retained in the component due to faster cooling rates associated with the weld metal. These stresses increase the dissolution rate of the material, deteriorating its corrosion properties. The major impact of residual stresses is felt on the SCC properties of the material. Many SCC failures have been reported on welded components during storage [12]. During service, residual stresses add on to the service load and accelerate SCC failures. Hence, the control and management of residual stresses assume significance.

Zamiryakin [13] reported that the proneness of austenitic chromium–nickel steels to SCC is determined by the magnitude of residual stresses. PWHT is most commonly employed to rid welded components of their residual stresses. In austenitic stainless steel (SS) components, PWHT can be of substantial benefit in avoiding intergranular SCC (IGSCC). In this regard, a stabilising anneal at 1143–1223 K is frequently applied to welded components in the petrochemical industry to guard against polythionic acid attack. For chloride-induced SCC, cracking occurs where environment conditions are adverse and the threshold stress for this form of failure is low. Service experience suggests that when loaded components suffer chloride SCC, cracking preferentially occurs in weld areas, strongly implying weld residual stresses to be a significant factor. Hence, PWHT is advisable, at least for critical applications. The high coefficient of thermal expansion and the extremely low limits of elasticity for austenitic SS would mean that residual stresses would readily arise during cooling from peak PWHT temperature, unless the operation is carefully controlled. Heating to over 1203 K is necessary to achieve maximum stress relief. However, heating at

such high temperatures can pose critical problems such as distortion and scaling. Slow heating and cooling is preferred, subject to avoidance of sensitisation during the cooling part of the cycle. Heat treatment at intermediate temperatures, say 823–1023 K, represents an easier operation but only about 60% residual stress will be relieved. However, the problems of sensitisation and formation of intermetallic brittle phases such as σ phase rule out this heat treatment cycle. Low temperature stress relief at 673 K has been advocated to avoid SCC even though less than 40% stress relief is achieved [14]. Owing to the above considerations, it may not be possible to guarantee that PWHT can avoid chloride SCC under the said service condition [15,16]. Elimination of chloride ions, minimising operating temperature and appropriate design to eliminate crevices could prevent SCC of austenitic SS weld joints in preference to PWHT. However, PWHT is definitely beneficial in countering chloride SCC and should be resorted to when other properties, such as creep and fatigue, render them essential.

Mochizuki [17] has reported methods of residual stress reduction for both in-process control during welding and post-weld control. The sequence optimisation of welding pass deposition for multi-pass welding in cruciform fillet-welded joints and butt-welded joints with an X-shaped groove helped minimise residual tensile stresses. He verified the effectiveness of this approach in preventing fatigue, and SCC in the in-process control method was verified by numerical analysis and actual experiment. He also investigated water jet peening and tungsten inert gas (TIG) cladding as post-weld control methods. The water jet peening was useful for obtaining compressive residual stress on the surface which helped to combat both fatigue and SCC. Cladding with a corrosion-resistant material was also effective in amelioration of SCC. Englehard *et al*. [18] reported that in addition to the use of low carbon stabilised grades of austenitic stainless steel, the risk of IGSCC during operation due to water chemistry and prevailing temperatures can be overcome by maintaining a controlled, uniform, and low heat input during welding. They also recommended that narrow-gap welding should be preferred to reduce the integral residual stress. The use of post-welding processes such as the last pass heat sink welding (LPHSW) process was also recommended. Dewald *et al*. [19] examined the effects of laser peening on Alloy 22, a nickel-based material, in reducing tensile stresses in the weld metal. Laser peening was found to produce compressive residual stress to a depth of 3.8 mm in 20 mm thick base material coupons. The depth of compressive residual stress was found to have a significant dependence on the number of peening layers. Additionally, laser peening produced compressive residual stresses to a depth of 4.3 mm in the 33 mm thick weld at the centre of the weld bead where high levels of tensile stress were initially present.

13.5 Corrosion of austenitic stainless steel weld joints

Several important changes that take place during cooling of the molten weld metal dictate the corrosion properties of the solidified weld metal. The welding of austenitic stainless steel has two major problems, viz. hot cracking of weld metal and sensitisation of the HAZ. Corrosion problems associated with austenitic stainless steel are best corrected by understanding the solidification of a stainless steel weld metal. The problem of hot cracking could be overcome by (i) reduction of the S + P content of the weld to less than 0.01% and (ii) addition of Mn to form high melting MnS instead of low melting FeS. However, the most common method adopted is retention of some amount of high temperature δ-ferrite to room temperature. δ-Ferrite can be retained by appropriate choice of the filler metal composition which could be done in consultation with the 70% iron isopleth (Fig. 13.2) [20].

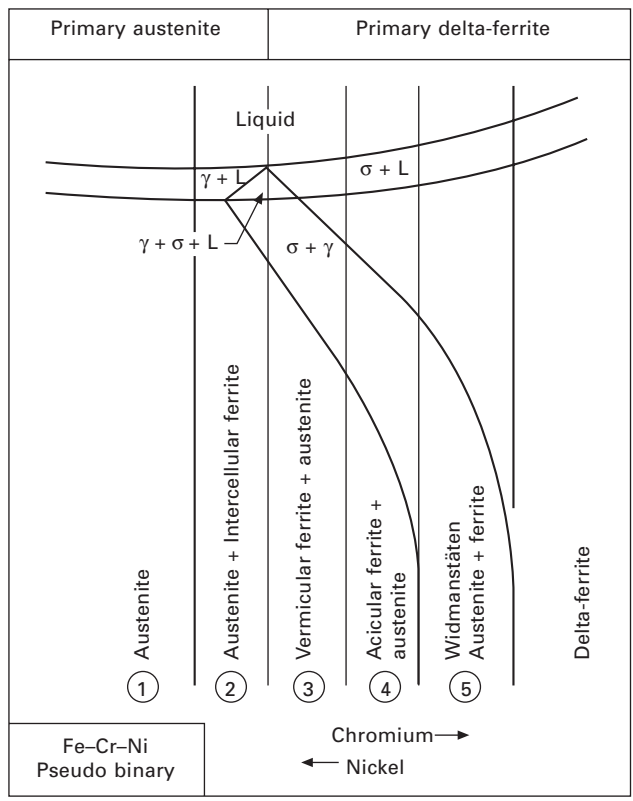

13.2 A schematic of the 70% iron cross-section showing the effect of composition on the austenite and δ-ferrite morphology in austenitic stainless steel weld metal [20].

This diagram determines the position of the alloy composition with respect to the liquidus minimum. Alloys with compositions located on the Ni-rich side solidify as primary austenite while those located on the Cr-rich side solidify as primary ferrite. In both the solidification modes, the δ-ferrite is enriched in ferritisers such as Cr, Mo and Si, while the austenite is enriched in austenitisers, such as Ni, Mn, C and N [21]. The extent of partitioning of alloying elements depends on heat input [22]. Apart from partitioning of alloying elements, impurities, such as S and P, segregate to the δ-ferrite/austenite (δ/γ) interface. The extent of segregation depends on the solidification mode and heat input [21, 22]. These micro-segregations cause preferential corrosion attacks of the weld.

13.5.1 Corrosion of weld metal

Effect of solidification and micro-segregation

The beneficial effect of δ-ferrite in controlling hot cracking is offset by the fact that in some corrosive media, it can cause severe localised corrosion attacks. However, δ-ferrite is not harmful under all conditions of environmental corrosivity. The attack on δ-ferrite is controlled by its chemical composition and does not solely depend on its mere presence in the austenite matrix. Also, preferential weld metal corrosion involving δ-ferrite takes two principal forms: attack on the δ-ferrite itself or attack along the δ/γ interface. Both these types of attack can occur in Mo-containing and Mo-free austenitic stainless steel weld metals. But attack along the δ/γ interface is more common in the former while attack on the δ-ferrite is often encountered in the latter. The difference in corrosion behaviour of weld metals of types 304 and 316 stainless steel is most pronounced in moderately oxidising media. The attack in this environment will occur at δ/γ interface for type 316 stainless steel, but will occur on the ferrite for type 304 stainless steel.

Marshall and Gooch reported lower pitting corrosion resistance (PCR) for weld metal vis-à-vis base metal with same chemical composition (Fig. 13.3) [23]. This was attributed to the detrimental effect of δ-ferrite on the PCR of the austenitic stainless steel [24]. Increasing the Mo content increased the PCR of welded 18Cr–12Ni stainless steel [25]. In the case of type 304 stainless steel weld metal, the most susceptible sites for pitting corrosion were the δ/γ interfaces, where extensive segregation of S and P caused difficulty in passivation [26]. In type 316 stainless steel weld metal, the preferential sites for pit initiation were found to be the core of the austenite cells where depletion of Mo occurred [27].

The difference in SCC behaviour of base and weld metals of austenitic stainless steels has been the subject of much disagreement in literature. The differences in SCC behaviour between the base and weld metals depend on

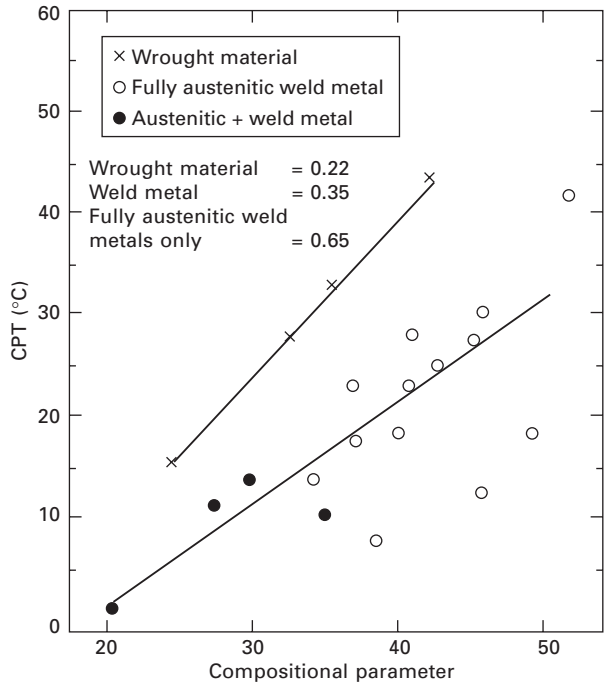

13.3 Comparison of PCR between base and weld metals of austenitic stainless steel [23].

the chemical composition, environment and testing techniques. Weld metal of austenitic stainless steel possessed equal or better SCC resistance than the base metal of similar composition when tested by slow strain rate technique (SSRT) in boiling 45% $MgCl_2$ solution [28–30]. The superior SCC resistance of the weld metal was attributed to the cathodic protection of the austenite due to the corroding δ/γ interface [31]. Tests on type 304 stainless steel in $MgCl_2$ boiling at 408 K and in 1 N HCl showed a much higher SCC resistance for the base metal [32]. Raja and Rao reported that the base metal of type 316 stainless steel had better SCC resistance than its autogenous weld in a 5 N H_2SO_4 + 0.5 N NaCl solution at room temperature [33]. Shaikh *et al*. [34] reported a lower K_{ISCC} (i.e. threshold stress intensity factor for SCC) and higher plateau crack growth rates for type 316N stainless steel weld metal vis-à-vis type 316LN base metal (Fig. 13.4). They attributed the poorer SCC resistance of the weld metal to its greater yield strength and higher microscopic defect density. Shaikh *et al*. [35] reported that a sensitised HAZ was the weakest link in a weld joint from SCC point of view. In case of a non-sensitised weldment, they reported failure in the weld metal.

The presence of δ-ferrite can appreciably alter both the SCC resistance and the crack morphology of the weld metal. The SCC resistance of the weld

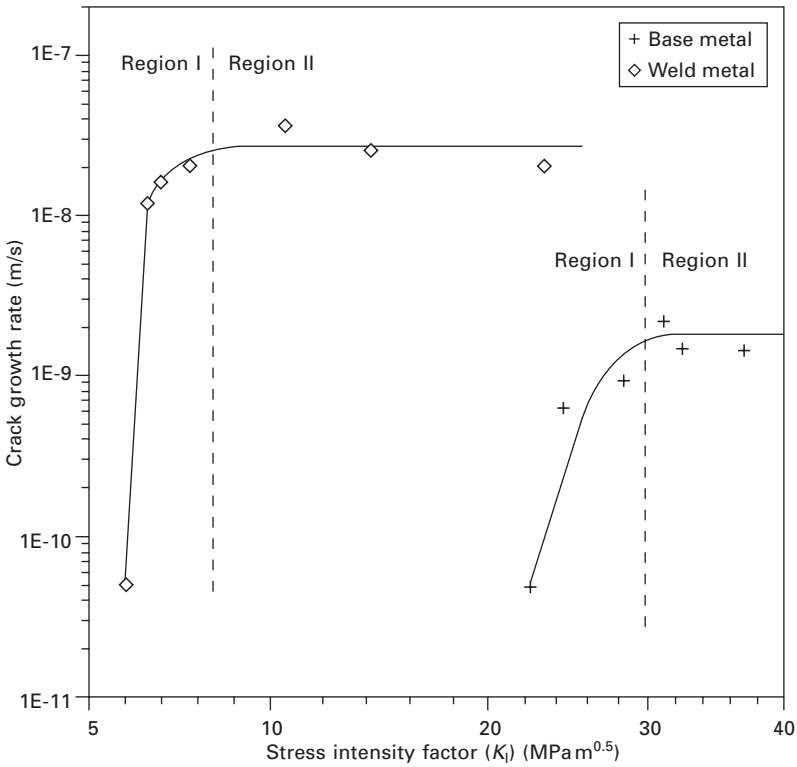

13.4 Comparison of SCC resistance of base and weld metals of austenitic stainless steel [34].

metal depends on the δ-ferrite content, its distribution and the solidification mode. Duplex weld metal, which solidifies in the primary ferritic or primary austenitic solidification mode, has SCC resistance similar to that of the base metal [36]. Fully austenitic weld metal has the most degraded SCC property and fails by IGSCC due to extensive segregation of S and P at the grain boundaries [37]. In NaCl and HCl solutions, both at ambient and high temperatures, the weld metal failed by stress-assisted dissolution (Fig. 13.5) of δ-ferrite and SCC of austenite [35]. In boiling 45% $MgCl_2$ solution, the failure occurred due to cracking of the δ/γ interface and SCC of austenite [29, 30, 32]. The amount, morphology and continuity of the δ-ferrite network influences the SCC resistance of the weld metal. A continuous network of δ-ferrite was most harmful for SCC of weld metal as it provided a continuous path for crack propagation. Shaikh *et al.* [35] reported that on polarising the weldments anodic to the critical cracking potential, a decrease in SCC resistance was observed, while slight cathodic polarisation prevented failure (Fig. 13.6). This suggested that a dissolution mechanism was operative during SCC of type 316 stainless steel weldments. Nage and Raja [38] reported that in high

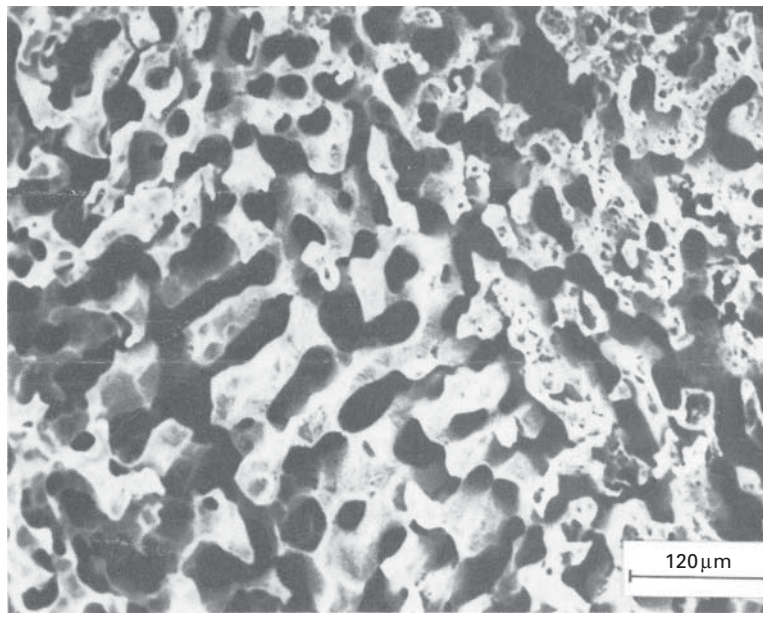

13.5 Stress assisted dissolution of δ-ferrite [35].

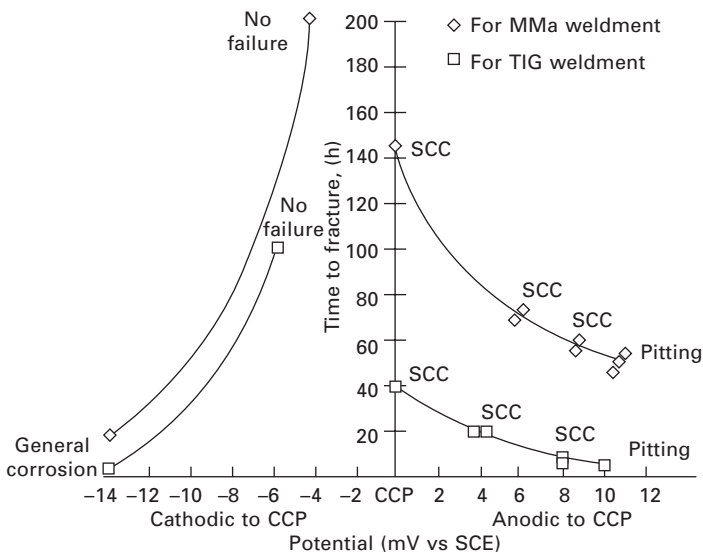

13.6 Effect of applied potential on the SCC of austenitic stainless steel weld (SCE = saturated calomel electrode) [35].

temperature water at 561 K, type 904L stainless steel welds, produced without nitrogen in the shielding gas, failed at the weld fusion zone. Small additions of nitrogen (0.5 vol.%) in the argon shielding gas imparted significant SCC resistance to the weld fusion zone such that the failure occurred in the base metal. Li and Congleton [39] reported that in the case of a heterogeneous weld of a low alloy steel and a stainless steel, the transition joint of the two steels had a greater susceptibility to SCC than individual susceptibility of either steel. The SCC in this zone was mainly intergranular in the austenitic zone but transgranular both at the interface and in the low alloy steel part of the joint.

Sensitisation of duplex weld metals of austenitic stainless steels is not commonly heard of since chromium depletion due to $M_{23}C_6$ precipitation at δ/γ interfaces does not readily occur. This is because any chromium depletion occurring due to $M_{23}C_6$ precipitation gets healed due to rapid diffusion of chromium from the chromium-rich δ-ferrite phase. However, this immunity from sensitisation and IGC can be severely compromised especially on heat treatment in the temperature range where $M_{23}C_6$ can form. The severity of this problem depends on the carbon content as well as the extent to which the duplex structure is lost through the dissolution/transformation of δ-ferrite. Sensitisation data on weld metal of austenitic stainless steel is rare. However, Hamada and Yamauchi [40] reported that type 308 stainless steel weld overlays on low alloy steel got sensitised on PWHT at 873 K. They evaluated the effect of δ-ferrite distribution on the sensitisation behaviour by using a microstructural parameter. Parvathavarthini *et al.* [41], in a very detailed study, reported that type 316N stainless steel weld metal was sensitised in the temperature range 898–998 K, when tested by ASTM A262 Practice E test (Fig. 13.7). They determined a critical cooling rate (CCR) of 160 K/h above which there was no risk of sensitisation. Figure 13.7 also shows that type 316L stainless steel weld metal was sensitised in the temperature range 900–950 K and the CCR was 1 K/h.

Corrosion problems related to partitioning of alloying elements and segregation in the weld metal can be overcome by a high temperature annealing treatment; or by choosing a filler metal with Mo content higher than base metal; or by employing cathodic or anodic protection.

The significance of the unmixed zone in corrosion service is evidenced when austenitic stainless steels are required to be welded with high Ni filler metal to give a fully austenitic structure. However, the microstructure in the unmixed zone would be duplex which will offset the beneficial effect of austenitic base and weld metals. The recently developed high Mo and N stainless steels, such as AL6XN and 254SMo, are designed for certain specific applications where considerable high corrosion resistance is required. However, autogeneous welds of these steels corrode preferentially because of extensive Mo segregation, thus necessitating a post-weld annealing. The high temperature

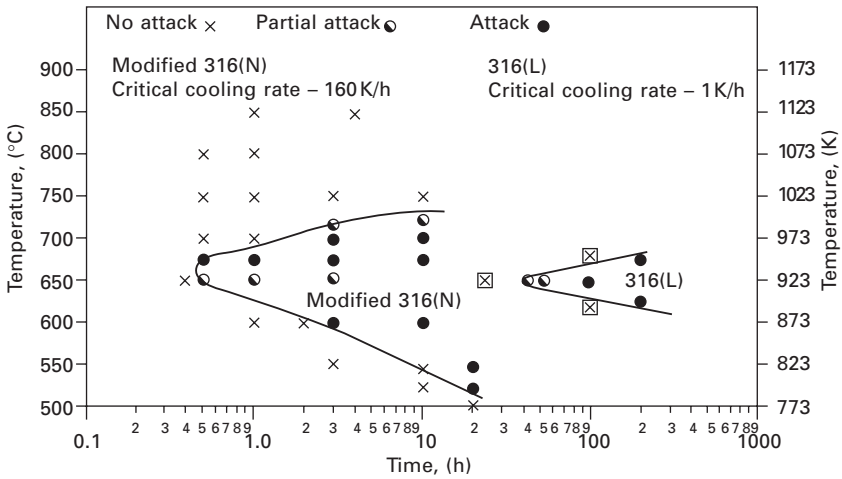

13.7 TTS diagram for types 316N and 316L stainless steel weld metals [41].

treatment is not always possible. Therefore, special filler materials with higher Mo content (C-22 and Incoloy 625) have been designed for welding. Lundin had reported preferential pitting attack in the unmixed zone of the weld metal [1].

Heat input

Heat input affects the microstructure and hence the microstructure-sensitive properties of the weld metal. Increasing heat input coarsens the δ-ferrite dendrites and increases the mean spacing between the dendritic arms [42]. Increasing the heat input decreases the cooling rate of the weld metal, which increases the partitioning of the alloying elements and segregation of S and P, coarsens the δ-ferrite dendrites and increases the mean spacing between its secondary arms [22]. This is because decrease in the cooling rate of the weld metal increases solid-state diffusion and aids the redistribution of the solute between the austenite and ferrite phases.

Critical pitting potential (E_{pit}) decreases with increasing heat input for multi-pass weld metal of type 316L SS [42]. The increased segregation of ferrite formers, such as chromium and molybdenum to δ-ferrite, resulting in impoverishment of austenite in these elements, coupled with depletion of chromium and molybdenum consequent to precipitation of $M_{23}C_6$ carbides at the δ/γ interface, caused the decrease in PCR [22]. Mudali *et al.* [43] reported that the PCR of weld metal, made by autogenous TIG welding on type 304 SS with addition of nitrogen through the argon shielding gas, decreased with increasing heat input. However, the deleterious effect of heat

input was readily offset by nitrogen additions (Fig. 13.8). Kumar *et al*. [44] reported an increase in E_{pit} and ΔE_{pass} with increasing heat input to a multi-pass weld metal of type 316N stainless steel (Fig. 13.9). They attributed this

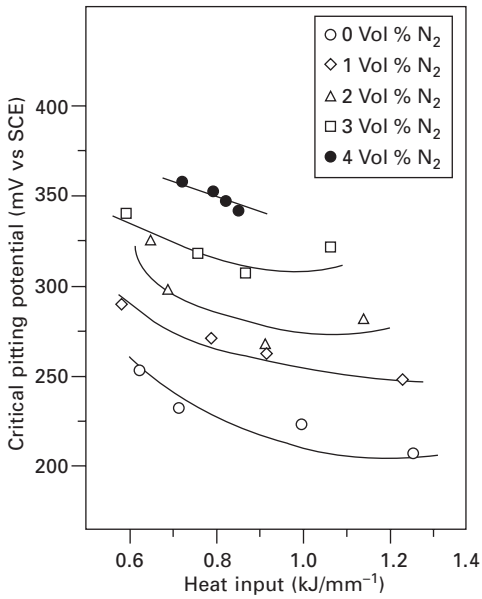

13.8 Effect of heat input and nitrogen content on PCR of weld metal of type 304 stainless steel [43].

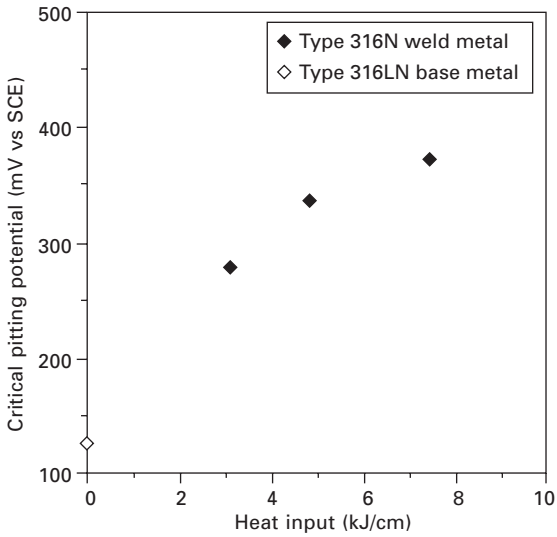

13.9 Improvement in critical pitting potential with increasing heat input in a multi-pass weld of type 316N stainless steel [44].

to the reheating of the previous passes, which led to reduction in continuity of δ-ferrite network, evening out of the composition and reduction in segregation at the δ/γ interface. Also, no $M_{23}C_6$ carbides were found to precipitate in the weld metal.

Very little work has been done on the influence of heat input on the SCC susceptibility of welds of austenitic stainless steels. Sensitivity to IGC is increased with increasing heat input and it would seem that IGSCC should also be promoted at higher heat inputs [31]. To a lesser extent, a similar adverse effect of high heat input has been found for transgranular SCC (TGSCC) [31]. However, Franco *et al*. reported an increase in SCC resistance of weld metal of AISI type 304 stainless steel with increasing heat input in boiling 45% $MgCl_2$ solution [45]. Anita *et al*. [42] reported an improvement in SCC resistance with increasing heat input of a multipass weld of AISI type 316N stainless steel in boiling acidified NaCl solution (Fig. 13.10). They attributed this to the softening of the austenite matrix by thermal recovery due to reheating of the previous passes to very high temperatures, which also led to reduction in continuity of the δ-ferrite network, homogenisation of the composition and decrease in segregation at the δ/γ interface. Also, no $M_{23}C_6$ carbides were found to precipitate in the weld metal.

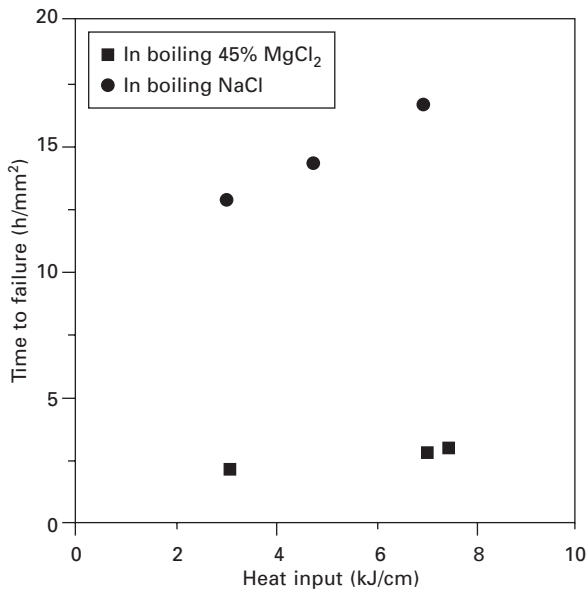

13.10 Increase in SCC resistance with increasing heat input in a multi-pass weld of type 316N stainless steel weld [42].

Secondary phases

The use of welded components of austenitic stainless steel would result in its degradation with time on exposure to elevated temperature during service or during PWHT. This happens when the δ-ferrite component of the duplex weld metal transforms to intermetallic phases, small quantities of which lead to large variations in the material's mechanical and corrosion properties. Hence, knowledge of the type, the amount and the physical parameters of phases such as size, and morphology distribution are vital in designing the optimum operational parameters for achieving the desired life for the austenitic stainless steel components. The transformation kinetics of δ-ferrite is complex and depends on various factors such as material composition, temperature, and the size and shape of δ-ferrite [46–48]. Shirley [10] and Garner [49] reported that formation of σ phase impoverishes the surrounding matrix of Cr and Mo, thus making the alloy susceptible to corrosion attack. σ phase precipitation leads to increase in critical corrosion current density (i_{CCD}), while the corrosion behaviour in the passive conditions remained unaffected [50]. Ageing the weld metal for long durations at 1023 K showed significant rise in the values of i_{CCD} [51]. Globularisation of σ phase caused an extensive rise in i_{CCD} [50]. Pujar *et al*. [51] reported that ageing type 316 stainless steel weld metal, with two different carbon concentrations, between 773 K and 1073 K, did not affect the corrosion rates at open circuit potentials (OCP) while the i_{CCD} increased steeply with ageing time. The weld metal with higher carbon content showed higher i_{CCD} on ageing.

Warren [52] showed that for type 316 stainless steel, pit initiation times decreased and weight loss due to pitting increased when σ phase was introduced to the microstructure. Shaikh *et al*. [50] reported lower E_{pit} and narrower ΔE_{pass} with increasing amount of σ phase in weld metal of aged type 316N austenitic stainless steel (Fig. 13.11). The reduction in E_{pit} was directly attributed to the dominating effect of depletion of Cr and Mo vis-à-vis the competing process of self-healing in the austenite matrix. Spherodisation of σ phase did not have a direct influence on the improvement in E_{pit} of aged weld metal [50]. Improvement in E_{pit} of type 316N stainless steel weld metal aged for long durations at 1023 K was attributed to the dominance of the process of self-healing rather than spherodisation of σ phase [50]. Since σ contains higher Cr and Mo than the austenite and exhibits more noble potentials in chloride solution, it is unlikely that the lower PCR is associated with direct attack on σ phase. Instead, Cr and Mo depletion occurring within austenite matrix just adjacent to the σ phase could cause the lowering of PCR [45]. Lo and Tsai [53] showed that the presence of intermetallic σ phase exerted an adverse effect on the pitting corrosion behaviour of weld overlays of type 347 stainless steel. Gill *et al*. [27] showed a sharp decrease in pitting potential of weld metal of type 316 stainless steel when the Cr +

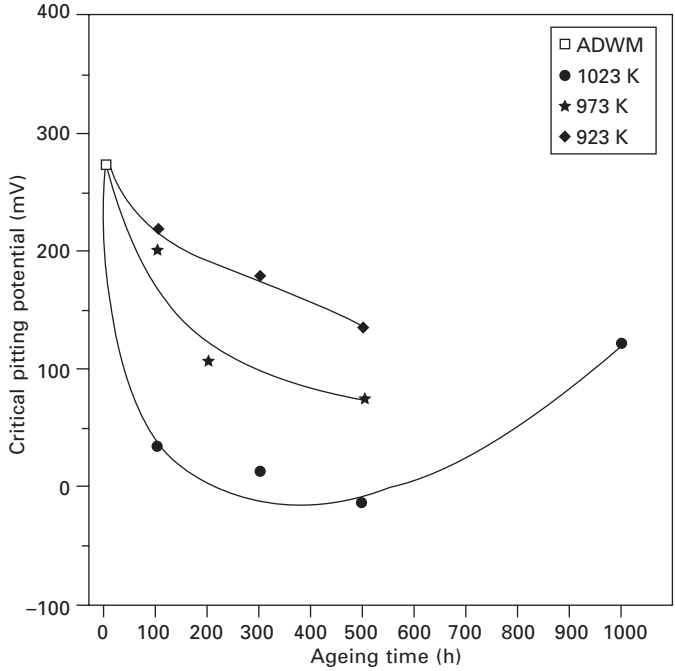

13.11 Dependence of E_{pit} of type 316N stainless steel weld metal on ageing time [50].

Mo content decreased from 20 to 19 wt% in the austenite matrix (Fig. 13.12).

SCC studies on aged weld metal of type 316L stainless steel showed that, on ageing at 873 K, the SCC resistance of the weld metal was governed by the occurrence of two complementary processes of matrix hardening and softening [54]. Maximum SCC resistance was observed for weld metal aged for 200 hours because effects of matrix softening, caused by processes such as dissolution of ferrite network, overwhelmingly dominated the effects of matrix hardening, caused by factors such as σ phase precipitation. Deterioration of SCC resistance was observed beyond 200 hours ageing because the effects of matrix hardening dominated [54]. The PWHT of weld metal of Nb-stabilised austenitic stainless steel, between 873 to 1073 K, resulted in decreased SCC resistance due to σ phase precipitation while improvement in SCC resistance was observed on ageing at 1073 K [55]. To overcome the corrosion problems associated with secondary phase precipitations in weld metal, it is recommended that a judicious choice of filler metal be made. In austenitic stainless steel, where δ-ferrite is expected to be attacked preferentially during service, its amount and morphology should be controlled. If the stainless steel weldment is to undergo PWHT to reduce the residual stresses, PWHT temperature should be selected so as to minimise formation of secondary phases.

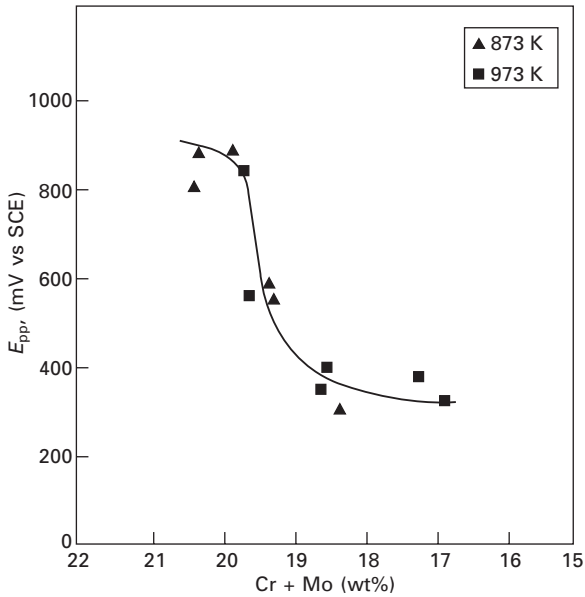

13.12 Variation of critical pitting potential with Cr + Mo contents of the remaining austenite matrix [27].

Corrosion of HAZ

The rapid thermal cycles experienced in the HAZ of a fusion weld promote some metallurgical changes that would significantly affect the corrosion resistance of the weld joint: for example in austenitic stainless steels, a degree of grain coarsening could be experienced just adjacent to the fusion line. However, the extent of grain coarsening is not significant enough to impair the SCC properties [31].

The more often encountered phenomenon, which degrades the corrosion resistance of an austenitic stainless steel weld joint, is the localised corrosion of the HAZ. Sensitisation of austenitic stainless steel occurs in the temperature range of 723–1123 K. During this high temperature exposure, depletion of Cr to less than 12% occurs in the region around the grain boundary, owing to the precipitation of a continuous network of $M_{23}C_6$ carbides. Sensitisation makes the steel susceptible to intergranular attack. The probability of the HAZ being sensitised during welding would depend on the time it spends in the sensitisation temperature range. The residence time spent by the HAZ in this temperature range depends on the heat input, which in turn depends on the heating and cooling rates. The use of higher inter-pass temperatures increases the probability of localised corrosion of the HAZ [56].

Sensitisation in austenitic stainless steels can take place after long exposure even at temperatures as low as 573 K, if such steels were first exposed briefly

in the sensitisation range prior to low temperature exposure. This kind of thermal cycle is experienced in welded stainless steels used in the boiling water reactor (BWR) and is termed low temperature sensitisation (LTS). Kain *et al*. [57] reported that type 304 stainless steel and its variants are more prone to LTS than the molybdenum-containing type 316 stainless steels. The kinetics of the chromium carbide precipitation, and, hence, the resultant sensitisation could be predicted from a TTS diagram [58–61]. These curves represent sensitisation during isothermal heat treatments (Fig 13.13) [60]. However, sensitisation during welding can be predicted by a continuous cooling sensitisation (CCS) diagram (Fig. 13.14) [60].

Susceptibility to IGC caused by sensitisation in austenitic stainless steel can be determined by systematically carrying out ASTM standardised tests. The ASTM tests for IGC are either chemical or electrochemical in nature

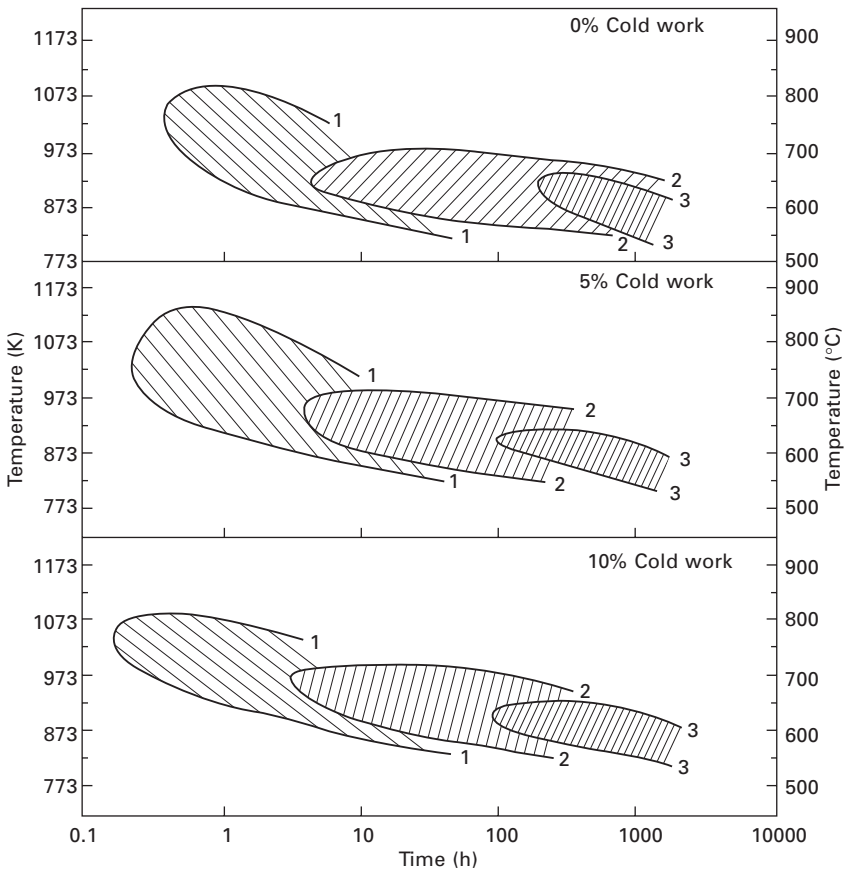

13.13 TTS diagram for types 316 (1-1), 316N (2-2) and 316LN (3-3) stainless steels [60].

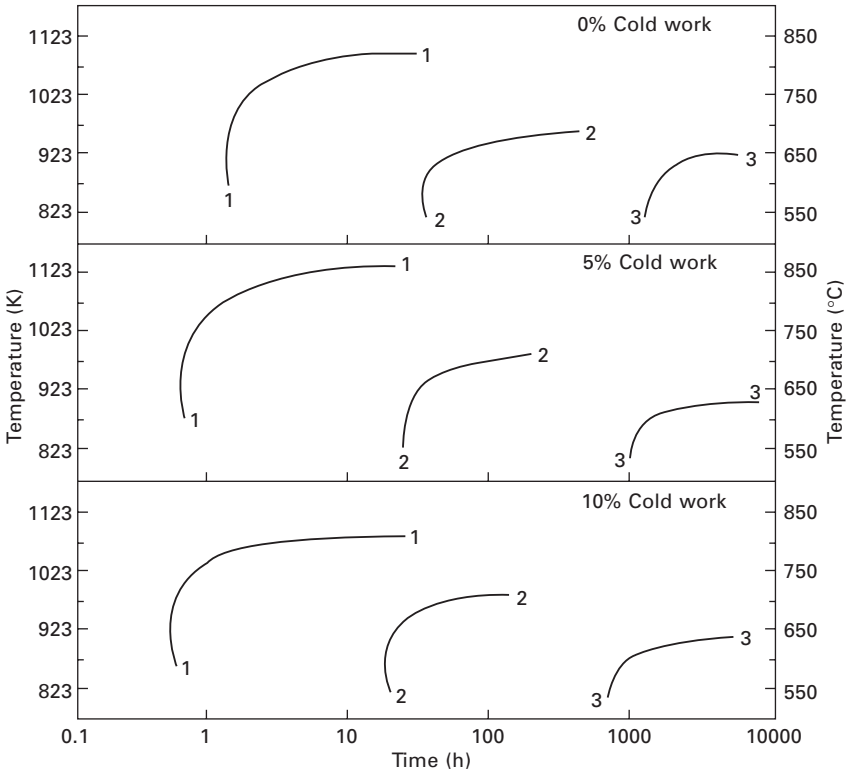

13.14 CCS diagram for types 316 (1-1), 316N (2-2) and 316LN (3-3) stainless steel [60].

and are applicable to austenitic stainless steel and some Ni–base alloys. ASTM Standard A 262 Practice A to F are the standards for chemical and metallographic tests to determine IGC in austenitic stainless steel [62]. These standard chemical tests are commonly used as qualification/acceptance criteria during purchase/fabrication stage. In order to quantify degree of sensitisation (DOS), an electrochemical technique, known as the electrochemical potentiokinetic reactivation (EPR) technique, has been developed [63–65]. This technique is a quantitative, non-destructive and rapid method, which is essentially suitable for field use. This technique was standardised by ASTM (standard G-108) to quantify the DOS in AISI types 304 and 304L stainless steel [66]. A comparative study on different test standards has been published by Parvathavarthini *et al*. [67]

Sensitisation of austenitic stainless steel requires the precipitation of Cr-rich carbides along grain boundaries, which makes carbon and Cr the predominant compositional variables for sensitisation. By reducing the carbon content in stainless steel, the TTS curve is displaced towards longer times

because carbon concentration in austenite becomes insufficient to form chromium-carbide readily [68]. The limit of C content for which steel is not sensitive to IGC is closely connected with the presence of other alloying elements such as Cr, Mo, Ni, N, Mn, B, Si as well as Ti and Nb in stabilised steel. The detrimental effect of C on sensitisation can be reduced by the addition of stabilising elements such as Ti and Nb. These elements form TiC and NbC, which results in a reduction in the amount of C available for chromium-carbide precipitation. Cr has a pronounced effect on the passivation characteristics of stainless steel. With higher Cr contents, the time to reach the resistance limit of Cr depletion at the grain boundaries becomes longer. Higher Cr contents facilitate the diffusion of Cr into depleted grain boundary area. Ni is required in austenitic stainless steel to stabilise the austenite and must be increased with increasing Cr concentration. Increasing the bulk Ni content decreases the solubility and increases the diffusivity of C. This effect is much more pronounced when the Ni content is greater than 20%. It is generally recommended that in 25/20 Cr–Ni steel, C content should be less than 0.02% to guarantee resistance to IGC.

Mo reduces the solubility of C in austenite. Carbide precipitation is accelerated at higher temperatures whereas at lower temperatures it is slowed down. When Mo is present, it is also incorporated in $M_{23}C_6$. Therefore, in addition to Cr depletion, Mo depletion is also revealed. In Mo-containing Cr–Ni austenitic stainless steel, $(Fe,Cr)_{23}C_6$ is precipitated first at 1023 K to 1123 K. With prolonged ageing, Mo is also incorporated as $(Fe,Cr)_{21}\,Mo_2C_6$ which is finally converted to χ phase. With increasing Mo contents, $M_{23}C_6$ precipitation and IGC become increasingly influenced by the precipitation of intermetallic phases.

The influence of Mn is of special importance because in fully austenitic welds, this element is added. Mn reduces the carbon activity and increases its solubility. Carbide precipitation is slowed down and hence it appears to inhibit carbide precipitation [69]. Boron retards the precipitation of chromium-carbide but, depending upon the heat treatment, it promotes IGC. Si promotes IGC of high purity and commercial stainless steel. Steels containing Mo were found to be much more sensitive to Si additions. The increased susceptibility to IGC in highly oxidising solution is due to the segregation of Si to grain boundaries [68]. One of the alloying additions studied extensively in the recent years is nitrogen. Its effect is quite complex and is dependent on the presence of other alloying additions. N content up to 0.16 wt% is reported to improve sensitisation resistance by retarding the precipitation and growth of $Cr_{23}C_6$ [70]. Parvathavarthini *et al.* have established that as the nitrogen content increases, the time required for sensitisation at the nose temperature increases from 0.5 hours (316 stainless steel) to as much as 80 hours (316 LN stainless steel), indicating the beneficial effect of N [71].

Based on numerous data in literature, the effect of chemical composition

on the sensitisation behaviour of austenitic stainless steels has been described by an effective chromium content, Cr^{eff}, by giving proper weightage to various elements [60,61]:

$$Cr^{eff} = Cr + 1.45Mo - 0.19Ni - 100C + 0.13Mn - 0.22Si - 0.51Al - 0.2Co + 0.01Cu + 0.61Ti + 0.34V - 0.22W + 9.2N$$

Table 13.1 [60] relates Cr^{eff} to the critical cooling rates. It is seen that as Cr^{eff} increases, the critical cooling rate, above which sensitisation will not occur, decreases.

A sensitised HAZ could fail by TGSCC or IGSCC. The most commonly encountered environments that cause failure in austenitic stainless steels are those containing chlorides. Figure 13.15 shows that the K_{ISCC} decreases and plateau crack growth rate increases with sensitising type 316 stainless steel because of the presence of pre-existing active paths in a sensitised stainless steel [72]. It is very difficult to specify chloride levels below which SCC will not occur since other environmental factors such as oxygen content and pH of environment play a role in the failure.

The problem of IGSCC in boiling water reactors can be overcome by resorting to modifications in welding processes, or by altering the material or by modifying the environment. Modifications in welding process include the following [73]:

- *Last pass heat sink welding*: A TIG welding arc is used as the heat source to heat the outer surface while simultaneously melting the filler metal. During the process, the inner surface is flushed with water, thus cooling it. A temperature difference is thus established between the outer and inner surfaces. The resulting thermal stresses produce localised plasticity, inducing compressive stresses on the inner surface of the pipe.

Table 13.1 Dependence of critical cooling rates on Cr^{eff} [60]

Percentage cold work	Critical cooling rates (K/h)		
	12.57*	14.36*	16.03*
0	365	17	0.43
5	710	22	0.54
10	765	27	0.73
15	515	27	0.76
20	815	26	0.93
25	790	18	0.97

*Cr^{eff} (wt.%)

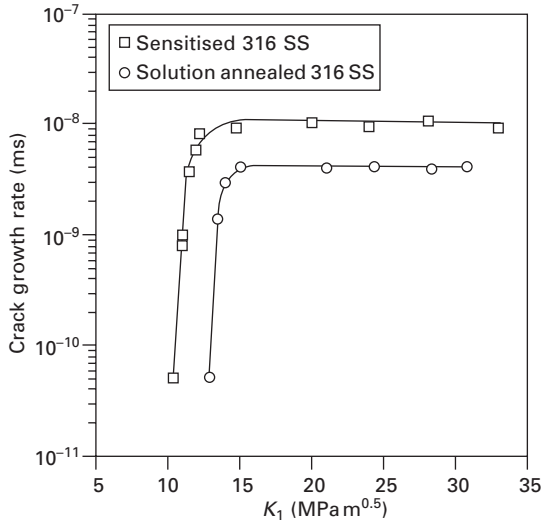

13.15 Effect of sensitisation on SCC resistance of type 316 stainless steel [72].

- *Induction heat stress improvement*: In this process, the weld area in the pipe is inductively heated from outside. The pipe is simultaneously cooled from inside with water. Just as in the above process, compressive stresses are induced on the inner surface of the pipe.
- *Mechanical stress improvement*: In this process, the pipe is radially compressed a slight amount on one side of the weld by means of hydraulic jaws to produce a permanent deformation. The deformation involved is less than 2%. The resulting curvature reduces the tensile stresses, produced by welding, on the root side of the weld area and produces compressive stresses in both the axial and radial directions.
- *Solution annealing treatment*: This helps in dissolving the grain boundary carbide network and homogenises the material composition.
- *Corrosion-resistant cladding*: The weld joint is deposited with weld overlays which have a duplex microstructure. In the BWR environment, the weld overlay may crack but complete resistance to IGSCC is ensured for the pipe.
- *Alternate pipe material*: Selection of superior materials for the application, such as types 304 LN stainless steel, which is resistant to sensitisation and hence to IGC.

13.6 Corrosion of ferritic steel weldments

Although carbon steels have some disadvantages related to fabricability and high temperature use, they are still extensively used in petroleum industries

and offshore structures. Chromium–molybdenum steels with Cr varying from 0.5 to 12 wt% and Mo from 0.25 to 1% are used extensively in fossil power plants, petrochemical industries and liquid metal cooled fast nuclear reactors as steam generator material. Since carbon steels and 'Cr–Mo' ferritic steels are the most widely used engineering materials, the corrosion issues in their weldments and the necessary precautions to be taken to avoid the premature failures are highlighted.

The corrosion behaviour of steel weldments are predominantly dependent on the microstructure developed across the weld metal and HAZ. The microstructural changes in HAZ are more pronounced in steels than stainless steels because the HAZ can easily undergo phase transformations during heating and cooling. Depending upon the heat input, preheating, thickness of the component and reheat effects (in multipass welding), cooling rates vary and a wide range of microstructures are developed. The various microstructures developed across Cr–Mo steel weldment due to fusion welding is discussed in the following section.

13.6.1 Microstructure of the weld metal

In Cr–Mo steels, the weld metal exhibits cast microstructure and base metal exhibits wrought microstructure which are either bainitic or martensitic or a mixture of both structures because hardenability of these steels is high. However, in high alloyed steel, the microstructure is fully martensitic irrespective of the cooling rates experienced during welding. If the wt% of Cr is 9 or more, weld metal may contain small volume fraction of δ-ferrite in the weld metal and HAZ. But morphology of the δ-ferrite will be different because it is formed from liquid metal during solidification and is retained and hence it has large grains with sharp boundaries.

Microstructure of HAZ

Depending on the peak temperature experienced, four main HAZ microstructures are observed in plain and modified 9Cr–1Mo steel weld joints [74]. Figure 13.16 is a schematic diagram indicating the various microstructures developed in the HAZ of steel weldment in terms of severity of the weld thermal cycle and the Fe–C equilibrium diagram. The region close to the fusion line experiences temperatures above AC_4 and results in the formation of coarse-grain martensite with δ-ferrite along prior austenite grain boundaries if Cr equivalent is high. The region next to this consists of coarse grain martensite and is known as coarse-grain HAZ (CGHAZ). The region of the HAZ which is heated to temperatures high enough for the transformation of ferrite to austenite but not sufficient for the growth of austenite is known as fine-grain HAZ (FGHAZ) which consists of fine-grain

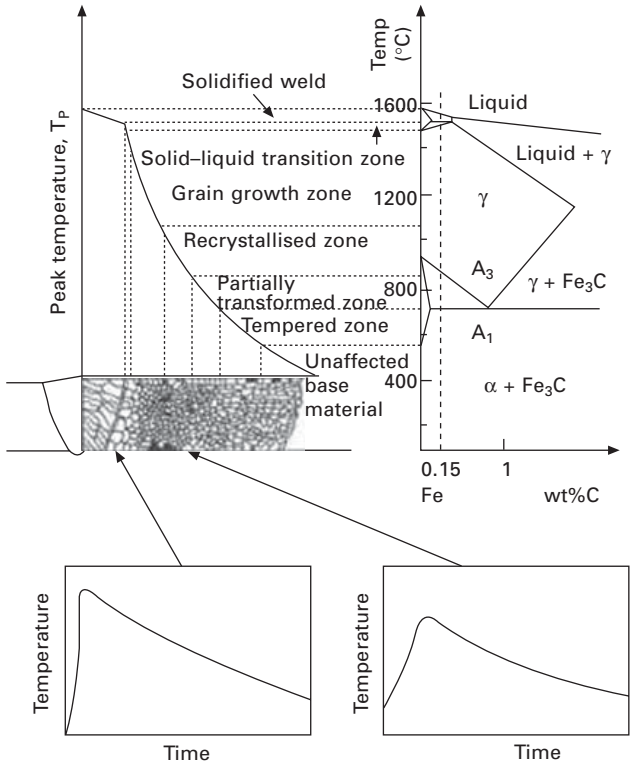

13.16 Schematic diagram indicating the various microstructures developed in the HAZ of steel weldment in terms of severity of the weld thermal cycle and the Fe–C equilibrium diagram [74].

martensite. The region of the base metal which is heated to a temperature range in which both austenite and ferrite are stable (between AC_1 and AC_3) is called intercritical HAZ (ICHAZ). The zone which experiences temperatures below AC_1 where no matrix transformation takes place is subcritical HAZ and it experiences tempering. It can be inferred that the steel weldment consists of weld metal, various HAZ and base metal of varying microstructure which introduces heterogeneities and reduces corrosion resistance in aggressive environments.

13.6.2 Corrosion of HAZ in steel weldments

In a wide range of aqueous environments, at pH values below 7 to 8, preferential weld corrosion in HAZ takes place. The reason for this is not fully understood. There is clearly a microstructural dependence and studies on HAZs show corrosion is severe when hardened microstructure is formed. Hardened steel

corrodes more rapidly in acid solutions than fully tempered material apparently because local microcathodes on the metal surface stimulate the cathodic hydrogen evolution reaction. Not much work is reported in the literature on the corrosion behaviour of weld metal, various HAZs and base metal. The authors have carried out extensive investigations on the general and localised corrosion resistance of plain and modified 9Cr–1Mo steel. Because of the difficulty in isolating microstructurally different adjacent regions of the HAZs, weld simulation heat treatments evolved by Laha *et al*. [75,76]. were followed to obtain specimen representing each microstructure. George *et al*. [77,78] have carried out electrochemical polarisation studies in 0.5 M H_2SO_4 for weld simulated plain 9Cr–1Mo steel and found the general corrosion resistance of FGHAZ, CGHAZ, normalised and tempered base metal >> ICHAZ >> PWHT weld metal. Parvathavarthini *et al*. [79] have reported similar work on modified 9Cr–1Mo weld simulated microstructures in acidic medium and found the general corrosion resistance of CGHAZ and FGHAZ > ICHAZ > over-tempered zone >> (CCGHAZ + δ-ferrite). Ranking of the various HAZ with respect to corrosion resistance in LiOH of pH = 10.2 is as follows [80]: CG HAZ + δ-ferrite > ICHAZ > FGHAZ > CGHAZ. In 0.001 M NaCl solution, the zone next to the fusion boundary containing CG martensite + δ-ferrite showed the highest susceptibility to pitting corrosion. The over-tempered zone was the next prone zone and the resistance of CGHAZ, FGHAZ and ICHAZ were almost identical. From the above data it is very clear that the general and pitting corrosion resistance of various HAZ are very different depending upon the pH and aggressiveness of the medium. Stability of the film formed depends upon the microstructure and microchemistry of the various zones. It has been reported that if the weld simulated specimens representing the as-welded microstructures are tempered (equivalent to PWHT) then all the different HAZ behave almost identically [79]. But the variations in the corrosion behaviour of HAZs with respect to microstructure are quite complex and not well understood.

13.6.3 General corrosion of weld metal

The weld metal often contains deoxidation products and, depending upon the flux system, the type and distribution of the deoxidation products, the corrosion resistance is affected. Consumable weld type plays a major role in determining weld metal corrosion rate. SMAW electrodes with basic coating show poor general corrosion resistance. For example in seawater the corrosion rate of a weld metal produced using a basic coated consumable weld is three times more than that of weld metal made using rutile coated electrode [81]. SMAW metal is predicted to have an intermediate corrosion rate between the weld metals prepared using basic coated and rutile coated electrodes.

13.6.4 Galvanic corrosion

Whenever a component is welded with an electrode in such a way that the weld metal is anodic to the base metal, severe galvanic corrosion of weld metal is likely to result. Several unexpected failures of pipings and pressure vessels have been reported in the literature which were attributed to the selection of wrong consumables which led to galvanically very dissimilar weld and base metal. For instance, Arnold [82] experienced premature weld failures due to galvanic corrosion in 100 mm (4 inch) ASTM A53 pipe that was used to transfer a mixture of chlorinated hydrocarbons and water when welding was carried out using E7010-A1 electrodes which were anodic to the base metal. By selecting nickel base electrodes, viz. InCo Weld A (AWS A5.11, class E NiCrFe 2) and Incoloy welding electrode 135, weld metal could be made cathodic and rapid corrosion was prevented. In another case, ASTM A285 grade C low carbon steel welded with E6013 electrodes failed within 18 months in seawater service at 298K whereas E7010-A1 was found most suitable. In raw brine solution, alkaline chloride and raw river water at 323K, ASTM A285 grade C base metal was cathodic to weld metal made of E7010-A1.When E 7010-G was exposed to the same environment, it was anodic to the base metal in raw brine and raw river water and was cathodic to ASTM A285 grade C base metal in alkaline chloride solution. When the base metal was changed to ASTM A53, grade B and A106 grade B it was found that E7010-A1 weld metal was cathodic to both, in raw brine at 323K. From these examples it is very clear that when components containing weld are exposed to an aqueous environment the possibility of galvanic corrosion should be carefully examined and use of higher alloyed filler metal may avoid rapid corrosion of the weld metal.

13.6.5 Stress corrosion cracking

As described earlier, during welding, the base metal, HAZ and underlying weld passes experience stresses due to thermal expansion and contraction. In addition geometric discontinuities such as weld reinforcement and lack of penetration may also result in stress concentration. Exposure of carbon steel components to caustics at temperatures above 323–353K, in the presence of residual stress may lead to caustic SCC. Such failures have been experienced in alumina processing, the pulp and paper industries, petrochemical plants and petroleum refineries. Traces of caustics can become concentrated in boiler feed water and cause caustic SCC. In boiler tubes, over-heating results in steam blanketing and, because of the alternate wetting and drying conditions, SCC takes place in locations such as cracked welds where steam pockets form with cyclic over-heating and quenching. Cracks mostly initiate at weld defects. Welded components which are intended for use above 323–353K

should be properly post-weld heat treated (1 h per 25 mm thickness at 893K). Even at ambient temperature, caustic SCC is possible, if pre-existing weld defects are present. The critical cracking potential for carbon steel is around –700 mV (SCE). Dissolved oxygen, chlorides, silicates, chromates and permanganates promote SCC, and phosphates, acetates and carbonates act as inhibitors. In anhydrous ammonia service at ambient temperatures and elevated pressures, carbon steel components containing hard welds have failed catastrophically in the presence of high stress and air contamination.

SCC of carbon steel by aqueous amine solutions which are used to remove H_2S and CO_2 from refinery and petrochemical plant is quite often reported. Intergranular cracking with crack surfaces covered with a thin film of magnetite was often observed at welds exposed to 323–368K to amines. Properly post weld heat treated components did not face the problem. Amine SCC appears to be a form of alkaline SCC and the failure mode is intergranular cracking. Carbon and low alloy steels are known to fail by SCC in hot nitrate solutions, ammonium carbonate solutions and aqueous solutions of CO_2 containing oxygen. Carbon steel refrigeration systems using 30% magnesium nitrate brine solutions have been reported to fail in HAZ due to SCC during shut down period.

In the oil and gas industry, sour water containing H_2S has caused spontaneous cracking of steel components containing hard welds. Failures are especially likely with the use of SAW for pressure vessel construction and where the weld metal had significantly higher hardness which led to transverse cracking in weld deposit. Whenever corrosion of steel takes place (aqueous H_2S corrosion, sour water or pickling solution) the cathodic reaction is the generation of atomic hydrogen from cathodic areas. When hydrogen recombination poisons such as suphide, arsenic or cyanide are present, atomic hydrogen concentration builds up at the surface and within the material, leading to blistering at the surface in low strength steel. If residual stresses arising due to fabrication processes such as welding, cold working or hardening are present, then hydrogen stress cracking (HSC) takes place. For example in sour water service HSC has been reported in a carbon steel vessel containing a hard weld [83, 84].

Because of the use of SAW for pressure vessels, weld deposits were harder and stronger and this led to the transverse cracking in the weld deposit. There is a direct relationship between H_2S concentration, allowable maximum hardness value of HAZ and threshold stress. The most effective way of preventing HSC is to ensure that the weld hardness is limited to 200 HB. Proper PWHT of fabricated component will reduce residual stress developed during welding as well as reduce hardness by tempering.

Less aggressive media such as boiler water (deionised and oxygen-free) can also result in HSC in unalloyed steels at high temperature (373–473K). The hydrogen is generated by the formation of magnetite (Fe_3O_4) on the

steel. Several failures were observed in the HAZ of repair welded boilers after a few years of service. The reason for the failures was the fact that PWHT after repair welding was overlooked, which resulted in an increase in hardness of HAZ [85].

13.6.6 Low cycle corrosion fatigue

Steel weldments are prone to low cycle corrosion fatigue which occurs due to the combined action of corrosive environment and cyclic loading. For instance, deaerator tanks which control free oxygen and other dissolved gases to acceptable levels in boiler feed water are subjected to great deal of stress-induced corrosion and low cycle corrosion fatigue [86]. Detailed investigation of the cracks indicated that cracking always occurs in welds and HAZs and are transverse to the weld HAZ, occurring both parallel and perpendicular to hoop stress direction. Cracks initiate from weld defects and pits. Combination of low cycle corrosion fatigue and stress-induced corrosion leads to such failures. Cracking at weld/HAZ boundaries suggested that residual weld shrinkage stress plays a major role in the failure. Improper PWHT coupled with poor vessel design (high localised bending stress around saddle support that fluctuates with water level) had led to the failure.

Chauhan [87] has reported cracking in the circumferential weld of a JIS-SM50B carbon manganese steel pipe used in CO_2 absorber which was in service for 18 years. All cracks were in the HAZ of the weld extending and branching into the base metal. The weld seam had been weld repaired twice and the repaired weld had been locally stress relieved. The initial weld was locally heat treated for stress relieving whereas after repair PWHT was not performed. The basic cause of this is SCC due to residual stress resulting from improper and inadequate stress relieving.

13.6.7 Sensitisation

In ferritic steels sensitisation is never considered as a serious problem and hence IGC has never been extensively examined. This is probably because of the fact that in air-hardenable ferritic steels such as 9Cr–1Mo steel, Cr depletion due to $M_{23}C_6$ precipitate is not expected because Cr diffusion in martensite/ferrite is quite rapid. Moreover at least 12% Cr is required for the formation of passive film and hence alloys containing less than 12% chromium will not exhibit active–passive behaviour in aqueous environment, which may result in enhanced attack at grain boundaries.

However, recently it has been reported [88] that creep strength enhanced 9–12% Cr ferritic steels can be susceptible to SCC in the fully hardened condition due to sensitisation. However, there were a few case histories reported earlier [88–93] which attributes some failures of 9Cr–1Mo steel to

sensitisation. Intergranular oxide presentation in caustic environment and poor SCC resistance of as-welded structures are attributed to the sensitisation of the weldments. Henry [88] has reported failure of dissimilar metal joint connecting T91 nipples to T22 safe end in a replacement SH outlet header and final SH assemblies header nipples in a coal-fired sub-critical utility boiler. Figure 13.17 shows the T91 to T22 safe end cracking on the T91 side of the weld. In some welds cracking had developed 360° around the weld to a depth greater than 50% of the total wall thickness. This failure has been attributed to sensitisation during cooling of the weld and the subsequent susceptibility to IGSCC from exposure to moisture/dampness. Even traces of aggressive contaminants such as sulphur species can lead to transgranular hydrogen stress cracking in the as-welded (hardened) condition. It must be added that in the context of Cr–Mo ferritic steels sensitisation refers to the change in microstructure, leading to further lowering of chromium in certain regions of the HAZ, which results in greater sensitivity to corrosion attack. As-welded 12Cr–1Mo, 9Cr–1Mo (plain as well as modified) and 5Cr–0.5Mo steels are sensitised in the regions of base metal–HAZ interface during welding.

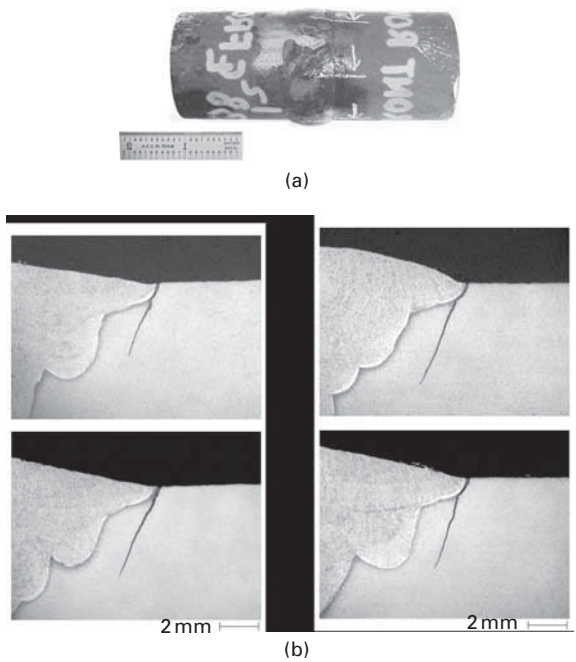

13.17 Cracking of dissimilar metal joint connecting T91 nipples to T22 safe end of a coal-fired sub-critical utility boiler. Cracking was present on the T91 side of the weld. Cracking had developed 360° around the weld to a depth greater than 50% of the wall thickness [88].

Detailed investigations were carried out by the authors to establish the influence of (i) initial microstructure, (ii) heat input, (iii) ageing, (iv) repair-welding and (v) ageing after repair welding on sensitisation behaviour of plain 9Cr–1Mo steel. It has been reported that quenched and tempered microstructure represents certain areas of HAZ of normalised and tempered ferritic steel weldments [94]. Plain 9Cr–1Mo steel weldments were austenitised, ice quenched and tempered for various durations to simulate various zones. A fully tempered specimen represents base metal while an insufficiently tempered specimen represents a sensitised specimen of a non-post-weld heat-treated weld. Using potentiostatic technique standardised by Poulson [89], sensitisation was evaluated. In this technique, all the specimens were subjected to potentiostatic etching in 16 wt% H_2SO_4 at +100 mV (SCE). Based on the current–time response the specimens were classified in three categories: (1) sensitised – instantaneous increase in current; (2) partially sensitised – current increase after some incubation time; (3) not sensitised – no increase in current. The potentiostatic curves for specimens tempered at 1023 K are collectively presented in Fig. 13.18 [95] and the TTS diagram established based on these results is presented in Fig. 13.19 [95].

The results of this study have unambiguously established that 9Cr–1Mo steel weldments undergo sensitisation if not properly post-weld heat treated. The proposed mechanism [89] is as follows: the initial microstructure of this steel in the normalised and tempered condition is ferrite and carbides of chromium. The schematic representation of chromium concentration profile is given in Fig. 13.20 [89]. Since these carbides are distributed uniformly throughout, there is no chromium-depleted zone in the initial microstructure.

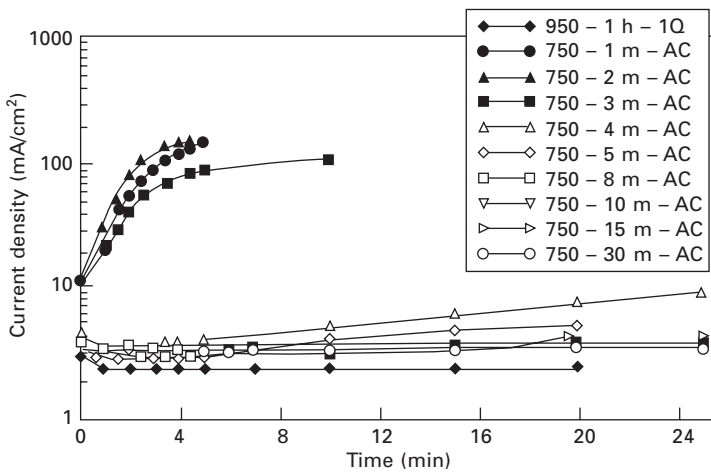

13.18 Potentiostatic curves for weld simulated 9%Cr–1%Mo steel in 16 wt% H_2SO_4 at +100 mV(SCE) [95]. Q = quenched, AC = air cooled. Temperature indicated in °C.

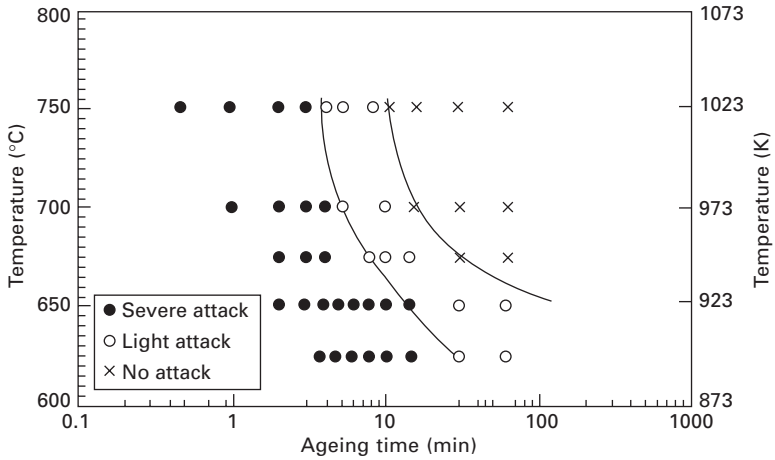

13.19 TTS diagram for 9%Cr–1%Mo steel established using potentiostatic etching technique [95].

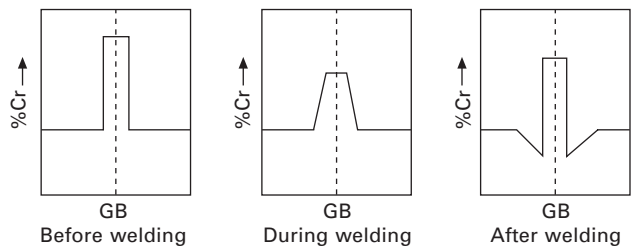

13.20 Schematic diagrams showing the proposed mechanism of sensitisation in 9Cr–1Mo steel weldment [89]. GB = grain boundary.

During welding, partial dissolution of carbides takes place and during cooling reprecipitation occurs, which results in chromium depletion in the immediate vicinity of the carbide particles. Because of the difference in chromium content between the matrix and the chromium-depleted zone, the passivation potential of these two zones will be different. Therefore in corrosive media, preferential attack leading to IGC can take place in zones leaner in chromium. When sufficiently tempered chromium diffusion from matrix to depleted zone may desensitise the HAZ.

It can be inferred that inadequate PWHT and insufficient tempering after normalising are risky from the sensitisation point of view. Results generated by the authors clearly indicate that the depth and width of the sensitised zone increases with increase in heat input and it moves away from the fusion line with increase in heat input. If repair welded components (without PWHT) are subjected to elevated temperature service, both weld metal and HAZ become prone to IGC. Potentiostatic hydrogen charging of a repaired SMAW

weldment resulted in hydrogen induced single sharp cracking in sensitised zone where gradient in hardness is maximum and the hydrogen-induced cracking (HIC) is shown in Fig 13.21 [95]. This means that the risk of HIC is also maximum in the sensitised zone in addition to susceptibility to IGC arising due to sensitisation. The practical implication of the above result is that delay or omission of tempering heat treatment may result in damage to the component due to SCC. Improper PWHT, insufficient tempering, rapid thermal transients at and above 1023 K and repair welding without proper PWHT lead to sensitisation. Inadequate PWHT can result in the sensitisation of entire HAZ and weld metal. This can be removed by proper PWHT.

Although PWHT is always recommended and practised after repair welding, sometimes it may not be possible. For example, once a component is in service in a nuclear or thermal station, repair welding itself is a difficult task. The components are invariably attached to a piping or support system and surrounded by process equipment and instrumentation which can present innumerable problems for pre-heating and PWHT. Although recent repair welding techniques such as temper bead welding which do not require PWHT are being developed to take care of hydrogen removal and refinement of HAZ microstructures, residual stresses are still a matter of concern. This problem can be easily avoided by (i) imposing limits on permissible time between completion of welding (or normalising) and completion of PWHT (or tempering), (ii) by maintaining the hardened component dry until tempering/PWHT and (iii) by examining both OD and ID surface by NDE after completion of PWHT/tempering.

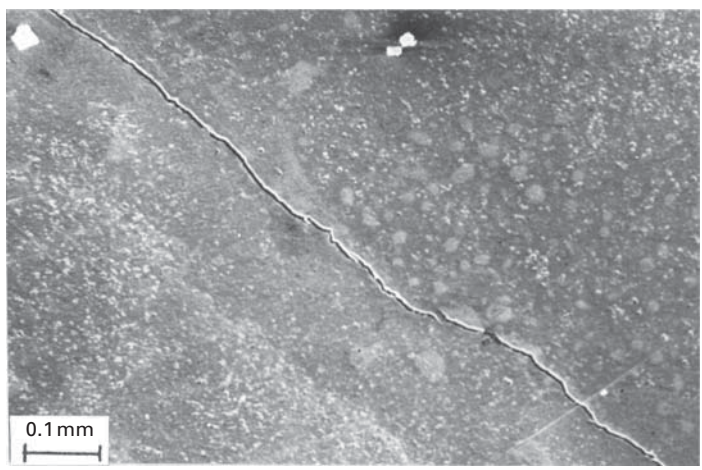

13.21 Scanning electron micrograph showing the hydrogen-induced cracking of 9%Cr–1%Mo steel weldment without PWHT due to hydrogen charging at –1.5 V (SCE) in 0.5 M H_2SO_4 containing 200 ppm As_2O_3 [95].

13.7 Conclusions

In the weld joints of austenitic stainless steels, the presence of δ-ferrite in the weld metal deteriorates the pitting and SCC properties of weld metal of austenitic stainless steels vis-à-vis the base metal. Higher heat input into the weld metal causes deterioration in its localised corrosion properties. High temperature ageing causes precipitation of a number of deleterious phases, which reduce the corrosion properties. Residual stresses are also detrimental from the weld metal corrosion point of view since the dissolution rate is increased. Sensitisation of HAZ leads to a decrease in all localised corrosion properties. The maximum impact of a sensitised HAZ is experienced on the IGSCC of the austenitic stainless steel weld joint. Careful examination of various corrosion issues in unalloyed and low alloyed steel weldments reported in several industries and case histories of failures indicates that (i) improper PWHT either during fabrication or after repair and (ii) faulty design accounts for most of the catastrophic failure of welded steel components. Lack of full weld penetration, for example, is dangerous because of likelihood of crevice corrosion and the possibility of fatigue crack. Cracks initiate from corrosion pits and weld defects can also become active sites for crack initiation.

During fabrication and commissioning of a new welded component, care is always taken to follow the various codes and regulations. However, when repair welding has to be carried out several points have to be remembered. Repair of component failed in service is more complex than repair carried out to remove defects during fabrication and commissioning stage. The success of repair welding operation depends on many factors such as weldability of the material, availability of suitable welding technique and welding consumable, possibility of pre-heating and post-weld heating, post-repair inspection by non-destructive testing. Sometimes welding consumables for repair may be different from those used for original fabrication. Under such conditions it should be ensured that any one of the several types of corrosion described above does not reoccur and faulty design, wrong selection of material and operational mistakes should not be repeated. A few remedies to the various problems of corrosion of weld joints of austenitic stainless steel and ferritic steels have been addressed.

13.8 References

1. C. D. Lundin, *WRC Progress Report* (1994) 64
2. K. Komai, *Proceedings of the International Conference on Case Histories on Integrity and Failures in Industry*, Italy, 1999
3. T. Rogne, J. M. Drugli and S. Valen, *Corrosion*, **48** (1992) 864
4. S. Szklarska-Smialowska and E. Lunarska, *Werkstoffe und Korrosion*, **32** (1981) 478
5. H. Holtan and H. Sigurdsson, *Werkstoffe und Korrosion*, **32** (1981) 478
6. S. Szklarska-Smialowska and J. Gust, *Corrosion Science*, **19** (1979) 753

7. R. L. Shamakian, A. R. Troiano and R. F. Hehemann, *Corrosion*, **36** (1980) 279
8. W. L. Clarke and G. M. Gordon, *Corrosion*, **29** (1973) 1
9. D. Kotecki and D. G. Howden, *WRC Bulletin* No. 184 (1973)
10. H. T. Shirley, *Journal of Iron and Steel Institute*, **174** (1954) 242
11. D. N. Noble, *Welding and Metal Fabrication*, **59** (1991) 295
12. H. S. Khatak, V. Seetharaman and J. B. Gnanamoorthy, *Practical Metallography*, **20** (1983) 570
13. L. K. Zamiryakin, *Materials Science*, **2** (1968) 439–441
14. C. L. Cole and J. D. Jones, *Proceedings of Conference on Stainless Steels*, ISI Publication 117, (1969) 71
15. C. Edeleanu, *Corrosion Technology*, **4** (1957) 49
16. T. G. Gooch, *Proceedings of the Conference on the Influence of Welding and Welds on Corrosion Behaviour of Constructions*, IIW Annual Assembly, Tel Aviv, (1975) 1.52
17. M. Mochizuki, *Nuclear Engineering and Design*, **237** (2007) 107
18. G. Engelhard, L. M. Habip, D. Pellkofer, J. Schmidt and J. Weber, *Nuclear Engineering and Design*, **198** (2000) 141
19. A. T. Dewald, J. E. Rankin, M. R. Hill, M. J. Lee and H. L. Chen, *Journal of Engineering Materials and Technology, Transactions of ASME*, **126** (2004) 465
20. J. C. Lippold and W. F. Savage, *Welding Journal*, **59** (1980) 362-s
21. J. A. Brooks and A. W. Thompson, *International Metals Review*, **36** (1991) 16
22. T. P. S. Gill, V. Seetharaman and J. B. Gnanamoorthy, *Corrosion*, **44** (1988) 511
23. P. I. Marshall and T. G. Gooch, *Corrosion*, **49** (1993) 514
24. H. J. Dundas and A. P. Bond, *NACE Corrosion/75*, (1975) Preprint No. 159
25. A. Garner, *Pulp and Paper Industry Corrosion Problems*, NACE, Vol. 2, (1977)
26. P. E. Manning, C. E. Lyrnan and D. J. Duquette, *Corrosion*, **36** (1980) 246
27. T. P. S. Gill, J. B. Gnanamoorthy and K. A. Padmanabhan, *Corrosion*, **43** (1987) 208
28. D. H. Sherman, D. J. Duquette and W. F. Savage, *Corrosion*, **31** (1975) 376
29. F. Stalder and D. J. Duquette, *Corrosion*, **33** (1977) 67
30. W. A. Baeslack III, W. F. Savage and D. J. Duquette, *Metallurgical Transactions A*, **10A** (1979) 1429
31. T. G. Gooch, *Welding in the World*, **22** (1984) 64
32. W. A. Baeslack III, D. J. Duquette and W. F. Savage, *Corrosion*, **35** (1979) 45
33. K. S. Raja and K. P. Rao, *Corrosion*, **48** (1992) 634
34. H. Shaikh, G. George, F. Schneider, K. Mummert and H. S. Khatak, *Werkstoffe und Korrosion*, **51** (2000) 719
35. H. Shaikh, H. S. Khatak and J. B. Gnanamoorthy, *Werkstoffe und Korrosion*, **38** (1987) 183
36. W. A. Baeslack III, W. F. Savage and D. J. Duquette, *Welding Journal*, **58** (1979) 83-s
37. A. Garner, *Materials Performance*, **21** (1982) 9
38. D. D. Nage and V. S. Raja, *Corrosion Science*, **48** (2006) 2317
39. G. F. Li and J. Congleton, *Corrosion Science*, **42** (2000) 1005
40. I. Hamada and K. Yamauchi, *Metallurgical and Materials Transactions A*, **33A** (2002) 1743
41. N. Parvathavarthini, R. K. Dayal, H. S. Khatak, V. Shankar and V. Shanmugam, *Journal of Nuclear Materials*, **35** (2006) 68
42. T. Anita, H. Shaikh, H. S. Khatak and G. Amarendra, *Corrosion*, **60** (2004) 873–880

43. U. K. Mudali, R. K. Dayal, T. P. S. Gill and J. B. Gnanamoorthy, *Corrosion*, **46** (1990) 454
44. R. Jithendra Kumar, T. Anita, H. Shaikh, R. K. Dayal and H. S. Khatak, *Proceedings of the National Welding Seminar*, Chennai, 24–26 November, (2006) 217
45. C. V. Franco, R. P. Barbosa, A. E. Martinelli and A. J. A. Buschinelli, *Werkstoffe und Korrosion*, **49** (1998) 496
46. T. P. S. Gill, M. Vijayalakshmi, P. Rodriguez and K. A. Padmanabhan, *Metallurgical Transactions A*, **20A** (1989) 1115
47. H. Shaikh, M. G. Pujar, N. Sivaibarasi, P. V. Sivaprasad and H. S. Khatak, *Materials Science and Technology*, **10** (1994) 1096
48. R. G. Thomas and D. Yapp, *Welding Journal*, **57** (1978) 361-s
49. A. Garner, *Metal Progress*, **127** (1985) 31
50. H. Shaikh, G. George, F. Schneider, K. Mummert and H. S. Khatak, *Transactions of the Indian Institute of Metals*, **54** (2001) 27
51. M. G. Pujar, R. K. Dayal, T. P. S. Gill and J. B. Gnanamoorthy, *Proceedings of the International Conference on Welding Technology*, University of Roorkee, Roorkee, (1988) II-33
52. D. Warren, *Microstructural and Corrosion Resistance of Austenitic Stainless Steel*, Sixth Annual Liberty Bell Corrosion Course, NACE, Philadelphia, PA, September 1968
53. I. H. Lo and W. T. Tsai, *Materials Science and Engineering A*, **355** (2003) 137
54. H. Shaikh, H. S. Khatak, S. K. Seshadri, J. B. Gnanamoorthy and P. Rodriguez, *Metallurgical and Materials Transactions A*, **26A** (1995) 1859
55. K. N. Krishnan and K. P. Rao, *Proceedings of the International Conference on Stainless Steel*, Indian Institute of Metals, New Delhi, (1992) 419
56. T. P. S. Gill, *Proceedings of the Corrosion Management Course*, The Indian Institute of Metals, Kalpakkam, October 1995, Paper No. L-6
57. V. Kain, K. Chandra, K. N. Adhe and P. K. De, *Journal of Nuclear Materials*, **334** (2004) 115
58. S. K. Mannan, R. K. Dayal, M. Vijayalakshmi and N. Parvathavarthini, *Journal of Nuclear Materials*, **126** (1984) 1
59. N. Parvathavarthini, R. K. Dayal, J. B. Gnanamoorthy and S. K. Seshadri, *Journal of Nuclear Materials*, **168** (1989) 83
60. N. Parvathavarthini and R. K. Dayal, *Journal of Nuclear Materials*, **305** (2002) 209
61. R. K. Dayal, N. Parvathavarthini and B. Raj, *International Materials Reviews*, **50** (2005) 129
62. ASTM Standard A262-93a, *ASTM Book of Standards*, American Society for Testing of Metals, Philadelphia PA, (1993) 42
63. V. Cihal, *Corrosion Science*, **20** (1980) 737
64. P. Novak, R. Stefec and F. Franz, *Corrosion*, **31** (1975) 344
65. W. L. Clarke, W. M. Romero and J. C. Danko, *Report GEAP-21382*, GEC, California, (1976)
66. ASTM Standard G 108-94, *ASTM Book of Standards*, American Society for Testing of Metals, Philadelphia PA, (1994) 444
67. N. Parvathavarthini, R. K. Dayal, R. Ravi and H. S. Khatak, *Transactions of the Indian Institute of Metals*, **56** (5) 2003, 499–504
68. E. Folkhard, *Welding Metallurgy of Stainless Steels*, Springer-Verlag, Vienna (1988)
69. C. L. Briant, R. A. Mulford and E. E. Hall, *Corrosion*, **38** (1982) 468
70. T. A. Mozhi, W. A. T. Clarke, K. Nishimoto, W. B. John and D. D. McDonald, *Corrosion*, **41** (1985) 555

71. N. Parvathavarthini, R. K. Dayal and J. B. Gnanamoorthy, *Corrosion*, **208** (1994) 251
72. T. V. Vinoy, H. Shaikh, H. S. Khatak, N. Sivaibharasi and J. B. Gnanamoorthy, *Journal of Nuclear Materials*, **238** (1996) 278
73. J. Schmidt, D. Pellkofer and E. Weiss, *Nuclear Engineering and Design*, **174** (1997) 301
74. R. Menon and K. K. Khan, Report No: ORNL/Sub/81-07685/02 & 77, Oak Ridge National Laboratory
75. K. Laha, K. S. Chandravathi, K. Bhanushankar Rao and S. L. Mannan, *International Journal of Pressure Vessels and Piping*, **62** (1995) 303
76. K. S. Chandravathi, K. Laha, K. Bhanushankar Rao and S. L. Mannan, *Materials Science and Technology*, **17** (2001) 1
77. G. George, H. Shaikh, N. Parvathavarthini, R. P. George and H. S. Khatak, *Journal of Materials Engineering and Performance*, **10** (4) (2001), 460–467
78. G. George, H. Shaikh, N. Parvathavarthini, R. P. George and H. S. Khatak, *Proceedings of International Welding Conference*, New Delhi, 21–23, February (2001), 305–321
79. N. Parvathavarthini, R. K. Dayal, H. S. Khatak and K. Laha, *Proceedings National Welding Seminar (NWS-2001)*, 7–9, January (2002), Chennai
80. L. Renuka, M. Sc thesis, September 2006, Bharathiyar University
81. J. R. Davis and J. D. Destefani, (eds.), *Metals Hand Book*, Vol. 13, 1987, ASM International, Ohio 44073, p 362
82. C. G. Arnold, Paper 71, presented at *Corrosion/80*, Chicago, IL, NACE, March, 1980
83. J. Gutzeit, R. D. Merrick, L. R. Scharfstein, *Metals Hand Book*, Vol. 13, p 1262–1287
84. E. L. Hildebrand, *Proc. API*, **50** (III) (1970) 593–613
85. M. Schutze, Vol II, Materials Science and Technology Series, series editors: R. W. Cahn, P. Haasen, E. J. Kramer, Wiley-VCH, 2000
86. G. E. Kerns, paper 310, presented at *Corrosion/86*, Houston, NACE, March, 1986
87. S. K. Chauhan, *Hand Book of Case Histories in Failure Analysis*, Vol. 1, ed. K. A. Esakul, ASM International, Materials Park, OH, 1992 191–193.
88. J. F. Henry, ALSTOM, IIW, AWS, Technical lectures on Cr–Mo steels, January/February 2006
89. B. Poulson, *Corrosion Science*, **18** (1978) 371
90. B. Poulson, *Proc. of Conference on Ferritic Steels for Fast Reactor Steam Generator*, eds. S. F. Pugh and E. A. Little, British Nuclear Energy Society, London, 1978, Paper No. 68, p 413–418
91. G. J. Bignold, *Proc. of Conference on Ferritic Steels for Fast Reactor Steam Generator*, Eds. S. F. Pugh and E. A. Little, British Nuclear Energy Society, London, 1978, Paper No. 58, 346–352
92. P. Hurst, REML, Risley, U.K, Private communication, 1977
93. D. Robinson, Clarke Chapman report No. ML/73/68/Dec. 1973
94. M. Wall, B. C. Edwards and J. A. Hudson, *Proc. Specialists Meeting on Mechanical Properties of Structural Materials Including Environmental Effects*, Chester 1988, Report IWGFR – 49, 1984, Vol. 2, 545
95. N. Parvathavarthini, Ph.D thesis, Madras University, May 1995.

14

Advances in techniques for determination of susceptibility of welds to stress corrosion cracking (K_{ISCC})

R K SINGH, Monash University, Australia

Abstract: Stress corrosion cracking (SCC) is a dangerous form of environment assisted degradation. Threshold stress intensity factor for SCC (K_{ISCC}), an important parameter in design and prediction of life of component, is a stress intensity limit below which any crack can not propagate in corrosive environment. Accurate determination of K_{ISCC} is vital for predicting life of a component. Welded components often suffer from SCC in the heat affected zone (HAZ). Determination of K_{ISCC} of narrow HAZ of actual welds is difficult with conventional techniques. Cracks in the specimens for these techniques can propagate out of HAZ plane. This paper describes a new simple, relatively fast, and inexpensive fracture mechanics-based technique (named circumferential notch tensile (CNT) technique), and its use in testing welded specimens.

Key words: stress corrosion cracking (SCC), fracture mechanics, threshold stress intensity factor for SCC (K_{ISCC}), circumferential notch tensile (CNT) technique.

14.1 Stress corrosion cracking (SCC) of welds and threshold stress intensity for SCC (K_{ISCC})

SCC is a premature cracking which occurs under a synergistic action of a tensile stress and corrosive environment. The most fundamental but extremely detrimental feature of cracking is that a ductile material that would have undergone considerable elongation before fracture suffers serious embrittlement in the presence of the corrosive environment, leading to a premature brittle fracture (i.e. without much elongation).

Some of the features that make SCC the most dangerous form of corrosion-assisted failure, and a critical consideration in selection of material for equipment operating in corrosive environment, are:

- it can occur at stresses below the design stresses (i.e. those required for failure of the material in the absence of the corrosive environment): the welded components are often most susceptible to SCC because of the presence of tensile residual stresses;
- environments that are only mildly corrosive may cause severe SCC; and
- sometimes, the alloy may virtually appear unattacked over most of its surface, and only a few fine and localised cracks may propagate undetected to failure.

SCC accounts for a great proportion of failures of industrial equipment, particularly the weldments exposed to corrosive environment. A reliable life assessment and extension of welded parts of ageing plants hinge critically on the reliable, cost-effective and rapid characterisation of SCC of in-service as well as failed components exposed to corrosive conditions. A few techniques have been used for monitoring SCC[1,2]. Common techniques, such as the U-bend and C-ring testing, have proved to be too simplistic in approach and the data generated can often represent overly accelerated conditions. Laboratory techniques, such as slow strain rate testing (SSRT), are suitable for providing a broad 'go, no-go' type of assessment[1] but fail to generate data for life prediction of in-service components.

Life extension/prediction of components exposed to in-service corrosive environments generally involves assessment of susceptibility of existing cracks to environment-assisted propagation. This susceptibility is also a critical consideration for design engineers when selecting construction materials for corrosive environments. Fracture toughness (K_{IC}) is the measure of a given material's resistance to crack growth. The driving force for extension of an existing defect (crack) is the stress intensity factor K_I. A crack will propagate when K_I exceeds some threshold value, K_{IC}, i.e. fracture toughness. Determination of the critical value of stress intensity factor necessary for propagation of an existing crack (i.e. K_{IC}) is a critical material selection criterion for any mechanical engineering design. For an alloy–environment system conducive to SCC, the threshold stress intensity with the influence of environment at the crack-tip (i.e. K_{ISCC}) is considerably lower than K_{IC}. K_{ISCC} has traditionally been determined using various specimen geometries, as shown in Fig. 14.1.

The prime and most stringent requirement for application of fracture mechanics is the validity of a rigorous plane strain condition (PSC) at the crack-tip, in order to eliminate/minimise the zone of the plastic deformation. In order for specimens of the commonly used geometries to comply with the requirements of valid plane strain condition, specimens require to be bulky (viz. compact tension specimen (CTS) and double cantilever beam (DCB) test specimens)[1,2].

CTS specimens (shown in Fig. 14.1), which is one of the most widely used specimen configurations for determination of fracture toughness (K_{ISCC}), is believed not to conform fully to the stringent requirements of PSC, in spite of the bulkiness of the specimens used. It is well known that the theoretical requirements, i.e. uniformly distributed applied stress over the thickness and plane strain condition, can never be realised as long as the free surfaces exist at both ends of a CTS specimen. The end effects will be further amplified when the thickness decreases to a thin plate. Consequently, specimens of greater thicknesses are used, which reduces (but never eliminates) the end effects. A large scatter in K_{IC} and K_{ISCC} data generated using CTS specimens

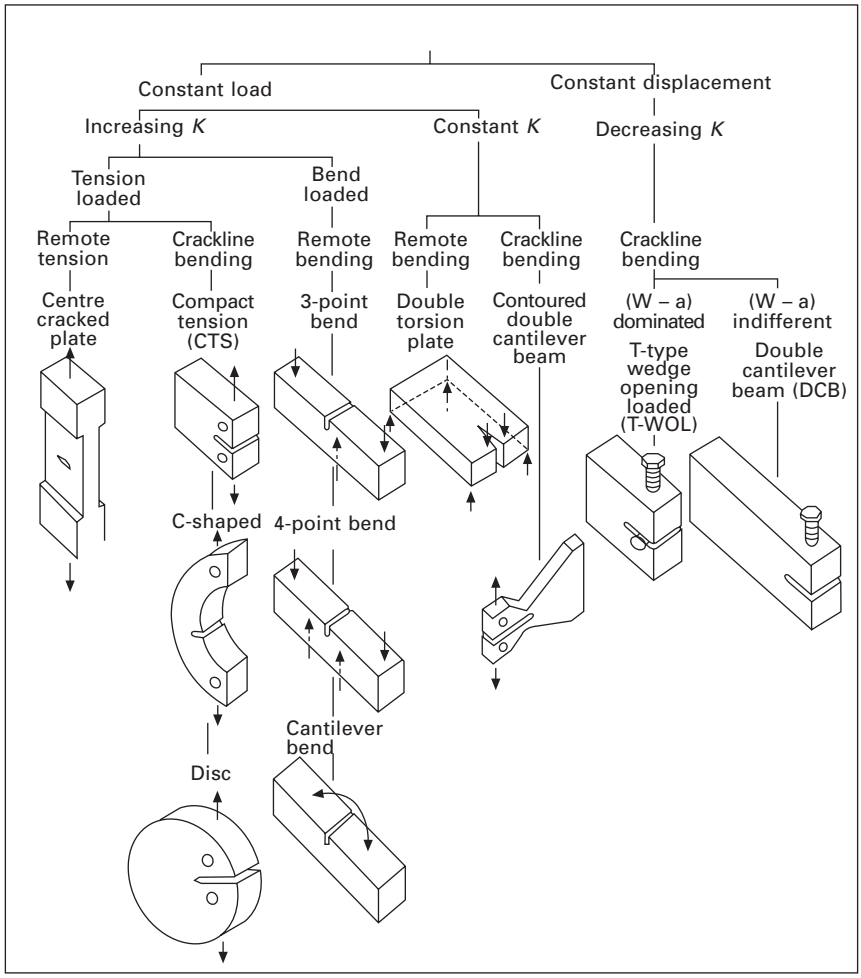

14.1 Different specimen geometries for SCC testing[1] (W = net width; a = effective crack length).

are attributed to end effects and to the conservative specimen size, which lead to an inability to control the direction of crack propagation, resulting in a zigzag or non-uniform crack front. The difficulties in controlling the crack direction during testing by the traditional techniques (such as CTS) may be prohibitively amplified while testing the small specimen such as the narrow area of a weldment.

Most importantly, a large scatter in data generated using CTS specimens forces a more conservative allowance in design, such as a large factor for safety. Large scatter in K_{IC} and K_{ISCC} data from CTS testing of the in-service components also leads to a conservative prediction of the remaining life of

a given component. Conservative estimates of the design data and remaining life have serious cost implications.

CTS and other specimen geometries that require use of bulky test specimens are also fraught with other disadvantages, such as the high cost of manufacture/testing of specimens, and requirements of a prohibitively long testing time, large number of tests and bulky piece of test materials. Therefore, an accurate, rapid and cost-effective determination of K_{ISCC} is of immense interest to prudent design and maintenance engineers as well as for accuracy in life prediction. With a view to addressing these requisites, a new technique for generation of K_{ISCC} data, namely, circumferential notch tensile (CNT) testing has been developed, tested and validated at Monash University. This technique is also being applied for testing specimens of weldments.

14.2 CNT testing

Specimens used for CNT testing, shown in Fig. 14.2, are one of the smallest possible specimens that can produce valid plane strain crack loading conditions[3–5]. Ahead of the notch of the CNT specimen, a uniform pre-crack is developed by subjecting the specimen to a controlled fatigue in a bending-rotating set-up[3–5]. The pre-cracked CNT specimen is then subjected to a constant load, until the specimen fails. Tests are carried out at different loads which translate to different magnitudes of stress intensity (K_I). K_I is correlated with the crack propagation parameters, viz. crack-growth velocity or time-to-failure (T_f)[3–5], in order to determine K_{IC} and K_{ISCC}. However, an accurate determination of K_I is the vital key to the successful application of the technique.

14.2.1 Determination of K_I

K_I is determined from the fractured specimen, using Equations 14.1–14.9[3–5]

$$K_I = (\sigma_t + \sigma_b)\sqrt{a\pi F_O} \qquad 14.1$$

where,

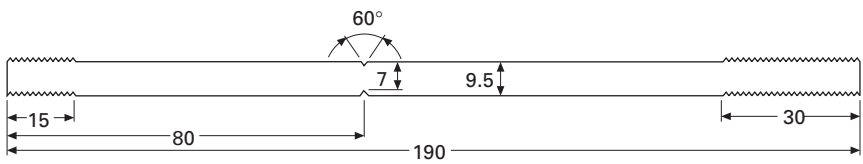

14.2 CNT specimen (all dimensions in mm).

$$a = \frac{D - d}{2} \tag{14.2}$$

$$\sigma_t = \frac{4P}{\pi D^2} \tag{14.3}$$

$$\sigma_b = \frac{16P\varepsilon}{\pi D^3} \tag{14.4}$$

$$F_O = Fe^{\alpha(\varepsilon/D)} \tag{14.5}$$

$$F = \frac{1.25}{\left[1 - \left(\frac{2a}{D}\right)^{1.47}\right]^{2.4}} \tag{14.6}$$

$$\alpha = 22.188e^{-4.889(2a/D)} \tag{14.7}$$

P is the applied load (N); D, the specimen's diameter (m); d, the equivalent ligament diameter (m); ε, the eccentricity (m); and a, the effective crack length (m).

The first estimate of K_I is obtained by using the effective crack length (a) in Equation (14.1). This estimate of K_I is used to get the Irwin correction factor (r_y) from Equation (14.8) and ($\bar{a}$) from Equation (14.9) and hence the quoted results for K_I from Equation (14.1).

$$r_y = \frac{1}{6\pi}\left(\frac{K_I}{\sigma_Y}\right)^2 \tag{14.8}$$

$$\bar{a} = a + r_y \tag{14.9}$$

where σ_y is 0.2% offset tensile yield stress (Pa). The basis of this correction term has been discussed thoroughly in the literature[6–9]. This correction term relates to a certain degree of plasticity at the crack-tip, given that the materials do not behave perfectly elastically and show some plastic deformation at the crack-tip. The first estimate of K_I is calculated by using the value of a in equation (14.2). Then, K_I is calculated using $\bar{a}$ in place of a.

14.2.2 Allowance for eccentricity (ε)

One of the critical issues in determination of K_{IC} by CNT method is the possible effects of the eccentric fatigue crack and the ligaments produced by the rotating bending fatigue crack machine of specimens. Examples of eccentric pre-cracks show that the ligaments are off-centre, which makes it difficult to locate the centroid of the ligament. This elliptical fatigue crack or eccentricity

occurs owing to the insufficient isotropy in its fatigue characteristics. When the ligament is off-centre, the final fracture of the specimen will not result from tension force only but will also have a contribution from the bending forces. Therefore, the effect of the eccentricity must be taken into account in calculating K_I. A specific method that is employed to account for the eccentricity is described elsewhere in detail[10,11].

14.2.3 Validity requirements for K_I measurements

Materials in non-ideal situations do not deform completely in elastic brittle manner as the linear elastic fracture mechanics (LEFM) approach assumes. The LEFM approach is only valid if the size of the plastic zone is negligible compared with the specimen geometry. Therefore, specifications for determining the validity of measuring K_I were developed. The validity requirements for measuring K_I are $a_f \geq 2r_y$ and $\sigma_N/\sigma_Y \leq 2.5$, where

$$a_f = \varepsilon + \frac{(D - 2a_m - d)}{2}$$

and σ_N is the nominal applied stress in the final ligament (Pa).

Validity limits require[3–5] the fatigue crack depth to be at least twice the Irwin plastic zone correction in depth, and that the average stress across the ligament after fatigue cracking should not exceed 2.5 times the yield strength. These limits were also applied to those cases where the final ligaments were eccentric to the specimen centreline. With an eccentric ligament, the maximum nominal stress considered was then a combination of tensile and bending stresses, which should not exceed 2.5 times the yield strength. Further, for such eccentric ligament cases the fatigue crack depth considered for the purposes of validity was taken to be the greatest depth of the crack.

The small size of the specimens used in CNT testing has the following advantages:

- The small cross-section of the specimen makes it possible to achieve quite high levels of stress intensities by using moderate loads.
- CNT testing reduces the amount/cross-section of material required for testing, which is critical when microstructures of limited size such as welds are to be investigated.
- In many cases thick section material may not be available. This is characteristic of many pressure vessels constructed out of expensive materials such as stainless steels or duplex stainless steels.
- The CNT specimen is cheap to produce because of its small cylindrical shape, reducing the cost of each specimen and overall testing.

Table 14.1 compares advantages and limitations of CNT with other ASTM standard tests/specimen configurations for determination of K_{IC} and K_{ISCC},

Table 14.1 Comparison of CNT with other specimen configurations for K_{IC} determination[10]

Comparison criteria	CNT	CTS	3PB	SNTT	CVN
Cost of sample	Low	High	Low	Low	Low
Size effect	Size dependent	Size dependent	Size dependent	Virtually none	N/A (dynamic test)
Direct K_{IC} determination	Yes, size dependent	Yes, with large specimen	Yes, test adjustment	Yes	No
Controlled crack propagation direction	No	No	No	Propagates perpendicularly toward central axis	N/A (dynamic test)
Statistical aspects	Large uncertainty	Large data scatter/uncertainty	Large uncertainty	Long/uniform crack front: less data scatter	Large uncertainty
Fatigue pre-crack (PC) characteristic/ requirement	Non-uniform front; PC required	Non-uniform front; PC required for both ductile and brittle materials	Non-uniform front; PC required for all materials	PC produces uniform crack front for ductile materials	N/A
Mixed mode testing	Not available	Needs large/complicated/ special set-up/specimen	Not available	Easy to carry out using different pitches for the notch	Not available

viz. CTS, 3-point bending (3PB) test, CNT, spiral notch torsion test (SNTT) and Charpy notched (CVN) bar impact test.

14.3 Determination of K_{ISCC} by CNT testing

First successful attempts have recently been made[11–13] for use of CNT testing for generation of K_{ISCC} data for mild steel in caustic solutions. The custom-built CNT rig for stress corrosion cracking testing using hot caustic solutions is shown in Fig. 14.3. The major components of the rig include a corrosion cell (made out of Monel 400), facilities for heating the corrosive solution, temperature control and thermal insulation. The rig also consists of facilities for electrochemical testing, such as the reference and counter-electrodes, which are used for the determination of K_{ISCC} under imposed electrochemical potentials. The CNT specimens (shown in Fig. 14.2) are machined out of 20 mm diameter rods of the cast iron. The diameter of the specimen is 9.5 mm with a 60° 'V' groove in the middle, which gives a minimum diameter of 7 mm. The notched specimens are subjected to fatigue pre-cracking, using a rotating bending fatigue machine. The pre-cracked specimens are cleaned and washed with ethanol and dried, before being installed into the rig.

For CNT testing, the corrosion cell was filled with 500 g/L NaOH solution and heated to the test temperature (100 °C) before applying the tensile load to the specimen. This procedure ensured that the applied load did not change as a result of the expansion of the specimen and surrounding metallic fittings. The specimen was held under a specific load until it failed. The time-to-failure (T_f) is recorded at the failure of the specimen. The K_I corresponding to a given applied load was determined from the fractured specimen. A detailed description of the technique and intricate measurement of various fracture parameters in order to accurately determine the stress intensity (K_I) are given in Section 14.2.

A plot of the calculated values of K_I against the time-to-failure (T_f) of mild steel in 500 g/L caustic solution at 100 °C is given in Fig. 14.4. As shown in the figure, the K_{ISCC} has been determined to be 42.9 MPa $m^{0.5}$, meaning thereby when steel specimens are in contact with 500 g/L caustic solution at 100 °C, any crack with a stress intensity (K_I) greater than 42.9 MPa $m^{0.5}$ will propagate quickly due to caustic embrittlement. Indeed, a specimen with a K_I less than 42.9 MPa $m^{0.5}$ did not fail during an extended testing for ~4000 h. Also, another specimen that was exposed to a condition which facilitated formation of a robust and thick oxide film did not fail even though the K_I was greater than 42.9 MPa $m^{0.5}$. These two examples demonstrate the profound role of both stress intensity and corrosion environment in facilitating SCC.

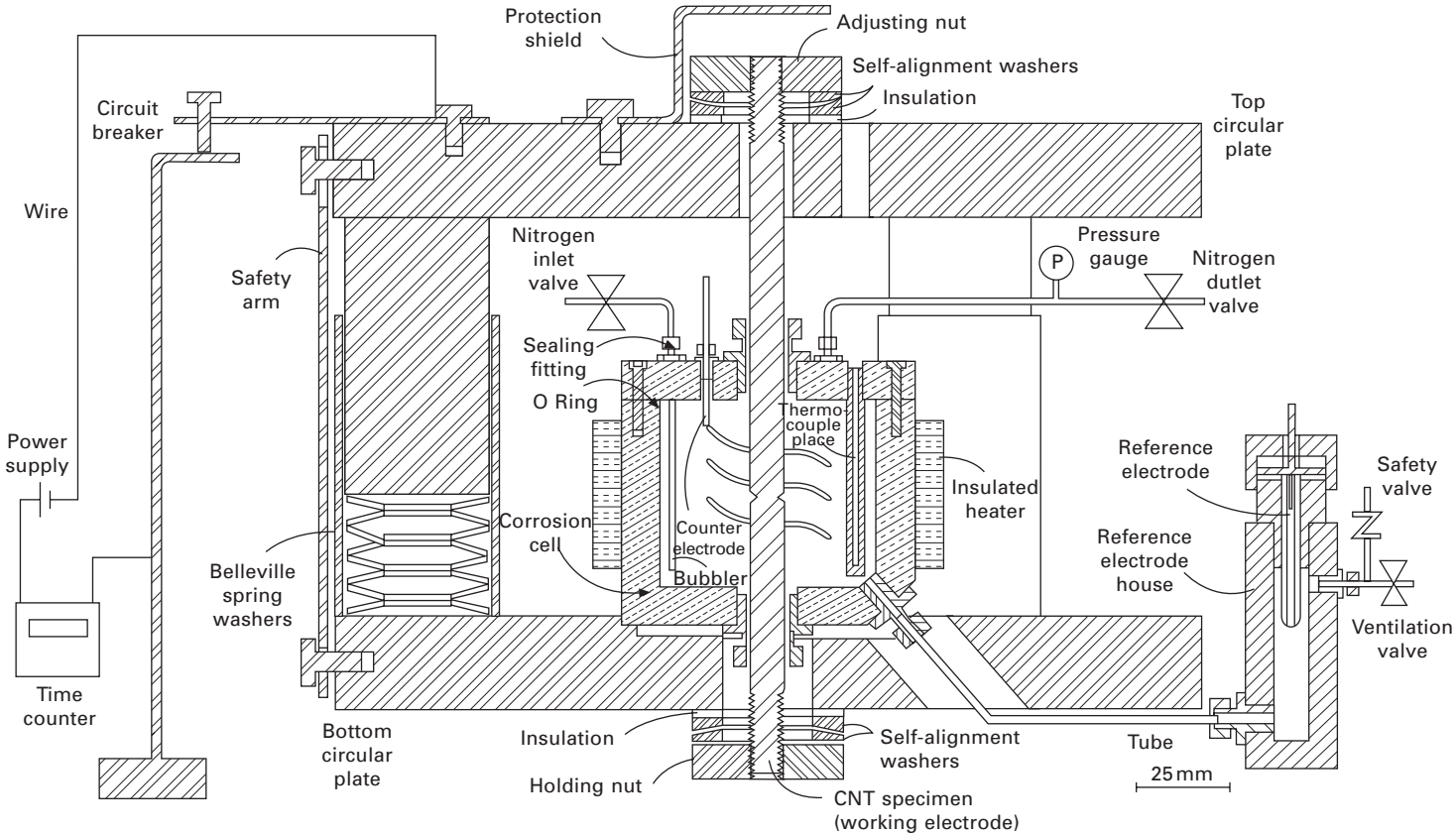

14.3 CNT rig for SCC testing[11].

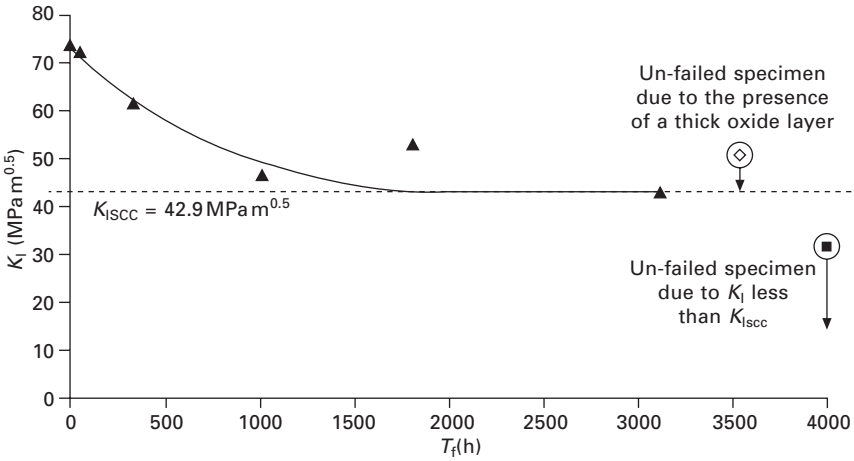

14.4 K_I vs. T_f of mild steel in 500 g/L NaOH at 100 °C[13].

14.4 CNT testing of welds

SCC is generally more prevalent in welded sections of the components since welding introduces residual tensile stresses which facilitate SCC. It is often deemed essential to take into account the greater susceptibility of welds to cracking while designing components for corrosive environment. Therefore, it is industrially more relevant and attractive to characterise susceptibility of the welds to SCC. Though there are abundant reports on SCC of welds, very few of them deal with the generation of data on the threshold stress intensity factor for propagation of stress corrosion cracks (K_{ISCC}). However, the determination of K_{ISCC} data of weldments can provide more accurate prediction of the life of the components, since the failures often occur in the welded area.

The newly developed CNT technique for determination of K_{ISCC} has recently been extended for testing welds, in an attempt to generate K_{ISCC} data. The testing of very small specimens becomes possible when the role of microstructures of limited size such as welds is to be investigated. The relevant microstructures need only be produced in the small volume of metal in the notched region of the CNT specimen.

The test material used in this investigation was AISI 1020 grade mild steel plates welded with the filler material Autocraft LW 1-6. The inert gas used for the welding was argon gas. The yield stresses (σ_y) of the weld and unwelded AISI 1020 mild steel were determined to be 430 and 580 MPa respectively. The fracture toughnesses (K_{IC}) of the welded and unwelded AISI 1020 mild steel were experimentally determined to be 34 and 100 MPa m$^{0.5}$ respectively. CNT specimens were machined from the welded plates, with a notch in the welded part.

The specimens were subjected to fatigue pre-cracking, using a rotating bending fatigue machine. The pre-cracked specimens were washed with ethanol and dried before being installed into the rig. The corrosion cell was filled with the given caustic solution (500 g/L). The test rig was heated to the test temperature (100 °C) before applying the tensile load to the specimen. The specimen was held at a given load until it failed. The time-to-failure (T_f) was recorded at the failure of the specimen. Tests were carried out at different applied K_I.

The K_{ISCC} of 1020 mild steel in 500 g/L NaOH at 100 °C was determined to be 47 MPa m$^{0.5}$ (as shown in Fig. 14.5), which is similar to K_{ISCC} of mild steel reported earlier[13]. As also shown in the figure, the weld specimens quickly failed even at low K_I values, suggesting their considerably greater susceptibility to cracking. The fractured specimens examined by scanning electron microscopy (SEM) showed features of intergranular cracking.

The data presented for welds in Fig. 14.5 are the first set generated using very small specimens such as CNT. The primary purpose of this exercise was to establish the capability of the CNT technique for testing welded specimens for generation of K_{ISCC} data. The traditional and commonly used techniques for generating K_{ISCC} data (CTS and DCB) may encounter prohibitive

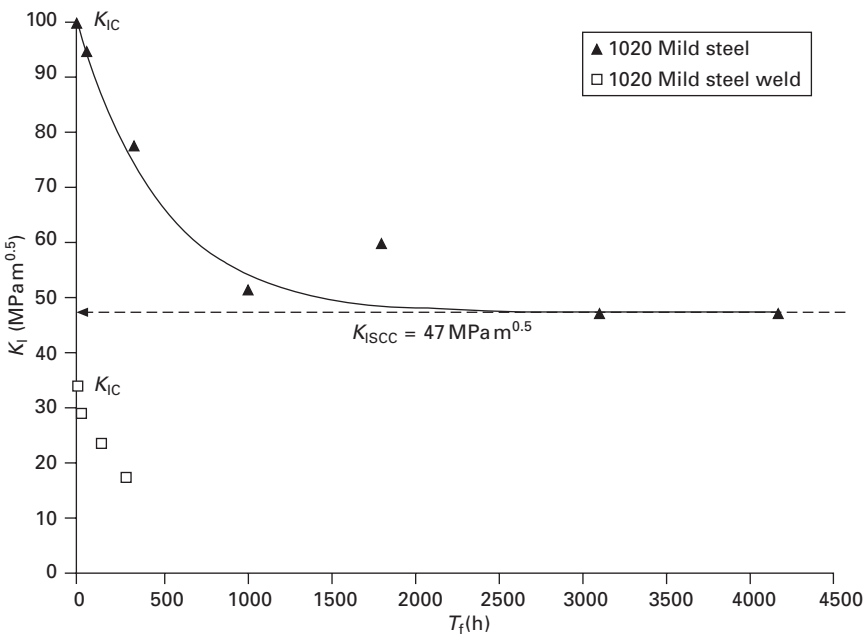

14.5 K_I vs T_f of 1020 mild steel and welded 1020 mild steel in 500 g/L NaOH solution at 100 °C.

difficulties in testing welded specimens for their inherent disadvantages. For example, for CTS specimens to achieve the plane strain condition they are required to be large and bulky in order to ensure that the free surface plane stress regions are negligible compared with the central plane strain regions. In an attempt to test welded specimen by CTS or DCB technique, one would have to first ensure that the advancing crack stays within the area of interest, such as welded area (which will obviously extend over a much larger length of bulky specimens of CTS and DCB). In contrast, the CNT specimen has much smaller cross-section and edge effect, making it easier for the advancing cracks to stay within the region of interest (such as weld metal in the present study).

14.5 Conclusions

Circumferential notch tensile (CNT) testing presents a potential for a simple and cost-advantageous possibility for generating K_{ISCC} data of welded specimens, which may overcome the prohibitive difficulties in testing welded specimens by the traditional and commonly used techniques for generating K_{ISCC} data (viz. CTS and DCB).

14.6 Acknowledgements

The CNT data on mild steel presented here constitute part of the PhD work of Dr Rihan Rihan (supervised by the author and Assoc. Prof. R. Ibrahim). The author acknowledges contributions of the two colleagues and the resulting publications.

14.7 References

1. A. Turnbull, *British Corrosion Journal*, **27** (1992) 271.
2. *Proc. Environment-sensitive Fracture Symposium*, ASTM Committee G-1, ASTM Special Technical Publication 821 (eds: S.W. Dean, E.N. Pugh and G.M. Ugiansky), Pub: ASTM, Philadelphia, 1982.
3. R. N. Ibrahim and H. L. Stark, *International Journal of Fracture*, **44** (1990) 179.
4. R. N. Ibrahim and H. L. Stark, *Engineering Fracture Mechanics*, **25** (1986) 395.
5. R. N. Ibrahim and H. L. Stark, *Engineering Fracture Mechanics*, **28** (1987) 455.
6. G. R. Irwin, '*Fracture Testing of High-strength Sheet Materials Under Conditions Appropriate for Stress Analysis*, Report 5486, Naval Research Laboratory, July 1960.
7. G. R. Irwin, 'Plastic zone near a crack and fracture toughness', *Sugamore Ordinance Materials Conference*, Syracuse University Research Institute, August (1961).
8. R. W. Hertzberg, *Deformation and Fracture of Engineering Materials*, Wiley, New York, pp 274–277 (1976).
9. F. A. McClintock and G. R. Irwin, *ASTM STP*, **381**, (1965) 84.
10. R. K. Singh R. Bayles, S. Knight, J.-A. Wang, B. R. W. Hinton and B. C. Muddle, in *Environment-Induced Cracking of Materials: Predictions, Industrial Developments*

and Evaluation, Eds: S. A. Shipilov, R. A. Jones, J.-M. Olive and R. B. Rebak, Elsevier, UK, p. 459 (2008).
11. R. K. Singh, R. Rihan and R. N. Ibrahim, *Metallurgical and Materials Transactions A*, **37A** (2006) 2963.
12. R. Rihan, R. K. Singh and R. N. Ibrahim, *Materials Science and Engineering A*, **425** (2006) 272.
13. R. K. Singh, R. Rihan and R. N. Ibrahim, *Corrosion Science*, **49** (2007) 4386.

15

Less explored types of environment-assisted cracking of welds: industrial issues and research opportunities

R K SINGH, Monash University, Australia

Abstract: The reported literature on the role of corrosion in degradation and cracking of welded components often deal with the influence of electrochemical corrosion. However, there are limited reports on the interesting influence of relatively less commonly explored factors, such as the role of the bacteria present in the marine environment in stress corrosion cracking, and the role of corrosive gases in degradation and cracking at elevated temperatures. This paper takes a stock of the currently available literature on the two phenomena, and also indentifies some important research opportunities.

Key words: environment-assisted cracking, high temperature corrosion, ferritic steels, internal oxidation, microbiologically-influnecd corrosion.

15.1 Introduction

Environment-assisted cracking of welds commonly concerns cracking caused or facilitated by the combined action of aqueous environment, stress and weld microstructure. One of the common examples is the stress corrosion cracking (SCC) of sensitised microstructure of austenitic stainless steel welds. However, there are instances of localised corrosion and cracking of steel welds caused or assisted by corrosive gases at high temperatures and microbiological organisms. This chapter presents a critique of the recent findings and research avenues of two distinctly different types of corrosion of steel weldments, viz. high temperature gaseous corrosion and microbiologically influenced corrosion. High temperature corrosion of weldments of chromium–molybdenum (Cr–Mo) steels is discussed in the context of corrosion-assisted microstructural degradation and life assessment of fossil fuel power plant components. The chapter also discusses microbiologically influenced corrosion and its likely influence on pitting of stainless steels and their weldments, which are becoming increasingly important in the context of failure of welded marine structures.

15.2 Cr–Mo ferritic steel welds: high temperature corrosion

Owing to their required combination of mechanical properties, weldability, formability and corrosion resistance[1,2], the low alloy Cr–Mo ferritic steels (viz. 2.25Cr–lMo and lCr–0.5 Mo steels) are used extensively for moderately high temperature (623–823 K) applications, such as steam generators of fossil-fuel power plants. For applications in harsh corrosive environments at temperatures higher than 823 K, steels with higher chromium contents (5–12%) have been developed. For example, 9Cr–1Mo steel possesses improved mechanical properties and corrosion resistance compared with its popular predecessor, 2.25Cr–1Mo steel[3,4].

Microstructures of Cr–Mo ferritic steels can be easily modified by thermo-mechanical treatments. Such thermo-mechanical susceptibilities of microstructures are often exploited to develop carbide precipitates of the required morphology and distribution in order to effect precipitation hardening. Owing to their metastable structure and morphology, the strengthening precipitates are known to undergo undesirable transformations[5–8] during welding. As a result, the creep rupture life of the weldments of Cr–Mo steels is reported to be poor[9–11], to the extent that the creep-rupture of the welds is often the life-limiting factor.

Since weldments are an indispensable part of most component fabrications, considerable effort has been directed in the past few decades to the correlation of the in-service failures with the microstructural degradation caused during welding of Cr–Mo steels[1,2,6,7,9,11,12]. Microstructural development of weldments of Cr–Mo steels and their role in weld cracking are described in detail in other chapters of this book. In recent years, limited studies have also been carried out to investigate the high temperature oxide scaling behaviour of the weldments[13–15] and its possible contribution to creep data generated by common testing[16]. The high susceptibility of microstructures of Cr–Mo ferritic steels to thermomechanical treatments is exploited in order to improve their creep strength. However, the metastable nature of their microstructure is also responsible for the deterioration in mechanical properties of the weldments of the steel[9–11]. Microstructural changes due to welding of 2.25Cr–1Mo steel include enrichment of Cr in the secondary precipitates and/or additional Cr-rich precipitate formation in the area adjoining the weld metal (i.e. the heat-affected zone, HAZ)[1,2,6,7,9,11,12]. Trapping of ‘free’ chromium through Cr-rich precipitation may result in the formation of a less-protective scale over the HAZ and greater oxidation rate of HAZ than the other regions of weldment of 2.25Cr–1Mo steel[8,13–15].

15.2.1 High temperature corrosion-assisted microstructural degradation and cracking in weldments

Investigations of oxide scaling of Cr–Mo steel welds have been limited generally to the environment of air[13–15]. Validity of the non-uniform oxidation rate across the Cr–Mo steel weldments (as observed in the air-oxidation of 2.25Cr–1Mo steel weldments) in the corrosive environments of direct relevance (viz. steam and sulphur) as well as its validity for the weldments of 9Cr–1Mo steel has never been studied. It is important to note that microstructural changes in the weldments of 9Cr–1Mo steel (particularly those changes that can influence oxide scaling behaviour) are considerably different from those in low chromium Cr–Mo steels[17,18].

In a critical investigation[19,20], specimen coupons of the weld metal, HAZ and base metal regions were sectioned from the weldments of a 2.25Cr–1Mo steel. These coupons were then oxidised at 873 K in an environment containing a mixture of 35% steam and nitrogen, and the morphology and structure of the oxidised specimens were characterised. A cross-section through a typical oxidised specimen (base metal) suggests the presence of at least three distinct regions in the scale/sub-scale, viz. a thick compact outer layer, a sub-scale region consisting of extensive internal oxide precipitates, and a thin inner layer which formed between the external layer and the subscale. The sub-scale region was populated with internal oxide precipitates, with the internal oxide precipitates forming more extensively at the alloy grain boundaries. X-ray mapping of the cross-section confirmed the internal oxide precipitates to be chromium-rich. Cross-sections of the oxidised weld metal had features similar to those in the oxidised base metal. However, the cross-section of the oxidised HAZ specimen could be distinguished from those of the weld metal and the base metal specimens by two features: a sub-scale region with extensive void formation and blocky internal precipitates, and an additional region in the alloy matrix adjacent to the sub-scale, with features of cavitation at the alloy grain boundaries in this region. Higher magnification showed these grain boundary features to be cavities. Sub-scale regions in the base and weld metal specimens were much less densely populated with internal precipitates than the subscale in the HAZ. More importantly, no grain boundary cavitation was observed in the region adjacent to the sub-scale regions in the oxidised specimens of weld metal and base metal.

Microchemical analysis across the scale and sub-scale regions in the cross-sections of the oxidised weld metal, HAZ and base metal specimens confirmed the formation of Cr-rich inner scales. However, a comparison of the Cr profiles suggested that the relative Cr content in the inner layer of the scale developed over the HAZ was considerably lower (~4 percent) than those detected in the similar layers of the scales developed over the base and the

weld metal (~12 percent). This variation in the chromium content of the inner oxide layer is very important since the chromium content of the inner layer of Fe/Cr oxides in low Cr steels governs the effective protectiveness of the scale[8,20].

It takes a specific combination of oxygen partial pressure beneath the external scale, alloy microstructure, temperature and the nature of resulting external scale to establish and sustain internal oxidation. The more protective inner scales (i.e. those scales with high Cr contents), which formed on both the weld metal and the base metal, resulted in a limited inward diffusion of oxygen ions, and hence a less extensive internal oxidation. A less protective inner scale, formed in the case of the HAZ, presumably permitted a greater inward diffusion of oxygen ions, thus facilitating a greater concentration of oxygen available for reaction with the chromium of the alloy matrix. More rapid diffusion of oxygen ions through the HAZ scale caused extensive internal oxidation and formation of a sub-scale zone densely populated with internal precipitates. Depletion of Cr, owing to extensive internal precipitation in the sub-scale zone of oxidised HAZ, would necessitate diffusion of Cr from adjacent areas in the alloy matrix, which will potentially lead to the generation of excess vacancies. These vacancies, preferentially annihilating at grain boundaries, could lead to the grain boundary void formation.

Grain boundary cavitation resulting from extensive internal oxidation can provide an easy path for crack propagation[21,22], and hence needs to be taken into account for high temperature component design because it has a direct bearing on the creep/fatigue life. In this context, the oxidation-assisted grain boundary formation in the alloy matrix neighbouring the sub-scale zone in the oxidised HAZ specimen is particularly important since in-service failures are commonly found to occur in the HAZ of the welded components of 2.25Cr–1Mo steel[9,11].

15.2.2 High temperature corrosion as a tool for life assessment and failure analysis

Since the life extension of in-service components and the issue of materials' ageing/degradation are becoming increasingly important, new approaches to life assessment and reliability analysis of aged components have been explored in recent years[23,24].

Life Assessment by scale thickness measurements

Life assessment of steam generating/handling systems by scale thickness measurement is an innovative use of existing information in the form of the oxide scales that generally develop over the in-service high temperature components. This emerging tool has been effectively used for determining

temperature history of steam generator tubes in fossil-fuel power plants[23,25,26]. A greater-than-average scale thickness is taken as indicative of an excessive high temperature, which could shorten the remaining creep life of a given component[23].

'Oxide dating' for crack growth measurement and failure analysis

For determining a crack growth history and crack velocity, 'oxide dating'[27] utilises an examination of oxide scales which form over a bare fracture surface created by a propagating crack. This technique has been applied in failure investigations of various Cr–Mo steel components, such as boiler headers, steam pipes, steam chests/castings, weldments and turbine blades[27]. The technique involves measurement of the thickness of oxide scales at locations between which the crack velocity is to be determined[23].

Non-homogeneous scaling across Cr–Mo steel weldments

Formation of a less-protective scale over HAZ during air-oxidation[8] resulted in the development of a thicker oxide scale over HAZ than the other regions of the weldment, viz., weld metal and base metal regions[14,15]. Surface profiles (as typically shown in Fig. 15.1) describing the difference in thickness of oxide scales over the weld metal and HAZ of a 2.25Cr–1Mo steel weldment have unambiguously established formation of a much thicker scale over the HAZ region.

As discussed earlier, thickness of oxide scale is used as a tool for life assessment, failure analyses and crack growth measurement by 'oxide dating'.

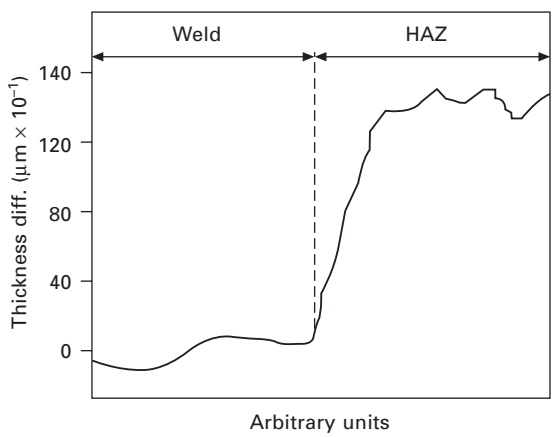

15.1 A surface profile describing the difference in thickness of oxide scales over weld metal and HAZ of 2.25Cr–1Mo steel, oxidised in air at 773 K for 500 h [14].

In relation to life assessment by scale thickness measurement[23–26], the possibility of a greater scale thickness developed exclusively over the HAZ of the weldment of 2.25Cr–Mo steel may misleadingly suggest that this region had experienced an excessive temperature. In the context of 'oxide dating'[27] by scale thickness measurement, a greater scale thickness developed exclusively over HAZ may misleadingly overestimate the exposure time (and, hence, underestimate the crack velocity). Therefore, in using scale thickness as a tool for life assessment and determining the crack growth history of welded components of Cr–Mo steels, it may be necessary to take into account the scaling rate data on the steel weldments[8,14]. Since studies on the oxide scaling of weldments of 2.25Cr–1Mo steels have been carried out only in the environment of air, it will be necessary to examine the phenomenon of non-uniform scale thickness across the weldment in steam and other environments of industrial significance. Non-uniform scale thickness across the weldments also calls for development of an improved model for accurately predicting the temperature history of welded in-service components.

15.2.3 Research opportunities

- Characterisation of high temperature corrosion-assisted microstructural degradation in the alloy matrix across the broadly different (microstructurally) zones (viz. weld metal, HAZ and base metal) of the steel weldments, in steam environment, and thus investigating the role of the environment in facilitating microstructural degradation.
- Examining the role of corrosion-assisted microstructural degradation on mechanical properties, by conducting creep tests in steam.
- Conducting similar studies in other aggressive environments (viz. sulphidation, sulphidation + oxidation) experienced in the petroleum, gas and petrochemical industries.
- Investigating the scaling behaviour of weldments of 9Cr–1Mo and 2.25Cr–1Mo steels in an industrial environment (viz. steam) and examining the validity of the recent results of non-uniform scaling observed during oxidation of 2.25Cr–1Mo steel weldments in air.
- Investigating the applicability of the recent practice of life assessment by scale thickness to the welded components, by establishing kinetics of the scale thickness growth over weld metal, HAZ and base metal of the steel weldments of 9Cr–1Mo and 2.25Cr–1Mo steels, in a steam environment.
- Developing a suitable model for life assessment by relating scale thickness with time-temperature history (and hence, creep damage) in the different zones of the steel weldments.

15.3 Microbiologically influenced corrosion of stainless steel weldments in the marine environment

This section presents an overview of the potential role of microbial activity in facilitating SCC of weldments of engineering stainless steels and the significance of the phenomenon in corrosion-assisted failures of marine structures. Premature failure of stainless steels (SS) and their weldments due to SCC has long been a major concern for marine infrastructure. There is generally a considerable degree of inconsistency in the SCC data. The industry experience calls for a fresh approach to investigations of SCC, and there is a distinct opportunity for investigating the role of microorganisms/MIC in SCC failures. Although some systematic failure analyses have indicated a profound role of microbiologically influenced corrosion (MIC) in initiating pitting, the widespread materials failures in marine environments would suggest the need for a development of a clear understanding of the synergistic influence and interplay of MIC and microstructure gradients in SCC of SS weldments.

15.3.1 Biofilms and MIC

In MIC, participation of the microorganisms initiates, facilitates and/or accelerates corrosion. Microorganisms can influence a corrosion process by one or a combination of the following phenomena[28]:

- patchy microbial deposits/colonies/tubercles/biocorrosion products can form discontinuous biofilms which create conditions for the formation of new galvanic cells and/or alter the conditions in the existing galvanic cells[29,30], as shown schematically in Fig. 15.2.

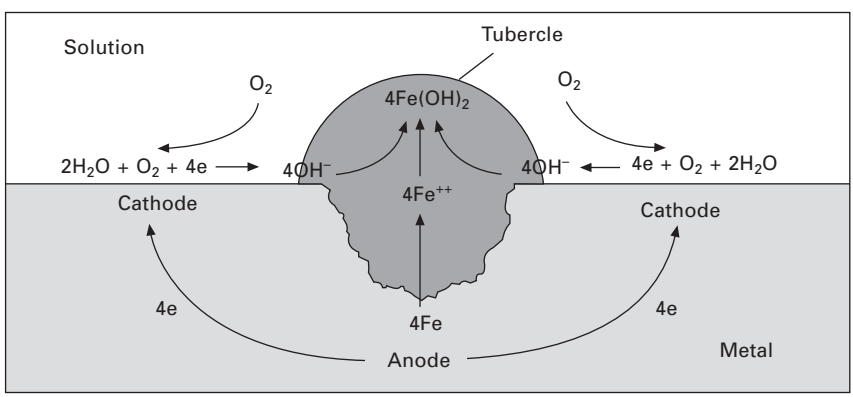

15.2 Schematic of a tubercle-assisted oxygen concentration cell pitting [31].

- metabolic processes of the microorganisms can destroy the existing protective films on the corrosion resistant alloys, for example, by production of acids during microbial metabolism.

Biofilms are composed of a matrix of microorganisms and their elaborated polymers on surfaces. Metal surfaces are known to develop biofilms, under both aerobic and anaerobic microhabitats. Hence, biofilms can support the mutual development of both aerobic and anaerobic microorganisms.

As a result of their ability to create and/or alter the galvanic cell conditions, biofilms are reported[32] to have a profound influence on localised corrosion, viz. pitting. This influence is particularly relevant for SCC since pitting is believed to be one of the critical factors in stress corrosion crack initiation. The marine environment supports growth of a wide variety of microorganisms (viz, *Vibrio, Bacillus* spp.) which can be active in developing biofilms[33], and thus causing microbiologically influenced localised corrosion. Sulphate-reducing bacteria (SRB) have long been identified as a most common cause of MIC. Biofilms of SRB generally develop in anaerobic regions. However, there are instances of biofilm formation in aerobic bulk water[34].

15.3.2 MIC of stainless steels

Stainless steels derive corrosion resistance from the formation of passive oxide films, which are stable in oxidising environments. Localised damage in the passive films can result in formation of pits and crevices. However, the presence of aerobic bacteria can deplete oxygen within such pits and thus cause acidification which will accelerate the pitting rate. Stoecker and Pope[35] have attributed the pitting of stainless steel in a water containing very low levels of chloride content (20 ppm, which should not normally cause pitting) to the presence of microbial activity in the environment.

The presence of microorganisms can be directly involved in increasing the corrosiveness of a chloride-containing environment. For instance, iron-oxidising bacteria in chloride-containing water when in contact with steel can produce ferric chloride, which is known to accelerate pitting processes[30].

15.3.3 SCC and MIC

Premature cracking of materials under the synergistic action of a tensile stress and a corrosive environment (which is SCC) is possibly the most dangerous form of corrosion-assisted failure. The difficulties in addressing the issue of SCC failures in marine environment include the great deal of inconsistency in SCC data for a given alloy–environment combination.

MIC can cause pitting and thus facilitate SCC crack initiation. Investigations of the role of MIC on SCC in saline environments will be particularly important

since the nature of microbial content of marine environments (and hence its influence on localised corrosion and SCC) at different marine locations varies considerably.

Microstructural dissimilarities across the weldments of stainless steels are known[31,36] to degrade SCC and MIC resistance. Analyses of ex-service welded SS components for marine application have suggested a synergistic role of MIC and SCC in weld failures[36].

15.3.4 SCC of weldments of duplex stainless steels

Duplex stainless steels (DSS) generally have a ferrite/austenite volume ratio of 1:1. For their considerable resistance to chloride-pitting and SCC, DSS are suitable for aggressive marine environments where traditional austenitic SS (viz. AISI 304 and 316) fail due to chloride-SCC[37,38]. Superior SCC resistance of the duplex SS (to both austenitic and ferritic SS) in chloride media is also attributed to the electrochemical behaviour of the two phases – austenite, which is more susceptible to SCC, is cathodically protected by the ferrite[37,38]. In fact, the chloride SCC resistance due to the presence of ferrite with austenite has been known to improve in the case of the weld metal region of austenitic SS weldments. In moving from the weld metal (fusion zone) to the unaffected base metal, at different distances, different thermal treatments are experienced during welding, which results in a variation of ferrite content. The presence of retained ferrite (5–10%) in the weld metal and its absence in the base metal of the austenitic SS weldment account for the superior SCC resistance of the weld metal[39]. However, at higher ferrite contents in the austenitic SS weld metal, crack growth is reported[40] to occur along the ferrite/austenite interface (due to a dissolution at the interface). It is relevant to recall the preferential pitting of the chromium-lean phase, austenite, when present in a duplex structure with chromium-rich phase, ferrite[39].

The influence of the ferrite content on SCC resistance of austenitic SS welds is reasonably well understood[39–43]. However, there is clearly a lack of understanding of the role of microstructural aspects of the ferritic phase in the SCC resistance of DSS, particularly their welds. A ferrite/austenite volume ratio of about 1:1 has been suggested to be the optimum for intergranular corrosion resistance of DSS[44,45]. However, in the case of DSS welds and the adjacent HAZ, the ferrite content will generally deviate from the optimum value due to the presence of some retained δ-ferrite. For the safe operation of welded components of DSS, it is necessary to know the role of the additional ferrite contents of the weld metal and HAZ in the SCC resistance of duplex DSS.

15.3.5 MIC of weldments of stainless steels

The role of MIC involves the influence of three factors, viz. metal, solution and microorganisms[30]. To that extent, the role of metal and its microstructure are appreciated by biocorrosion scientists[30,36]. The metallurgical features, such as deformation of the grain structure or presence of inclusions, are reported[44] to act as sites of decreased MIC resistance.

The influence of metal microstructure on MIC is reported[29,31,33,46] to be most marked in the case of weldments of stainless steels. Borenstein[29,36] has reported the duplex microstructure which is generally present in the weld metal. The neighbouring heat-affected zone (HAZ) of the weldments of austenitic stainless steels is preferentially attacked by MIC, whereas the fully austenitic structure in the base metal region is less often attacked. Borenstein[29] has also reported that MIC (by iron-oxidising bacteria, such as *Gallionella*) showed no preference for one or other phase in the duplex (austenitic + ferritic) structure. However, Videla[30] has reported that in a preferential attack on the duplex weld structure, *Gallionella* selectively attacks the austenitic phase. In this regard, it may be interesting to understand how MIC will be influenced by the additional ferrite contents of the weld metal and HAZ in the weldments of DSS[31] on MIC.

Welding of austenitic stainless steels can also result in another microstructural heterogeneity, viz. sensitisation in the HAZ which facilitates intergranular corrosion because of the depletion of chromium from the area neighbouring grain boundaries as a result of chromium carbide precipitation[47]. A sensitised structure is reported[29] to be susceptible to MIC, though the lack of sensitisation did not guarantee protection from MIC.

15.3.6 Research avenues

- Examining the hypothesis that under MIC conditions, the pitting that can be associated with preferential austenite attack is also responsible for the enhanced SCC susceptibility of welds in DSS.
- Application of the understanding of the role of MIC in SCC of SS and their weldments in explaining the large scatter in SCC data for SS in marine environment at different locations.

15.4 References

1. A.K. Khare (ed.), Ferritic steels for high temperature applications: *ASM Intl. Conf.*, Warrendale, PA, 1981.
2. S.F. Pugh and E.A. Little (eds.), *Proc. BNES Intl. Conf Ferritic Steels for Fast Reactor Steam Generators, Pub:* BNES, London, 1978.
3. J.A.G. Holmes, *Nucl Energy*, **20** (1981) 23.

4. J. Orr and S.J. Sanderson, *Proc AIME Topical Conf on Ferritic Steels for Use in Nuclear Energy Technologies*, Snowbird, Utah, 1983, p.261.
5. J. Pilling and N. Ridley, *Metall. Trans.*, **13A** (1982) 557.
6. P. Roy and T. Lauritzen, *Welding J.*, **65** (1986) 45s.
7. S.D. Mann and B.C. Muddle: *Proc. Microstructure and Mechanical Properties of Ageing Material,* TMS, 1993, pp. 301–08, Warrendale, PA.
8. R.K. Singh, *Metall. Mater. Trans.*, **26A** (1995) 1847.
9. K. Laha, K.B.S. Rao and S.L. Mannan, *Mater. Sci. Eng.*, **129** (1990) 183.
10. ASME Boiler and Pressure Vessel Code, Code Case N-47, 1986.
11. B. Chew and P. Harris, *Metal Construction*, **11**(5), (1979) ll.
12. R.G. Baker and J. Nutting, *J. Iron and Steel Inst.*, **192** (1959) 257.
13. R.K. Singh, *Metall. Mater. Trans.*, **31A** (2000), 3101.
14. R.K. Singh and A.K. Tyagi, *Mater. Sci. Eng. A*, **185** (1994) 97.
15. R.K. Singh and J.B. Gnanamoorthy, *Welding Journal – Research Suppl.*, April 1995, p.133-s.
16. R.K. Singh and A. Al-Mazrouee, *Metall. Mater Trans A*, **38A** (8) (2007) 1750.
17. S.J. Sanderson, *Proc. BNES lnt. Conf Ferritic Steels for Fast Reactor Steam Generators*, BNES, London, 1978, p.120.
18. F.B. Pickering *et al.*, *Met. Technol.*, Oct 1980, 409.
19. R.K. Singh, *Metall. Mater. Trans.*, **29A** (1998) 577.
20. R.K. Singh, *Metall. Mater. Trans.*, **30A** (1999) 2103.
21. E.R. Johnson, C.R. Barrett and W.D. Nix, *Metall Trans*, **3** (1972) 695.
22. E.C. Scaife and P.L. James, *Metal Sci J.*, **2** (1968) 217.
23. EPRI Report TR-102433-V2, 'Boiler Tube Failure Metallurgical Guide', 1993, Palo Alto, CA.
24. D.O. Harris and R.M. Tilley, *Proc EPRI Intl Conf. on Advanced in Life Assessment and Optimization of Fossil Power Plants*, Orlando, March 2002.
25. L.W. Pinder, *Corr. Sci.*, **21** (1981) 749–63.
26. R.E. Kessler, *Proc EPRI Intl Conf. on Advanced in Life Assessment and Optimization of Fossil Power Plants*, Orlando, March 2002.
27. Brochure: *Oxide Dating for Failure Analysis*, PowerGen, Power Technology Centre, Ratcliffe on Soar, Nottingham, UK, 1999.
28. H.A. Videla, *Proc. Argentine-USA Workshop on Biodeterioration 7 (CONICET-NSF)*, H.A. Videla, Ed., Aquatec Quimica, S.A., Sao Paulo, Brazil, 1986, p.43.
29. S.W. Borenstein, *Materials Performance*, **August** (1988) 62.
30. H.A. Videla, *Manual of Biocorrosion*, CRC Lewis, 1996, p.8 and p.5.
31. R.K. Singh, B.C. Muddle and B.W. Cherry, *Proc., 10th International Congress on Marine Corrosion and Biofouling*, Melbourne, February 1999 (ed.: J. Lewis, Pub: DSTO, DSTO-GD-0287), pp.229–236.
32. R.C. Newman, W.P. Wong and A. Garner, *Corrosion*, **42** (1986) 489.
33. J.G. Stoecker, *Materials Performance*, May 1995, 49.
34. H.A. Videla, *Biofouling*, **15** (2000) 37.
35. J. Stoecker and D. Pope, *Materials Performance*, **135/6** (1986) 55.
36. S.W. Borenstein, *Materials Performance*, January 1991, 52.
37. N. Neilsen, *Corrosion*, **20** (1964) 105.
38. S. Shimodaira, M. Takano, Y. Taleizawa and H. Kamida, *SCC and Hydrogen Embrittlemant of Iron-base Alloys*, NACE 1977, p.1003.
39. T.G. Gooch, Doc. IIS/IIW-783-83, p.64.
40. W.A. Baeslack, *Welding J. - Res. Suppl.*, **58** (1979) 83s.

41. D.J. Duquette and R.E. Ricker, *Biologically Induced Corrosion* (S.C. Dexter, ed.), NACE-8, International Corrosion Conference Series, NACE, Houston, TX, 1986, pp.121–130.
42. W.A. Baeslack, W.F. Savage and D.J. Duquett, *Metall. Trans*, **10A** (1979) 1429.
43. W.A. Baeslack, D.J. Duquett and W.F. Savage, *Corrosion*, **35** (1979) 45.
44. S. Bernhardsson, R. Mellstrom and J. Oredsson, *Proc. NACE – Corrosion 1981*, paper#13.
45. I.A. Ward and L.H. Keys, *Stainless Steels '84*, Gothenberg, 1984.
46. S.W. Borenstein, *Proc. Corrosion '91*, Paper # 107, NACE International, Houston, 1991.
47. M.G. Fontana and N.D. Greene, *Corrosion Engineering*, McGraw-Hill International Book Co., 1984.

Index

70 wt%^{Fe} isopleth 11
316L(N) stainless steel
  estimation of delta-ferrite content in welds 75–6, 77, 78
  joint with A48P2 carbon steel 68–73
  joint with Alloy 800 55, 56–61, 62
  weldability 39–47
475°C embrittlement 6

A (austenitic) solidification mode 18–19, 20
  susceptibility to cracking 20–1
A48P2 carbon steel/316L(N) stainless steel joint 68–73
absolute hardness 260
acoustic Barkhausen noise (ABN) 291–2, 327–8
acoustic emission technique (AET) 297, 298–9, 300–2, 327
acousto-elastic effect 289
AF (austenite–ferrite) solidification mode 19, 20
  susceptibility to cracking 20–1
ageing
  316L(N) stainless steel/Alloy 800 joint 56–9
  Alloy 800/9Cr–1Mo ferritic steel joint 63–8
  hardface deposits on austenitic stainless steels 89–92
allowable stress intensity 106–7
Alloy 800 182, 320
  joint with 9Cr–1Mo steel 55, 61–8
  joint with 316L(N) stainless steel 55, 56–61, 62
alternating current (AC) magnetisation/demagnetisation 236, 239
aluminium 401
American Association of Railroads (AAR) Code 140–1, 142–4
American Welding Society 141
anode 479
artificial neural networks (ANNs) 75–6, 77, 78
  evaluation of resistance spot welding process 299–300
ASME Boiler and Pressure Vessel Code 226–8
  section III division 1 code 102–13
  section VIII division 1 code 97–102, 135–6
  section VIII division 2 code 137–8
ASTM G35 procedure 274, 275
ASTM G46 procedure 275–6
austenite colonies 355
austenitic filler metal 30
austenitic stainless steels 8–13, 154, 223, 244, 354
  corrosion of weld joint 490–506
    HAZ corrosion 501–6
    heat input 496–8
    secondary phases 499–501
    solidification and micro–segregation 490–6
  creep behaviour of welds 166–74
    influence of nitrogen 170–4
    microstructural changes during creep deformation 173–4
  dissimilar welds with ferritic steels 181–2, 319–20
  failure mechanisms 320–1
  hardfacing of austenitic stainless steel components 35, 38–9, 78–92
  precipitation hardened 15, 16

weldability 34, 35–6, 39–47
compositions 39, 40
effect of titanium and nitrogen on hot cracking 44–6
hot cracking assessment criteria 46–7
hot cracking tests 39–44
Australian pipeline construction practice 396–8, 425–6

bainite 176
ball valve 337–40
Barkhausen noise analysis 291–4, 295, 327–8
Bayesian neural network (BNN) model 75–6, 77, 78
Beachem's slip softening model 423–4
bead shape 27–8, 410–11
bearing pad welding 302, 304
bellow sealed valve 340–2
Bennet hardness scale 260
beta carbon nitride 260
biofilms 540–1
booms, mining dragline 144–7
borescope 231–2
boron 26, 180, 504
Bragg equation 464
Brinell hardness test 260, 261–2
British Standard 7910 (BS 7910) 205–6, 465–72, 473
brittle striations 385–6
brittleness temperature range (BTR) 39, 42, 43, 46–7
brittleness transition temperature 198–200
buckling 284
butt welds 244, 252, 253
buttering technique 448, 450

carbides 23–4
carbon
effect on weld cracks 434–5
iron–carbon phase diagram 413–15
sensitisation of austenitic stainless steel 503–4
carbon equivalent (CE) 421
carbon nitride 260
carbon steels 222–3
low alloy 223, 317–18
carrier gas, spray test with 257, 258
categorisation of welds 98–9, 103
cathode 479
cavitation damage 482–3
cellulosic girth welds 393–432
hollow bead defect 398–406, 428–9, 430
hydrogen-assisted cold cracking 421–30
keyhole welding 394–5, 403–5
pipeline construction 396–8
solidification cracking 406–21, 428–30
cellulosic welding 395–6, 397
centreline cracks 436
solidification cracking 407, 408
Charpy test piece 270
Charpy V-notch impact (CVN) test 186, 187, 197–9, 325, 527
chromium
chromium-rich inner scales in ferritic steels 536–7
Creq/Ni_{eq} ratio 13, 15, 18–19, 25–6, 42–4, 320–1
effective chromium content 505
iron–nickel–chromium ternary system 10–11
sensitisation of austenitic stainless steels 503–4, 505
chromium depletion 481–2, 515
chromium–molybdenum (Cr–Mo) ferritic steels 34, 198, 199
Alloy 800/9Cr–1Mo joint 55, 61–8
corrosion 506–16
creep 174–81
2.25Cr–1Mo 174–8
mismatch 123–5
modified 9Cr–1Mo 179–81
failure mechanisms 318–20
high temperature corrosion 535–9
modified *see* modified Cr–Mo ferritic steels
circular patch test 46
circumferential notch tensile (CNT) testing 524–32
stress intensity factor 524–8
allowance for eccentricity 525–6
validity requirements 526–8
threshold intensity for SCC 528–30
CNT testing of welds 530–2

clusters 144–6
coarse-grain HAZ (CGHAZ) 442, 443, 507, 509
codes 134–5, 302
  see also ASME Boiler and Pressure Vessel Code; RCC-MR code
cold cracking *see* hydrogen-assisted cracking (HAC)
cold welding 455
cold working 5
Colmonoy hardfacing alloys 38, 78–92
  metallurgical and ageing behaviour of hardface deposits on austenitic stainless steel 89–92
  selection of hardfacing process and hardfacing alloy type 81–8
compact tension specimens (CTSs) 522–4, 527, 531–2
composite zone *see* fusion zone
composition
  effect on cracks 434–5, 439
  and hollow bead defect 400–2
  liquation cracking 23, 28
  solidification cracking 20–1, 25–6
  and weldability of Cr–Mo ferritic steels
    HAC 49–51
    toughness of SMAW metal 51–5
compression hold tests 162–5
condenser tube 330–3
conical inlet 347–9
constitution diagrams 12–13
constitutional liquation 22–3
consumable qualification 225–7
consumables, choice of 323
contact ultrasonic testing 243
controlled deposition technique 453
cooling sensitisation diagram 502, 503
cooling time 420–1
  prevention of HAC 428
copper 180, 274
copper sulphate 274
corrosion 477–520, 534–45
  austenitic stainless steel weld joint *see* austenitic stainless steels
  effects of defects 486–8
  effects of residual stresses 488–9
  ferritic steel weldments *see* ferritic stainless steels
  forms of 479–86
  high temperature corrosion 535–9
  MIC of stainless steel weldments in the marine environment 540–3
  resistance of superduplex stainless steel welds 361–4
  testing methods 271–7
    ASTM G35 specification 274, 275
    cyclic testing 276
    HIC test 276
    humid sulphur dioxide tests 276
    IGC test 273–4
    immersion tests 271–2
    passivation testing 277
    pitting corrosion 275–6
    SCC test 274–5
    sour service testing 276
    SSCC tests 275
    standards 311
  see also under individual forms
corrosion cracking processes 483–5
  see also corrosion fatigue; hydrogen embrittlement; stress corrosion cracking
corrosion fatigue 485
  low cycle corrosion fatigue in ferritic steel weldments 512
  superduplex stainless steel welds 366–87
    crack propagation in a benign environment 372–8
    crack propagation in seawater under high ECP 378–81
    crack propagation in seawater under negative imposed ECP 381–7
    experimental details 366–72
corrosion-resistant cladding 506
Cottam Power Station 452–3
Cr_{eq}/Ni_{eq} ratio 13, 15, 18–19, 320–1
  austenitic stainless steels and hot cracking 42–4
  prevention of solidification cracking 25–6
crack growth/propagation 128–30, 131–2
  creep crack growth 190–2, 213–15
  creep–fatigue crack growth 192, 214–15
  fatigue crack growth 189–90, 212–13

measurement by 'oxide dating' 538
stages 128, 129
subcritical crack growth parameters 189–92
characterisation of welds 212–15
superduplex stainless steel welds 368–72
benign environment 372–8
seawater under high ECP 378–81
seawater under negative imposed ECP 381–7
crack initiation 131
crack initiation time 213, 214
crack-like defects, weld design with 115–22
life prediction of fast breeder reactor fuel pin end plug weld 119–22
σ_d approach for benchmark solution 115–19
crack repair *see* repair welds
crack tip, stress fields around 190–1
crack tip opening displacement (CTOD) 187, 208
cracks 434–40
effect of chemical composition 434–5, 439
effect of thermal history 434
effect of welding process conditions 435
in parent material 439–40
in weld metal 436–9
creep 110, 111, 153–5, 160–82
austenitic steel welds 166–74
creep crack initiation life for welds with crack-like defects 118–19, 120–2
damage and design of welds 111–12, 115
welds with crack-like defects 117, 118–19
dissimilar weld joints 181–2
ferritic steel weld joint 174–81
mismatch creep properties and weld design 122–5
rupture strength of ferritic steel weld joint 174–81
creep brittle materials 192
creep cavitation 178
creep crack growth (CCG) 190–2
characterisation of welds 213–15
creep ductile materials 192
creep–fatigue crack growth (CFCG) 192, 214–15
creep–fatigue damage 112–13, 114, 115
creep–fatigue interaction 112, 113
stainless steel welds and weld joints 160–6
creep hard welds 122
creep soft welds 122
crevice corrosion 362, 480–1
critical pitting potential 496–8, 499–500, 501
critical pitting temperature (CPT) tests 363
critical preheat temperature 49, 50
current
magnetising 236
welding 399–400, 402–3, 406
CVN test 186, 187, 197–9, 325, 527
cyclic corrosion testing 276

D9 alloys 39–47
damage tolerance approach 142, 148, 187
dealloying 480
defects 130, 133–4, 326, 434–41
arising from design, fabrication and service 316–17
cracks 434–40
effect on corrosion properties 486–8
excessive spatter 441
and importance of their evaluation 229–30
lack of fusion 246, 441
lack of penetration 441
LCF of stainless steel weldments 159, 161
porosities 159, 161, 440, 487
slag inclusions 159, 161, 246, 440, 487
testing and evaluation *see* testing and evaluation
undercut 441
delayed cracking *see* hydrogen-assisted cracking (HAC)
delayed lifting 420–1
delayed neutron monitoring (DNM) system 349–51
delta-ferrite (δ-ferrite) 51, 193

austenitic stainless steels 37, 320–1
corrosion 490–1, 492–5
creep deformation of welds 173
estimation of content in 316L(N) stainless steel welds 75–6, 77, 78
LCF testing of stainless steel weldments 157–9
demagnetisation 238–9
depth to width ratio 409–10
design 96–126
against fatigue *see* fatigue design
effect of mismatch creep properties 122–5
need to consider operating conditions and service requirements 316–17
RCC–MR 113–15
rules for pressure vessels
conventional 97–102
nuclear 102–13
reducing failures in weldments 322–3
weld failures and design problems 127–33
welds with crack-like defects 115–22
design by analysis approach 102, 137–8
design by rule approaches 135–6
design by thumb rule 98
destructive testing 264–71, 325–6
etching test for macro-assessment 271
free-bend test 265–6
guided-bend test 267–8, 325
impact tests *see* impact tests
nick-break test 268–9
standards 312
tensile testing *see* tensile testing
detail classification approach 140–1, 147
developers 233–4
diamond 260
diffusible hydrogen content 318–19
dilution 81, 82–8
direct current electrode negative (DCEN) welding 396, 406
direct current electrode positive (DCEP) welding 396, 406
direct current (DC) magnetisation/demagnetisation 236, 239
discontinuities 324
dished end failure 335–7
dissection method 286, 295
dissimilar weld joints 35, 37–8, 55–73
316L(N) stainless steel/Alloy 800 joint 55, 56–61, 62
A48P2 carbon steel/316L(N) stainless steel joint 68–73
Alloy 800/9Cr–1Mo steel joint 55, 61–8
creep 181–2
failure mechanisms 319–20
strength mismatch 195
dissolution 380–1
distortion 277
double cantilever beam (DCB) specimens 522, 531–2
double vee welds 244, 248
double wall penetration radiography 252–4, 255
double image radiography 254, 255
single image radiography 253–4, 255
dragline booms, mining 144–7
drop-weight testing 187, 197, 198, 199, 325
ductile-brittle transition 186–7
ductile fracture toughness 61, 62, 66–7
ductile striations 375, 376, 385, 386
ductility
A48P2 carbon steel/316L(N) stainless steel joint 69, 70
free-bend test for 265–6
rupture ductilities of austenitic stainless steel welds 170, 171, 172, 173
duplex stainless steels (DSS) 13–15, 223–4, 353, 354, 355
SCC of weldments 542
superduplex stainless steel welds *see* superduplex stainless steel welds
dynamic fracture properties 187–92
weld characterisation 197–205
irradiation effects 204–5
dynamic hardness 260

eccentricity 525–6
eddy current imaging (ECI) technique 327
eddy current testing (ECT) 239–42, 326–7
standards 309

effective chromium content 505
effective primary stress 113–14
effective secondary stress 111–12
effective stress intensity 189–90
efficiency index 114
elastic cycling 110
elastic plastic fracture mechanics (EPFM) 187
elastic stress analysis 105–7
electrochemical potential (ECP) 362–3
  corrosion fatigue cracking of superduplex stainless steel welds 378–87
    high ECP 378–81
    negative imposed ECP 381–7
electrochemical potentiokinetic reactivation (EPR) technique 503
electrodes 226–7
  special purpose electrodes 73–8, 79
electron beam welding (EBW) 394
embrittlement
  ferritic stainless steels 6–8
  hydrogen embrittlement *see* hydrogen embrittlement
  irradiation embrittlement 186, 204–5
  temper embrittlement 6
embrittlement index (EI) 422
end plug welding 119–22, 300–1
endoscope 232
energy beam welding methods 314, 394
environment-assisted cracking 534–45
  high temperature corrosion 535–9
  MIC of stainless steel weldments in the marine environment 540–3
environmental effects 285, 131
  superduplex stainless steel welds 366–87
    benign environment 372–8
    seawater under high ECP 378–81
    seawater under negative imposed ECP 381–7
erosion corrosion 482
etching test for macro-assessment 271
eutectic melting 22–3
extensometer (strain gauge) 264, 265

F (ferrite) solidification mode 20
  susceptibility to solidification cracking 21
FA (ferrite–austenite) solidification mode 19–20
  resistance to solidification cracking 21
failure analysis
  high temperature corrosion and 537–9
  'oxide dating' and 538
  stages in 328–30
failure analysis report 330
failure assessment diagrams (FADs) 187, 195
failures 314–52
  case studies in failure investigation 328–51
    ball valve 337–40
    bellow sealed valve 340–2
    condenser tube 330–3
    conical inlet 347–9
    pipe fittings 344–7
    pipeline in fire-fighting system 342–4
    pipeline reducer 333–5
    stainless steel dished end 335–7
    stainless steel tubes under insulation 349–51
  defects due to design, fabrication and service 316–17
  design problems and 127–33
  in fast breeder reactors 96–7
  general failure mechanisms relating to weldments 317
  major failure mechanisms 317–22
    Cr–Mo steels 318–20
    low alloy carbon steels 317–18
    sensitisation in stainless steel 321–2
    stainless steels 320–1
  reducing failures in weldments 322–8
    choice of welding processes, parameters and consumables 323
    design 322–3
    plant operational practices 328
    quality assurance and quality control 324–8
    welding process optimisation 323–4
fast breeder reactors 96–7, 182

fuel pin end plug weld 119–22
RCC-MR design rules *see* RCC-MR code
fatigue 153–4, 155–66
behaviour of stainless steel weldments 155–60, 161
creep–fatigue damage 112–13, 114, 115
creep–fatigue interaction 112, 113, 160–6
damage 112
see also fatigue design
fatigue failure at a weld paradigm 128–33
residual stress and fatigue strength 284
fatigue crack growth (FCG) 189–90
characterisation of welds 212–13
fatigue design 127–50
assessing the strength of welds 135
case studies 142–7
concepts and their influence 133–4
current approaches 135–42, 147–8
manufacturing codes 134–5
weld failures and design problems 127–33
fatigue tests 325–6
ferric sulphate–sulphuric acid test 273
ferrite number (FN) 75–6, 78
ferritic stainless steels 6–8, 154–5, 223, 354
corrosion of weldments 506–16
galvanic corrosion 510
general corrosion of weld metal 509
HAZ corrosion 508–9
high temperature corrosion 535–9
low cycle corrosion fatigue 512
microstructure 507–8
SCC 510–12
sensitisation 512–16
creep rupture strength of weld joint 174–81
fatigue design of rail wagons 142–4
ferritic/austenitic dissimilar weld joints 181–2, 319–20
ferritic/ferritic dissimilar weld joints 181
see also chromium–molybdenum (Cr–Mo) ferritic steels
ferromanganese particles 487
fertiliser plant condenser tube 330–3
filiform corrosion 482
fillet welds 252, 254
fine-grain HAZ (FGHAZ) 442–3, 507–8, 509
finite element analysis 123–5
fire-fighting system pipeline failure 342–4
fitness-for-purpose (FFP) approach 229–30
fitness-for-purpose codes and residual stresses 465–8, 469
flaws in welding *see* defects
flexible fibre-optic borescope (flexiscope) 232
fluorescent penetrants 233, 234
fracture properties 185–221
damage-tolerant design 187
dynamic properties 187–92
weld characterisation 197–205
importance of 185–6
materials qualification 186–7
metallurgical inhomogeneities 192–3
quasi-static properties 187–92
fracture toughness 205–12
residual stresses 195–7
strength mismatch 193–5, 196–7, 202–4, 210–12
subcritical crack growth 189–92
weld characterisation 212–15
fracture surface
examination 329–30
preservation 329
fracture toughness 186, 187–8, 325, 522
ductile 61, 62, 66–7
dynamic and strength mismatch 202–4
quasi-static 204–12
superduplex stainless steels 361, 376–8
free-bend test 265–6
fretting corrosion 483
fuel pin end plug weld 119–22, 300–1
fusion, lack of 246, 441
fusion reactors 182
fusion welds 315–16
radiography 252–5

fusion zone 272, 478
solidification cracking 17–21
preventing 24–8
fuzzy logic 299

galvanic corrosion 479, 510
gamma rays 245–6, 247–9
see also radiography
gas metal arc welding (GMAW) 30
gas tungsten arc welding (GTAW) 30, 394–5
hardfacing with Colmonoy 78–9
superduplex stainless steel welds 356, 358, 361, 366–8
toughness of Cr–Mo ferritic steels 51–5
general corrosion 479, 509
girth welds *see* cellulosic girth welds
global heat treatments 446
grade 91 weld metal 47–55
hydrogen-assisted cracking studies 48–51
impact toughness 53–5
microstructure and hardness 51–3
grain boundary liquation 21–2, 23
grain growth 27–8, 356, 357
grain refinement techniques 447–55
grinding 419
guided-bend test 267–8, 325

half-bead technique 448, 451
hardening behaviour 110, 111
hardfacing 35, 38–9, 78–92
metallurgical and ageing behaviour of hardface deposits 89–92
selection of hardfacing process and hardfacing alloy type 81–8
hardness 60
Cr–Mo ferritic steels 51–3
creep behaviour of ferritic steel 176, 177
dissimilar weld joints 60, 63–4
hardfacing with Colmonoy alloys 80, 82, 84–8
hardface deposits on austenitic stainless steel 89–92
TBW technique and PWHT 453–4
hardness testing 259–64
Brinell hardness 260, 261–2
indentation hardness 260–3
Knoop hardness 262–3
micro-hardness testing 263
rebound hardness 260
Rockwell hardness 260, 261
scratch hardness 260
standards 311–12
Vickers hardness 260, 262–3
of welds and HAZ 263–4
Hazelwood power station steam drums 452
heat-affected zone (HAZ) 223, 272, 316, 439, 442–3, 478, 479
coarse-grain HAZ 442, 443, 507, 509
corrosion of austenitic stainless steels 501–6
corrosion of ferritic steel weldments
HAZ corrosion 508–9
microstructure of HAZ 507–8
ferritic steel weld joints 174, 175
width 180
fine-grain HAZ 442–3, 507–8, 509
flaws in and FADs 195
hardness testing 263–4
intercritical HAZ 443, 508, 509
liquation cracking 21–3
prevention 28–9
tempering and grain refinement without PWHT 447–55
heat exchangers 105
heat input
corrosion of austenitic stainless steels 496–8
hollow bead defect 399–400
prevention of cracking 26–7, 29, 30
solidification cracking 26–7, 411
helium leak testing 256–8
high carbon steels 223
high energy beam (HEB) welding 314, 394
high temperature corrosion 535–9
life assessment and failure analysis 537–9
microstructural degradation and cracking 536–7
research opportunities 539
high temperature embrittlement 8
high temperature properties 438–9
hold-time tests 162–5
hole-drilling strain gauge technique 287–8, 295

hollow bead (HB) defect 396–406, 428–9, 430
  characteristics 398–9
  effect of processing conditions 399–402
  mechanisms 402–5
  prevention 406
hot cracking *see* liquation cracking; solidification cracking
hot pass remelting 419
hot spot stresses 138–9
HSE Steel 2001/015 report 141
Huey test 273–4
Hui–Riedel zone 191
humid sulphur dioxide tests 276
Hutchinson–Rice–Rosengren (HRR) zone 191
hydrogen
  atomic hydrogen adsorption 386–7
  effect on cracking in modified Cr–Mo steels 49, 50, 318–19
  hollow bead defect 405
  solidification cracking 418
hydrogen-assisted cracking (HAC) 24, 439–40, 516
  cellulosic girth welds 421–30
    characteristics 421–3
    effect of processing conditions 423
    mechanisms 423–5
    prevention 425–8
  Cr–Mo ferritic steels 318–19
    modified 47–51
  low alloy carbon steels 318
  prevention 30
  test 276
hydrogen embrittlement (HE) 423–4, 484–5
  superduplex stainless steel welds 364–6
    corrosion fatigue cracking 383–7
hydrogen stress cracking (HSC) 511–12
hypothetical defect approach 142, 148

illuminator luminance 251
image quality indicators (IQIs) 250
imaging techniques 327
immersion tests 271–2
immersion ultrasonic testing 243
impact tests 269–70
  CVN test 186, 187, 197–9, 325, 527
impact toughness
  Cr–Mo ferritic steels 53–5
  dissimilar weld joints 69–70, 71
impingement corrosion 482
impurities
  liquation cracking 23
  solidification cracking 20–1, 42–3, 44
    prevention 25–6
in-service inspection (ISI) programme 328
inclusions
  non-metallic 425, 486–7
  slag 159, 161, 246, 440, 487
indentation hardness 260–3
induction heat stress improvement 506
inelastic stress and strain analysis 107–13
inspection, levels of 134–5
insulation 349–51
intelligent welding process 298–300
intercritical HAZ (ICHAZ) 443, 508, 509
intergranular corrosion (IGC) 321–2, 481–2
  austenitic stainless steel 502–3
  test 273–4
internal flaws 484
inter-pass temperature control 445
inverted metallographic microscope 259
iron–carbon phase diagram 413–15
iron–nickel–chromium ternary system 10–11
irradiation embrittlement 186, 204–5
irreversible traps 424–5
Izod test piece 270

J–R curves 187, 200–1, 208–10, 211
joint efficiencies 100–2

keyhole welding 394–5
  hollow bead defect 403–5
knife line attack 322
Knoop hardness test 262–3

Larsen–Miller parametric approach 89–90, 91
laser beam welding (LBW) 394
laser peening 489
last pass heat sink welding 505
lattice spacing 462–5
leak testing 255–8
LEEB hardness scale 260

life assessment 537–9
life prediction 118–19, 120–2
linear elastic fracture mechanics (LEFM) 187, 526
liquation cracking 21–3
  prevention 28–9
  weldability of austenitic stainless steels 39–47
liquid penetrant testing 232–4, 326
  standards 310
local progressive heat treatments 446
local uniform heat treatments 446
longitudinal residual stresses 466–73
longitudinal Varestraint test 39–42
low alloy carbon steels 223
  failure mechanisms 317–18
low cycle fatigue (LCF) 155–60, 161
low temperature sensitisation (LTC) 502

macro-residual stresses 279–80
magnetic Barkhausen noise (MBN) 291–4, 327–8
  case study for tube to tube sheet weld joints 292–4
magnetic particle testing (MPT) 235–9, 326
  standards 309
magnetisation 235–6
magnetomechanical acoustic emission (MAE) 291–2, 327–8
manganese 504
  effect on weld cracks 434–5
manufacturing codes 134–5, 302
  see also ASME Boiler and Pressure Vessel Code; RCC–MR code
marine environments 540–3
  corrosion fatigue cracking of superduplex stainless steel welds 371–2, 378–87
martensite 434, 443
martensitic stainless steels 3–6, 223, 354
  precipitation hardened 15, 16, 17
master curves 188, 189
master tempering curves 5–6
materials qualification 186–7
maximum crack length (MCL) 39
maximum likelihood (MML) estimation procedure 206–7
mechanical methods for residual stresses 286
mechanical properties
  dissimilar metal welding 60–1, 62, 64–8, 69–70, 71
  superduplex stainless steel welds 359–60
mechanical stress improvement 506
metallography 258–9
  preparing samples 259
  standards 311
microbiologically influenced corrosion (MIC) 486
  stainless steel weldments in the marine environment 540–3
    biofilms and MIC 540–1
    influences on MIC 543
    SCC and MIC 541–2
microdensitometer 251–2
micro–hardness testing 263
micro-residual stresses 279–80
microscope 231
micro-segregation 192–3, 491–6
minimum detectable leak 256
minimum of three equivalent (MOTE) concept 206, 207
mining dragline booms 144–7
mismatch
  creep properties and weld design 122–5
  strength mismatch 193–5, 196–7, 202–4, 210–12
mixed zone *see* fusion zone
modified Cr–Mo electrode 76–7, 79
modified Cr–Mo ferritic steels
  creep behaviour of 9Cr–1Mo weld joints 179–81
  joint with Alloy 800 55, 61–8
  weldability 36–7, 47–55
    effect of composition and PWHT on toughness of SMAW metal 51–5
    hydrogen-assisted cracking studies 48–51
modified E316-15 electrodes 73–5
  delta-ferrite content in 316L(N) stainless steel welds 75–6, 77, 78
Mohs scale of hardness 260
molybdenum
  Cr–Mo ferritic steels s*ee* chromium–

molybdenum (Cr–Mo) ferritic steels
sensitisation of austenitic stainless steels 504
monitoring, on-line 294–302

narrow gap welding 298–9
National Board Inspection Code (NBIC) 453
Neuber's rule 108, 109
neutron diffraction (ND) 288–9, 295
residual stresses in weld repairs 460–1, 465, 466
nick-break test 268–9
nickel 10
Cr_{eq}/Ni_{eq} ratio 13, 15, 18–19, 25–6, 42–4, 320–1
iron–nickel–chromium ternary system 10–11
nickel-based alloys 244
nickel-based welding (cold welding) 455
nitric acid 273–4
nitrogen
austenitic stainless steels
effect on hot cracking 44–6
influence on creep properties 170–4
sensitisation 322, 504
superduplex stainless steel welds 357–9
non-destructive testing and evaluation (NDT/NDE) 97, 230–58, 329
ASTM material specifications with NDT requirements 310
eddy current testing 239–42, 309, 326–7
and FFP approach 229–30
leak testing 255–8
liquid penetrant inspection 232–4, 310, 326
magnetic particle testing 235–9, 309, 326
radiographic testing 245–55, 307–8, 327
reducing failures in weldments 326–8
advanced NDT methods 327–8
standards 307–10
ultrasonic testing 134–5, 242–5, 246, 247, 248, 308–9, 327
visual inspection 134, 230–2, 326
non-homogeneous scaling 538–9
non-metallic inclusions 425, 486–7
normalised residual stress (NRS) 468–72
notch sensitivity 8
nozzle welds 103–4, 248
nuclear power plants
design codes for pressure vessels 102–13
design of welds with crack-like defects 115–22
fast breeder reactors *see* fast breeder reactors
reactor pressure vessel weld repair 452
weld monitoring of fuel element components 300–2, 303, 304

O'Donnel–Porowski Diagram (OPD) 108, 109
on-line weld monitoring 294–302
acoustic emission technique 297, 298–9, 300–2
intelligent welding 298–300
nuclear fuel element components 300–2, 303, 304
thermography 296–7, 298–9
operating conditions 316–17
operating practices 328
optical instruments 231–2
oxalic acid 273
oxidation 485–6
'oxide dating' 538
oxide scales 535–9
non-homogeneous scaling 538–9
scale thickness measurements 537–8

Pacary diagram 26
parent material cracks 439–40
parent material zone 442, 443
partially melted zone (PMZ) 21–2, 272
partitioning coefficient 416
passivation testing 277
passive film 223
peak stress approach 137–8, 147
penetrants 233
penetration, lack of 441
penetration time 234
performance qualification 228

peritectic reaction 413–15
phase transformation 438
  residual stresses due to 282–3
    superimposition with other residual stresses 283–4
phosphorus
  liquation cracking 23
  solidification cracking 20–1, 42–3, 44, 416, 417
    prevention 25–6
pipe fittings failure 344–7
pipeline reducer 333–5
pipelines
  cellulosic girth welds *see* cellulosic girth welds
  construction 396–8
    sequence of operations 396, 397
  failure in fire-fighting system 342–4
pipes, fusion welds in 252–5
pitting corrosion 480
  austenitic stainless steels 491, 492, 496–8, 499–500, 501
  critical pitting potential 496–8, 499–500, 501
  critical pitting temperature (CPT) tests 363
  superduplex stainless steel welds 362–4
  test 275–6
pitting resistance equivalent (PRE) 363
planar defects 317
plant operating practices 328
plasma arc welding (PAW) 394, 395
plasma transferred-arc welding (PTAW) 79, 80
  Colmonoy hardfacing alloys 81–8
plastic zone 467
polarity 53–5
polythionic acid 274, 275
porosities 159, 161, 440, 487
post–emulsifiable fluorescent penetrant system 234
post-heating 447
post-welding heat treatment (PWHT) 444, 446–7
  Cr–Mo ferritic steels
    Alloy 800/Cr–Mo ferritic steel joint 61–8
    cracking 319
    toughness 51–5
  MBN analysis for residual stress measurements 293–4
  prevention of SCC 488–9
  PHWT cracking *see* reheat cracking
  sensitisation of ferritic steels 515–16
potentiostatic etching technique 514, 515
precipitation hardened stainless steels 15–17, 224, 354
pre-cracked Charpy V (PCCV) testing 189, 200–4
preheating 30, 445
  critical preheat temperature 49, 50
  prevention of HAC 427–8
preliminary inspection 329
pressure vessels
  fracture mechanics 188–9
  reactor pressure vessel weld repair 452
  weld design rules 97–113
    conventional 97–102
    nuclear power plants 102–13
primary bending stress intensity 106
primary membrane stress intensity 106
primary solidification mode 18–21
primary stresses 196
  effective primary stresses 113–14
  weld design for nuclear power plant pressure vessels 102, 105–7
probabilistic approach 142
procedure qualification 227–8
prod magnetisation 236–8
pulse echo technique 243, 290
PVR test 46

qualification 224–8
quality assurance 224–5, 324–8
quality control 131, 324–8
quasi–static fracture properties 187–92
  fracture toughness 205–12
quenching residual stresses 281–2
  superimposition with other residual stresses 283–4

R6 procedure 465–72, 473
radiographic testing 245–55, 327
  applications 252–5
  defect evaluation 251–2
  film viewing 251

geometric factors 246–7
industrial X-ray films 250–1
radiographic sensitivity 250
sources 247–9
standards 307–8
radioisotope camera 249
rail wagons 142–4
ratcheting 110
RCC-MR code 113–15
creep rupture strength for austenitic stainless steel welds 170–2
design of welds with crack–like defects 115–22
real leaks 256
rebound hardness 260
reduction in area 61, 62, 65, 67, 70
reheat cracking 23–4
prevention 29–30
relative distance 211–12
relaxation of stresses 118, 162, 163, 286
repair welding 433–58, 516, 517
guidelines 444
heat treatment 445–7
measurement of residual stresses in weld repairs 459–74
tempering and grain refinement of the HAZ without PWHT 447–55
weld cracks 434–40
weld defects 434–41
welding process microstructures 441–3
replacement costs 444
residual stresses 130–1, 195–7, 277–94, 323, 440
dissimilar weld joint 70–3
effects on corrosion properties 488–9
effects on performance 284–5
factors affecting 280–1
measurement 285–94, 295
selection of method 294, 295
standards 313
measurement in weld repairs 459–74
comparison with FFP codes 465–72, 473
distribution of stresses 469–72
experimental procedure 461–5, 466
welding procedure 462, 463
mechanisms of generation 277–9
sources 281–4
superduplex stainless steel welds 360, 369, 370
types of 279–80
resistance spot welding 299–300
restraint forces 29
hydrogen cracking 30, 427–8
solidification cracking 26–7, 411–12
reversible traps 424
Robinson's time fraction rule 111
robust design guidelines 104–5
robust welding technologies 34–95
development of special purpose electrodes 73–8, 79
dissimilar metal welding 35, 37–8, 55–73
hardfacing of austenitic stainless steel components 35, 38–9, 78–92
weldability of austenitic stainless steels 34, 35–6, 39–47
weldability of modified Cr–Mo ferritic steels 36–7, 47–55
Rockwell hardness test 260, 261
root pass pipeline girth welds 397–8
rupture strength
austenitic stainless steel welds 166–70
influence of nitrogen 170–2, 173–4
creep rupture strength of ferritic steel weld joint 174–81

S–N curves 387
fatigue design approach 133–4, 137–8, 147
safety factor approach 135–6, 147
scale thickness measurements 537–8
scanning electron microscope (SEM) 259
Schaeffler diagram 12–13
scratch hardness 260
seawater 362
condition and ECPs of stainless steels 363
corrosion fatigue cracking of superduplex stainless steel welds 371–2
seawater under high ECP 378–81
seawater under negative imposed ECP 381–7
see also marine environments
secondary phases 499–501
sigma phase 10–11, 173, 193, 499–501

secondary stresses 196
creep relaxation 118
RCC–MR code 113–15
weld design for nuclear power plant pressure vessels 102, 107–13
selective leaching 480
semi-austenitic precipitation hardened stainless steels 15, 16, 17
semi-destructive testing 258–9
standards 311
sensitisation 321–2
austenitic stainless steels 495, 496
HAZ 501–5, 506
ferritic steel weldments 512–16
service requirements 316–17
shakedown 110
shielded metal arc welding (SMAW) 30, 393, 395
cellulosic *see* cellulosic girth welds
Cr–Mo ferritic steels 51–5
superduplex stainless steel welds 356, 358, 361, 366–8
shrinkage residual stresses 281, 282
superimposition with other residual stresses 283–4
σ_d approach 115–22
benchmark solution 115–19
life prediction of fast breeder reactor fuel pin end plug weld 119–22
sigma (σ) phase 10–11, 173, 193, 499–501
sigma (σ) phase embrittlement 6
Sigmajig test 46
silicon 504
content and hollow bead defect 400–1
simulation 330
single V butt welds 244, 247, 248
single wall penetration radiography 252, 255
skirt-supported vessels 104, 105
slag 403, 405
inclusions 159, 161, 246, 440, 487
stringers 398
slip softening model 423–4
socket welds 104
solidification
corrosion of austenitic stainless steel joints 490–6
modes 18–21
prediction of solidification mode in 316L(N) stainless steel welds 75–6, 77
solidification cracking 17–21, 436–8
cellulosic girth welds 406–21, 428–30
characteristics 406–7, 408
effect of processing conditions 407–12
mechanisms 412–18
prevention 24–8, 419–21
weldability of austenitic stainless steels 39–47
solution annealing treatment 506
solvent-removable fluorescent penetrant system 234
sour service corrosion testing 276
spacer pad welding 301–2, 303
spatter, excessive 441
special purpose electrodes 73–8
delta-ferrite content in 316L(N) stainless steel welds 75–6, 77, 78
modified 9Cr–1Mo electrode 76–7, 79
specifications 304
ASTM material specifications with NDT requirements 310
specimen dimensions 280
speed, welding 399–400, 409–10
spiral notch torsion test (SNTT) 527
spray test 257–8
stainless steels 3–33, 223
cracking mechanisms in welds 17–24
hydration cracking 24
liquation cracking 21–3
reheat cracking 23–4
solidification cracking 17–21
creep–fatigue interaction behaviour of welds and weld joints 160–6
failure of dished end 335–7
failure mechanisms 320–1
failure of tubes under insulation 349–51
fatigue behaviour of weldments 155–60, 161
microbiologically influenced corrosion in the marine environment 540–3
nitrogen steels 322
prevention of weld cracking 24–30
hydrogen cracking 30

liquation cracking 28–9
reheat cracking 29–30
solidification cracking 24–8
sensitisation *see* sensitisation
types of 3–17
see also under individual types
standards 302–4
NDT of welds 307–10
for semi-destructive and destructive techniques 311–13
star crater cracks 437
steam generators 182
Stellite 38–9
stovepipe welding 396, 419
strain
preferential creep strain accumulation 176–7
secondary stress and strain limits in ASME section III division 1 code 107–13
weldability of modified Cr–Mo ferritic steels 49, 50
strain age cracking *see* reheat cracking
strain concentration factor (SNCF) 139
strain gauge rosettes 287–8
strain hardening 360
Strauss test 274
Streicher test 273
strength mismatch 193–5, 196–7, 202–4, 210–12
stress
around crack tip 190–1
concentration at welds 130
elastic stress analysis 105–7
inelastic stress and strain analysis 107–13
primary stresses *see* primary stresses
secondary stresses *see* secondary stresses
solidification cracking 411–12
stress concentration factor (SCF) 138–9
stress corrosion cracking (SCC) 483–4, 521–33
austenitic stainless steels 491–5, 498, 500
CNT testing 524–8
determination of threshold stress intensity for SCC 528–30
of welds 530–2
ferritic steel weldments 510–12
residual stresses and 488–9
stainless steel weldments in marine environment 540–3
MIC and 541–2
SCC of weldments of duplex stainless steels 542
test 274–5
and threshold stress intensity for SCC 521–4
stress intensity
allowable 106–7
effective 189–90
stress intensity factor 116–17, 187, 198, 199, 522
determination using CNT testing 524–8
allowance for eccentricity 525–6
validity requirements 526–8
threshold stress intensity for SCC 521–4
determination using CNT testing 528–32
stress relaxation 118, 162, 163, 286
stress relieving heat treatment 447
Colmonoy hardfacing alloys 81–2, 84, 88
stress–to–rupture curves 112, 114
stretch zone height (SZH) 200
stringer welding 460, 462, 463, 469–73
structural steel code 140–1
subcritical crack growth 189–92
characterisation of welds 212–15
subcritical HAZ 508
sulphate-reducing bacteria (SRB) 541
sulphide inclusions 486–7
sulphide SSC (SSCC) test 275
sulphur 434–5
hollow bead defect 401
liquation cracking 23
solidification cracking 20–1, 42–3, 44, 416, 417
prevention 25–6
sulphur dioxide 276
sulphuric acid 274
superduplex stainless steel welds 353–92
corrosion fatigue cracking of welds 366–72
corrosion resistance 361–4

crack propagation 372
in a benign environment 372–8
in seawater under high ECP 378–81
in seawater under negative imposed ECP 381–7
future trends 387
hydrogen embrittlement 364–6
microstructure 354–61
toughness 361, 376–8
supervisor visual inspection 134
surface inspection 134
Suutala diagram 25–6
synthetic aperture focusing technique (SAFT) 327

T-welds 248
temper bead welding (TBW)
residual stresses in weld repairs 460, 462, 463, 464, 469–73
tempering and grain refinement of HAZ 448, 450–5
temper embrittlement 6
temperature
brittleness transition temperature 198–200
BTR 39, 42, 43, 46–7
critical preheat temperature 49, 50
fatigue life of stainless steels 165–6
high temperature corrosion 535–9
high temperature embrittlement 8
high temperature properties 438–9
tempering
martensitic stainless steels 5–6
techniques without PWHT 447–55
tensile loading 284–5
tensile strains 29, 418
tensile testing 135, 264–5, 325
dissimilar metal welding 60–1, 62, 64–6, 67–8, 69, 70, 71
tension hold tests 162–5
testing and evaluation 222–313
corrosion 271–7
destructive testing 264–71
hardness testing 259–64, 311–12
intelligent welding 298
measurement of residual stresses 277–94, 295
non–destructive tests 230–58
on–line weld monitoring 294–302, 303, 304
quality assurance and qualification 224–8
semi-destructive testing 258–9, 311
specifications 304, 310
standards 302–4, 307–10, 311–13
weld imperfections and importance of their evaluation 229–30
welding codes 302
thermal cycle effects 130
thermal demagnetisation 238–9
thermal history 434
thermography 296–7, 298–9
thickness
estimation in ASME section VIII division 1 code 99–100
scale thickness measurements 537–8
three-point bending (3PB) 527
threshold stress intensity for SCC 521–4
determination using CNT testing 528–30
CNT testing of welds 530–2
time of diffraction (TOFD) technique 327
titanium 44–6
toe cracks 436
total crack length (TCL) 39, 46–7
toughness *see* fracture toughness; impact toughness
tramp elements *see* impurities
transformation residual stresses 282–3, 438
superimposition with other residual stresses 283–4
trans–Varestraint test 39–42
transverse residual stresses 466–73
trap theory 424–5
traverse cracks 436
trimetallic transition joints 35, 37–8, 55–73, 182, 320
316L(N) stainless steel/Alloy 800 joint 55, 56–61, 62
A48P2 carbon steel/316L(N) stainless steel joint 68–73
Alloy 800/9Cr–1Mo steel joint 55, 61–8
tube to tube sheet weld joints 292–4
tungsten inert gas (TIG) welding 80, 81–8

tunnel pore defects 403–4
two-layer approach 447–55

ultimate tensile strength (UTS) 359–60
  dissimilar metal welding 60–1, 62, 64, 65, 67, 70, 71
ultrasonic methods for residual stress 289–91, 295
ultrasonic testing 134–5, 242–5, 246, 247, 248, 327
  standards 308–9
under-bead cracks 436, 439
undercuts 441
uniform corrosion 479, 509
University of Tennesse (UT)–modified hydrogen sensitivity test 47–9
unmixed zone 272, 478–9

validity limits 526–8
Varestraint tests 39–44, 46–7
vertical cracks 436, 437–8
Vickers hardness test 260, 262–3
virtual leaks 256
visual inspection 134, 230–2, 326
volumetric defects 317
volumetric inspection 134–5

'wagon tracks' 398
waste heat boiler conical inlet 347–9
water washable fluorescent system 234
Weibull plots 201, 203
weld angle 124, 125
weld bead shape 27–8, 410–11
weld categorisation 98–9, 103
weld classification approach 140–1, 147
weld configurations
  ASME section III division 1 code 103–4, 105
  ASME section VIII division 1 code 99, 100, 101
weld design *see* design
weld metal cracks 436–9
weld pool shape 27–8, 410–11
weld repairs *see* repair welds
weld strength reduction factors 115
weldability testing 324
welder performance qualification 228
welding consumable qualification 225–7
welding consumables 323
welding current 399–400, 402–3, 406
welding heat treatment 445–7
welding inserts 488
welding procedure qualification 227–8
welding processes 315–17
  processing conditions 435
    and hollow bead defect 399–402
    and hydrogen–assisted cracking 30, 49–51, 423
    and solidification cracking 407–12
  reducing failures in weldments
    choice of process 323
    process optimisation 323–4
  and residual stresses 281
welding sequence 281
welding speed 399–400, 409–10
welding zone 441–2
WIC test 426–8, 429–30
WRC diagram 12–13
  control of solidification cracking 24–5

X-radiography 245–6, 247, 327
  industrial X-ray films 250–1
  see also radiography
X-ray diffraction (XRD) 327
  measurement of residual stresses 288–9, 295
X-ray intensity profiles 82, 84, 85

Y-groove test 46
yield strength 64, 65, 70, 71, 359–60
yield zone 467
yoke magnetisation/demagnetisation 236–8, 239

zinc 362–3
zones in a weld 271, 272, 441–3, 478–9